20030205083

AD-A208 880

GC-TR-88-1639

VOLUME I

RESEARCH AND DEVELOPMENT IN SUPPORT OF THE SURFACE CHEMISTRY BRANCH

GEO-CENTERS, INC

89 6 06 066

GC-TR-88-1639

VOLUME I

RESEARCH AND DEVELOPMENT

IN SUPPORT OF THE

SURFACE CHEMISTRY BRANCH

FINAL REPORT

PREPARED FOR
NAVAL RESEARCH LABORATORY
4555 OVERLOOK DRIVE, S.W.
WASHINGTON, D.C. 20375-5000
UNDER CONTRACT NUMBER N00014-86-C-2096

PREPARED BY
GEO-CENTERS, INC.
7 WELLS AVENUE
NEWTON CENTRE, MA 02159

JUNE 1988

GEO-CENTERS, INC.

UNCLASSIFIED

SECURITY CLASSIFICATION OF THIS PAGE

REPORT DOCUMENTATION PAGE

1a. REPORT SECURITY CLASSIFICATION UNCLASSIFIED	1b. RESTRICTIVE MARKINGS
2a. SECURITY CLASSIFICATION AUTHORITY	3. DISTRIBUTION/AVAILABILITY OF REPORT Approved for public release; distribution unlimited.
2b. DECLASSIFICATION/DOWNGRADING SCHEDULE	
4. PERFORMING ORGANIZATION REPORT NUMBER(S) GC-TR-88-1639	5. MONITORING ORGANIZATION REPORT NUMBER(S)
6a. NAME OF PERFORMING ORGANIZATION GEO-CENTERS, INC. 6b. OFFICE SYMBOL (If applicable) Code 6170	7a. NAME OF MONITORING ORGANIZATION
6c. ADDRESS (City, State, and ZIP Code) 7 Wells Avenue Newton Centre, MA 02159	7b. ADDRESS (City, State, and ZIP Code)
8a. NAME OF FUNDING/SPONSORING ORGANIZATION Naval Research Laboratory 8b. OFFICE SYMBOL (If applicable) Code 6170	9. PROCUREMENT INSTRUMENT IDENTIFICATION NUMBER Contract Number N00014-86-C-2096
8c. ADDRESS (City, State, and ZIP Code) 4555 Overlook Avenue, S.W. Washington, DC 20375-5000	10. SOURCE OF FUNDING NUMBERS PROGRAM ELEMENT NO. / PROJECT NO. / TASK NO. / WORK UNIT ACCESSION NO.

11. TITLE (Include Security Classification)

Research and Development in Support of the Surface Chemistry Branch (U)

12. PERSONAL AUTHOR(S)
D. Ballantine

13a. TYPE OF REPORT	13b. TIME COVERED	14. DATE OF REPORT (Year, Month, Day)	15. PAGE COUNT
Final	FROM 12/85 TO 4/88	June 1988	750

16. SUPPLEMENTARY NOTATION

17. COSATI CODES		
FIELD	GROUP	SUB-GROUP

18. SUBJECT TERMS (Continue on reverse if necessary and identify by block number)
Surface analysis, surface modification and tribological characterization, chemical microsensors, air purification and detection, ~~electrochemical~~ (ES)

19. ABSTRACT (Continue on reverse if necessary and identify by block number)

GEO-CENTERS, INC. programs in support of the Naval Research Laboratory Surface Chemistry Branch of the Chemistry Division have addressed problems dealing with the properties of and chemistry occurring on/at surfaces and interfaces. Of particular interest to the Navy are the programs and advances described below:

Modified ceramic and metal surfaces demonstrated significant improvements in tribological characteristics such as friction and wear resistance. In addition to the characterization and analysis of these materials, a large materials database was compiled. This information will assist in identifying important factors affecting stress propagation and tribological performance, and will aid in the development of models. → over →

(Continued on back of sheet)

20. DISTRIBUTION/AVAILABILITY OF ABSTRACT ☒ UNCLASSIFIED/UNLIMITED ☐ SAME AS RPT. ☐ DTIC USERS	21. ABSTRACT SECURITY CLASSIFICATION UNCLASSIFIED
22a. NAME OF RESPONSIBLE INDIVIDUAL Dr. James S. Murday	22b. TELEPHONE (Include Area Code) (202) 767-3550 / 22c. OFFICE SYMBOL Code 6170

DD FORM 1473, 84 MAR — 83 APR edition may be used until exhausted. All other editions are obsolete.

SECURITY CLASSIFICATION OF THIS PAGE

UNCLASSIFIED

18. kinetics and interface chemistry.

19. In chemical microsensors, both SAWs and optical waveguides were evaluated with respect to sensitivity, selectivity, and reproducibility. Application of these sensors for the detection of specific vapors was demonstrated. A model based on solubility interaction effectively predicts SAW coating behavior. In the area of decontamination, various charcoal substrates were evaluated, and models were developed to predict adsorbent behavior and performance.

The effects of interfaces on electron transport were investigated. Instrumentation and software were developed to identify electron transport mechanisms in transition metal complexes. Such complexes will be used as catalysts in the oxidation/reduction of toxic dissolved gases.

Keywords →

TABLE OF CONTENTS

Section	Page
INTRODUCTION	1
I. SURFACE MODIFICATION AND ANALYSIS	4
A. Friction/Wear Characterization of Tribological Materials	4
1. Ti-Implanted Engineering SiC and Si_3N_4	5
2. Carbon and Boron Implanted Ti-6Al-4V	6
3. Other Accomplishments	7
B. Surface Analyses and Characterization	8
1. Tribological Materials/Superconducting Ceramics	8
2. Surface Modification/Manufacture of Electronic Devices	10
3. Radiation Hard Devices	12
4. Miscellaneous Program Efforts	16
II. DETECTION AND DECONTAMINATION	20
A. Microsensors and Chemical Vapor Detection	21
1. Optical Sensors	21
2. Automated Vapor Generation/Data Acquisition Apparatus	23
3. SAW Device/Coating Evaluation	24
B. Air Purification and Decontamination	32
1. Water on Activated Charcoal	33
2. Adsorption Isotherms for CW-Agents	34
3. Fixed-Bed Adsorptive Reactor	35

GEO-CENTERS, INC.

TABLE OF CONTENTS, cont'd

Section | Page

III. SOLUTION ELECTROCHEMISTRY 36
A. Intermodulation Interference Studies (LOCUS) . . . 36

B. Solution Electrochemistry 36
1. Data Acquisition/Control Software for CARY 2390 37
2. Electron Transfer in Transition Metal Complexes 38
3. Spectral Analysis of High-T Superconducting Ceramics 40

NMR Results 43

IV. TOXI-LAB STUDIES 67
A. Introduction 67

B. Results 68
1. Toxi-Lab A - Basic Drugs 70
2. Toxi-Lab B - Barbiturates 72
3. Benzodiazepines 72

C. Conclusions 74

APPENDIX A
APPENDIX B
APPENDIX C
APPENDIX D
APPENDIX E

INTRODUCTION

In support of Naval Research Laboratory (NRL) Contract Number N00014-86-C-2096, GEO-CENTERS has met all technical requirements and summarizes results in this report. During the period of performance, December 31, 1985 through April 30, 1988, work was carried out at the Naval Research Laboratory in the Chemistry Division and the Electronics Technology Division. The majority of this work has subsequently been the subject of numerous publications, reports and presentations at scientific meetings.

The individual research projects in which GEO-CENTERS' technical staff members have been involved under this contract can be organized into four general areas, which are described below. More detailed discussions relating to progress and accomplishments, as well as listings of relevant publications and presentations, are included in the body of this report.

(1) Surface Modification and Analysis. Work in the Chemistry Division centered on the modification of metal and ceramic materials to improve the tribological performance of these materials. Work performed in the Electronics Technology Division involved the analysis of modified materials and surfaces for use in electronic devices. In addition, GEO-CENTERS' personnel maintained the Chemistry Division Cameca Ion Microscope facility and performed numerous analyses in support of these programs.

(2) Detection and Decontamination. The majority of work has involved the development and evaluation of detector

technologies, including optical wave guide sensors and surface acoustic wave (SAW) devices. A vapor generation/data acquisition apparatus was constructed, and detailed data reduction software was developed and implemented, which significantly increased the research capabilities of the technical staff. In addition, SAW device coating responses were analyzed to elucidate vapor/coating interaction mechanisms. This information is useful in the selection and design of new coating materials for specific applications. In the area of decontamination, the use of carbon bed collectors was investigated. Models were developed to describe the adsorption behavior of activated charcoals and to identify the affect of changes in ambient conditions, such as relative humidity, on the adsorption of chemical vapors.

(3) Solution Electrochemistry. One area of particular interest is the development of electrochemically active transition metal complexes for the catalytic conversion/decomposition of dissolved gases, such as CO_2. In support of this effort, significant software developments made it possible to investigate the electron transport kinetics and mechanisms of a model system. Studies on transition metal complexes have produced information which will be useful in the production of future catalytic systems for use by the Navy. In conjunction with research personnel from LOCUS, a program to investigate intermodulation interference effects was carried out. The results of these studies are also discussed briefly, with supporting documentation included under separate cover.

(4) Toxi-Lab Studies. The Navy is currently investigating a number of methodologies which will provide rapid and accurate evaluation of urine samples for the major classes of drugs of

abuse. Although lacking somewhat in sensitivity to some analytical procedures, thin layer chromatography has proven to be extremely practical as a technique for screening a broad spectrum of drugs. As a part of supplementing the capabilities of the Navy to detect and quantify illicit drugs, thin layer chromatography was used to examine samples for the presence of these substances. The technique of choice involved the application of a commercially available product called TOXI-LAB, which is a two-system thin layer chromatographic screen for over 250 of commonly prescribed and often abused drugs. The choice of this product was made because of its relative low cost, speed, and ability to detect the large number of substances, in an effort to supplement the detection capabilities of the Navy Drug Screening Laboratory (NDSL) in Norfolk, VA. These investigations were not conducted to determine the efficacy of the technique, or the quality of this particular product.

I. SURFACE MODIFICATION AND ANALYSIS

A. Friction/Wear Characterization of Tribological Materials

Modified surfaces are currently being investigated by the Navy for a variety of applications. Of particular interest is the improved wear and friction properties of materials. GEO-CENTERS' technical personnel have been involved in both the preparation of modified surfaces and in the testing and evaluation of modified materials during the period of performance. Efforts in support of the NRL program have resulted in over five publications and/or presentations in these areas.

The work performed in support of this task involved the direct preparation, modification and testing of surfaces. Other work performed by GEO-CENTERS' personnel involving the analysis of modified surfaces using the Cameca Ion Microscope and other surface analytical techniques is described in detail at the end of this section.

Materials that have been tested to date include a variety of ceramics, such as silicon nitride (Si_3N_4), silicon carbide (SiC), and aluminum oxide (Al_2O_3), as well as silicon crystals, metals and metal alloys. Surfaces were modified by ion beam enhanced deposition (IBED), by ion implantation, and by the formation of surface layers by sputtering (TiN) or by crystal growth (SiC on Si). These materials were prepared by polishing and other appropriate techniques and were subsequently tested using a variety of methods. Typical testing included evaluation of hardness (crack propagation), toughness (indentation), stress, and relative wear resistance (friction/wear, stick-slip, and pin-on-disk).

These materials were implanted or modified at both elevated temperatures (900°C) and at room temperature. Implantation usually was performed until a high dosage level was achieved. The effects of these parameters on the material surface properties were then determined. Significant results of investigations on these materials will be discussed in detail below. Other significant accomplishments achieved during the period of performance will also be presented and discussed.

1. Ti-Implanted Engineered Si_3N_4 and SiC

Most research in the area of tribological properties of ceramic materials has focused on single crystal ceramics. Engineering ceramics, however, usually include more than one phase, such as glasses, sintering agents, or milling impurities, which affect the surface mechanical properties. Studies were undertaken at NRL to identify ion implantation treatments that would improve the surface mechanical properties of these materials when exposed to an oxidizing environment (1,2).

Titanium ions were implanted to a high dose (near 50 at. % peak concentration) at both room temperature and at 900°C. The resulting surfaces were then evaluated using Knoop and Vickers hardness testers. Implantation at room temperature resulted in softer surfaces, lowering indentation fracture toughness values for Si_3N_4 by 20%. While the resulting surfaces exhibited lower indentation fracture toughness, crack propagation was reduced due to the closing of cracks and pores in the surface microstructure. Hot implantation also reduces indentation toughness, but without the accompanying decrease in surface hardness. Both implanted and non-implanted surfaces became embrittled when exposed to high temperature under vacuum conditions. XPS studies indicate that this may be due to a depletion of subsurface oxygen.

These Si_3N_4 samples were further studied. Composition vs. depth profiles were obtained by RBS, a quantitative non-destructive depth profiling technique, and microstructures were examined by TEM and diffraction. Results indicate that Si concentration was considerably reduced at the Ti peak depth, but was enriched near the surface. These results were interpreted using a Si-Ti-N ternary phase diagram (3).

2. Carbon and Boron Implanted Ti-6Al-4V

Titanium and engineering alloys of Ti are known for their poor wear resistance. Improvement in the tribological properties of these materials has been observed as a result of N^+ ion implantation. Studies performed at NRL have focused on the use of two other interstitial implant species, boron and carbon (4).

The titanium boride and titanium carbide surfaces that were formed as a result of high dose B^+ and C^+ implantation were examined for wear resistance and other performance parameters. Results of surface analysis show that the implantation of Ti-6Al-4V with carbon or boron to a very high dose produces a thick implanted layer with nearly uniform carbon or boron distribution. High dosage C^+ implants produced a continuous TiC layer which exhibited the largest observed increase in wear resistance of the implants studied. This C^+ implant requires less than half the dose than that required for B^+. Even the B^+ implantation provided substantial improvement in wear resistance vs. untreated Ti-6Al-4V. In addition, the B^+ implantation process produced an amorphous matrix, which may be beneficial in situations where corrosion accelerates the wear process.

Included in Appendix A are copies of published papers that GEO-CENTERS contributed to during the period of performance of this contract.

3. Other Accomplishments

In addition to the preparation, testing and evaluation of sample materials, GEO-CENTERS' personnel have been involved in other support activities. One of the more significant tasks involves the development of a materials testing data base. This data base was produced using Super Calc-4 with the intention of organizing the large set of existing data into an easily manageable, logically ordered data base. This data base can be utilized for the rapid retrieval of data (from 1980 to the present) relating to specific material constants, such as Hertzian stress, or hardness/fracture information. Such a system will facilitate the interpretation of data and the generation of reports and publications. In addition to the data base, several spread sheets have been created for the organization and storage of data.

Another task in progress involves the use of XRF and Michelson Interferometry to determine the coating thickness of as-deposited and worn MoS_2 films. XRF data could be used to determine the relative percent of film to underlying substrate by examining the S+Mo(film)/Fe(substrate), Ni (film)/Fe(substrate), and Mo(film)/Fe(substrate) ratios. For the excitation wavelength (40 keV at .492 A) the depth of penetration of the X-rays is much greater than the film thickness. Therefore, the S+Mo/Fe and Mo/Fe ratios are directly proportional to film thickness. The constant of proportionality was determined from RBS data on MoS_2 films.

A comparison was made between worn and as-deposited MoS_2 films. XRF data indicated a difference between the two films of 1.1 um. A film thickness difference of 1.1 um was also calculated calculated using MI results. Thus, XRF is a plausible, non-destructive method for the rapid determination of MoS_2 film thicknesses.

B. Surface Analyses and Characterization

GEO-CENTERS' scientists have assisted in the research efforts of the Navy relating to surface modification and surface analysis. The results of efforts into the determination of tribological performance characteristics of modified and unmodified surfaces have been discussed in detail under the heading of friction and wear. Some additional analysis of tribological materials will be discussed here.

In addition to the analysis of tribological materials, there has been significant support for ongoing projects in the electronics Technology Division of NRL, as well as in the areas of high temperature superconducting ceramic materials. The results of these analyses will also be included in the following discussions.

1. Tribological Materials/Superconducting Ceramics

In addition to the sample preparation and testing already discussed, surface analytical techniques were applied to the characterization of these surfaces to determine the depth of species distribution. This information can be used to evaluate the effectiveness of ion implantation conditions. This data could also be correlated with microstructures and tribological performance to elucidate implantation/redistribution mechanisms, and the resulting wear characteristics of modified surfaces. Both modified and unmodified surfaces were studied. Materials of interest included ion-implanted iron and steel, stainless steel, implanted ceramics and chrome-plated nickel.

Other areas of interest to the Navy include high temperature superconducting ceramic materials. Current investigations involve the manufacture of ceramic materials composed of Y, Ba, Cu, and O. These materials were evaluated both as bulk pellets and as thin films deposited onto a Al_2O_3 substrate. Surface analytical techniques are useful in identifying relevant elemental composition and distributions which may affect superconductive properties of these materials.

Analyses were performed using the CAMECA IMS-300 SIMS instrument located in the NRL Chemistry Division. Results of these studies have been detailed in periodic reports. Representative titles are listed below. Copies of these reports are included in Appendix B.

- SIMS Analysis of Ti-Implanted Steel and Ceramics
- SIMS Depth Profiling of ^{13}C-Implanted Iron
- SIMS Depth Profiling and Imaging Analysis of Chrome-Plated Nickel Samples
- SIMS Depth Profiling of 304 Stainless Steel and Fe/C Steel
- SIMS Depth Profiling of ^{13}C, ^{14}N, and ^{15}N-Implanted Iron
- SIMS Analysis of High Temperature Superconducting Ceramics

2. Surface Modification/Manufacture of Electronic Devices

The Electronic Technologies Division of NRL (ETD - Code 6800) is involved in the evaluation of a variety of electronic devices, as well as in investigations of novel methods for the manufacture of these devices. In support of these efforts, GEO-CENTERS' scientists have performed numerous surface analyses using the CAMECA SIMS instrument, interferometry techniques, surface profilometry, and Scanning Auger Microscopy. In some cases, the sensitivity of the CAMECA IMS-300 was not sufficient for the analyses to be performed, and samples were sent to the US Army LABCOM at Ft. Monmouth. The LABCOM facility includes a CAMECA IMS-3f ion microanalyzer capable of performing imaging analyses.

Electronic devices usually consist of semiconductor materials whose surfaces have been modified either by ion-implantation, by the deposition of a doped semiconductor layer, or by deposition of a different material. Typical semiconductor substrates include GaAs, GaAlAs, InP, and InSb. Another substrate material of particular interest in electronic devices is Si.

Typical dopants used in the manufacture of these devices include Be and In. Ion-implantation was performed using As, Be, B, Mg, and N (in Si). Surface modification can be readily achieved using molecular beam epitaxy (MBE) for the deposition of thin layers of material on a substrate. Studies have been performed to evaluate the effectiveness of alternative methods in producing high quality electronic devices. Methods such as organometallic chemical vapor deposition (OM-CVD) or organometallic vapor phase epitaxy (OM-VPE) are potentially faster and cheaper than MBE.

Ion-implantation had been selected as an alternative method for the development of p^+/n junction diodes. The resulting p-layer, produced by Be implantation of GaAlAs, had to be shallow enough and highly doped enough for low sheet resistivity, and had to possess low leakage for photoconductivity. Suitable devices were manufactured and tested by NRL personnel in ETD. Surface analyses were performed by GEO-CENTERS' scientists to verify both the doping levels and layer thicknesses of the resulting devices.

A representative list of these and other studies is given below. Copies of internal reports relating to these studies are included as an Addenda to this report.

- SIMS Analysis of Be-Doped GaAs
- SIMS Analysis of Be Distribution in Thermally Annealed GaAlAs
- SIMS Analysis of Be Distribution in Be-Implanted GaAlAs
- SIMS Analysis of Be Distribution in as-Implanted GaAlAs
- SIMS Analysis of B-Implanted InP and B and As-Implanted Si
- SIMS Analysis of In-Doped GaAs
- Results of Imaging Analysis of InP Substrate by US Army LAB-COM, Ft. Monmouth
- SIMS Analysis of Mg Distribution in Mg-Implanted GaAs
- Determination of As Detection Limit in Si

- SIMS Analysis of SiC Films on Si
- SIMS Analysis of As Distributed in As-Implanted Si
- SIMS Analysis of Be Distribution in MBE Grown InSb Films
- SIMS Analysis of Chemically Etched GaAs Films on GaAlAs
- SIMS Analysis of N-Implanted Si Substrates
- Scanning Auger Imaging Analysis of As in InP
- SIMS Analysis of Boron Implanted Silicon
- SIMS Analysis of Be and Si Distribution in GaAs
- SIMS Analysis of Be Distribution in as Grown InSb Films

3. Radiation Hard Devices

Another application for modified surfaces is in the manufacture of "radiation hard" devices. The material of greatest interest is silicon grown on sapphire (SOS). The analytical technique used in the diagnostic evaluation of this material is the transmission electron microscope (TEM).

In the process of growing SOS films, crystal defects occur which affect the quality and characteristics of the resulting films. One such defect, called microtwinning, plays an important role in accommodating stresses that accompany the growth of SOS films. During the contract period, GEO-CENTERS' personnel have studied SOS films by TEM to determine micrctwin densities and morphologies in films grown by chemical vapor deposition (CVD) and by molecular beam epitaxy (MBE). In addition, the effects of annealing temperatures and growth temperatures on the quality of grown films were evaluated. Detailed discussions of the significant results of these investigations are included below.

a. Microtwin Morphology and Density for SOS. Despite the importance of microtwins in SOS growth, few investigations have addressed their actual morphology. Some previous studies have relied on TEM of cross-section TEM samples (XTEM). The XTEM geometry is useful for studying the silicon/sapphire interface, and for obtaining a qualitative estimate of defect density as a function of distance from the interface. It is difficult, however, to assess microtwin morphology in an XTEM sample because most microtwins imaged in these samples are artificially terminated by the sample preparation process. In other studies, plan view TEM (PVTEM) was used for determining microtwin density profiles in SOS, but density measurements were not associated with microtwin morphology. Work performed during the period of performance has focused on a quantitative determination of the morphology and volume fraction of microtwin defects, rather than simply on the number of defects per unit volume (1). The volume fraction is a particularly useful quantity for describing crystal perfection in SOS. By obtaining a geometric description of microtwins in a given sample, the volume fraction can be measured. Most of the details of microtwin morphology can be obtained from dark field (DF) images of PVTEM samples. In addition, stereo-imaging of PVTEM samples in DF can be used to provide details of microtwin morphology that are not always evident in a two-dimensional micrograph.

Several interesting observations were made as a result of these studies. The microtwin volume fraction does not appear to be greatest at the silicon/sapphire interface. Rather, the density is greatest about 100 A from the interface. While microtwin density does not drop significantly below the interface value for distances up to 1000 A, the volume of individual microtwins increases markedly over the first several hundred angstroms, increasing the volume fraction of these defects. Also, the PVTEM observations indicate that the microtwins are heavily faceted and grow from nucleation sites at the interface.

b. Structure of SOS Thin Films Grown by MBE. The microstructure of SOS films grown by CVD has been widely studied. These films are known to be extremely defective, with the predominant defect being microtwins. As-grown MBE SOS films appear to be superior to CVD SOS films, but little work has been performed addressing the nature of defects in the MBE-grown films. By applying TEM to the analysis of MBE films, GEO-CENTERS' personnel have studied these defects in MBE grown SOS films (2).

Sapphire substrates were subjected to annealing treatment at 900°C in ultra-high vacuum. Films of 150 A thick silicon were grown at both 750°C and at 900°C. On this second substrate, an additional 2500 A of silicon was grown at 750°C. At 900°C, the silicon films grew as islands with either the (001) or the (110) planes parallel to the (1012) plane. As is true for CVD-grown SOS, most of the silicon grows as (001) rather than as (110). By following the initial 150 A with 2500A grown at 750°C, a continuous (001) film was grown in which microtwins appeared to be the predominant defect. Twinning activity in the MBE-grown SOS follows substrate orientation in the same way as CVD-grown SOS.

c. Annealing Temperature Effects on SOS Films. Rapid thermal annealing (RA) has been shown to substantially improve the crystalline quality of as-grown CVD SOS. To understand this material improvement, the effects of maximum RA on crystalline quality of the silicon epilayer was studied (3). Dramatic improvements in crystalline quality occur even at the lowest RA studied (1160°C). At the highest annealing temperature (1320°C), crystalline quality at the surface is similar to that of bulk silicon. At these annealing temperatures, only a few microtwins extend toward the surface, and defect microstructure in the region of the silicon/sapphire interface is substantially reduced. Defect elimination can be explained in terms of the motion of the incoherent boundaries of the microtwins.

In other studies, the effect of pre-deposition substrate annealing was investigated for MBE-grown SOS films (4). Both the annealing temperature and the growth temperature were found to have a marked effect on the quality of MBE grown SOS. On substrates annealed at 900°C, (001) oriented silicon islands will grow at 900°C but not at a growth temperature of 750°C. At this lower temperature, the islands are randomly oriented and unsuitable as growth sites for good device material. When the substrate is annealed at 1450°C prior to growth, well oriented islands do grow at 750°C. This is significant since SOS grown at lower temperatures may show less damage due to thermal stresses that develop as the deposited film is brought down to room temperature. This problem is particularly great for SOS films because the thermal expansion coefficient for sapphire is twice that of silicon.

4. Miscellaneous Program Efforts

Additional studies performed in support of Navy programs include the analysis of Mg-flare powders for NWSC in Crane, Indiana. Problems had arisen from the fact that some samples of Mg-flare Powder were difficult to ignite and did not exhibit the desired combustion behavior, even though they satisfied current procurement specifications.

As a result of surface analyses performed by GEO-CENTERS' personnel, the cause of failure was determined. It is believed that failure was due to the formation of an excessively thick oxide or hydroxide coating which passivated the surface. The nature of this coating was identified using X-Ray Photoelectron Spectroscopy. Based on the results of these analyses, procurement specifications could be appropriately modified to avoid the purchase of "bad" Mg-flare powders.

Other efforts include the design and construction of a time-of-flight (TOF) SIMS instrument for use by NRL Chemistry Division personnel. The TOF SIMS has several advantages relative to the CAMECA IMS-300. Among these advantages are:

- higher sensitivity (nearly 4 orders of magnitude)
- higher mass range (potential detection of 5000 amu fragments)
- the ability to detect neutral as well as ionic species.

This instrument will significantly increase the analytical capabilities of the Chemistry Division. As of the end of the period of performance of this contract, the instrument was fully operational and being used for support of several research efforts.

a. Other Accomplishments. In collaboration with NBS, NRL scientists and GEO-CENTERS' personnel are in the process of calibrating and analyzing the electron optics of the Philips 430 TEM at NBS. They identified a vibration problem, which has since been remedied. Reduction of this vibration has improved the resolution of the instrument, and it is being evaluated for potential use in future investigations.

GEO-CENTERS' personnel have also been successful in adapting image-simulation programs for the electron microscope to run on the NRL Cray computer. These programs can be used in current and future efforts. Other current efforts include TEM studies on device materials grown via the silicon implanted oxygen (SIMOX) process.

REFERENCES

A. Friction and Wear

1. I.L. Singer, "Indentation Fracture and Near Surface Chemistry on Ti-Ion Implanted Engineering Si_3N_4 and SiC," Jan 1987.

2. I.L. Singer, "Surface Chemistry and Mechanical Behavior of Silicon Carbide and Silicon Nitride Implanted with Titanium to High Fluence and High Temperature," Surface Coat. technol. 33, 487 (1987).

3. I.L. Singer, R.G. Vardimann, C.R. Gossett, "Composition and Structure of Si_3N_4 Implanted with Ti^+ at 900°C," presented at MRS, Dec 1987.

4. R.N. Bolster, I.L. Singer, R.G. Vardimann, "Composition Studies and Wear Resistance of Ti-6Al-4V Implanted with Carbon and Boron to High Doses," <u>Surface Coat. Technol.</u> <u>33</u>, 469 (1987).

B. Surface Modification and Analysis

1. M.E. Twigg, E.D. Richmond, "Microtwin Morphology and Density for Silicon on Sapphire," submitted to J. Appl. Phys, Dec 1987.

2. M.E. Twigg, J.G. Pellegrino, E.D. Richmond, "The Structure of Silicon Thin Films Grown on Sapphire by MBE," presented at MRS Fall Meeting, Dec 1987.

3. E.D. Richmond, G. Campisi, M. Twigg, "Temperature Dependence of Rapid Thermal Annealing of Silicon on Sapphire," presented at MRS Fall Meeting, Dec 1987.

4. J. Pellegrino, M.E. Twigg, E.D. Richmond, "Substrate Annealing and the MBE Growth of Silicon on Sapphire," presented at MRS Fall Meeting, Dec 1987.

5. J. Zahavi, P. Pehrsson, G.J. Campisi, R.F. Greene, "UV-Laser-Induced Metal Deposition on Semiconductor and Metals from Electroplating Solution," (contributed), submitted.

6. B. Molnar, H.B. Dietrich, S. Hues, G. Kelner, R. Magno, "The Use of Co-Implantation to Achieve Shallow, Highly Doped p+ Be-Implanted AlGaAs Layers," presented at 14th Int'l Symp. on GaAs and Related Compds, Heraklio, Crete (Sept. 1987).

7. P.D. Ehni, S.M. Hues, I.L. Singer, "Nitrogen and Carbon Solute Redistribution During High Fluence Nitrogen Implantation into Iron," presented at MRS Fall Meeting, Dec 1987.

8. R.S. Sillman, S.M. Hues, D.K. Gaskill, N. Bottka, "OM-VPE Growth of Modulation-doped p-AlGaAs/GaAs Heterojunctions Using Diethylberylium," submitted for presentation at 1988 Elect. Mat. Conf, U. of Colo. (June 1988).

II. DETECTION AND DECONTAMINATION

A. Microsensors and Chemical Vapor Detection

The Navy has a growing interest in the use of microsensors as chemical vapor detectors, specifically as personnel and system monitors, detector/alarm systems for hazardous materials, and for biological diagnostics. Microsensors are particularly attractive for many of these applications because of their potential sensitivity, ruggedness and low cost. During the period of performance, GEO-CENTERS personnel have made significant advances and contributions in the area of chemical microsensor testing and evaluation. Specific advances include the development of a reliable and reproducible optical waveguide humidity sensor, the construction and calibration of an automated vapor generation apparatus for microsensor testing, and the elucidation of vapor/coating interaction mechanisms that affect microsensor response. Additional efforts have involved the further evaluation of the optical waveguide, the evaluation of several coating materials as SAW sensor coatings, the generation of SAW sensor coatings, the generation of SAW sensor response data bases for use in the development of pattern recognition algorithms, and the development of data collection/data reduction software to facilitate the interpretation of SAW response data.

Work performed in these areas has resulted in at least 13 presentations and 11 publications and technical reports. One publication was cited with a 1986 Alan Berman Award for Applied Research. Included in Appendix C are copies of technical reports and published papers which were generated as a result of the work conducted during the period of performance of this contract.

1. Optical Sensors

Optics-based sensors have been studied because of the inherent sensitivity and selectivity of spectroscopic methods of analysis. The response of these sensors are also less sensitive to changes in the ambient conditions, such as temperature and pressure, than their electronics-based counterparts. The major problem to date in developing a reliable optical waveguide sensor was the lack of reproducibility.

Reproducibility problems most likely arise from two sources: variations in the coatings applied to the devices, and the inability to obtain optimum alignment of the waveguide and the optical components. Both of these problems were addressed in the course of developing and evaluating an optical waveguide humidity detector (1). Plastic couplers were designed that held the waveguides and optical components in a rigid, reproducible alignment. This resulted in better reproducibility of response for the waveguide detector. In addition, the use of plastic couplers increased the amount of light transmitted to and from the waveguide, resulting in increased sensitivity. Several coating application methods were then evaluated for their affect on response: dip-coating, and air-brush application.

In dip-coating, a device is dipped into a reagent/polymer solution and is slowly extracted. As the solvent is evaporated (using a heat gun), a thin polymer film containing the reagent remains on the surface. In general, dip-coating resulted in thicker, less uniform films which contained areas of high reagent concentration. In air-brushing, a fine aerosol spray is generated and deposited on the surface of the waveguide. This technique allows for greater control during film application. These films were usually thinner and more uniformly distributed.

Quantitatively, the response was slightly dependent on the amount of reagent in the film, but results for films of both types were comparable. Qualitatively, the thinner films applied using the air-brush exhibited much faster response times.

Further evaluations of the optical waveguide sensor were performed (2). These studies were conducted to verify the performance of the system and to elucidate the relationship between the solubility parameter (δ_H) of the polymer coating and the response of the waveguide to specific vapors. In this study, no colorimetric reagents were incorporated in the films. Responses of the devices were due primarily to changes in the amount of scattering, or changes in the refractive index of the polymer upon exposure to vapors.

The results indicate good long-term reproducibility of a given device, but poor reproducibility between multiple devices with the same coating. This indicates that, for non-colorimetric measurements, the morphology of the polymer coating on the waveguide surface is an important factor. Responses of coating devices are semi-selective, but selectivity has not been unequivocally correlated with δ_H. As in the humidity study, the use of optical couplers with the polymer coated waveguide resulted in increased sensitivity by increasing the transmission of light to and from the waveguide.

These studies have shown that the waveguide has the potential for use as a reliable, reproducible sensor. Further evaluation of the mechanisms involved in non-colorimetric applications are needed before the device can be fully utilized for such applications.

2. Automated Vapor Generation/Data Acquisition Apparatus

The multiple vapor exposures necessary for the testing and evaluation of coating materials make such testing labor intensive and time consuming. The data bases needed for the development of pattern recognition algorithms demand large volumes of reduced data. To aid in the generation of such large data bases, an automated system was needed for the continuous testing of coated sensors. With the assistance of GEO-CENTERS personnel, such a system has been designed and constructed (3). The system consists of two modular vapor sources and a master/dilution control module. Vapors can be generated from either permeation tubes or bubblers in concentrations ranging < 1 mG/M^3 (permeation tubes) to > 10,000 mG/M^3 (bubblers). Vapor streams for 12 different vapors can be individually generated and sent to the sensor at a pre-programmed flow rate. Two component vapor mixtures can also be generated.

The system is fully automated using two Apple IIe personal computers. One computer is dedicated to managing the vapor generator apparatus, while the other computer controls the real-time sensor data collection and data-file storage duties. The two computers communicate via a game-controller port communications linkage to synchronize the vapor generation and data acquisition tasks. Parameters for controlling the vapor source and concentration can be pre-selected and stored on floppy disk. While the system is fully operational, more than sixty-four separate experiments can be run sequentially. This is equivalent to over 96 hours of unattended operations. By expanding the number of frequency-counters, up to five sensors can be tested simultaneously.

Initially, the number of experiments was limited by the number of data files that could be stored on floppy disk. Incorporation of a 10 M-byte hard disk in the system enabled us to increase our data storage capability, and to separate the data collection software from the data reduction software. The hard disk can currently be accessed from a separate micro-computer connected to the network. Data files stored on the hard disk can be systematically retrieved and reduced. This facilitates the rapid turn around of data for other projects (i.e. pattern recognition) and aids in the interpretation of data.

The data reduction software also routinely determine such sensor operating conditions as baseline rms noise, initial frequency, long-term drift, and initial and final flow rate to the sensor. These values can be useful in interpreting results and diagnosing problems with individual sensors. In addition, the frequency shifts associated with individual vapor exposures are calculated, calibration curves are plotted for visual inspection of data, and response factors (log R) are calculated and tabulated for rapid comparison and evaluation of coatings. More details on the log R are included in the discussion of SAW coating studies below.

3. SAW Device/Coating Evaluations

During the period of performance, GEO-CENTERS personnel have performed extensive coating testing and evaluation. The majority of data have been collected in attempts to identify and quantify the vapor/coating solubility interactions which are responsible for observed responses. Other areas of study have included coating structure/response correlations, investigations of possible elastic modulus effects, and the identification/evaluation of new coatings for the detection of specific hazardous vapors. Progress in these areas will be discussed separately.

a. Solubility Interactions

The most significant progress during these studies has come in the identification of vapor/coating solubility interactions. The initial intent of the program was to identify coating materials for the detection of G-agents. Preliminary tests using a simulant (dimethyl, methylphosphonate - DMMP) had identified some materials that would be potentially sensitive to these chemical agents. Additional vapor exposures were performed to determine the selectivity of these materials for the simulant vs a variety of interferences and to estimate the limits of detectability. The response data from these tests would then be analyzed using pattern recognition techniques. Pattern recognition would be useful in determining the minimum number of coatings that would be needed to correctly classify a given vapor as an interference or as an agent/simulant.

A set of ten coatings were studied and the frequency responses for these sensors were monitored as the devices were exposed to varying concentrations of twelve vapors. The majority of these coatings exhibited excellent sensitivity to the simulants DMMP and dimethylacetamide (DMAC), and were less sensitive to the interferences. When pattern recognition techniques were applied to these data, the vapor responses tended to cluster together based on their solubility properties (4). In addition, the presence of hydrogen bonding functional groups in the chemical structures of the coatings correlated well with the responses of these coatings to water vapor and other hydrogen bonding vapors. Reduction of this data set by pattern recognition revealed that excellent discrimination between simulants and interferences was achievable with a reduced set of four coatings. These coatings were identified as fluoropolyol (FPOL), poly(ethylene maleate) (PEM), poly(vinyl pyrrolidone) (PVP), and octacedyl vinyl ether/maleic anhydride copolymer (OVEMAC).

The results of this study indicated the correlation between structural features and the hydrogen bonding ability of the coatings, and identified hydrogen bonding as an important mechanism in the vapor/coating interactions. Subsequent work has focused on exploring the issues of solubility properties and structural effects.

To quantify the vapor/coating interactions, the SAW responses for a given coating (FPOL) were compared with the retention volume data for the same material used as a stationary phase in gas-liquid chromatography (GLC). The assumptions inherent in this work are as follows: First, the vapor/coating interactions can be modelied as the dissolution of a solute vapor in a solvent coating. The extent of such interactions are determined by solubility properties such as hydrogen bonding, dipole-dipole interactions and dispersion forces. Quantitatively, these interactions can be described by a partition coefficient, K, where

$$K = C_S/C_V.$$

The terms C_S and C_V refer to the concentrations of the solute vapor in the stationary phase/coating material and the gaseous phase, respectively. The derivations of equations relating SAW responses and GLC retention volumes to partition coefficients are described in detail in reference (5).

The second assumption was that the observed SAW response are due only to changes in mass on the surface of the device. Contribution to the observed response from changes in the elastic modulus of the coating were considered to be minimal or negligible. In addition, the total amount of vapor absorbed by the coating should be relatively small compared to the mass of the coating. If significantly large amounts of vapor are absorbed, changes in the density of the coating would occur which would affect the accuracy of calculated K values.

In general, the comparison between K values calculated from SAW data and from GLC data reveals a similar trend. Quantitative agreement between the two sets of data are not good, with the K values from SAW data being consistently higher. Hydrogen bonding is associated with strong interactions and large K values, while dispersion forces are associated with weak interactions and smaller K values. Vapors and coatings capable of multiple interactions showed higher K values overall. The relatively good qualitative agreement, however, is significant. It emphasizes the role of solubility interactions in SAW coating responses, and indicates that GLC data from the literature can be used as a good first approximation to predict the SAW response behavior of a coating material.

While the agreement was qualitatively good, the lack of good quantitative agreement indicates that more work remains to be done before the mechanisms responsible for SAW response are fully understood. Error arises from the lack of accurate temperature control and from possible variations in the concentration of the vapor streams. In addition, the assumption that mechanical effects are negligible may not be strictly valid. To further determine the relative magnitude of errors due to these factors, additional studies were performed.

b. Temperature Effects

Temperature studies were performed on two coatings, FPOL and PEM. Since equilibrium partition coefficients are dependent on the temperature of the system, then the response of the coated SAWs should also change as a function of temperature. Results of these studies indicated a linear dependence of K_{SAW} values on temperature, with higher responses being observed at lower temperatures (6). Furthermore, the slope of the temperature/K value plots were different for the two coatings. Two conclusions can be derived from these data. First, the sensitivity of the SAW device can be improved by operating the devices at lower temperatures. The potential of condensation of vapors in the sensor may pose problems if the temperature is reduced significantly below ambient and if the relative humidity is high. Secondly, since the rate of change of K with temperature varies for each coating/vapor pair, operating sensor arrays at more than one temperature will yield more information than operation at only one temperature. This information can be used in the development of discrimination algorithms for pattern recognition.

c. Elastic Modulus

Investigations into the contributions from mechanical effects were prompted by observed frequency responses from dual SAW devices that were inconsistent with the assumption that mass loading was the predominant mechanism for producing frequency shifts. The appearance of negative frequency shifts from the dual devices could only be explained by either increases in the frequency due to a stiffening of the film, or by a larger amount of adsorption on the uncoated reference side than on the coated side of the device.

Uncoated devices that had been ultrasonically cleaned were exposed to vapor streams of varying concentrations. These tests indicated that there was a significant amount of adsorption on the reference side of the device, and that the amount of adsorption was not consistent from one device to another (7). These devices also exhibited some sensitivity to flow rate changes, but when operated in the dual mode these effects were negligible. Efforts to circumvent problems from adsorption on the reference side by passivation or treatment of the surface of the crystal are in progress.

Studies have also been performed in conjunction with the Electronics Technology Division of NRL to study the possibility of elastic modulus effects. Coated devices were analyzed using a HP Network Analyzer to determine insertion losses and phase shifts (7). Of the coatings studied, one appeared to be fairly stable in terms of phase shift and insertion losses over time. One of the coatings, however, exhibited increases in insertion losses and decreases in the phase shifts over time. Decreases in the phase shift could be the result of a stiffening of the film or of losses of material from the surface due to evaporation. The fact that the insertion losses increased may be indicative of changes in the mechanical properties of this coating over time.

d. Structure/Response Studies

A set of experiments were designed in an attempt to identify the relationship between specific functional groups or structural features and observed solubility properties. A series of 10 polymers were synthesized, with each polymer representing slight variations on the structure of the coating PEM. These coatings were then exposed to vapor tests and the responses were analyzed for possible correlation with specific structural features (8). Results of this study indicated that the coating responses were more dependent on changes in the chemical formula/structure of the coatings than in physical parameters such as the Hildenbrand solubility parameter, density, T_g, or molecular weight/chain length. Without a more controlled set of experiments and more rigorous data reduction and analysis (such as pattern recognition), no definite correlations could be made between observed responses and specific functional groups or structural features.

e. Sensitivity, Selectivity and Reproducibility

During the period of performance, several large data sets were collected. Results from these studies can be used to evaluate the SAW sensors with respect to the issues of sensitivity, selectivity and reproducibility. These efforts included a coordinated study between the Army/CRDEC at Aberdeen and NRL (9), and between NRL and Bendix/ESD in Baltimore (10).

The issue of sensitivity is of particular importance to the Air Force because of problems arising from myosis at very low concentrations of agent. We have identified several candidate coatings during these studies that have excellent sensitivity to agent simulants (DMMP and DMAC). Concurrent live agent testing at CRDEC, and subsequently at Bendix, have verified that these coatings are also sensitive to agent, although not at the desired limits of detection. As a result of the knowledge gained from the work on solubility interactions if should now be possible to design or identify materials with a higher sensitivity to these materials. Alternatively, operation of the sensor at a lower temperature will also increase the sensitivity of response. In conjunction with pattern recognition algorithms, an array of sensors can be developed with the required detection capabilities. In addition, progress has been made in the identification of coating materials that are sensitive to mustard and other compounds.

Selectivity of the agent sensitive coatings has been very good. During this work, materials have been identified that would be selective to specific interference. Again, the use of pattern recognition algorithms will enhance the selective detection of targeted compounds.

Reproducibility is crucial if these devices are to be mass produced and put into operation service-wide. To date, the best results have been obtained with FPOL. It is very reproducible in all respects. Response behavior can be reproduced from one coated device to another, these responses can be reproduced during tests at different facilities, and these responses can be reproduced even after the devices have aged up to a year at a time. Other coatings have not been as well behaved. While it has been possible to obtain consistent response behavior between different labs and over time, it has been very difficult to reproduce response behavior from one coated device to another. In some cases, this is due to changes in the property of the coating as it ages. In other cases, it may be due to differences in the morphology of the coating or surface area of the coating on a given device.

This lack of reproducibility is particularly a problem in devices coated with non-sensitive materials. Since adsorption on the uncoated reference side can be significant in these cases, the use of a passivated reference, or a separate, sealed reference may eliminate this problem. If the problem is due to elastic modulus effects, then the surface coverage on the device and the surface morphology of the coating will be crucial. Coating applications must be made in a reproducible fashion to eliminate variations in response arising from these factors.

B. Air Purification and Decontamination

The majority of Navy applications using adsorbent media involve the purification and regeneration of contaminated air streams. The adsorbent of choice is generally activated charcoal, or an impregnated charcoal medium, such as Whetlerite. Past GEO-CENTERS' effort have focused on the desorption of small molecules (O_2, N_2, CO, and CO_2) from activated charcoals (1), as well as the use of impregnated charcoals for the collection and catalytic decomposition of toxic vapors (2), and the evaluation of Navy shipboard environments (3). For the purpose of purification of air streams several factors must be considered. The collection efficiency and adsorption isotherm of the charcoal for a given vapor must be well characterized so that breakthrough volumes and, hence, the lifetime of a carbon bed can be accurately determined. The effect of adsorbed water, or of relative humidity (RH) on efficiency and breakthrough must also be known. Finally, factors such as heat of adsorption, pore volume distributions and hysteresis effects for both pure and multicomponent vapor streams must be addressed.

During the period of performance, considerable effort has been applied to address these concerns. GEO-CENTERS' scientists have investigated the adsorption properties of activated carbon adsorbents with respect to the factors listed above, and have developed mathematical equations and models to predict the adsorption behavior of water, chemical agents, and multicomponent vapor streams on charcoal. These models can be used to predict the adsorption characteristics of charcoal for other vapors of interest. The specific studies of interest are discussed below.

1. Water on Activated Carbon

It is important to understand the behavior of water for two reasons: (1) it can adversely affect filter performance against challenges of toxic vapors, and (2) the transient behavior of water itself can result in adverse behavior. During this work, water isotherms were measured for BPL carbon at various temperatures and conditions of relative humidity. The adsorption onto a bed can be described in terms of a material balance equation, an energy balance equation, and a rate expression. The rate expression describes the rate at which the material of interest is transferred from a passing vapor stream to the surface of the carbon. It was found that the water isotherm has both favorable and unfavorable regions. The most unfavorable region occurs between 0% and 50% RH.

The mathematical model developed could adequately describe the adsorption and desorption behavior of the bed as a function of temperature and ambient RH. It was also noted that significant heating of the bed occurred as a result of water adsorption (4).

In other studies, the water vapor equilibria on a variety of activated carbons was used to obtain an understanding of the capacity and temperature dependence of adsorption. Capillary condensation was found to be primarily responsible for adsorption of water by activated carbon. This condensation produces a hysteresis effect, which can be used to determine the pore volume distribution from the Kelvin equation. It was found that water vapor adsorption could be used in lieu of nitrogen adsorption, since the former provides valuable phase equilibria data as well as a means of characterizing pore volume distributions (5).

2. Adsorption Isotherms for CW-Agents

Adsorption phase equilibrium relationships are required to accurately predict the performance of carbon filters designed to protect personnel from exposure to toxic vapors. Experimentally determined isotherm data for both single and multicomponent vapor streams are needed to design reliable protection systems. Results of studies by GEO-CENTERS' scientists indicate that empirical equations can be used to describe these isotherms. These equations have the advantage of facilitating reliable extrapolation to conditions outside the ranges of partial pressure and temperature explored experimentally. At low partial pressures, these equations converge to Henry's Law, while at high partial pressures they approximate Antoine's vapor pressure equations. Values of the coefficients for these equations have been determined for the chemical agents cyanogen chloride (CK), phosgene (CG) and hydrogen cyanide (AC) (6).

3. Fixed Bed Absorptive Reactor

Also of interest to the Navy is the use of impregnated carbon materials for the adsorption and catalytic decomposition of toxic vapors. The use of a fixed-bed reactor for the degradation of CW-agents was explored by GEO-CENTERS' scientist. The fixed-bed reactor consisted of a cylindrical bed of activated carbon treated with reactive metal salts (Whetlerite). Models developed to describe the reactor behavior include both an external mass transfer resistance term to account for relatively low effluent concentrations, as well as an internal mass transfer resistance term since the reaction takes place in the adsorbed phase. This model can be used to predict breakthrough times as a function of bed depth and velocity (7).

Appendix D contains the results of the work conducted on this task during the period of performance on this contract.

III. SOLUTION ELECTROCHEMISTRY

GEO-CENTERS has been involved in the investigation of corrosion and catalysis related problems of concern to the Navy, both through the direct research efforts of the Company's scientific and technical staff, or in conjunction with the efforts of LOCUS, Inc. Problems dealing with inter-modulation interference (IMI) were addressed by LOCUS personnel and will be discussed separately. The discussion that follows deals with the efforts of scientists and technicians of GEO-CENTERS personnel working in the Chemistry Division of NRL.

A. Intermodulation Interference Studies (LOCUS)

The results of this work are presented in their entirety in Part III of this final report, which is provided under separate cover.

B. Solution Electrochemistry

The majority of work required for the completion of the above tasks involved extensive spectrophotometric investigations using the CARY 2390 UV-Vis-NIR Spectrophotometer. The capabilities of the instrument, however, were not sufficient to perform the required analyses with the necessary resolution and sensitivity. Specifically, specialized spectrum addition/subtraction routines were necessary to identify the intervalence transfer bands of the intermediate transition metal complexes under study. This task was further complicated by the presence of spectral features from both the starting materials and final products. Also, the implementation of digital data acquisition capabilities could be exploited to study electronic spectra of superconductor materials of interest to the Navy.

Details of these studies, as well as discussion of the software enhancements of the Cary 2390 are presented below. A detailed description of the program is included in Appendix E.

1. Data Acquisition/Control Software for CARY 2390

The CARY 2300 and 2400 series spectrophotometers are high quality, microprocessor controlled analytical instruments intended for measurements of the UV-visible and Near IR absorption spectra of solids, liquids, and gases. When equipped with an optional IEEE-488 standard interface these instruments and their accessories are programmable by an external computer enabling acquisition of spectral measurements in digital form. During the period of performance, GEO-CENTERS researchers developed and tested a FORTRAN 77 program designed for single scan acquisition of spectra from the CARY 2390 instrument using a Hewlett-Packard minicomputer running the multi-user CI shell and RTE-6/VM operating system. The program uses very few machine specific functions and could be modified easily to run on other host systems supporting the IEEE-488 interface standard.

The program implements a large subset of the programmable instrument control functions of the CARY 2300 in a menu driven format closely resembling the menu displays on the instrument. Therefore, no special training is required for users already familiar with operation of the instrument. The control functions implemented reproduce the facilities of the spectrophotometer's instrument Settings, Baseline Setup, Lamp and Detector Modes and Accessory Setup menus, as well as a number of single keypad functions. To make the program as user friendly as possible, full error trapping of keyboard entries has been implemented.

The collection of spectrophotometric data in digitized form provides both a permanent means of storage and the ability to perform more sophisticated analysis. While the instrument obtains spectral measurements as absorbance vs. wavelength (nm), plotting programs can rescale the raw data into more meaningful units such as molar absorptivity vs. wavenumber (cm^{-1}). Techniques such as difference spectroscopy no longer need to be performed in real time since data files can be manipulated easily to achieve this function by scaling and subtraction. Noise can be used to generate derivative spectra which are more accurate than those produced in real time by the CARY 2300-2400 series spectrophotometers on their internal pen recorders. Such benefits make it worthwhile to develop software for data transfer between the CARY spectrophotometer and an external computer system.

In addition to the previously detailed capabilities, the program will also permit the plotting of first and second derivative spectra, correction and editing of data file parameters and spectral data, and quartic polynomial least square curve smoothing to remove random noise from spectrum. A full explanation of the program capabilities, as well as the source code for the program and subroutines, is included in Appendix E.

2. Electron Transfer in Transition Metal Complexes

Because of the Navy's interest in homogeneous catalysis for the activation of small molecules, the kinetics and mechanisms of electron transfer and ligand exchange in transition metal complexes has been under study. Enhancements to the CARY 2390 spectrophotometer have enabled GEO-CENTERS' scientists to study the spectral features of these reaction intermediates, thereby elucidating the electron transfer mechanisms. The mode system studied to confirm the mechanism of electron transfer of these complexes was a monoformylated Ru(III) complex. This complex was reacted with Ti(III), and the spectra of starting materials, products and intermediates were to be obtained.

The presence of the monoformylated-acac ligand in the Ru(III) complex was believed to increase the rate of electron transfer. The overall reaction involved is given below.

$$\mathrm{Ti(III)} + \mathrm{Ru(III)} \text{ -----> } \mathrm{Ti(IV)} + \mathrm{Ru(II)}$$

In the presence of oxygen, this reaction can be cycled repeatedly.

The specialized spectrum addition/subtraction capabilities of the CARY 2390 could be utilized to identify intervalence transfer bands of the Ti-ligand-Ru species, a labile intermediate in the reaction between the Ti(III) and $Ru(acac)_2$(3-CHO-acac) species. This task is normally complicated by the spectral features from both starting materials and final products.

From purified $Ru(acac)_3$, the monoformylated complex was synthesized following published syntheses. As published, the synthesis has a very low expected yield (<10%). Attempts were made to improve the yield of the monoformylated product by increasing the ratio of $POCl_3$:$RU(acac)_3$ from 2:1 to 4:1. This resulted, however, in the presence of significant amounts of the diformylated complex, as was verified by NMR. Ti(III) solutions were prepared by the dissolution of TiH_2 in 3 M HCl. Absorption spectra, proton and ^{13}C NMR spectra of the starting materials are given in Figures 1-5.

Results of these experiments indicate that the formylated Ru complex is more easily air oxidized than the parent $Ru(acac)_3$ complex, and reacts more rapidly with the Ti(III) species. During reaction it eventually consumes excess Ti(III), leaving most of the formylated Ru complex as Ru(III), preventing significant hydrolysis. After the addition of sufficient Ti(III) to purge the system of oxygen, a stable solution of Ru(II) is obtained.

For the parent complex [$Ru(acac)_3$], reaction with Ti(III) is slow and can be followed spectrophotometrically for over an hour. For the formylated complex [$Ru(acac)_2$(3-CHO-acac)], the reaction was almost instantaneous. Over the course of several days, however, the Ru(II) species formed undergo significant hydrolysis.

Kinetics of the cross reaction between Ti(III) and Ru(III) complexes are in progress. There is already good evidence for facile electronic coupling via ligand bridges connecting the 3-C position to other transition metals. Confirmation of the kinetics and mechanisms of electron transfer by NMR, EPR and UV-VIS-NIR spectrum will pave the way for investigations into other transition metal complexes.

3. Spectral Analysis of High-T Superconducting Ceramics

Because of the Navy's interest in the application of superconducting ceramics, recent studies have focused on the production and characterization of these materials. Currently, the preparation of the superconducting orthorhombic phase of $YBa_2Cu_3O_7$ in bulk quantities requires repeated high temperature cycling and thermal decomposition above 900°C. These temperatures are incompatible with the various substrate materials and electronic materials with which these superconducting ceramics would ultimately be used. Therefore, studies were performed to determine the feasibility of preparing suitable materials at lower temperatures with less temperature cycling. The preparation of superconducting ceramics in this way would enhance the technological capabilities of superconducting devices.

GEO-CENTERS' scientists assisted in the characterization of these materials. Samples of $YBa_2Cu_3O_7$ were prepared and characterized using transmission spectroscopy and reflectance spectroscopy at both room temperature and at liquid nitrogen temperature (77 K). The purpose of these investigations was to determine whether the plasma edge of the metallic state can be observed at room temperatures. The spectra obtained at room temperature revealed that the samples had both localized and delocalized Cu sites. In addition, the low temperature spectra exhibited the same spectral bands observed at room temperature without significant band narrowing or shifts in band positions. Subsequent magnetization measurements using a superconducting quantum interference device (SQUID) magnetometer indicated that a significant portion of the superconducting phase was present. A superconduction onset temperature of 95 K was observed, with a magnetic-flux expulsion of 5% at lower temperatures (2).

REFERENCES

1. R.A. Binstead, J.C. Cooper, "CARYSPEC: A FORTRAN 77 Program for Spectral Data Acquisition and Control of the Varian CARY 2390 UV-VIS-NIR Spectropnotometer," submitted as NRL Memorandum Report 1988 (preprint included as Addendum to this report).

2. Rm. Panayappan, J.T. Guy, Jr., R. Binstead, V. LeToyrneau, J.C. Cooper, "Preparation of Superconduction Y $Ba_2Cu_3O_7$ from the Corresponding Metal Formates," Phys. Rev. B 37(7), March 1988.

TABLE I

Results of NMR Spectra for [Ru(acac)$_3$] in $CDCl_3$

Nuclei	δ (ppm)	Ratio	Comment
^1H:			
$-CH_3$	-5.51	6.056	Singlet
>C-H	-30.5	1.000	Singlet, broad
^{13}C: (decoupled)			
$-CH_3$	-21.3		Singlet, NOE
>C=O	+140.5		Singlet
>C-H	+307.5		Singlet, broad, NOE
^{13}C: (coupled)			
$-CH_3$	-23.9 (av)	6.000	Quartet
>C=O	+138.3	5.343	Singlet
>C-H	+315.0 (av)	2.855	Doublet

TABLE II

Results of NMR Spectra for [Ru(3-CHO-acac)(acac)$_2$] in $CDCl_3$

Nuclei	δ (ppm)	Ratio	Comment
^{1}H:			
$-CH_3$	-13.01	6.000	Singlet
$-CH_3$	-10.30	5.924	Singlet
$-CH_3$(F)	+7.465	6.139	Singlet
OC-H(F)	+12.89	1.082	Singlet
>C-H	-46.7	1.967	Singlet, broad
^{13}C: (decoupled)			
$-CH_3$	-18.17		Singlet, NOE
$-CH_3$	-8.51		Singlet, NOE
$-CH_3$(F)	+3.69		Singlet, NOE
>C=O	-12.00		Singlet, broad
>C=O	+65.52		Singlet, broad
>C=O(F)	+326.7		Singlet, broad
O=C-H(F)	+204.2		Singlet, NOE
>C-Formyl	+313.5		Singlet
>C-H	+358.7		Singlet, broad, NOE
^{13}C: (coupled)			
$-CH_3$	-20.23 (av)	1.96*	Quartet, overlaps >C=O
$-CH_3$	-9.94 (av)	1.959	Quartet
$-CH_3$(F)	+1.87 (av)	1.960	Quartet
>C=O	-26.48	1.72*	Singlet, broad
>C=O	+57.52	1.704	Singlet, broad
>C=O(F)	+338.2	1.782	Singlet, broad
O=C-H(F)	+206.8 (av)	0.999	Doublet
>C-Formyl	+320.4	1.000	Singlet
>C-H	+370.9	1.766	Unresolved Doublet

* Overlapping Peaks - Redistributed Excess Methyl Intensity To >C=O Resonance

TABLE III

Results of NMR Spectra for $[Ru(acac)(3\text{-}CHO\text{-}acac)_2]$ in $CDCl_3$

Nuclei	δ (ppm)	Ratio	Comment
^1H:			
$-CH_3$	-15.9	6.000	Singlet
$-CH_3(F)$	-1.205	5.934	Singlet
$-CH_3(F)$	+8.622	6.073	Singlet
OC-H(F)	+11.72	2.235	Singlet
>C-H	-57.00	0.990	Singlet, broad

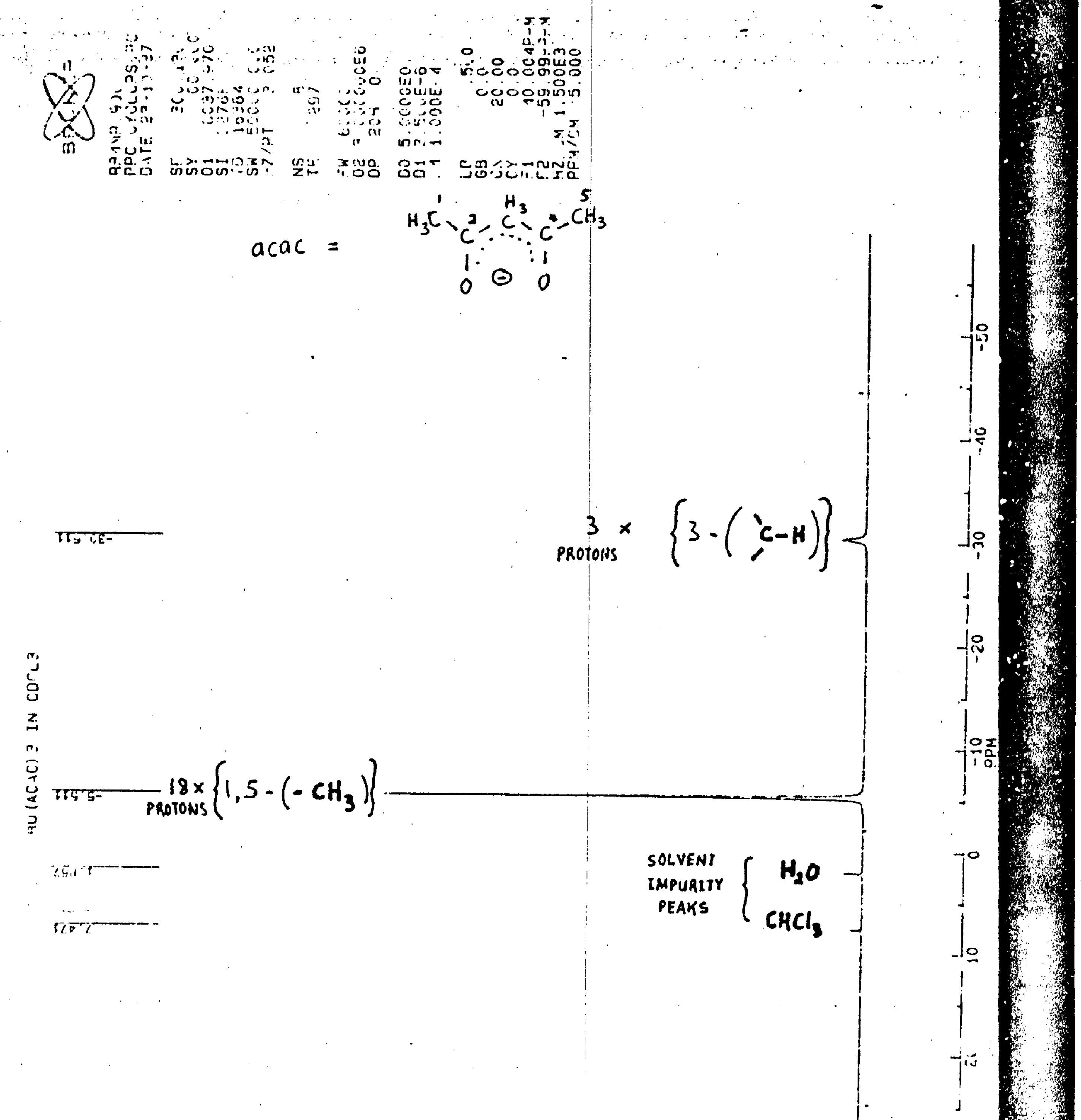

Figure 1a:
^{1}H NMR spectrum of [$Ru^{III}(acac)_3$] in $CDCl_3$
(External Reference: TMS in $CDCl_3$)

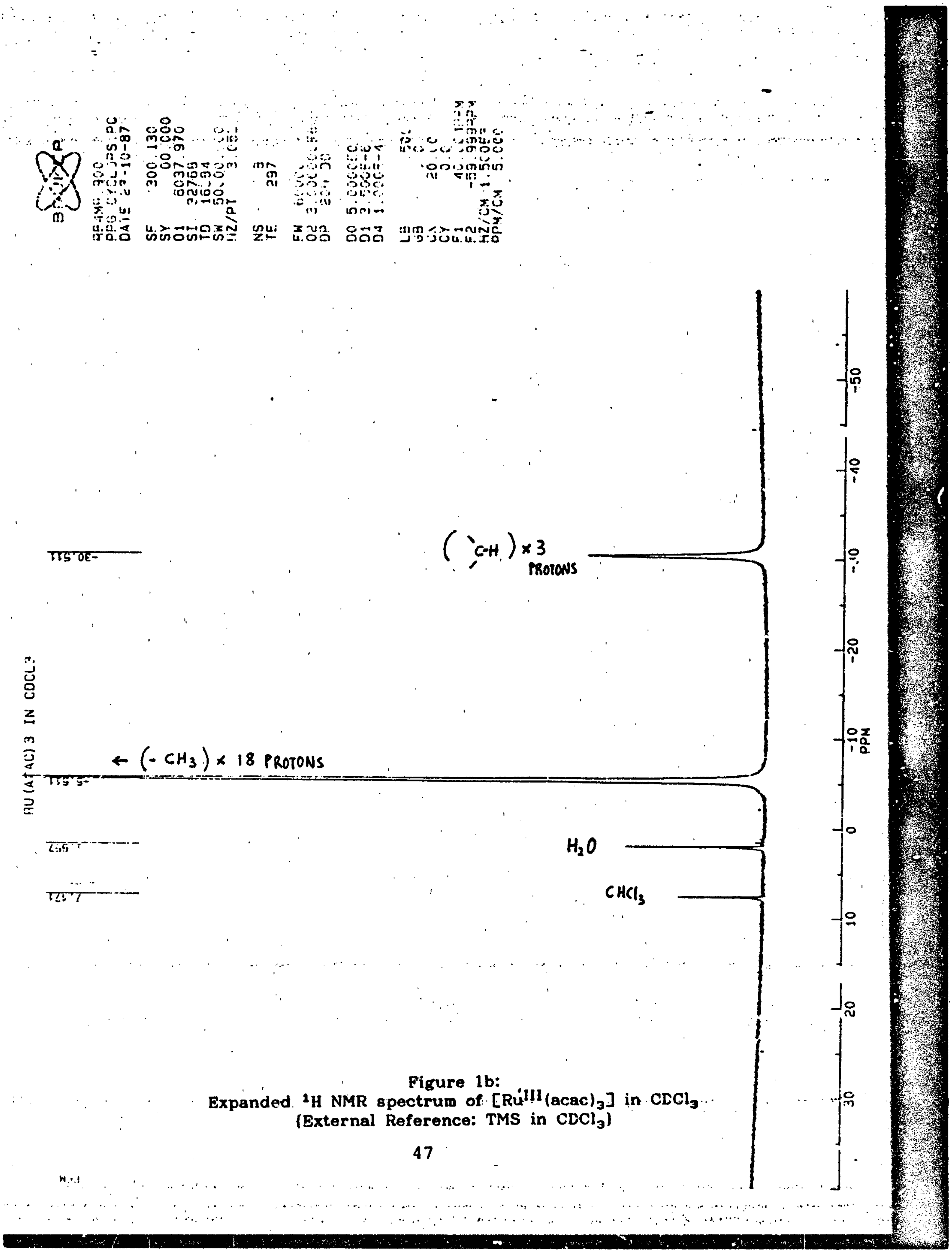

Figure 1b:
Expanded ^1H NMR spectrum of $[Ru^{III}(acac)_3]$ in $CDCl_3$
(External Reference: TMS in $CDCl_3$)

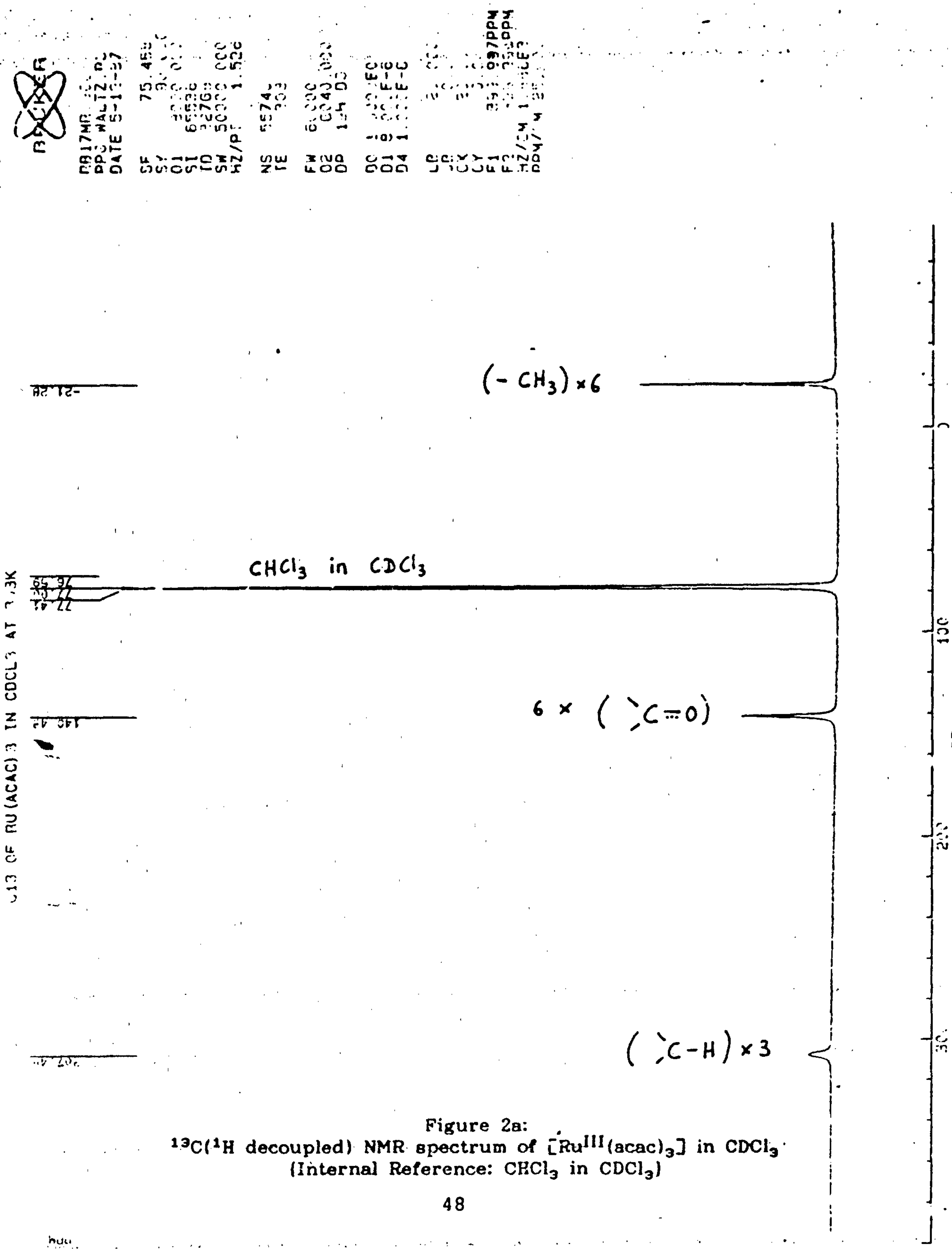

Figure 2a:
$^{13}C(^1H$ decoupled) NMR spectrum of $[Ru^{III}(acac)_3]$ in $CDCl_3$
(Internal Reference: $CHCl_3$ in $CDCl_3$)

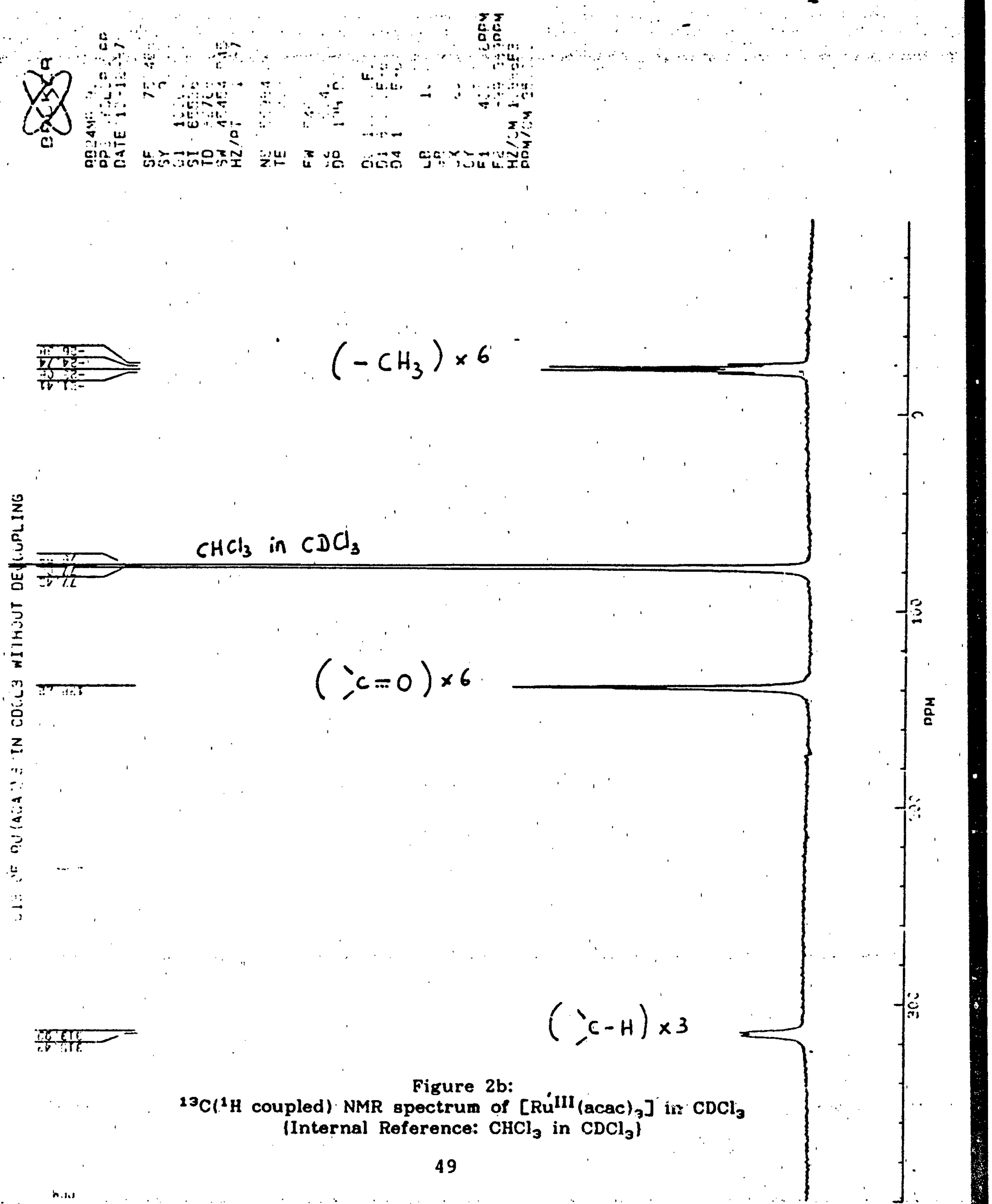

Figure 2b:
$^{13}C(^{1}H$ coupled) NMR spectrum of $[Ru^{III}(acac)_3]$ in $CDCl_3$
(Internal Reference: $CHCl_3$ in $CDCl_3$)

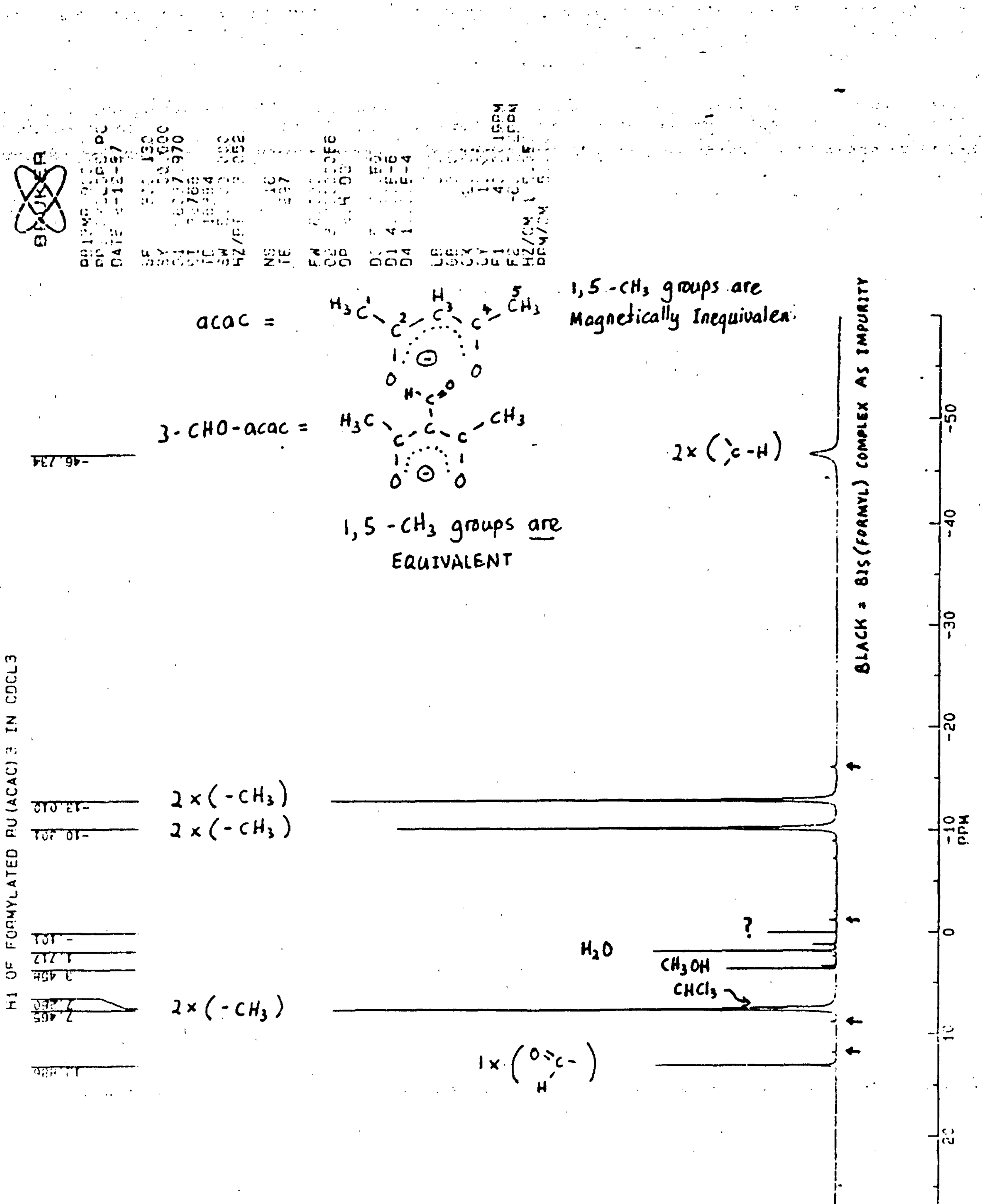

Figure 3:
^{1}H NMR spectrum of $[Ru^{III}(3\text{-CHO-acac})(acac)_2]$ in $CDCl_3$
(External Reference: TMS in $CDCl_3$)

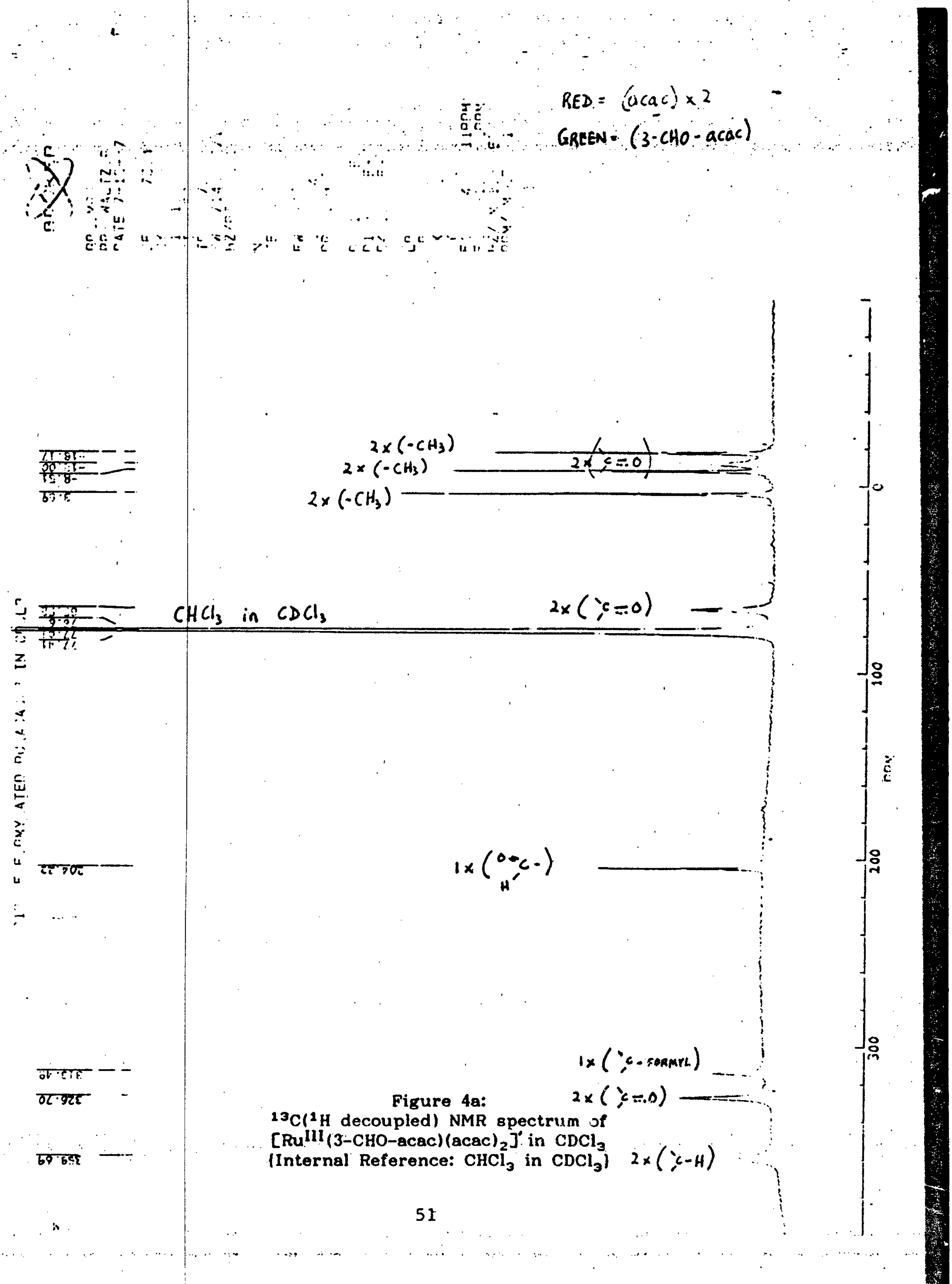

Figure 4a:
$^{13}C(^{1}H$ decoupled) NMR spectrum of $[Ru^{III}(3\text{-}CHO\text{-}acac)(acac)_2]$ in $CDCl_3$
(Internal Reference: $CHCl_3$ in $CDCl_3$)

RED = (acac) × 2

GREEN = (3-CHO-acac)

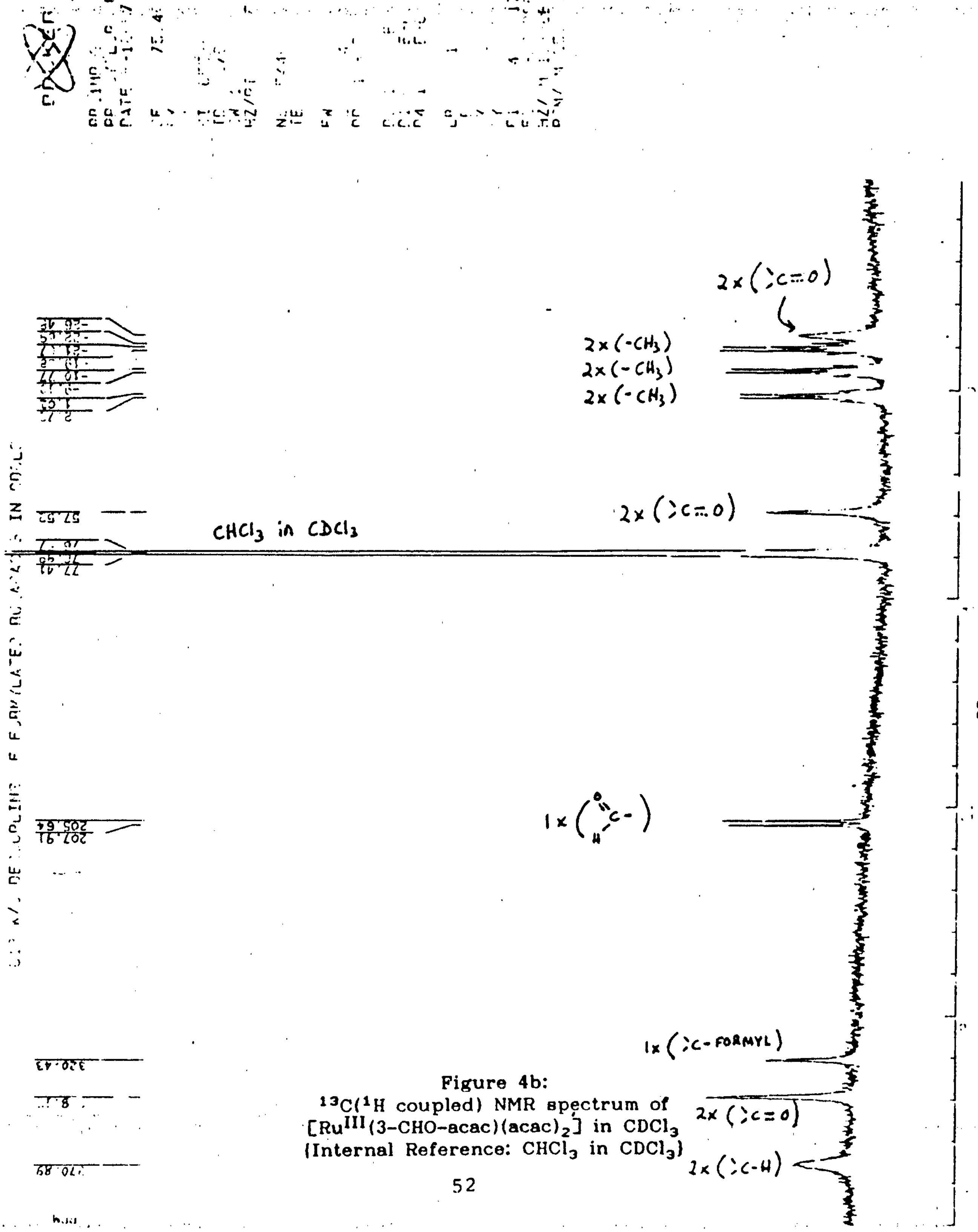

Figure 4b:
^{13}C(^{1}H coupled) NMR spectrum of [Ru^{III}(3-CHO-acac)(acac)$_2$] in $CDCl_3$
(Internal Reference: $CHCl_3$ in $CDCl_3$)

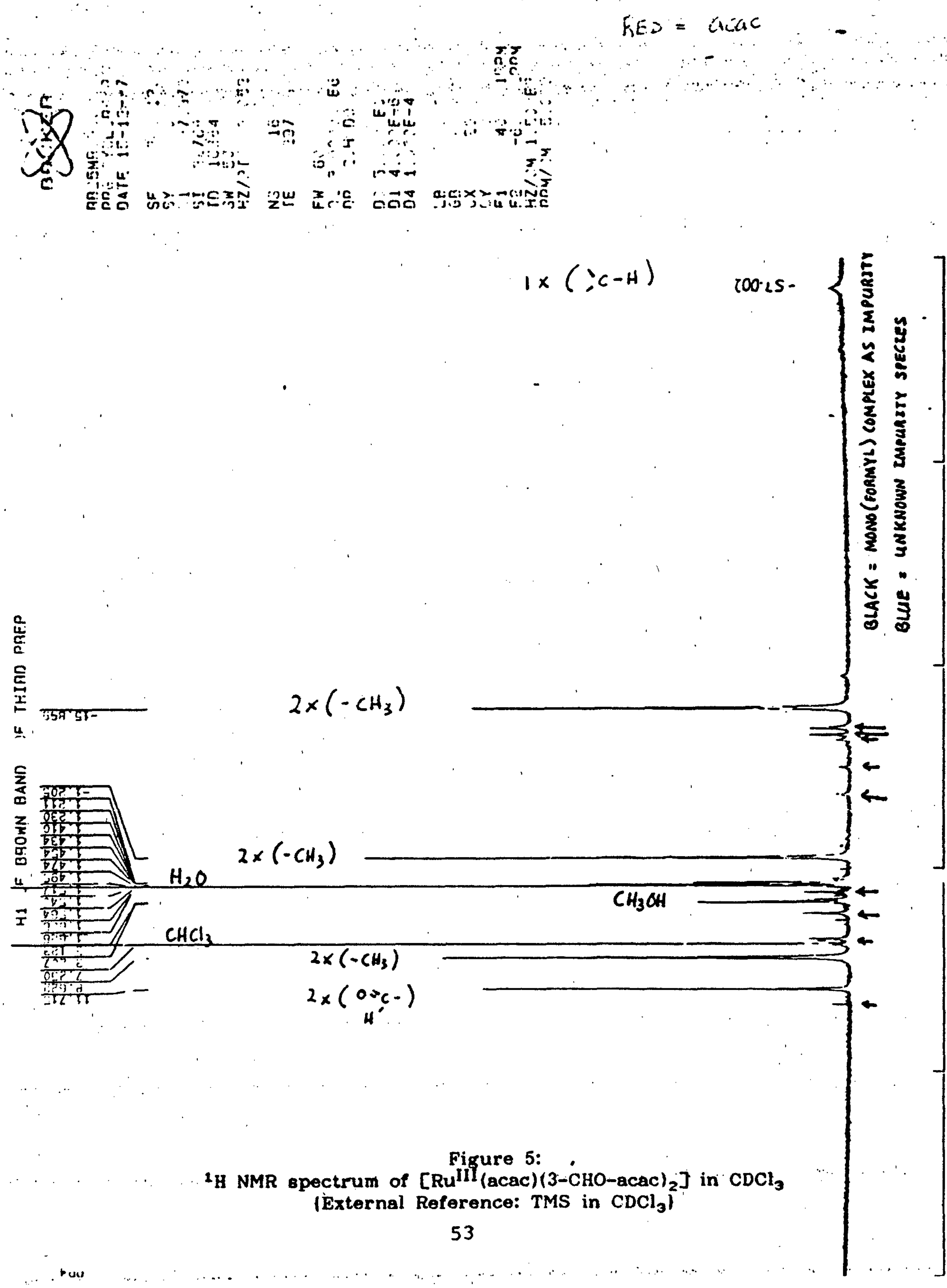

Figure 5:
^1H NMR spectrum of $[Ru^{III}(acac)(3\text{-}CHO\text{-}acac)_2]$ in $CDCl_3$
(External Reference: TMS in $CDCl_3$)

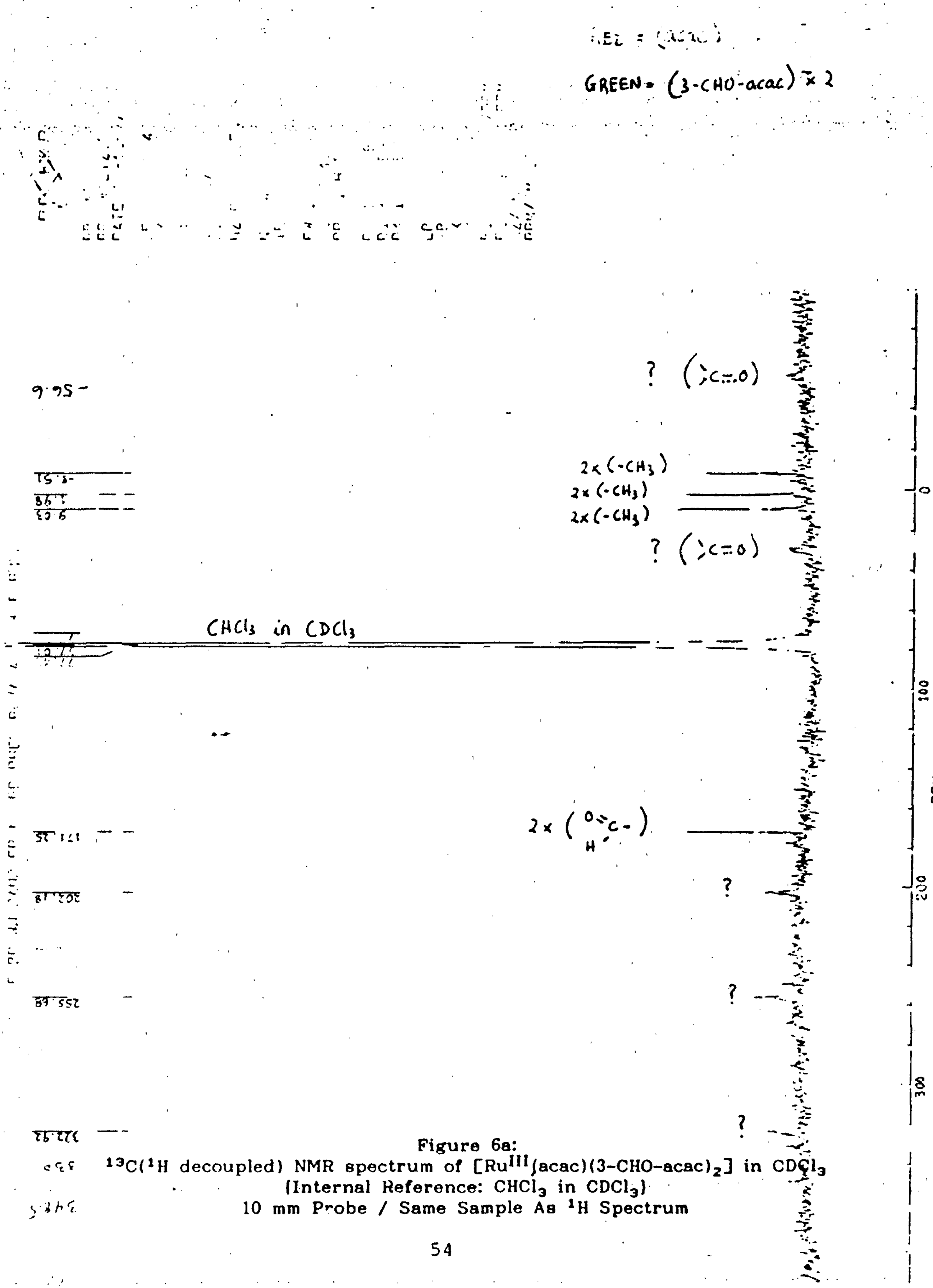

Figure 6a:
$^{13}C(^1H$ decoupled) NMR spectrum of $[Ru^{III}(acac)(3\text{-}CHO\text{-}acac)_2]$ in $CDCl_3$
(Internal Reference: $CHCl_3$ in $CDCl_3$)
10 mm Probe / Same Sample As ^1H Spectrum

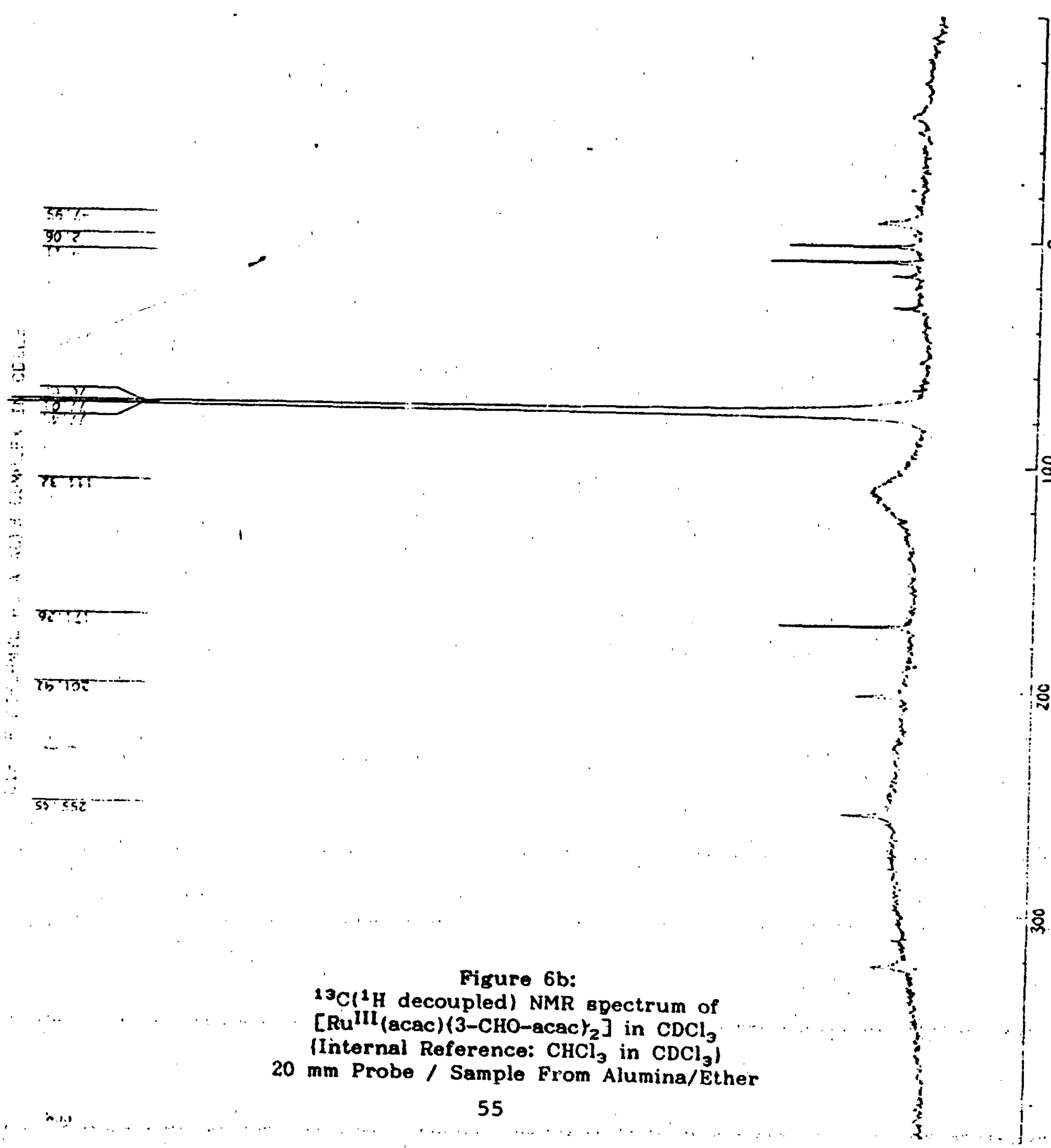

Figure 6b:
$^{13}C(^{1}H$ decoupled) NMR spectrum of
$[Ru^{III}(acac)(3\text{-}CHO\text{-}acac)_2]$ in $CDCl_3$
(Internal Reference: $CHCl_3$ in $CDCl_3$)
20 mm Probe / Sample From Alumina/Ether

TABLE I

Results of NMR Spectra for [Ru(acac)$_3$] in $CDCl_3$

Nuclei	δ (ppm) (303 K)	δ (ppm) (313 K)	Δ Shift (ppm)
^{13}C: (^1H coupled)			
$-CH_3$	-23.9 (av)	-21.3	+2.6
>C=O	+138.3	+140.45	+2.15
>C-H	+315.0 (av)	+307.3	-7.7

TABLE II

Results of NMR Spectra for [Ru(3-CHO-acac)(acac)$_2$] in $CDCl_3$

Nuclei	δ (ppm) (303 K)	δ (ppm) (313 K)	Δ Shift (ppm)
^{13}C: (^1H coupled)			
$-CH_3$	-20.23 (av)	-18.39	+1.84
$-CH_3$	-9.94 (av)	-8.66	+1.28
$-CH_3$(F)	+1.87 (av)	+3.52	+1.65
>C=O	-26.48	-13.46	+13.0
>C=O	+57.52	+64.77	+7.25
>C=O(F)	+338.2	+327.7	-10.5
O=C-H(F)	+206.8 (av)	+204.4	-2.4
>C-Formyl	+320.4	+314.2	-6.2
>C-H	+370.9	+360.1	-10.8

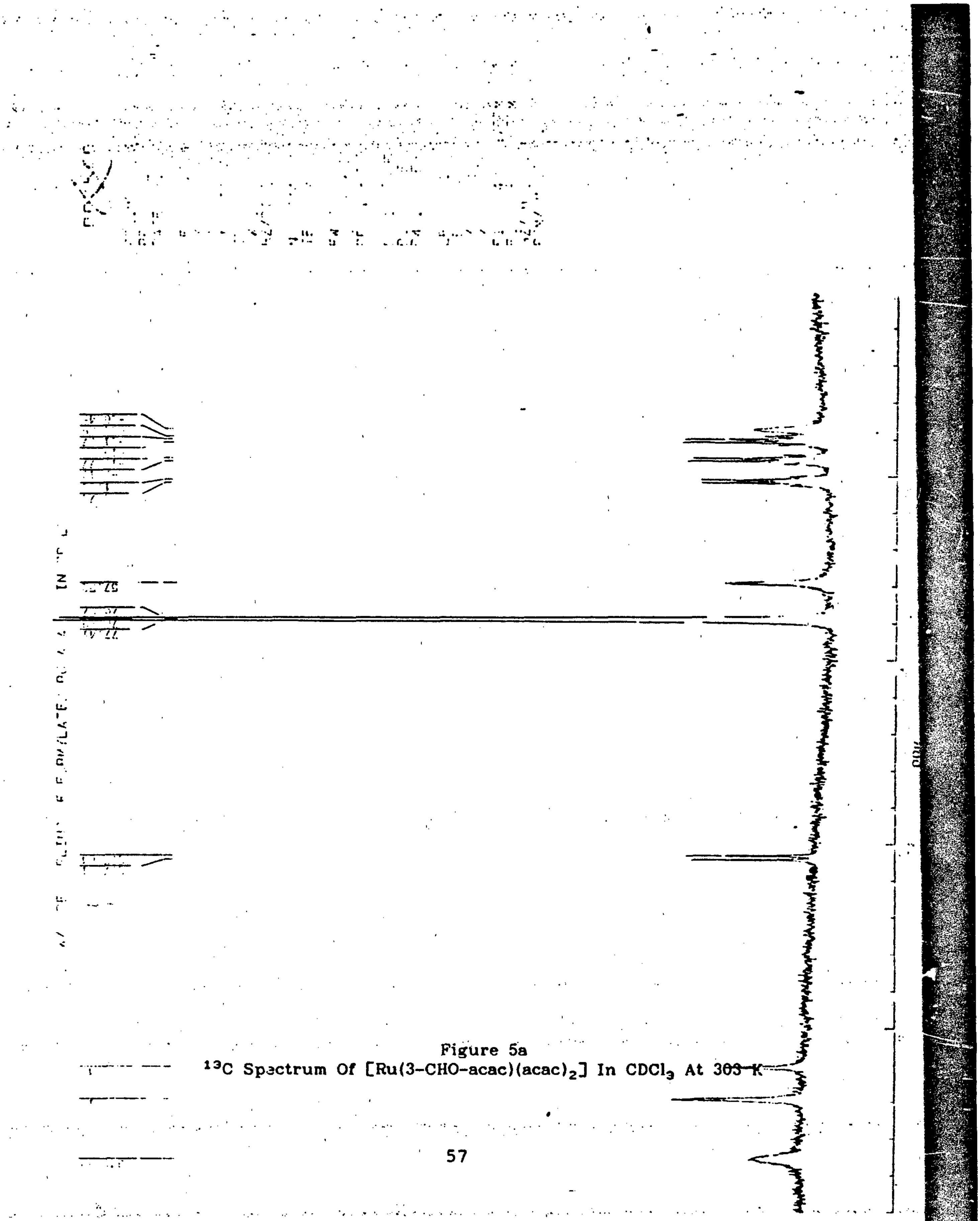

Figure 5a

^{13}C Spectrum Of [Ru(3-CHO-acac)(acac)$_2$] In $CDCl_3$ At 303 K

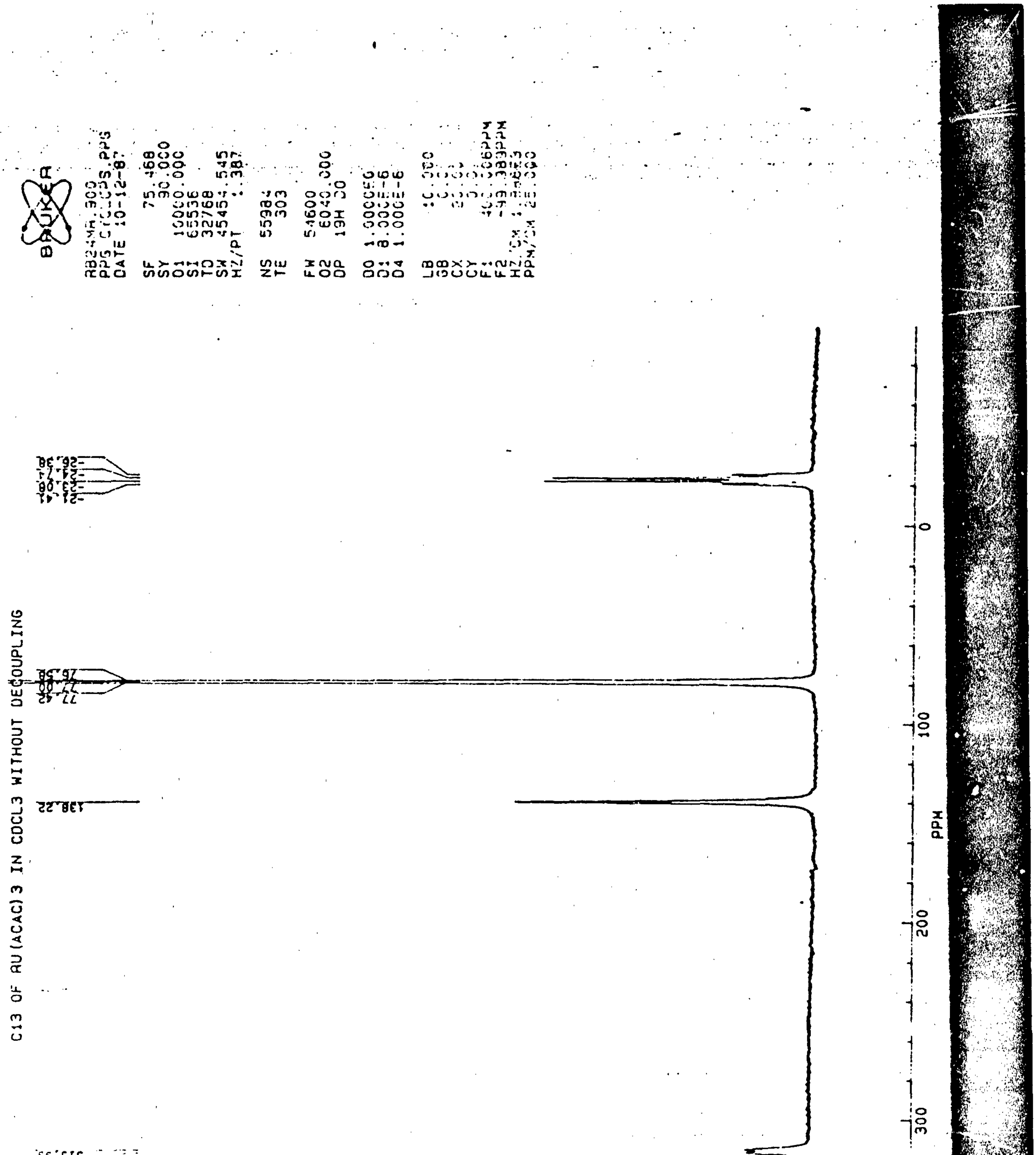

Figure 4a
^{13}C Spectrum Of $[Ru(acac)_3]$ In $CDCl_3$ At 303 K

Figure 2
UV-Visible Spectrum [Ru(acac)$_3$] In Water

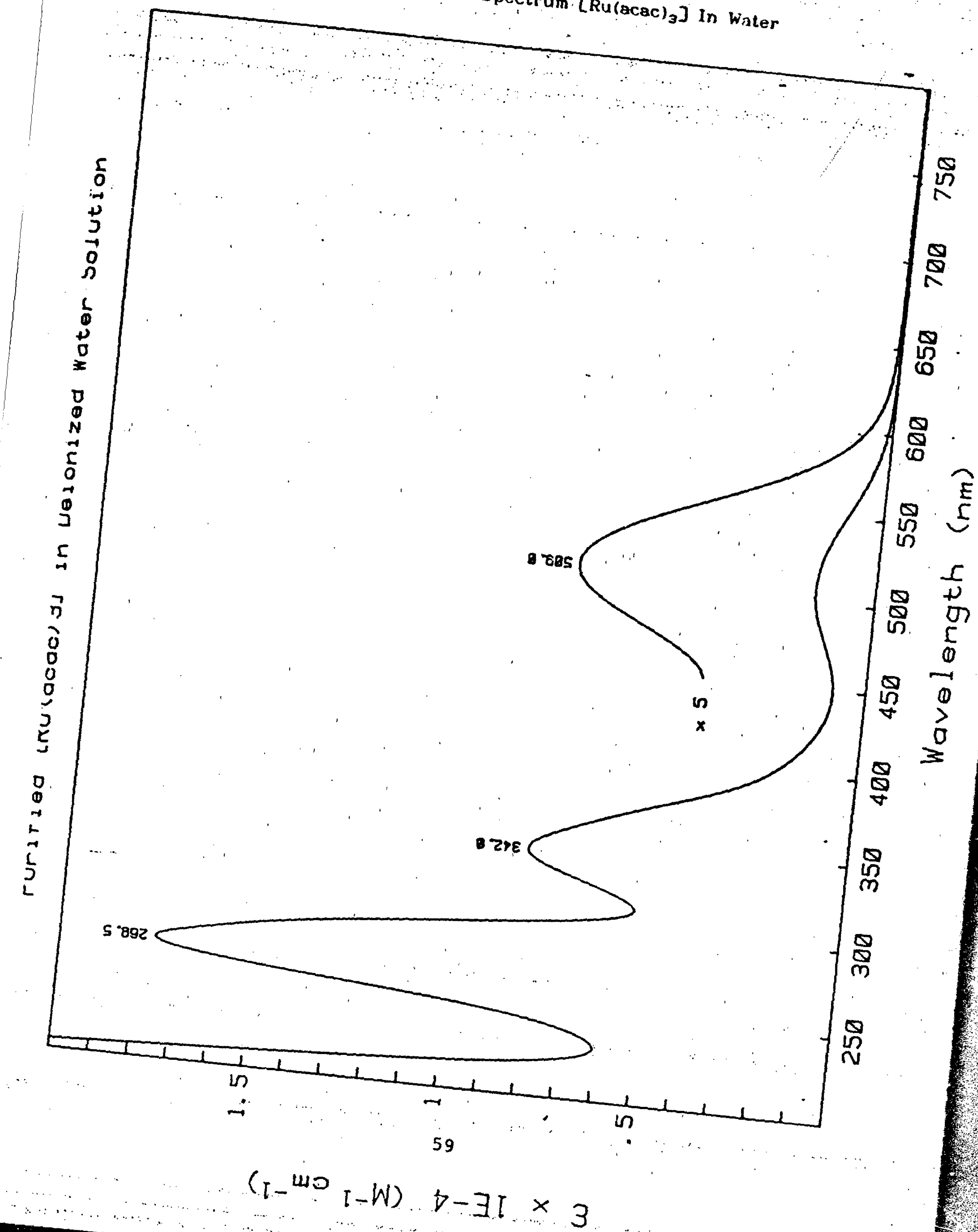

Figure 3a
Uv-Visible Spectrum Of [Ru(3-CHO-acac)(acac)$_2$] In Water
One Day After Dissolution

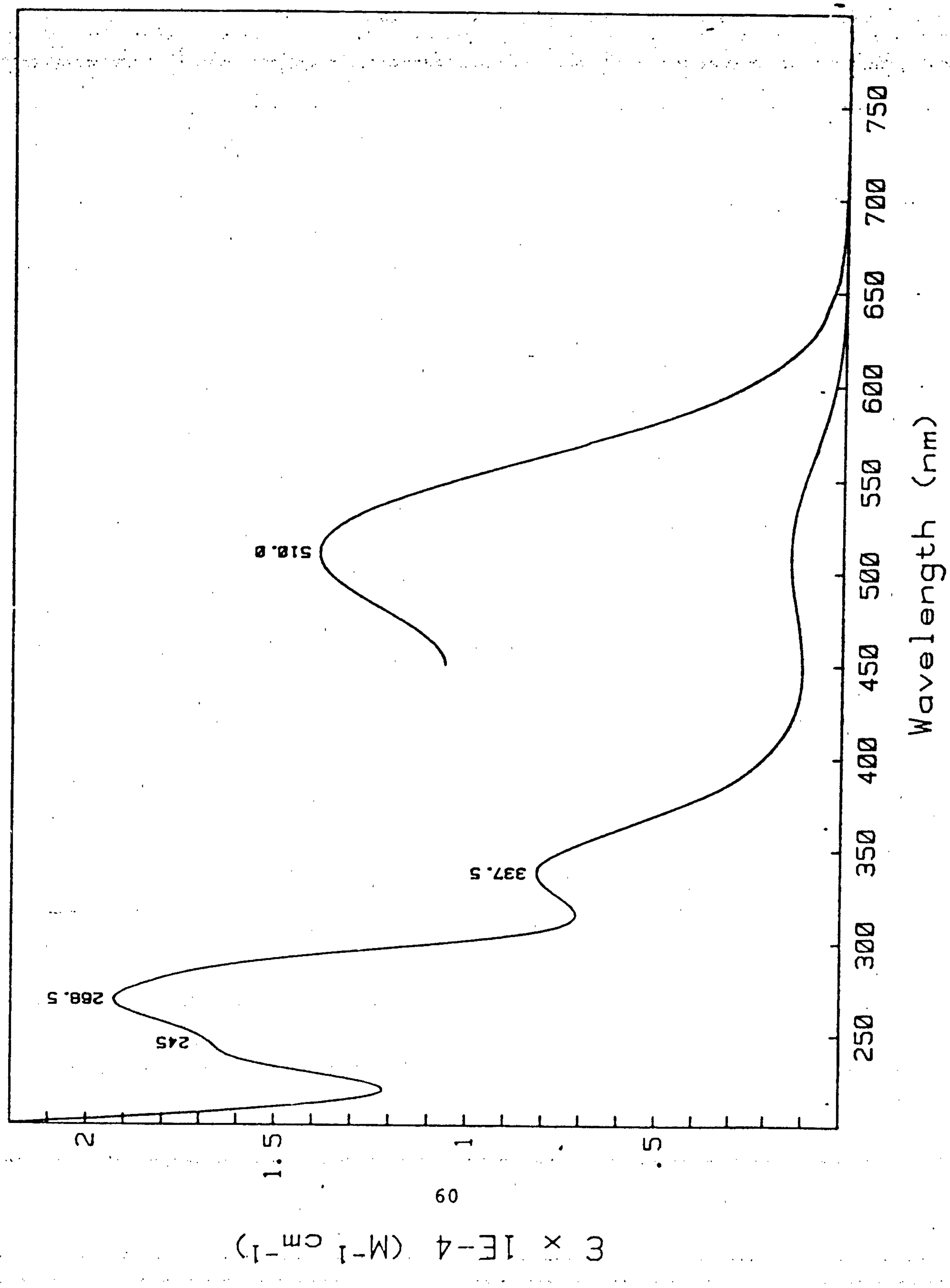

Figure 3b
UV-Visible Spectrum Of [Ru(3-CHO-acac)(acac)$_2$] In Water
Three Days After Dissolution

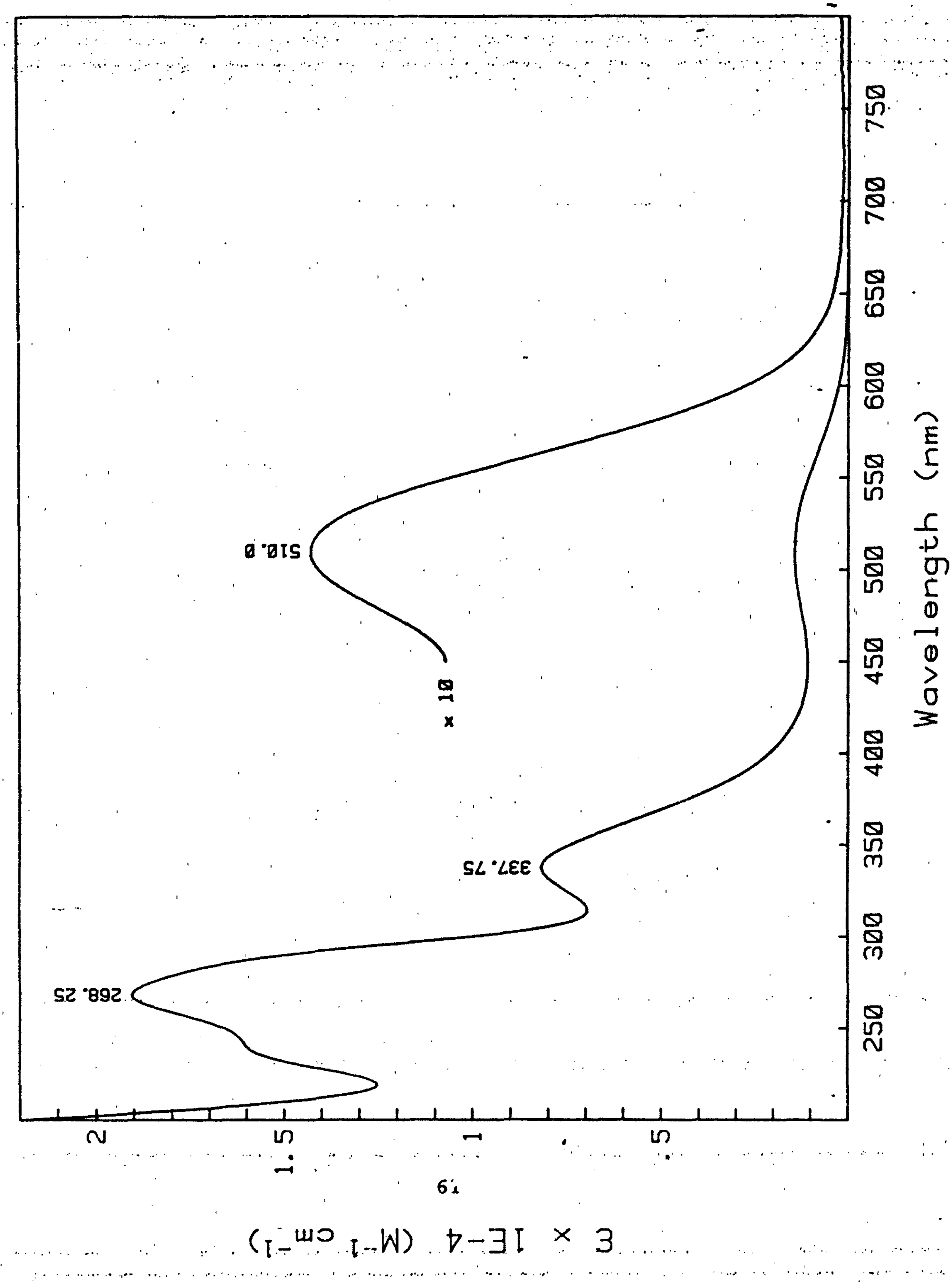

Figure 3c
UV-Visible Spectrum Of [Ru(3-CHO-acac)(acac)$_2$] In Water
Three Weeks After Dissolution

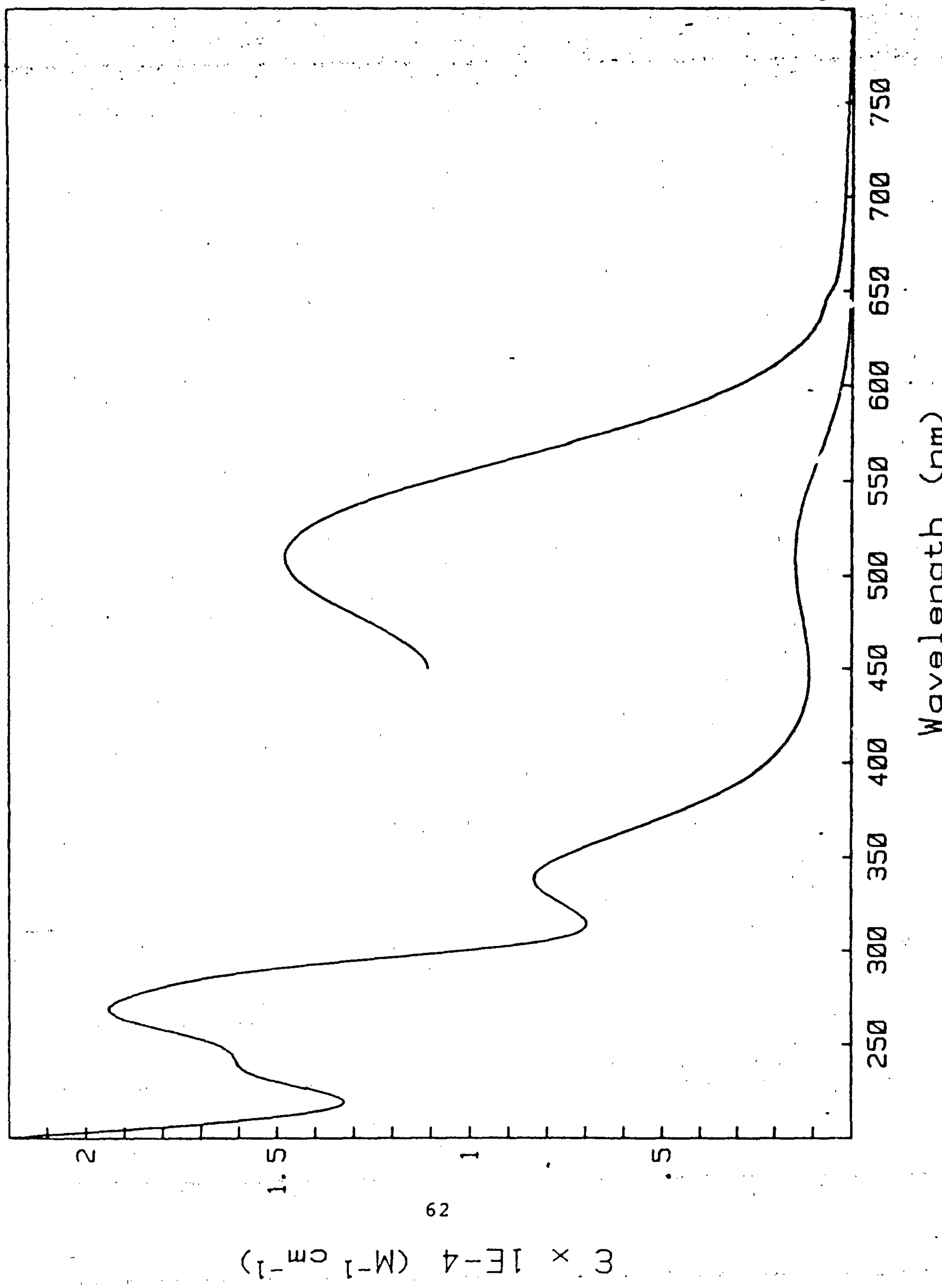

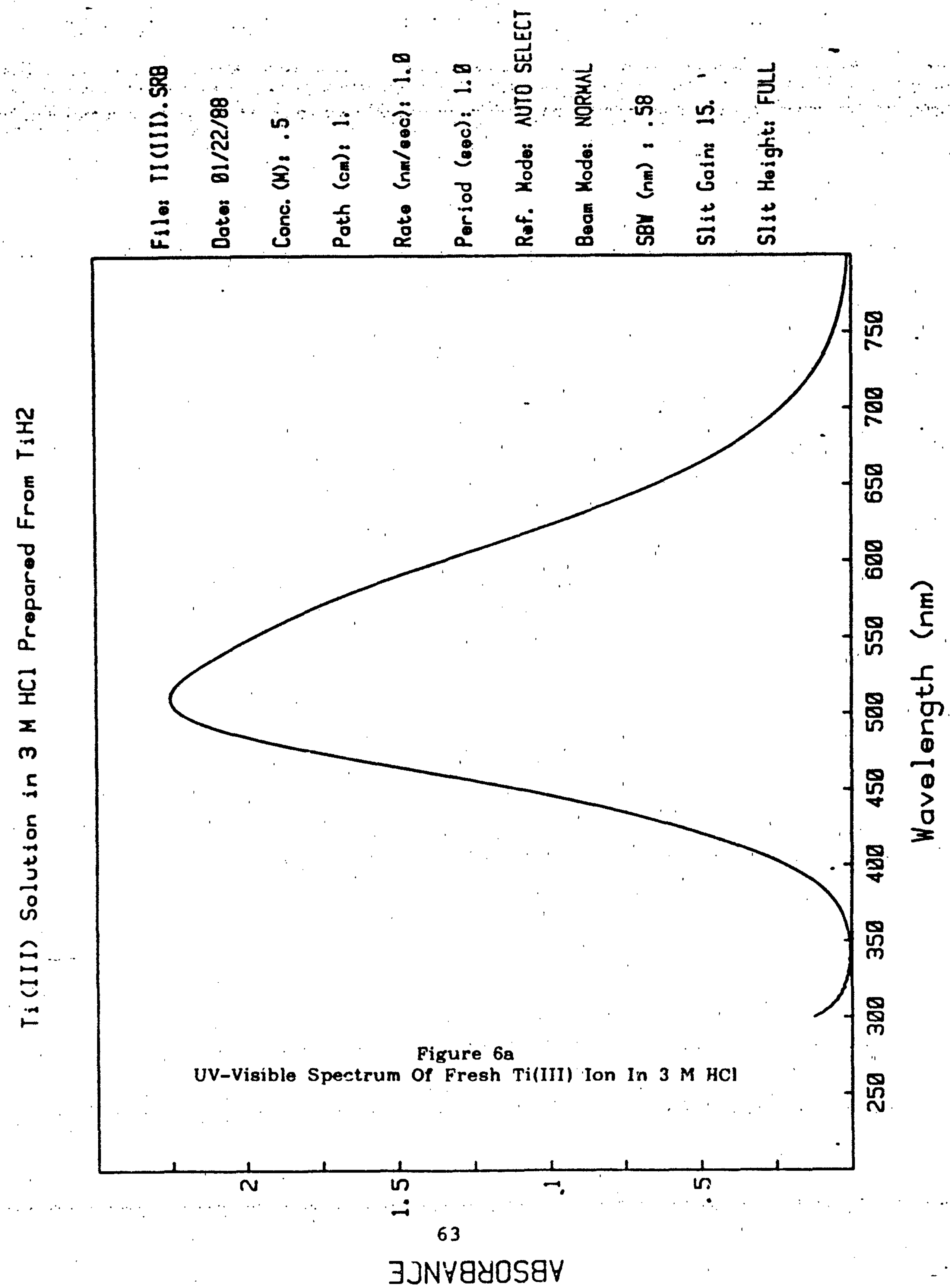

Figure 6a
UV-Visible Spectrum Of Fresh Ti(III) Ion In 3 M HCl

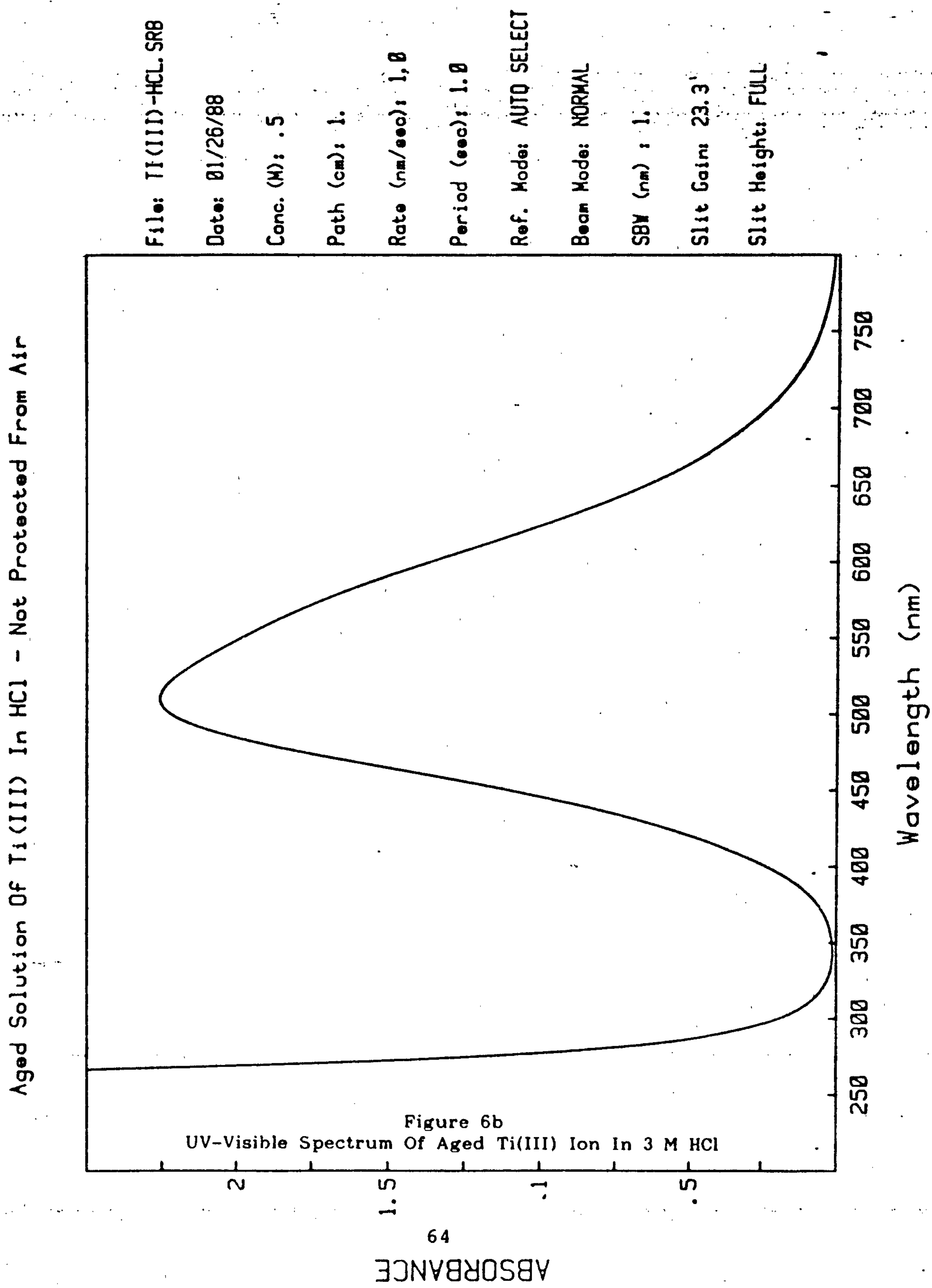

Figure 6b
UV-Visible Spectrum Of Aged Ti(III) Ion In 3 M HCl

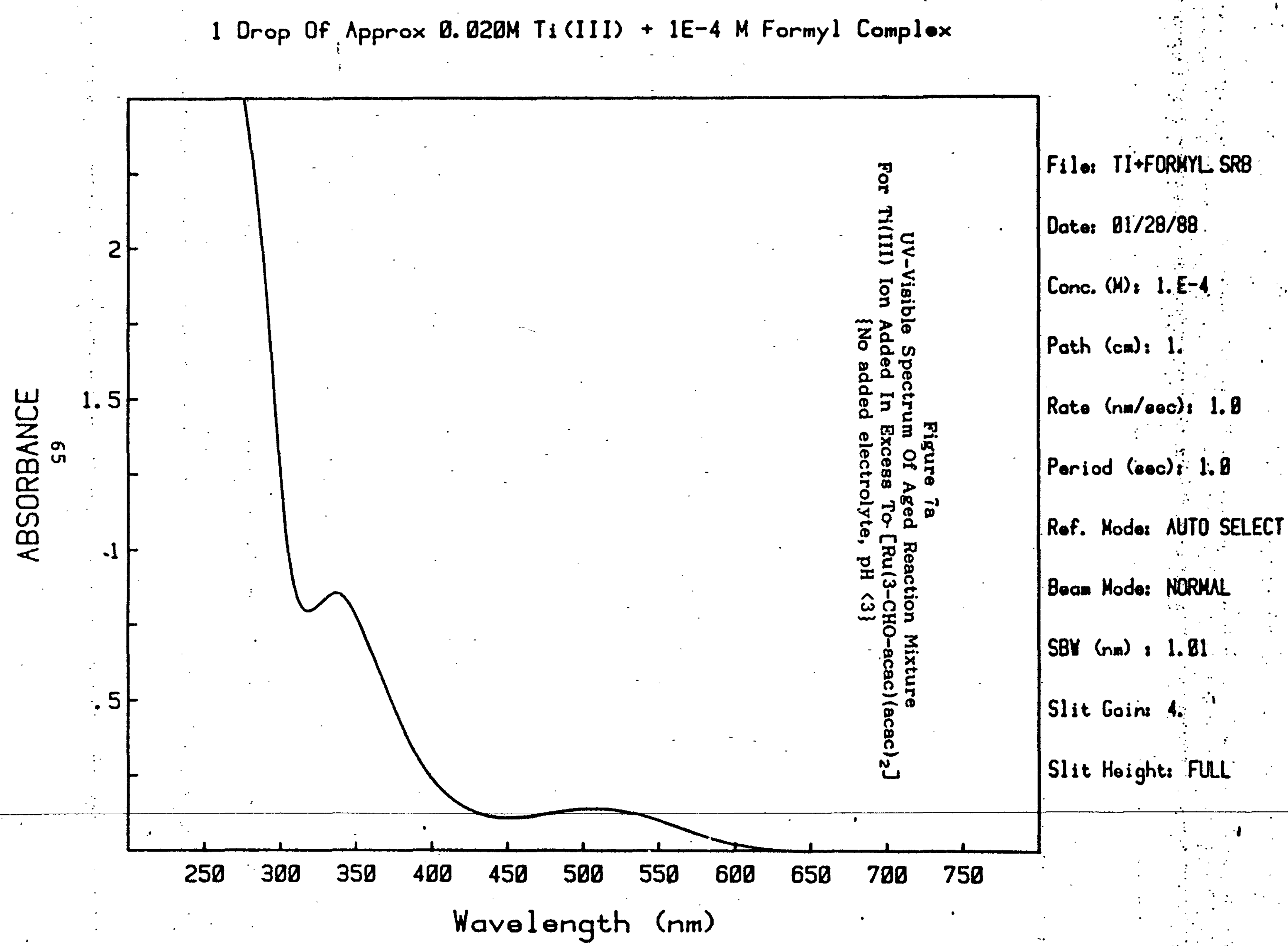

Figure 7a
UV-Visible Spectrum Of Aged Reaction Mixture
For Ti(III) Ion Added In Excess To [Ru(3-CHO-acac)(acac)$_2$]
{No added electrolyte, pH <3}

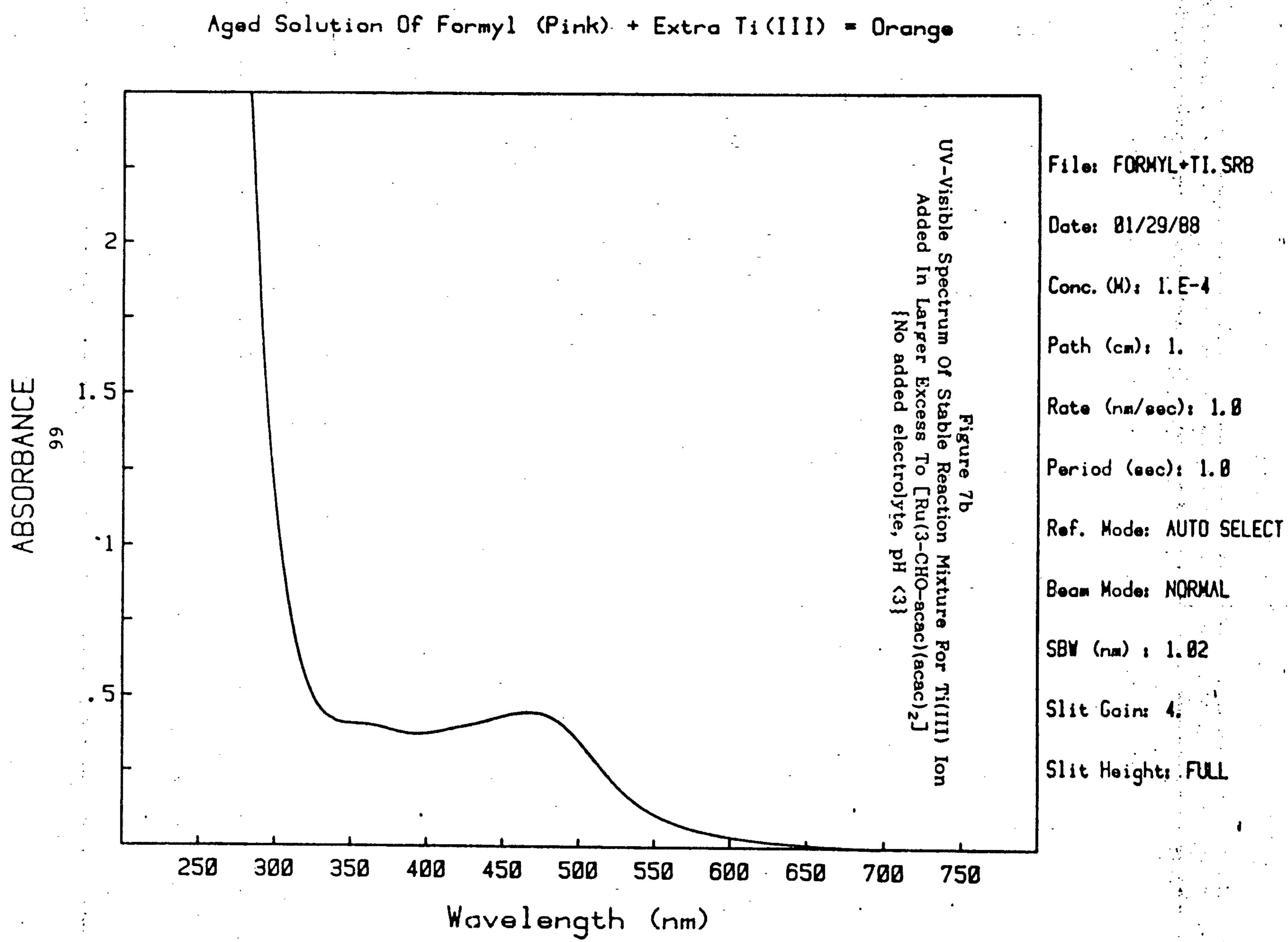

Figure 7b
UV-Visible Spectrum Of Stable Reaction Mixture For Ti(III) Ion Added In Larger Excess To [Ru(3-CHO-acac)(acac)$_2$]
{No added electrolyte, pH <3}

IV. TOXI-LAB STUDIES

A. INTRODUCTION

The purpose of this project was to rescreen numerous urine samples obtained from the Navy Drug Screening Lab (NDSL) in Norfolk, VA. These samples had already been screened for the following drugs of abuse: morphine, benzoylecgonine (cocaine metabolite), amphetamine/methamphetamine, phenobarbital, PCP, and THC metabolite by RIA (radioimmunoassay).

Since RIA is very specific for the classes of drugs mentioned above, other drug classes would go undetected, even in high concentrations. Thin layer chromatography is not as sensitive as RIA, but can detect a much broader spectrum of drugs. It is therefore a logical, rapid and inexpensive way to look for patterns of abuse among Navy personnel.

Toxi-Lab is a two-system (A,B) thin-layer chromatographic screen for a large number (250+) of commonly prescribed and often abused drugs. The A system detects basic and neutral drugs, most of which are analgesics, tranquilizers, decongestants, anti-depressants and stimulants. The B system detects acidic and neutral drugs, most of which are barbiturates or hypnotics. Toxi-Lab is often used in emergency situations in hospitals to determine what material was taken in an overdose or what materials may be ruled-out. Toxi-Lab is also finding its way into mass screening programs run by commercial laboratories. Therefore, a close examination of its potential to the screening of Navy urine specimens is warranted.

The sensitivity of Toxi-Lab ranges from 0.5 µg/ml-5.0 µg/ml per compound. Toxi-Lab uses an initial salt/solvent extraction procedure for separating the drug of interest from the urine matrix and metabolic by-products. The solvent is then evaporated onto a small disc of chromatographic paper to concentrate the extracted components. The disc, now coated with materials, is inserted into a chromatogram. The chromatogram is supplied with four other disks containing various drug standards. The chromatogram is then developed in an organic solvent to elute the unknown and the standard drugs. Various dipping procedures are then employed to reveal the compounds on the chromatogram. A positive identification is made when a spot in the unknown lane matches a standard in migration characteristics and color in all the dipping procedures.

B. RESULTS

The first 41 urine samples sent to NRL were selected to be those from potential drug abusers. They were divided into subgroups according to RIA test results:

No. of samples	Drug present
8	LSD negative
12	Low positive
12	THC 50-100 ng/ml
9	Cocaine 0-150 ng/ml

No unusual substances were found in these samples except that the cocaine urine samples had a larger number of cold tablet medications compared to the other urine samples. However, the number of urine samples is too small to come to any definite conclusions. After the first 41 samples were screened by

Toxi-Lab; another 378 samples were obtained at random. These samples had all been screened negative for drugs of abuse by RIA. The results for all 429 samples are summarized in Table 1. (Note that the total number of drugs found is greater than 429. Some samples had several drugs present.)

TABLE 1 - Toxi-Lab Results
Total # of Samples (429)

Nic	Caff	Acet	SMA	A Neg	Unconf	β-phenethyl amine conf	β-phenethyl amine unconf	B unconf	B neg
218	25	9	9	116	48	17	57	45	366
50.8%	5.8%	2.1%	2.1%	27%	11.2%	4.0%	13.3%	10.5%	85.3%

Explanation of column headings: OTC = over the counter

1. Nic = # of samples testing positive for nicotine
2. Caff = # of samples testing positive for caffeine
3. Acet = # of samples testing positive for acetaminophen
4. SMA = sympathomimetic amines; a broad class of drugs (stimulants) including amphetamine/methamphetamine and ephedrine/pseudoephedrine (found in most OTC decongestants, e.g., Bronkaid, Nyquil).
5. Neg = negative - no classifiable drugs were found.
6. Unconf = a spot of interest was detected that did not exactly match any of the 26 standards on the chromatogram.

7. β-Phenethylamine conf = of the samples sent to Analytical Systems, several (17) had a drug concentration too low to confirm, but the drug was presumed to be β-phenethylamine because of color and migration characteristics. (β-phenethylamine is a putrefaction base found here because of old, mishandled specimens.)
8. β-Phenethylamine unconf = a number of samples were sent to Analytical Systems (manufacturers of Toxi-Lab) and run against their standards. These did not match any of their known standards.
9. B unconf = dark spots that made the sample look positive for barbiturates, even though it was screened negative by NDSL.
10. B neg = nothing of interest on the B side.

1. TOXI-LAB A - BASIC DRUGS

Toxi-Lab A detects basic and neutral drugs. The most common material found was an unknown amine that appeared similar to methamphetamine in color at various detection stages and Rf. This amine was not β-phenethylamine. Examination of its mass spectrum on a number of derivatives was not helpful in determining its structure.

The electron impact mass spectrum of the trifluoroacetyl derivative is shown in Figure 1. A molecular ion is not observed. This derivative was also run by negative and positive chemical ionization. The molecular weight appears to be 329. Several possible compounds were synthesized and their mass spectra taken. In all cases, the retention time or mass spectrum was different than the unknown. A literature search uncovered several possible structures derived from β-phenethylamine. The most likely is N-acetyl-α-hydroxy-β-phenethylamine, based on the similarity of the mass spectra. However, the trifluoroacetyl derivative of this material has a molecular weight of 371 not 329. Since this material is unlikely to be a drug of abuse due to the frequency of its occurrence, no further work to determine its identity was undertaken.

Due to the degraded nature of most of the urine samples, many spots and streaks also appeared. These lowered the detection sensitivity for drugs of abuse by concealing potential drugs and gave rise to a high number of unconfirmed positives (11.2%). Presumably, all or most of these unconfirmed positives were false positives.

The use of Toxi-Lab for older urine specimens (greater than a few days old) and specimens without preservatives is called into question. Although this system is being employed by some commercial laboratories, we believe that it should not be used for routine drug screening because of the chance for testing older specimens and the large number of false positives that would result. More importantly, the lower sensitivity due to the high background in degraded samples, would generate a large number of false negatives.

Several methods for modifying the extraction methodology were tried. Most relied upon a back extraction into 1N HCL from the organic layer after the Toxi-Lab A initial extraction. The aqueous layer was then made basic and re-extracted with another Toxi-Lab A tube. This resulted in cleaner chromatograms, but it eliminated the detection of neutral drugs, an important asset for Toxi-Lab. Also, some loss in sensitivity occurred due to the two, one step extractions. The increased analysis time would be a detriment in mass screening.

2. TOXI-LAB B - BARBITURATES

Toxi-Lab B detects acidic drugs, most of which are barbiturates. Since these urine samples had been screened by RIA for barbiturates, none should be found. Over 10% of the samples had spots present that appeared exactly the same as phenobarbital. Several of these samples were tested by GC/MS and found to be negative for phenobarbital. Likewise, running the Toxi-Lab B system in an unconventional manner showed that this substance was neutral, not acidic as phenobarbital would be. This substance was not further identified.

Based upon the limited lack of confirmation by GC/MS and negative nature of these samples by RIA, it can be assumed that all of the unconfirmed positives detected by Toxi-Lab B were false positives. Since there were a large number of false positives in Toxi-Lab B, its use in mass screening can be called into question.

3. BENZODIAZEPINES

The first 200 samples were tested for benzodiazepines (Librium, Valium, etc.) by EMIT. EMIT was employed due to the lack of sensitivity of Toxi-Lab with these urine specimens and the low reported sensitivity of Toxi-Lab with this class of drugs. Benzodiazepines were screened because of their reported high abuse by the general population. The EMIT test is a homogeneous enzyme immunoassay. Since EMIT relies upon antibody-antigen reactions it tends to be quite specific. The EMIT test for benzodiazepines best detects oxazepam and the other species at three-four times higher concentrations. EMIT detects oxazepam at a level of approximately 0.3 µg/ml or more.

Of the 200 samples tested by EMIT, one was strongly positive and another sample indicated the presence of a benzodiazepine concentration below the cut-off level. These two samples were extracted using the Toxi-Lab procedure and hydrolyzed to diphenylketones with hydrochloric acid. The hydrolysis procedure destroys information on the type of benzodiazepine presence since it converts many of the benzodiazepines and their metabolites to the same diphenylketone. However, hydrolysis simplifies the mass spectrometric detection since only three diphenylketones must be examined. Also, sensitivity may be improved since many of the metabolites are converted to the same compound. Standards of Librium and Valium were also extracted and hydrolyzed to provide reference standards of diphenylketones.

Both urine samples were found to contain benzodiazepines. Neither of the two samples tested positive with the Toxi-Lab hydrolysis confirmation procedure, probably due to its lower sensitivity.

No information is available on these urine samples. Therefore, it is not known if these drugs were abused or prescription drugs. A 1% use rate for benzodiazepines bears further study as this use rate is higher than the abuse of every drug except marijuana. Also, benzodiazepines are commonly available on the street and are undetected by the current Navy drug screening program. Several benzodiazapines recently were rescheduled to Schedule 2 in light of their abuse potential.

C. CONCLUSIONS

Toxi-Lab was used to screen 429 urine samples from the Norfolk NDSL. Due to the degraded nature of many of these specimens, the reported sensitivity of Toxi-Lab could not be reached. Samples (200) were also tested by EMIT for benzodiazpines. One sample was positive and another was a suspected positive. Both were found positive by GC/MS. The use of benzodiazpines by Navy personnel warrants further study.

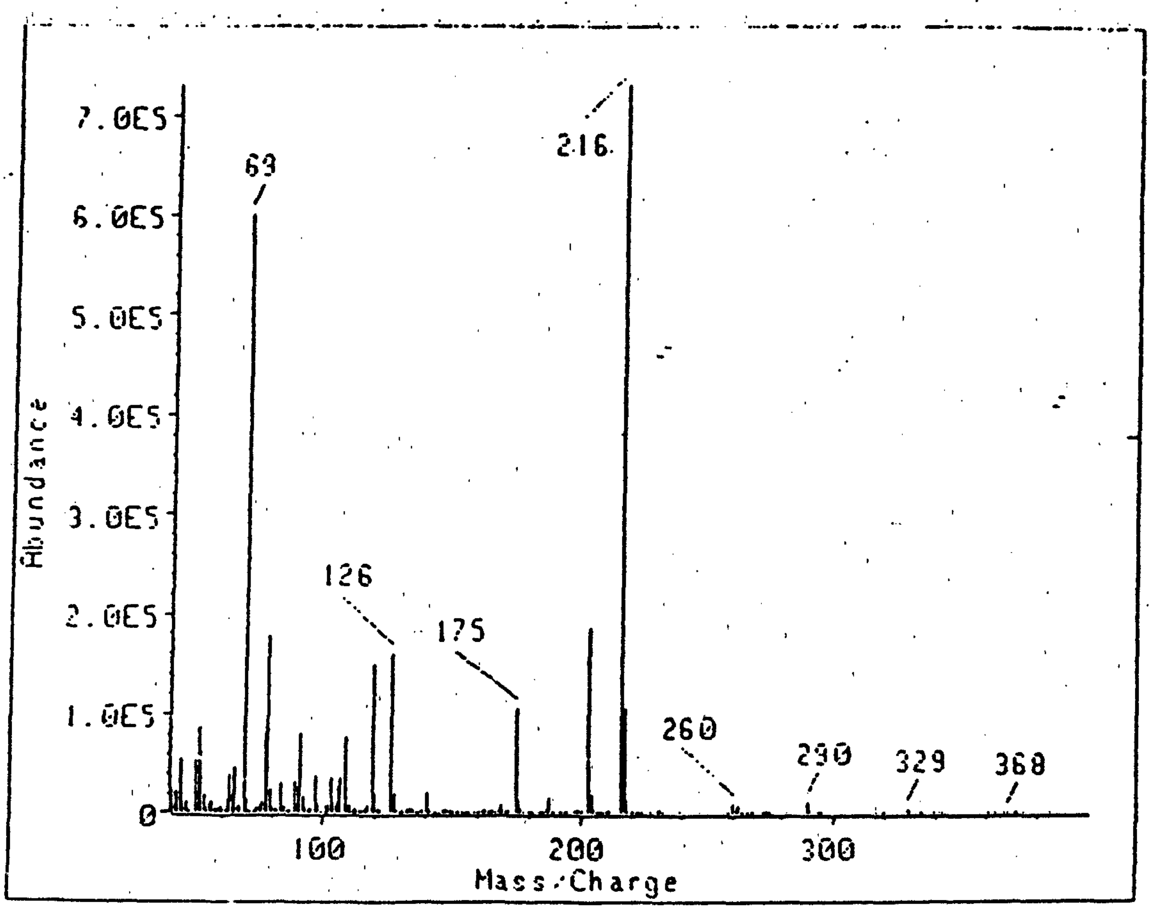

Figure 1 - EI mass spectrum of unknown amine

GEO-CENTERS, INC.

APPENDIX A

GEO-CENTERS, INC.

SURFACE CHEMISTRY AND MECHANICAL BEHAVIOR OF SILICON CARBIDE AND SILICON NITRIDE IMPLANTED WITH TITANIUM TO HIGH FLUENCES AND HIGH TEMPERATURES*

I. L. SINGER

Naval Research Laboratory, Washington, DC 20375 (U.S.A.)

(Received April 6, 1987)

Summary

Ti^+ ions have been implanted to high fluences (4×10^{17} cm^{-2} at 190 keV) into commercial SiC and Si_3N_4 substrates heated up to 900 °C. X-ray photoelectron spectroscopy depth profiles showed expected gaussian-like profiles at room temperature (approximately 45 at.% peak concentration). At the highest temperatures, solutes redistributed and phases formed consistent with the corresponding ternary phase diagrams. Implantation at room temperature softened the surfaces and reduced the indentation fracture toughness values of Si_3N_4 by about 20% but also closed cracks and pores on the surface and considerably reduced microstructural control of propagating cracks. Hot implantation produced no loss in surface hardness but some loss (10% - 25%) in indentation toughness. Heating in vacuum, however, produced oxygen depletion from both the implanted and the non-implanted surfaces of several substrates and resulted in catastrophic embrittlement of the Si_3N_4 surface.

1. Introduction

Ion implantation is capable of modifying the surface chemistry, structure and mechanical properties of ceramics. Previous investigations by researchers at Oak Ridge National Laboratory [1], at Cambridge University [2] and Toyota Laboratories [3] have demonstrated many benefits of implanting ceramics including increased surface hardness, fracture toughness and bend strength. However, while many implanted ceramics displayed increased surface toughness, *e.g.* Al_2O_3 [1 - 3], TiB_2 [1], SiC [1] and fully stabilized ZrO_2 [4], others such as glass, SiAlON and some ZrO_2 ceramics [5] showed decreased fracture toughness, particularly at high

*Paper presented at the 14th International Conference on Metallurgical Coatings, San Diego, CA, U.S.A., March 23 - 27, 1987.

0257-8972/87/$3.50

fluences. SiC and Si_3N_4, the ceramics of interest here, were expected to behave like the ceramics in the latter category, so it was necessary to investigate implantation processes which would not be so deleterious to the surface mechanical properties. One method of reducing the structural damage produced by ion implantation is to implant "hot", *i.e.* to implant into a heated substrate [6].

The influence of one implant species, Ti^+ ions, on the surface mechanical properties of SiC and Si_3N_4 implanted to high fluences and high temperatures, with the goal of improving the properties by hot implantation, is examined in this paper. Surface compositions were analyzed by X-ray photoelectron spectroscopy (XPS) sputter depth profiles, surface morphologies by optical and electron microscopies, and surface mechanical properties by indentation hardness and fracture techniques. Several effects of thermally assisted solute redistribution and phase formation on surface mechanical properties are discussed.

2. Experimental details

2.1. Substrates

Commercial SiC and Si_3N_4 substrates (SiC, ESK high-density sintered alpha; Si_3N_4, Norton NC132, MgO hot pressed, and Ceradyne 147-1, Y_2O_3 hot pressed) were polished to a 3 μm diamond finish. Several NC132 substrates, which arrived with commercially polished surfaces, were subsequently ground, lapped and repolished to generate new surfaces.

2.2. Ion implantation

Ion implantation was performed at the Naval Research Laboratory in a Varian–Extrion high current implanter. Base pressures before implantation were in the 10^{-7} Torr range. ^{48}Ti ions were implanted at 190 keV to fluences up to 4×10^{17} ions cm^{-2}. The predicted range and range straggling values for both of the substrates are about 116 nm and 36 nm respectively [7]. These parameters give peak concentrations, assuming a gaussian range distribution, of about 45 at.%.

During implantation, substrates were either held at room temperature or implanted hot. Hot implantation denotes direct heating of the substrates by the intense ion beam and is achieved by suspending the substrates in a molybdenum sheet basket during implantation. An optical pyrometer, calibrated by a thermocouple, was used to monitor the substrate temperature. During hot implantation, performed with ion current densities up to 40 μA cm^{-2}, substrates reached temperatures from 500 to 900 °C within a few minutes. For both cold and hot implantation conditions, substrates were masked in order to retain a non-implanted area of each surface. The non-implanted areas of the hot substrates were subjected to what will be called a "vacuum heating" treatment.

2.3. *Surface analysis*

The near surface composition was investigated by XPS. XPS was performed with monochromatized aluminum X-rays in a Surface Science Laboratory small-spot analyzer. Sputter depth profiling was accomplished using 3 keV Ar^+ ion bombardment. Ion milling rates were 14 nm min^{-1}, according to the depths of the ion-milled craters as measured by Michelson interferometry. Data analysis was performed using Surface Science Laboratory software routines. Binding energies were referenced to 84.0 eV for Au $4f_{7/2}$; the adventitious C 1s, observed at 284.9 ± 0.2 eV, served as a secondary standard. Composition *vs.* depth profiles were quantified by integrating the photoelectron spectra and normalizing them using Surface Science Laboratory's modified Scofield cross-sections. Rutherford backscattering (RBS) was used to verify the elemental depth profiles.

2.4. *Indentation hardness and toughness*

Knoop and Vickers indenters were used to evaluate the surface mechanical properties of the polished, titanium-implanted, ion-milled and vacuum-heated surfaces. Indentation crack lengths were measured using light microscopy. Indentation toughness values were calculated according to the formula proposed by Lawn *et al.* [8] and critically evaluated by Anstis *et al.* [9]. By this method, one measures the radial crack length c at a given load P on the Vickers diamond and computes the indentation toughness as

$$K_c = 0.016 \times \left(\frac{E}{H}\right)^{1/2}\left(\frac{P}{c^{3/2}}\right) \tag{1}$$

where E is the elastic modulus and H is the hardness. In this study, we compute the change in indentation toughness as

$$\frac{(K_c)_{\mathrm{impl}} - (K_c)_{\mathrm{non}}}{(K_c)_{\mathrm{non}}} = \left(\frac{c_{\mathrm{non}}}{c_{\mathrm{impl}}}\right)^{3/2} - 1 \tag{2}$$

Although this formulation of indentation toughness does not strictly apply to implanted layers, it does provide numbers like hardness numbers to compare various treatments.

3. Results and discussion

3.1. *General observations*

Titanium implantation at 4×10^{17} ions cm^{-2} gave a metallic luster to both cold and hot implanted substrates: both of the cold implanted substrates had a "silvery" appearance, whereas the hot SiC substrate had a dark, metallic appearance and the hot Si_3N_4 substrate developed a golden hue. Implantation also produced conductive surfaces on otherwise highly insulating Si_3N_4 (about 10^{24} Ω m). The resistance was approximately 100 Ω with a 1 cm separation of the probes of a volt–ohmmeter. Because of the high conductivity, XPS analysis could be performed without the charging problems commonly encountered with insulators.

3.2. X-ray photoelectron spectroscopy analysis of SiC and Si_3N_4

XPS sputter depth profiles of the room temperature implants into SiC and Si_3N_4 are shown in Figs. 1(b) and 2(b) respectively. The Ti profile showed the expected gaussian-like distribution, with peak concentrations from 40 to 45 at.% at a depth of 120 nm as predicted. The carbon or nitrogen and silicon concentrations dropped then rose in inverse proportion to the titanium concentration, indicating that the bulk constituents had simply been diluted by the implanted titanium. The C:Si and N:Si ratios varied systematically with the titanium concentration in XPS depth profiles but not in RBS depth profiles (not shown) of the same samples. The variations are believed to be due to preferential sputtering during ion milling in the XPS depth profiles [10]. A second feature of the profiles, oxygen depletion, was also seen in several of the commercially polished Si_3N_4 substrates. The oxygen appears to have migrated out of the peak depth region during implantation, becoming trapped near the surface. However, after grinding, repolishing and implanting, these substrates showed no oxygen depletion.

XPS sputter depth profiles in SiC and Si_3N_4 substrates heated to approximately 900 °C during titanium implantation are represented in Figs. 1(a) and 2(a). Both of these profiles differ from their room temperature counterparts (verified by RBS profiles) in ways suggesting that solute redistribution and phase formation took place during hot implantation. The SiC profile suggests TiC formation with silicon depleted from

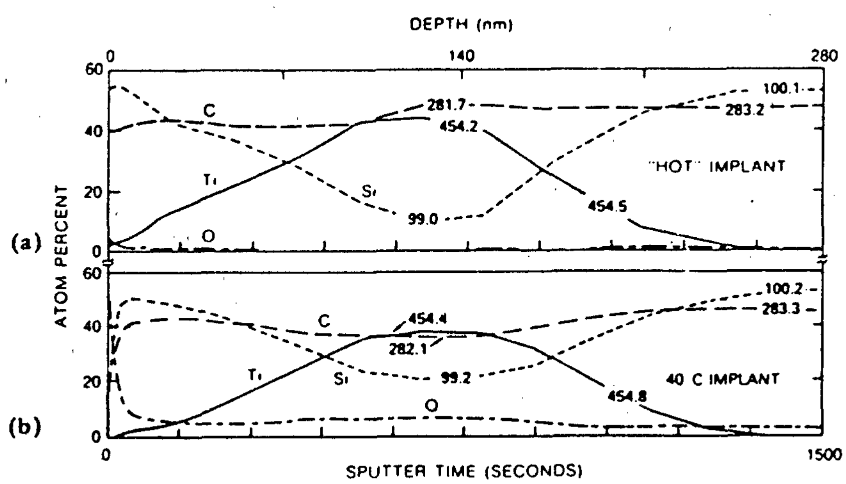

Fig. 1. XPS sputter depth profiles of titanium-implanted SiC (peak binding energy (electronvolts) is given at selected depths): (a) 900 °C implant; (b) room temperature implant.

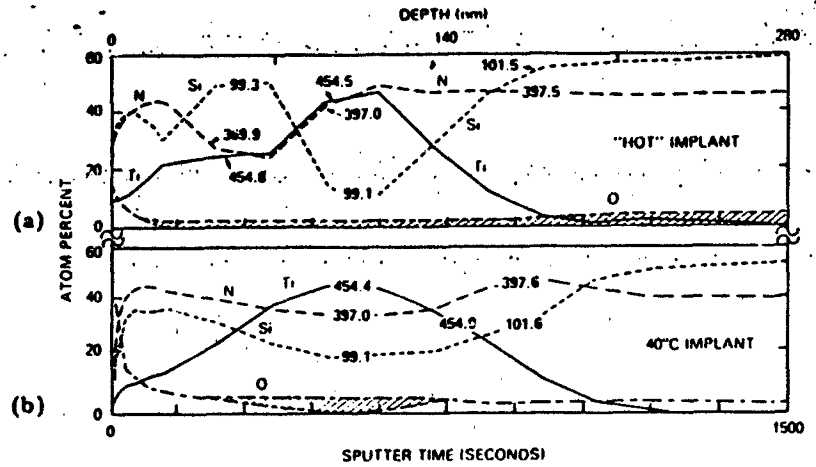

Fig. 2. XPS sputter depth profile of titanium-implanted Si_3N_4 (peak binding energy (electronvolts) is given at selected depths): (a) 900 °C implant; (b) room temperature implant.

the peak titanium concentration region. The Si_3N_4 profile appears now to have at least three layers, passing from the surface to the titanium peak-depth region: first, a thin silicon-nitride-rich layer containing titanium and a small amount of oxygen; next a layer probably containing TiN + Si in approximately equal concentrations; finally, a layer containing TiN (and probably titanium) and some silicon.

The hot implantation profile of Si_3N_4 is consistent with phases predicted by the ternary phase diagram for Ti–Si–N at 700 - 1000 °C [11]. (It should be noted that there is an error in the Ti–Sn–N drawing in ref. 11, Fig. 4. The position of Si_3N_4 along the N–Si line was incorrectly placed at 33% Si and actually belongs at 43% Si.) The reaction of titanium with Si_3N_4 should produce the following:

$$Si_3N_4 + Ti \longrightarrow Si_3N_4 + TiN + Si \quad 0\% < [Ti] < 36\%$$

$$Si_3N_4 + Ti \longrightarrow TiN + Si + TiSi_2 \quad 36\% < [Ti] < 45\%$$

These phases are consistent with the binding energies obtained from the XPS data, given at selected depths in Figs. 1 and 2, and from reference compounds listed in Table 1. In particular, the binding energy for titanium at lower concentrations is that of TiN, while at maximum concentration it shows a mix of TiN and probably titanium silicide. Similar arguments can be made for phase formation in titanium-implanted SiC.

A second finding from sputter depth profiles was that, in the commercially polished substrates (those that showed oxygen depletion in the room temperature implants), the oxygen concentration rapidly fell to zero and remained there. XPS sputter depth profiles of the non-implanted

TABLE 1

Binding energies for photoelectrons of silicon, titanium, nitrogen and carbon

Photoelectron	*Binding energies* (eV)		
	Metal	*Nitride*	*Carbide*
Si 2p	99.1[a, b], 99.4[c]	102.1[c]	100.2[d], 100.2[b]
Ti $2p_{3/2}$	453.9[a]	454.9[a], 454.7[b]	454.8[a]
N 1s	—	397.1[b] (TiN)	—
C 1s	—	—	281.2[a] (TiC)

[a]Reference 12.
[b]Present work.
[c]Reference 10.
[d]Reference 13.

portions of these substrates also showed oxygen depletion, indicating that substrate heating (in vacuum), and not ion implantation, caused the oxygen depletion. Several Si_3N_4 substrates were later ground, lapped and repolished; they did not show oxygen depletion after hot implantation. These results suggest that grinding and/or polishing can destabilize the oxygen chemistry in sintered or hot-pressed ceramics.

In summary, titanium implantation was capable of forming unique surface alloys in SiC and Si_3N_4. XPS analysis suggested that a solid state reaction occurs, *i.e.* titanium bonds replaced silicon bonds to nitrogen and, at high temperatures, the atoms redistributed, allowing the thermodynamically stable phases to begin to form. The golden coloration of the hot titanium-implanted Si_3N_4 substrate supports the interpretation of the XPS data that TiN was formed.

3.3. Surface mechanical properties

3.3.1. Surface morphology: SiC

The shiny black, polished surface, as seen by the naked eye, was observed in a microscope to contain many pits and protrusions. Surface textures around Vickers indents exemplify the brittleness of the surface. Grain pull-out, circumferential cracking and radial cracking occurred at low loads (less than 1 N). Cracks propagated along pores, second phases or grain boundaries, indicating that propagation in the surface is controlled by the near-surface microstructure. Similar microstructural control of indentation fracture has been observed by Naylor and Page [14] in hot-pressed and reaction-bonded SiC substrates.

Heating these commercially polished SiC substrates in vacuum to temperatures above 500 °C smoothed the surface considerably but also increased the brittleness of the surface. Around Vickers indents, the radial cracks became more jagged and circumferential cracks more pronounced. These features are readily seen in Fig. 3, a scanning electron microscopy (SEM) stereo micrograph of a Vickers' indent (at 4.9 N) in the non-

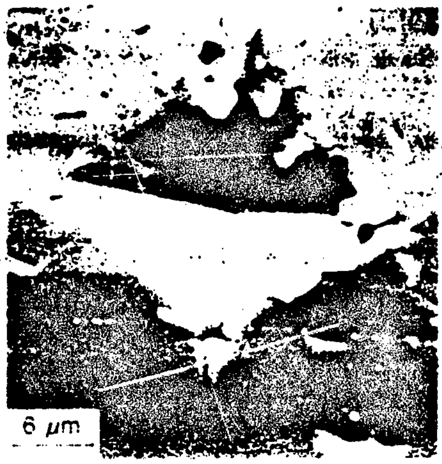

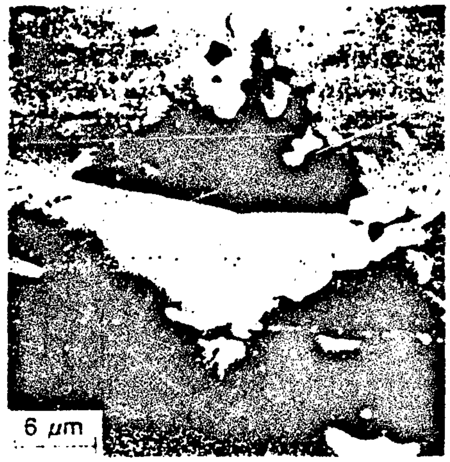

(a) (b)

Fig. 3. SEM stereo pair of a Vickers' indent (at 4.9 N) in sintered SiC vacuum heated to 900 °C.

implanted portion of a substrate heated in vacuum to 900 °C. At higher loads, chunks of material often popped out of the indented surface.

Both cold and hot titanium implantation into SiC substrates greatly reduced grain pull-out and circumferential cracking and decreased the microstructural control of radial crack propagation. Chipping, observed on the long edge of Knoop indents, was replaced by extrusion, indicating plastic flow of the titanium-implanted surface. Roberts and Page [15] have reported similar resistance to chipping for high fluence, room temperature implants of N^+ and B^+ into SiC.

The increased resistance to chipping is illustrated dramatically in Fig. 4, which shows Vickers indents (at 49 N) in the hot implanted surface and in an ion-milled crater on the same surface. While chipping was suppressed and radial cracks were less jagged on the implanted surface, the brittle textures that typified non-implanted surfaces had returned in the ion-milled crater.

3.3.2. *Surface morphology: Si_3N_4*

As happened on SiC, polishing left the Si_3N_4 surfaces quite pitted and, in certain areas, particle-like protrusion could be seen. In contrast, titanium implantation closed polishing pores and Vickers-induced radial cracks as seen in the optical micrographs in Fig. 5. In particular, Fig. 5(b) illustrates the closing of radial cracks by implantation: Fig. 5(a) shows an indent before implantation and the middle photo shows the same indent after implantation. The closing of cracks is believed to be due to subsurface compressive stresses that developed in response to implantation-induced surface tension; however, a quantitative discussion of these effects is beyond the scope of this paper. Implantation also reduced the microstructural control of

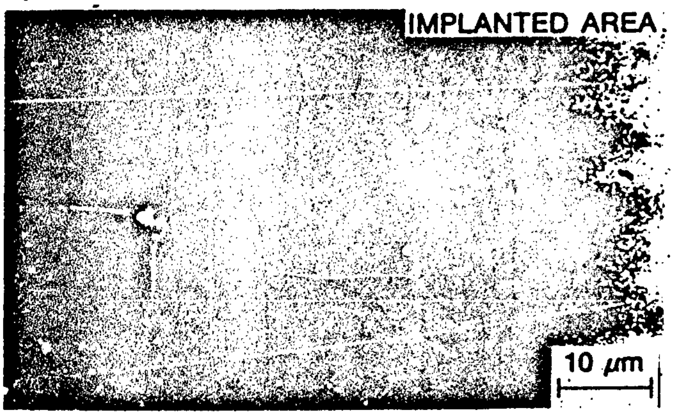

(a)

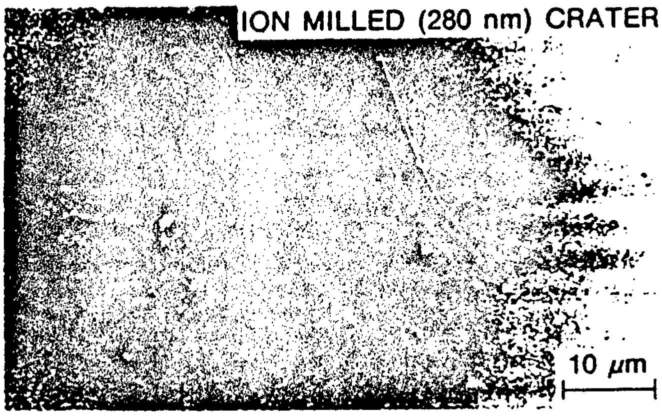

(b)

Fig. 4. Optical micrographs of Vickers indents (at 49 N) in hot titanium-implanted (900 °C) sintered SiC: (a) implanted surface; (b) ion-milled crater.

propagating cracks, similar to that reported by Burnett and Page [5] for titanium-implanted SiAlONs.

Vacuum heating to 900 °C produced no significant morphology changes in most Si_3N_4 substrates. However, several substrates from one batch of Si_3N_4 developed brittle surfaces after heating to temperatures greater than 500 °C in vacuum. Figure 6 shows both optical and SEM micrographs of surfaces of one such substrate heated to 900 °C during implantation. Both implanted and non-implanted areas developed a network of cracks, with quilt-like patches from 20 to 50 μm in diameter. Crack propagation around indentations was deflected by, then followed, the borders of the patches. The surfaces became extremely smooth, making them quite transparent and enabling one to see features several micrometers below the surface (*e.g.* subsurface lateral cracks in Fig. 6(b)). These surfaces were the same

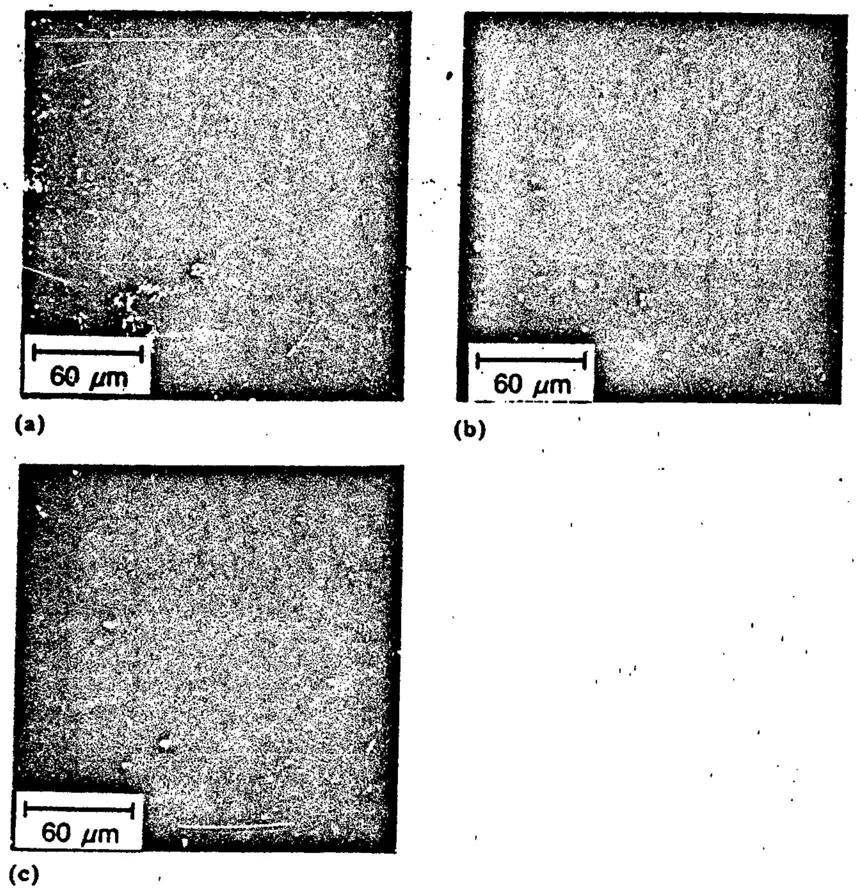

Fig. 5. Optical micrographs of Vickers indents (at 49 N) in hot-pressed Si_3N_4: (a) non-implanted; (b) indented then titanium implanted; (c) titanium implanted then indented.

as those found to be oxygen depleted. Not all Si_3N_4 substrates became embrittled during vacuum heating. However, those which did also showed oxygen depletion, leading us to speculate that loss of oxygen led to embrittlement of the surface. At present, however, we do not know what caused these substrates to lose oxygen.

3.3.3. Swelling

Implantation at room temperature caused the surfaces of both SiC and Si_3N_4 to swell about 70 ± 10 nm, similar to values reported for high fluence implants into SiC [15, 16] and Al_2O_3. However, no swelling was observed on substrates implanted at high temperatures. The swelling is attributed to the accumulation and retention of defects, consistent with the "atomic stuffing" depth profiles observed during room temperature implantation. The absence of swelling in the hot implanted substrates is consistent with

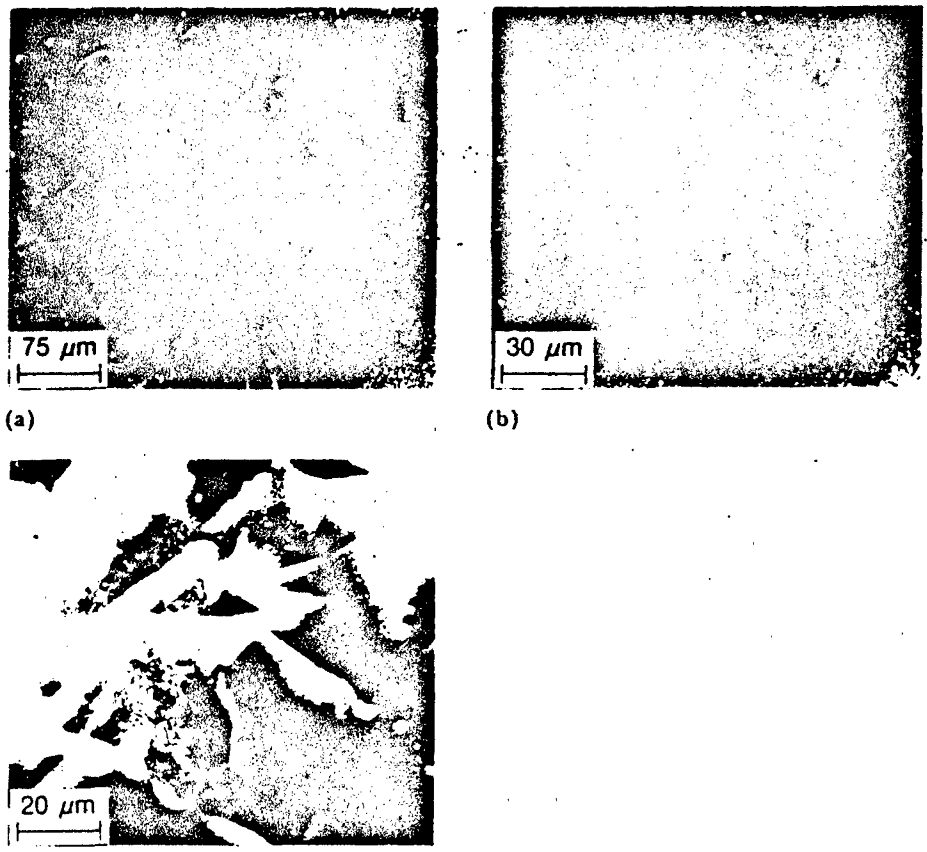

(a) (b) (c)

Fig. 6. Micrographs of Vickers indents in surfaces of hot-pressed Si_3N_4 heated to 900 °C in vacuum: Nomarski micrographs of 4.9 N indents in (a) non-implanted and (b) titanium-implanted areas; (c) SEM micrograph of 0.20 N indent in non-implanted area.

the removal of defects during the solute redistribution and phase formation that occurred at higher temperatures.

3.3.4. Surface hardness

The near-surface hardness of the SiC and Si_3N_4 substrates was measured with a Knoop indenter at loads of 150 mN and 98 mN respectively. The indenter penetrated 200 - 300 nm into the surface, comparable with the implantation depth. As seen in Table 2, room temperature titanium implantation lowered the surface hardness of both SiC and Si_3N_4. Hot implantation did not lower the hardness of SiC significantly and appears to have returned the hardness of Si_3N_4 to its room temperature value. The recovery of surface hardness after hot implantation is probably due to the avoidance of amorphization, which is responsible for softening ceramic substrates [6]. Vacuum heating lowered the hardness of all Si_3N_4

TABLE 2

Knoop hardness of titanium-implanted SiC and Si_3N_4

Area indented	Hardness[a] of SiC (HK)		Hardness[a] of Si_3N_4 (HK)	
	$T < 40$ °C	$T = 900$ °C	$T < 40$ °C	$T = 900$ °C
Non-implanted	42 ± 2	45 ± 3	29 ± 6	23 ± 7
Ti^+	24 ± 2	38 ± 5	23 ± 5	28 ± 2

[a]Load, 0.15 N.

substrates, both oxygen depleted and non-depleted, for reasons not at present understood.

3.3.5. Indentation toughness

Indentation toughness measurements were performed with a Vickers' indenter at loads from 10 to 98 N. The indentation toughness values were calculated from crack lengths measured at a load $P = 49$ N. The results, too lengthy to present in this paper, are summarized in Table 3. Indentation toughness values decreased by 10% - 25% for all the implant conditions except for the room temperature SiC implant, which showed no change in indentation toughness. In addition, non-implanted Si_3N_4 surfaces that were oxygen depleted by vacuum heating had indentation toughness values 15% - 25% lower than the original surfaces.

XPS depth profiles might provide insight into the toughness of hot-pressed Si_3N_4 and sintered SiC. Since oxygen depletion led to increased brittleness of the surface in many substrates, it is tempting to suggest that the oxide phase(s) contribute to the toughness of these materials. We note that the room temperature SiC implant, which did not lose oxygen from the implanted layer, was the only substrate that showed no drop in indentation toughness. It would be useful to learn whether the glasses [17], SiAlONs and ZrO_2 ceramics [5] that lost fracture toughness after implantation might also have lost oxygen during implantation.

TABLE 3

Indentation toughness changes of titanium-implanted SiC and Si_3N_4

Substrate	SiC	SiC	Si_3N_4	Si_3N_4
Implantation temperature	< 40 °C	900 °C	< 40 °C	900 °C
Indentation toughness change	None	Decreased 15% - 20%	Decreased 20% - 25%	Decreased 10% - 25%

. Summarizing remarks and conclusions

Composition and morphology studies of high fluence titanium nplantation indicate atomic stuffing of the lattice at room temperature but ignificant solute redistribution and phase formation at the higher temperaures (up to 900 °C). The swelling observed on room temperature implants, ut lost in high temperature implants, is consistent with defect removal ccompanying solute redistribution. Recovery of surface hardness at high emperatures is probably due to phase formation and defect removal.)xygen destabilization, which may result from grinding or polishing, appears o contribute to decreased fracture toughness.

\cknowledgments

I would like to thank Mike Gardos (Hughes Aircraft) for the motivation o investigate such messy engineering materials, and DARPA for providing inancial support. I am also deeply appreciative of the hospitality, facilities nd learning environment provided by the Department of Materials Science nd Metallurgy, Cambridge, England. I am especially grateful to Dr. Trevor 'age and his students for their advice and assistance during my stay in Camoridge last year. I also thank Rich Colton (Naval Research Laboratory) or helping me to acquire the XPS data, Bob Gossett for RBS analysis, Cathy Pollock (Geo-Centers) for preparing most of the samples and John Vegand (Geo-Centers) for assistance in obtaining the indentation data.

References

1 C. S. Yust and C. J. McHargue, *J. Am. Ceram. Soc.*, *67* (1984) 117.
2 P. J. Burnett and T. F. Page, *J. Mater. Sci.*, *19* (1984) 3524.
3 T. Hioki, A. Itoh, M. Ohkubo, S. Noda, H. Doi, J. Kawamoto and O. Kamigaito, *J. Mater. Sci.*, *21* (1986) 1328.
4 K. O. Legg, J. K. Cockran, H. F. Solnick-Legg and X. L. Mann, *Nucl. Instrum. Methods, Phys. Res. B*, *7 - 8* (1985) 535.
5 P. J. Burnett and T. F. Page, in E. A. Almond (ed.), *Science of Hard Materials*, Adam Hilger, Bristol, 1986, p. 789.
6 C. J. McHargue, G. C. Farlow, C. W. White, J. M. Williams, B. R. Appleton and H. Naramoto, *Mater. Sci. Eng.*, *69* (1985) 123.
7 I. Manning and G. P. Mueller, *Comput. Phys. Commun.*, *7* (1974) 85.
8 B. R. Lawn, A. G. Evans and D. B. Marshall, *J. Am. Ceram. Soc.*, *63* (1980) 574.
9 G. R. Anstis, P. Chantikul, B. R. Lawn and D. B. Marshall, *J. Am. Ceram. Soc.*, *64* (1981) 533.
0 L. Kubler, R. Huag, E. K. Hill, D. Bolmont and G. Gewinner, *J. Vac. Sci. Technol. A*, *4* (1986) 2323.
1 R. Beyers, R. Sinclair and M. E. Thomas, *J. Vac. Sci. Technol. B*, *2* (1984) 781.
2 *PHI Handbook of X-ray Photoelectron Spectroscopy*, Perkin–Elmer, Eden Prairie, MN, 1979.
3 Y. Mizokawa, K. M. Geib and C. M. Wilmsen, *J. Vac. Sci. Technol. A*, *4* (1986) 1696.

14 M. G. S. Naylor and T. F. Page, *J. Microsc.*, *130* (1983) 345.
15 S. G. Roberts and T. F. Page, *J. Mater. Sci.*, *21* (1986) 457.
16 C. J. McHargue and J. M. Williams, *Proc. Mater. Res. Soc.*, *7* (1982) 303.
17 T. Jensen, B. R. Lawn, R. L. Dalglish and J. C. Kelly, *Radiat. Eff.*, *28* (1976) 245.
B. R. Lawn and E. R. Fuller, *J. Mater. Sci.*, *19* (1984) 4061.

ce and Coatings Technology, 33 (1987) 469 - 477

IPOSITION, STRUCTURE AND WEAR RESISTANCE OF Al–4V IMPLANTED WITH CARBON OR BORON TO HIGH DOSES*

BOLSTER, I. L. SINGER and R. G. VARDIMAN
' *Research Laboratory, Washington, DC 20375-5000 (U.S.A.)*
:ived March 23, 1987)

mary

High-dose ion implantation of carbon or boron into Ti–6Al–4V alloy uced flat-topped concentration profiles indicating considerable solute tribution. Carbon implantation produced precipitates of TiC, which me a continuous layer at the highest doses. This layer showed very high ;ion resistance, at least 70 times that of the substrate. Boron implanta- ; generated increasingly dense layers of TiB_2 dispersed in amorphous ium. Boron and lower-dose carbon provided appreciable increases in resistance (by about ten times). Wear of these ultra-adherent but thin s (less than 300 nm) was not uniform.

troduction

Ion implantation has been shown to improve the tribomechanical erties of a wide variety of engineering materials [1 - 3]. Its most nota- uccesses have generally been obtained in those engineering alloys known heir poor wear resistance; titanium and its alloys are prime examples. ous tribomechanical studies of ion-implanted titanium have focused on on implantation, which has been shown to harden the surface [4 - 7], ase durability during sliding wear [8 - 13] and greatly improve the)sive wear resistance of prosthetic devices [14 - 16]. The best results are :ved at highest doses where nearly continuous layers of TiN are formed 7 - 19].

This investigation examined two other interstitial implant species, n and carbon, capable of improving the wear resistance of titanium s. High-dose B^+ [20, 21] and C^+ [22] implantations are known to form le and carbide precipitates, and titanium borides and carbides are known : harder than and, perhaps, more wear resistant than titanium nitride is

Paper presented at the 14th International Conference on Metallurgical Coatings, iego, CA, U.S.A., March 23 - 27, 1987.

8972/87/$3.50

[23]. Previous studies have shown, with one exception [11], that C^+ implantation provides comparable tribomechanical benefits with N^+ [16, 24]. Moreover, C^+ implantation has been shown to benefit the fatigue resistance of α-Ti by strengthening the surface [22]. Some tribological benefits of B^+ implanted titanium have also been reported [25].

The purpose of this paper is to demonstrate the benefits of implanting B^+ or C^+ to high doses into the alloy Ti–6Al–4V. Doses for B^+ implants were chosen to give peak concentrations capable of forming TiB and TiB_2 and doses for C^+ implants were chosen to give peak concentrations up to that needed to form TiC. Although there is evidence that post-implantation heat treatments can benefit tribomechanical properties [12, 24], we restricted this study to unannealed, room-temperature implants.

2 Experimental procedure

Samples of mill-annealed Ti–6Al–4V (Ti–11.2at.%Al–3.8at.%V) alloy from two sources were used. They were similar in hardness and abrasive wear resistance. The samples were machined disks, 12.7 mm in diameter and 2.8 mm thick, ground, fine ground, and polished with 3 μm diamond to a steady-state finish on the polishing machine to be used for the abrasive wear studies.

Ion implantations were performed in the Naval Research Laboratory high current Varian–Extrion implanter. Polished Ti–6Al–4V disks were mounted on a water-cooled holder and the target chamber was cryogenically pumped to pressures of 2×10^{-6} Torr or better. B^+ ions were implanted at 40 keV to doses of 8×10^{17} cm^{-2} or 16×10^{17} cm^{-2}, and C^+ ions at 50 keV or 75 keV to doses of $(2 - 8) \times 10^{17}$ cm^{-2}. Concentrations at peak depth predicted from range straggling data (Table 1 and Appendix give details) varied from 56 to 71 at.% for B^+ and from 21 to 52 at.% for C^+.

Auger sputter depth profiles were performed using Ar^+ ion milling. Compositions were computed by standard normalization procedures using sensitivity factors obtained from well-characterized TiC films and

TABLE 1

Range R_p, range straggling ΔR_p and peak concentrations for Ti–6Al–4V implanted with $^{11}B^+$ or $^{12}C^+$ [26]

Ion	*B^+*		*C^+*	*C^+*		
Energy (keV)	40		50	75		
R_p (nm)	104		109	151		
ΔR_p (nm)	44		41	52		
Dose ($\times 10^{17}$ cm^{-2})	8	16	6	2	4	8
Peak concentration (at.%)	56	71	51	21	35	52

TiB_2 substrates: S(Ti420 eV)/S(B) = 2.2 and S(Ti420 eV)/S(C) = 1.0 were used on data obtained with a 2 keV electron beam. Depth scales, where given, were obtained from depths of ion-milled craters measured interferometrically; uniform sputtering rates were assumed.

To prepare specimens for transmission electron microscopy (TEM), the surfaces of polished, then implanted; disks were sliced off using a thin diamond saw, mechanically polished on the sawed surface, cut in 3 mm disks, and electrolytically thinned from the unimplanted side. These were then examined in a 200 keV electron microscope and selected area electron diffraction (SAD) patterns taken.

Abrasive relative wear resistances (RWRs) were determined by polishing of the sample disks with 3 μm diamond paste [27 - 29]. In this procedure, implanted and reference (non-implanted) disks were polished simultaneously under controlled conditions. Wear depth increments of 10 nm could be resolved. Most of the experiments were done with three implanted and six reference disks.

The boron and high-dose (8×10^{17} cm^{-2}) carbon-implanted surfaces were polished on the wheel polisher with a pressure of 6400 Pa and a mean speed of 23 cm s^{-1}. Low-dose (2×10^{17} cm^{-2}) carbon-implanted surfaces were polished on the wheel polisher at 2700 Pa and 10.9 cm s^{-1}, and on a vibratory polisher with a pressure of 6400 Pa. The implanted surfaces were examined at various wear depths for changes in surface texture, hardness and composition.

3. Results and discussion

3.1. Composition

Composition *vs.* depth profiles for C^+ implanted Ti-6Al-4V, shown in Fig. 1 for medium and high doses, evolved with increasing dose from a

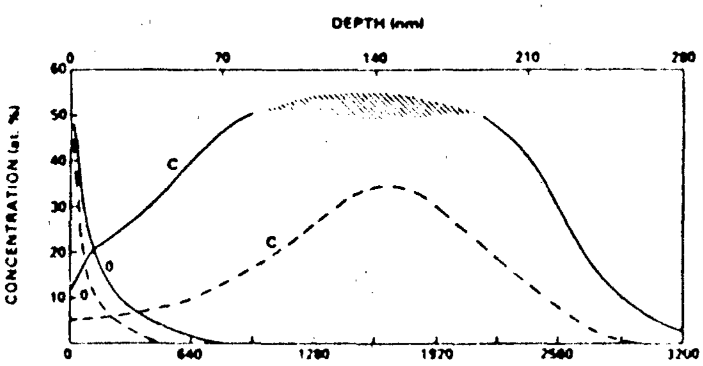

Fig. 1. Composition *vs.* depth profiles for 75 keV carbon ions implanted in Ti-6Al-4V at two doses: — — —, nominally 2×10^{17} cm^{-2}; ——, 8×10^{17} cm^{-2}.

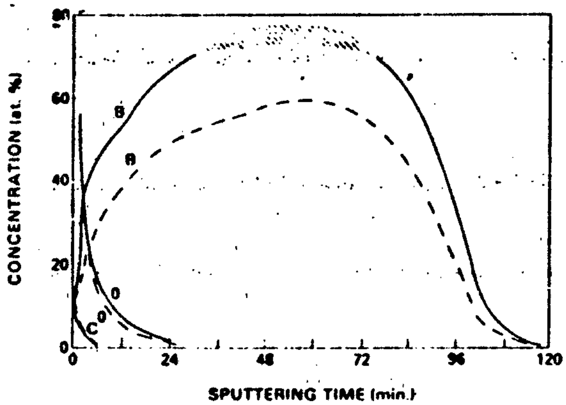

Fig. 2. Composition *vs.* depth profiles for 40 keV boron ions implanted in Ti–6Al–4V at two doses: – – –, 8×10^{17} cm^{-2}; ——, 16×10^{17} cm^{-2}.

slightly broadened gaussian to a near flat-top distribution as the maximum concentrations approached 50 at.%, suggesting considerable redistribution of (solute) carbon. (The apparent retained dose is approximately twice the nominal implanted dose for reasons as yet unexplained.) The lineshape of the carbon (KLL) Auger spectrum was like that of titanium carbide up to carbon concentrations of about 50 at.%. At higher concentrations, the carbon (KLL) lineshape indicated admixtures of elemental carbon, which, for the highest dose implant, led to the uncertainty in peak concentrations (indicated by the cross-hatched region of the profile curve). The peak concentration was found in the predicted range near a depth of 140 nm. The 6×10^{17} cm^{-2} profile for 50 keV C^+ (not shown) was identical with that of 8×10^{17} cm^{-2} at 75 keV, except for the shorter range. Finally, infusion of oxygen was seen for C^+ implantation at these high doses.

Composition *vs.* depth profiles for 40 keV B^+ implants to 8×10^{17} cm^{-2} and 16×10^{17} cm^{-2} are shown in Fig. 2. (No depths were measured, but it was assumed from the projected range data that the peak boron concentration lies near 100 nm.) At both doses, the boron profiles are considerably broader than a gaussian, indicating considerable redistribution of (solute) boron, especially toward the surface. The lineshape of the boron (KLL) Auger spectra were like that of titanium boride, up to boron concentrations of about 65 - 70 at.%. At higher concentrations, the boron (KLL) lineshape indicated significant admixtures of elemental boron, which again led to the uncertainty in peak concentrations for the higher-dose implant (indicated by the cross-hatched region of the profile curve). Infusion of oxygen (but not carbon) is seen at both doses, far more than is found in non-implanted substrates.

3.2. Structure

The structure of the Ti–6Al–4V implanted layer for the carbon dose of 2×10^{17} ion cm^{-2} at 75 keV has been reported previously [22]. This and the current TEM structure observations are summarized in Table 2. At

TABLE 2

Summary of phases observed by TEM for carbon and boron implantations of Ti-6Al-4V

Implant	*Dose* (ion cm^{-2})	*Energy* (keV)	*Matrix*	*Precipitate*	*Size* (nm)
C^+	2×10^{17}	75	α Ti	TiC	5 - 20
C^+	6×10^{17}	50	TiC	—	
B^+	8×10^{17}	40	Amorphous	TiB_2	10 - 30
B^+	1.6×10^{18}	40	Amorphous	TiB_2	30 - 100

6×10^{17} ion cm^{-2} carbon (50 keV), the TiC layer was continuous, and SAD showed α titanium spots only from the thickest parts of the foil which remained electron-transparent. A continuous TiC layer was also found for a carbon dose of 7×10^{17} ion cm^{-2} at 75 keV.

For the boron dose of 8×10^{17} ion cm^{-2}, a diffuse ring indicating an amorphous matrix was readily apparent in the diffraction pattern. All crystalline ring reflections indexed to TiB_2. At 1.6×10^{18} ion cm^{-2}, the amorphous ring was much weaker, and the TiB_2 reflections stronger, corresponding to the observed increase in size and density of the precipitate. No indication of the TiB phase was found, in agreement with results of Okamoto *et al.* [21].

The formation and growth of TiC and TiB_2 precipitates may account for the observed broadening and flattening of the carbon and boron concentration profiles. As the precipitates grow, they occupy larger volumes than the metal matrix (16% for TiC and 47% for TiB_2). Compressive stresses, generated symmetrically about the peak depth (the likely nucleation depth) combined with lowered solubility in the precipitated phase and radiation-assisted segregation would drive the solutes initially towards the surface. At higher doses, solute drag by defects may reverse the flow towards the internal precipitate–matrix interfaces [7]. Therefore, at high doses, one might expect broad, uniform distributions even for single energy implants (with the caveat that some blistering may occur at high doses).

3.3. *Abrasive wear resistance*

Two abrasive wear experiments with low-dose carbon implanted in Ti–6Al–4V were done with the vibratory polisher, and one with the wheel polisher at higher speed and lower load. All the results were similar. The data from the wheel polisher are shown in the lower curve of Fig. 3. Each point shown is the mean of the data for three disks. The peak RWRs with the vibratory polisher were 7 and 8, at depths of 80 and 120 nm.

The high-dose carbon implant produced the much greater effect shown by the upper curve in Fig. 3. Its peak RWR value was comparable (70 and 66 respectively) with that of a sputter-deposited TiN film (from W. Sproul, Borg–Warner Corporation) polished with the same reference disks. Moreover,

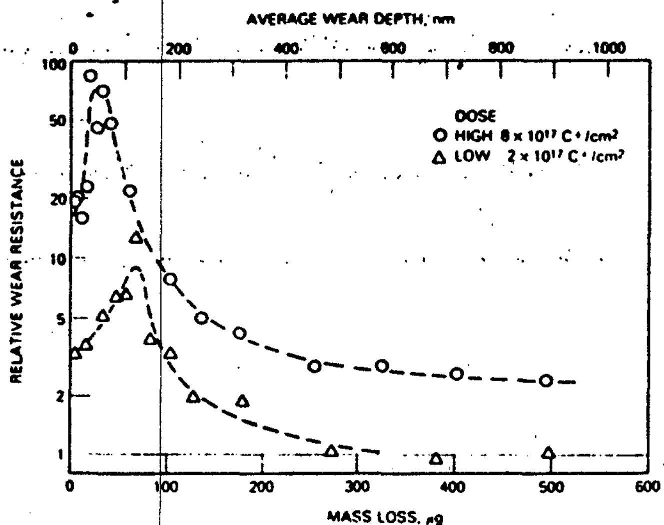

Fig. 3. Abrasive wear resistance *vs.* mass loss and average wear depth of Ti–6Al–4V implanted with high and low doses of carbon ions at 75 keV.

this RWR value far exceeds the largest RWR increases measured in previous implantation studies: about 10 for titanium-implanted AISI M2 tool steel [30] and titanium-implanted 304 stainless steel [27], and about 6 for titanium-implanted 52100 bearing steel [31].

At depths beyond the peak, the implanted layer began to wear non-uniformly, with some portion of the bare substrate exposed. After 100 μg of wear, two distinct zones on the titanium disks were visible to the naked eye. The curves are therefore plotted as functions of mass loss rather than of wear depth. The corresponding average wear depth is given at the top. Although one might expect that polishing in such a controlled manner would remove material layer by layer, this is not the case for ion-implanted Ti–6Al–4V. Although the initial segments of the RWR curves reflect the RWR of the more wear-resistant implanted layer, the rapid drop in the high-dose curve and the shallow peak depth relative to the carbon concentration shown in Fig. 1 indicate that wear of the substrate was occurring. Tailing of the curve is also the result of this composite wear process. After 400 - 500 μg of wear, these disks were still about half-covered by the wear-resistant layer, resulting in RWRs of around 2. Auger sputter depth profiles of the remaining layer (not shown) indicated that only 50 nm of the implanted layer had been worn away. This wear depth also matches the depth of the RWR curve peak.

Boron implantation also produced large increases, from 8 to 13 times, in the RWR of Ti–6Al–4V. With the boron implantations, however, the RWR peaks, shown in Fig. 4, did not differ greatly between high and low doses, the curves being similar to that of the low-dose carbon. (The mass loss scale of Fig. 4 is half that of Fig. 3.) One anomalous result is that, in one run with the high dose, two of the three disks had very low mass losses,

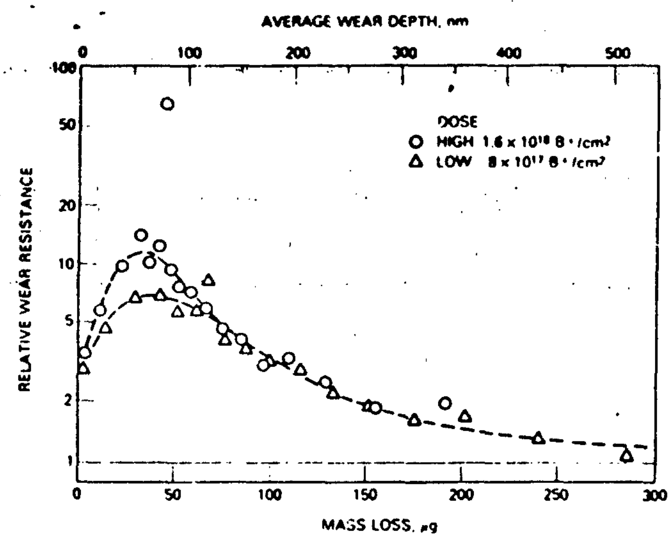

Fig. 4. Abrasive wear resistance *vs.* mass loss and average wear depth of Ti–6Al–4V implanted with high and low doses of boron ions at 40 keV.

producing the point at an RWR of 65. Non-uniform wear was also observed with the B^+-implanted layer, as with the C^+-implanted layer, suggesting that non-uniform wear may have reduced the apparent RWRs beyond the peak depth. Again, the RWR peaks are at shallower depths than would be expected from Fig. 2.

Two implications may be drawn from the non-uniform wear behavior during polishing of hard, thin layers on softer substrates. Firstly, the RWR curves may give only lower bounds on the maximum wear resistance of the implanted layer. The larger the RWR of the implanted layer, the less likely the true RWR would be measured. Secondly, because polishing does not produce uniform layer-by-layer wear, composition analysis of polished surfaces may not be used indiscriminately to assess migration of implanted species during wear [13].

4. Conclusions

Implantation of Ti–6Al–4V with carbon or boron to very high doses produces a thick implanted layer (about twice the projected range) with a nearly uniform carbon or boron distribution. In the carbon-implanted layer, TiC precipitates grow in a titanium matrix ultimately to a continuous TiC layer at highest doses. In the B^+-implanted layer, TiB_2 precipitates grow in an amorphous titanium matrix toward a uniform TiB_2 layer.

The high dose C^+ implant, corresponding to a continuous TiC layer, produced the largest increase in wear resistance of the implants studied. Its wear resistance was comparable with if not greater than a TiN film produced by physical vapor deposition. Moreover, from a production point of view, the C^+ implant required less than half the dose (*i.e.* half the implantation time and cost) that the highest dose B^+ implant required. However, the B^+ implant, even at 8×10^{17} cm^{-2}, provided a respectable improvement (eight times) in wear resistance for Ti–6Al–4V. In addition, the B^+-implantation process produced an amorphous matrix, which may be beneficial where corrosion accelerates the wear process, *e.g.* in prosthetic components.

Acknowledgments

We thank Randy Walker and the NRL Materials Modification and Analysis Branch for implantation of the samples, Catherine Pollock and John Wegand for assisting with the abrasive wear measurements, and Pete Ehni and Nancy Finnegan (DOE Center for Microanalysis of Materials, Urbana, IL) for obtaining some of the Auger data.

References

1 I. L. Singer, in G. K. Hubler, O. W. Holland, C. R. Clayton and C. W. White (eds.), *Ion Implantation and Ion Beam Processing of Materials*, North-Holland, New York, 1984, p. 585.
2 G. K. Hubler and F. A. Smidt, *Nucl. Instrum. Methods Phys. Res. B*, *7/8* (1985) 151.
3 S. T. Picraux, *Am. Rev. Mater. Sci.*, *14* (1984) 335.
4 J. B. Pethica, in V. Ashworth, W. Grant and R. Procter (eds.), *Ion Implantation into Metals*, Pergamon, Oxford, 1982, p. 147.
J. B. Pethica and W. C. Oliver, in S. T. Picraux and W. J. Choyke (eds.), *Metastable Materials Formation by Ion Implantation*, Elsevier, New York, 1982, p. 373.
5 J. B. Pethica, R. Hutchings and W. C. Oliver, *Nucl. Instrum. Methods*, *209/210* (1983) 995.
6 R. Hutchings, W. Oliver and J. B. Pethica, in R. Kossowsky and S. C. Singhal (eds.), *Surface Engineering*, Martinus Nijhoff, Boston, 1984, p. 170.
7 J. C. Pivin, F. Pons, J. Takadoum and H. M. Pollock, *J. Mater. Sci.*, *22* (1987) 1087.
8 S. R. Shepard and N. P. Suh, *J. Lubr. Technol.*, *104* (1982) 29.
9 R. Hutchings and W. C. Oliver, *Wear*, *92* (1983) 143.
10 W. C. Oliver, R. Hutchings and J. B. Pethica, *Metall. Trans. A*, *15* (1984) 2221.
11 W. C. Oliver, R. Hutchings, J. B. Pethica, E. L. Paradis and A. J. Shuskus, in G. K. Hubler, O. W. Holland, C. R. Clayton and C. W. White (eds.), *Ion Implantation and Ion Beam Processing of Materials*, North-Holland, New York, 1984, p. 705.
12 R. Martinella, G. Chevallard and C. Tosello, in G. K. Hubler, O. W. Holland, C. R. Clayton and C. W. White (eds.), *Ion Implantation and Ion Beam Processing of Materials*, North-Holland, New York, 1984, p. 711.
13 S. Fayeulle, *Wear*, *107* (1986) 61.
14 P. Sioshansi, R. W. Oliver and F. D. Matthews, *J. Vac. Sci. Technol. A*, *3* (1985) 2670.
15 J. M. Williams and R. Buchanan, *Mater. Sci. Eng.*, *69* (1985) 237.
16 J. M. Williams, R. A. Buchanan and E. D. Rigney, in R. F. Hochman (ed.), *Ion Plating and Implantation*, American Society of Metals, Metals Park, OH, 1986, p. 141.
17 R. Hutchings, *Mater. Sci. Eng.*, (1985) 129; *Mater. Lett.*, *1* (1983) 137.
18 J.-P. Gauthier, D. Fleche, J. Pivot and J.-A. Roger, *Vacuum*, *34* (1984) 1013.
19 B. Rauschenbach and K. Hohmuth, *Phys. Status Solidi A*, *94* (1986) 833.

20 J. G. Han, R. F. Hochman and S. D. Antolovich, in R. F. Hochman (ed.), *Ion Plating and Implantation*, American Society of Metals, Metals Park, OH, 1986, p. 189.
21 S. Okamoto, A. Kawai, K. Kobayashi, M. Takata, T. Yamashita and S. Yamashita, *J. Am. Ceram. Soc.*, *66* (1983) C78.
22 R. G. Vardiman and R. A. Kant, *J. Appl. Phys.*, *53* (1982) 690.
23 H. Holleck, *J. Vac. Sci. Technol. A*, *4* (1986) 2661.
24 R. G. Vardiman, in G. K. Hubler, O. W. Holland, C. R. Clayton and C. W. White (eds.), *Ion Implantation and Ion Beam Processing of Materials*, North-Holland, New York, 1984, p. 699.
25 A. K. Suri, R. Nimmagadda and R. F. Bunshah, *Thin Solid Films*, *64* (1979) 191.
26 J. F. Ziegler, J. P. Biersack and U. Littmark, Pergamon, New York, 1985 (TRIM version 2.1).
27 R. N. Bolster and I. L. Singer, *ASLE Trans.*, *24* (1981) 526.
28 R. N. Bolster and I. L. Singer, in T. R. Shives and M. B. Peterson (eds.), *Mechanical Properties, Performance, and Failure Modes of Coatings*, Cambridge University Press, Cambridge, 1984, p. 201.
29 I. L. Singer, R. N. Bolster, S. A. Wolf, E. G. Skelton and R. A. Jeffries, *Thin Solid Films*, *107* (1983) 207.
30 I. L. Singer, R. N. Bolster, J. A. Sprague, K. Kim, S. Ramalingam, R. A. Jeffries and G. O. Ramseyer, *J. Appl. Phys.* *58* (1985) 1255.
31 I. L. Singer, R. N. Bolster and C. A. Carosella, *Thin Solid Films*, *73* (1980) 283.

Appendix

The maximum concentration of implanted ions, assuming a gaussian range distribution, occurs at a depth given by the projected range. This peak concentration N_p (*i.e.* at peak depth) depends only on the range straggling ΔR_p and dose, and is calculated as

$$N_p = \frac{0.4 \times \text{dose}}{\Delta R_p}$$

The peak atomic percentage concentration for ions I which enter a lattice interstitially can be calculated as

$$[\mathrm{I}] = \frac{N_p}{N_p + \rho}$$

where ρ is the atomic density of the unimplanted lattice. For Ti–6Al–4V, an atomic density of $\rho = 5.76 \times 10^{22}$ atom cm^{-3} was assumed.

Note added in proof

Non-destructive composition depth profiles of carbon-implanted Ti–6Al–4V have been obtained by Rutherford backscattering spectroscopy (RBS) (R. Gossett, May 1987) in order to quantify better the high dose profile data. RBS values for the peak carbon concentrations in the high dose implants (6×10^{17} cm^{-2} at 50 keV and 8×10^{17} cm^{-2} at 75 keV) were about 67 at.%. For the lower dose implants, RBS values agreed to better than 10% with Auger values. RBS also indicated a 10% - 20% narrower straggling range for the high dose implants than that obtained by Auger sputter depth profiles. We attribute the "broadening" of the Auger profiles in Figs. 1 and 2, where uniform sputtering was assumed, to slower sputtering rates of the TiC and TiB_2 phases relative to the metallic titanium phase.

COMPOSITION AND STRUCTURE OF Si_3N_4 IMPLANTED WITH Ti^+ AT 900°C.

I.L. SINGER, R.G. VARDIMAN AND C.R. GOSSETT
Naval Research Laboratory, Washington, DC 20375.

ABSTRACT

Ti^+ ions were implanted to high fluences (up to $5 \times 10^{17}/cm^2$) into Si_3N_4 substrates heated to around 900°C. Composition vs depth profiles were obtained by RBS (in conjunction with RUMP analysis) and microstructures were examined by TEM. At a fluence of $4 \times 10^{17}/cm^2$, the Si concentration was considerably reduced at the Ti peak depth but enriched near the surface. By $5 \times 10^{17}/cm^2$, Si was nearly depleted from the implanted layer, leaving a Ti-rich nitride layer merging continuously into Si_3N_4. TEM detected TiN precipitates up to several µm in diameter, and coherent with Si_3N_4 crystallites. A Si-Ti-N ternary phase diagram is used to interpret the observed solid state reactions.

INTRODUCTION

Ion implantation is capable of modifying the surface chemistry, structure and mechanical properties of ceramics. Investigations by researchers at Oak Ridge National Laboratory[1], at Cambridge University[2] and Toyota Laboratories[3] have demonstrated many benefits of implanting ceramics including increased surface hardness, fracture toughness and bend strength. These enhanced properties can be lost, however, if the implantation fluence gets too high and the surface becomes amorphous.[4,5] One method of reducing the structural damage produced by ion implantation is to implant "hot," that is implant into a heated substrate.[6] We recently took this approach to investigate the influence of Ti^+ ions on the surface mechanical properties SiC and Si_3N_4 implanted to high fluences and at high temperatures.[7] One unexpected result was that Si appeared to be quite mobile in hot implanted Si_3N_4, but not in hot implanted SiC. This mobility warranted further examination of the phases formed during hot implantation.

This paper examines in more detail the chemistry and structure of Ti implanted Si_3N_4 at high fluences and high temperatures. Near surface compositions were analyzed by RBS, a quantitative nondestructive depth profiling technique ideally suited for implants of heavier atoms into lighter solids. Microstructures were obtained by transmission electron microscopy (TEM) and diffraction. Solute redistribution and phase formation accompanying high fluence implantation is discussed in terms of the Si-N-Ti ternary-phase diagram.

EXPERIMENTAL

Commercial Si_3N_4 substrates (Norton NC132, hot-pressed with MgO) were polished to a 3-µm diamond finish. Ion implantation was performed at NRL in a Varian/Extrion high current implanter. Base pressures before implantation were in the 10^{-7} Torr range. ^{48}Ti ions were implanted at 170 or 190 keV to fluences up to 5×10^{17} ions/cm². The predicted range and range straggling values are about 115 nm and 35 nm[8], giving peak concentrations, assuming a gaussian range distribution, up to 60 at. %.

During implantation, substrates were either heat sunk on a well-cooled substrate holder (T ≤ 40°C) or implanted "hot." "Hot" implantation denotes direct heating of the substrates by an intense ion beam and is achieved by thermally isolating substrates in a suspended Mo sheet basket during implantation. An optical pyrometer, calibrated by a thermocouple, was used to monitor the substrate temperature. During "hot" implantation, performed with ion current densities up to 40 μA/cm², substrates reached temperatures between 800 and 900 °C within a few minutes.

Composition vs depth profiles were obtained by RBS using 2.00 MeV-alpha particles. Spectra were obtained in a coplanar geometry at 30°, to 60° grazing exit to enhance depth resolution. The spectra were fit by the simulation program RUMP[9]. Depth scales at the top of the figures were calculated using the atomic density of 9.6×10^{22} atoms/cm³ for Si_3N_4 which differs from that of TiN (1.05×10^{23} atoms/cm³) by less than 5%.

For TEM studies, disks 3 mm in diameter received a fine mechanical polish on the side to be implanted, then after implantation were ground to a thickness of 100 μm on the unimplanted side. The implanted face was then masked and the back side ion milled to perforation. Masking was done with a silicon rubber compound applied wet with a hardening catalyst and removed with freon.

RESULTS

Composition vs depth profiles of Si_3N_4 implanted with Ti to high fluences are shown in Figs. 1 and 2. To illustrate the effects of substrate temperature, Fig. 1 presents compositions obtained at a fluence of 4×10^{17}/cm² with 190 keV Ti ions in substrates held at T<40°C (left) and beam heated to about 900°C (right). The lower temperature profile gives the expected gaussian-like Ti distribution, with Si_3N_4 diluted in proportion to the incorporated Ti. The hot implantation profile, in contrast, suggests that three or four distinct layers were formed. Hot implantation clearly promoted solute redistribution. In particular, Si appears to have been displaced from the Ti-rich layer and moved towards the surface. This profile resembles the layered structure found when Ti was reacted with Si_3N_4 at these temperatures.[10,11]

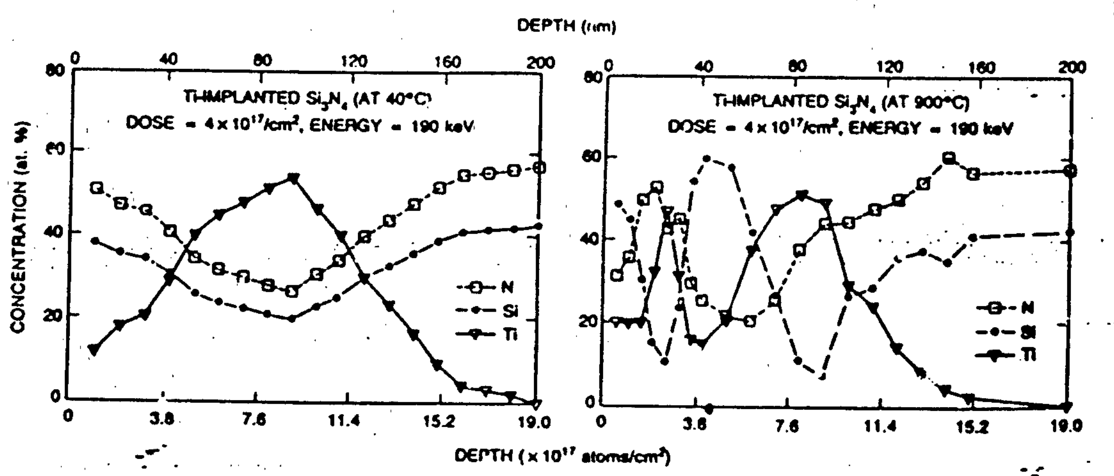

Fig. 1. RBS depth profiles of Si_3N_4:Ti^+ (4×10^{17}/cm² at 190 keV). Left, substrate temperature ≤ 40°C; right, Substrate temperature approximately 900°C.

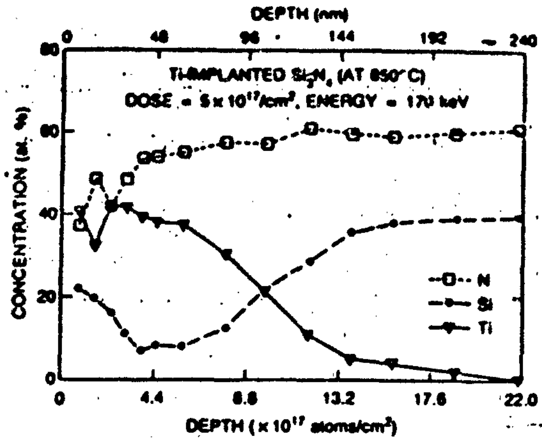

Fig. 2. RBS depth profile of Si_3N_4:Ti$^+$ ($5 \times 10^{17}/cm^2$ at 170 keV, sample temperature approximately 850°C).

At a fluence of $5 \times 10^{17}/cm^2$ with 170 keV Ti ions, the hot implantation profile (Fig. 2) looked more like a "sputter limited" curve, but with most of the near-surface Si missing. The fall off in the Si profile as it enters the Ti-rich layer suggests that the elemental Si might have moved to the surface then desorbed into the vacuum during implantation. The composition achieved is that of a Ti-rich nitride layer merging continuously with a Si nitride substrate.

TEM studies of the hot implanted Si_3N_4 ($5 \times 10^{17}/cm^2$) showed TiN present as both fine particles approximately 10-50 nm in diameter (Fig. 3) and as large grains several microns in size (Fig. 4). No amorphous material was observed. Si_3N_4 was detected in some diffraction patterns, usually showing coherency with any large TiN particles present, as seen in Fig. 5. However, it cannot be definitely ascertained from these results whether the pattern arose from Si_3N_4 present in the implanted layer or from the underlying substrate.

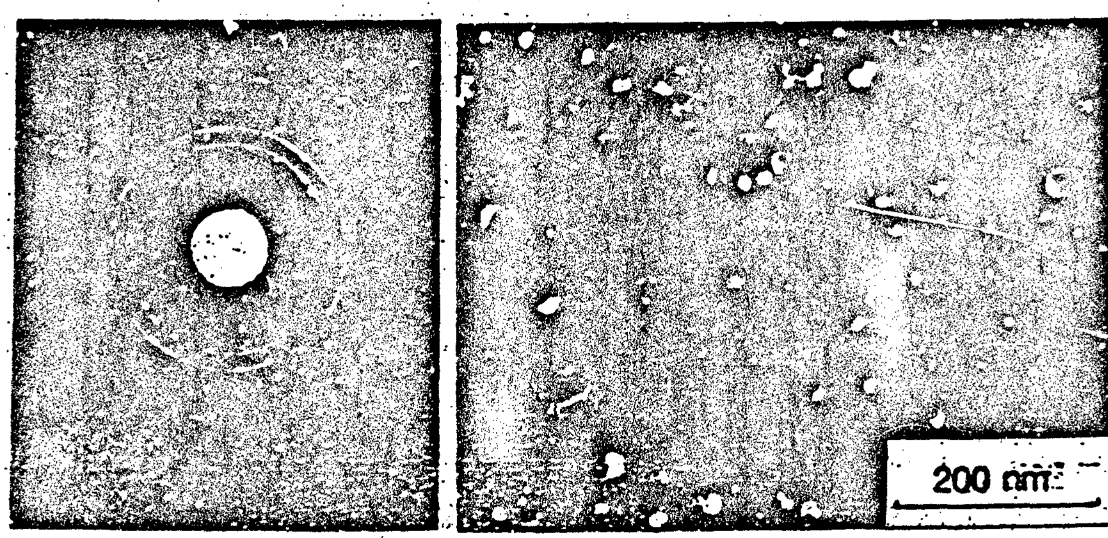

Fig. 3. Dark Field TEM micrograph imaged using the two inner rings (111 and 200) of the inset electron diffraction pattern. Si_3N_4 spots can be seen just inside the innermost (111) ring.

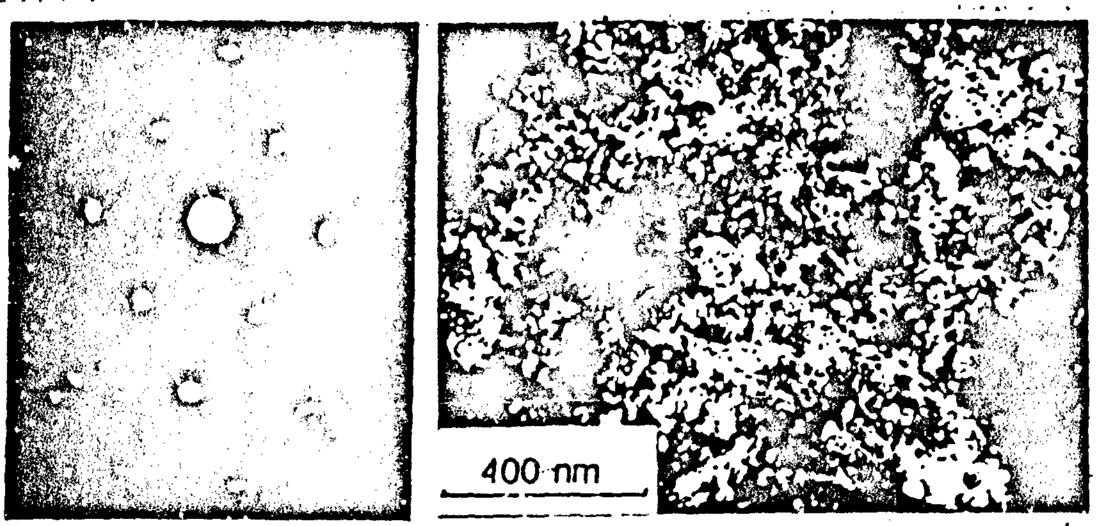

Fig. 4. Dark field TEM micrographic showing a large TiN grain. Inset diffraction pattern shows a (110) orientation for the grain.

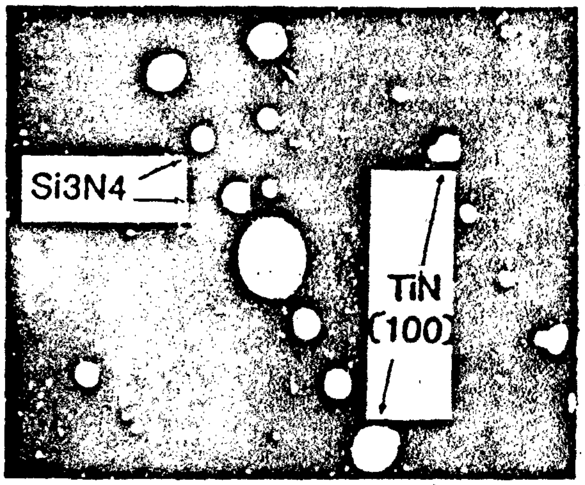

Fig. 5. Electron diffraction pattern showing both Si_3N_4 and TiN reflections. TiN pattern is (100), and Si_3N_4 reflections show coherency with TiN.

DISCUSSION

Predicted Phases. An idealized model is presented here for assessing the phases expected in Ti-implanted Si_3N_4. A ternary phase diagram calculated for the Si-N-Ti system at temperatures between 700 and 1000°C is shown in the upper right of Fig. 6. Although calculated phase diagrams are oversimplifications, this one has been shown consistent with phases observed at 1000°C in Ti-metallized Si_3N_4[12].

We have used this diagram to compute the thermodynamically stable phases expected for Ti-implanted Si_3N_4 assuming no elemental redistribution. The compositions obtained by alloying Si_3N_4 with Ti fall on the dashed line drawn from the Ti corner to Si_3N_4. Implanting Ti at 170 keV to a fluence of 5 x $10^{17}/cm^2$ into Si_3N_4 would give, to a first approximation, a gaussian profile with a peak concentration of about 60 at % centered at a depth of 120 nm. Using this gaussian profile (depicted schematically along the dashed line), we have calculated and presented in Fig. 6 the phases expected at each depth. At Ti concentrations up to 36 at %, Si_3N_4 decomposes to TiN and Si. At higher Ti concentrations, Si_3N_4 no longer appears but Ti silicides and Ti_2N are present.

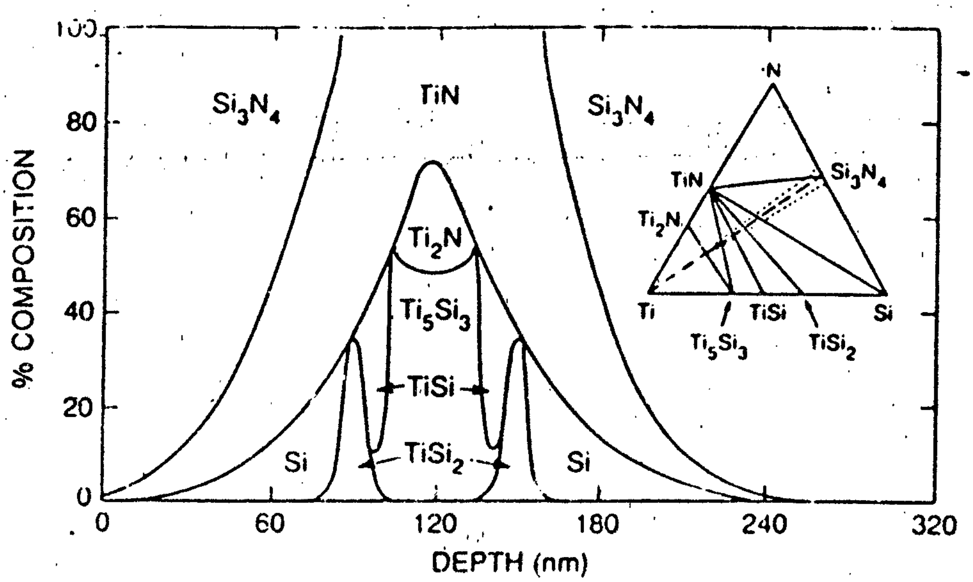

Fig. 6. Predicted phase vs depth profile for Si_3N_4:Ti^+ (5 x $10^{17}/cm^2$ at 170 keV). Inset shows ternary phase diagram for Ti-N-Si with schematic of elemental Ti profile used to compute the phase profile.

Actual Phases. In fact, the only two phases observed for the highest fluence (5 x $10^{17}/cm^2$) hot implanted Si_3N_4 were TiN and Si_3N_4. The TiN phase would account for the golden coloration observed on the hot-implanted surface. The presence of coherent, crystalline phases and the absence of amorphous material in the implanted layer is attributed to hot implantation. Room temperature implantation of Si-based covalent ceramics such as SiC and Sialon produces an amorphous phase at fluences two orders of magnitude lower than used here.[5] Thus, hot implantation in the 900°C temperature range can provide sufficient defect annealing to produce crystalline surfaces. The absence of Ti silicide phases or Ti_2N may be due to a non-ideal composition: The peak Ti concentration is lower than predicted (40 vs 60 at %) and substantial quantities of Si have been lost from the implanted layer. Although not examined in detail in this study, Si depletion has previously been seen from silicides[13] and SiC[14] heated in vacuum above 800°C and during sputtering of Ti-implanted Si_3N_4.[7]

A reexamination of the ternary phase diagram (in Fig. 6) for Ti implanted into a Si-depleted Si_3N_4, i.e. the actual composition of the implanted layer, would now predict high concentrations of TiN and some Si_3N_4, as observed and, perhaps, free N (e.g. N_2 gas). And, in hindsight, the ternary phase diagram could have forewarned of possible Si redistribution. Free Si, according to the ternary phase diagram, is a thermodynamically stable decomposition product of the Ti/Si_3N_4 reaction. By contrast, free Si is not a stable decomposition product of SiC alloyed with Ti,[15] and parallel studies conducted on Ti-implanted SiC showed no Si solute redistribution under identical hot implantation conditions[7]. Ternary phase diagrams, therefore, should be valuable for predicting solute redistribution during high temperature implantation of alloys where elemental constituents, and not compounds, are stable decomposition products.[16]

SUMMARY AND CONCLUSIONS

A crystalline TiN layer has been formed in the surface of Si_3N_4 by implanting Ti to high fluences into a beam-heated substrate. The TiN layer merged continuously into the underlying Si_3N_4 substrate and, in places, exhibited coherence with Si_3N_4. This composition was brought about by the loss of Si from the implanted layer. Ternary phase diagrams proved useful in accounting for both the phases formed and the Si solute redistribution.

ACKNOWLEDGEMENT

I.L.S. would like to thank John Vegand for sample preparation, Colette Einloth for programming the ternary phase calculations and DARPA for financial support.

REFERENCES

1. C.S. Yust and C.J. McHargue, J. Am. Ceram. Soc., 67, 117 (1984).
2. P.J. Burnett and T.F. Page, J. Mater. Sci., 19, 3524 (1984).
3. T. Hioki, A. Itoh, M. Ohkubo, S. Noda, H. Doi, J. Kawamoto and O. Kamigaito, J. Mater. Sci., 21, 1328 (1986) .
4. P. J. Burnett and T. F. Page, in Science of Hard Materials, edited by E.A. Almond (Adam Hilger, London, 1986) p. 789.
5. P.J. Burnett and T.F. Page, Radiat. Effects, 97, 283 (1986)
6. C.J. McHargue,G.C. Farlow, C.W. White, J.M. Williams, B.R. Appleton, H. Naramoto Mater. Sci. Eng., 69, 123 (1985).
7. I.L. Singer, Surf. Coat.and Tech. 33, 487 (1987).
8. I. Manning and G.P. Mueller, Computer Phys. Commun. 7, 85 (1974).
9. L.R. Doolittle, Nucl. Instrum. and Methods, B9, 344 (1985).
10. A.E. Morgan, E.K. Broadbent, and E.K. Sadana Appl. Phys. Lett. 49, 1236 (1986).
11. J.C. Barbour, A.E.T. Kuiper, M.F.C. Willemsen, and A.H. Reader Appl. Phys. Lett. 50, 953 (1987).
12. R. Beyers, R. Sinclair and M.E. Thomas, J. Vac. Sci. Technol. B2, 781 (1984). [Note an error in the Ti-Sn-N drawing in Fig. 4. The position of Si3N4 along the N-Si line was incorrectly placed at 33% Si and actually belongs at 43% Si.]
13. A.E.T. Kuiper, G.C.J. van der Ligt, W.M. van de Wijgert, M.F.C. Willemsen and F.H.P.M. Habraken, J. Vac. Sci. Technol. B3, 830 (1985).
14. Kazuhisa Miyoshi and Donald H. Buckley, Applications of Surf. Sci. 10, 357 (1982).
15. E. Rudy, Ternary Phase Equilibria in Transition Metal-B-C-Si Systems, Part V,Technical Report AFML-TR-65-2 (Air Force Materials Lab, Wright-Patterson Air Force Base, OH, May 1969), p. 522.
16. I.L. Singer and J.H. Wandass (unpublished).

Prob. # 61-25[illegible]

INDENTATION FRACTURE AND NEAR SURFACE CHEMISTRY OF Ti-ION IMPLANTED ENGINEERING Si_3N_4 AND SiC

I. L. Singer
Naval Research Lab.
Washington DC 20375.

ABSTRACT

The surface mechanical behavior of ion-implanted Si_3N_4 and SiC has been investigated by indentation fracture techniques. Ti ions were implanted to a high dose (near 50 at.% peak concentration) into substrates at room temperature and at 900°C. In a sintered alpha-SiC, implantation reduced the grain pullout, circumferential cracks and microstructural control of radial cracks characteristic of Vickers indents in nonimplanted surfaces. Implantation was particularly effective in reducing the surface brittleness caused by heating SiC substrates to 900°C in vacuum. Implantation into a hot-pressed Si_3N_4 ceramic reduced the critical load for radial cracking under Vickers indentation from about 10 N to 1 N and decreased the indentation fracture toughness values for Si_3N_4 substrates implanted at room temperature from 5 to less than 4 $MPa\text{-}m^{1/2}$. On the other hand, room temperature implantation apparently produced compressive stresses sufficiently large to close pores on the surface and considerably reduced microstructural control of propagating cracks. Both implanted and nonimplanted surfaces of Si_3N_4 exposed to high temperatures in the vacuum became embrittled, developing a quilt-like texture, with patches from 20 to 50 um in diameter. XPS depth profiles indicated that heating in vacuum depleted the subsurface of oxygen (presumably from the grain boundaries). The depth profiles also indicated that TiN and TiC formed during high temperature Ti implantation of Si_3N_4 and SiC, respectively.

1. INTRODUCTION

Ceramics, by virtue of their light weight, high strength, thermal stability and hot hardness have great potential as triboelements in moving mechanical assemblies. However, ceramics generally have rather poor surface mechanical properties: they tend to fail catastrophically by surface chips, cracks, and by releasing sharp abrasive particles with subsequent high wear rates Moreover, engineering ceramics are not monolithic solids i.e. they have many other phases (glasses, sintering agents, milling impurities), and these other phases can and often do control both surface mechanical properties and oxidation behavior. This research effort was undertaken to understand the surface-controlled failure modes of engineering ceramics operating at high (850°C) temperatures, with the goal of designing surface treatments capable of improving tribological behavior.

Ion implantation is a surface treatment capable of modifying the tribomechanical behavior of ceramics. Researchers at Oak Ridge National Laboratory[1] in the USA and at Cambridge University[2] in England have demonstrated that ion implantation can increase (or decrease) hardness, increase fracture toughness and reduce friction. To date, however, most research has focused on single crystal ceramics, and virtually nothing is known about the effects of ion implantation on engineering ceramics. This research program was undertaken with the purpose of identifying ion implantation treatments that improve the surface mechanical properties of engineering ceramics exposed to an oxidizing environment.

Encl: (1) to 6170-32

During the first year of the program, experimental and theoretical studies were performed both at NRL and at Cambridge University in England (with Dr. Trevor Page and coworkers). The work at Cambridge, which is the focus of this report, concentrated on determining the surface mechanical behavior of ion-implanted as well as CVD-coated engineering ceramics. Surface analytical and mechanical studies were performed on two of the engineering ceramics, SiC and Si_3N_4, under consideration as bearing materials in the DARPA/Hughes "Solid Lubricated Ceramics" program. (The substrates were provided by Mike Gardos of Hughes Aircraft). Given the limited amount of time and the vast number of implantation parameters that could be varied, an implantation "design" philosophy was followed for improving surface mechanical properties. Ceramics were implanted with ions selected to produce unique (i.e. unobtainable without ion implantation) phase mixtures: Hence, Ti ions were implanted into SiC or Si_3N_4 to very high doses in order to form tough TiC- or TiN-like surface phases within the more brittle matrix; Al ions into Si_3N_4 to produce sialon-like compounds; N ions into SiC and C into Si_3N_4 to produce Si carbonitrides. The metal implant treatments were also expected to improve adhesion of nitride or carbide hardcoatings to the ceramic surfaces, e.g. TiC and TiN coatings on Ti-implanted SiC and Si_3N_4, respectively.

This report covers the preliminary studies on the room-temperature surface mechanical properties and compositions of ion implanted substrates. (Reports on the high temperature mechanical properties and oxidation behavior will follow.) Section 2 presents the implantation parameters chosen and the ion concentrations expected, the indentation hardness and tougnness methods used, and the surface analytical techniques employed. Section 3 presents both qualitative and quantitative evaluation of the surface mechanical properties of Ti-implanted and nonimplanted SiC and Si_3N_4 substrates. It demonstrates that ion implantation can produce unique surface alloys on ceramics with both outstanding and poor tribological properties. But more importantly, the investigation uncovers many of the potential failure modes of these engineering ceramics and provides an approach to improve their surface mechanical properties.

2. EXPERIMENTAL

2.1 Substrates

Si_3N_4 and SiC substrates were provided by Mike Gardos, Hughes Aircraft Co. The substrates were rectangular solid blocks, 1 cm x 1 cm x 0.5 or 0.3 cm thick, from batches of materials listed in Table 1. Selected substrates were given identification numbers then diamond polished (to #3 diamond) in order to obtain a reproducible finish. To the naked eye, the substrates had a shiny black finish. However, under high magnification of an optical microscope, the surface showed polishing pits, pores and perhaps second phase compounds.

TABLE 1: SUBSTRATE MATERIAL AND IDENTIFICATION NUMBERS FOR ION IMPLANTATION STUDIES.

ENGINEERING CERAMIC	MANUFACTURER/TYPE	SUBSTRATE PREFIX	IDENTIFICATION NUMBERS
Si_3N_4	Norton NC132 MgO Hot-Pressed	SN	1,2,11,12,13,14,20,2[illegible]
SiC	ESK high-density sintered alpha	SC	1,2,7,8,9,10

2.2 Ion Implantation

Implantation parameters were chosen in order to achieve nearly equal concentrations of implantation-induced and bulk phases for each of the three implanted species: Ti^+, Al^+ and C^+ (in Si_3N_4) or N^+ (in SiC). After implantation at a single energy, implanted ions are distributed in a Gaussian-like depth profile, characterized by a projected range, R_p, and a straggling range, dR_p.[3] The maximum concentrations of implanted ions, $[C]_{max}$, is located at R_p, the depth of the Gaussian peak (hereafter referred to as the peak depth) and may be calculated and expressed in at. % as follows:

$$[C]_{max} = N_p / N_b \times 100 \qquad (1a)$$

or

$$[C]_{max} = N_p / (N_p + N_b) \times 100 \qquad (1b)$$

where N_p is the maximum density of implanted ions, given by

$$N_p = 0.4 \times dose / dR_p \qquad (2)$$

and N_b is the density of the bulk material. Eq. (1a) gives an upper limit of the maximum concentration whereas (1b) gives a lower limit (it assumes complete substitutional dilution of the substrate atoms). Atomic densities for Si_3N_4 and SiC are 9.54×10^{22} at/cm^3 and 9.64×10^{22} at/cm^3, respectively. Table 2 gives the implantation parameters used in these calculations, as well the doses chosen to achieve nearly equal concentrations of implantation-induced and bulk phases for each of the implanted species.

TABLE 2: IMPLANTATION PARAMETERS AND PREDICTED RANGES AND CONCENTRATIONS FOR ION IMPLANTED Si_3N_4 AND SiC

SUBSTRATE	ION	ENERGY (keV)	DOSE ($\times 10^{17}$/cm^2)	RANGES R_p (nm)	RANGES dR_p (nm)	CONCENTRATION[a] (at. %)
Si_3N_4	Ti^+	190	4	116	3[illegible]	31-45
Si_3N_4	Al^+	110	4	115	37	31-45
Si_3N_4	C^+	75	4	148	33	34-50
SiC	Ti^+	190	4	116	36	32-46
SiC	Al^+	190	4	115	35	32-47
SiC	C^+	85	4	150	34	33-48

[a] Low and upper limits, see Eqs. (16) and (1a), respectively.

Ion implantation was performed at NRL in a Varian/Extrion high current implanter. Base pressures before implantation were in the 10^{-7} Torr range. Two sets of substrates were prepared at each implantation condition: one set was maintained at room temperature during implantation while a second set was implanted "hot." "Hot" implantation denotes direct heating of the substrates by the intense ion beam and is achieved by thermally isolating the substrates, e.g. by suspending the substrates in a Mo sheet basket, during implantation. The substrate is therefore given what might be called a "vacuum annealing" treatment. An optical pyrometer was used to monitor the temperatures of the substrates during implantation. For both cold and hot implantation conditions, substrates were masked in order retain a nonimplanted area of each surface. Table 3 identifies and lists the implantation conditions for each of the substrates.

TABLE 3: IMPLANTATION CONDITIONS FOR Si_3N_4 AND SiC SUBSTRATES

SUBSTRATE	ION	IMPLANTATION PARAMETERS ENERGY (keV)	DOSE (x $10^{17}/cm^2$)	FLUX (uA/cm^2)	SUBSTRATE TEMP. (°C)
SN11	Ti^+	190	4	5	<40
SC7	Ti^+	190	4	5	<40
SN12	Ti^+	190	4	38	900
SC8	Ti^+	190	4	38	900
SN1	Al^+	110	4	51	<40
SC1	Al^+	110	4	51	<40
SN2	Al^+	110	4	63	900
SC2	Al^+	110	4	63	900
SN13	C^+	75	4	---[a]	---[a]
SN14	C^+	75	4	19	500
SC9	N^+	85	4	32	<40
SC10	N^+	85	4	16	460

[a] Not measured.

2.3 Indentation Hardness and Toughness.

Knoop and Vickers hardness tester(s) were used to evaluate the surface mechanical properties of the nonimplanted, Ti-implanted, ion-milled and vacuum-annealed surfaces. The near-surface hardness was measured with a Knoop indenter loaded with 15 gf and 10 gf, respectively, for SiC and Si_3N_4. At these loads, the Knoop indenter penetrated 200-300 nm into the surface, comparable to the implantation depth (although the indenter samples the hardness to a depth about 4 to 10 times greater).

The load above which radial cracks appeared around Vickers indentations i.e. the critical load, P*, was determined by observing indents from loads of 100 gf upwards.

Indentation toughness values were determined according to the method proposed by Lawn et al[4] and critically evaluated by Anstis et al[5]. By this method, one measures the radial crack length, c, at a given load, P, and computes the indentation toughness as:

$$K_c = 0.016 \times (E/H)^{1/2}(P/c^{3/2}). \qquad (3)$$

We have chosen to use a constant (E/H) value for each of the calculations, even though H values were measured, because of the uncertainty in measured H values and the unavailability of a value of E for our substrates. The ratios chosen were taken from Anstis' compilation of materials property data and are given below:

TABLE 4: ELASTIC MODULUS AND HARDNESS VALUES USED IN INDENTATION TOUGHNESS CALCULATIONS (TAKEN FROM ANSTIS ET AL[6])

MATERIAL	E (GPa)	H (GPa)	E/H
Si_3N_4	300	18.5	16.2
SiC	436	24.0	18.2

2.4 Surface Analysis.

The near surface composition was investigated by Energy-Dispersive Xray Analysis (EDX) and by Xray Photoelectron Spectroscopy (XPS). EDX was performed in an ISI-200 scanning electron microscope (at NRL) to determine the concentrations of implanted Ti retained in the four substrates. A 20 keV electron beam, rastered over a 20 um x 20 um area, gave sufficiently good signal-to-noise ratios (10:1) to perform this measurement. XPS was performed with monochromatized Al Xrays in a Surface Science Laboratory (SSL) small-spot analyzer. Sputter depth profiling was accomplished using 3 keV Ar^+ ion bombardment. Ion milling rates were 14 nm/min, based on depths of the ion-milled craters as measured by Michelson interferometry. Data analysis was performed using SSL software routines. Binding energy/depth profiles were obtained directly from the acquired data. Composition vs depth profiles were quantified using Gaussian fits to the photoelectron spectra and normalized using SSL's modified Scofield cross sections.

3. RESULTS AND DISCUSSION

3.1 Surface Mechanical Properties of SiC.

<u>Surface morphology.</u> Polishing produced a shiny black surface as seen by the naked eye. However under a microscope, the polished surface was seen to contain many pits and protrusions. Indentation studies indicated that the surface was very brittle. Grain pullout, circumferential and radial cracking occurred at low loads (<100 gf) with a Vickers diamond indenter. Cracks propagated along pores, second phases or grain boundaries, indicating that the toughness of the surface is controlled by the near surface microstructure. Fig. 1 shows the surface morphology and the various crack patterns in and around a Vickers indentation (at 5 kgf) on a polished, nonimplanted SiC surface. Similar microstructural control of indentation fracture has been observed by Naylor and Page[7] in hot-pressed and reaction bonded SiC substrates.

Heating the SiC substrate in vacuum to a temperature of about 900°C smoothed the surface considerably, but also increased the brittleness of the surface. Around Vickers indents, the radial cracks became more jagged and circumferential cracks more pronounced. These features are readily seen in the SEM stereo micrographs of a Vickers indent (at 500 gf) in the nonimplanted portion of the vacuum heated substrate SC8, shown in Fig. 2. At higher loads, chunks of material often popped out of the indented surface.

Both cold and hot Ti implantation into SiC substrates greatly reduced grain pullout and circumferential cracking and decreased the microstructural control of radial crack propagation. In Fig. 1, very different crack patterns are seen around a 5 kgf Vickers indent in the nonimplanted and Ti-implanted substrate SC7. The increased toughness provided by Ti implantation at the high temperature is seen even more dramatically in Fig. 3, which shows Vickers indents (at 5 kgf) in the implanted surface and in an ion-milled crater of substrate SC8. [The ion milled crater represents the SiC surface but with the Ti^+ layer (about 280 nm thick) removed.] On the Ti^+ surface, chipping was suppressed and radial cracks ran on straighter paths.

TABLE 5: SURFACE HARDNESS (IN GPa) OF Ti-IMPLANTED SiC.

Substrate	Area Indented	Surface Hardness HK(15 gf)	# of hits
SC7	nonimplanted	42 ± 2	6
	Ti^+	24 ± 2	5
	ion milled crater	29 ± 2	3
SC8	nonimplanted	45 ± 3	6
	Ti^+	38 ± 5	5
	ion milled crater	50 ± 1	3

Surface Hardness. The near-surface hardness of the SiC substrates was measured by a Knoop indenter loaded with 15 gf. The indenter penetrated 200-300 nm into the surface, comparable to the implantation depth (although the indenter samples the hardness to a depth about 4 to 10 times greater). As seen in Table 5, Ti implantation appears to have lowered the surface hardness of SC7 but not as much for SC8. It also appears that SC8, the substrate heated in vacuum, may be somewhat harder than the original substrate. However, one cannot rely too much on the calculated hardness at these loads, because of 1) the difficulties of measuring endpoints of indentations only 8 to 10 um long, and 2) the increased plastic flow observed in implanted surfaces.

TABLE 6: CRITICAL LOAD (P^*), INDENTATION TOUGHNESS AND HARDNESS OF Ti-IMPLANTED SiC.

Substrate	P^* (in kgf)	Area Indented	Load (in kgf)	Indentation Toughness K_c (in $MPa\text{-}m^{1/2}$)	Hardness HV (in GPa)
SC7	0.3	nonimplanted	1.0	4.3 ± 0.5	29 ± 4
	0.3	Ti^+		4.0 ± 0.4	
		nonimplanted	5.0	3.5 ± 0.6	23 ± 3
		Ti^+		3.5 ± 0.5	
SC8	0.1	nonimplanted	1.0	4.7 ± 0.3	27 ± 2
	0.1	Ti^+		4.0 ± 0.5	
		nonimplanted	5.0	4.4 ± 0.7	27 ± 2
		Ti^+		3.8 ± 0.5	

Toughness and Hardness. Indentation toughness measurements were performed with a Vickers indenter at loads from 0.1 to 10 kgf. The critical load at which surface radials appeared, P^*, and indentation fracture toughness are given in Table 6; and, for completeness, HV values are also given. Note that the Vickers indenter, at 5 kgf, penetrated about 6 μm. First, it is seen that P^* hot < P^* at room temperature. This is consistent with the more brittle nature of the hot implanted SC8. Second, P^* is the same for non and Ti-implanted surfaces, on both room temperature and hot implanted substrates. Third, the K_c values of the nonimplanted and Ti-implanted room temperature substrates were nearly the same, suggesting that implantation does not significantly affect the radial crack system. A similar conclusion was reached by Roberts and Page for N-implanted SiC[8].

Finally, an increase in measured hardness at lower loads can be seen for the SiC room temperature substrate. The rise indicates an indentation size effect (ISE) index < 2, as is well documented for ceramics[9]. It is interesting that no change in measured hardness with load was seen in the substrate heated to high temperatures.

3.2 Surface mechanical properties of Si_3N_4.

Surface Morphology. Polishing left the Si_3N_4 surfaces quite pitted, and in certain areas, particle-like protrusion could be seen. (These are seen in Fig. 4 and will be identified later.) Indentation studies showed that the hot-pressed Si_3N_4 (NC132) surface was quite resistant to cracking; radial cracks did not form until loads of about 1 kgf, and chipping was uncommon. Room temperature implantation of Ti decreased the critical load for radial fracture considerably. The optical micrographs in Fig. 4 of Vickers indent (at 500 gf) in SN11 show radials in the Ti-implanted surface but not in the polished or ion-milled surfaces. It is quite clear that Ti implantation reduced the resistance to surface radial fracture, but when the implanted layer was removed, the radial fracture resistance returned.

On the other hand, Ti implantation at room temperature produced large compressive stresses, sufficiently large to close polishing pores on the surface. Implantation also reduced considerably the microstructural control of propagating cracks. These two effects are easily seen in Fig. 5, optical micrographs of Vickers indents (at 10 kgf) in nonimplanted and Ti-implanted SN11.

Heating Si_3N_4 to high temperatures in vacuum completely embrittled the surface. Fig. 6 shows both optical and SEM micrographs of surfaces of Si_3N_4 heated to 900°C in vacuum. Heated surfaces developed a network of cracks, with quilt-like patches from 20 to 50 um in diameter. Crack propagation around indentations followed the crazes of the patchy surface. Curiously, though, vacuum heating caused the Si_3N_4, like the SiC, surfaces to become smooth. Lastly, implantation of Ti had no discernable effect on the surface mechanical properties of vacuum heated Si_3N_4 substrates. However, it did change the color of the surface from shiny black to gold, suggesting that TiN had been formed.

TABLE 7: SURFACE HARDNESS (IN GPa) OF Ti-IMPLANTED Si_3N_4.

Substrate	Area Indented	Surface Hardness HK(10 gf)	# of hits
SN11	nonimplanted	29 ± 6	5
(cold)	Ti^+	23 ± 5	5
	ion milled crater	24 ± 4	5
SN12	nonimplanted	23 ± 7	5
(hot)	Ti^+	28 ± 2	5
	ion milled crater	26 ± 7	5

Surface Hardness. The near-surface hardness of the Si_3N_4 substrates was measured by a Knoop indenter at a load of 10 gf. The indenter penetrated 200-300 nm into the surface, comparable to the implantation depth (although the indenter samples the hardness to a depth about 4 to 10 times greater). As seen in Table 7, Ti implantation may have lowered the surface hardness of SN11, the room temperature implant, but raised the hardness of SN12, the substrate heated in vacuum. The surface hardness of SN11 and SN12 is not, however, very different, unlike the hardness values for SC7 and SC8.

TABLE 8: CRITICAL LOAD (P^*), INDENTATION TOUGHNESS AND HARDNESS OF Ti-IMPLANTED Si_3N_4.

Substrate	P^* (in kgf)	Area Indented	Load (in kgf)	Indentation Toughness K_c (in $MPa\text{-}m^{1/2}$)	Hardness HV (in GPa)
SN11	1.0	nonimplanted	2.5	5.0 ± 0.4	17.9 ± 0.7
	0.2	Ti^+		3.8 ± 0.5	
		nonimplanted	5.0	4.7 ± 0.4	16.3 ± 0.6
		Ti^+		3.6 ± 0.3	
SN12	<0.1	nonimplanted	2.5	4.3 ± 1.0	18.9 ± 1.0
	<0.1	Ti^+		2.9 ± 0.2	
		nonimplanted	5.0	3.7 ± 0.4	18.9 ± 1.0
		Ti^+		3.5 ± 0.5	

Toughness and Hardness. Indentation toughness measurements were performed with a Vickers indenter at loads from 0.1 to 10 kgf. The critical load, P^*, and indentation fracture toughness and hardness are given in Table 8. First, in the room temperature Si_3N_4 substrates, P^* implanted << P^* nonimplanted, verifying that high dose Ti implantation promoted surface radial cracking in Si_3N_4. Second, the indentation fracture toughness values obtained from the room temperature NC132 Si_3N_4 agree well with published values for NC132 Si_3N_4 by indentation techniques: Naylor obtained values from 4.0 to 6.2 MPa-$m^{1/2}$[10] while Anstis, using the formalism leading to Eq. 3, obtained 4.0 mPa-$m^{1/2}$.[11] Indentation toughness measurements suggest that the decrease in critical load corresponds to a decrease in toughness. In room temperature substrates, Ti implantation caused a reduction in K_c of about 20 to 25%. Thirdly, in the high temperature Si_3N_4 substrate, P^* was below 100 gf for both the non- and Ti-implanted side, and K_c was also reduced significantly, both presumably caused by the same effect which produced the embrittled surface appearance.

Finally, the cold and hot Si_3N_4 substrates showed the same measured hardness behavior as did the comparably prepared SiC substrates. The room temperature substrate showed an increase in measured hardness at lower loads, hence an indentation size effect (index < 2), whereas the hot implanted substrate again appeared to have constant hardness. The mechanisms responsible for this increase cannot presently be explained.

3.3 Surface Composition

EDX analysis. EDX analysis was performed in order to assess the retention of Ti^+ ions in the Si_3N_4 and SiC substrates at the two temperatures and to identify the fine particle-like features on substrate SN11 (see Fig. 4). The particles were found to contain W and Fe, in addition to Si, suggesting that these are impurities obtained during the ball-milling process of Si_3N_4.

TABLE 9: EDX ANALYSIS OF Ti^+-IMPLANTED Si_3N_4 AND SiC SUBSTRATES

Substrate	Counts Si	Counts Ti	Ratio
SN11	10,000	830	0.083
SN12	10,000	580	0.058
SC7	10,000	540	0.054
SC8	10,000	540	0.054

The retention of Ti^+ ions was assessed by comparing the Ti/Si ratios in the two sets of Si_3N_4 and SiC substrates. The results, listed in Table 9, indicate that Si_3N_4 and SiC retained the same amount of implanted Ti at room and high temperatures. The ratio for SN11, which shows an anomalously high Ti retention, can be rationalized as follows: W-rich precipitates partially covered the Si_3N_4 substrate, thereby masking the EDX signal emanating from Si. Since Ti was implanted into both precipitates and the Si_3N_4 substrate, its EDX signal would not be attenuated. Hence, the increased Ti/Si ratio doesn't constitute excess Ti (a physical impossibility), but rather an attenuated Si signal.

XPS of SiC. The XPS sputter depth profiles of the room temperature implant SC7 (see Fig. 7) show the expected Gaussian-like distribution for Ti with concomitant dilution of the Si and C. The maximum concentration of 42 at. % at a depth of 120 nm is consistent with the value predicted in Table 2. The [O] does not vary appreciably throughout the implanted layer, except for a slight rise in the Ti peak-depth region. The rise there is probably a sputtering artifact; oxygen is probably preferentially sputtered from the SiC more than from the Si-Ti-C. The variation in the Si/C ratio with [Ti] also suggests preferential sputtering of Si in the Ti peak-depth region and of C (slightly) in the bulk SiC.

The binding energies for the three major constituents of the implanted layer are listed above the profile. (We note that SiC did not charge up during the XPS analysis.) The Si(2p) peak shifted continuously from 100.2 eV to 99.2 eV at the [Ti] peak-depth and back to 100.2 eV in the bulk. At the same time, the C(1s) shifted from 283.3 eV to 282.1 eV at the Ti peak-depth then back. The Ti($2p_{3/2}$) shifted down in energy from about 454.8 eV to 454.4 eV at the Ti peak-depth then back up to 454.7 eV as it disappeared.

XPS sputter depth profiles in vacuum-heated substrate SC8 are shown in Fig. 8. Although the Ti profile remains Gaussian-like, it appears less spread out than the room temperature implant. The C and Si profiles do not appear to be simply diluted as they were in the room temperature implant in Fig. 8. Instead, the [C] appears to remain high, whereas the [Si] seems to have been displaced from the Ti peak-depth region. Also, the oxygen is gone from the implanted region and below. This depletion is probably due to heating of the substrate in vacuum and not an effect of implantation.

The binding energies for this high temperature implant are seen at the top of Fig. 8. Entering the Ti peak-depth region, the Si(2p) peak at 100.1 eV (that of SiC) disappears while one at 99.0 eV (that of Si) appears. At the same time, the C(1s) line at 283.2 eV shifts down in energy and broadens, then disappears as a 281.7 eV line appears concurrent with increasing [Ti]. The Ti($2p_{3/2}$) binding energy remains nearly constant at 454.4 eV for all concentrations. (See Table 10 for binding energies of reference samples.) The binding energy shifts in Ti-implanted SiC suggest that the solid state reaction

$$SiC + Ti \longrightarrow TiC + Si$$

proceeds as the Ti concentration increases. This reaction likely forms a TiC layer in the hot implanted substrate, similar to that formed in steels during the "hot" implantation of Ti[12].

TABLE 10. BINDING ENERGIES FOR PHOTOELECTRONS (PEs) OF Si, Ti, N AND C.

PEs	Metal	Nitride	Carbide
Si(2p)	99.1[a,d], 99.4[b]	102.1[b]	100.2[c],100.2[d]
Ti($2p_{3/2}$)	453.9[a]	454.9[a],454.7[d],	454.8[a]
N(1s)	-------	397.1[d] (TiN)	-------
C(1s)	-------	-------	281.2[a],281.1d(TiC)

a PHI handbook of Xray Photoelectron Spectroscopy (Perkin-Elmer, MN, 1979).
b L.Kubler, R.Huag, E.K.Hill, D.Bolmont and G.Gewinner J. Vac. Sci. Technol. A 4 (1986) 2323.
c Y.Mizokawa, K.M.Geib and C.W.Wilmsen J. Vac. Sci. Technol A 4 (1986) 1696.
d Present author.

XPS of Si_3N_4. Fig. 9 shows XPS sputter depth profiles of the room temperature and hot implanted Si_3N_4 substrates, as well as that of an electronics-grade LPCVD Si_3N_4 film, shown for reference purposes. Perhaps the most notable difference between the cold-and, hot-implanted Si_3N_4 substrates can be found in their oxygen profiles. (Recall that the sputtering rates here are about 14 nm/min.) The oxygen quickly leveled off to near bulk value in the cold substrate whereas it more slowly fell to zero in the hot substrate. Continued sputtering on the hot substrate for hundreds of nms failed to detect any oxygen. Hence, as with the SiC, heating in vacuum tended to drive off oxygen from the Si_3N_4 substrate.

The XPS sputter depth profile in the room temperature implant (see Fig. 10) shows Ti distributed in the expected Gaussian-like distribution, with a peak concentration of about 48 at. % at a depth of 120 nm as predicted in Table 2. The N and Si concentrations drop then rise inversely proportional to the Ti concentration, indicating that the Si_3N_4 has simply been diluted by the implanted Ti. The N/Si ratio also varies systematically with the Ti concentration: it increases as the [Ti] increases. This variation, however, is believed to be an artifact of the sputter depth profile process due to preferential sputtering of N. The oxygen profile is somewhat unusual. Immediately below the surface there appears to be an enhanced [O] concentration which then falls to zero (from a bulk value of about 4 at %) in the Ti peak-depth region. This profile is interpreted as showing oxygen migrating out of the peak depth region during implantation, but becoming trapped below the surface as it tries to leave. The consequences of oxygen depletion at room temperature will be discussed later.

The changes in binding energies of the Si(2p), N(1s) and Ti($2p_{3/2}$) lines with depth in the implanted region are given in Fig. 10 and shown in full detail in Fig. 11. (Note that the spectra in Fig. 11 were not taken at equal depth intervals.) Si shows two discrete peaks: a 101.6 eV peak associated with Si_3N_4 (see Table 10), which disappears in the Ti implanted region; and a 99.1 eV metallic Si peak , which appears in proportion to the growth of [Ti]. The Ti peak appears to shift from 454.9 eV at low concentrations to 454.4 eV at high concentrations. The simplest interpretation of these shifts is that Ti is bound as TiN for [Ti] $<$ [N] and as a mixture of TiN and Ti for [Ti] $>$ [N]. The N peak also shifts from 397.6 eV at lowest [Ti] to 397.0 at the Ti peak-depth; this shift is interpreted as a change in bonding from Si_3N_4 to TiN.

The binding energies of Si and N abruptly shifted 2 - 3 eV negative at a depth where [Ti] fell below a few at. %, indicative of charging. At this depth, the binding energies were identical to those obtained with the insulating LPCVD Si_3N_4 film. Note, however, that the binding energy data obtained in the implanted layer showed no evidence of charging. This is because Ti-implantation at these high-doses produces conductive surfaces on otherwise highly insulating ceramics.

XPS sputter depth profiles in SN12, the Si_3N_4 substrate heated to approx. 900°C during Ti implantation, are shown in Fig.12. None of the elemental profiles resembles those of the room temperature implantation of Fig. 10. There appear to be at least 3 layers passing from the surface to the Ti peak-depth region: first, a thin Si+N rich layer containing Ti and a small amount of oxygen; next a TiN/Si layer, in approximately equal concentrations; finally, a TiN layer diluted by Si. These phase identifications are also indicated, qualitatively, by the binding energies listed above the profiles and shown in Fig. 13. The discrete binding energies in the three depth regions attests to the phase formation. A second feature of the sputter depth profile is that the [O] rapidly goes to zero, and remains there to at least twice that depth. Recall that XPS sputter depth profiles of the nonimplanted portion also showed no oxygen depletion. Therefore, it may be concluded that substrate heating (in vacuum), and not ion implantation, caused the oxygen depletion.

3.4 Composition and Surface Mechanical Properties

Ti ion implantation is capable of forming unique surface alloys in SiC and Si_3N_4. XPS analysis has demonstrated that Ti bonds replace Si bonds to both N and C in Si_3N_4 and SiC, respectively. At high temperatures and/or sufficiently high irradiation-induced mobility, the atoms can redistribute allowing the thermodynamically stable phases to form. According to the ternary phase diagram for Ti-Si-N at 900°C , TiN is a stable phase for [Ti] up to 50 at %, with Si then $TiSi_2$ stable by-products of the reaction[13]. The golden coloration of the hot Ti-implanted Si_3N_4 substrate supports the interpretation of the XPS data that TiN grains have been formed. In addition, the high dose implantation of Ti produced an electrically conductive layer on the Si_3N_4 surface.

XPS depth profiles also provide new insights into the diminished toughness of ion implanted Si_3N_4 substrates. Since most of the oxygen is likely present in the grain boundaries and its absence leads to increased brittleness of the surface, it can be concluded that the toughness of Si_3N_4 is controlled by the oxide phases present at the grain boundaries. In the case of SiC, room temperature Ti implantation did not cause oxygen depletion (perhaps because the Oxygen was more tightly bound by the Al sintering agent) and resistance to chipping was increased.

Heating either substrate in vacuum caused Oxygen depletion of both the implanted and nonimplanted surfaces. This deoxygenation is likely responsible for the increased brittleness and hardness of the SiC and for the disastrous embrittling of the Si_3N_4 surface. This is additional evidence that some of the plasticity (i.e. their ability to plastically deform without cracking) of these ceramic substrates resides in the oxygen-containing phases. As to the origin of the cracking, we note that the crack network on Si_3N_4 resembles that seen in (dried) mud after the water evaporates. By analogy, the Si_3N_4 surface may develop a crack network as the Oxygen is driven off by heating in vacuum. If this rather simple hypotheses were correct, however, it would be very surprising since ceramics are considered to be very stable in this temperature range (500 to 900°C).

4. CONCLUSIONS AND RECOMMENDATIONS

1. The studies so far have demonstrated that it is possible to form metastable, if not stable, compounds of pseudo-binary carbides and nitrides in ceramic surfaces. Further studies on the effects of these phases on the oxidation behavior and subsequent surface mechanical properties are in progress.

2. High dose, room temperature Ti-implantation can reduce the circumferential cracking and surface fracture controlled by the microstructure (e.g. grain boundaries, pores, ...) in Si_3N_4 and SiC. However, indentation fracture toughness--as determined by the length of surface radial cracks--is not reduced and may be increased when oxygen-containing phases are depleted. Further investigations of these effects should lead to a better understanding of the chemical basis for toughness in engineering ceramics.

3. Hot implantation studies have indicated a chemical basis for embrittling ceramics at unexpectedly low temperatures. SIMS and SAM analyses will be performed on these embrittled surface to identify the compounds responsible for this embrittlement. Since coating processes such as CVD and PVD subject Si_3N_4 substrates to high

temperatures under low pressure or vacuum conditions, it is important to pursue this study in order to understand and control of deoxygenation and embrittlement of heated substrate.

ACKNOWLEDGEMENTS

I would like to thank Mike Gardos (Hughes Aircraft), to whom the back page of this manuscript is dedicated, for the motivation and moral support to carry out this messy task. I'm also deeply appreciative of the hospitality, facilities and learning environment provided by the Dept. of Material Science and Metallurgy, Cambridge England. I'm especially grateful to Dr. Trevor Page and his students for their advice and assistance during my stay in Cambridge last year. I also thank Rich Colton (NRL) for helping me acquire the XPS data, Bruce Sartwell (NRL) for the implantation, Cathy Pollock (Geo-Centers) for preparing most of the samples and John Wegand (Geo-Centers) for assistance with the fracture toughness measurements.

IRWIN L. SINGER

REFERENCES

1. C.J. McHargue and C.S. Yust, J. Am. Ceram. Soc., 67 (1984) 117.
2. P.J. Burnett and T.F. Page, J. Mater. Sci., 19 (1984) 3524.
3. I. Manning and G.P. Mueller, Computer Phys. Commun. 7 (1974) 85
4. B.R. Lawn, A.G. Evans and D.B. Marshall, J. Amer. Ceram. Soc., 63 (1980) 574.
5. G.R. Antis, P. Chantikul, B.R. Lawn and D.B. Marshall, J. Amer. Ceram. Soc. 64 (1981) 533.
6. Anstis et al., op cit.
7. M.G.S. Naylor and T.F. Page, J. Microsc. 130 (1983) 345
8. S.G. Roberts and T.F. Page, J. Mater. Sci 21 (1986) 457-468.
9. P.M. Sargent and T.F. Page, Proc. Brit. Ceram. Soc. 26 (1978) 209
10. M.G.S. Naylor, Ph.D. Dissertation, U. of Cambridge, England, 1981, unpublished.
11. Antis, et al., op cit.
12. I.L. Singer et. al., J. Appl. Phys., 58 (1985) 1255
13. R. Beyers, R. Sinclair and M.E. Thomas, J. Vac. Sci. Technol. B2 (1984) 781.

FIGURES

FIG. 1. Optical micrographs of Vickers indents (at 5 kgf) in sintered SiC. Non-implanted and Ti-implanted.

FIG. 2. SEM stereo pair of Vickers indent (at 500 gf) in sintered SiC; vacuum annealed at 900°C.

FIG. 3. Optical micrographs of Vickers indents (at 5 kgf) in vacuum annealed (900°C), sintered SiC. Implanted and ion milled (280 nm crater).

FIG. 4. Optical micrographs of Vickers indent (at 500 gf) in hot-pressed Si_3N_4. Non-implanted, Ti-implanted and ion milled crater.

FIG. 5. Optical micrographs of Vickers indents (at 10 kgf) in Si_3N_4. Non-implanted and Ti-implanted.

FIG. 6. Micrographs of Vickers indents in surfaces of Si_3N_4 heated to 900°C in vacuum. Nomarski micrographs of a) non-implanted, and b) Ti-implanted (at 500 gf); SEM of Al-implanted (at 200 qf).

FIG. 7. XPS sputter depth profile of Ti-implanted SC7. (Sputtering rate = 23 nm/100 sec).

FIG. 8. XPS sputter depth profile of Ti-implanted SC8. (Sputtering rate = 23 nm/100 sec).

FIG. 9. XPS sputter depth profiles of non-implanted Si_3N_4 substrates. (Sputtering rate = 23 nm/100 sec).

FIG. 10. XPS sputter depth profile of Ti-implanted SN11. (Sputtering rate = 23 nm/100 sec).

FIG. 11. XPS binding energy/depth profiles of Ti-implanted SN11.

FIG. 12. XPS sputter depth profile of Ti-implanted SN12. (Sputtering rate = 23 nm/100 sec.

FIG. 13. XPS binding energy/depth profiles of Ti-implanted SN12.

OPTICAL MICROGRAPHS OF VICKERS INDENTS
(AT 5 KGF) IN SINTERED SiC

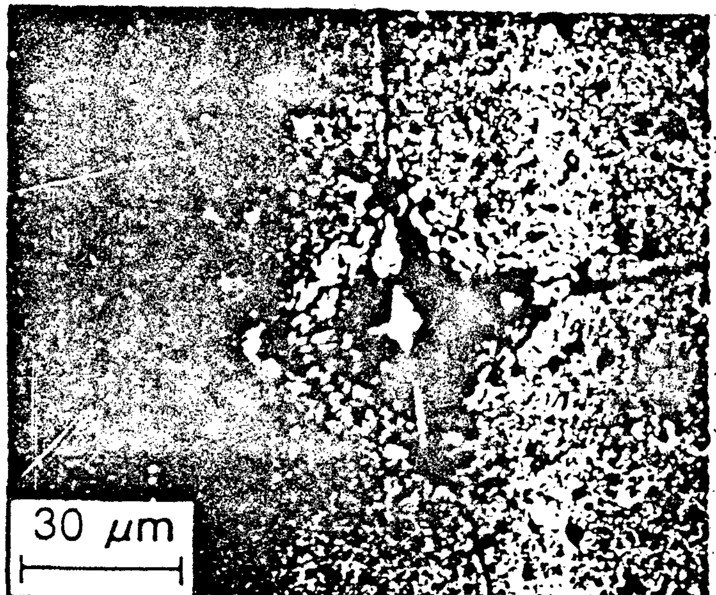

NON IMPLANTED

Ti IMPLANTED

Figure 1

SEM STEREO PAIR OF VICKERS INDENTS (AT 500 GF)
SINTERED SiC; VACUUM ANNEALED AT 900°C

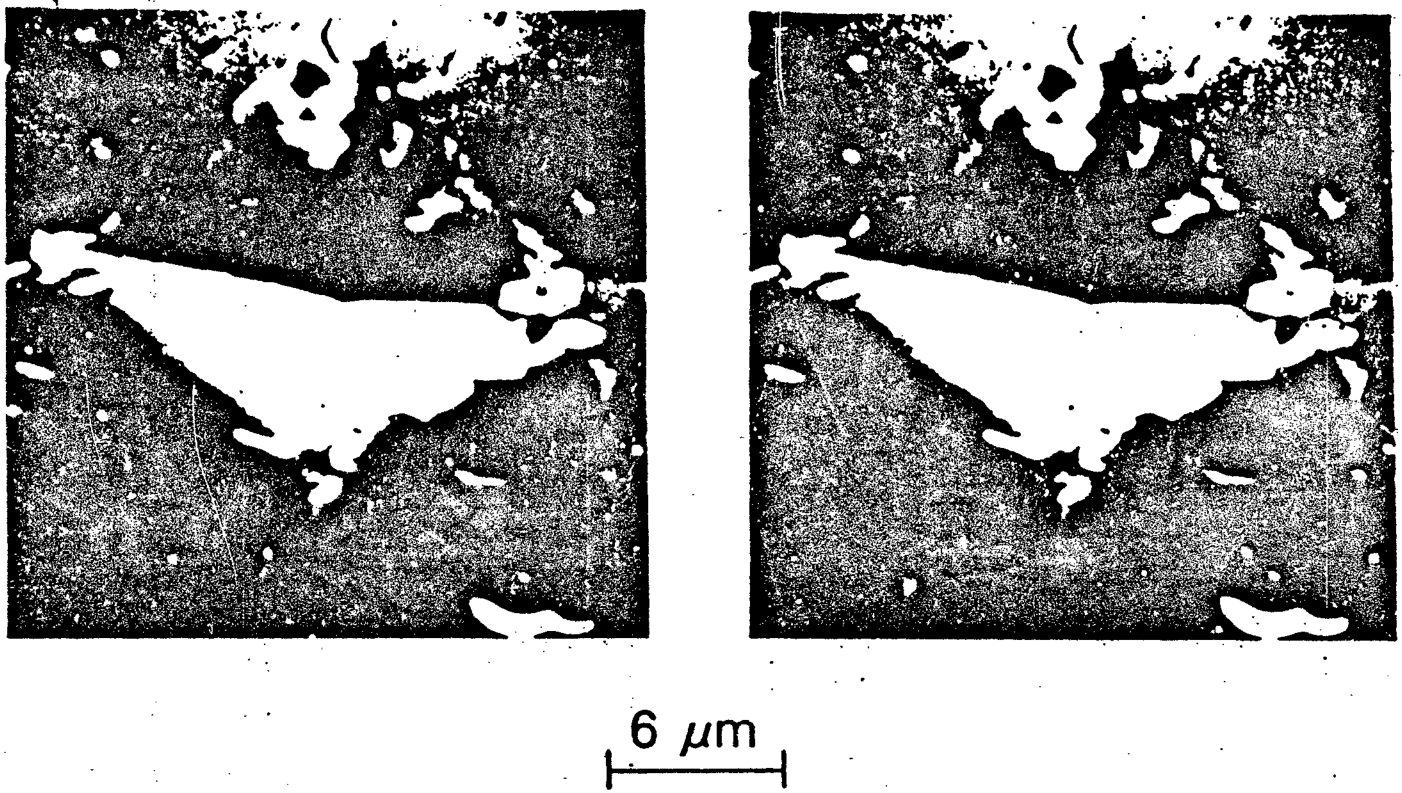

Figure 2

OPTICAL MICROGRAPHS OF VICKERS INDENTS (AT 5 KGF)
SINTERED SiC; Ti IMPLANTED AT 900°C

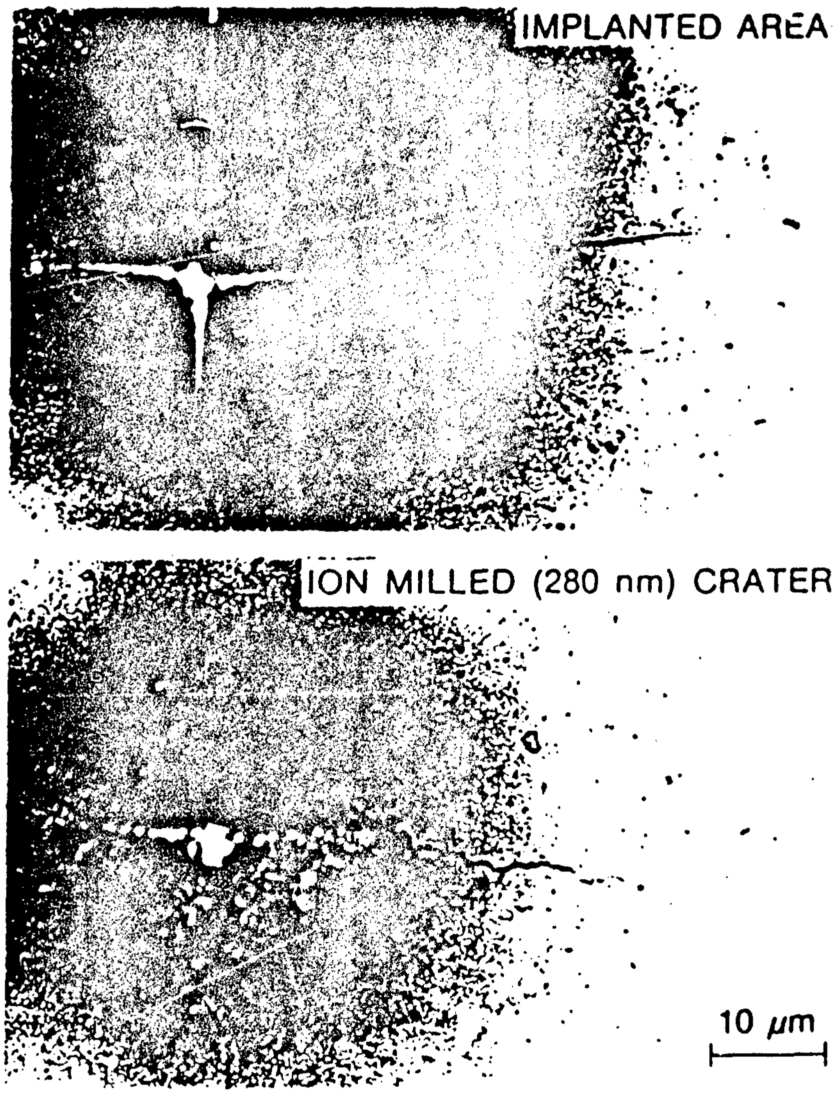

Figure 3

OPTICAL MICROGRAPHS OF VICKERS INDENT (AT 500 GF)
HOT-PRESSED Si3N4

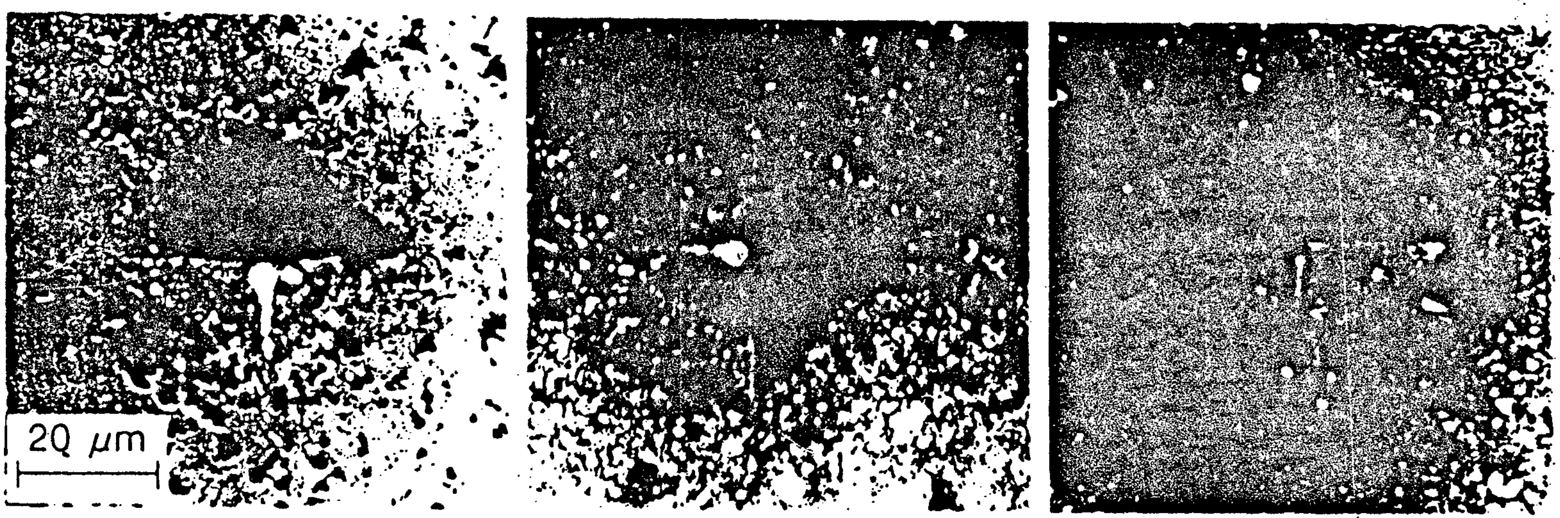

NON IMPLANTED — Ti IMPLANTED — ION MILLED (280 nm)

Figure 4

OPTICAL MICROGRAPHS OF VICKERS INDENTS (AT 10 KGF) IN HOT-PRESSED Si3N4

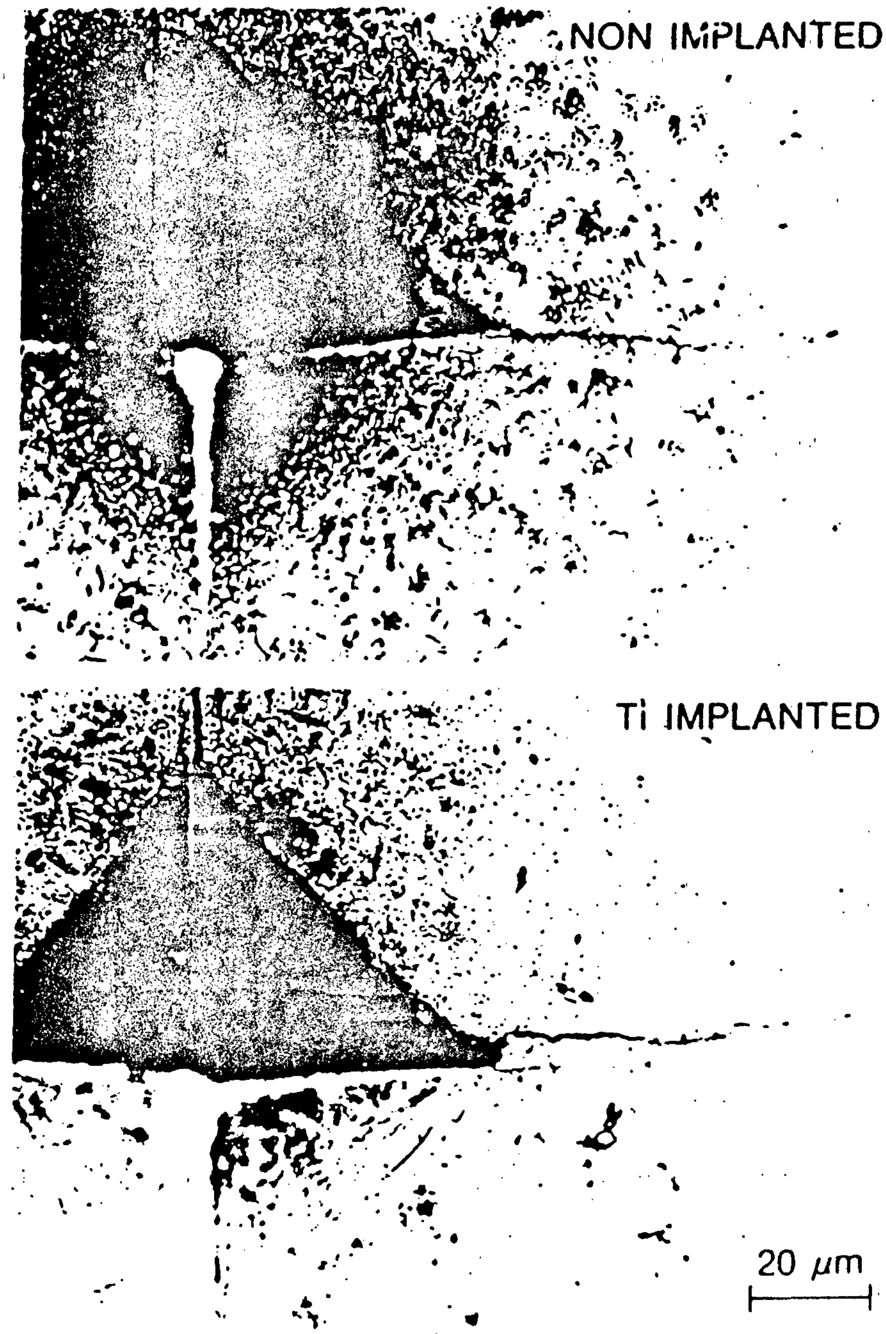

Figure 5

MICROGRAPHS OF VICKERS INDENTS IN SURFACES
OF HOT-PRESSED Si_3N_4 HEATED TO 900°C IN VACUUM

NOMARSKI | SEM

Ti IMPLANTED | NON IMPLANTED | NON IMPLANTED

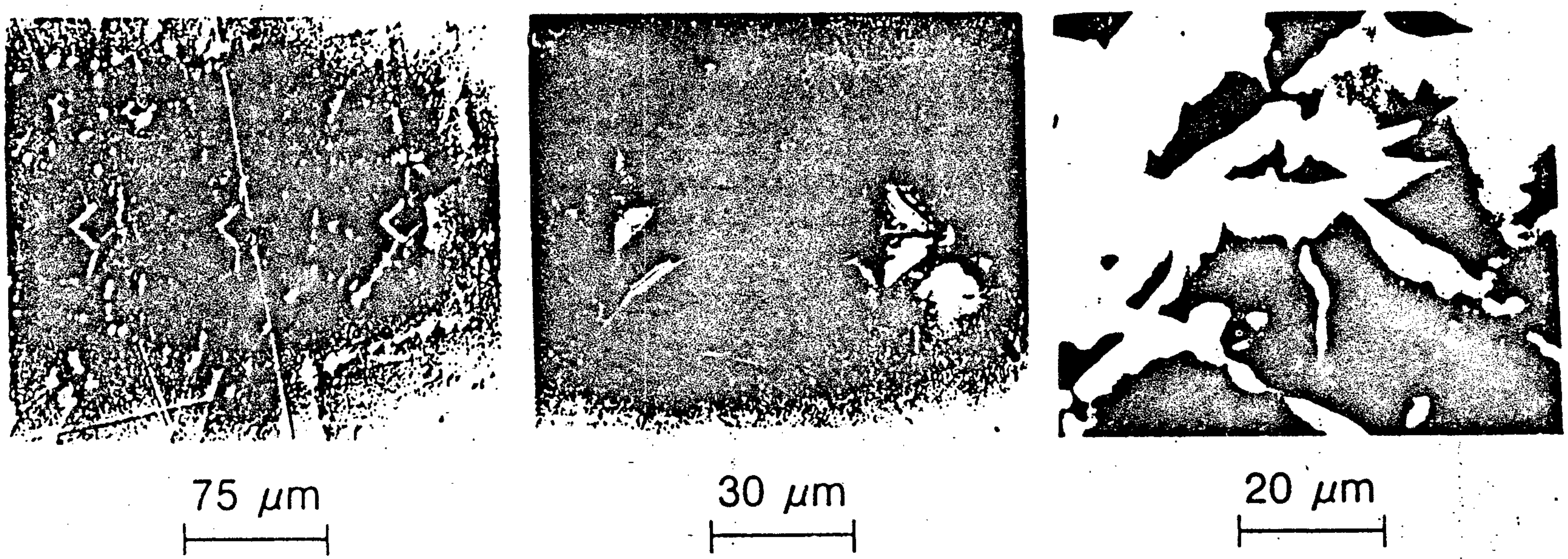

Figure 6

File: ..7TI2	Date: 5/17/1986 Disc: 89826	Sp : Size: 300 u	Flood Gun: 0.0 e Resolution: 3
Description: DEPTH PROFILE-TI IMPLANTED SiC (ROOM TEMP) P 4 E-7 Ar -10 mA - 2mm x 2mm - 3kV-			Operator: ILS

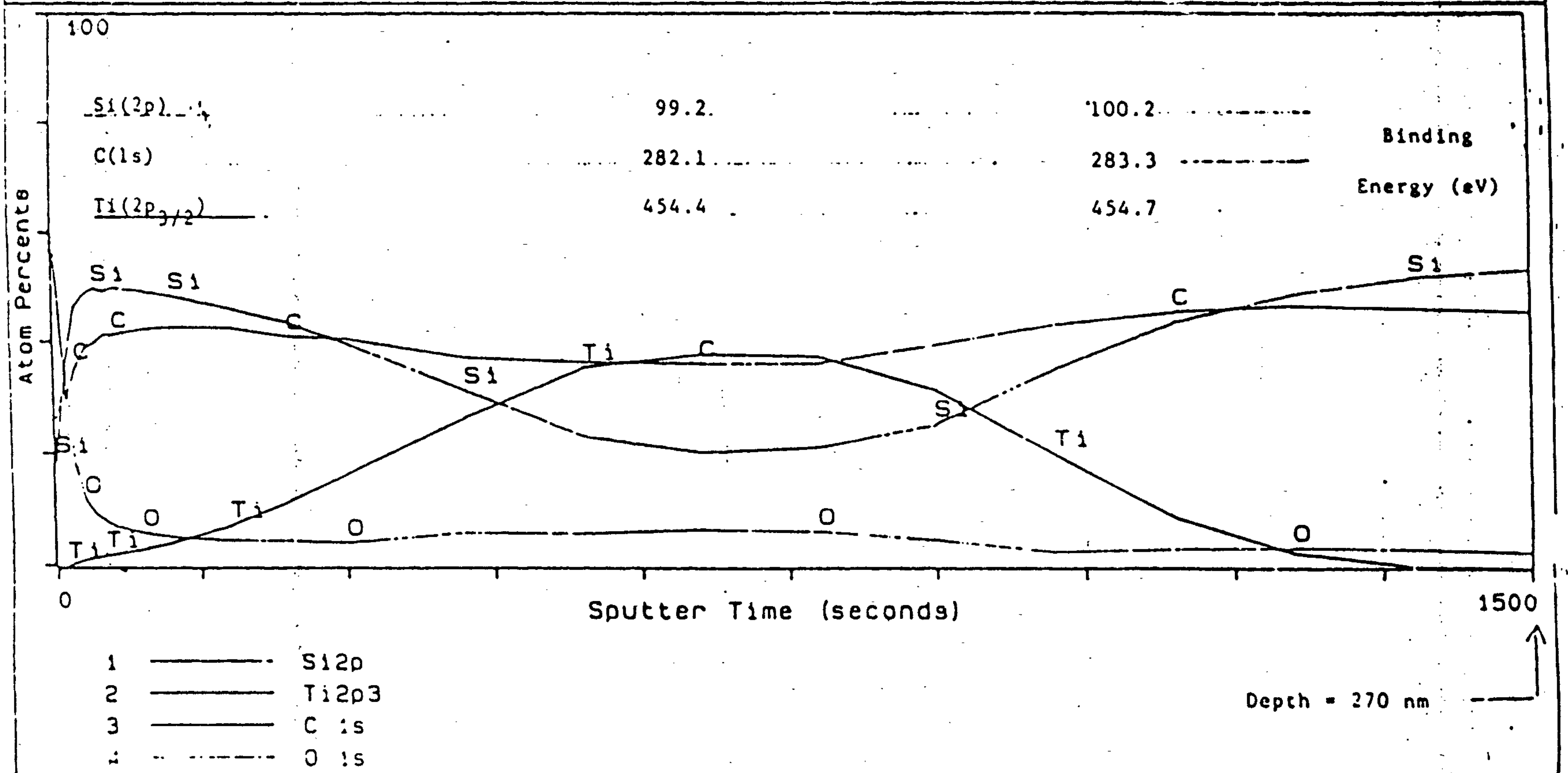

Fig. 7

NAVAL RESEARCH LABORATORY

Flood Gun: 0.0

Disc: 89826

Resolution: 3

Description: DEPTH PROFILE- Ti IMPLANTED SiC (900 DEG C)
P 4 E-7 Ar -10 mA - 2mm x 2mm - 3kV-

Operator: ILS

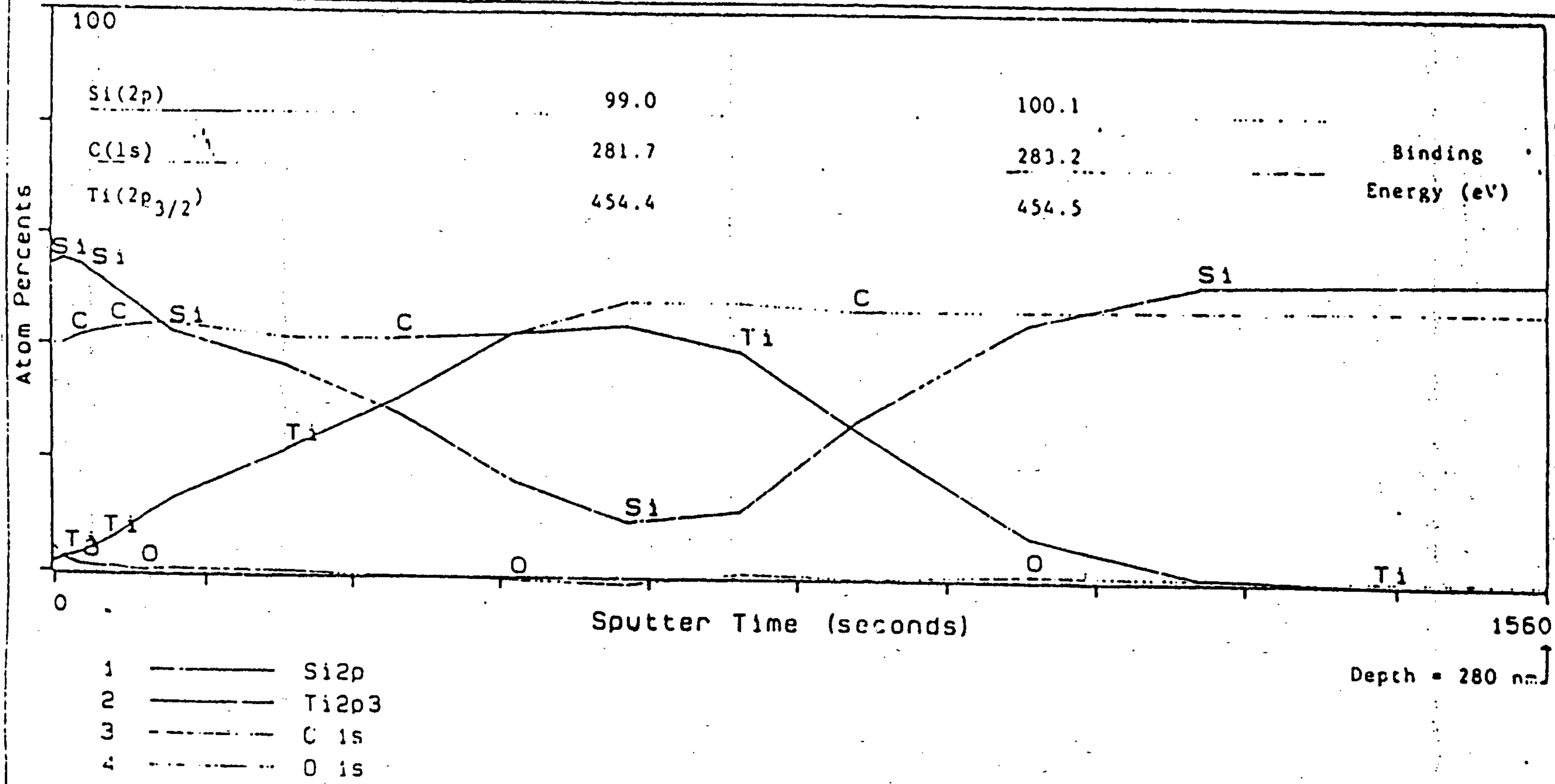

Fig. 8

NAVAL RESEARCH LABORATORY

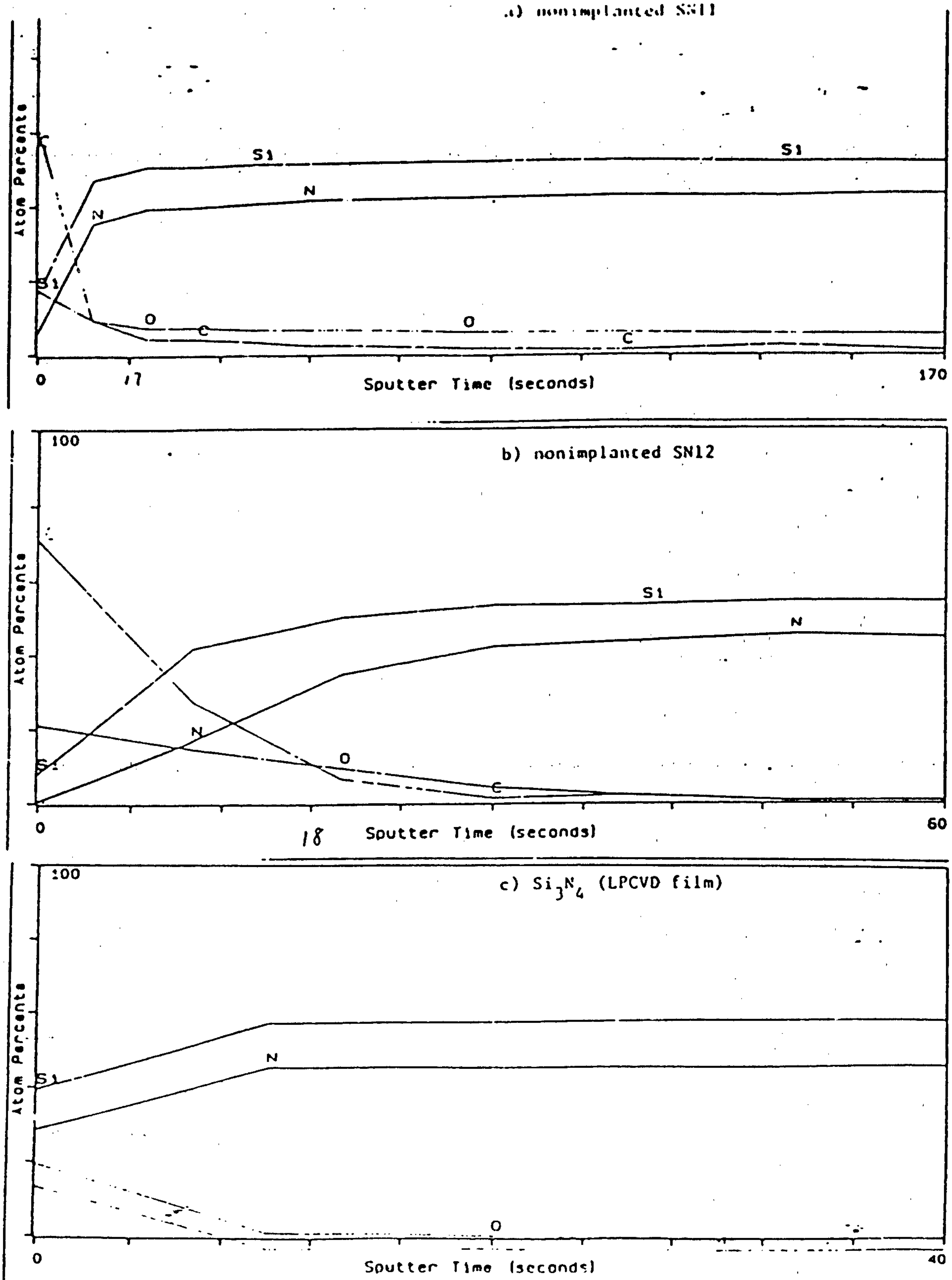

1 ———— Si2p
2 ———— N 1s
3 - - - - - O 1s
4 - · - · — NOT ASIGND C

Fig. 9. XPS Sputter depth profiles of Si_3N_4 substrates.

File: SN11TI2	Date: 5/15/1986 Disc: 89826	Spot Size: 300 u	Flood Gun: 0.0 e. Resolution: 3

Description: DEPTH PROFILE- Ti IMPLANTED SiN (ROOM TEMP) P 4 E-7 Ar -10 mA - 2mm x 2mm - 3kV- Operator: ILS

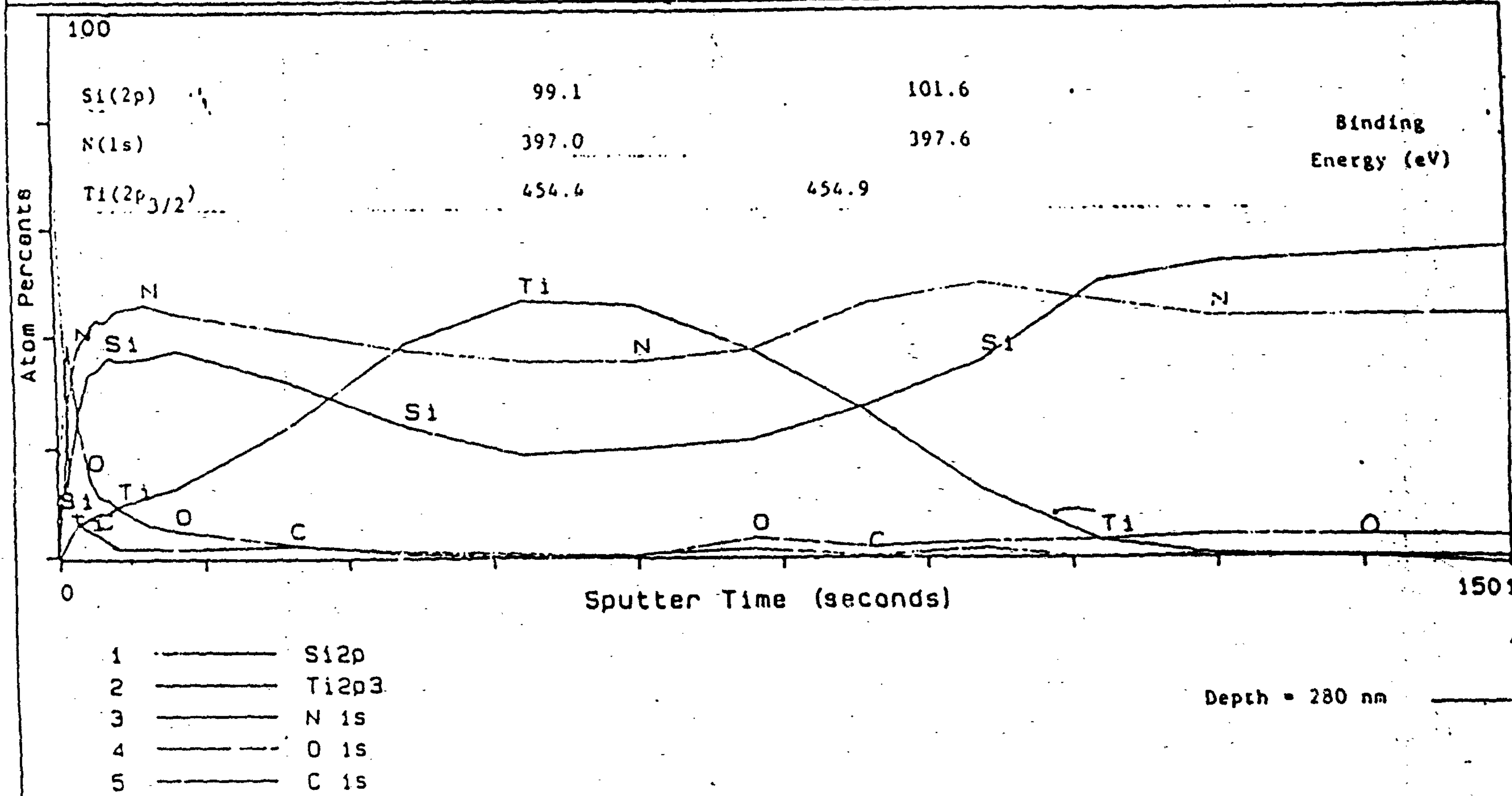

Fig. 10

NAVAL RESEARCH LABORATORY

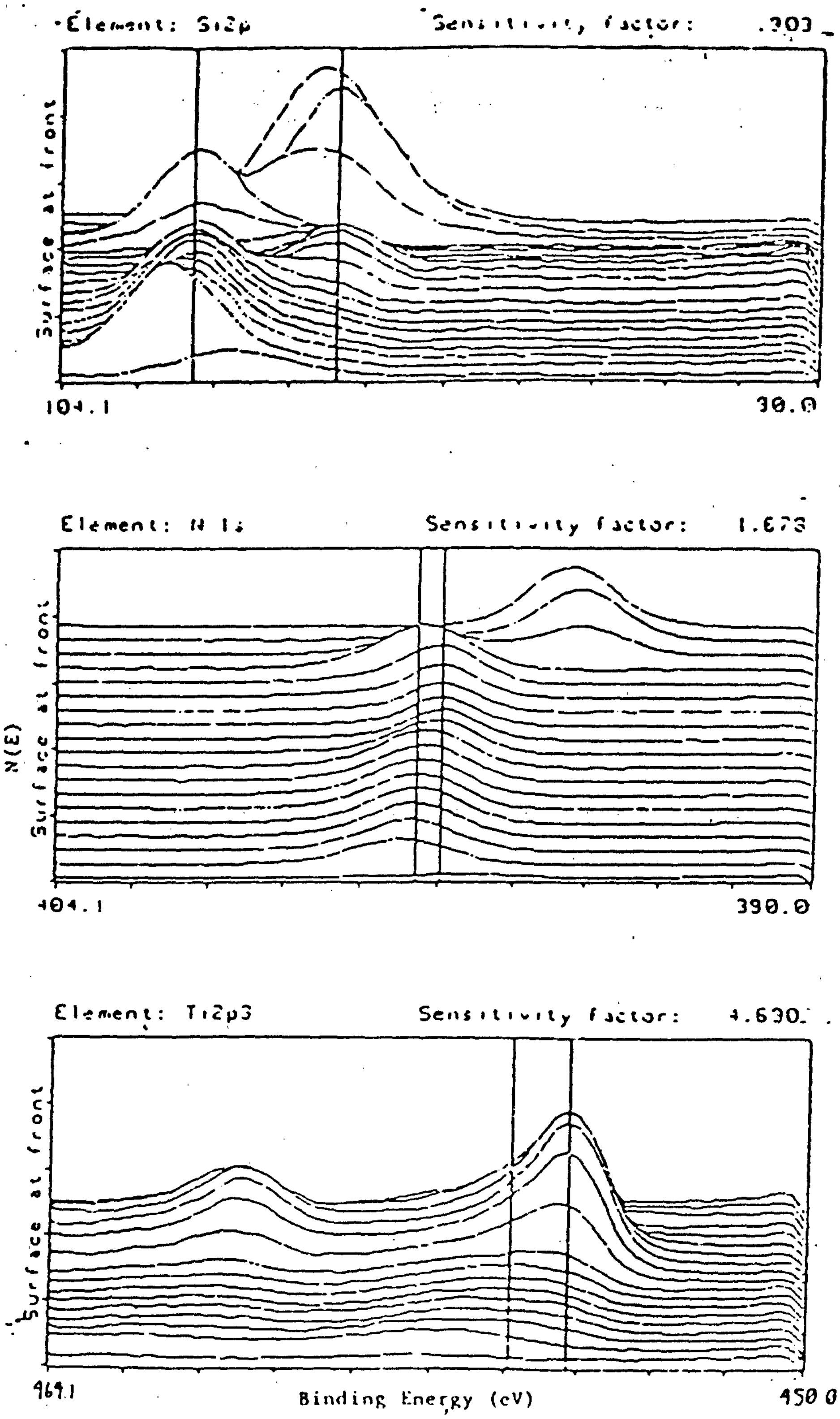

Fig. 11. XPS binding energy/depth profiles of Ti-implanted Si_3N_4 (cold) SN11.

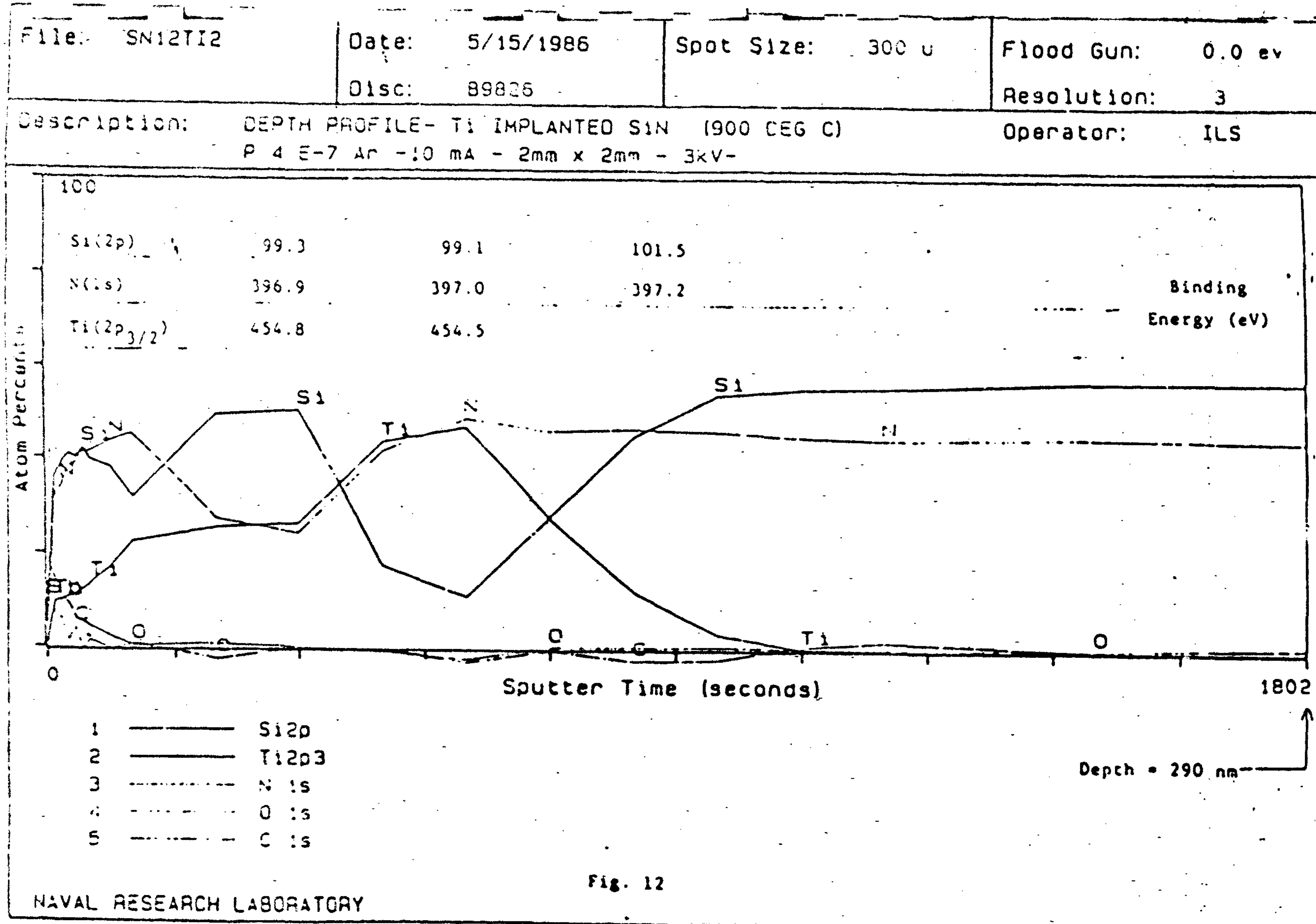
File: SN12TI2
Date: 5/15/1986
Disc: 89826
Spot Size: 300 u
Flood Gun: 0.0 ev
Resolution: 3
Description: DEPTH PROFILE- Ti IMPLANTED SiN (900 DEG C)
P 4 E-7 Ar -10 mA - 2mm x 2mm - 3kV-
Operator: ILS
100
Si(2p) 99.3 99.1 101.5
N(1s) 396.9 397.0 397.2
Ti(2p3/2) 454.8 454.5
Binding Energy (eV)
Atom Percent
Si
Ti
N
O
C
0
Sputter Time (seconds)
1802
Depth = 290 nm
1 Si2p
2 Ti2p3
3 N 1s
4 O 1s
5 C 1s
NAVAL RESEARCH LABORATORY
Fig. 12

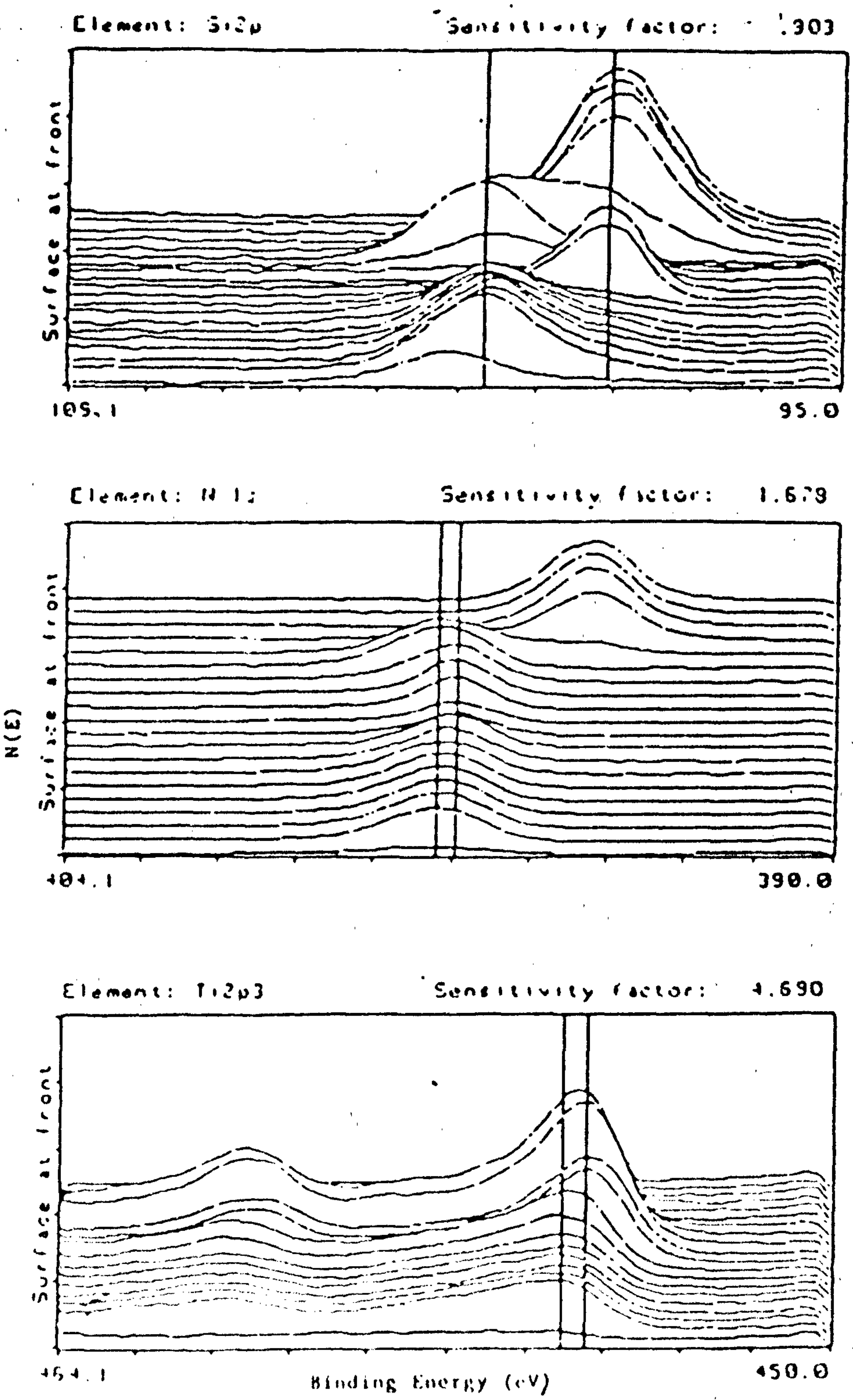

Fig. 13. XPS binding energy/depth profiles of Ti-implanted Si_3N_4 (hot) SN12.

APPENDIX B

GEO-CENTERS, INC.

SIMS DEPTH PROFILING OF ^{13}C-IMPLANTED IRON

Ref: Code 6170-56:SH:al memo dated 30 Jan 87

1. On 27 January 1987 I. Singer, Code 6176, requested that sample 4 (reference (a)) be depth profiled in a oxidized area of the surface and that the depth profile of sample 8 be repeated.

2. The samples were depth profiled with a CAMECA IMS-300 ion microscope using 5.5 keV O_2^+ primary ions at a primary current of 500 nA. The primary beam was rastered over an area of approximately 500 x 800 um. In the center of this raster an area 250 um in diameter was analyzed. Because of the difference in size between the rastered and analyzed areas the contributions of analyte atoms residing at the crater walls to the detected signals were eliminated. Some details concerning the CAMECA IMS-300 ion microscope are given in the appendix.

3. Figs. 1, 2, and 3 show depth profiles for mass 13 ($^{13}C^+$), mass 54 ($^{54}Fe^+$), and mass 72 ($^{56}Fe^{16}O^+$) of samples 4 (oxidized area), 4 (nonoxidized area), and sample 8, respectively. As may be seen the no significant differences are observed in the depth profiles of the oxidized and nonoxidized regions of sample 4. The differences in absolute signal levels may be attributed in a slight drift of primary current during the analyses. Of interest is the fact that the oxidized surface actually shows a lower FeO^+ signal relative to Fe^+. The sample 8 profile no longer displays the high signal noise of the previous analysis and now has a signal/noise ratio comparable to the other profiles.

4. Appendix:

The CAMECA IMS-300 ion microscope employs an energetic (0-10 keV) primary ion beam (typically O_2^+, Ar^+, or O^-) to analyze solid materials. The interaction of the primary ions with the sample erodes the target surface liberating secondary ions which are subsequently mass analyzed. The instrument design is such that the lateral distribution of the secondary ions is reformed at the detector resulting in a magnified mass analyzed image of the sample surface. This image may be observed visually or recorded on electron sensitive film with a field of view of 250 microns and a lateral resolution of one micron. The ion microscope is also capable of providing a three dimensional characterization of solids by monitoring the secondary ion signal of interest as a function of time. Provided the sputter yield (sputtered atoms/incident ion) is constant (or the layer thicknesses of a heterogeneous sample are known) this time scale may be converted to a depth scale by measurement of the crater depth. Crater depth measurements are normally made in this laboratory by interferometry. Secondary ion mass spectrometry (SIMS) is capable of detecting all elements in the periodic table, with detection limits in the ppm to ppb range. With proper standards, quantification may be performed with accuracies of ~ 10% or less. The instrument is normally operated as a low resolution mass spectrometer (M/M = 300), but may also be operated in a high resolution mode (M/M = ~2500).

GEO-CENTERS, INC.

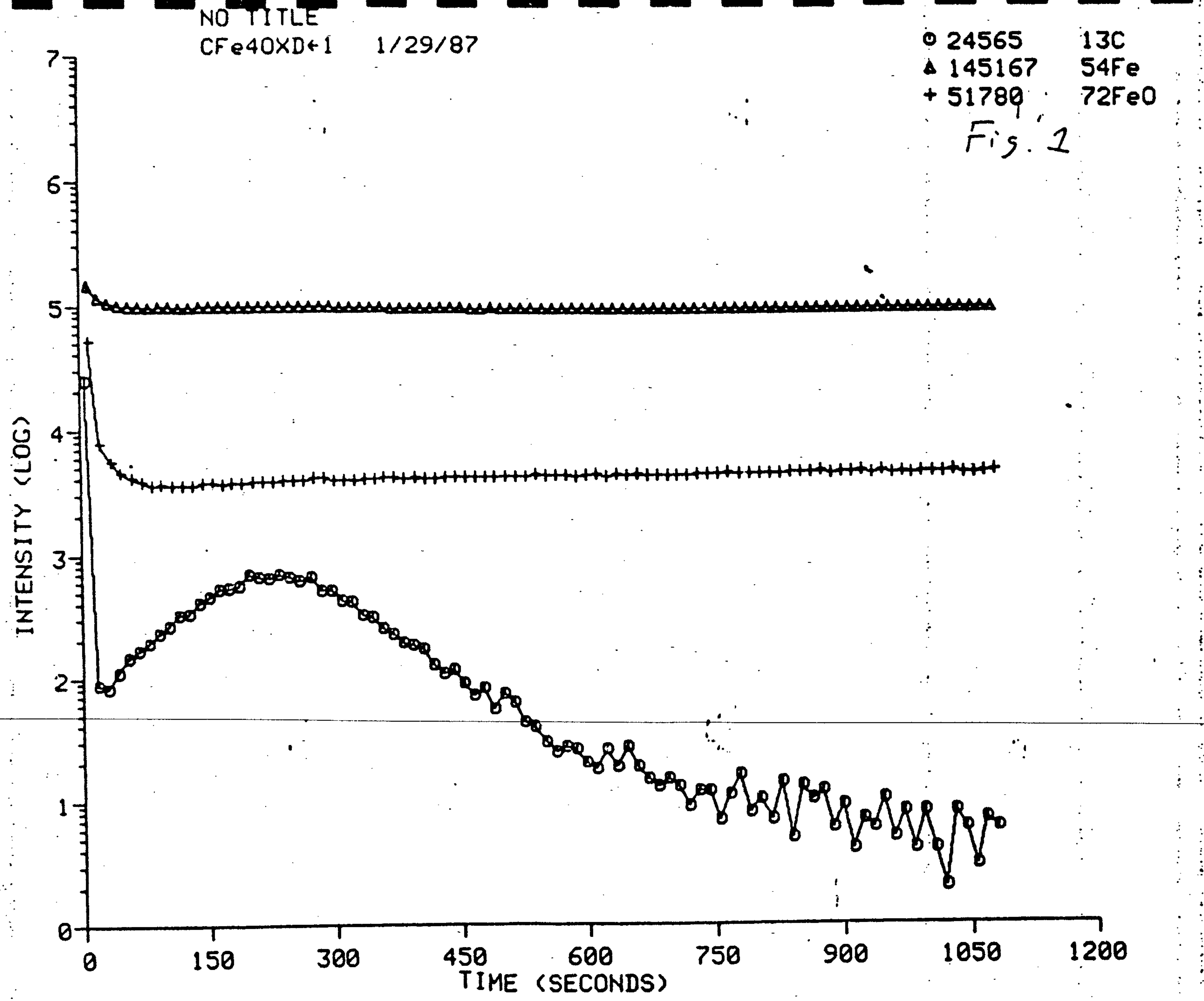
NO TITLE
CFe4OXD+1 1/29/87
24565 13C
145167 54Fe
51780 72FeO
INTENSITY (LOG)
0
1
2
3
4
5
6
7
0
150
300
450
600
750
900
1050
1200
TIME (SECONDS)

Fig. 1

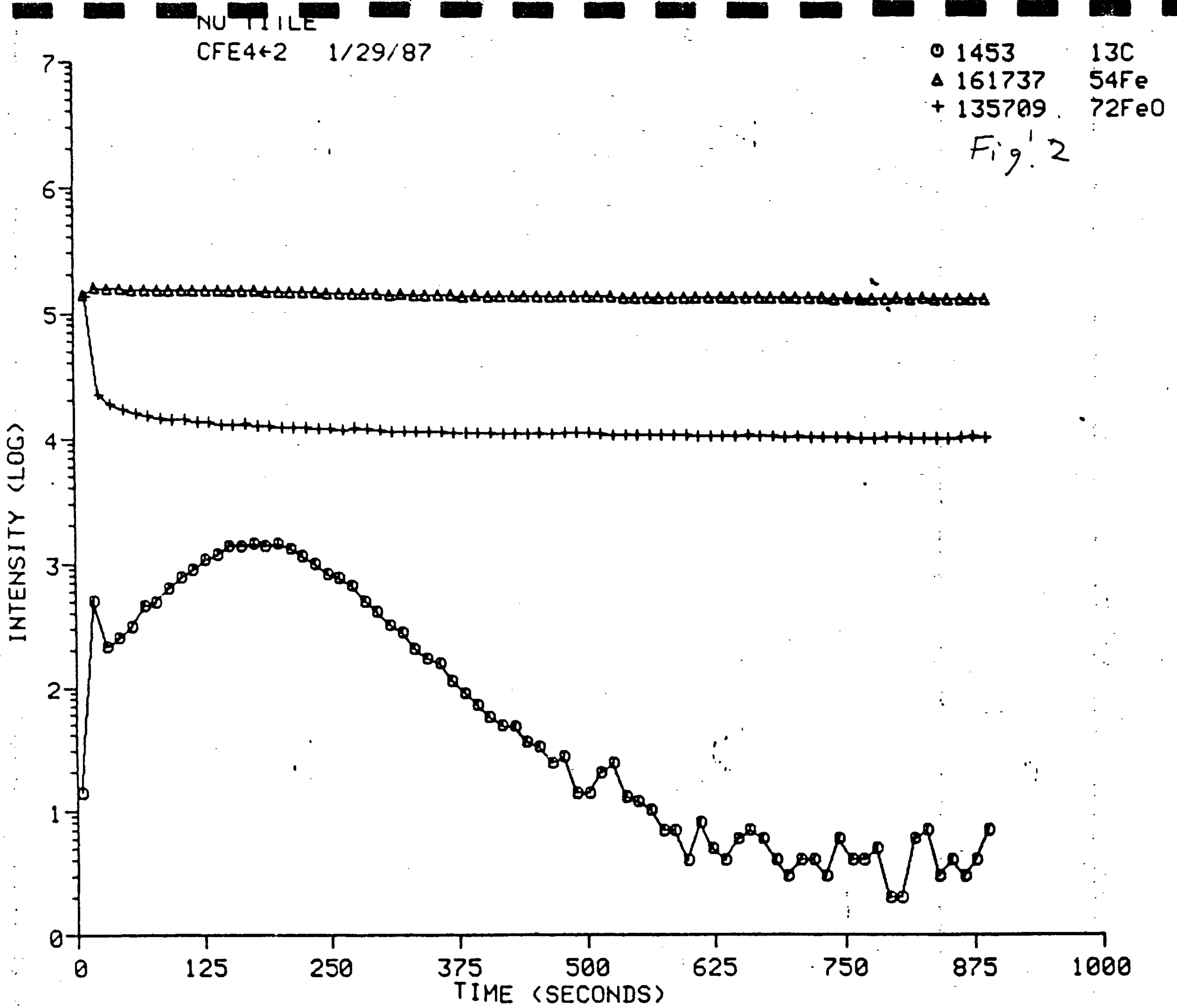
NU TITLE
CFE4←2 1/29/87
⊙ 1453 13C
△ 161737 54Fe
+ 135709 72FeO
Fig. 2
INTENSITY (LOG)
0
1
2
3
4
5
6
7
0
125
250
375
500
625
750
875
1000
TIME (SECONDS)

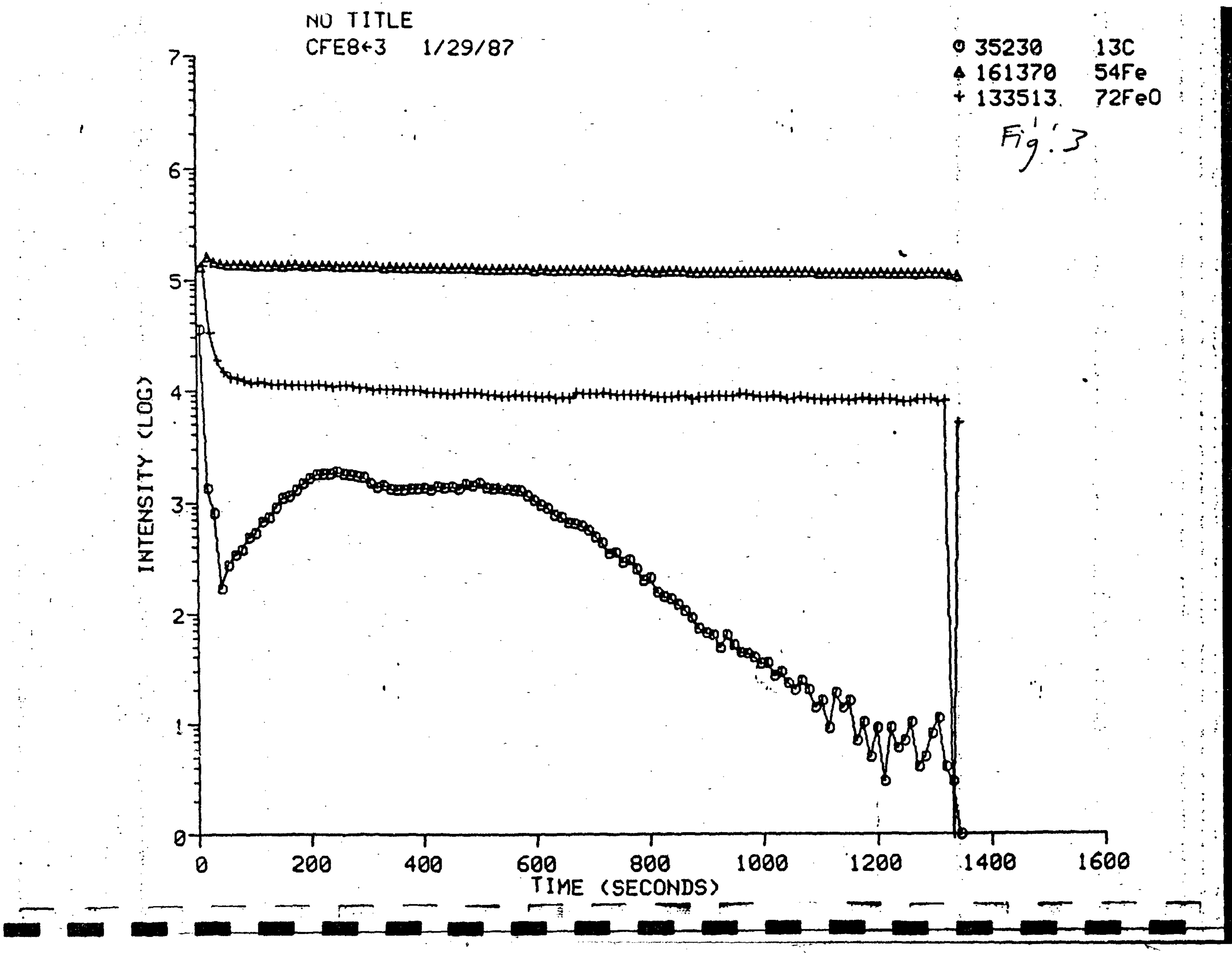
NO TITLE
CFE8+3 1/29/87
o 35230 13C
▲ 161370 54Fe
+ 133513 72FeO
Fig. 3
INTENSITY (LOG)
0
1
2
3
4
5
6
7
0
200
400
600
800
1000
1200
1400
1600
TIME (SECONDS)

SIMS DEPTH PROFILING OF ^{13}C-IMPLANTED IRON

1. On approximately 16 January 1987, I. Singer, Code 6176, submitted three samples for analysis by secondary ion mass spectrometry. These samples consisted of Fe substrates which had been implanted with ^{13}C. Sample 4 had been implanted at an energy of 70 keV, sample 12 at 190 keV, and sample 8 at both of these energies. Of interest was the depth distribution of ^{13}C.

2. The sample was depth profiled with a CAMECA IMS-300 ion microscope using 5.5 keV O_2^+ primary ions at a primary current of 400 nA. The primary beam was rastered over an area of approximately 500 x 800 um. In the center of this raster an area 250 um in diameter was analyzed. Because of the difference in size between the rastered and analyzed areas the contributions of analyte atoms residing at the crater walls to the detected signals were eliminated. Some details concerning the CAMECA IMS-300 ion microscope are given in the appendix.

3. Figs. 1, 2 and 3 show depth profiles for mass 12 ($^{12}C^+$), mass 13 ($^{13}C^+$), mass 54 ($^{54}Fe^+$), and mass 72 ($^{56}Fe^{16}O^+$) of samples 4, 8 and 12, respectively. As may be seen the level of ^{12}C which would be present as a contaminant is below the detection limit. As the profile of sample 8 was taken between those for samples 4 and 12 and since all samples were analyzed one immediately after the other, it is unlikely that the noise in the secondary ion signals are an instrumental artifact. This noise may have been caused by slight surface charging due to a high carbon concentration produced by the deeper implant diffusing to the surface and possibly forming small islands of an insulating phase. This is presently a subject of investigation and any significant results will be presented in a later report. Even with the decreased signal/noise ratio it is apparent that the high energy implant in sample 8 has migrated closer to the surface.

4. Appendix:

The CAMECA IMS-300 ion microscope employs an energetic (0-10 keV) primary ion beam (typically O_2^+, Ar^+, or O^-) to analyze solid materials. The interaction of the primary ions with the sample erodes the target surface liberating secondary ions which are subsequently mass analyzed. The instrument design is such that the lateral distribution of the secondary ions is reformed at the detector resulting in a magnified mass analyzed image of the sample surface. This image may be observed visually or recorded on electron sensitive film with a field of view of 250 microns and a lateral resolution of one micron. The ion microscope is also capable of providing a three dimensional characterization of solids by monitoring the secondary ion signal of interest as a function of time. Provided the sputter yield (sputtered atoms/incident ion) is constant (or the layer thicknesses of a heterogeneous sample are known) this time scale may be converted to a depth scale by measurement of the crater depth. Crater depth measurements are normally made in this laboratory by interferometry. Secondary ion mass spectrometry (SIMS) is capable of detecting all elements in the periodic table, with detection limits in the ppm to ppb range. With proper standards, quantification may be performed with accuracies of ~10% or less. The instrument is normally operated as a low resolution mass spectrometer (M/M = 300), but may also be operated in a high resolution mode (M/M = ~2500).

GEO-CENTERS, INC.

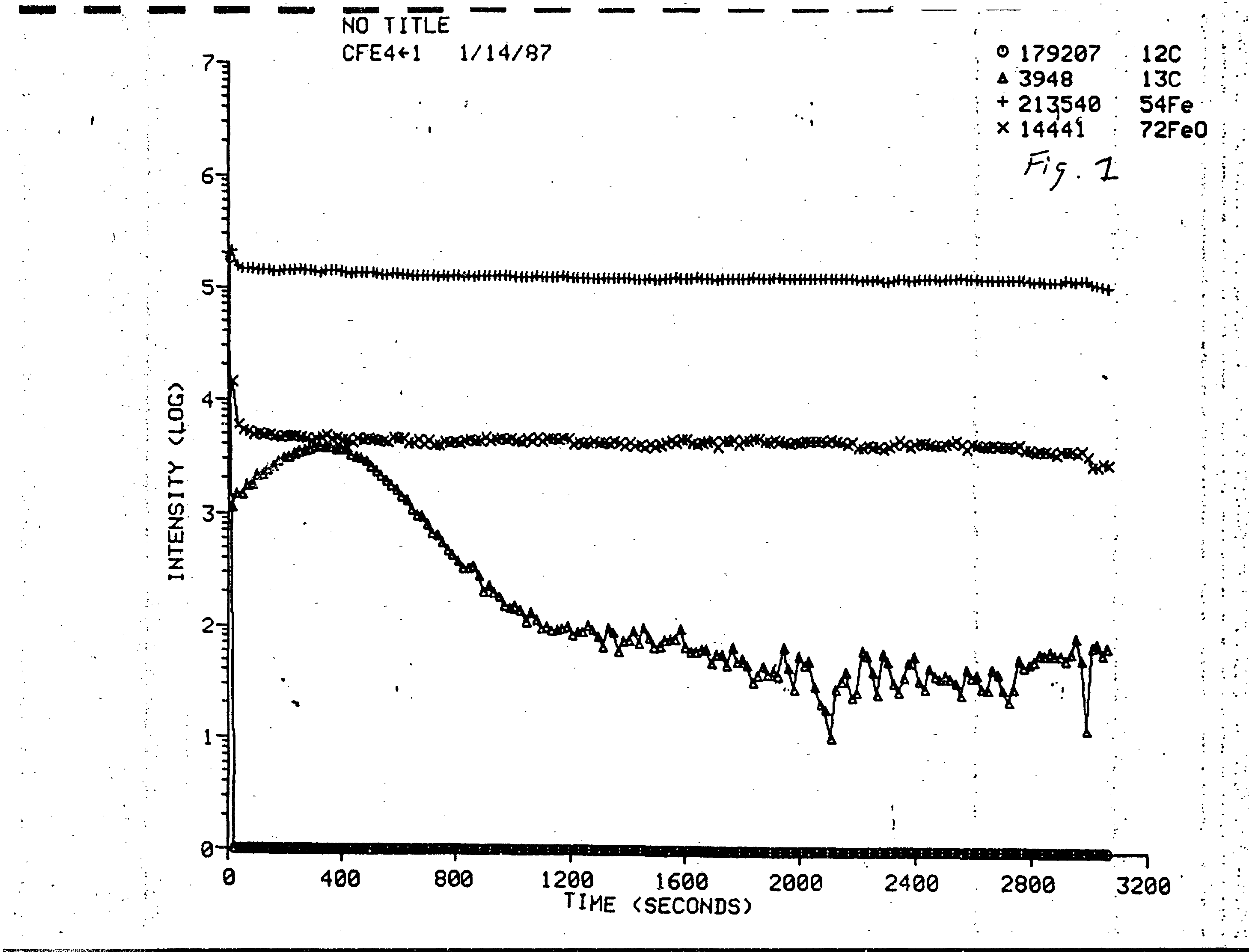

NO TITLE
CFE4←1 1/14/87
⊙ 179207 12C
▵ 3948 13C
+ 213540 54Fe
× 14441 72FeO
INTENSITY (LOG)
0
1
2
3
4
5
6
7
0
400
800
1200
1600
2000
2400
2800
3200
TIME (SECONDS)

Fig. 1

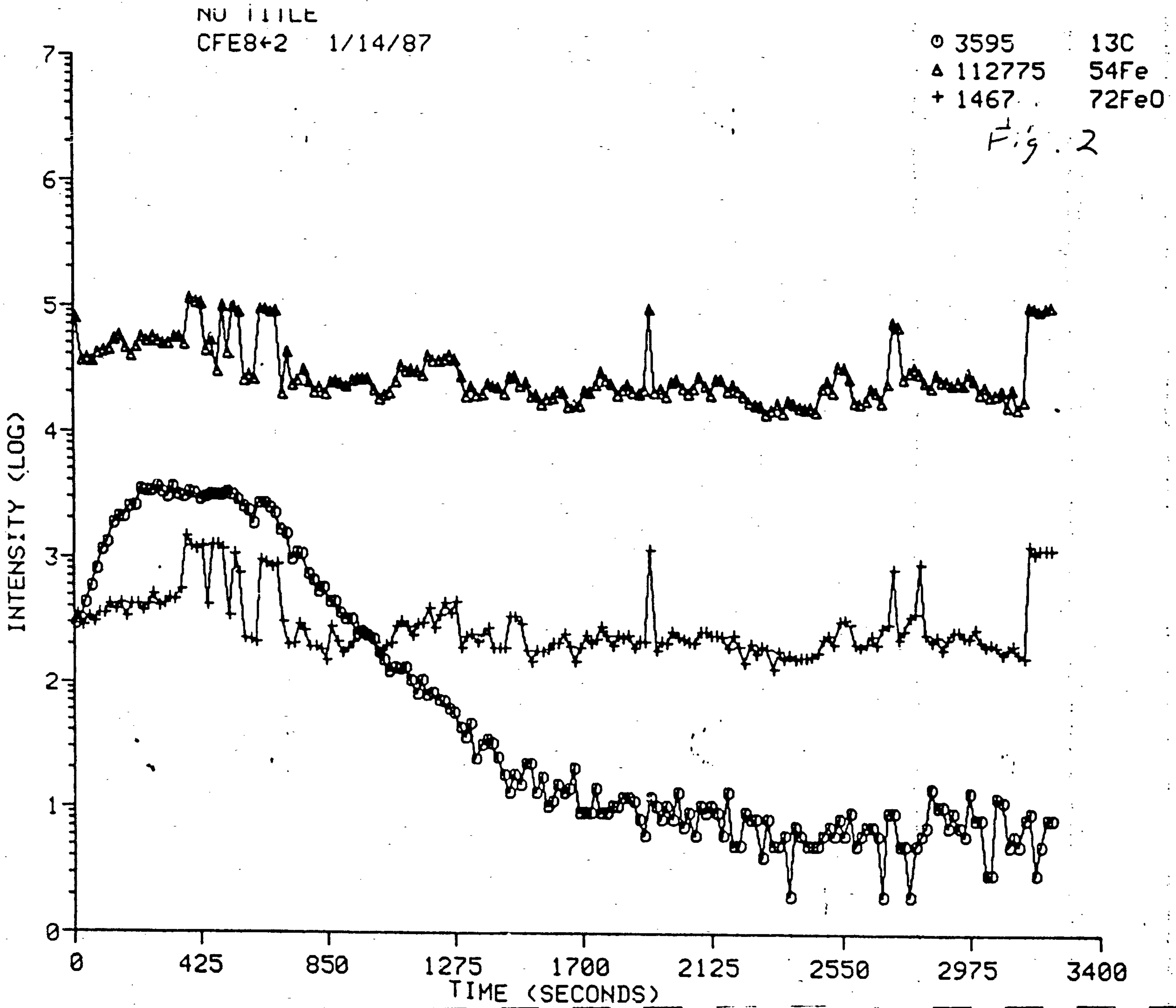
NO TITLE
CFE8+2 1/14/87
⊙ 3595 13C
△ 112775 54Fe
+ 1467 72FeO
INTENSITY (LOG)
0
1
2
3
4
5
6
7
0
425
850
1275
1700
2125
2550
2975
3400
TIME (SECONDS)

Fig. 2

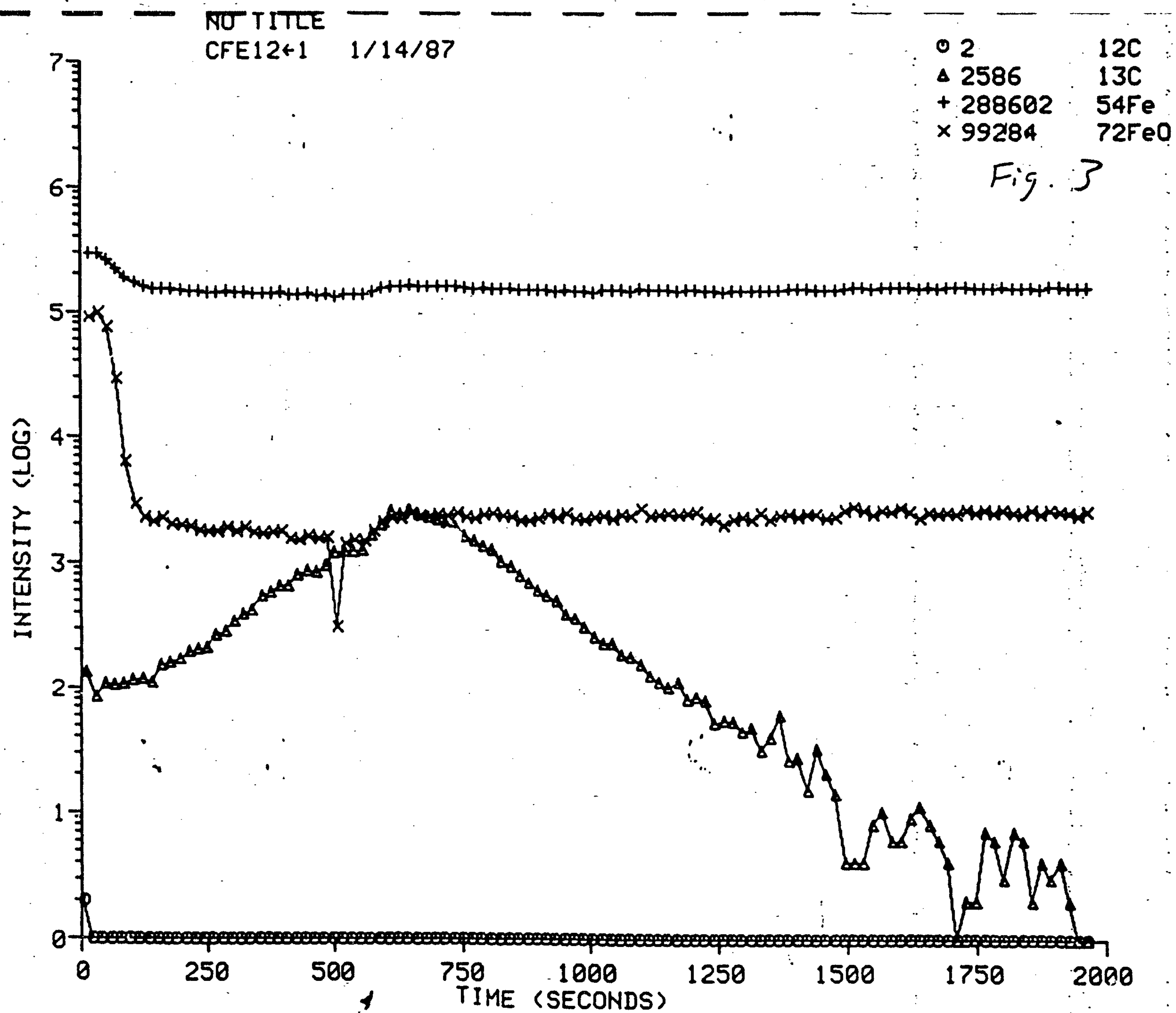
NO TITLE
CFE12+1 1/14/87
ʘ 2 12C
△ 2586 13C
+ 288602 54Fe
× 99284 72FeO
INTENSITY (LOG)
TIME (SECONDS)

Fig. 3

SIMS DEPTH PROFILING AND IMAGING ANALYSIS OF CHROME PLATED NICKEL SAMPLES

1. On 30 December 1986, I. Singer, Code 6176, submitted two samples for analysis by secondary ion mass spectrometry. these samples, labeled C-49 (work hardened) and N-16 (non-work hardened), consist of chrome plated nickel substrates which show surface crack patterns. Of interest was the lateral distribution of species having a significant secondary ion signal and the relative concentrations and depth distribution of oxygen in the two samples.

2. The samples were analyzed with a CAMECA IMS-300 ion microscope using 5.5 keV Ar^+ primary ions at a primary current of 500 nA (C-49) and 1.0uA (N-16) for depth profiles and mass spectra. The primary beam was rastered over an area of approximately 500 x 800 um. In the center of this raster an area 250 um in diameter was analyzed. Because of the difference in size between the rastered and analyzed areas the contributions of analyte atoms residing et the crater walls to the detected signals were eliminated.

Imaging analysis was performed by recording the secondary ion image on electron sensitive film. Images were taken at a primary current of 1.0 uA with the beam rastered over an area slightly greater than 250 x 250 um. Some details concerning the CAMECA IMS-300 ion microscope are given in the appendix.

3. Figs. 1 and 2 show depth profiles of mass 16 (O^+), mass 39 (K^+), and mass 52 (Cr^+) for C-49 and N-16, respectively. As may be seen in both samples the oxygen is near background levels. Sample N-16 however, does show a higher mass 39 signal level, relative to mass 52, than sample C-49.

Mass spectra taken of the samples N-16 and C-49 show significant secondary ion signals (greater than 1000 total counts) indicative of Ni, Cr, K, and Na.

An index of the images taken of the sample surfaces is given in Table I. An image of the Al focusing grid is provided for scale. The grid spacings are 25 um. The change in the mass 39 image of N-16 from the "peak shaped structures to the "crack pattern" is most probably due to the eroding action of the primary ion beam. Whether the "crack pattern" is the cause or a product of the surface cracking is presently unknown. A more in-depth study of these samples is planned and will be detailed in a subsequent report.

4. Appendix:

The CAMECA IMS-300 ion microscope employs an energetic (0-10 keV) primary ion beam (typically O_2^+, Ar^+, or O^-) to analyze solid materials. The interaction of the primary ions with the sample erodes the target surface liberating secondary ions which are subsequently mass analyzed. The

GEO-CENTERS, INC.

instrument design is such that the lateral distribution of the secondary ions is reformed at the detector resulting in a magnified mass analyzed image of the sample surface. This image may be observed visually or recorded on electron sensitive film with a field of view of 250 microns and a lateral resolution of one micron. The ion microscope is also capable of providing a three dimensional characterization of solids by monitoring the secondary ion signal of interest as a function of time. Provided the sputter yield (sputtered atoms/incident ion) is constant (or the layer thicknesses of a heterogeneous sample are known) this time scale may be converted to a depth scale by measurement of the crater depth. Crater depth measurements are normally made in this laboratory by interferometry. Secondary ion mass spectrometry (SIMS) is capable of detecting all elements in the periodic table, with detection limits in the ppm to ppb range. With proper standards, quantification may be performed with accuracies of approximately 10% or less. The instrument is normally operated as a low resolution mass spectrometer (M/M = 300), but may also be operated in a high resolution mode (M/M = ~ 2500).

STEVEN HUES

GEO-CENTERS, INC.

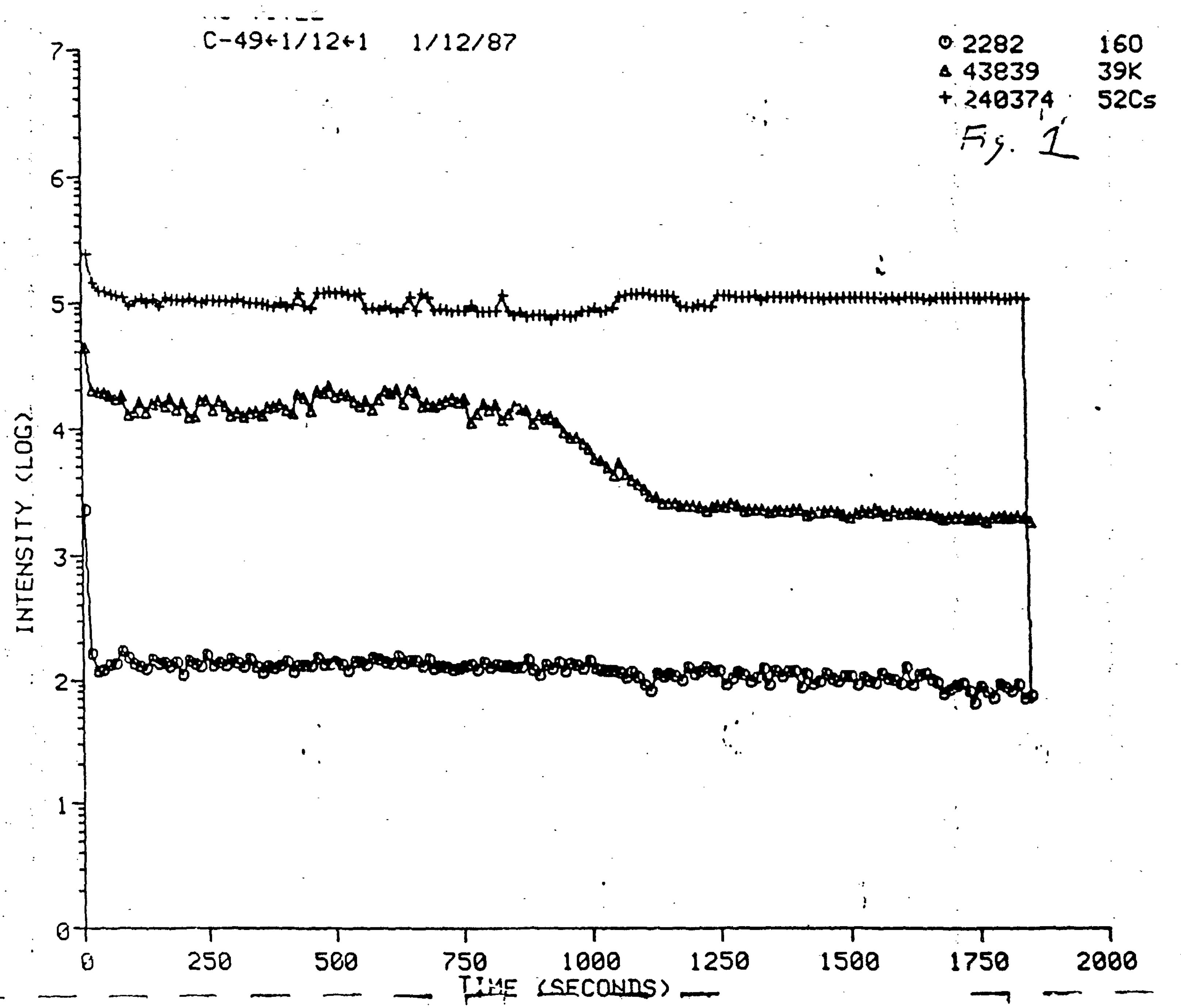
C-49+1/12+1 1/12/87
○ 2282 16O
△ 43839 39K
+ 240374 52Cs
INTENSITY (LOG)
TIME (SECONDS)
0
1
2
3
4
5
6
7
0
250
500
750
1000
1250
1500
1750
2000

Fig. 1

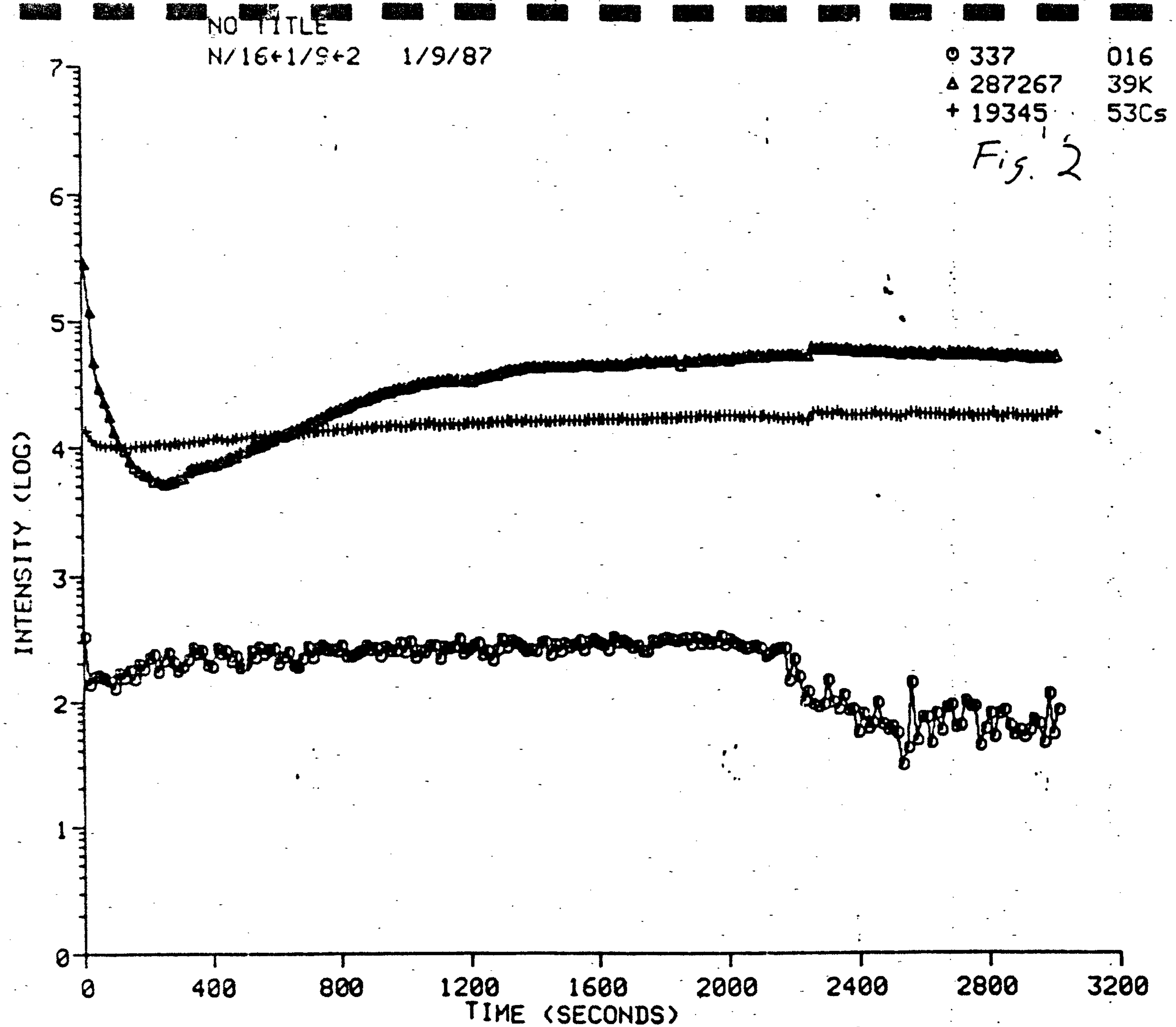
NO TITLE
N/16+1/9+2 1/9/87
o 337 016
Δ 287267 39K
+ 19345 53Cs
INTENSITY (LOG)
0
1
2
3
4
5
6
7
0
400
800
1200
1600
2000
2400
2800
3200
TIME (SECONDS)

Fig. 2

TABLE I

IMAGE	SAMPLE	MASS
1	C-49	16
2	C-49	39
3	N-16	16
4	N-16	39
5	N-16	52
6	N-16	39
7	N-16	52
8	Grid	27

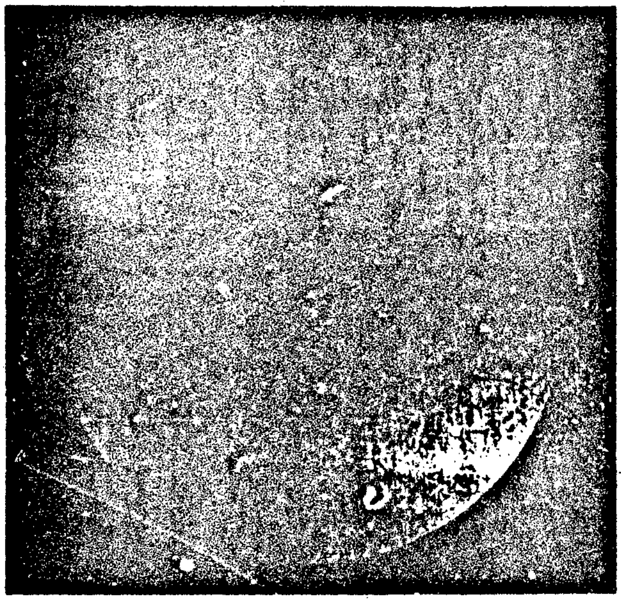

1

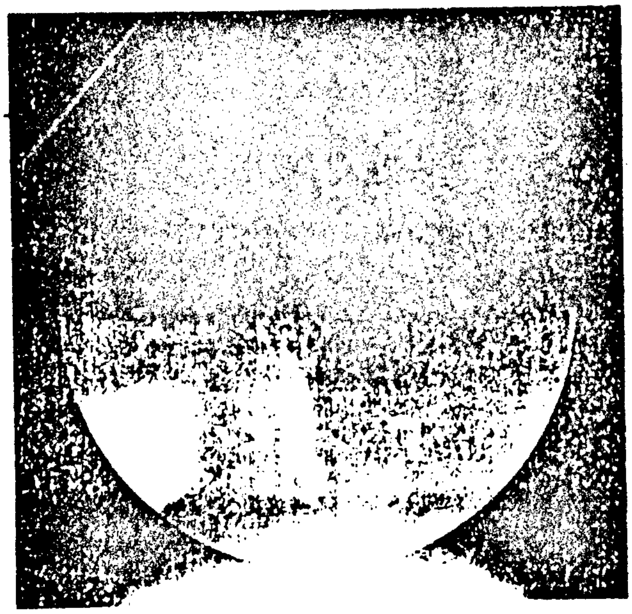

2

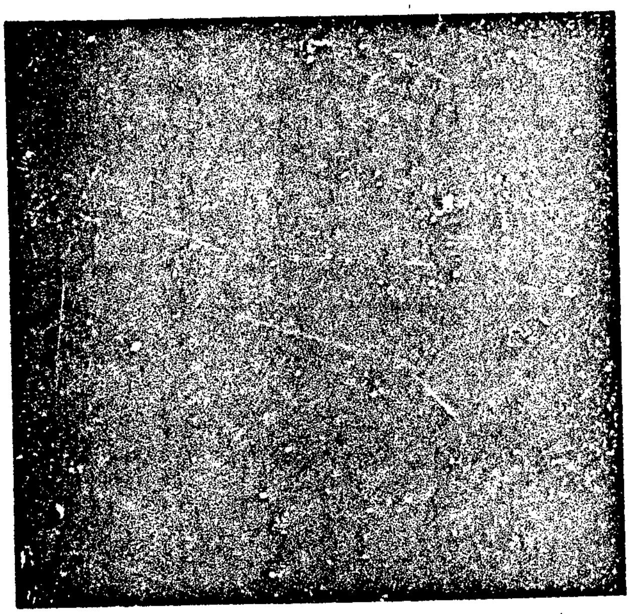

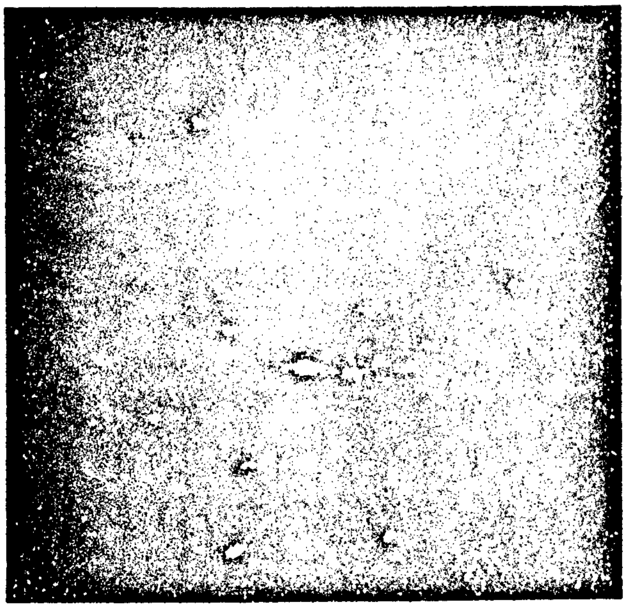

4

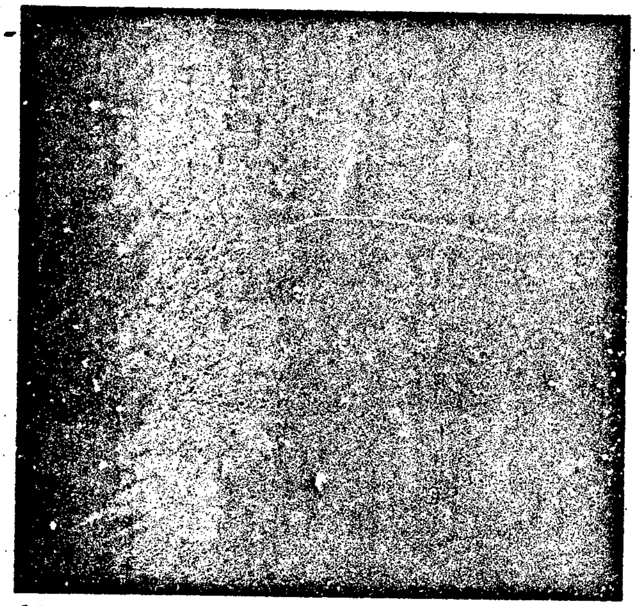

5

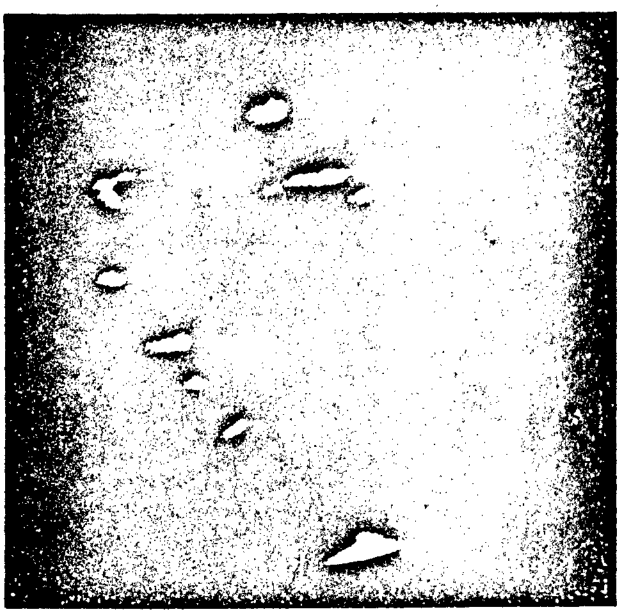

6

7

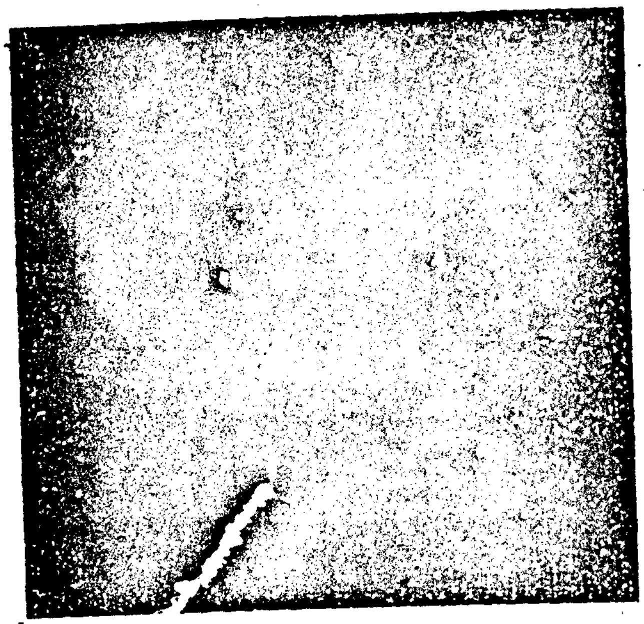

8

SIMS DEPTH PROFILING OF 304 STAINLESS STEEL AND Fe/C STEEL

1. On 18 February 1987 I. Singer, Code 6176, submitted two samples, one a sample of 304 stainless steel, labeled 304SS, and the other a sample of FeC steel, labeled QQT508, for analysis by secondary ion mass spectrometry. On 19 February 1987 a third sample of Fe steel, labeled 35 was also submitted. The first two samples had been implanted with N^+ in an atmosphere of ^{13}CO to a fluence of 5.5 x 10^{17} atoms/cm^2, the third sample had been implanted with N^+ to a fluence of 4 x 10^{17} atoms/cm^2 under normal vacuum conditions. Of interest was the depth distribution of ^{13}C and ^{14}N.

2. The samples were depth profiled with a CAMECA IMS-300 ion microscope using 5.5 keV O_2^+ primary ions. The primary beam was rastered over an area of approximately 500 x 800 μm. In the center of this raster an area 250 μm in diameter was analyzed. Because of the difference in size between the rastered and analyzed areas the contributions of analyte atoms residing at the crater walls to the detected signals were eliminated. Some details concerning the CAMECA IMS-300 ion microscope are given in the appendix.

3. Fig. 1 shows a depth profile of 304SS for mass 12 ($^{12}C^+$), mass 13 ($^{12}CH^+$, $^{13}C^+$), mass 14 ($^{14}N^+$), mass 50 ($^{50}Cr^+$), and mass 57 ($^{57}Fe^+$) taken at a primary current of 300 nA. Two features of note in this profile are that the mass 57 signal follows the N^+ signal. This is most likely due to a matrix effect caused by the presence of nitrogen. A second feature is that the mass 13 signal decreases at the backside of the nitrogen implant. The cause of this is not known at present. Causes that have been speculated are diffusion of ^{13}C throughout the implanted region or the presence of hydrogen in the implanted region contributing to the $^{12}CH^+$ signal. Fig. 2 is a second profile of 304SS taken on the following day to confirm the reproducibility of the mass 13 signal decrease. Fig. 3 is a profile of the front side of the 304SS nitrogen implant performed at a primary current of 100 nA. Fig. 4 is a depth profile of QQT580 taken under the same conditions and immediately following the profile shown in Fig. 1. Although a mass 50 signal is seen in this profile, isotope ratio measurements do not verify that the signal is due to the presence of Cr. Fig. 5 is a depth profile of the front side of the QQT580 nitrogen implant performed at a primary current of 100 nA. Fig. 6 is a profile of the front side of nitrogen implant in sample 35. Of interest was the apparent mass 14 ($^{14}N^+$) peak before the nitrogen implant. Although a peak in the mass 14 signal does appear, no conclusions concerning the nitrogen concentration can safely be drawn as the ion yields in this near surface region, as evidenced by the mass 57 signal, are changing greatly as a result of surface contaminants being sputtered and the implanted oxygen concentration attaining steady state.

4. Appendix:

The CAMECA IMS-300 ion microscope employs an energetic (0-10 keV) primary ion beam (typically O_2^+, Ar^+, or O^-) to analyze solid materials. The interaction of the primary ions with the sample erodes the target surface liberating secondary ions which are subsequently mass analyzed. The instrument design is such that the lateral distribution of the secondary ions is reformed at the detector resulting in a magnified mass analyzed image of the sample surface. This image may be observed visually or recorded on electron sensitive film with a field of view of 250 microns and a lateral resolution of one micron. The ion microscope is also capable of providing a three dimensional characterization of solids by monitoring the secondary ion signal of interest as a function of time. Provided the sputter yield (sputtered atoms/incident ion) is constant (or the layer thicknesses of a heterogeneous sample are known) this time scale may be converted to a depth scale by measurement of the crater depth. Crater depth measurements are normally made in this laboratory by interferometry. Secondary ion mass spectrometry (SIMS) is capable of detecting all elements in the periodic table, with detection limits in the ppm to ppb range. With proper standards, quantification may be performed with accuracies of ~ 10% or less. The instrument is normally operated as a low resolution mass spectrometer (M/M = 300), but may also be operated in a high resolution mode (M/M = ~2500).

GEO-CENTERS, INC.

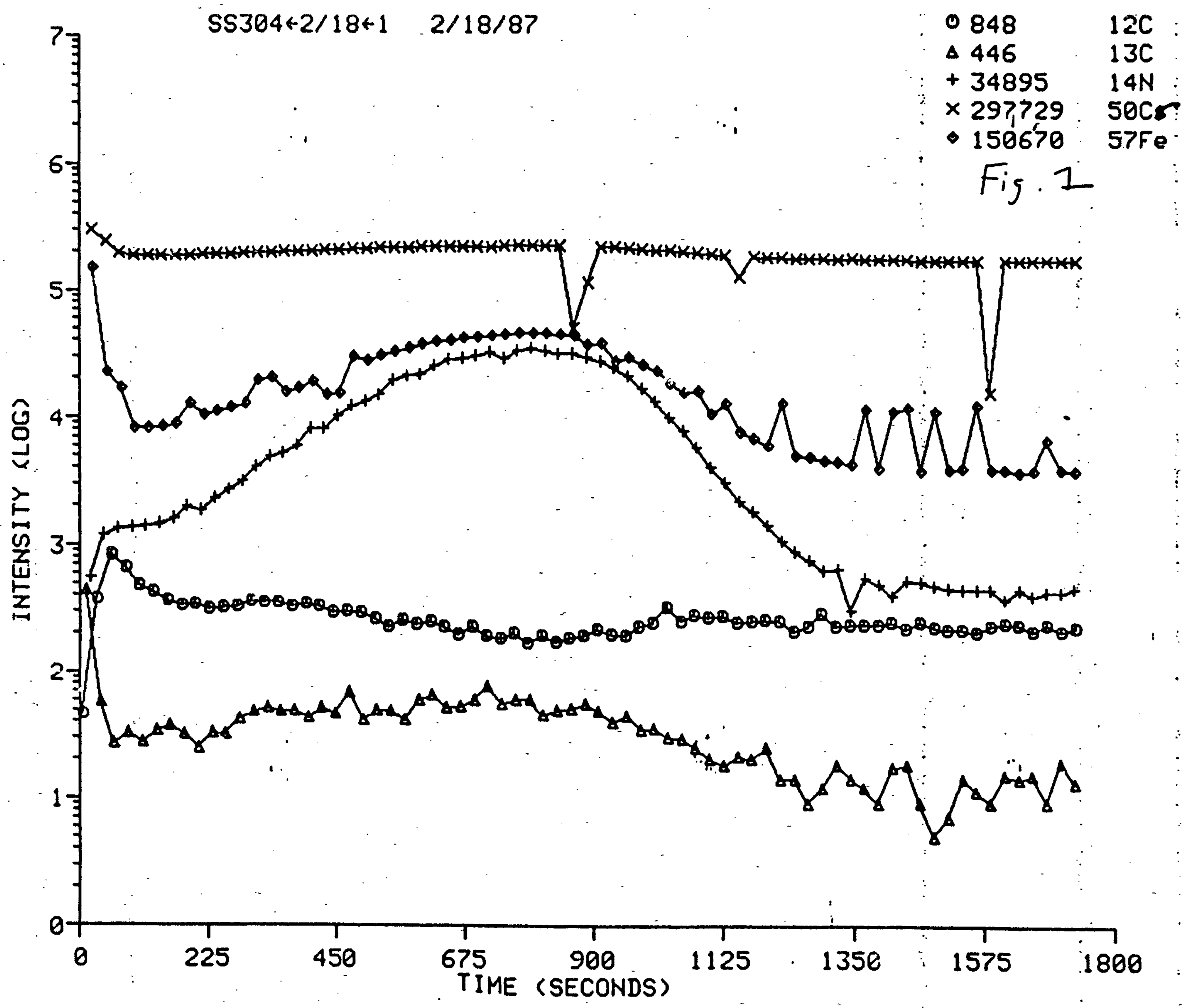
SS304+2/18+1 2/18/87
o 848 12C
Δ 446 13C
+ 34895 14N
× 297729 50Cr
◊ 150670 57Fe
INTENSITY (LOG)
0
1
2
3
4
5
6
7
0
225
450
675
900
1125
1350
1575
1800
TIME (SECONDS)

Fig. 1

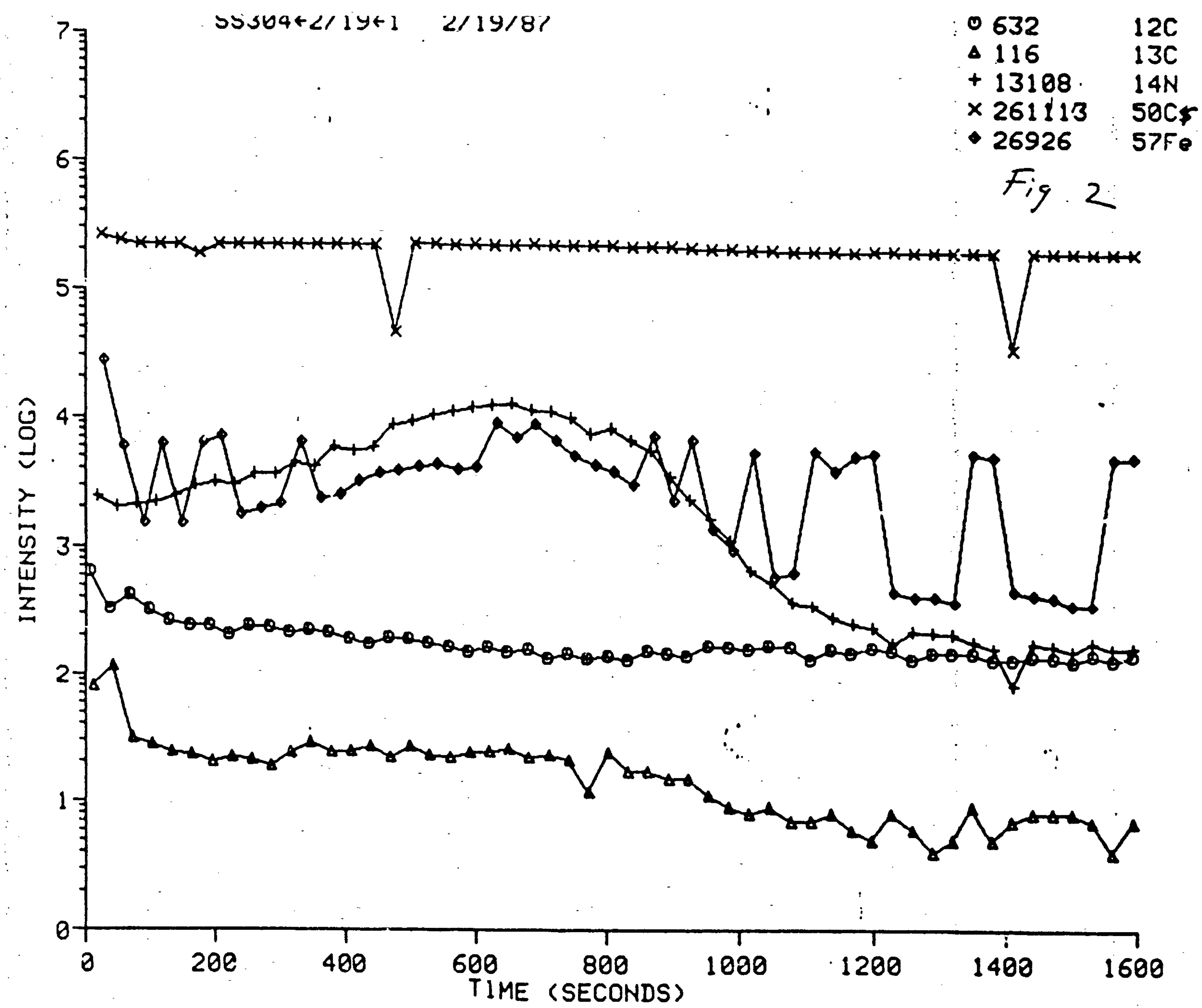
SS304+2/19+1 2/19/87
ο 632 12C
Δ 116 13C
+ 13108 14N
× 261113 50Cr
◆ 26926 57Fe
INTENSITY (LOG)
0
1
2
3
4
5
6
7
0
200
400
600
800
1000
1200
1400
1600
TIME (SECONDS)
Fig 2

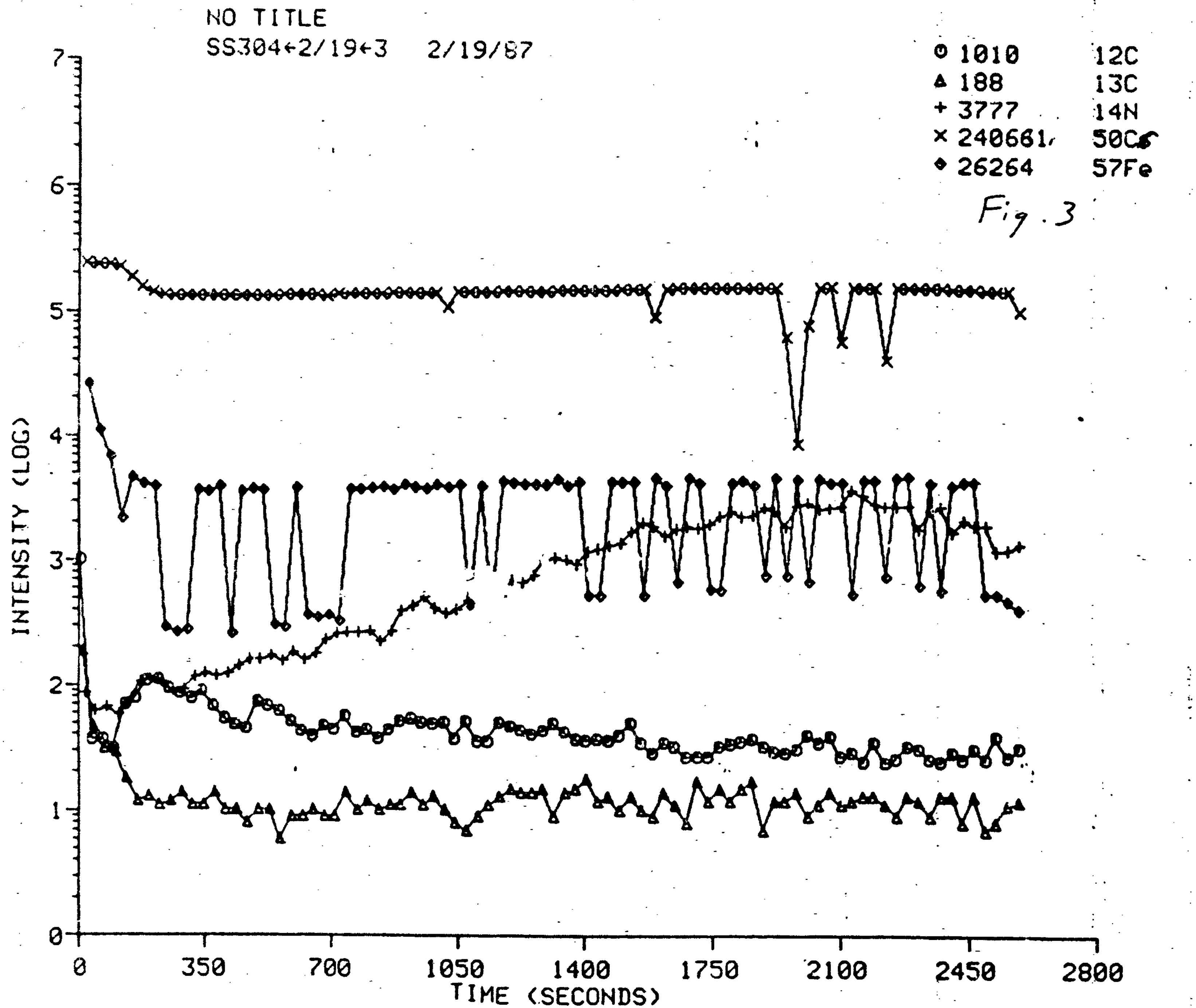
NO TITLE
SS304+2/19+3 2/19/87
1010 12C
188 13C
3777 14N
240661 50Cr
26264 57Fe
INTENSITY (LOG)
TIME (SECONDS)
0
1
2
3
4
5
6
7
0
350
700
1050
1400
1750
2100
2450
2800
Fig. 3

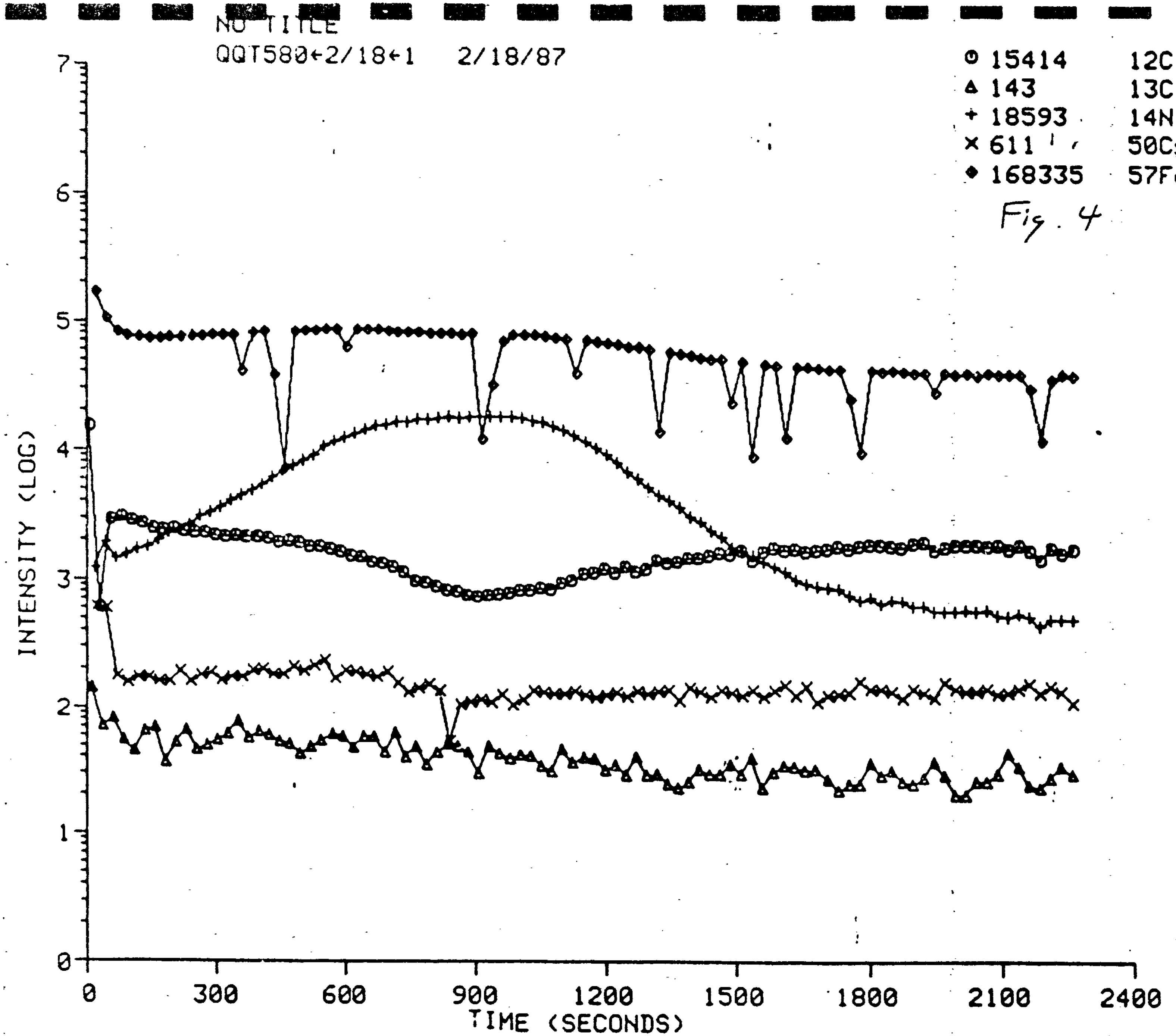
NO TITLE
QQT580←2/18←1 2/18/87
15414 12C
143 13C
18593 14N
611 50Cr
168335 57Fe
INTENSITY (LOG)
TIME (SECONDS)
0
1
2
3
4
5
6
7
0
300
600
900
1200
1500
1800
2100
2400

Fig. 4

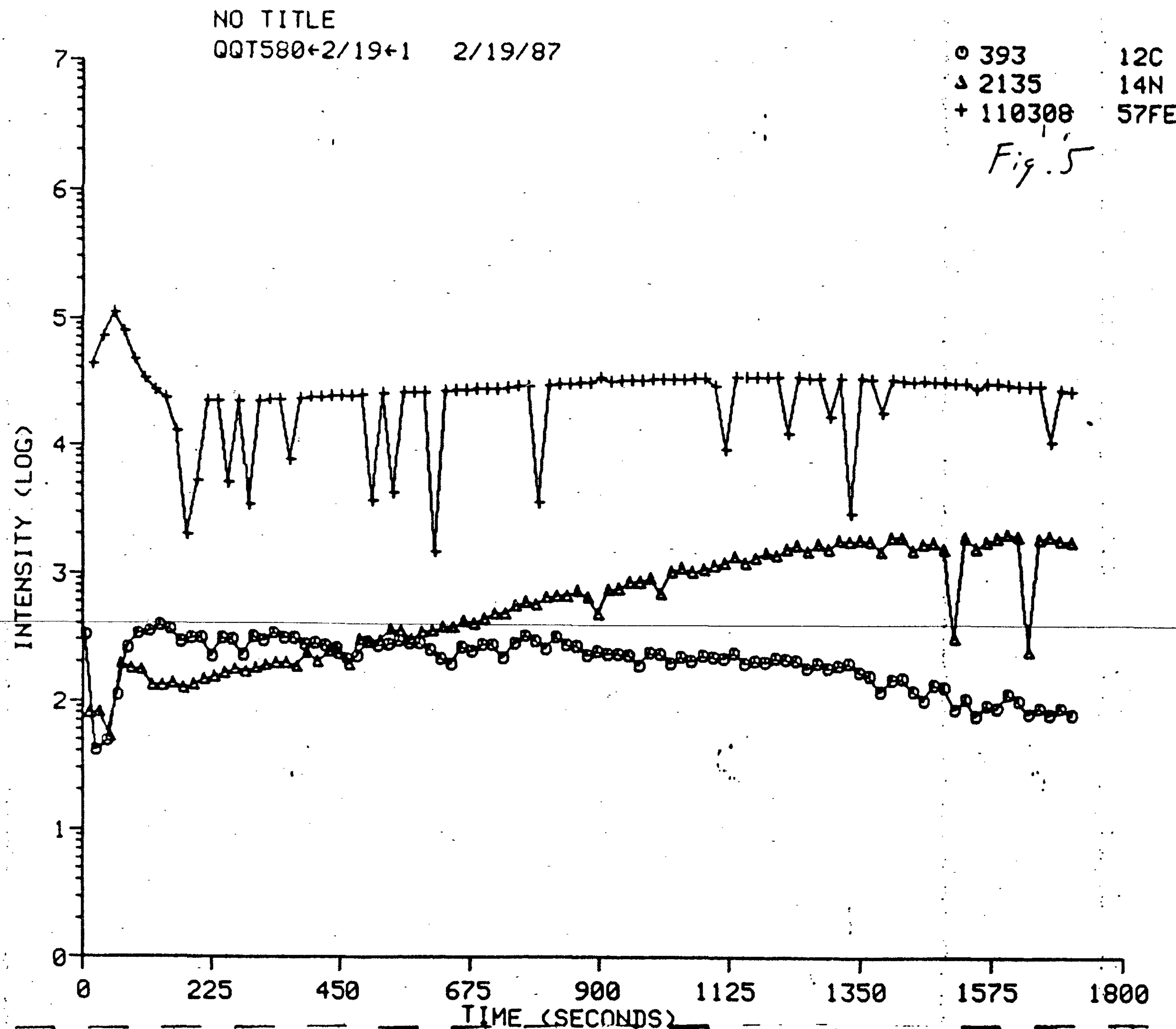

NO TITLE
QQT580←2/19←1 2/19/87
⊙ 393 12C
△ 2135 14N
+ 110308 57FE
INTENSITY (LOG)
TIME (SECONDS)
0
225
450
675
900
1125
1350
1575
1800
1
2
3
4
5
6
7

Fig. 5

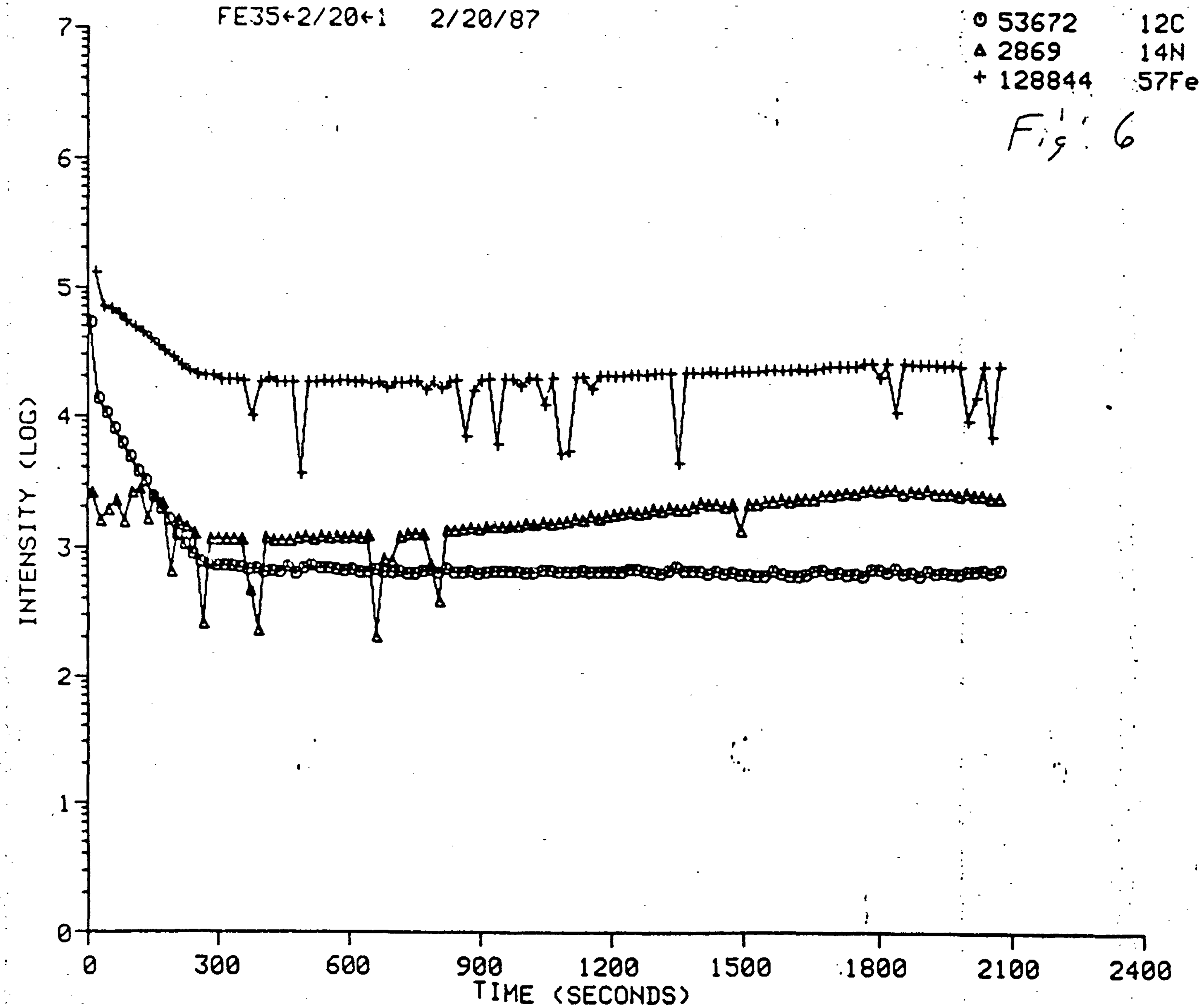
FE35←2/20←1 2/20/87
o 53672 12C
Δ 2869 14N
+ 128844 57Fe
INTENSITY (LOG)
0
1
2
3
4
5
6
7
0
300
600
900
1200
1500
1800
2100
2400
TIME (SECONDS)

Fig. 6

SIMS DEPTH PROFILING OF ^{13}C, ^{14}N, AND ^{15}N-IMPLANTED IRON

1. On 27 February 1987 I. Singer, Code 6176, submitted three samples for analysis by secondary ion mass spectrometry. These samples consisted of Fe substrates which had been implanted with ^{13}C. Sample 4 had been implanted at an energy of 70 keV, sample 12 at 190 keV, and sample 8 at both of these energies. The samples were then implanted with ^{14}N and ^{15}N to a projected range midway between the two carbon implants. These samples had previously been analyzed prior to nitrogen implantation (1). Of interest was the depth distribution of ^{13}C, ^{14}N, and ^{15}N.

2. The specimen was depth profiled with a CAMECA IMS-300 ion microscope using 5.5 keV O_2^+ ions at a primary current of 150 nA. The primary beam was rastered over an area of approximately 500 x 800 μm. In the center of this raster an area of 250 μm in diameter was analyzed. Because of the difference in size between the rastered and analyzed areas, contributions of analyte atoms residing at the crater walls to the detected signal were eliminated. Some details concerning the CAMECA IMS-300 ion microscope are presented in the appendix.

3. Fig. 1 shows a depth profile of sample 4 for mass 12 ($^{12}C^+$), mass 13 ($^{13}C^+$), mass 14 ($^{14}N^+$, $^{13}CH^+$), mass 15 (^{15}N, $^{14}NH^+$), mass 54 ($^{54}Fe^+$), mass 70 ($^{56}Fe^{14}N^+$) and mass 71 ($^{56}Fe^{15}N^+$). Fig. 2 shows, for clarity, the same depth profile for masses 13, 14, 15, and 54 only. Figs. 3, 4, 5, and 6 show comparable profiles for samples 8 and 12, respectively. Fig. 7 shows a comparable profile for an N-unimplanted area of sample 4 showing the background levels of the species of interest. Figs. 8 and 9 show depth profiles of sample 8, plotted on a linear scale, prior to (1) and after N implantation, respectively. Although there is a small difference in ^{13}C valley resolution between the two linear replots, this may be due to differences in primary current density. In conclusion, it may be stated that the ^{13}C distribution in the implanted samples were not significantly affected by the ^{14}N and ^{15}N implants.

4. Appendix:

The CAMECA IMS-300 ion microscope employs an energetic (0-10 keV) primary ion beam (typically O_2^+, Ar^+, or O^-) to analyze solid materials. The interaction of the primary ions with the sample erodes the target surface liberating secondary ions which are subsequently mass analyzed. The instrument design is such that the lateral distribution of the secondary ions is reformed at the detector resulting in a magnified mass analyzed image of the sample surface. This image may be observed visually or recorded on electron sensitive film with a field of view of 250 microns and a lateral resolution of one micron. The ion microscope is also capable of providing a three dimensional characterization of solids by monitoring the secondary ion signal of interest as a function of time. Provided the sputter yield (sputtered atoms/incident ion) is constant (or the layer thicknesses of a heterogeneous sample are known) this time scale may be converted to a depth scale by measurement of the crater depth. Crater depth measurements are normally made in this laboratory by interferometry. Secondary ion mass spectrometry (SIMS) is capable of detecting all elements in the periodic table, with detection limits in the ppm to ppb range. With proper standards, quantification may be performed with accuracies of ~ 10% or less. The instrument is normally operated as a low resolution mass spectrometer (M/M = 300), but may also be operated in a high resolution mode (M/M = ~2500).

STEVEN HUES

GEO-CENTERS, INC.

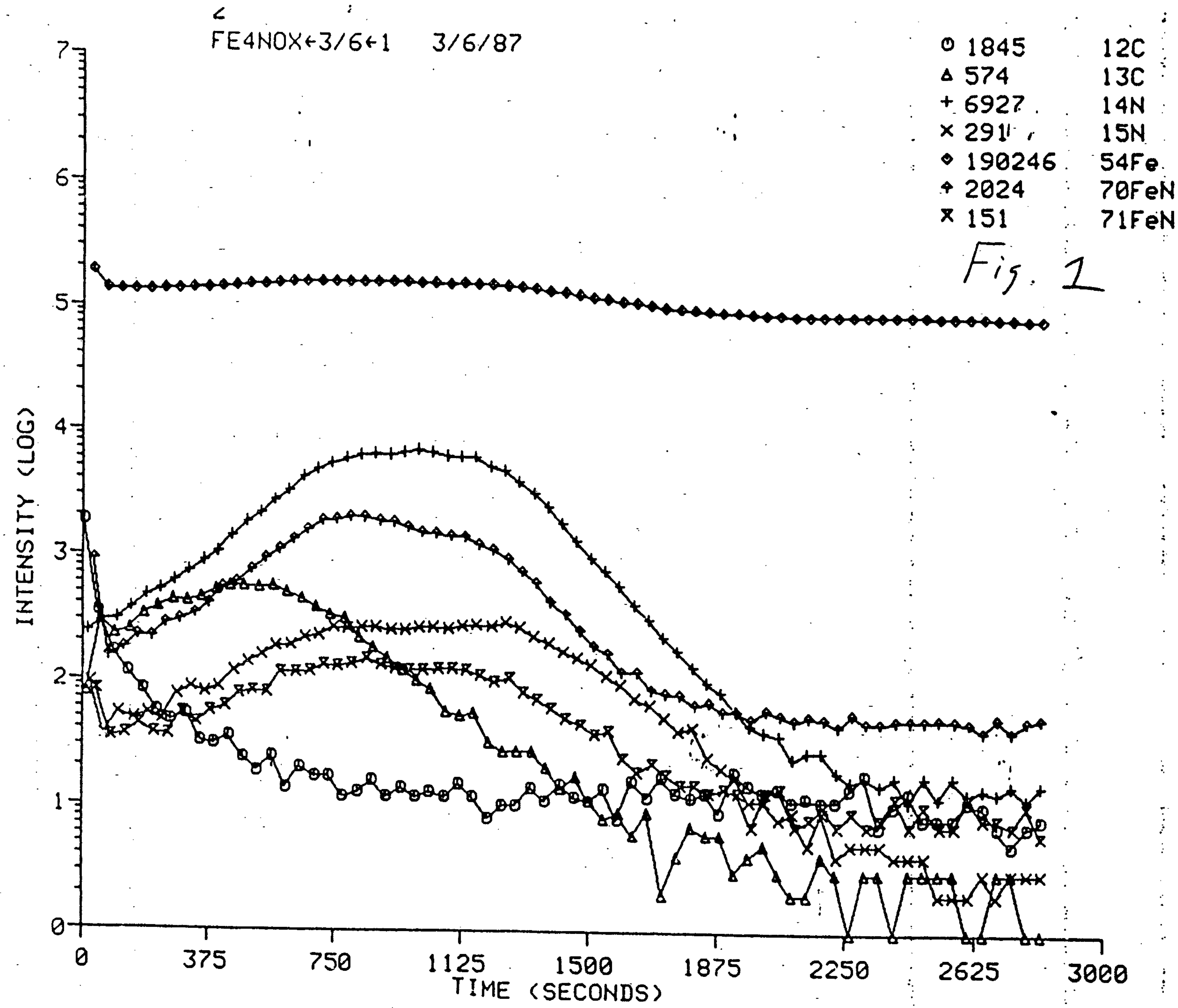
FE4NOX+3/6+1 3/6/87
o 1845 12C
△ 574 13C
+ 6927 14N
× 291 15N
◇ 190246 54Fe
✧ 2024 70FeN
ⵅ 151 71FeN
Fig. 1
INTENSITY (LOG)
0
1
2
3
4
5
6
7
0
375
750
1125
1500
1875
2250
2625
3000
TIME (SECONDS)

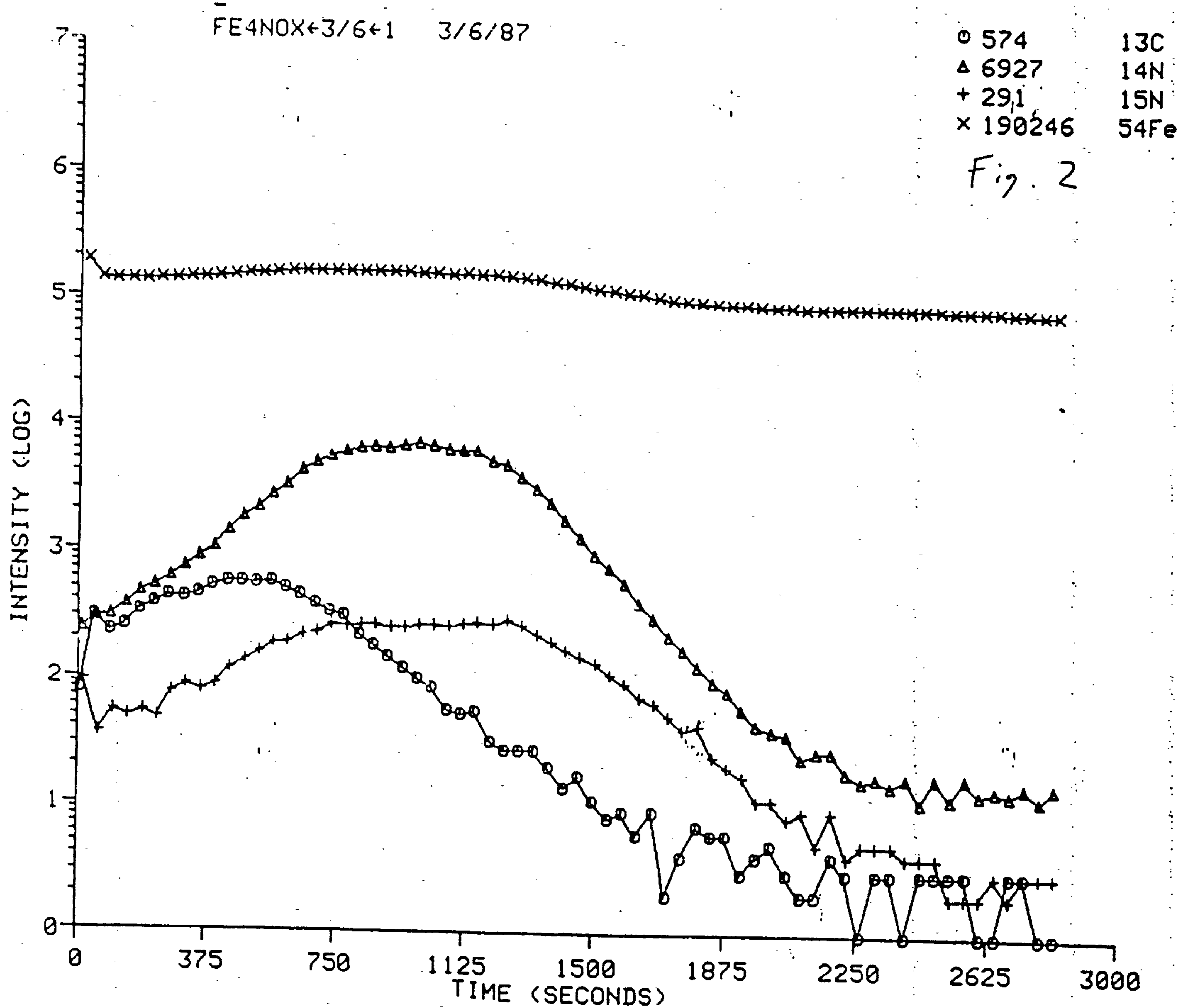
FE4NOX←3/6←1 3/6/87
○ 574 13C
△ 6927 14N
+ 291 15N
× 190246 54Fe
INTENSITY (LOG)
0
1
2
3
4
5
6
7
0
375
750
1125
1500
1875
2250
2625
3000
TIME (SECONDS)

Fig. 2

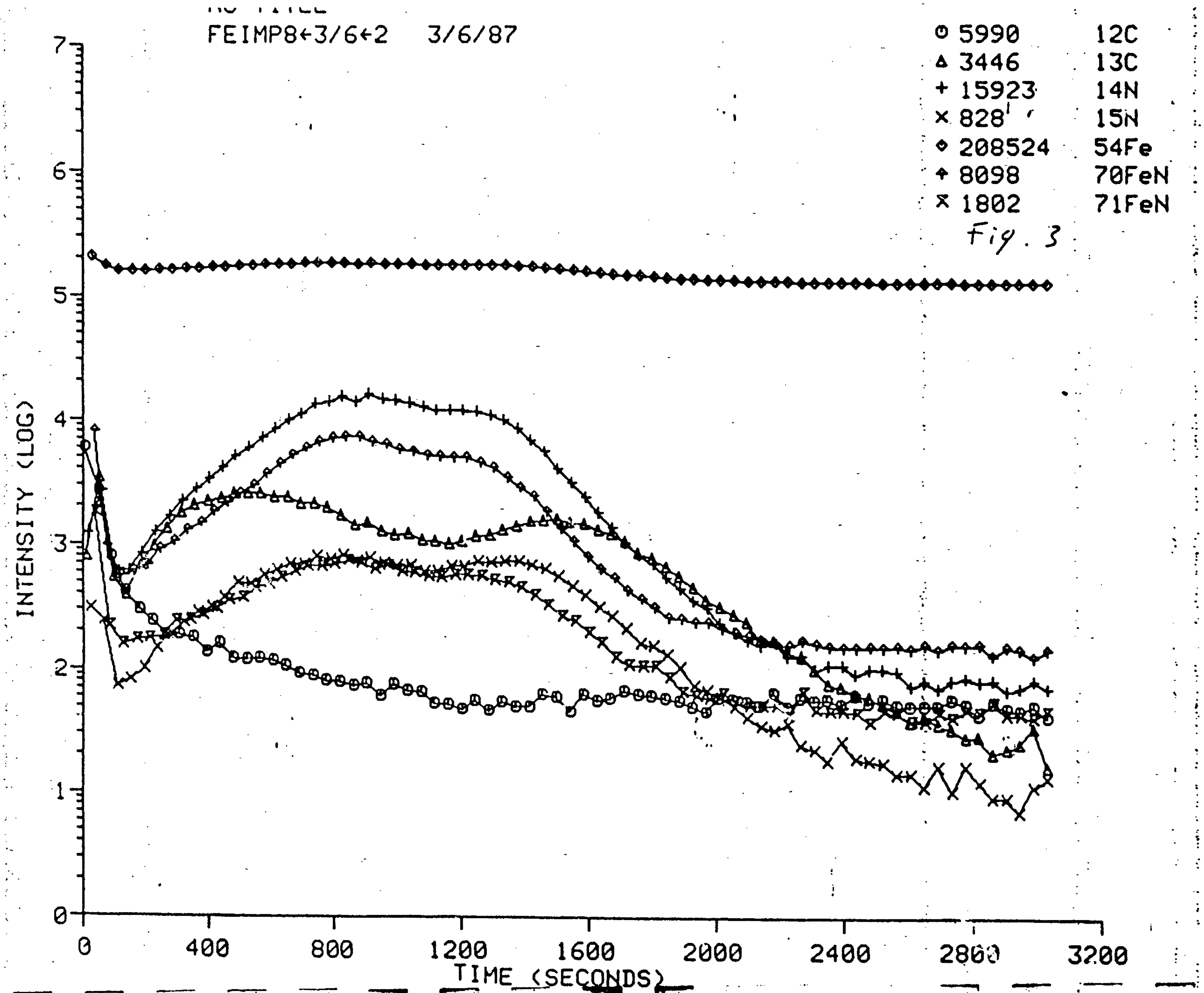

FEIMP8←3/6←2 3/6/87
5990 12C
3446 13C
15923 14N
828 15N
208524 54Fe
8098 70FeN
1802 71FeN
INTENSITY (LOG)
TIME (SECONDS)
0
1
2
3
4
5
6
7
0
400
800
1200
1600
2000
2400
2800
3200

Fig. 3

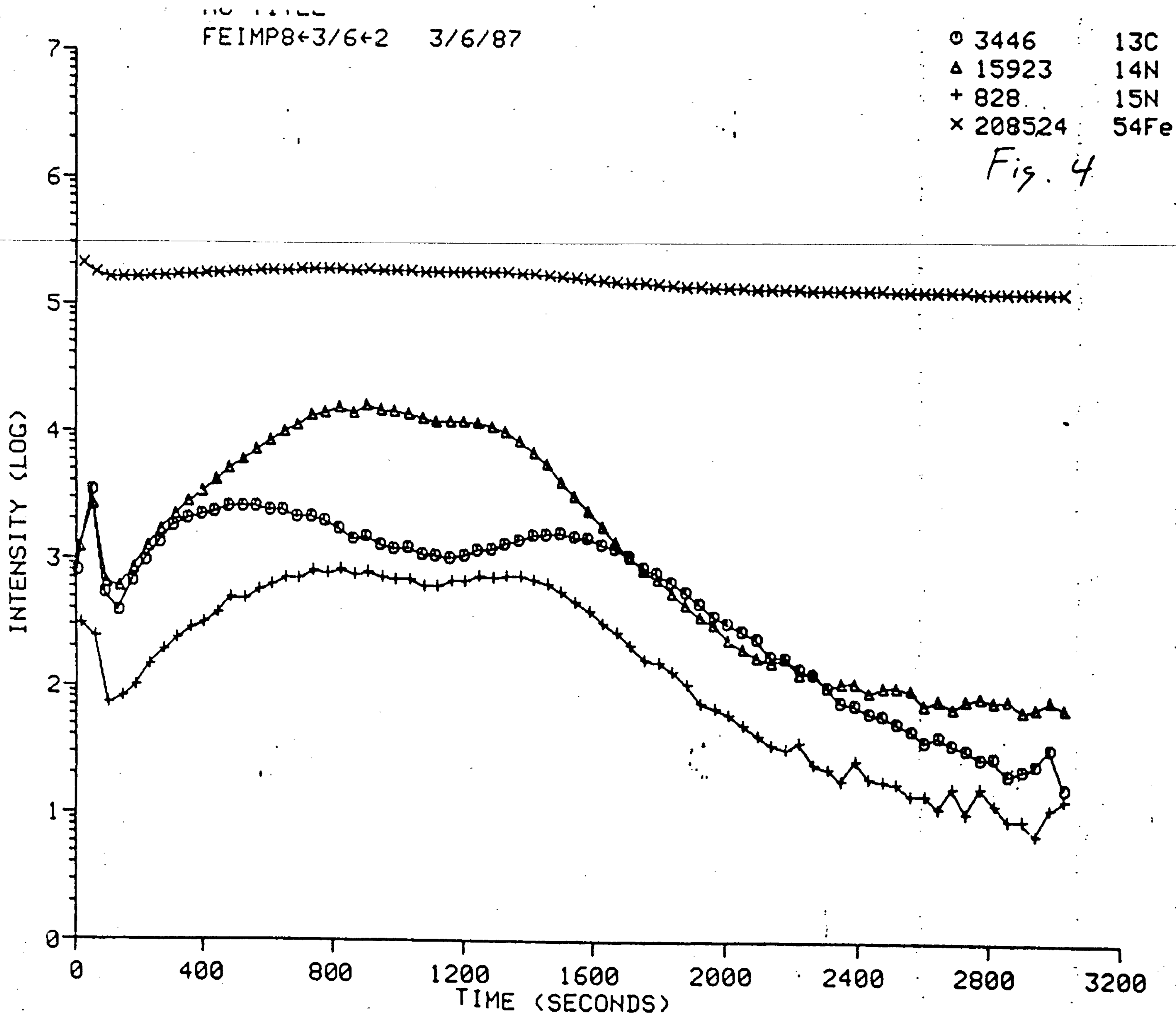
NO TITLE
FEIMP8←3/6←2 3/6/87
o 3446 13C
Δ 15923 14N
+ 828 15N
× 208524 54Fe
INTENSITY (LOG)
TIME (SECONDS)
0
1
2
3
4
5
6
7
0
400
800
1200
1600
2000
2400
2800
3200

Fig. 4

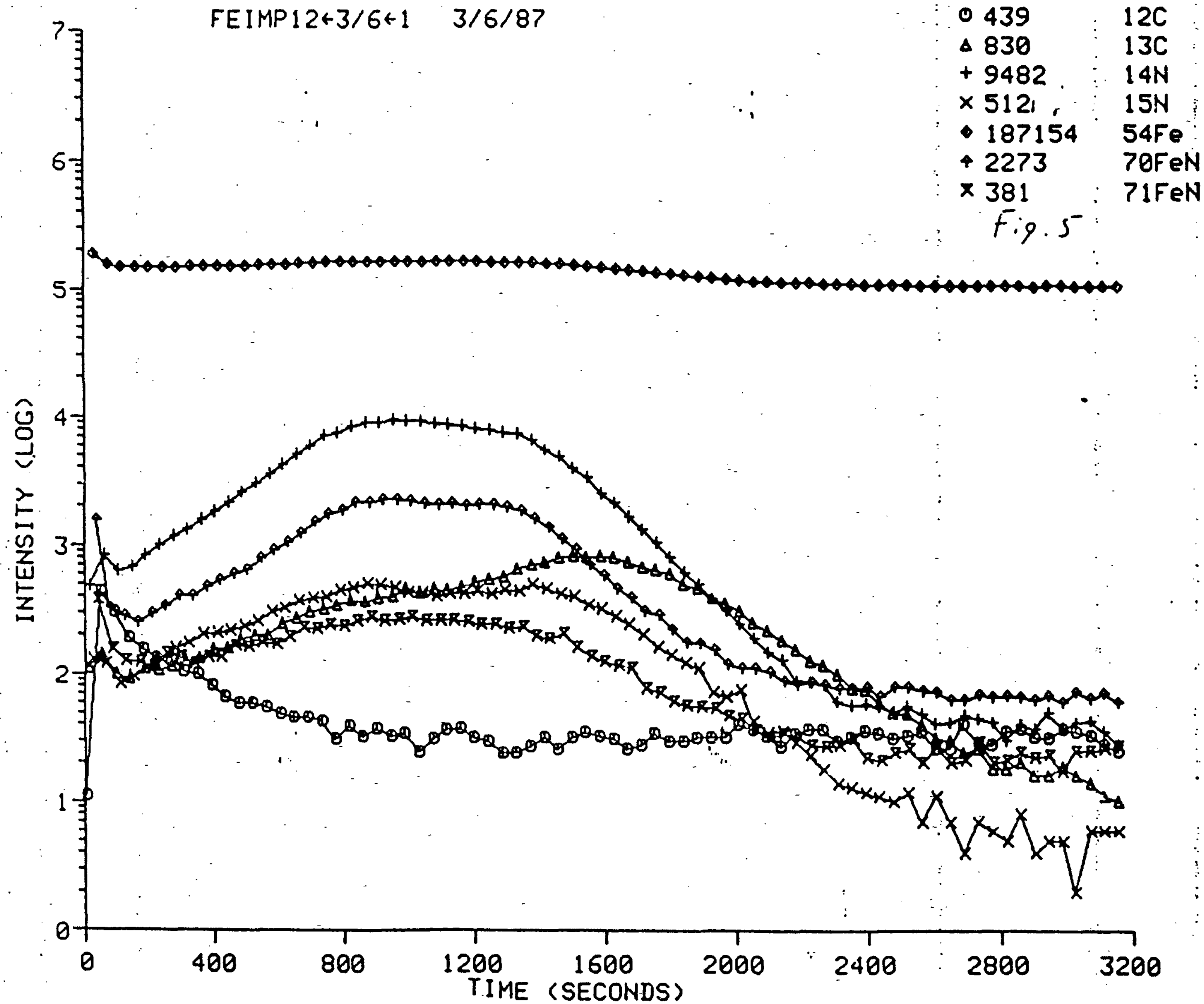
FEIMP12←3/6←1 3/6/87
439 12C
830 13C
9482 14N
512 15N
187154 54Fe
2273 70FeN
381 71FeN
INTENSITY (LOG)
TIME (SECONDS)
0
1
2
3
4
5
6
7
400
800
1200
1600
2000
2400
2800
3200

Fig. 5

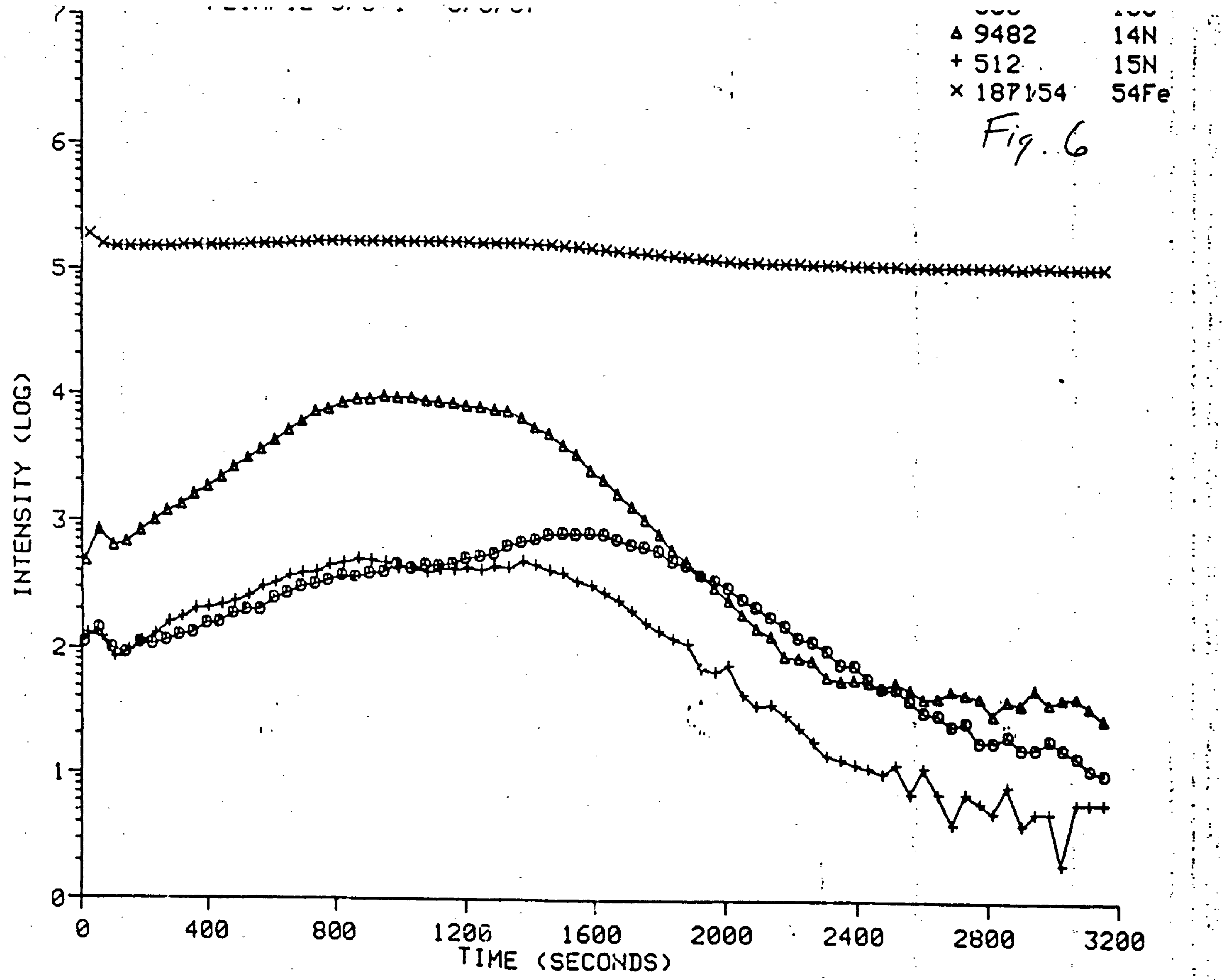

△ 9482 14N
+ 512 15N
× 187154 54Fe
INTENSITY (LOG)
0
1
2
3
4
5
6
7
0
400
800
1200
1600
2000
2400
2800
3200
TIME (SECONDS)

Fig. 6

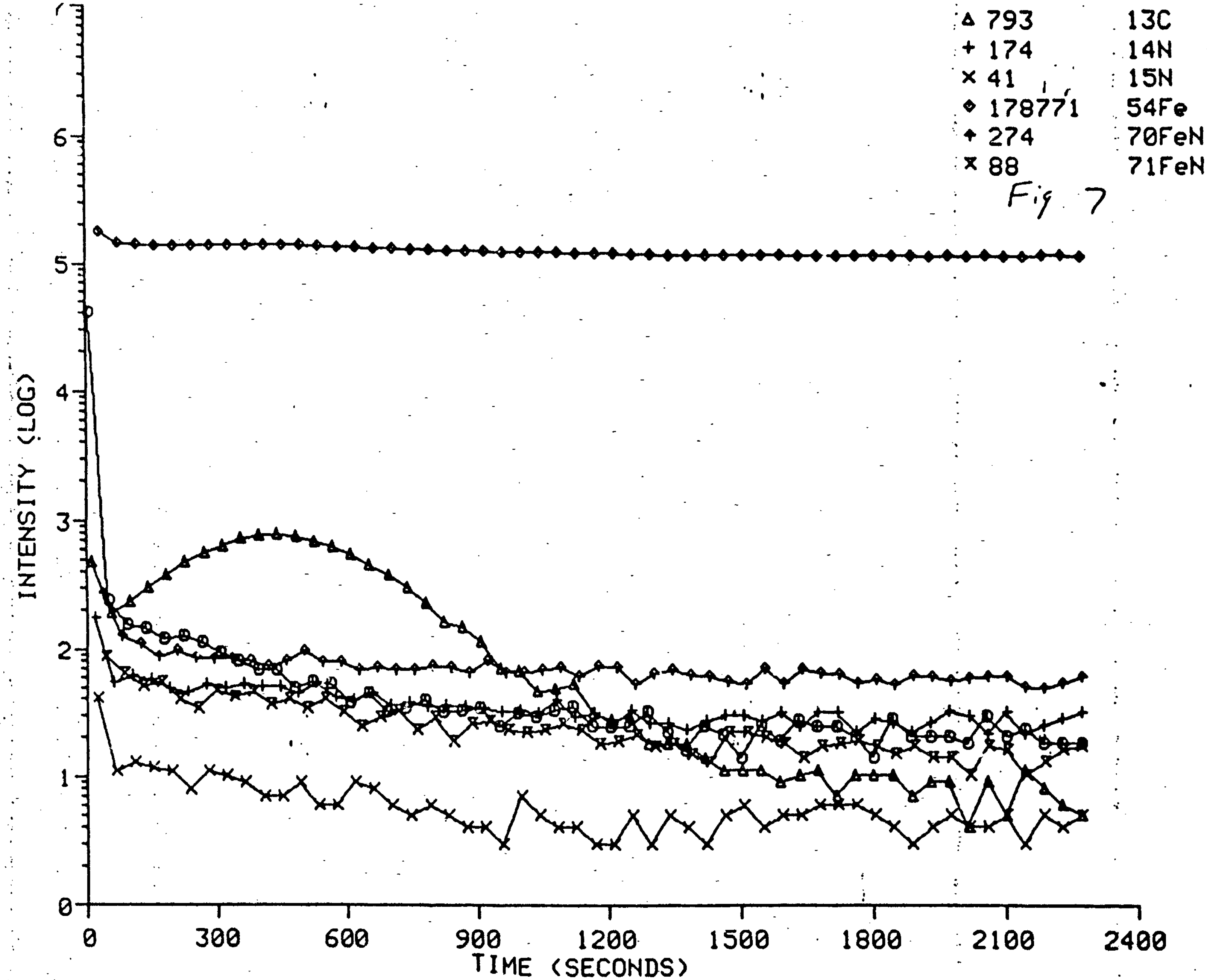

△ 793 13C
+ 174 14N
× 41 15N
◇ 178771 54Fe
✦ 274 70FeN
⌧ 88 71FeN
INTENSITY (LOG)
0
1
2
3
4
5
6
0
300
600
900
1200
1500
1800
2100
2400
TIME (SECONDS)

Fig 7

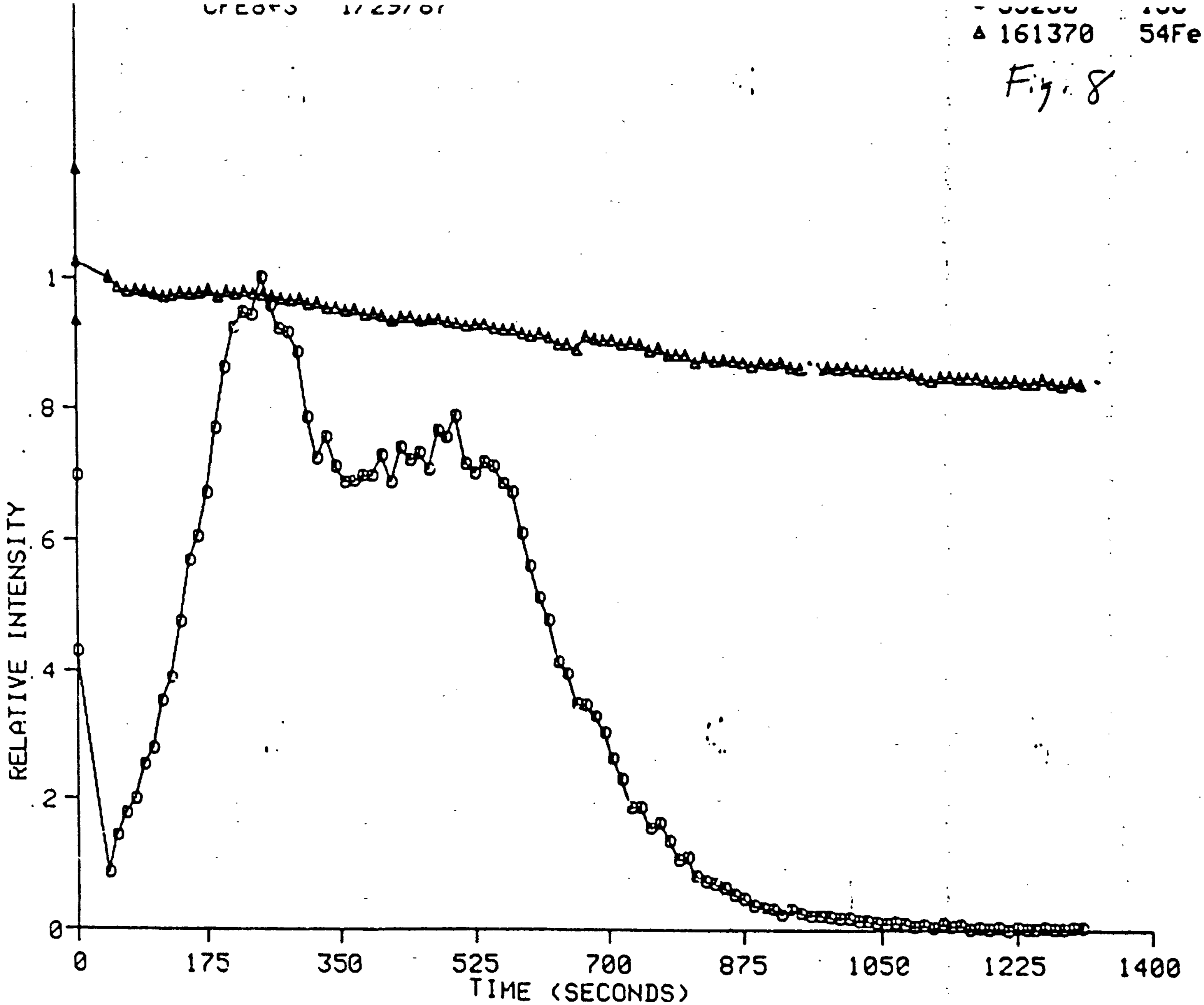
△ 161370 54Fe
RELATIVE INTENSITY
TIME (SECONDS)
0
.2
.4
.6
.8
1
0
175
350
525
700
875
1050
1225
1400

Fig. 8

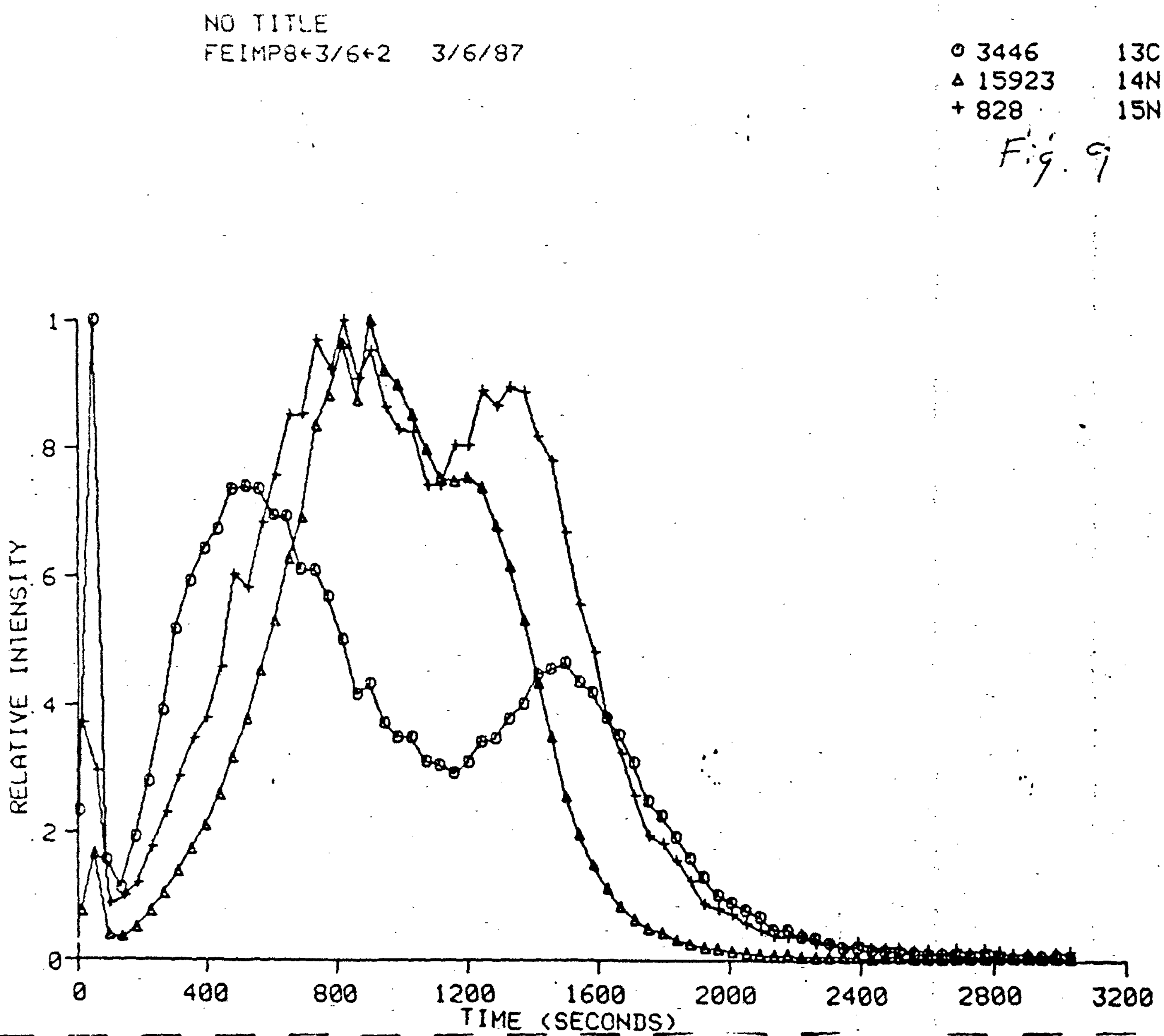
NO TITLE
FEIMP8+3/6+2 3/6/87
⊙ 3446 13C
△ 15923 14N
+ 828 15N
RELATIVE INTENSITY
TIME (SECONDS)
0
400
800
1200
1600
2000
2400
2800
3200
0
.2
.4
.6
.8
1

Fig. 9

SIMS DEPTH PROFILING OF ^{13}C, ^{14}N, AND ^{15}N-IMPLANTED IRON

1. On 21 April 1987 I. Singer, Code 6176, submitted six samples for analysis by secondary ion mass spectrometry. These samples consisted of Fe substrates which had been implanted with ^{13}C. Samples 2 and 4 had been implanted at an energy of 70 keV, samples 10 and 12 at 190 keV, and samples 6 and 8 at both of these energies. All samples were then implanted with ^{15}N to a fluence of 10^{16} atoms/cm^2 with projected range midway between the two carbon implants. Samples 2, 6, and 10 were also implanted with ^{14}N to a fluence of 5.3×10^{17} atoms/cm^2 at the same energy as the ^{15}N. The samples were masked over approximately 1/2 their area during N implantation in order that the original ^{13}C distribution could be determined. These samples had previously been analyzed prior to nitrogen implantation (1). Of interest was the depth distribution of ^{13}C, ^{14}N, and ^{15}N.

2. The specimens were depth profiled with a CAMECA IMS-300 ion microscope using 5.5 keV O_2^+ ions at a primary current of 200 nA. The primary beam was rastered over an area of approximately 500 x 800 μm. In the center of this raster an area of 250 μm in diameter was analyzed. Because of the difference in size between the rastered and analyzed areas, contributions of analyte atoms residing at the crater walls to the detected signal were eliminated. Some details concerning the CAMECA IMS-300 ion microscope are presented in the appendix.

3. Depth profiles of samples 2, 4, 6, 8, 10, and 12 were obtained for mass 12 ($^{12}C^+$), mass 13 ($^{13}C^+$), mass 14 ($^{14}N^+$, $^{13}CH^+$), mass 15 ($^{15}N^+$, $^{14}NH^+$), mass 54 ($^{54}Fe^+$), mass 70 ($^{56}Fe^{14}N^+$) and mass 71 ($^{56}Fe^{15}N^+$). For clarity the depth profiles are shown for masses 13, 14, 15, and 54 only; the depth profiles for the other masses are available upon request. Figs. 1-12 show the depth profiles of samples 2-12, respectively. The implantation history for each sample may be easily deduced from the depth profile.

4. Appendix:

The CAMECA IMS-300 ion microscope employs an energetic (0-10 keV) primary ion beam (typically O_2^+, Ar^+, or O^-) to analyze solid materials. The interaction of the primary ions with the sample erodes the target surface liberating secondary ions which are subsequently mass analyzed. The instrument design is such that the lateral distribution of the secondary ions is reformed at the detector resulting in a magnified mass analyzed image of the sample surface. This image may be observed visually or recorded on electron sensitive film with a field of view of 250 microns and a lateral resolution of one micron. The ion microscope is also capable of providing a three dimensional characterization of solids by monitoring the secondary ion signal of interest as a function of time. Provided the sputter yield (sputtered atoms/incident ion) is constant (or the layer thicknesses of a heterogeneous sample are known) this time scale may be converted to a depth scale by measurement of the crater depth. Crater depth measurements are normally made in this laboratory by interferometry. Secondary ion mass spectrometry (SIMS) is capable of detecting all elements in the periodic table, with detection limits in the ppm to ppb range. With proper standards, quantification may be performed with accuracies of ~ 10% or less. The instrument is normally operated as a low resolution mass spectrometer (M/M = 300), but may also be operated in a high resolution mode (M/M = ~2500).

STEVEN HUES

GEO-CENTERS, INC.

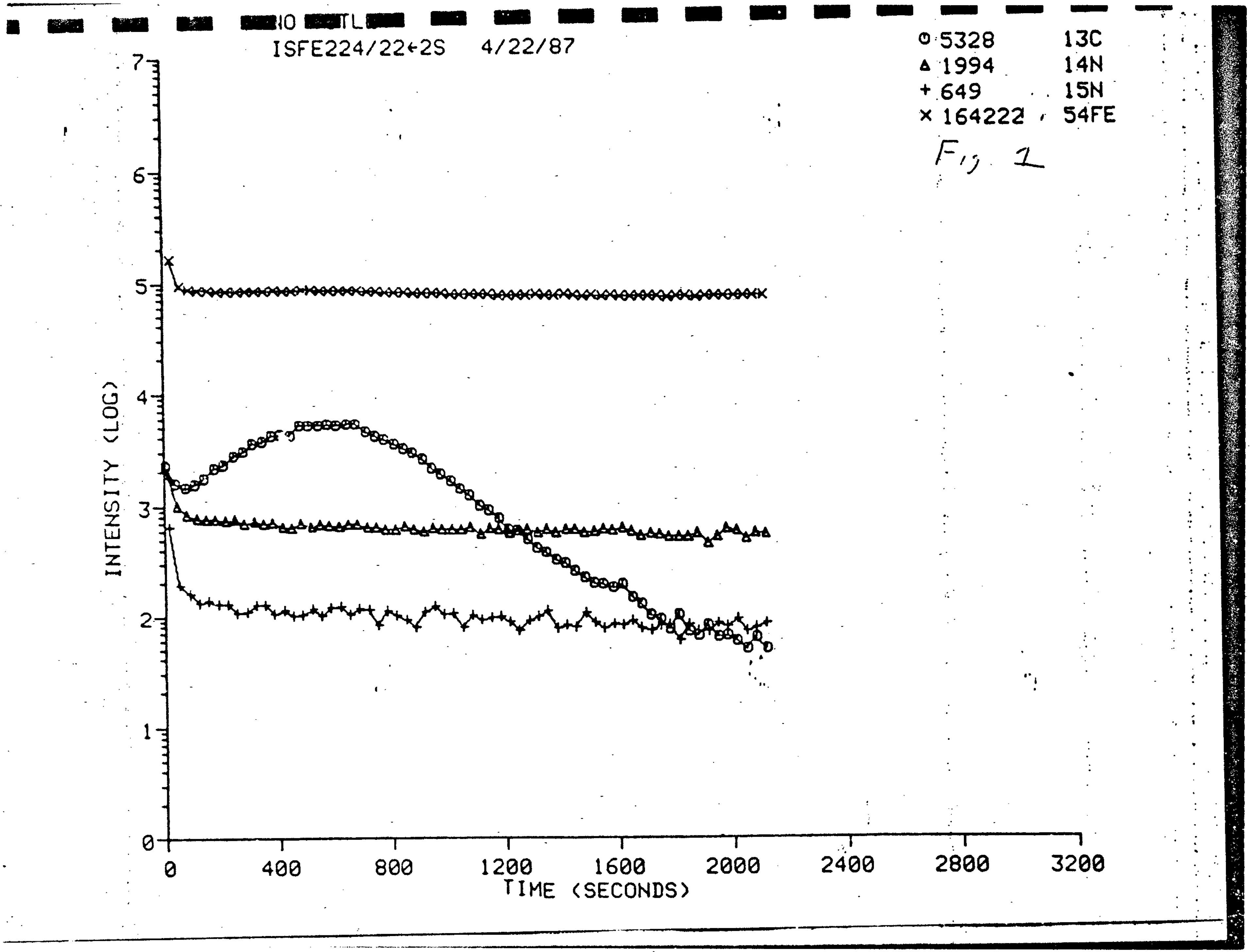
ISFE224/22+2S 4/22/87
o 5328 13C
Δ 1994 14N
+ 649 15N
× 164222 54FE
Fig 1
INTENSITY (LOG)
7
6
5
4
3
2
1
0
0
400
800
1200
1600
2000
2400
2800
3200
TIME (SECONDS)

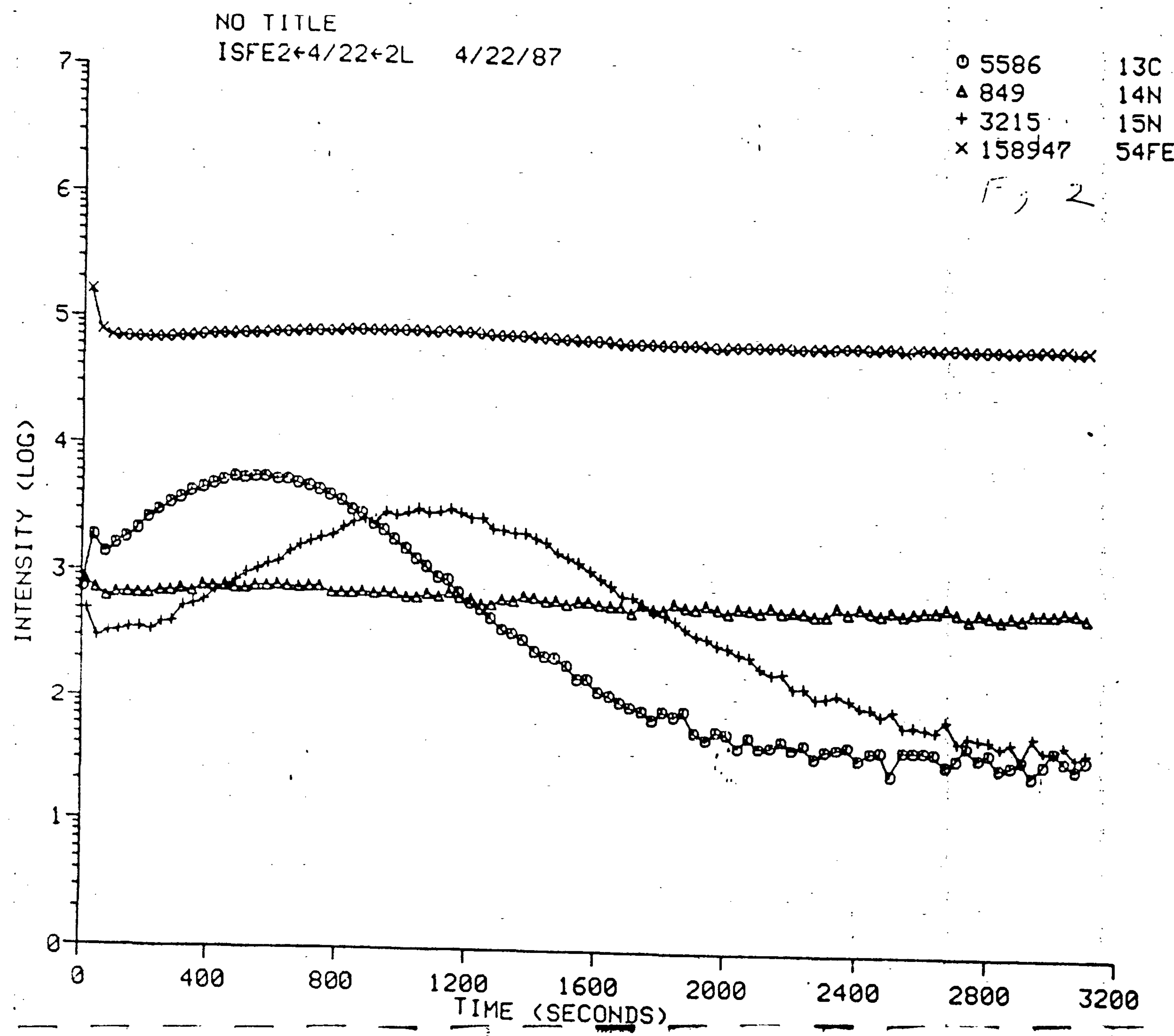
NO TITLE
ISFE2←4/22←2L 4/22/87
⊙ 5586 13C
△ 849 14N
+ 3215 15N
× 158947 54FE
Fig 2
INTENSITY (LOG)
0
1
2
3
4
5
6
7
0
400
800
1200
1600
2000
2400
2800
3200
TIME (SECONDS)

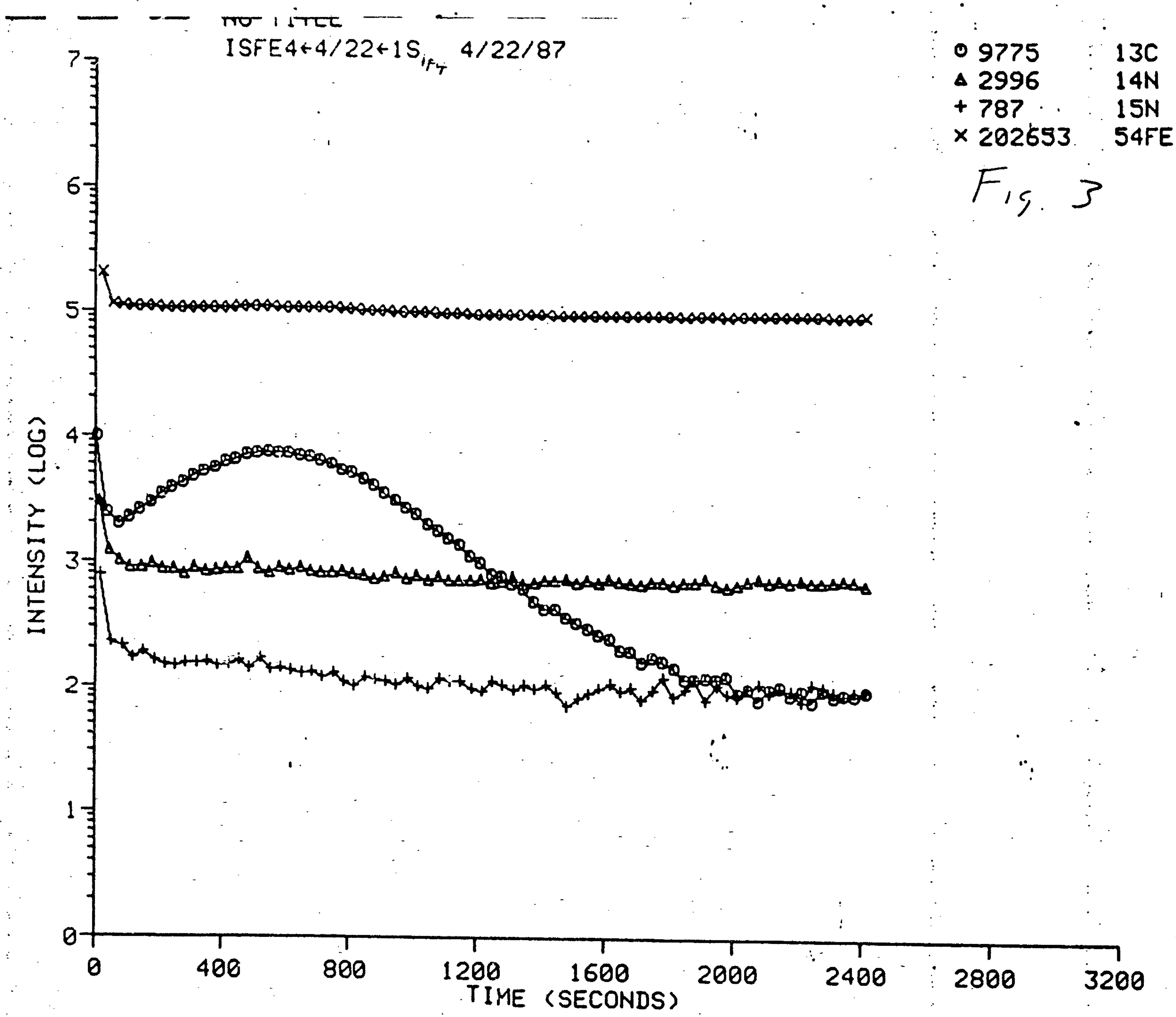
NO TITLE
ISFE4+4/22+1S 4/22/87
ʘ 9775 13C
▲ 2996 14N
+ 787 15N
× 202653 54FE
INTENSITY (LOG)
TIME (SECONDS)
0
400
800
1200
1600
2000
2400
2800
3200
1
2
3
4
5
6
7

Fig. 3

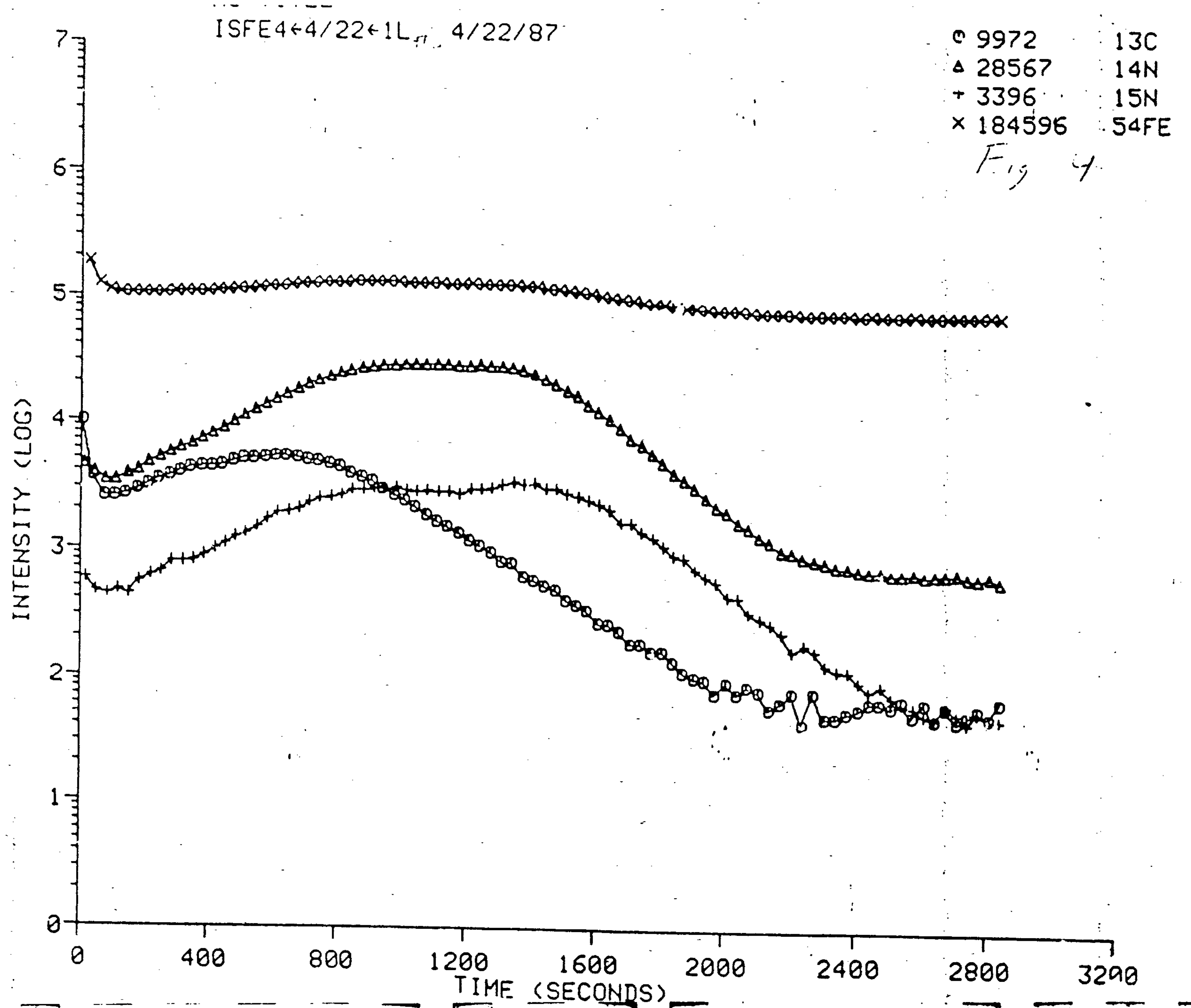
ISFE4←4/22←1L, 4/22/87
9972 13C
28567 14N
3396 15N
184596 54FE
Fig 4
INTENSITY (LOG)
TIME (SECONDS)
0
1
2
3
4
5
6
7
0
400
800
1200
1600
2000
2400
2800
3200

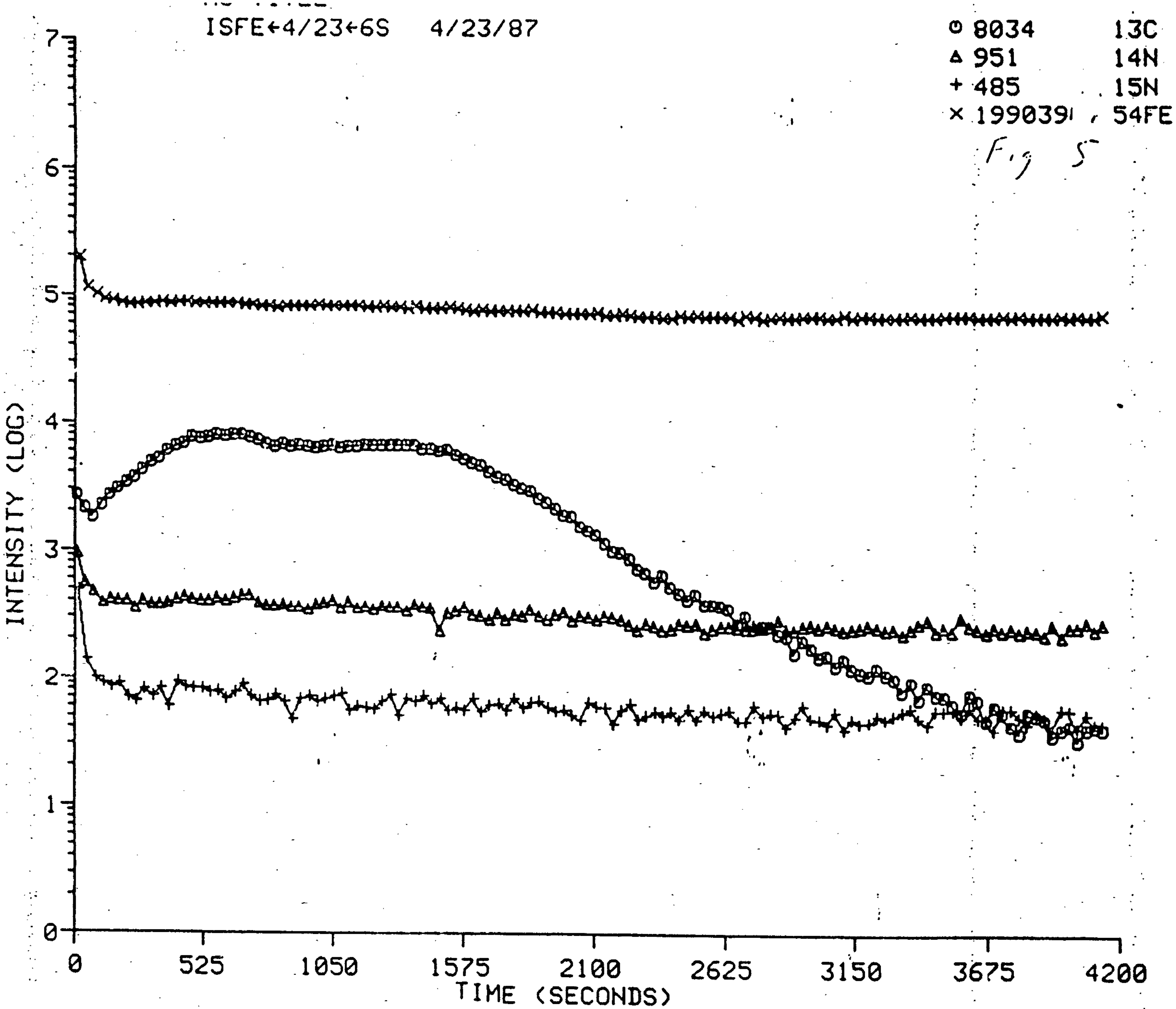
ISFE←4/23←6S 4/23/87
ο 8034 13C
Δ 951 14N
+ 485 15N
× 199039 , 54FE
Fig 5
INTENSITY (LOG)
7
6
5
4
3
2
1
0
0
525
1050
1575
2100
2625
3150
3675
4200
TIME (SECONDS)

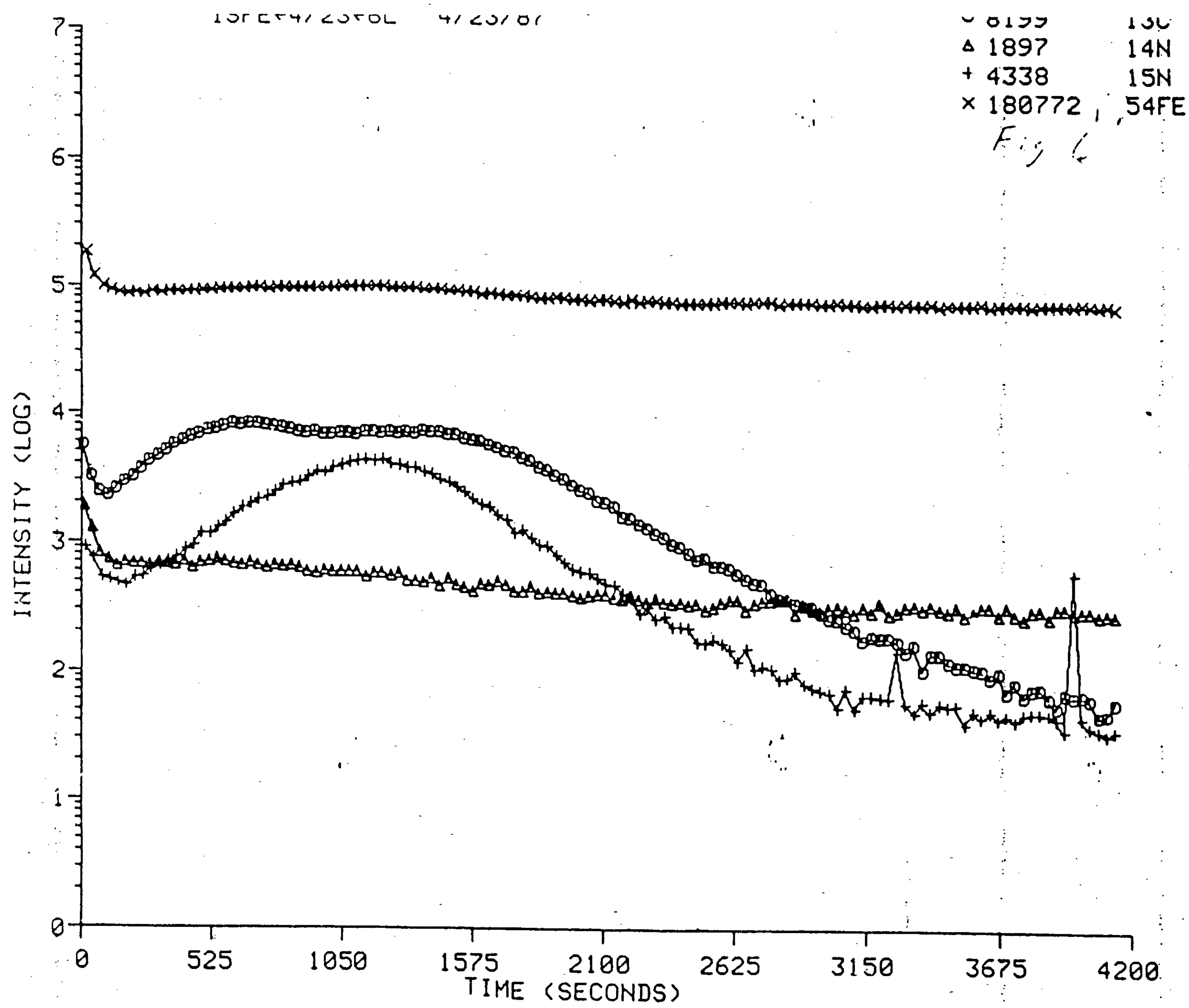

△ 1897 14N
+ 4338 15N
× 180772 54FE
INTENSITY (LOG)
TIME (SECONDS)
0
525
1050
1575
2100
2625
3150
3675
4200
1
2
3
4
5
6
7

Fig 6

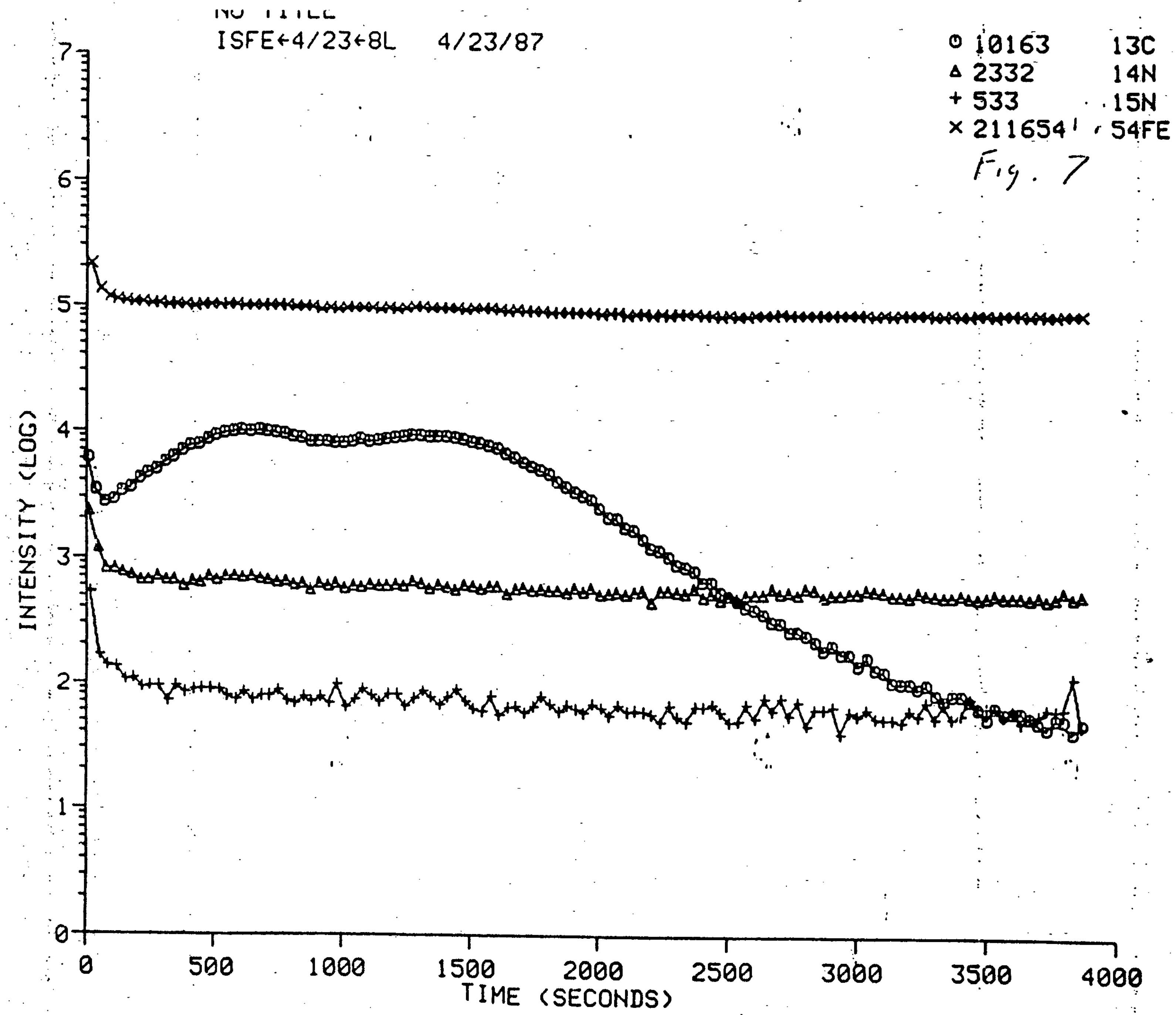

NO TITLE
ISFE←4/23←8L 4/23/87
o 10163 13C
Δ 2332 14N
+ 533 15N
× 211654 54FE
Fig. 7
INTENSITY (LOG)
TIME (SECONDS)

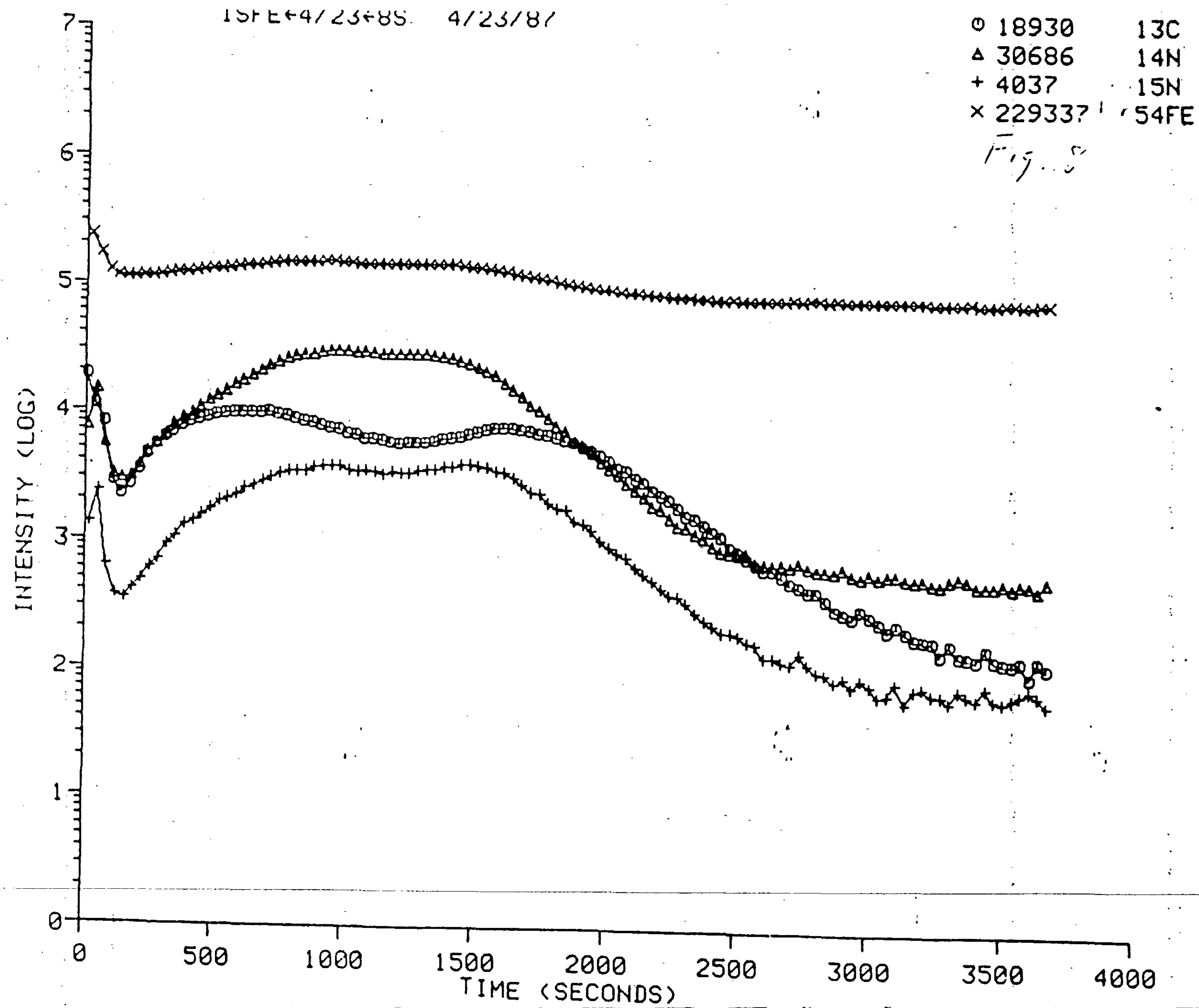

ISFE+4/23+8S 4/23/87
⊕ 18930 13C
△ 30686 14N
+ 4037 15N
× 229337 54FE
INTENSITY (LOG)
TIME (SECONDS)
0
500
1000
1500
2000
2500
3000
3500
4000
1
2
3
4
5
6
7

Fig. 5

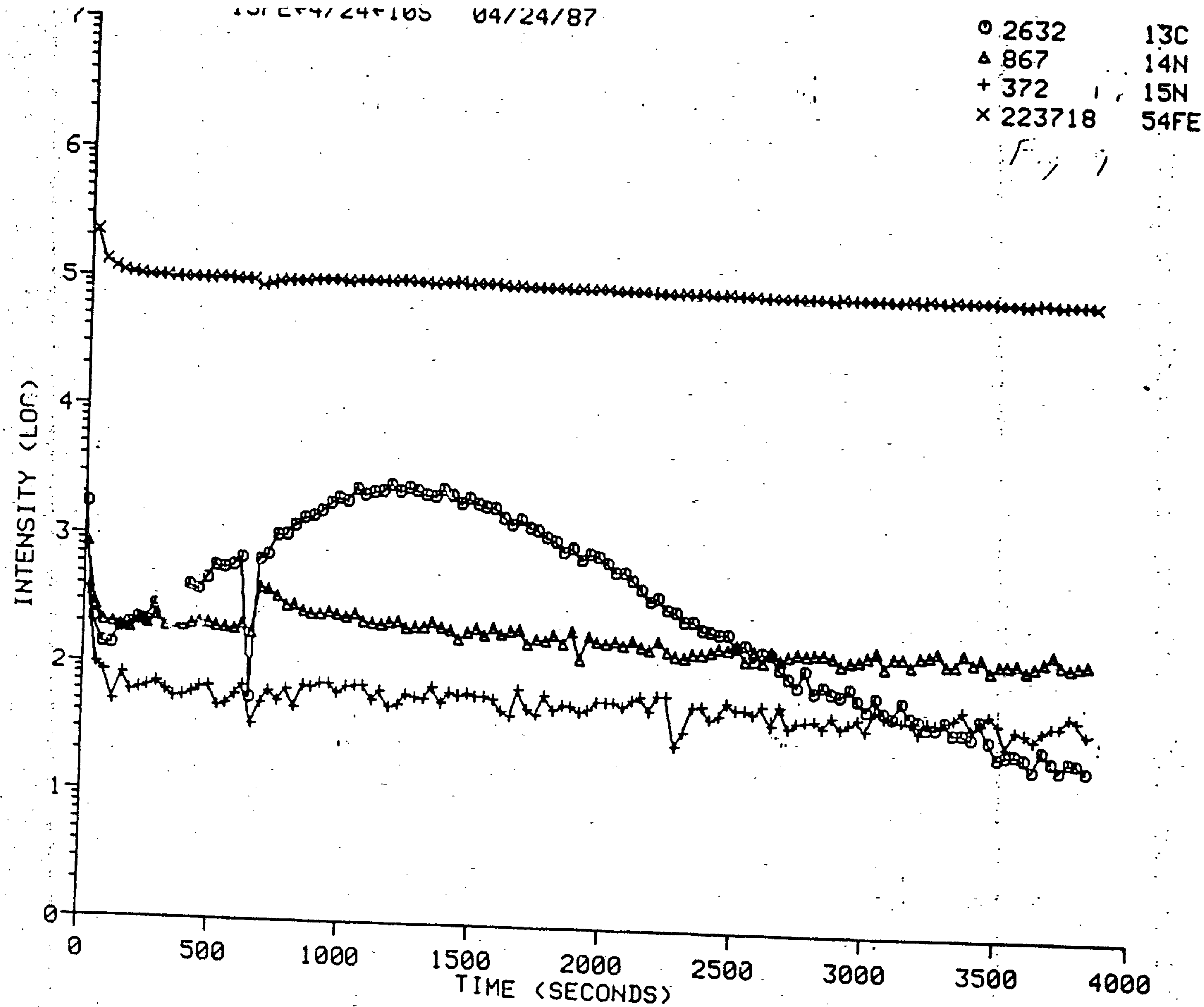
04/24/87
○ 2632 13C
△ 867 14N
+ 372 15N
× 223718 54FE
INTENSITY (LOG)
0
1
2
3
4
5
6
7
0
500
1000
1500
2000
2500
3000
3500
4000
TIME (SECONDS)

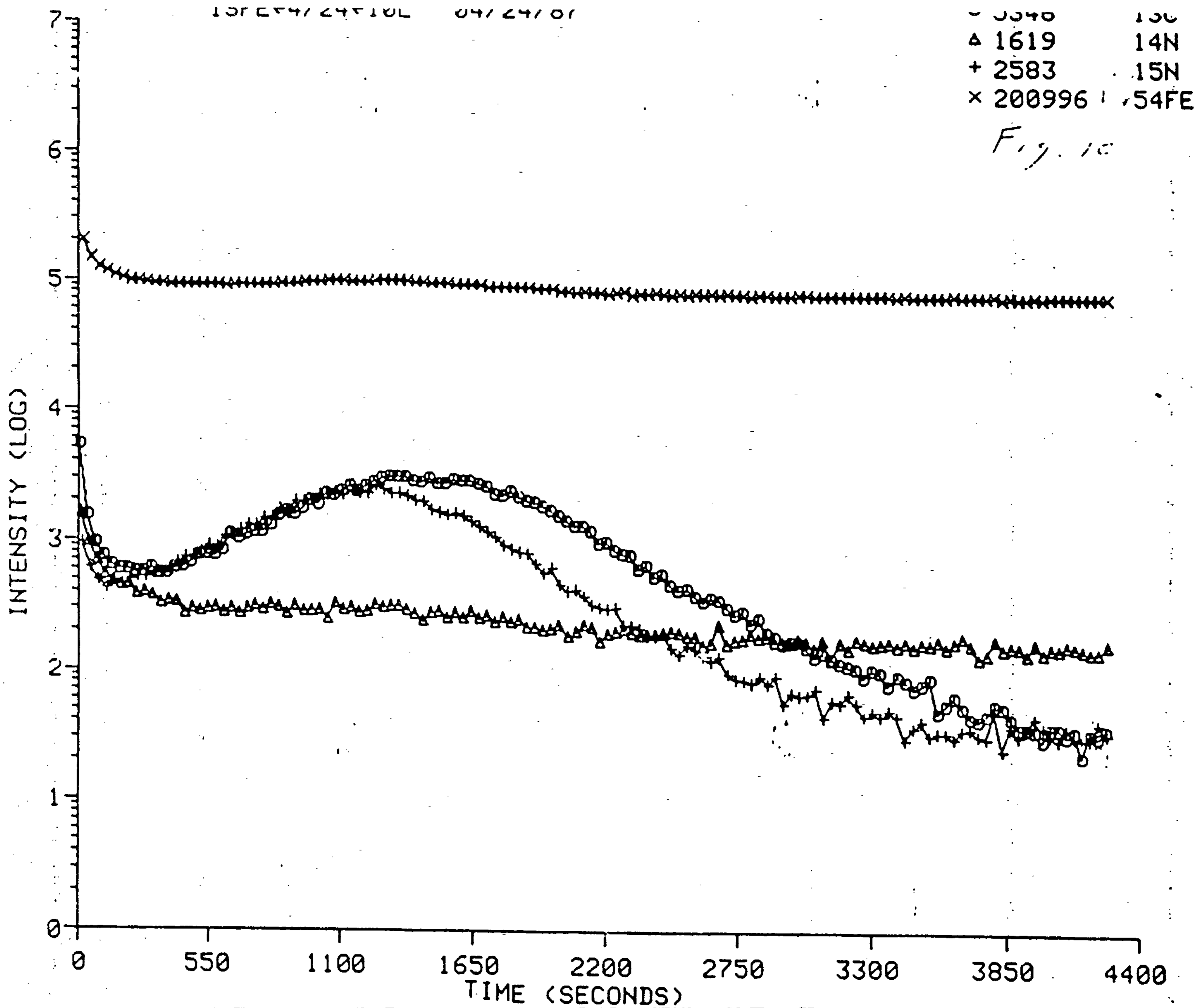

INTENSITY (LOG)
TIME (SECONDS)
0
550
1100
1650
2200
2750
3300
3850
4400
0
1
2
3
4
5
6
7
△ 1619 14N
+ 2583 15N
× 200996 54FE
Fig. 1c

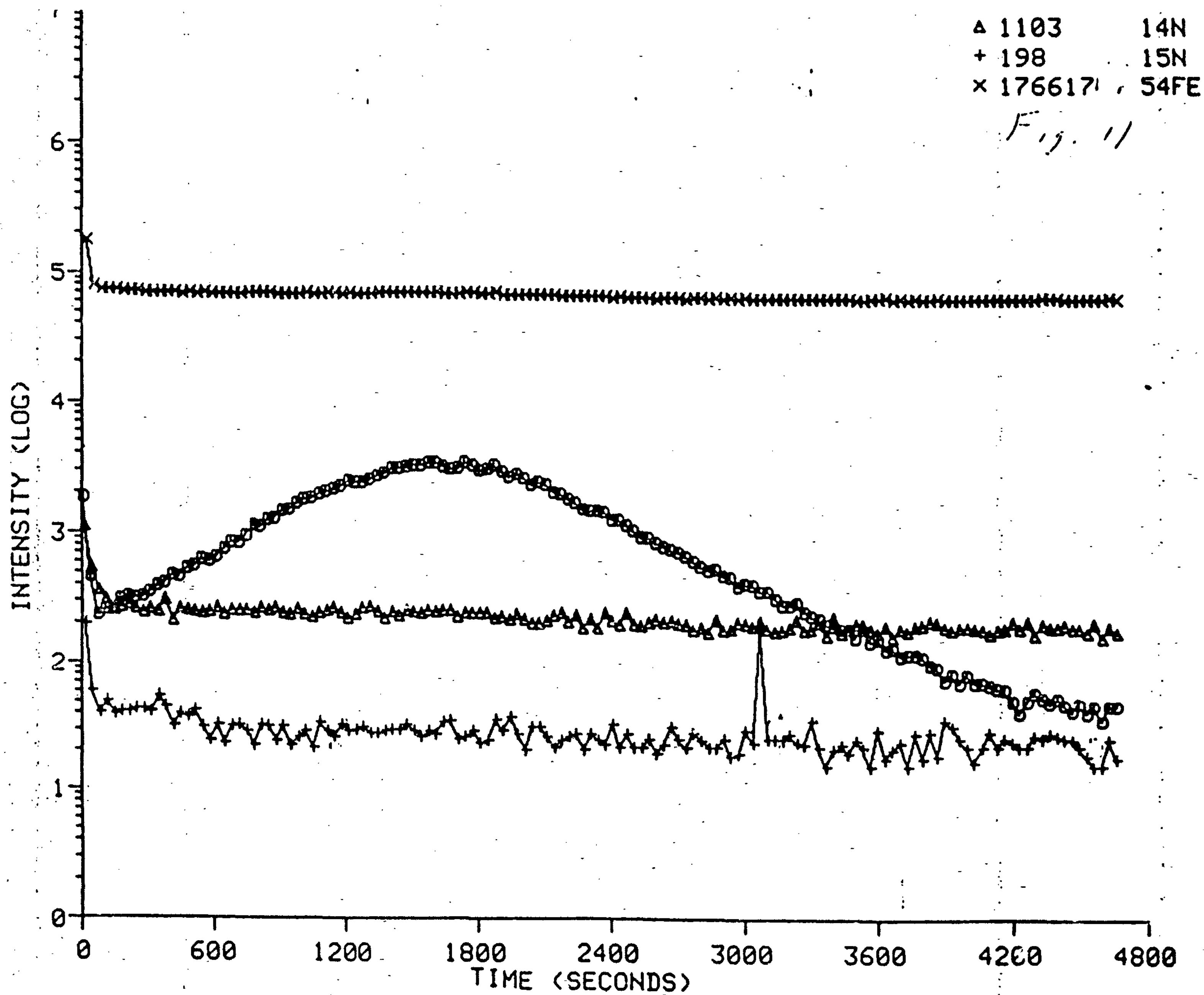

△ 1103 14N
+ 198 15N
× 176617 , 54FE
INTENSITY (LOG)
0
1
2
3
4
5
6
0
600
1200
1800
2400
3000
3600
4200
4800
TIME (SECONDS)

Fig. 11

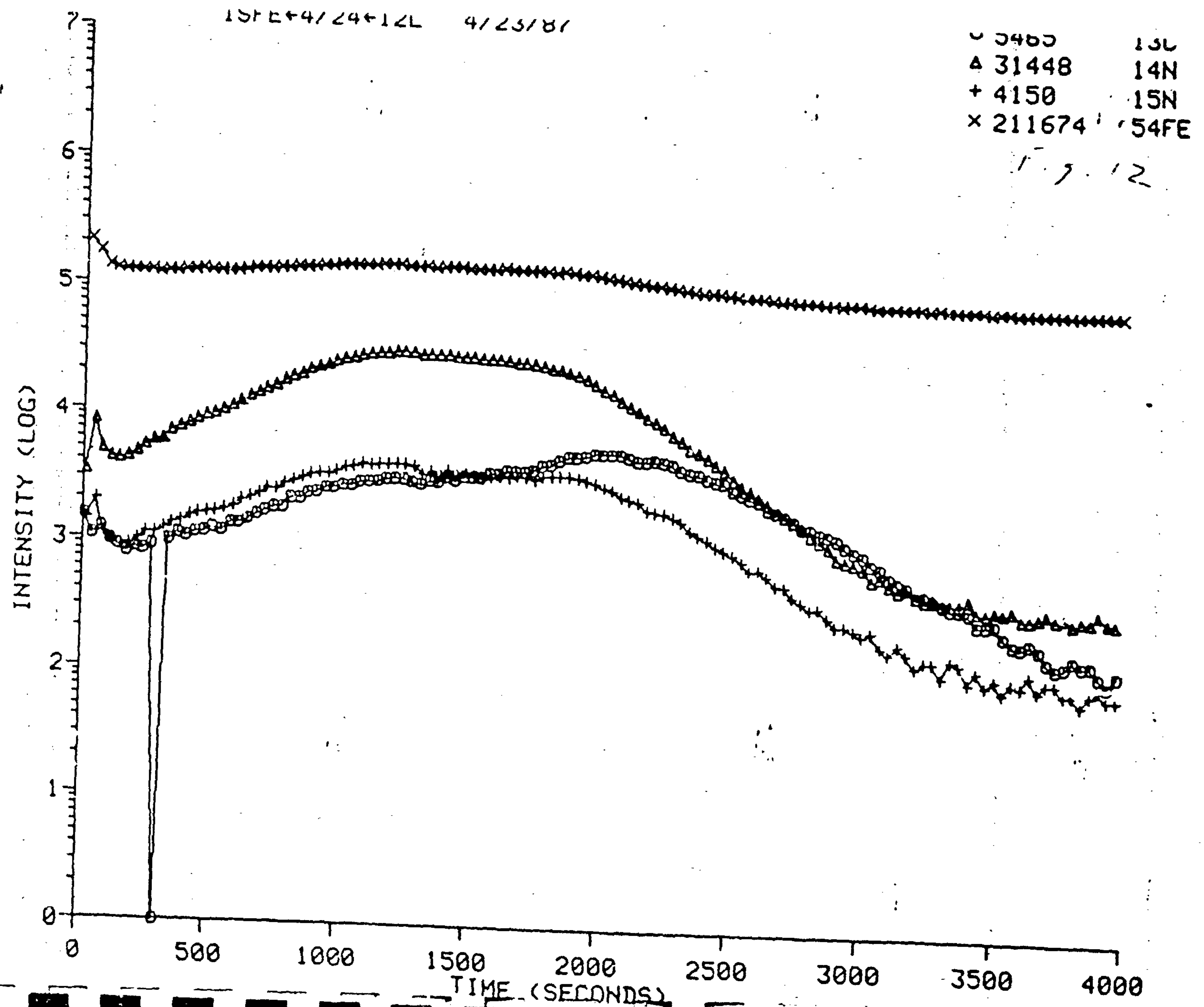

△ 31448 14N
+ 4150 15N
× 211674 54FE
INTENSITY (LOG)
TIME (SECONDS)
0
1
2
3
4
5
6
7
0
500
1000
1500
2000
2500
3000
3500
4000

Fig. 12

GEO-CENTERS, INC.

SIMS ANALYSIS OF HIGH TEMPERATURE SUPERCONDUCTING CERAMICS

1. On 5 June 1987 Noel Turner, Code 6177, submitted two samples of a high temperature superconducting ceramic composed of Y, Ba, Cu, and O. One sample consisted of a bulk ceramic pellet. The other sample was a thin ceramic film several thousand angstroms in thickness deposited onto a Al_2O_3 substrate. A comparative analysis of these two samples was requested.

2. The specimens were depth profiled with a Cameca IMS-300 ion microscope using 5.5 keV O_2^+ ions. The primary beam was rastered over an area of approximately 500 x 800 um. In the center of this raster an area of 250 um in diameter was analyzed. Because of the difference in size between the rastered and analyzed areas contributions of analyte atoms residing at the crater walls to the detected signal were eliminated. Some details concerning the Cameca IMS-300 ion microscope are presented int he appendix.

3. Depth profiles of the bulk ceramic and the thin film for mass 16 ($^{16}O^+$)m mass 63 ($^{63}Cu^+$), mass 89 ($^{89}Y^+$), and mass 136($^{136}Ba^+$) performed at a primary current of 500 nA are shown in Figs. 1 and 2 respectively. A depth profile of the thin film performed at a primary current of 200 nA is shown in Fig. 3.

Comparison of Figures 1 and 2 show that there is a dramatic decrease in the mass 89 signal along with a smaller decrease in the mass 16 and mass 63 signals. Whether these decreases in signal intensity are due to a decrease in the analyte concentration or ion yield or both cannot be determined. One observation which may be drawn from this analysis is that, regardless of whether the variations in ion intensity are a result of concentration or ion yield differences, the composition of the two samples are not identical.

4. Appendix:

The Cameca IMS-300 ion microscope employs an energetic (0-10 keV) primary ion beam (typically O_2^+, Ar^+, or O^-) to analyze solid materials. The interaction of the primary ions with the sample erodes the target surface liberating secondary ions which are subsequently mass analyzed. The instrument design is such that the lateral distribution of the secondary ions is reformed at the detector resulting in a magnified mass-analyzed image of the sample surface. This image may be observed visually or recorded on electron sensitive film with a field of view of 250 microns and a lateral resolution of one micron. The ion microscope is also capable of providing a three dimensional characterization of solids by monitoring the secondary ion signal of interest as a function of time. Provided the sputter yield (sputtered atoms/incident ion) is constant (or the layer thicknesses of a heterogenous sample are known) this time scale may be converted to a depth scale by measurement of the crater depth. Crater depth measurements are normally made in this laboratory by interferometry. Secondary ion mass spectrometry (SIMS) is capable of detecting all elements in the periodic table,

10903 Indian Head Highway
Fort Washington • Maryland • 20744
(301) 292-1010

BOSTON
WASHINGTON,
ALBUQUERQU

with detection limits in the ppm to ppb range. With proper standards, quantification may be performed with accuracies of ~10% or less. The instrument is normally operated as a low resolution mass spectrometer (M/ M =300), but may also be operated in a high resolution mode (M /M = ~2500).

STEVEN HUES

Copy to: R. Colton, Code 6177

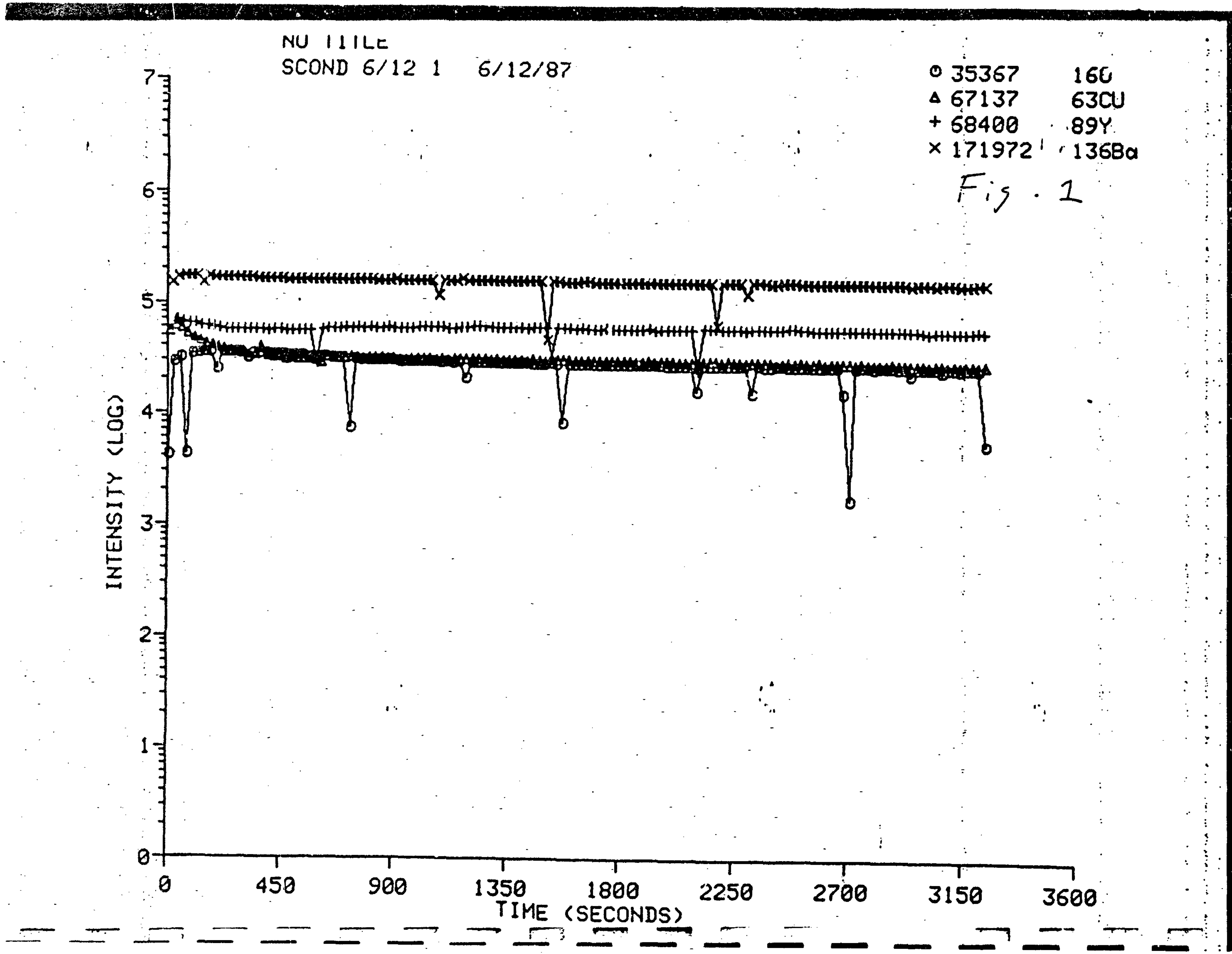
NO TITLE
SCOND 6/12 1 6/12/87
35367 16O
67137 63CU
68400 89Y
171972 136Ba
INTENSITY (LOG)
0
1
2
3
4
5
6
7
0
450
900
1350
1800
2250
2700
3150
3600
TIME (SECONDS)

Fig. 1

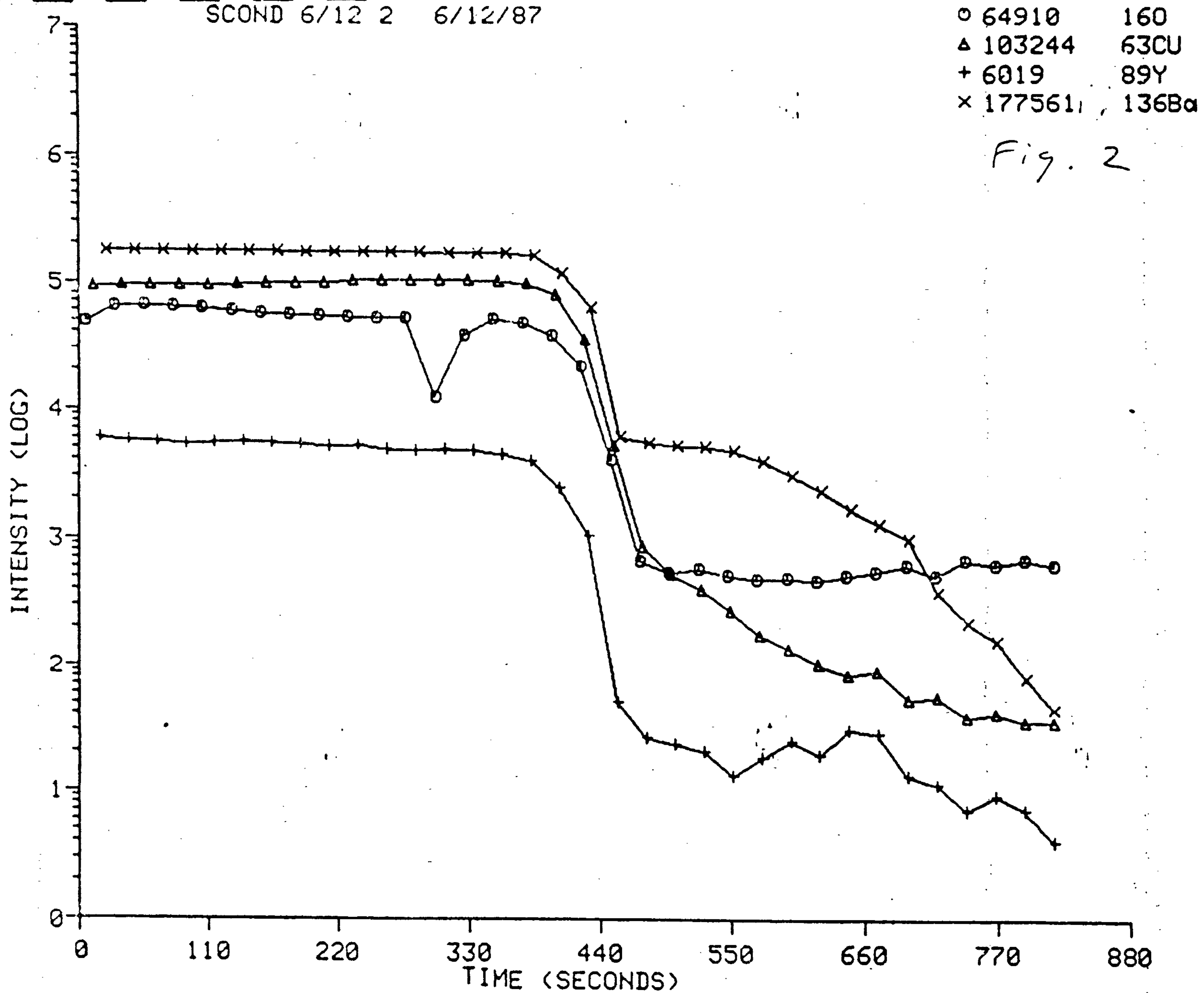

SCOND 6/12 2 6/12/87
o 64910 16O
Δ 103244 63CU
+ 6019 89Y
× 177561 136Ba
INTENSITY (LOG)
0
1
2
3
4
5
6
7
0
110
220
330
440
550
660
770
880
TIME (SECONDS)

Fig. 2

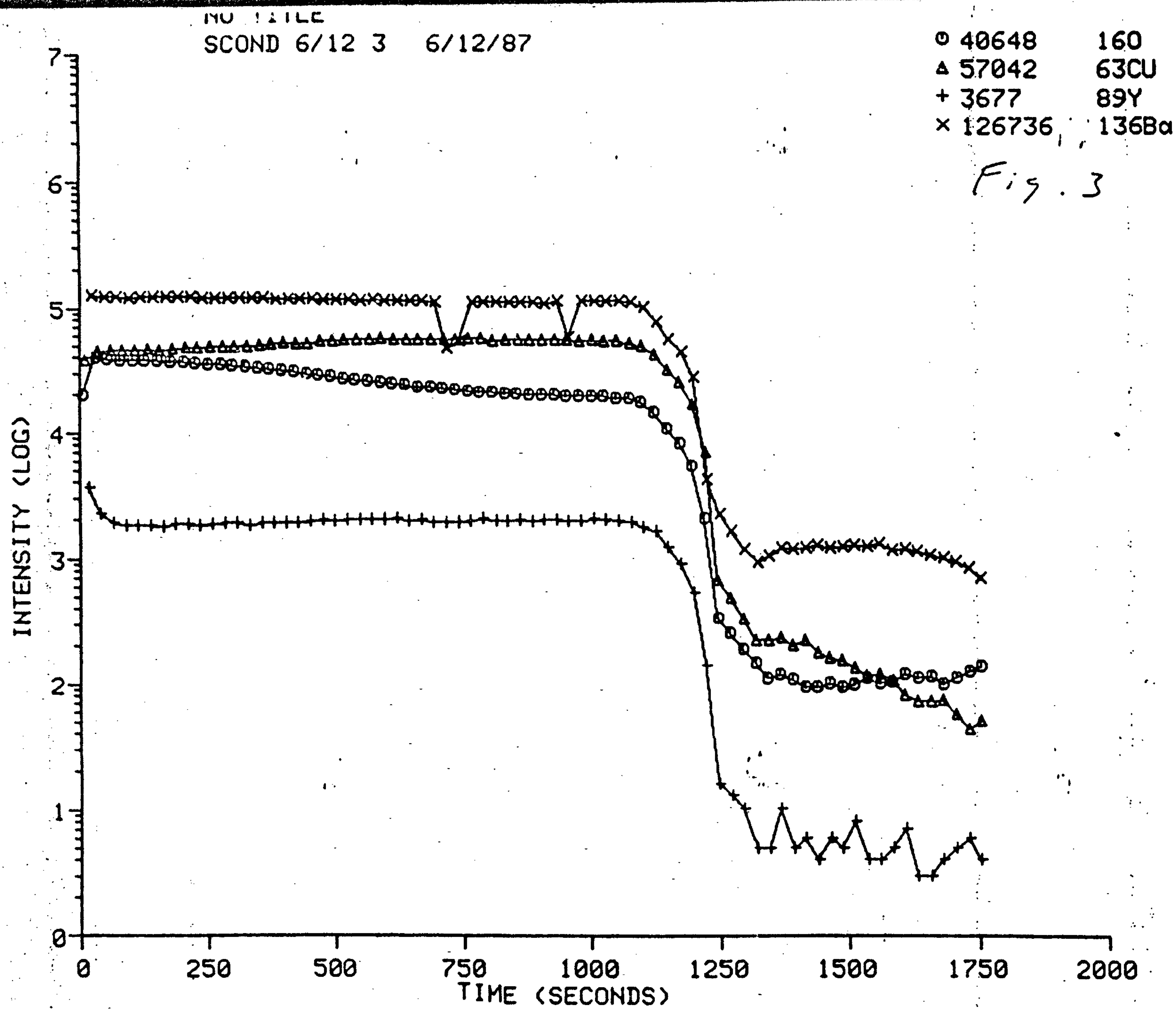
NO TITLE
SCOND 6/12 3 6/12/87
40648 16O
57042 63CU
3677 89Y
126736 136Ba
INTENSITY (LOG)
0
1
2
3
4
5
6
7
0
250
500
750
1000
1250
1500
1750
2000
TIME (SECONDS)

Fig. 3

SIMS ANALYSIS OF Be-DOPED GaAs

On 17 November 1986, R. Sillmon, Code 6821, requested that the deposited Be-doped layer in sample OM-344 (memorandum 6170-732:SH:al) be analyzed for the presence of Hg.

The specimen was depth profiled with a CAMECA IMS-300 secondary ion mass spectrometer using 5.5 keV O_2^+ ions at a primary current of 500 nA. The primary beam was rastered over an area of approximately 700 x 800 µm. In the center of this raster an area 250 µm in diameter was analyzed. Because of the difference in size between the rastered and analyzed areas, contributions of analyte atoms residing at the crater walls to the detected signal were eliminated. Some details concerning the CAMECA IMS-300 ion microscope are presented in the appendix.

Before analyzing the deposited layer in OM-344 for Hg it was necessary to determine the background signal level for the masses corresponding to the Hg isotopes. Fig. 1 shows a short range mass spectrum of a sample of the GaAs substrate sputtered to steady state signal intensities. As may be seen the low intensity peaks present do not correspond to the isotopic distribution of Hg and are in all probability due to vacuum contaminants. Fig. 2 shows a short range mass spectrum, over the same region, of the deposited Be-doped deposited layer in OM-344. As in the substrate material the observed peak intensities do not correspond to those of the Hg isotopes. In order to determine the relative contaminant levels between the deposited layer and the substrate a depth profile of OM-344 was preformed for mass 9 (Be^+), mass 75 (As^+) and mass 200, this depth profile is shown in fig. 3. As may be seen the mass 200 signal is more intense in the deposited layer region. This may be due either to contaminants introduced during layer growth or a matrix effect from the high Be concentration.

Based upon these findings, it is concluded that the level of Hg present in the deposited layer is below the detection limit of the instrument. This detection limit may be quantified, if desired, at a later date if suitable standards are provided.

Appendix:

The CAMECA IMS-300 ion microscope employs an energetic (0-10 keV) primary ion beam (typically O_2^+, Ar^+, or O^-) to analyze solid materials. The interaction of the primary ions with the sample erodes the target surface liberating secondary ions which are subsequently mass analyzed. The instrument design is such that the lateral distribution of the secondary ions is reformed at the detector resulting in a magnified mass analyzed image of the sample surface. This image may be observed visually or recorded on electron sensitive film with a field of view of 250 microns and a lateral resolution of one micron. The ion microscope is also capable of providing a three dimensional characterization of solids by monitoring the secondary ion signal of interest as a function of time. Provided the sputter yield (sputtered atoms/incident ion) is constant (or the layer thicknesses of a heterogeneous sample are known) this time scale may be converted to a depth scale by measurement of the crater depth. Crater depth

GEO-CENTERS, INC

measurements are normally made in this laboratory by interferometry. Secondary ion mass spectrometry (SIMS) is capable of detecting all elements in the periodic table, with detection limits in the ppm to ppb range. With proper standards, quantification may be performed with accuracies of - 10% or less. The instrument is normally operated as a low resolution mass spectrometer (M/M = 300), but may also be operated in a high resolution mode (M/M = -2500).

STEVEN HUES

GEO-CENTERS, INC.

Fig. 1

AK NUMBER 1
SS = 196.179167 MIDPT = 55661.5
ART = 55641.5 END = 55681.5
AK MAX = 55661.5 WIDTH = 40
EA = 224

AK NUMBER 2
SS = 198.223485 MIDPT = 55935.5
ART = 55893.5 END = 55977.5
AK MAX = 55921.5 WIDTH = 84
EA = 1972

AK NUMBER 3
SS = 199.102273 MIDPT = 56051.5
ART = 56045.5 END = 56057.5
AK MAX = 56057.5 WIDTH = 12
EA = 68

AK NUMBER 4
SS = 200.164122 MIDPT = 56191.5
ART = 56153.5 END = 56229.5
AK MAX = 56189.5 WIDTH = 76
EA = 2460

AK NUMBER 5
SS = 201.263359 MIDPT = 56335.5
ART = 56329.5 END = 56341.5
AK MAX = 56341.5 WIDTH = 12
EA = 76

AK NUMBER 6
SS = 202.148855 MIDPT = 56451.5
ART = 56417.5 END = 56485.5
AK MAX = 56453.5 WIDTH = 68
EA = 924

AK NUMBER 7
SS = 204.103846 MIDPT = 56707.5
ART = 56681.5 END = 56733.5
AK MAX = 56713.5 WIDTH = 52
EA = 516

0

OM-314

Fig. 2

AK NUMBER 1
SS = 196.129167 MIDPT = 55655.5
ART = 55633.5 END = 55677.5
AK MAX = 55665.5 WIDTH = 44
EA = 384

AK NUMBER 2
SS = 197.174658 MIDPT = 55785.5
ART = 55765.5 END = 55805.5
AK MAX = 55789.5 WIDTH = 40
EA = 276

AK NUMBER 3
SS = 198.299243 MIDPT = 55945.5
ART = 55889.5 END = 56001.5
AK MAX = 55925.5 WIDTH = 112
EA = 2352

AK NUMBER 4
SS = 199.260726 MIDPT = 56077.5
ART = 56053.5 END = 56101.5
AK MAX = 56073.5 WIDTH = 48
EA = 392

AK NUMBER 5
SS = 200.089686 MIDPT = 56199.5
ART = 56153.5 END = 56245.5
AK MAX = 56189.5 WIDTH = 92
EA = 1912

AK NUMBER 6
SS = 202.179389 MIDPT = 56455.5
ART = 56421.5 END = 56489.5
AK MAX = 56445.5 WIDTH = 68
EA = 1044

AK NUMBER 7
SS = 204.180769 MIDPT = 56717.5
ART = 56709.5 END = 56725.5
AK MAX = 56717.5 WIDTH = 16
EA = 124

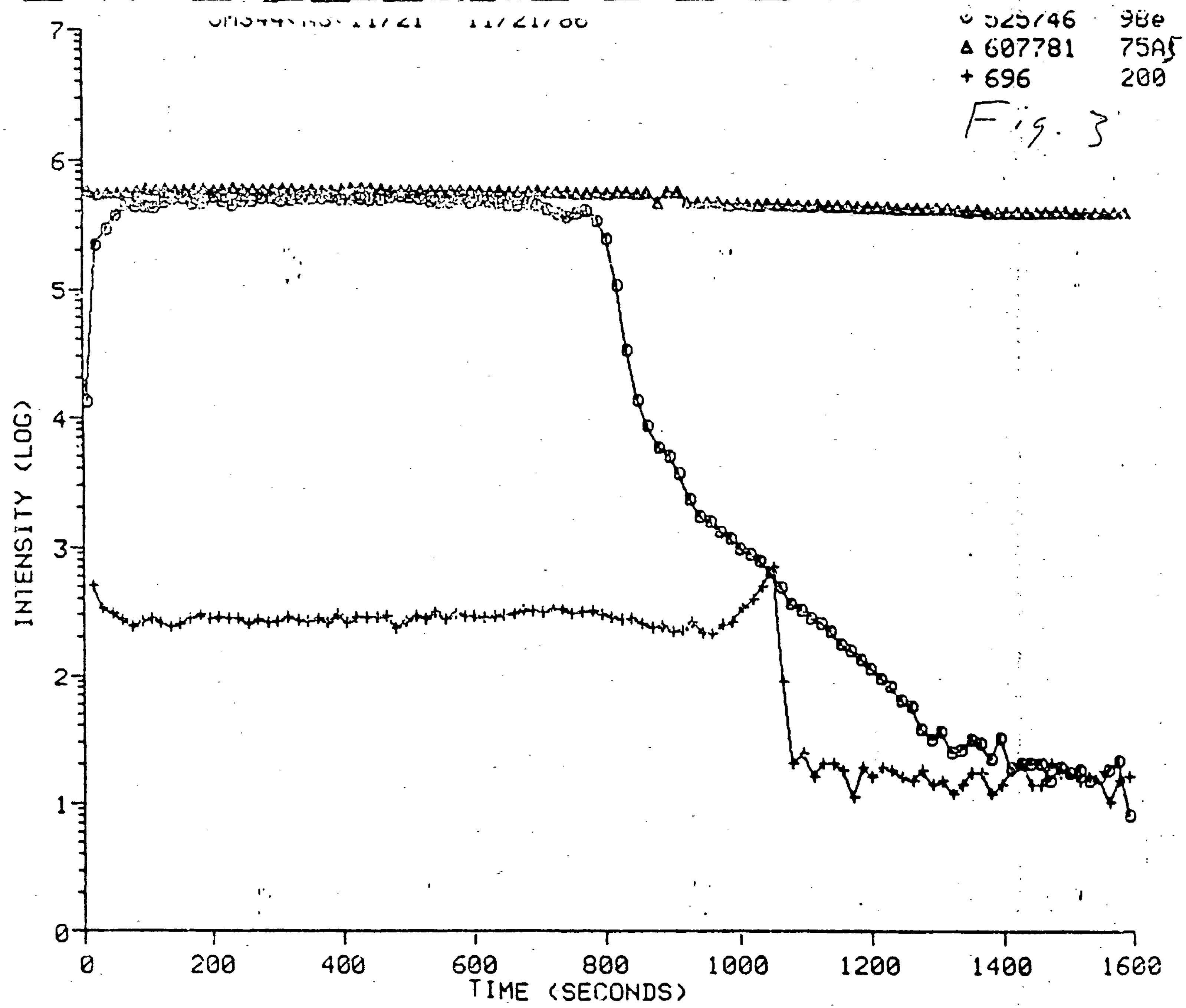

Fig. 3

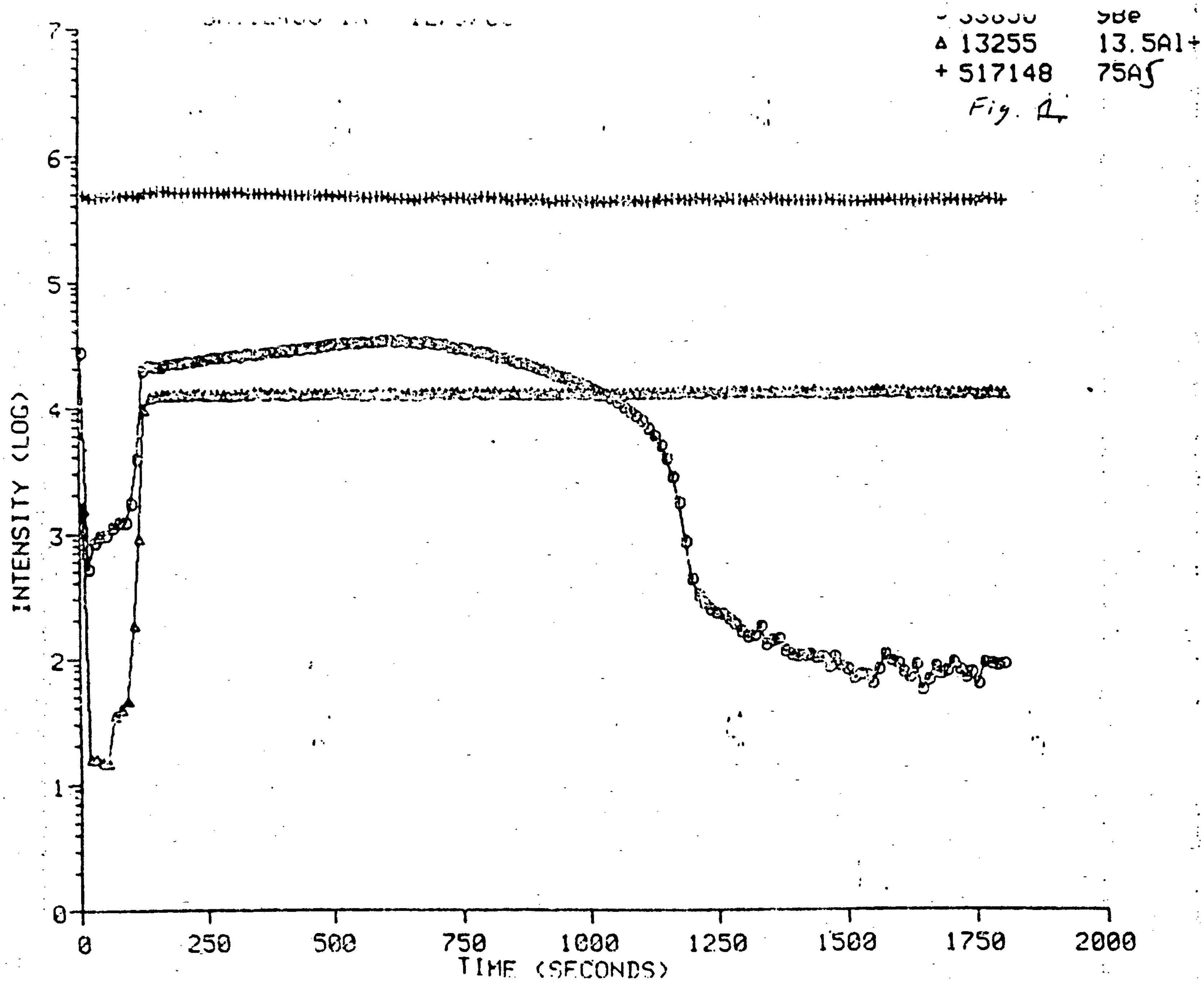
△ 13255 13.5Al+
+ 517148 75As
INTENSITY (LOG)
TIME (SECONDS)
0
1
2
3
4
5
6
7
0
250
500
750
1000
1250
1500
1750
2000

Fig. 4

SIMS ANALYSIS OF Be DISTRIBUTION IN THERMALLY ANNEALED GaAlAs

On 9 December 1986, B. Molnar, Code 6812, requested that sample 112486-1 (memo 6170-795:SH:a1) be analyzed for the depth distribution of Al.

The specimen was depth profiled with a CAMECA IMS-300 ion microscope using 5.5 keV O_2^+ ions at a primary current of 400 nA. The primary beam was rastered over an area of approximately 500 x 800 μm. In the center of this raster an area of 250 μm in diameter was analyzed. Because of the difference in size between the rastered and analyzed areas contributions of analyte atoms residing at the crater walls to the detected signal were eliminated. Some details concerning the CAMECA IMS-300 ion microscope are presented in the appendix.

A depth profile of 112486-1 for mass 9 (Be^+, $^{27}Al^{+3}$), mass 13.5 ($^{27}Al^{+2}$), and mass 75 (As^+) is shown in fig. 1. The increase of the mass 9 signal level in the beginning of the profile is due to an increase in the Al concentration and to a matrix effect arising from the increased oxygen gettering efficiency of Al over that of GaAs.

Appendix:

The CAMECA IMS-300 ion microscope employs an energetic (0-10 keV) primary ion beam (typically O_2^+, Ar^+, or O^-) to analyze solid materials. The interaction of the primary ions with the sample erodes the target surface liberating secondary ions which are subsequently mass analyzed. The instrument design is such that the lateral distribution of the secondary ions is reformed at the detector resulting in a magnified mass analyzed image of the sample surface. This image may be observed visually or recorded on electron sensitive film with a field of view of 250 microns and a lateral resolution of one micron. The ion microscope is also capable of providing a three dimensional characterization of solids by monitoring the secondary ion signal of interest as a function of time. Provided the sputter yield (sputtered atoms/incident ion) is constant (or the layer thicknesses of a heterogeneous sample are known) this time scale may be converted to a depth scale by measurement of the crater depth. Crater depth measurements are normally made in this laboratory by interferometry. Secondary ion mass spectrometry (SIMS) is capable of detecting all elements in the periodic table, with detection limits in the ppm to ppb range. With proper standards, quantification may be performed with accuracies of ~ 10% or less. The instrument is normally operated as a low resolution mass spectrometer (M/M = 300), but may also be operated in a high resolution mode (M/M = ~2500).

GEO-CENTERS, INC.

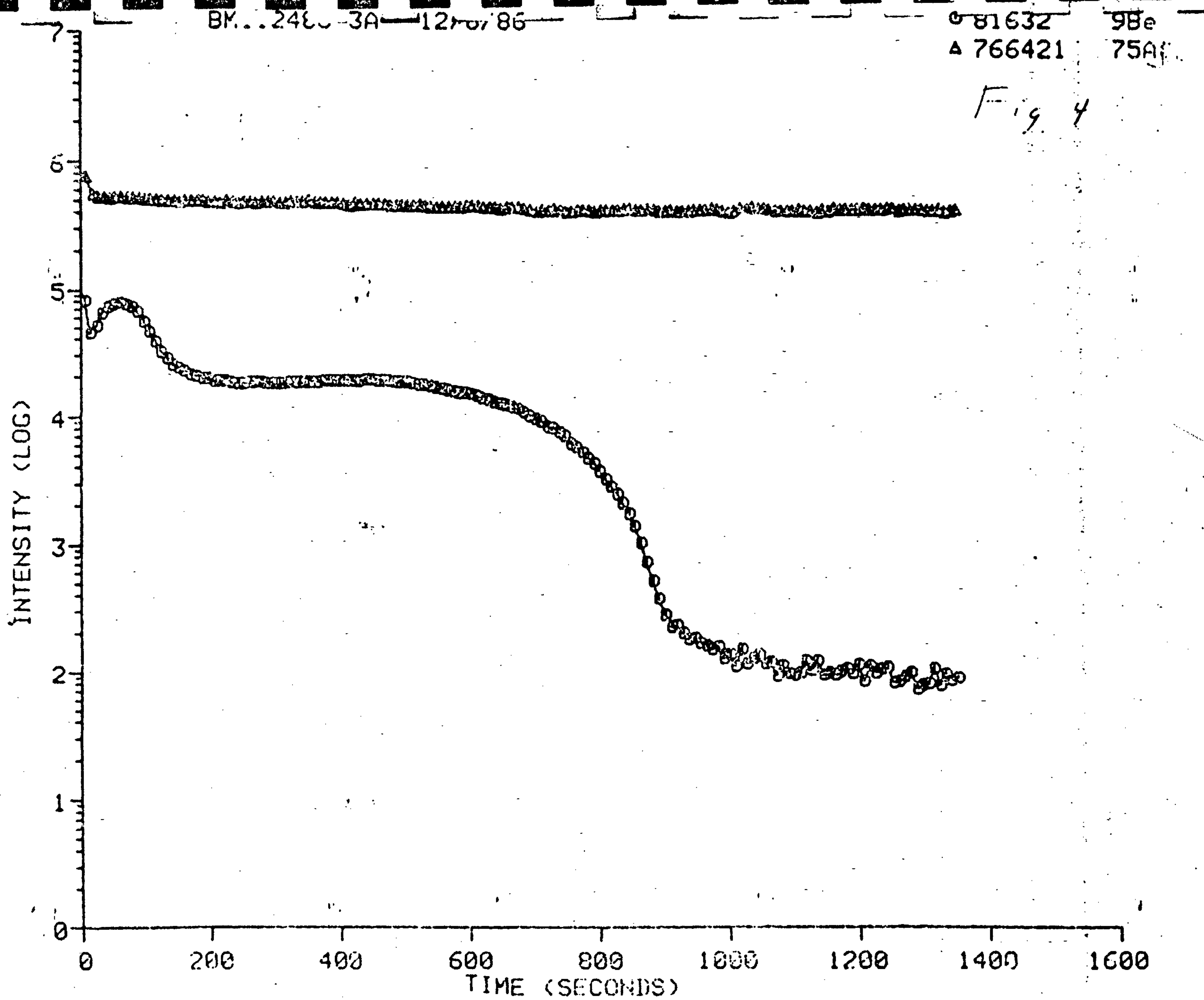
BM...24 -3A 12/ /86
81632 9Be
766421 75A
INTENSITY (LOG)
TIME (SECONDS)
0
1
2
3
4
5
6
7
0
200
400
600
800
1000
1200
1400
1600

Fig. 4

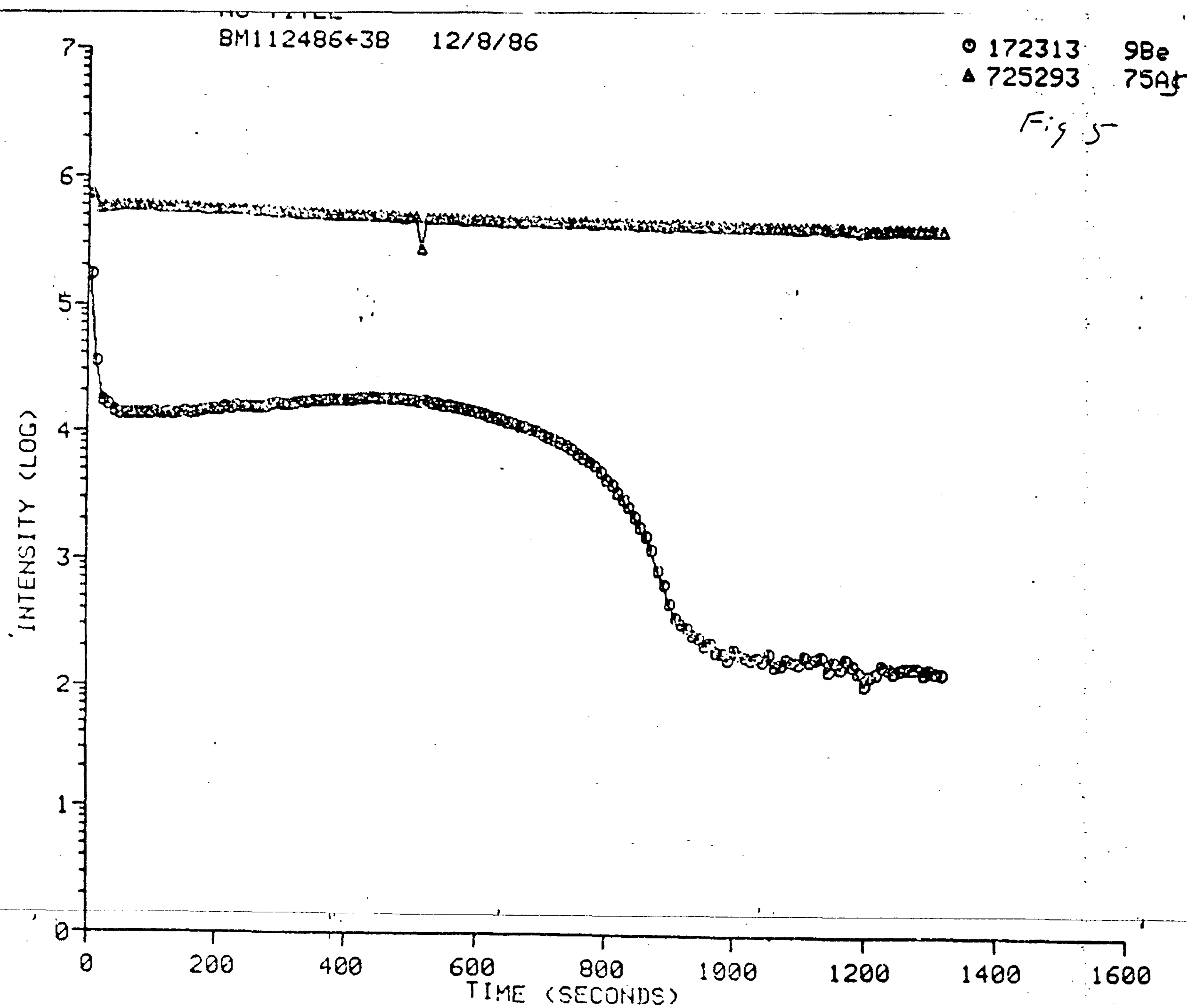

NO TITLE
BM112486+3B 12/8/86
172313 9Be
725293 75As
Fig 5
INTENSITY (LOG)
TIME (SECONDS)

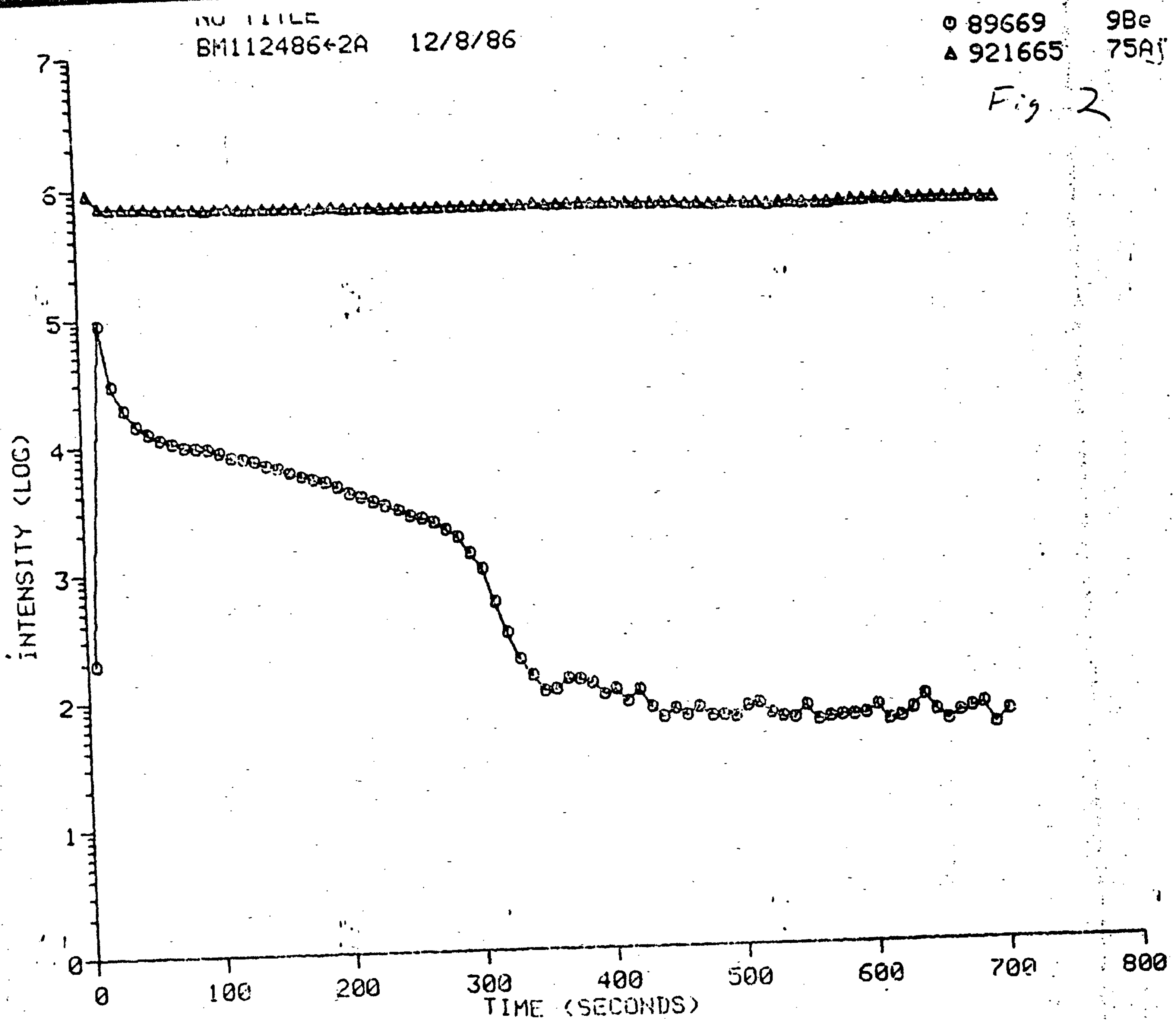
NO TITLE
BM112486+2A 12/8/86
⊙ 89669 9Be
△ 921665 75As
INTENSITY (LOG)
TIME (SECONDS)
0
1
2
3
4
5
6
7
0
100
200
300
400
500
600
700
800

Fig. 2

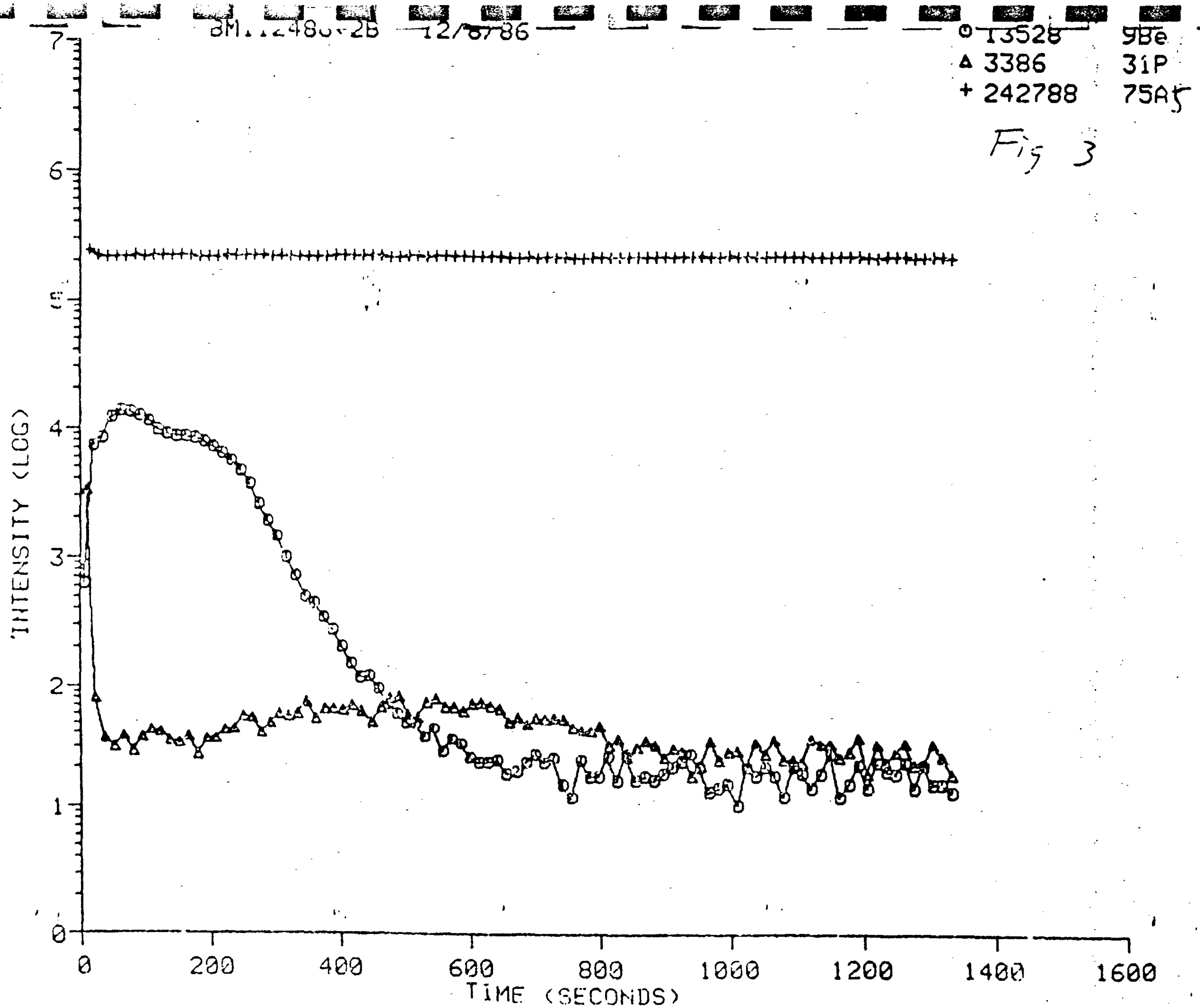

12/8/86
ʘ 13528 9Be
Δ 3386 31P
+ 242788 75As
INTENSITY (LOG)
0
1
2
3
4
5
6
7
0
200
400
600
800
1000
1200
1400
1600
TIME (SECONDS)

Fig 3

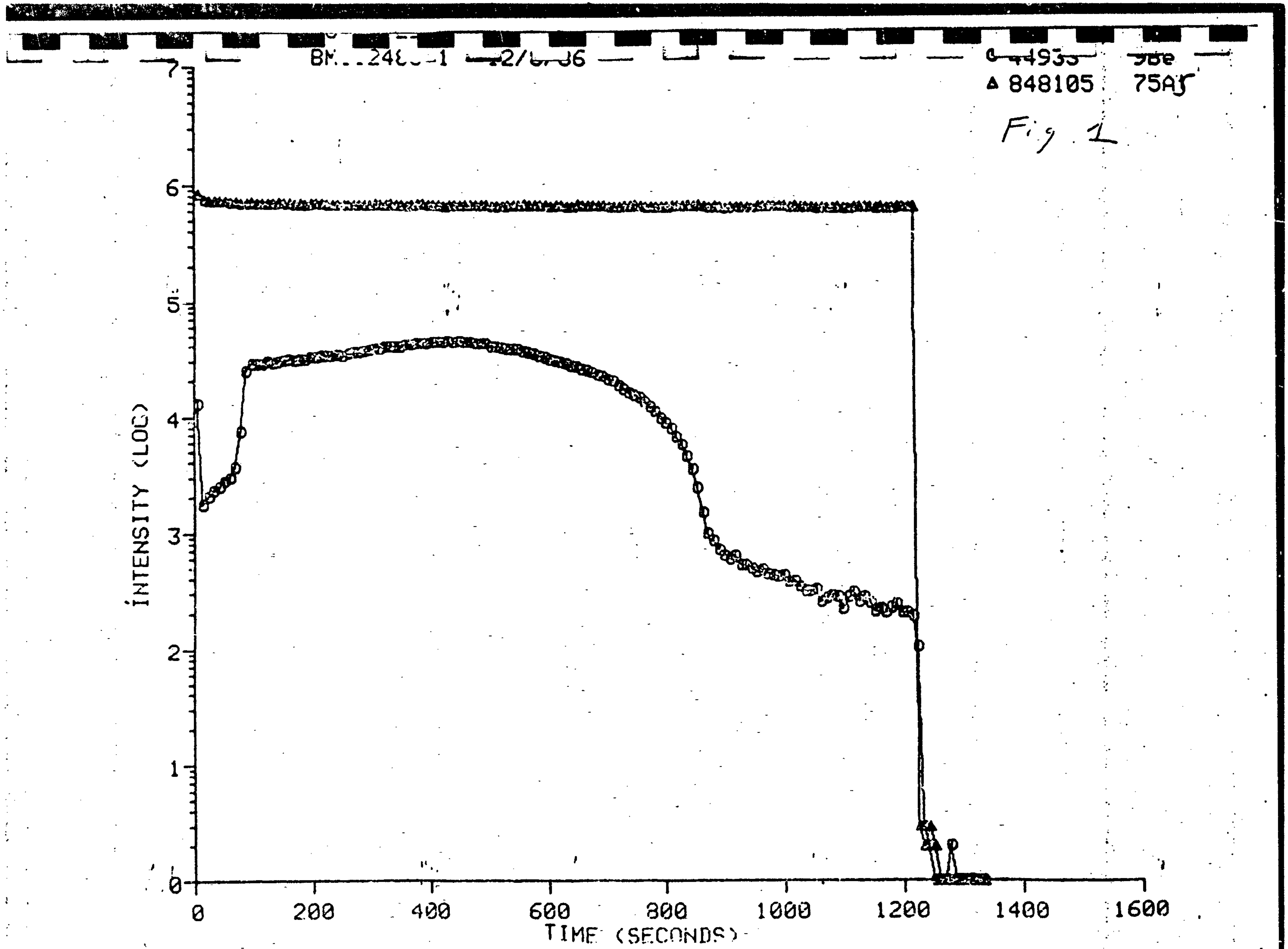

▵ 848105 75A
INTENSITY (LOG)
TIME (SECONDS)
0
200
400
600
800
1000
1200
1400
1600
1
2
3
4
5
6
7

Fig 1

SIMS ANALYSIS OF Be DISTRIBUTION IN THERMALLY ANNEALED GaAlAs

On 24 November 1986 B. Molnar, Code 6812, submitted five samples of beryllium implanted GaAlAs samples for analysis by secondary ion mass spectrometry. These samples were designated 112486-1, 112486-2a, 112486-2b, 112486-3a, and 112486-3b. All samples had been implanted with Be to a fluence of 8×10^{13} ions/cm^2. In addition, 112486-2b was also implanted with 400 keV P to a fluence of 3×10^{14}.

The specimens were depth profiled with a CAMECA IMS-300 ion microscope using 5.5 keV O_2^+ ions. The primary beam was rastered over an area of approximately 500 x 800 μm. In the center of this raster an area of 250 μm in diameter was analyzed. Because of the difference in size between the rastered and analyzed areas contributions of analyte atoms residing at the crater walls to the detected signal were eliminated. Some details concerning the CAMECA IMS-300 ion microscope are presented in the appendix.

Depth profiles of samples 112486-1, 2a, 3a, and 3b for mass 9 ($^{9}Be^+$, $^{27}Al^{+3}$) and mass 75 ($^{75}As^+$) obtained at primary currents of 600 nA, are shown in figs. 1, 2, 3, and 4, respectively. The low signal level for mass 9 in the beginning of fig. 1 is due to a matrix effect caused by the presence of a GaAs cap layer. A depth profile of sample 112486-2b for mass 9, mass 75, and mass 31 (P^+), obtained at a primary current of 300 nA, is shown in fig. 5.

Appendix:

The CAMECA IMS-300 ion microscope employs an energetic (0-10 keV) primary ion beam (typically O_2^+, Ar^+, or O^-) to analyze solid materials. The interaction of the primary ions with the sample erodes the target surface liberating secondary ions which are subsequently mass analyzed. The instrument design is such that the lateral distribution of the secondary ions is reformed at the detector resulting in a magnified mass analyzed image of the sample surface. This image may be observed visually or recorded on electron sensitive film with a field of view of 250 microns and a lateral resolution of one micron. The ion microscope is also capable of providing a three dimensional characterization of solids by monitoring the secondary ion signal of interest as a function of time. Provided the sputter yield (sputtered atoms/incident ion) is constant (or the layer thicknesses of a heterogeneous sample are known) this time scale may be converted to a depth scale by measurement of the crater depth. Crater depth measurements are normally made in this laboratory by interferometry. Secondary ion mass spectrometry (SIMS) is capable of detecting all elements in the periodic table, with detection limits in the ppm to ppb range. With proper standards, quantification may be performed with accuracies of ~ 10% or less. The instrument is normally operated as a low resolution mass spectrometer (M/M = 300), but may also be operated in a high resolution mode (M/M = ~2500).

GEO-CENTERS, INC.

SIMS ANALYSIS OF Be DISTRIBUTION IN THERMALLY ANNEALED GaAlAs

Ref: 6170-795:SH:al memo

1. On 28 January 1987 B. Molnar, Code 6812, requested that a depth scale be placed on the depth profile of sample 112486-1 (reference (a)) assuming a GaAs cap layer thickness of 100 nm.

2. The specimen was depth profiled with a CAMECA IMS-300 ion microscope using 5.5 keV O_2^+ ions at a primary current of 700 nA. The primary beam was rastered over an area of approximately 500 x 800 um. In the center of this raster an area of 250 um in diameter was analyzed. Because of the difference in size between the rastered and analyzed areas contributions of analyte atoms residing at the crater walls to the detected signal were eliminated. Some details concerning the CAMECA IMS-300 ion microscope are presented in the appendix.

3. A depth profile of 112486-1 for mass 9 (Be^+, $^{27}Al^{+3}$) and mass 75 (As^+) is shown in fig. 1. The increase of the mass 9 signal level in the beginning of the profile is due to an increase in the Al concentration and to a matrix effect arising from the increased oxygen gettering efficiency of Al over that of GaAs. A broken depth scale may be placed upon this profile using the GaAs cap thickness of 100 nm and the total depth, determined by interference microscopy utilizing a Nikon OPTIHOT optical microscope of 1360 nm.

4. Appendix:

The CAMECA IMS-300 ion microscope employs an energetic (0-10 keV) primary ion beam (typically O_2^+, Ar^+, or O^-) to analyze solid materials. The interaction of the primary ions with the sample erodes the target surface liberating secondary ions which are subsequently mass analyzed. The instrument design is such that the lateral distribution of the secondary ions is reformed at the detector resulting in a magnified mass analyzed image of the sample surface. This image may be observed visually or recorded on electron sensitive film with a field of view of 250 microns and a lateral resolution of one micron. The ion microscope is also capable of providing a three dimensional characterization of solids by monitoring the secondary ion signal of interest as a function of time. Provided the sputter yield (sputtered atoms/incident ion) is constant (or the layer thicknesses of a heterogeneous sample are known) this time scale may be converted to a depth scale by measurement of the crater depth. Crater depth measurements are normally made in this laboratory by interferometry. Secondary ion mass spectrometry (SIMS) is capable of detecting all elements in the periodic table, with detection limits in the ppm to ppb range. With proper standards, quantification may be performed with accuracies of ~ 10% or less. The instrument is normally operated as a low resolution mass spectrometer (M/M = 300), but may also be operated in a high resolution mode (M/M = ~2500).

GEO-CENTERS, INC.

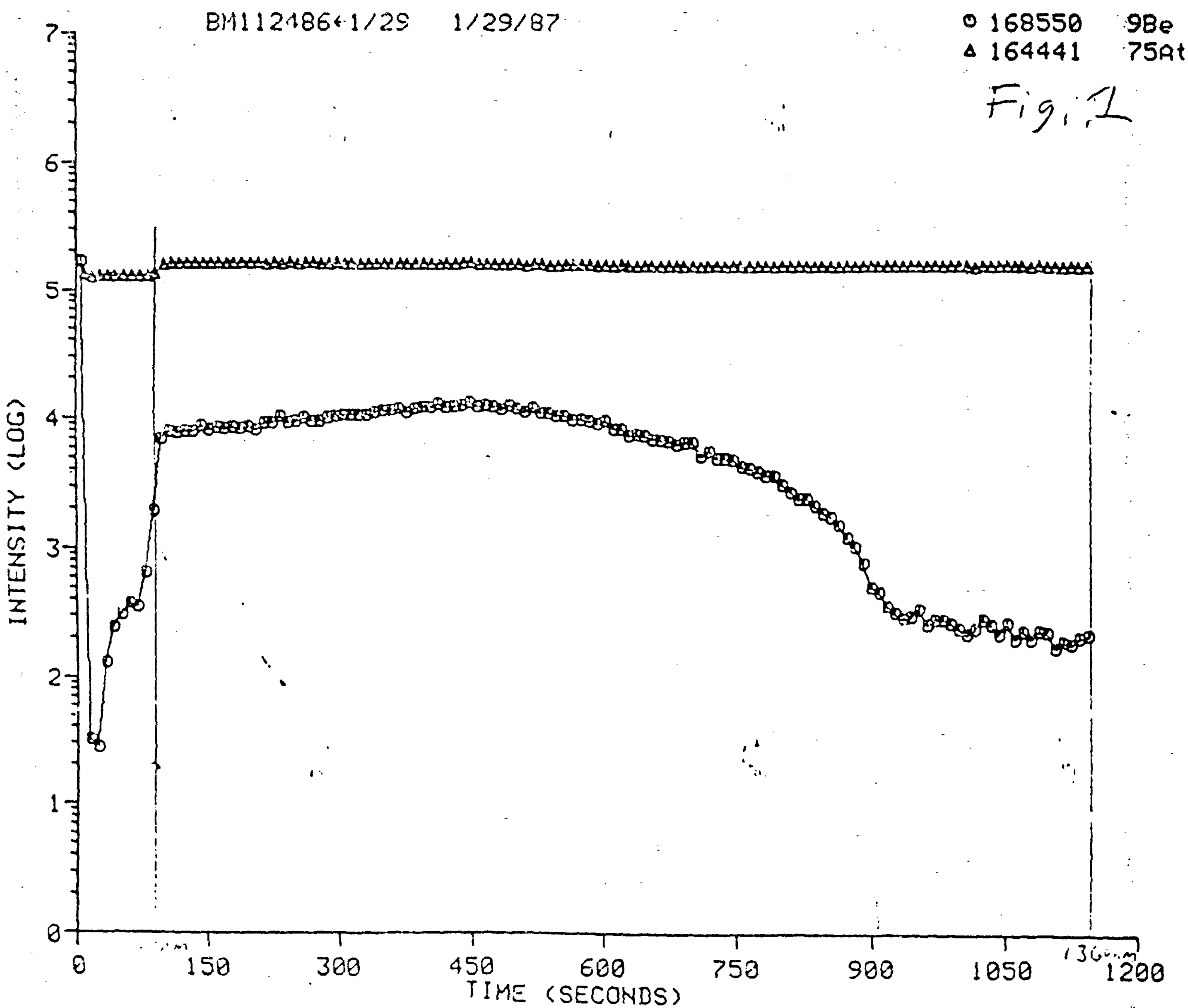

BM112486+1/29 1/29/87
o 168550 9Be
Δ 164441 75At
INTENSITY (LOG)
0
1
2
3
4
5
6
7
0 150 300 450 600 750 900 1050 1200
TIME (SECONDS)

Fig. 1

SIMS ANALYSIS OF Be DISTRIBUTION IN THERMALLY ANNEALED GaAlAs

Ref: 6170-795:SH:al memo

1. On 28 January 1987 B. Molnar, Code 6812, requested that a depth scale be placed on the depth profile of sample 112486-1 (reference (a)) assuming a GaAs cap layer thickness of 100 nm.

2. The specimen was depth profiled with a CAMECA IMS-300 ion microscope using 5.5 keV O_2^+ ions at a primary current of 700 nA. The primary beam was rastered over an area of approximately 500 x 800 um. In the center of this raster an area of 250 um in diameter was analyzed. Because of the difference in size between the rastered and analyzed areas contributions of analyte atoms residing at the crater walls to the detected signal were eliminated. Some details concerning the CAMECA IMS-300 ion microscope are presented in the appendix.

3. A depth profile of 112486-1 for mass 9 (Be^+, $^{27}Al^{+3}$) and mass 75 (As^+) is shown in fig. 1. The increase of the mass 9 signal level in the beginning of the profile is due to an increase in the Al concentration and to a matrix effect arising from the increased oxygen gettering efficiency of Al over that of GaAs. A broken depth scale may be placed upon this profile using the GaAs cap thickness of 100 nm and the total depth, determined by interference microscopy utilizing a Nikon OPTIHOT optical microscope of 1360 nm.

4. Appendix:

The CAMECA IMS-300 ion microscope employs an energetic (0-10 keV) primary ion beam (typically O_2^+, Ar^+, or O^-) to analyze solid materials. The interaction of the primary ions with the sample erodes the target surface liberating secondary ions which are subsequently mass analyzed. The instrument design is such that the lateral distribution of the secondary ions is reformed at the detector resulting in a magnified mass analyzed image of the sample surface. This image may be observed visually or recorded on electron sensitive film with a field of view of 250 microns and a lateral resolution of one micron. The ion microscope is also capable of providing a three dimensional characterization of solids by monitoring the secondary ion signal of interest as a function of time. Provided the sputter yield (sputtered atoms/incident ion) is constant (or the layer thicknesses of a heterogeneous sample are known) this time scale may be converted to a depth scale by measurement of the crater depth. Crater depth measurements are normally made in this laboratory by interferometry. Secondary ion mass spectrometry (SIMS) is capable of detecting all elements in the periodic table, with detection limits in the ppm to ppb range. With proper standards, quantification may be performed with accuracies of ~ 10% or less. The instrument is normally operated as a low resolution mass spectrometer (M/M = 300), but may also be operated in a high resolution mode (M/M = ~2500).

GEO-CENTERS, INC.

SIMS ANALYSIS OF Be DISTRIBUTION IN Be-IMPLANTED GaAlAs

1. On 28 January 1987 B. Molnar, Code 6812, submitted a sample of Be-implanted GaAlAs, labeled B-1, for analysis by secondary ion mass spectrometry. The implant dose was 10^{13} atoms/cm^2 and of interest was the present detection limit of Be from GaAlAs.

2. The specimen was depth profiled with a CAMECA IMS-300 ion microscope using 5.5 keV O_2^+ ions at a primary current of 700 nA. The primary beam was rastered over an area of approximately 500 x 800 um. In the center of this raster an area of 250 um in diameter was analyzed. Because of the difference in size between the rastered and analyzed areas contributions of analyte atoms residing at the crater walls to the detected signal were eliminated. Some details concerning the CAMECA IMS-300 ion microscope are presented in the appendix.

3. A depth profile of B-1 for mass 9 (Be^+, $^{27}Al^{+3}$) and mass 75 (As^+) is shown in fig. 1. Assuming a peak concentration of 10^{18} atoms/cm^3 and defining the detection limit as that concentration necessary to produce 10 counts/sec the present detection limit for Be in GaAlAs is determined to be approximately 3 x 10^{17} atoms/cm^3. The detection limit in this case is background limited by $^{27}Al^{+3}$ to approximately 6 x 10^{17} atoms/cm^3.

4. Appendix:

The CAMECA IMS-300 ion microscope employs an energetic (0-10 keV) primary ion beam (typically O_2^+, Ar^+, or O^-) to analyze solid materials. The interaction of the primary ions with the sample erodes the target surface liberating secondary ions which are subsequently mass analyzed. The instrument design is such that the lateral distribution of the secondary ions is reformed at the detector resulting in a magnified mass analyzed image of the sample surface. This image may be observed visually or recorded on electron sensitive film with a field of view of 250 microns and a lateral resolution of one micron. The ion microscope is also capable of providing a three dimensional characterization of solids by monitoring the secondary ion signal of interest as a function of time. Provided the sputter yield (sputtered atoms/incident ion) is constant (or the layer thicknesses of a heterogeneous sample are known) this time scale may be converted to a depth scale by measurement of the crater depth. Crater depth measurements are normally made in this laboratory by interferometry. Secondary ion mass spectrometry (SIMS) is capable of detecting all elements in the periodic table, with detection limits in the ppm to ppb range. With proper standards, quantification may be performed with accuracies of ~ 10% or less. The instrument is normally operated as a low resolution mass spectrometer (M/M = 300), but may also be operated in a high resolution mode (M/M = ~2500).

GEO-CENTERS, INC.

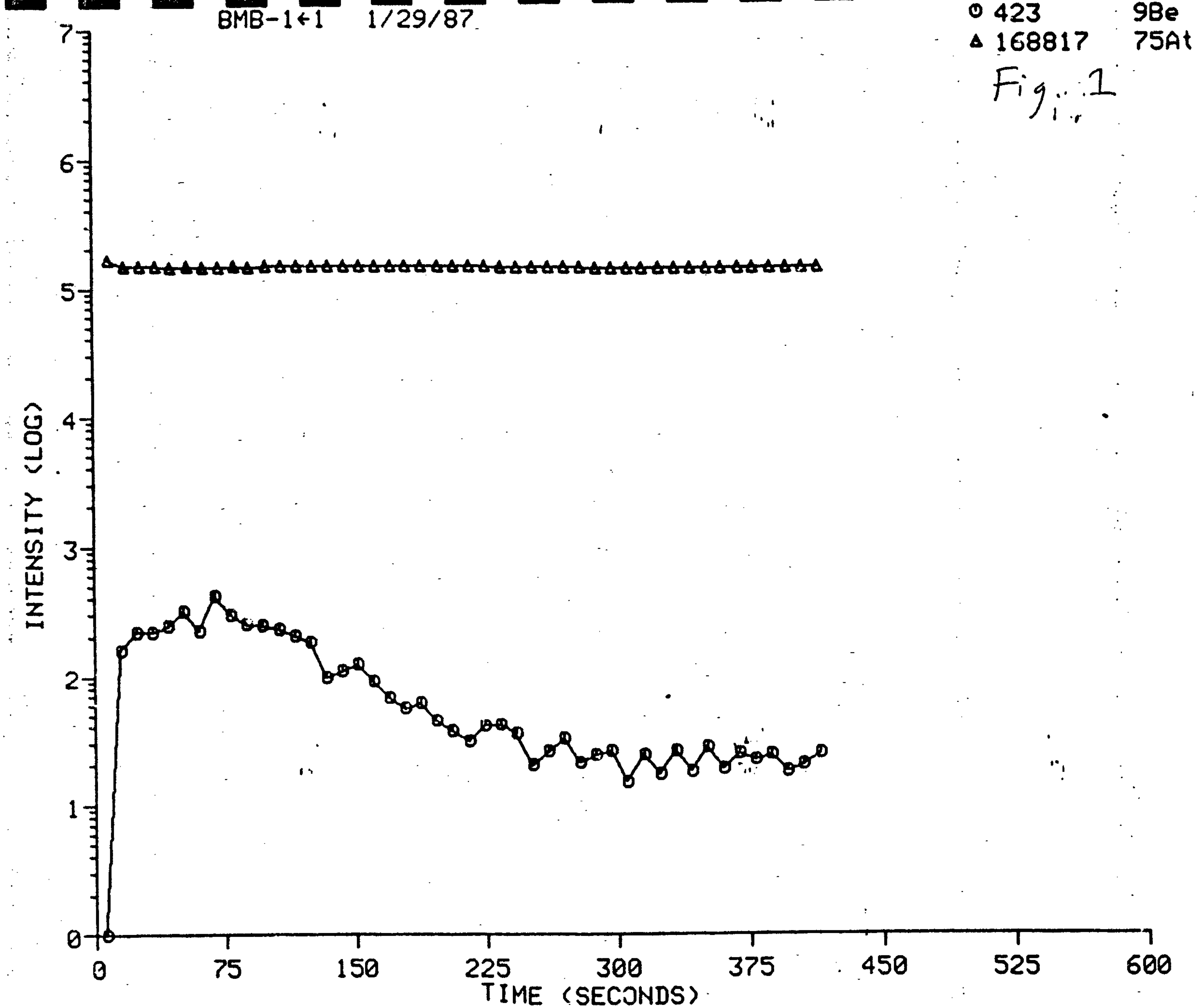
BMB-1←1 1/29/87
⊙ 423 9Be
△ 168817 75At
INTENSITY (LOG)
0
1
2
3
4
5
6
7
0
75
150
225
300
375
450
525
600
TIME (SECONDS)

Fig. 1

SIMS ANALYSIS OF Be DISTRIBUTION IN AS-IMPLANTED GaAlAs

1. On 30 January 1987 B. Molnar, Code 6812, submitted a sample of Be-implanted GaAlAs, labeled 1739, for analysis by secondary ion mass spectrometry. The sample had been implanted with Be at 25 keV and 300 keV. Of interest was the depth distribution of Be.

2. The specimen was depth profiled with a CAMECA IMS-300 ion microscope using 5.5 keV O_2^+ ions at a primary current of 700 nA. The primary beam was rastered over an area of approximately 500 x 800 um. In the center of this raster an area of 250 um in diameter was analyzed. Because of the difference in size between the rastered and analyzed areas contributions of analyte atoms residing at the crater walls to the detected signal were eliminated. Some details concerning the CAMECA IMS-300 ion microscope are presented in the appendix.

3. A depth profile of 1739 for mass 9 (Be^+, $^{27}Al^{+3}$) and mass 75 (As^+) is shown in fig. 1. The depth scale was established by interferometry utilizing a Nikon OPTIHOT optical microscope, assuming a uniform sputter rate throughout the analyzed depth. The sharp downward peaks at approximately 900 nm are instrumental artifacts and may be ignored.

4. Appendix:

The CAMECA IMS-300 ion microscope employs an energetic (0-10 keV) primary ion beam (typically O_2^+, Ar^+, or O^-) to analyze solid materials. The interaction of the primary ions with the sample erodes the target surface liberating secondary ions which are subsequently mass analyzed. The instrument design is such that the lateral distribution of the secondary ions is reformed at the detector resulting in a magnified mass analyzed image of the sample surface. This image may be observed visually or recorded on electron sensitive film with a field of view of 250 microns and a lateral resolution of one micron. The ion microscope is also capable of providing a three dimensional characterization of solids by monitoring the secondary ion signal of interest as a function of time. Provided the sputter yield (sputtered atoms/incident ion) is constant (or the layer thicknesses of a heterogeneous sample are known) this time scale may be converted to a depth scale by measurement of the crater depth. Crater depth measurements are normally made in this laboratory by interferometry. Secondary ion mass spectrometry (SIMS) is capable of detecting all elements in the periodic table, with detection limits in the ppm to ppb range. With proper standards, quantification may be performed with accuracies of ~ 10% or less. The instrument is normally operated as a low resolution mass spectrometer (M/M = 300), but may also be operated in a high resolution mode (M/M = ~2500).

GEO-CENTERS, INC.

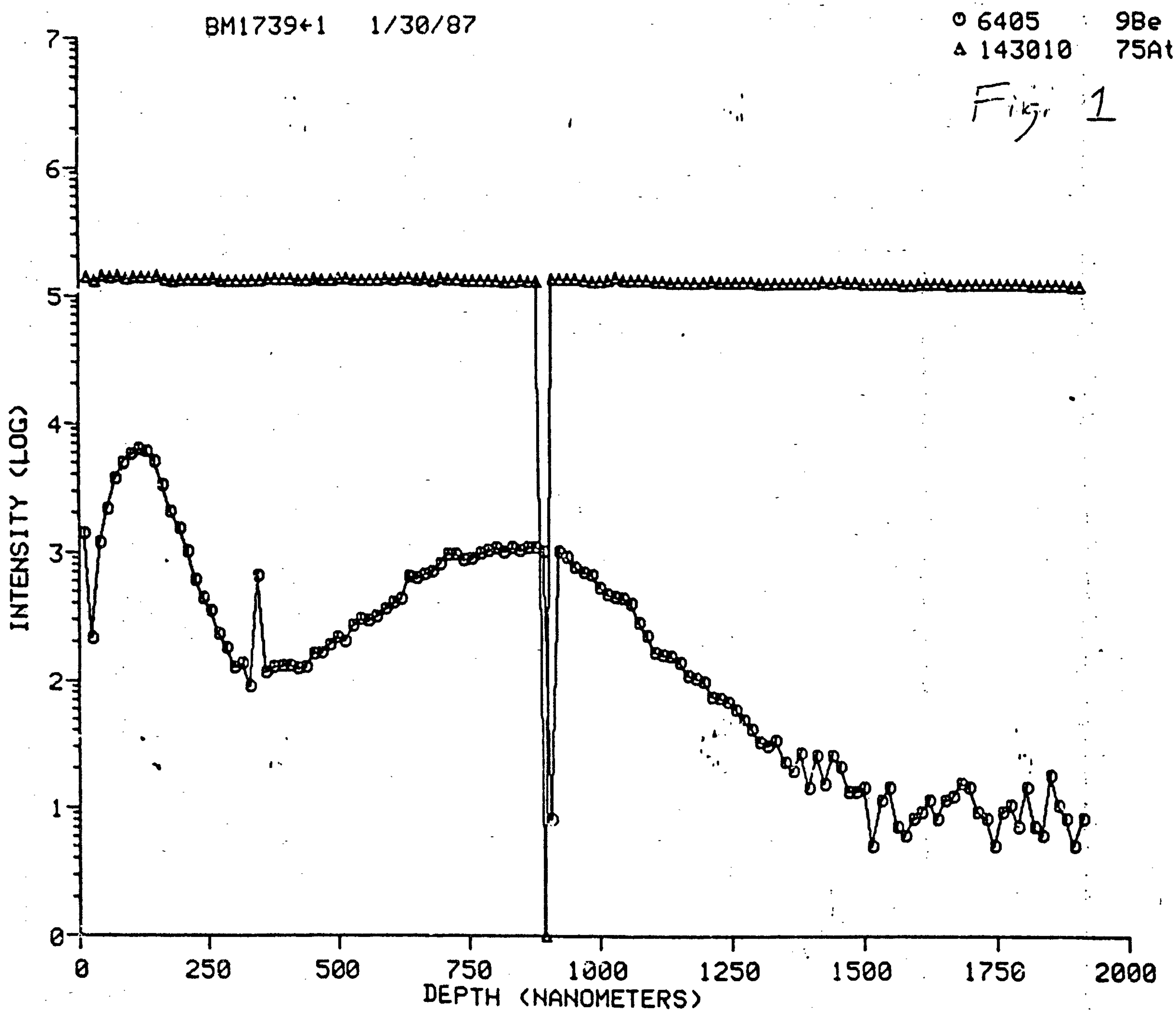
BM1739+1 1/30/87
○ 6405 9Be
△ 143010 75At
INTENSITY (LOG)
DEPTH (NANOMETERS)
0
1
2
3
4
5
6
7
0
250
500
750
1000
1250
1500
1750
2000

Fig. 1

SIMS ANALYSIS OF B-IMPLANTED InP AND B AND As-IMPLANTED Si

1. On 23 December 1986 B. Molnar, Code 6812, submitted two samples for analysis by secondary ion mass spectrometry. One sample was a Si substrate which had been implanted with As to a depth of 3000A to a peak concentration of 10^{20} atoms/cm^3 and B to a depth of 1 um and a peak concentration of 10^{16} atoms/cm^3. The second sample was an InP substrate which had been implanted with B to a depth of 4000 and a peak concentration of 10^{17} atoms/cm^3. Of interest was the depth distribution of each of the implanted species.

2. The specimens were depth profiled with a CAMECA IMS-300 ion microscope using 5.5 keV O_2^+ ions at a primary current of 500 nA (Si sample) and 650 nA (InP sample). The primary beam was rastered over an area of approximately 500 x 800 um. In the center of this raster an area of 250 um in diameter was analyzed. Because of the difference in size between the rastered and analyzed areas contributions of analyte atoms residing at the crater walls to the detected signal were eliminated. Some details concerning the CAMECA IMS-300 ion microscope are presented in the appendix.

3. The presence of As was not detected in the Si sample while monitoring for As^+, As^-, or AsO^-. While As in Si detection limit for this particular instrument is not known, due to a lack of suitable standards, other researchers have reported detection limits, under these analysis conditions, in the 10^{19} atoms/cm^3 range (1). In order to ascertain if the instrument was operating normally a depth profile of a previously analyzed B implanted Si sample was obtained, Fig. 1, showing sensitivity within normal limits. Improved detection limits may be obtained by monitoring negative ions and using Cs^+ primary ions which acts to increase the negative secondary ion yield. This capability is, however, not presently available at NRL. Fig. 2 shows a depth profile of the B distribution in the InP sample. The depth scale was established by interference microscopy of the sputtered crater using a Nikon OPTIHOT optical microscope.

4. Appendix:

The CAMECA IMS-300 ion microscope employs an energetic (0-10 keV) primary ion beam (typically O_2^+, Ar^+, or O^-) to analyze solid materials. The interaction of the primary ions with the sample erodes the target surface liberating secondary ions which are subsequently mass analyzed. The instrument design is such that the lateral distribution of the secondary ions is reformed at the detector resulting in a magnified mass analyzed image of the sample surface. This image may be observed visually or recorded on electron sensitive film with a field of view of 250 microns and a lateral resolution of one micron. The ion microscope is also capable of providing a three dimensional characterization of solids by monitoring the secondary ion signal of interest as a function of time. Provided the sputter yield (sputtered atoms/incident ion) is constant (or the layer thicknesses of a heterogeneous sample are known) this time scale may be converted to a depth scale by measurement of the crater depth. Crater depth measurements are normally made in this laboratory by interferometry. Secondary ion mass spectrometry (SIMS) is capable of detecting all elements in the periodic table, with detection limits in the ppm to ppb range. With proper standards, quantification may be performed with accuracies of approximately 10% or less. The instrument is normally operated as a low resolution mass spectrometer (M/M = 300), but may also be operated in a high resolution mode (M/M = 2500).

(1) Methods of Surface Analysis, A.W. Czanderna, Ed., Elsevier Scientific Publishing, 1975, pg. 307.

STEVEN HUES

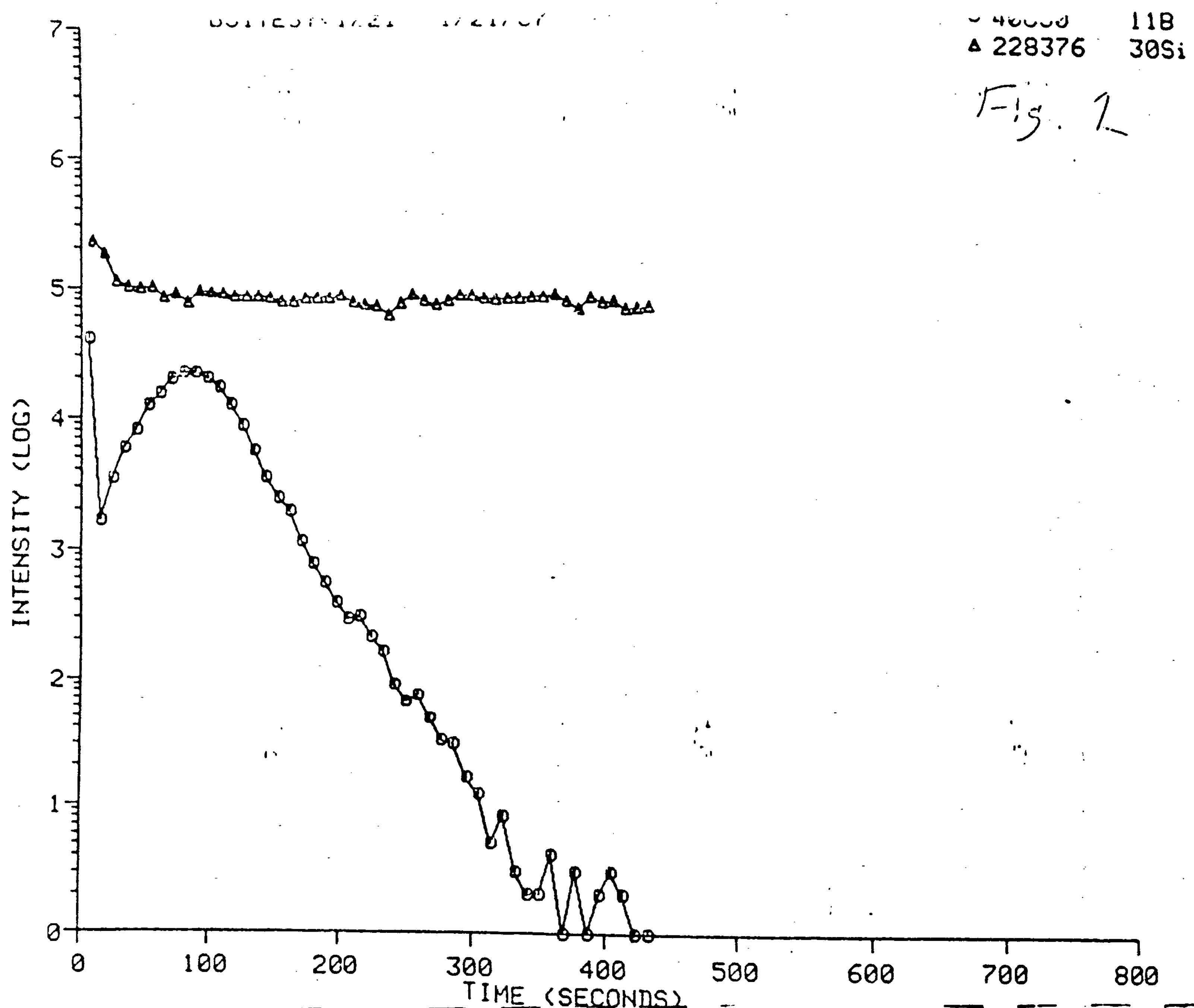
11B
▵ 228376 30Si
INTENSITY (LOG)
TIME (SECONDS)
0
1
2
3
4
5
6
7
0
100
200
300
400
500
600
700
800

Fig. 1

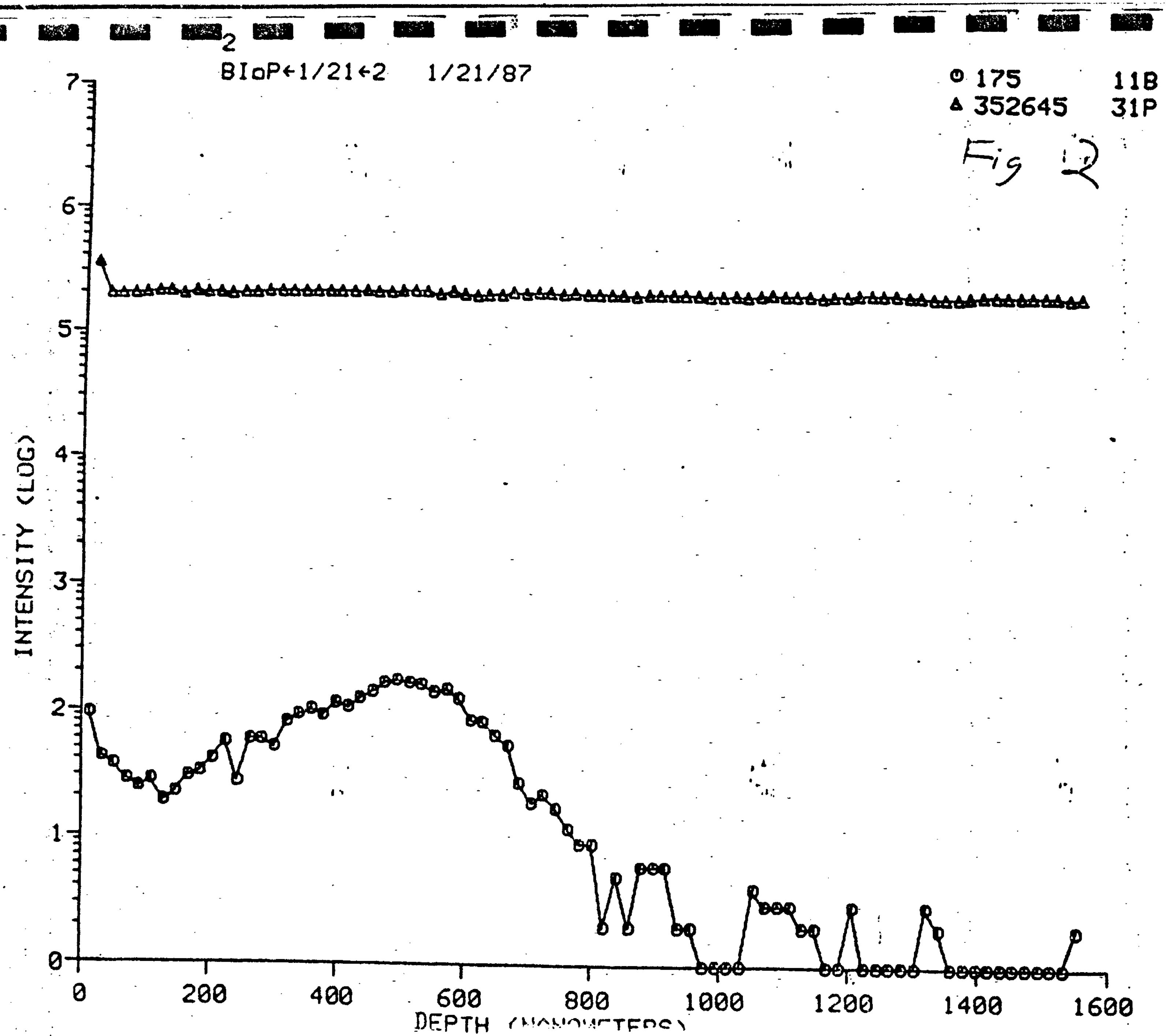

BIoP←1/21←2 1/21/87
175 11B
352645 31P
INTENSITY (LOG)
DEPTH
0
200
400
600
800
1000
1200
1400
1600
0
1
2
3
4
5
6
7

Fig 2

SIMS ANALYSIS OF In-DOPED GaAs

1. On 25 February 1987 N. Bottka, Code 6821, submitted three samples of In doped GaAs for analysis by secondary ion mass spectrometry. One sample, labeled OM-374 consisted of a MODFET structure having a GaAs cap layer 100A in thickness, followed by an In and Si doped AlGaAs layer 500A in thickness, an In doped AlGaAs layer 100A in thickness, and an In doped GaAs layer 7000A in thickness deposited on a GaAs substrate. The other two samples, labeled OM-379-1 and OM-363, were In doped GaAs layers ~6-7μm in thickness deposited on GaAs substrates. The In concentrations as measured by photo reflectance spectroscopy were 0.98% and 0.42%, respectively. These samples were to be used as standards for quantifying the In concentration in the 7000A layer in OM-374. Based upon the results for OM-374 two further samples similar to OM-374, labeled OM-380 and OM-383, were submitted on 27 February 1987.

2. The specimens were depth profiled with a CAMECA IMS-300 secondary ion mass spectrometer using 5.5 keV O_2^+ ions. The primary beam was rastered over an area of approximately 700 x 800 μm. In the center of this raster an area 250 μm in diameter was analyzed. Because of the difference in size between the rastered and analyzed areas, contributions of analyte atoms residing at the crater walls to the detected signal were eliminated. Some details concerning the CAMECA IMS-300 ion microscope are presented in the appendix.

3. Figs. 1, 2 and 3 show depth profiles of OM-379-1, OM-363, and OM-374 for mass 27 ($^{27}Al^+$), mass 28 ($^{28}Si^+$, $^{27}AlH^+$), mass 75 ($^{75}As^+$), and mass 115 ($^{115}In^+$) taken at a primary current of 100 nA. Using the two standard samples and normalizing the mass 115 signal to the mass 75 signal the concentration of In in the plateau region reached immediately after the AlGaAs layer had been sputtered through is determined to be 0.03%. Fig. 4 shows a depth profile of OM-379-1 taken at a primary current of 2.0 μA. As may be seen, the In doping is constant throughout the grown film. Figs. 5, 6 and 7 show depth profiles of OM-383, OM-380, and OM-374 taken at a primary current of 150 nA. The spikes in the mass 115 signals in figs. 6 and 7 do not appear to be the result of electronic noise in the instrument. Since these spikes are occurring in the interfacial region they may be the result of either a true increase in the In concentration or a matrix effect, possibly due to an increased amount of oxygen at these interfaces relative to the one in OM-383. However, since the mass 27 signal spike is approximately the same for all three profiles it is probable that some of the increase is due to an increased concentration of In at the interface.

4. Appendix:

The CAMECA IMS-300 ion microscope employs an energetic (0-10 keV) primary ion beam (typically O_2^+, Ar^+, or O^-) to analyze solid materials. The interaction of the primary ions with the sample erodes the target surface liberating secondary ions which are subsequently mass analyzed. The instrument design is such that the lateral distribution of the secondary ions is reformed at the detector resulting in a magnified mass analyzed image of the sample surface. This image may be observed visually or recorded on electron sensitive film with a field of view of 250 microns and a lateral resolution of one micron. The ion microscope is also capable of providing a three dimensional characterization of solids by monitoring the secondary ion signal of interest as a function of time. Provided the sputter yield (sputtered atoms/incident ion) is constant (or the layer thicknesses of a heterogeneous sample are known) this time scale may be converted to a depth scale by measurement of the crater depth. Crater depth measurements are normally made in this laboratory by interferometry. Secondary ion mass spectrometry (SIMS) is capable of detecting all elements in the periodic table, with detection limits in the ppm to ppb range. With proper standards, quantification may be performed with accuracies of ~ 10% or less. The instrument is normally operated as a low resolution mass spectrometer (M/M = 300), but may also be operated in a high resolution mode (M/M = ~2500).

STEVEN HUES

GEO-CENTERS, INC.

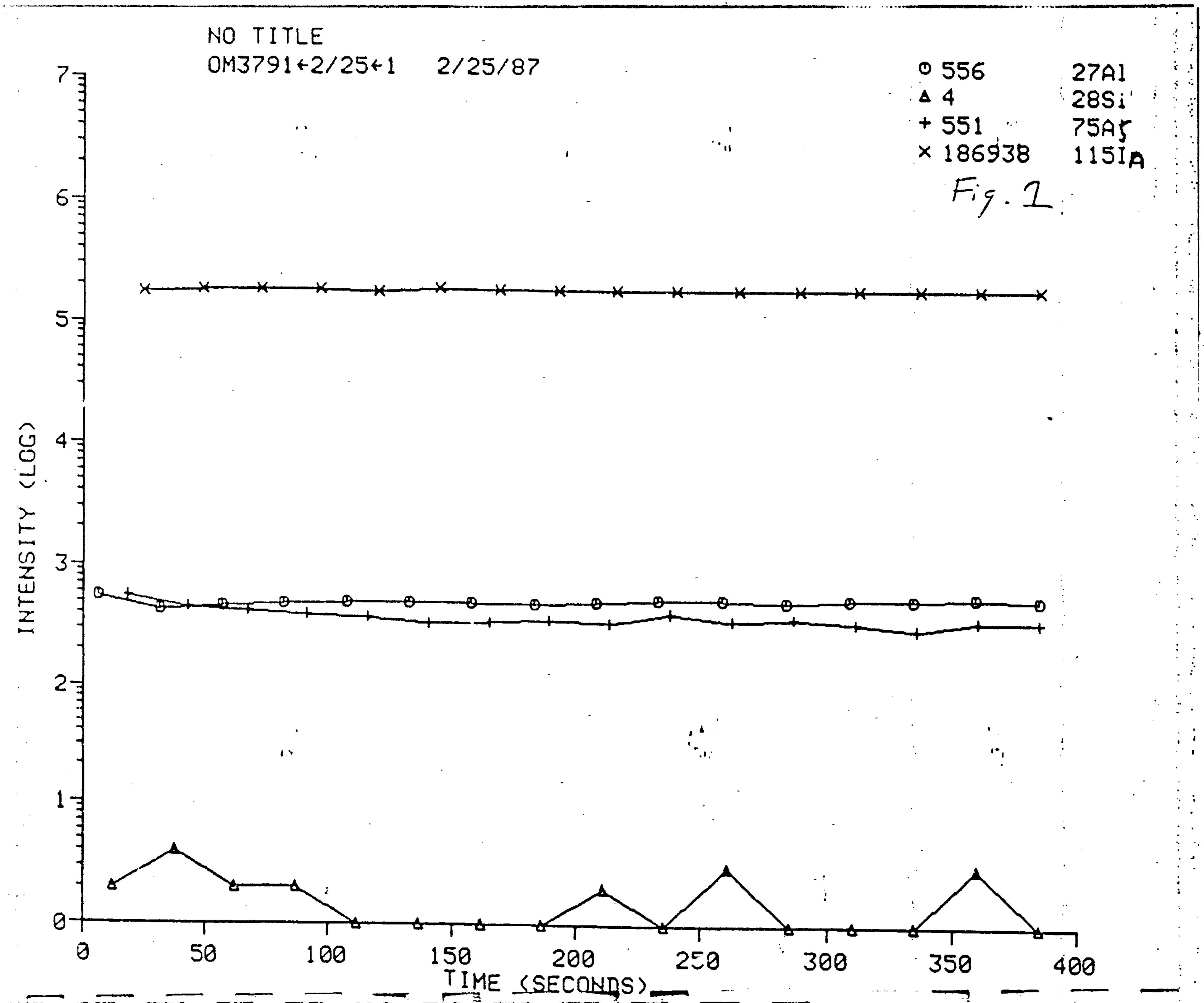

NO TITLE
OM3791←2/25←1 2/25/87
○ 556 27Al
△ 4 28Si
+ 551 75As
× 186938 115In
Fig. 1
INTENSITY (LOG)
TIME (SECONDS)
0
1
2
3
4
5
6
7
0
50
100
150
200
250
300
350
400

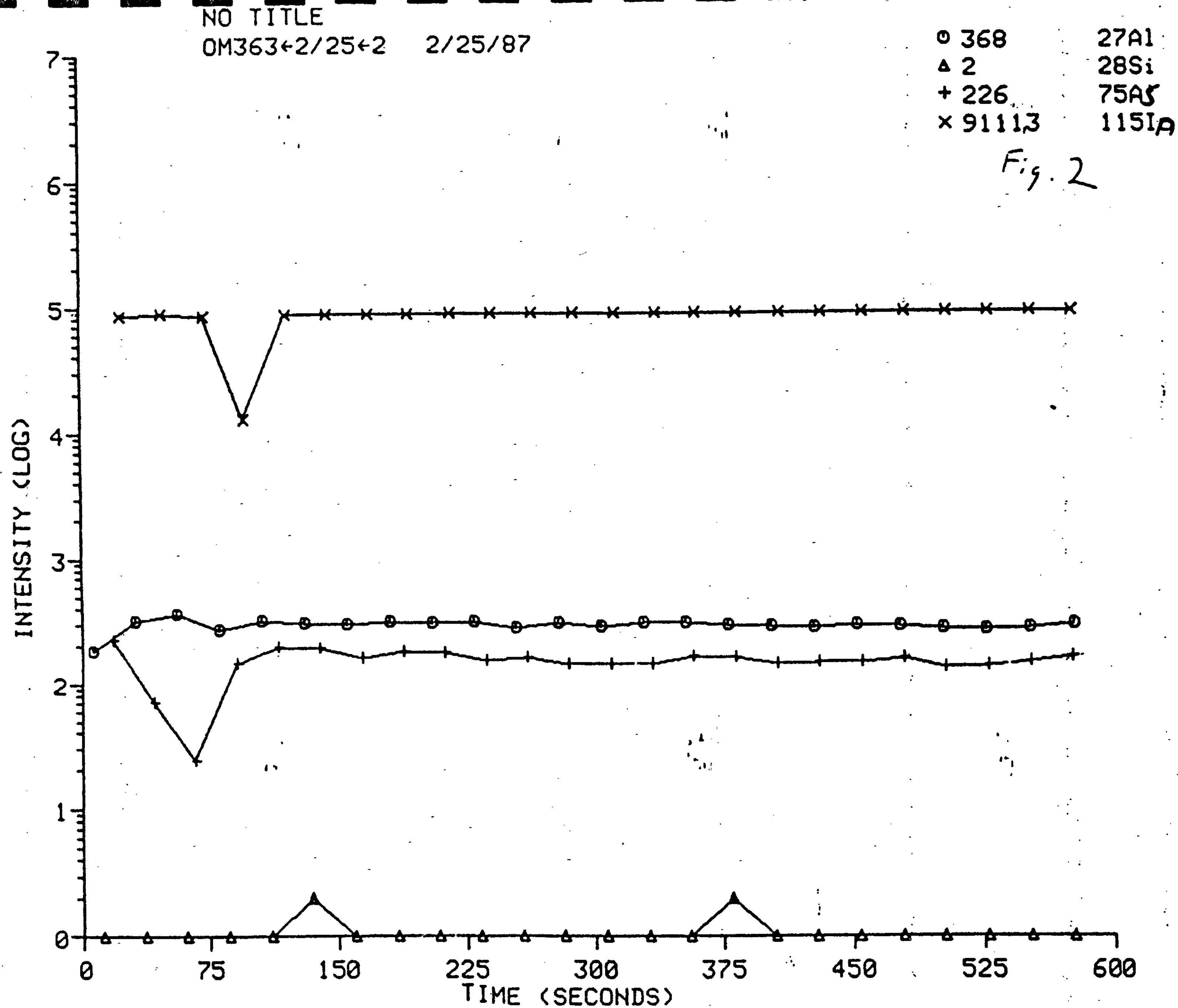

NO TITLE
OM363←2/25←2 2/25/87
⊖ 368 27Al
▵ 2 28Si
+ 226 75As
× 91113 115In
INTENSITY (LOG)
7
6
5
4
3
2
1
0
0
75
150
225
300
375
450
525
600
TIME (SECONDS)

Fig. 2

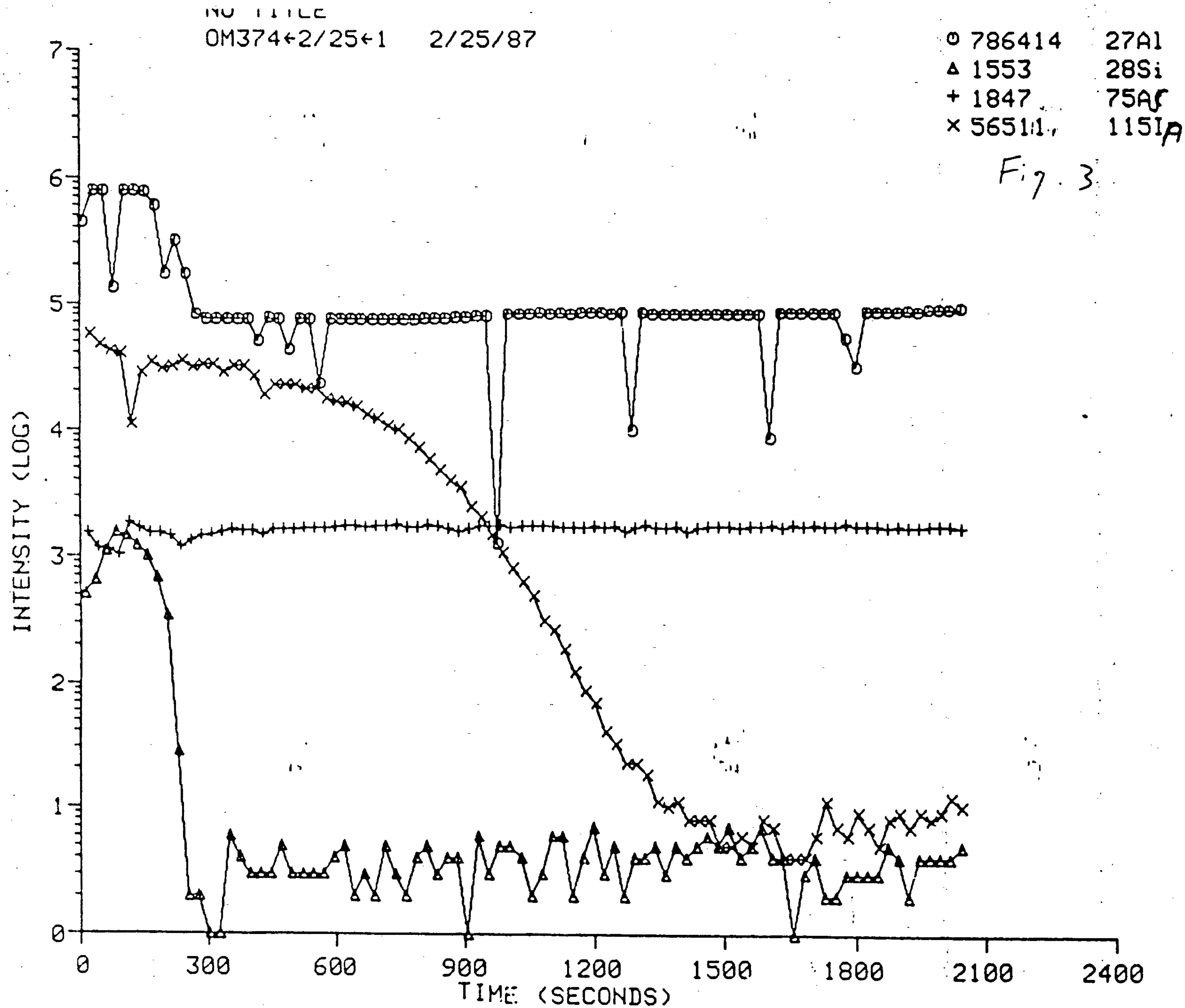

NO TITLE
OM374←2/25←1 2/25/87
ⓞ 786414 27Al
△ 1553 28Si
+ 1847 75As
× 56511 115In
INTENSITY (LOG)
7
6
5
4
3
2
1
0
0
300
600
900
1200
1500
1800
2100
2400
TIME (SECONDS)

Fig. 3

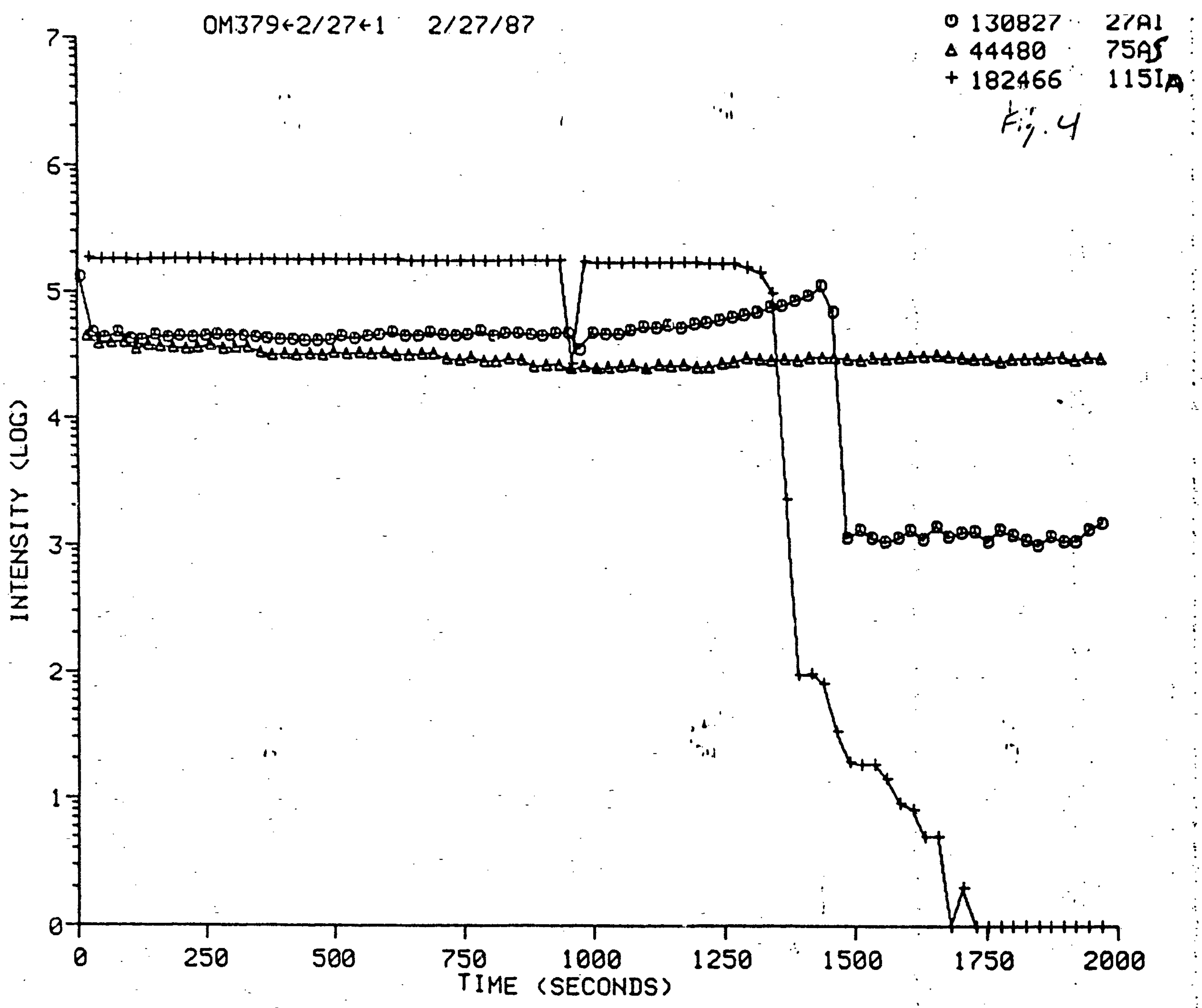
OM379←2/27←1 2/27/87
⊙ 130827 27Al
△ 44480 75As
+ 182466 115In
Fig. 4
INTENSITY (LOG)
0
1
2
3
4
5
6
7
TIME (SECONDS)
0
250
500
750
1000
1250
1500
1750
2000

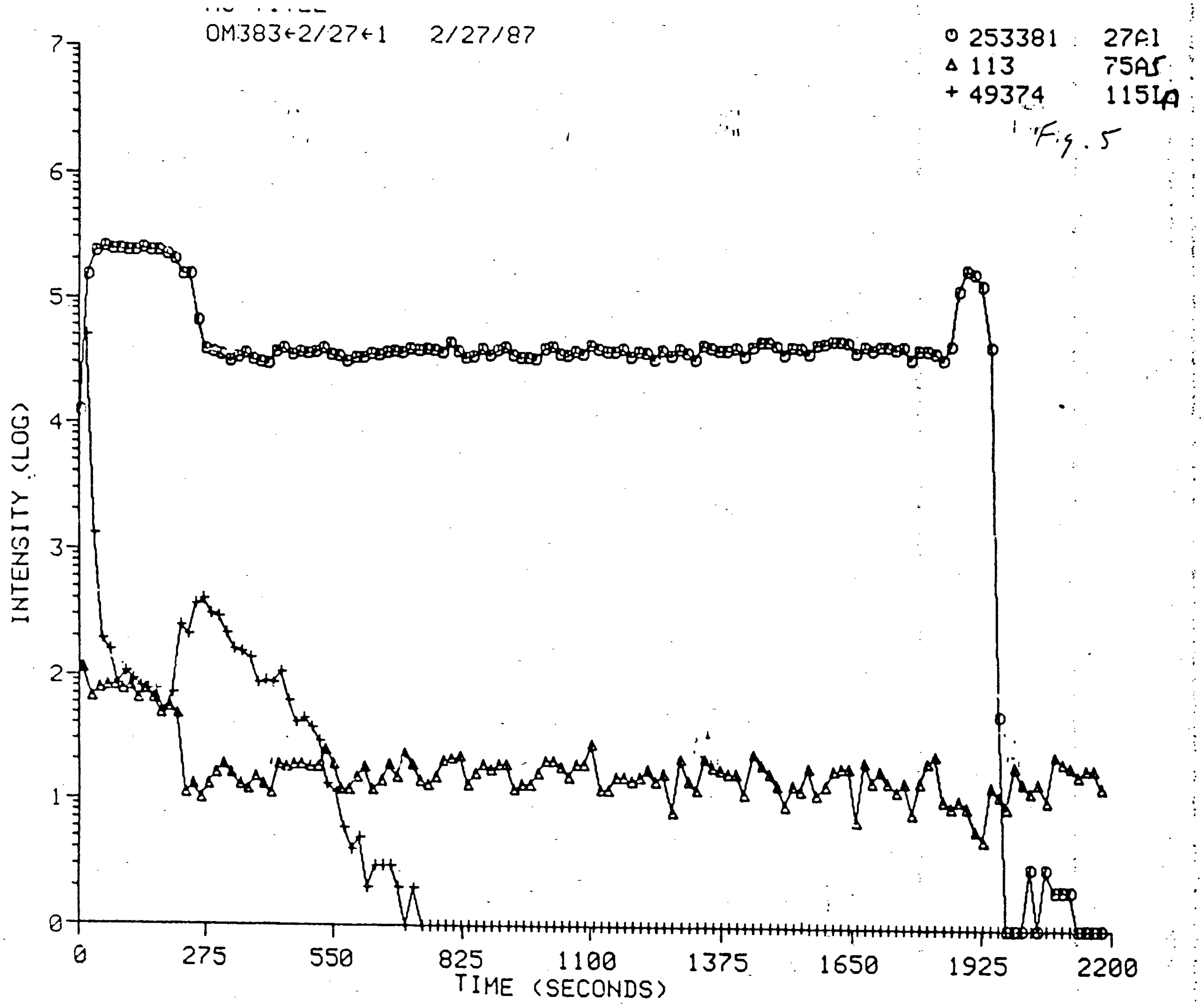

OM383+2/27+1 2/27/87
○ 253381 27Al
△ 113 75As
+ 49374 115In
INTENSITY (LOG)
TIME (SECONDS)
0
275
550
825
1100
1375
1650
1925
2200
7
6
5
4
3
2
1
0

Fig. 5

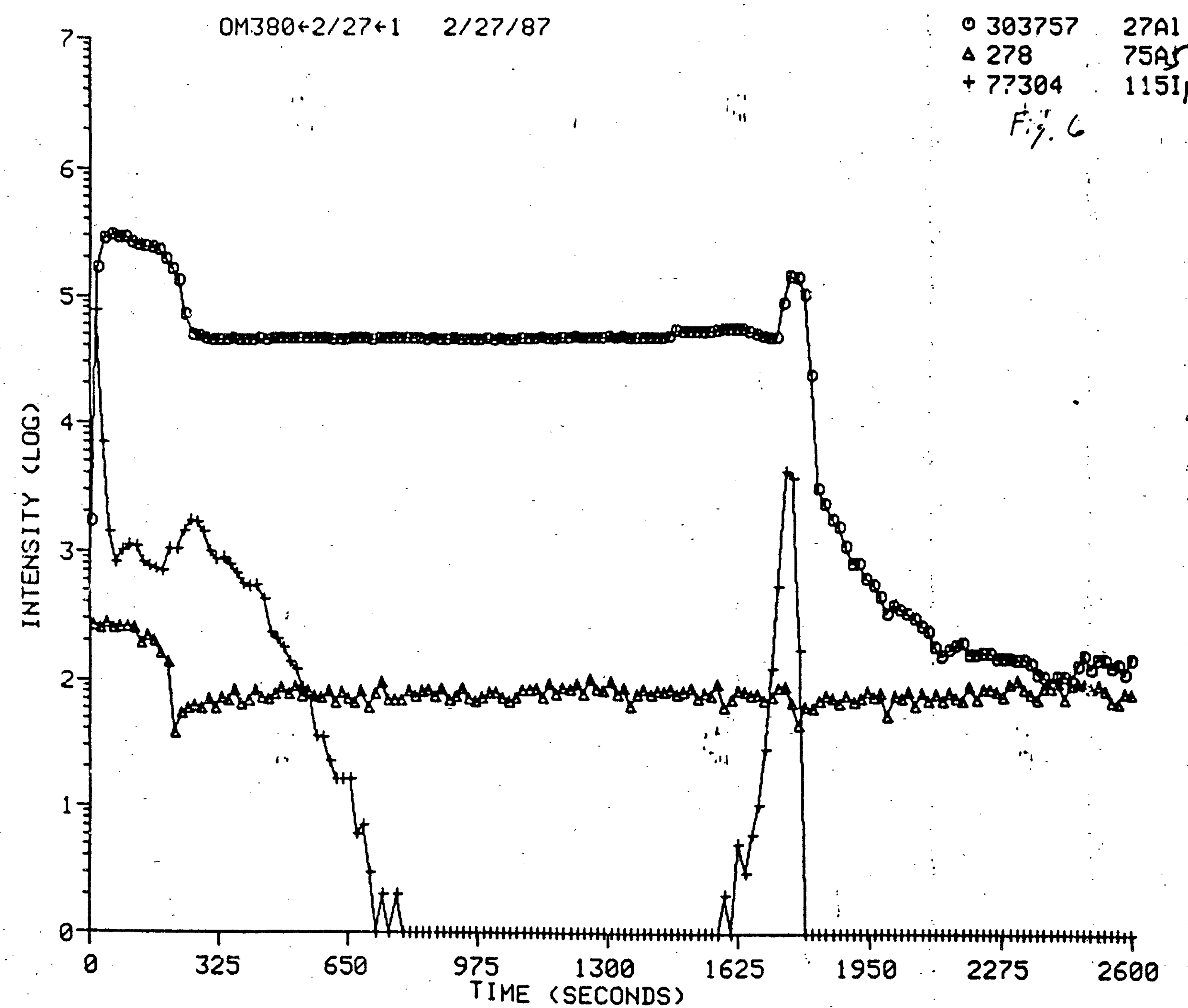
OM380←2/27←1 2/27/87
⊙ 303757 27Al
△ 278 75As
+ 77304 115In
INTENSITY (LOG)
0
1
2
3
4
5
6
7
0
325
650
975
1300
1625
1950
2275
2600
TIME (SECONDS)

Fig. 6

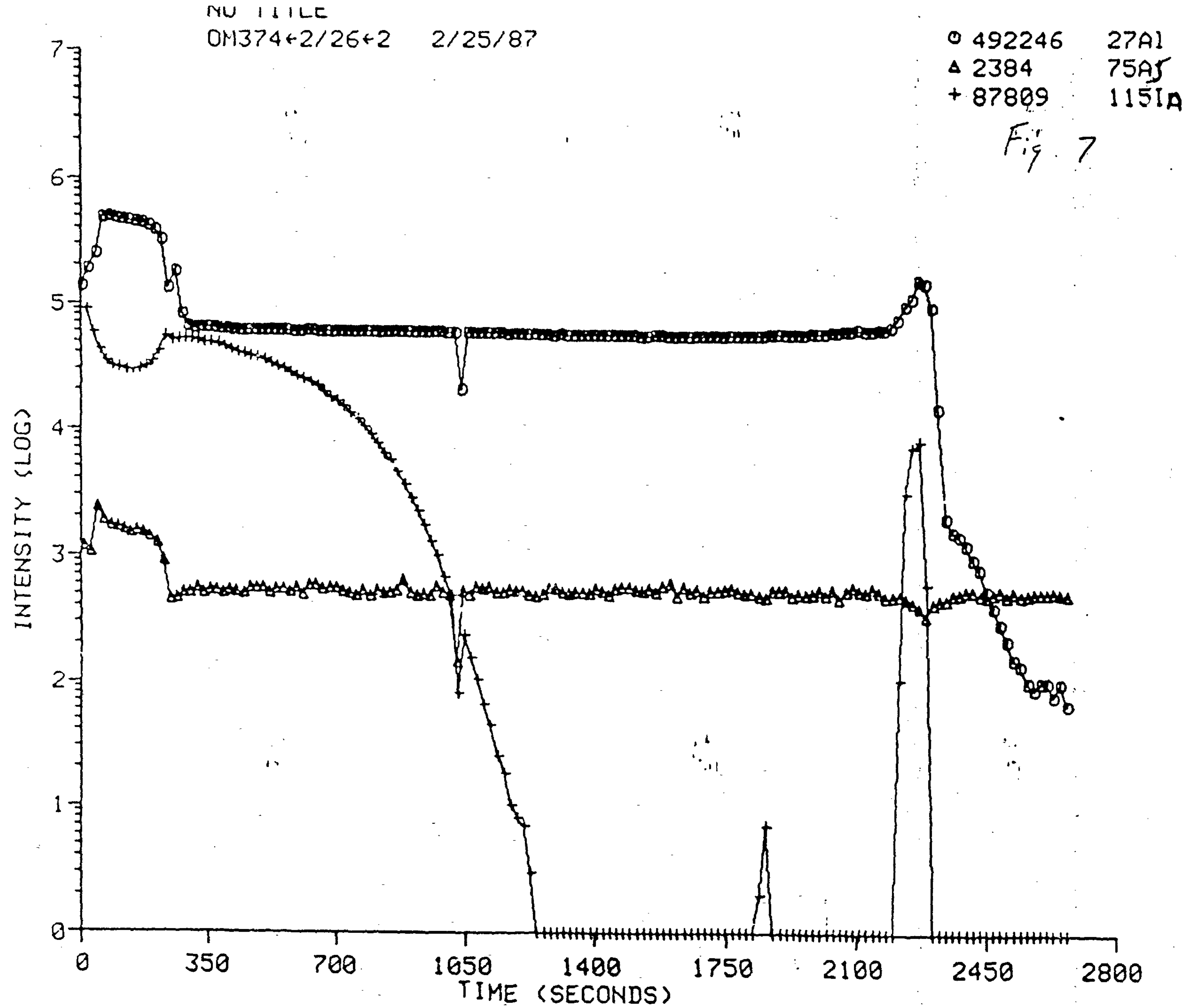

NO TITLE
OM374+2/26+2 2/25/87
o 492246 27Al
▵ 2384 75As
+ 87809 115In
INTENSITY (LOG)
7
6
5
4
3
2
1
0
0
350
700
1050
1400
1750
2100
2450
2800
TIME (SECONDS)

Fig 7

RESULTS OF IMAGING ANALYSIS OF InP SUBSTRATE BY U.S. ARMY LABCOM, FT. MONMOUTH

1. On approximately 12 September 1986, B. Molnar, Code 6812 submitted a sample of InP with visible striations in its surface. An imaging analysis using secondary ion mass spectrometry to determine the lateral distribution of any As which might be present was requested. The level of As present was below the detection limit of the CAMECA IMS-300 imaging system (memo 6170-655), therefore the sample was forwarded to the U.S. Army Electronic Technology and Development Laboratory, Ft. Monmouth, NJ for imaging analysis on the CAMECA IMS-3f ion microanalyzer. The results of this analysis performed by Dr. Richard T. Lareau are presented in this report.

2. Figs. 1 and 2 are depth profiles of the sample with the analysis conditions specified on each profile. The photos are ion micrographs taken using O_2^+ primary ions. Micrographs 1-10 are mass/charge specific images of the sample surface. The field of view in each image is approximately 150 μm. Images 1 and 2 (mass 115) indicate irregular surface features such as pitting or precipitate formation. Images 3, 4, and 5 show further examples of these features; (HR) indicates that the image was taken using high mass resolution. No variation in As^+ or P^+ signal was observed in these areas. Images 6-10 show ion images of masses 28, 27, 115, 31, and 75, respectively, showing localized surface contamination present. Photo 11 is an optical image of the surface showing the striations of interest. These striations are larger than the field of view of the ion images, they do not appear to have excess concentrations of As and appear to be a result of topographical features. Figs. 3 and 4 are computer generated images of the sample surface utilizing a resistive anode encoder (RAE). This device allows the computer to generate images of a sample surface based upon electronically detected signals. The color contrast is related to the signal intensity at that pixel as indicated in the color scale provided. The field of view for each image is 150 μm and all images were taken using Cs^+ primary ions and negative secondary ions. The species corresponding to each image is noted in the figure. Of note is that the As distribution (fig. 1 image D) is fairly uniform throughout the field of view. Also in fig. 4, images E and F are of the same area and images G and H are of the same area.

3. Appendix:

The CAMECA IMS-3f ion microscope employs an energetic (0.5-22 keV), mass-filtered, primary ion beam (typically O_2^+, Ar^+, O^-, or Cs^+) to analyze solid materials. The interaction of the primary ions with the sample erodes the target surface liberating secondary ions which are subsequently mass analyzed. The instrument design is such that the lateral distribution of the secondary ions is reformed at the detector resulting in a magnified mass-analyzed image of the sample surface. This image may be observed visually or recorded on photographic film or video cassette with a field of view of either 25, 150, or 400 microns and a lateral resolution of one micron. The ion microscope is also capable of providing a three dimensional characterization of solids by monitoring the secondary ion signal of interest as a function of time. Provided the sputter yield (sputtered atoms/incident ion) is constant (or the layer thicknesses of a heterogeneous sample are known) this time scale may be converted to a depth scale by measurement of the crater depth. Crater depth measurements are normally made in this laboratory by interferometry. Secondary ion mass spectrometry (SIMS) is capable of detecting all elements in the periodic table, with detection limits in the ppm to ppb range. With proper standards, quantification may be performed with accuracies of - 10% or less. The instrument is normally operated as a low resolution mass spectrometer (M/M = 300), but may also be operated in a high resolution mode (M/M = - 10,000).

DEPTH PROFILE
317H1
18
12/17/86
0H 31M 52S 1812 Sec.

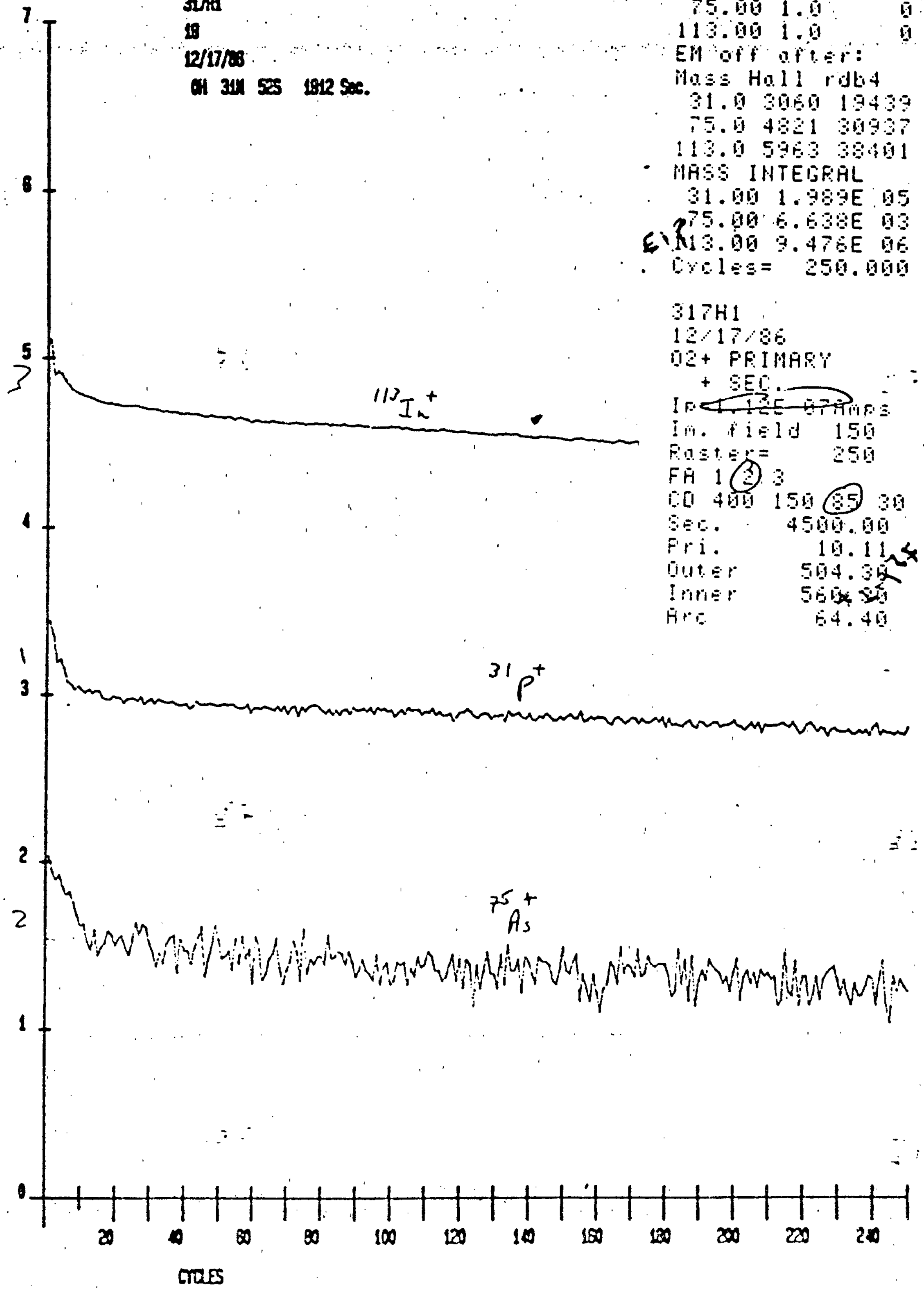


```
Mass time offset
 31.00 1.0      -0
 75.00 1.0       0
113.00 1.0       0
EM off after:
Mass Hall rdb4
 31.0 3060 19439
 75.0 4821 30937
113.0 5963 38401
MASS INTEGRAL
 31.00 1.989E 05
 75.00 6.638E 03
113.00 9.476E 06
Cycles=  250.000

317H1
12/17/86
O2+ PRIMARY
  + SEC.
Ip 1.12E 07Amps
Im. field  150
Raster=    250
FA 1 2 3
CO 400 150 85 30
Sec.     4500.00
Pri.       10.11
Outer     504.30
Inner     560.50
Arc        64.40
```

Fig. 2

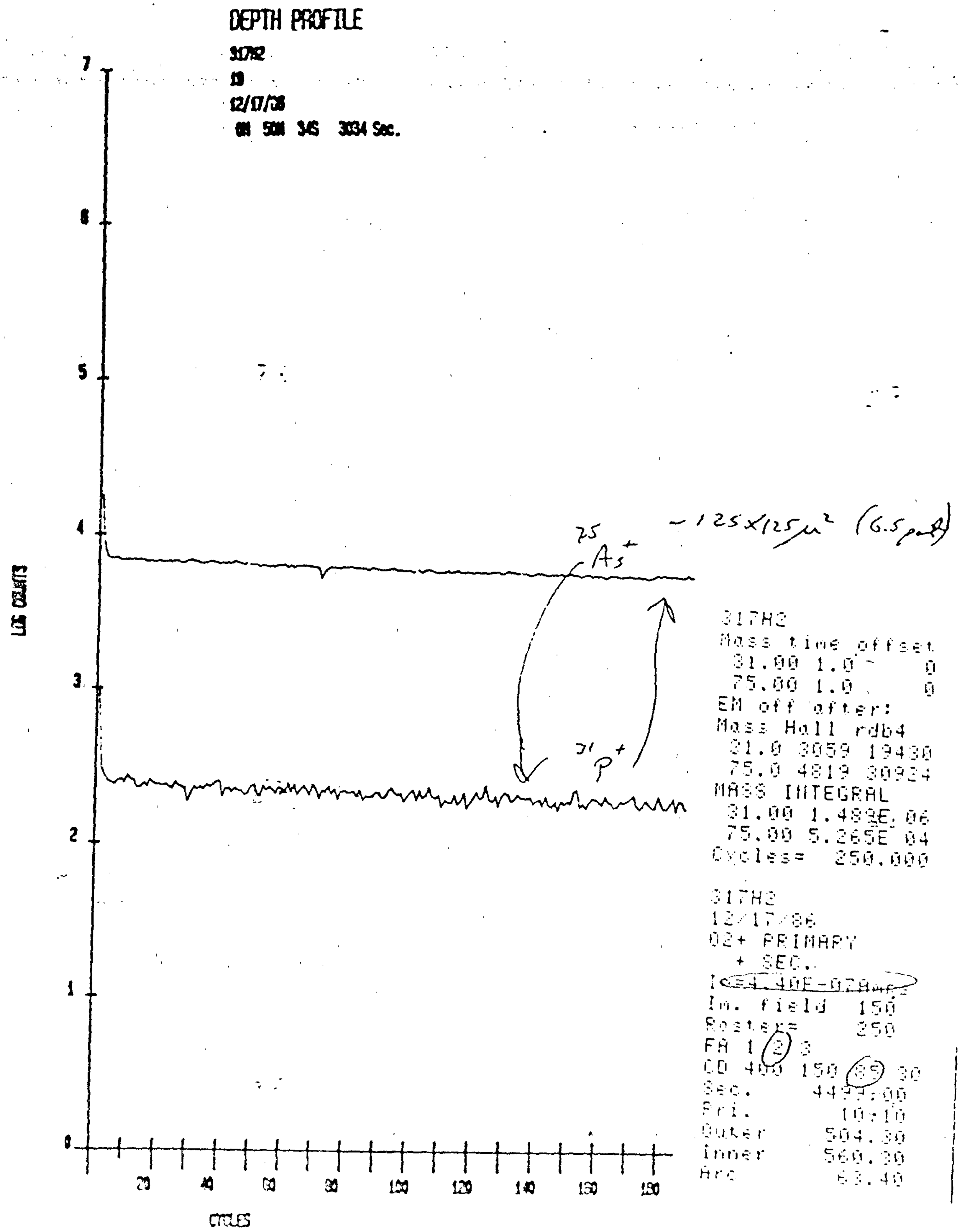
DEPTH PROFILE
317H2
19
12/17/86
0H 50M 34S 3034 Sec.
LOG COUNTS
CYCLES
$^{75}As^{+}$
$^{31}P^{+}$
~125x125μ² (6.5 part)
317H2
Mass time offset
31.00 1.0 0
75.00 1.0 0
EM off after:
Mass Hall rdb4
31.0 3059 19430
75.0 4819 30924
MASS INTEGRAL
31.00 1.489E 06
75.00 5.265E 04
Cycles= 250.000
317H2
12/17/86
O2+ PRIMARY
+ SEC.
I=4.40E-07Amps
Im. field 150
Raster= 250
FA 1 2 3
CD 400 150 85 30
Sec. 4497.00
Pri. 10.10
Outer 504.30
Inner 560.30
Arc 63.40

5

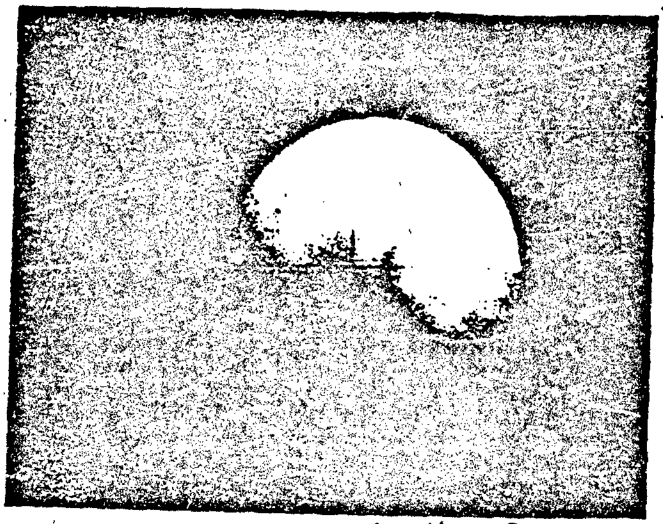

(HR) $^{115}In^{+}$

6

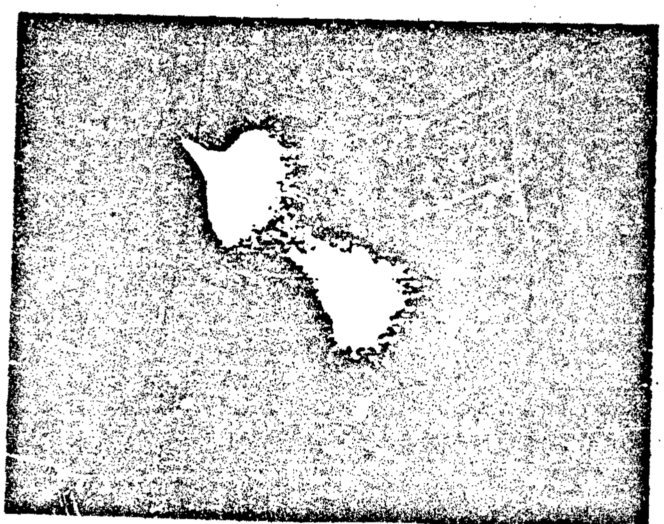

$^{28}Si^{+}$?

7

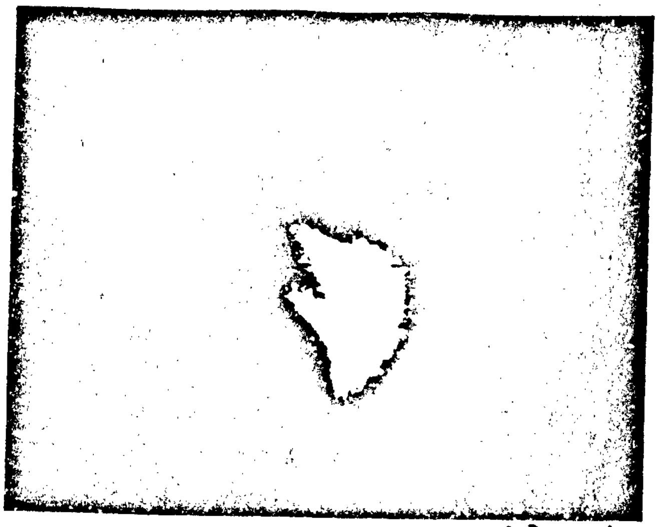

$^{27}Al^+$

8

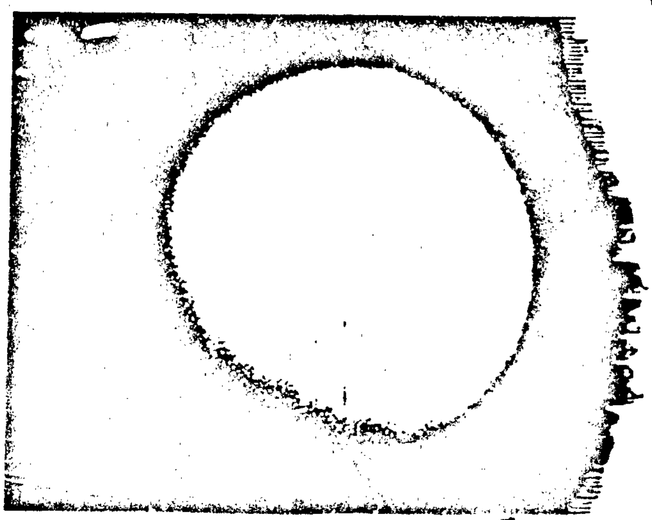

$^{115}In^+$

1

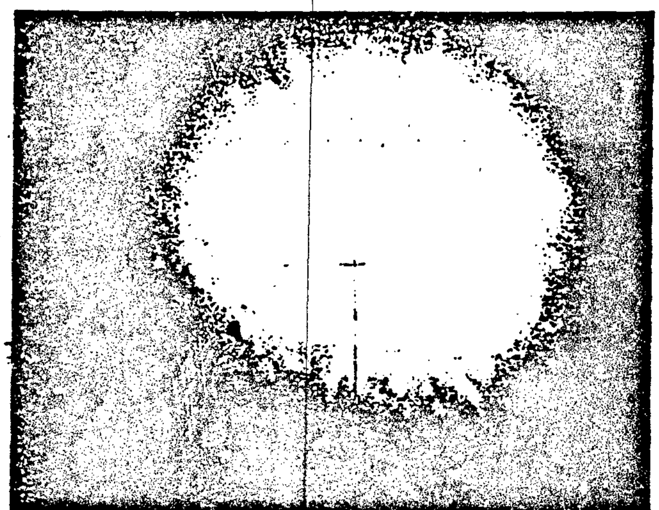

115 In+

2

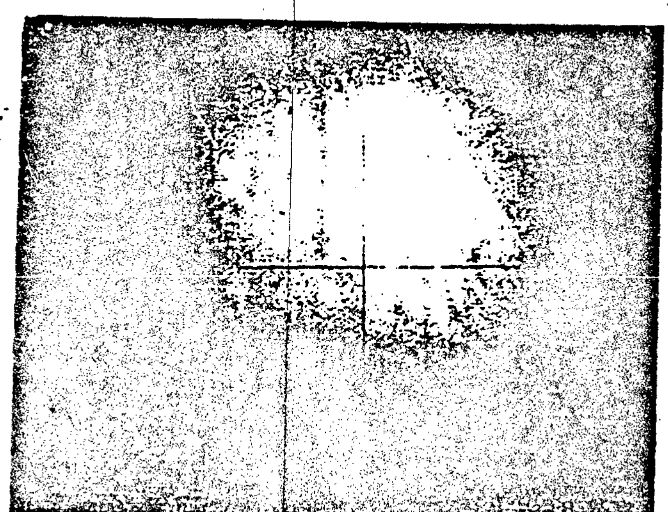

115 In+

3

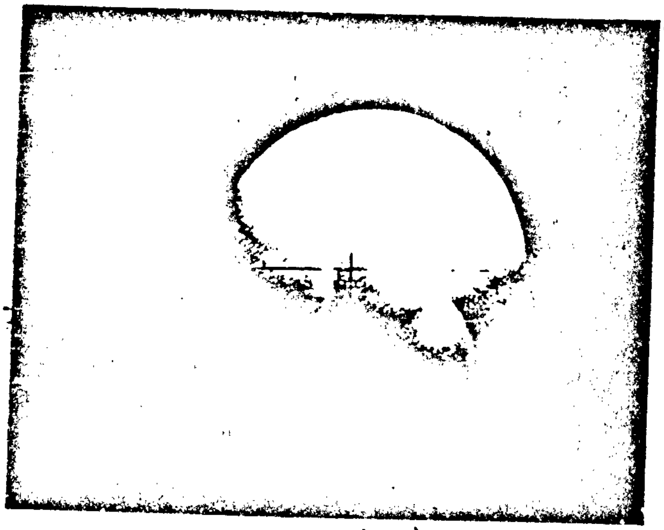

(HR) 115 Int

4

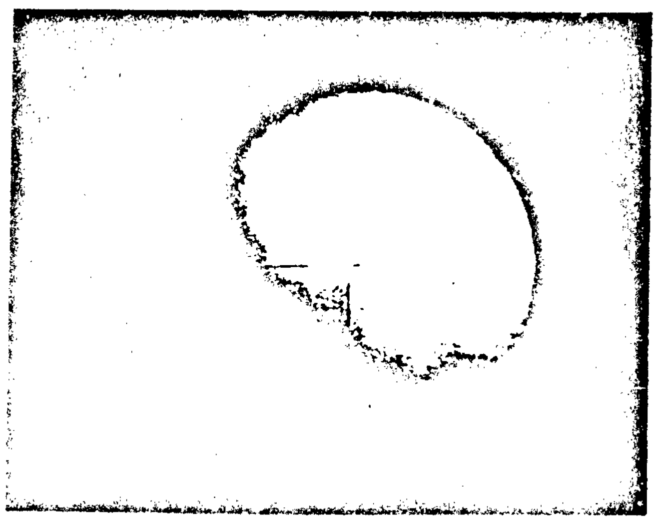

115 Int

9

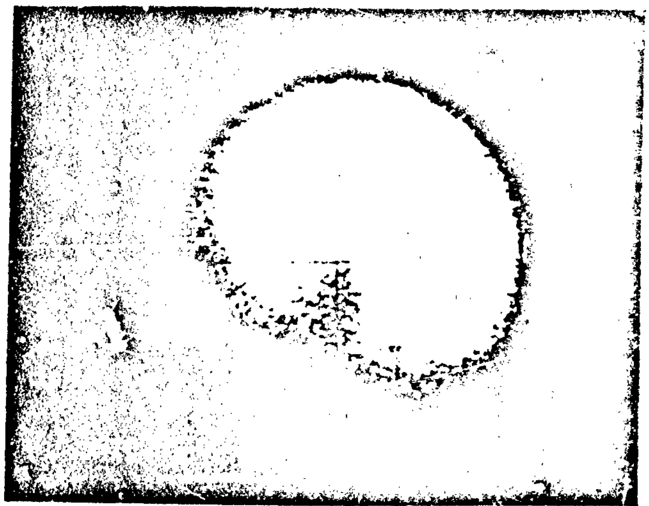

16

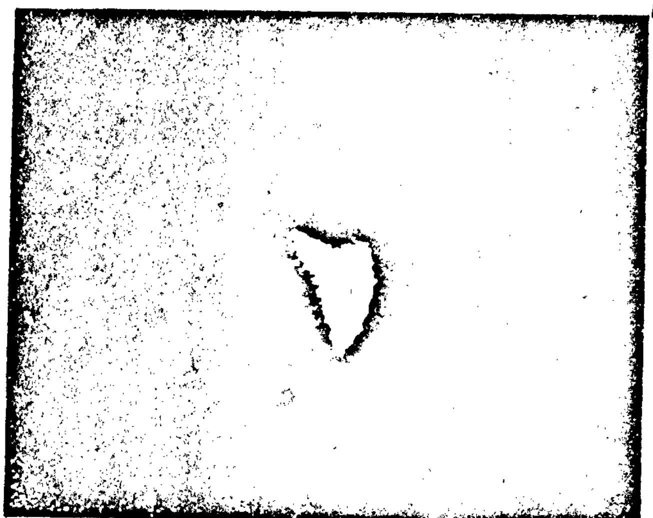

A

16
0

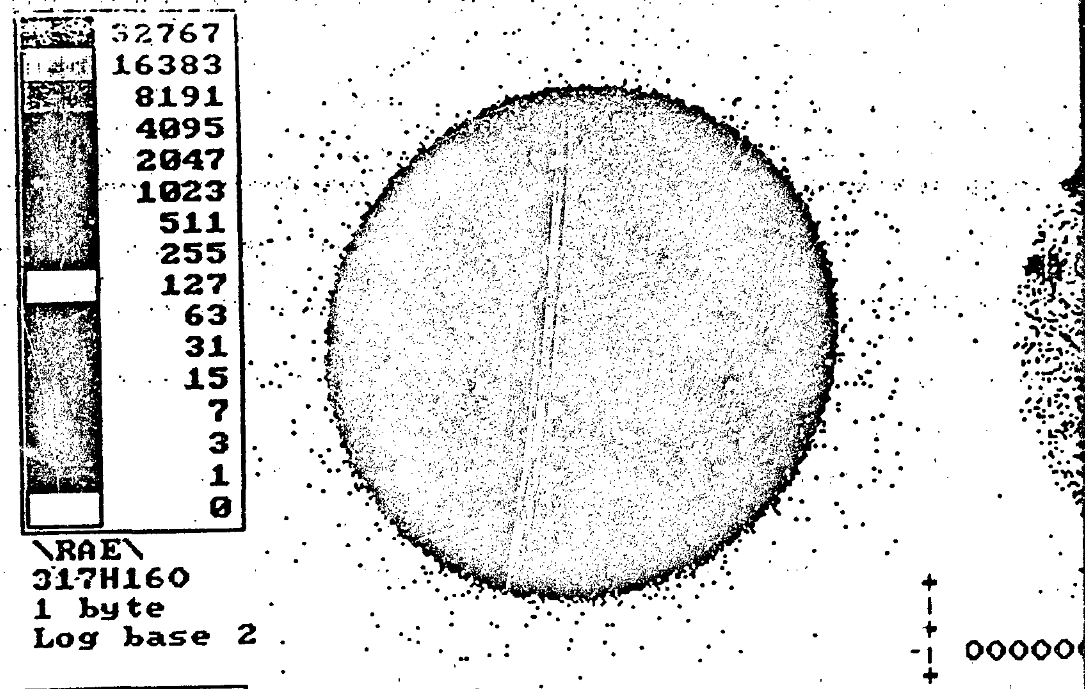
32767
16383
8191
4095
2047
1023
511
255
127
63
31
15
7
3
1
0
\RAE\
317H160
1 byte
Log base 2
00000

B

As

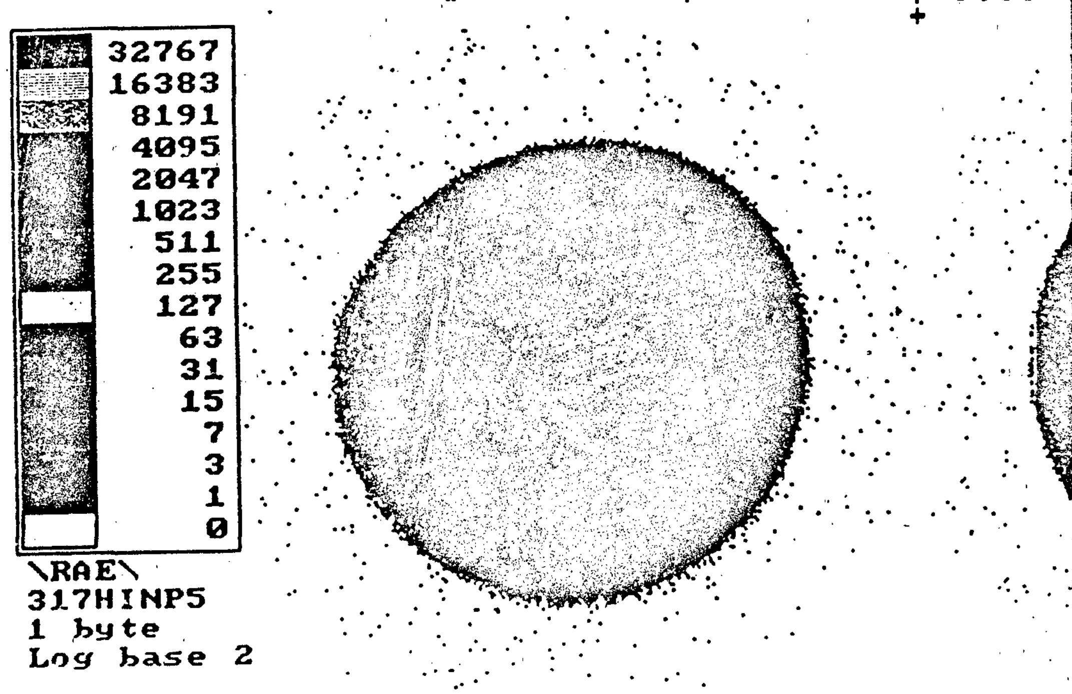
32767
16383
8191
4095
2047
1023
511
255
127
63
31
15
7
3
1
0
\RAE\
317HINP5
1 byte
Log base 2

Fig 3

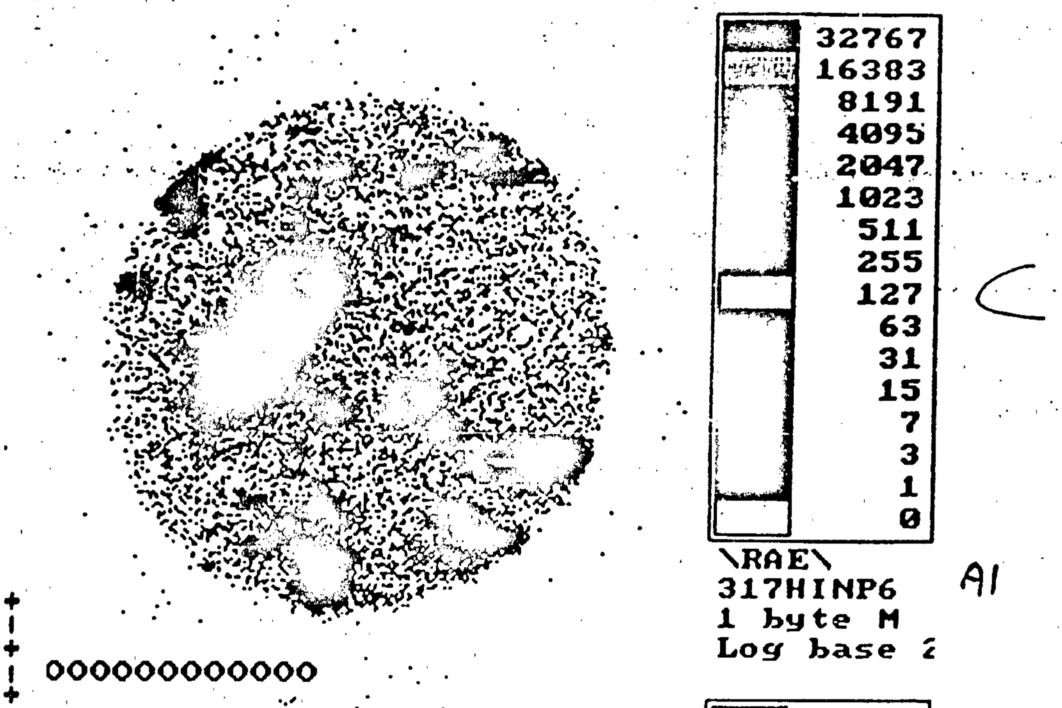
32767
16383
8191
4095
2047
1023
511
255
127
63
31
15
7
3
1
0
C
\RAE\
317HINP6
1 byte M
Log base 2
A1
000000000000

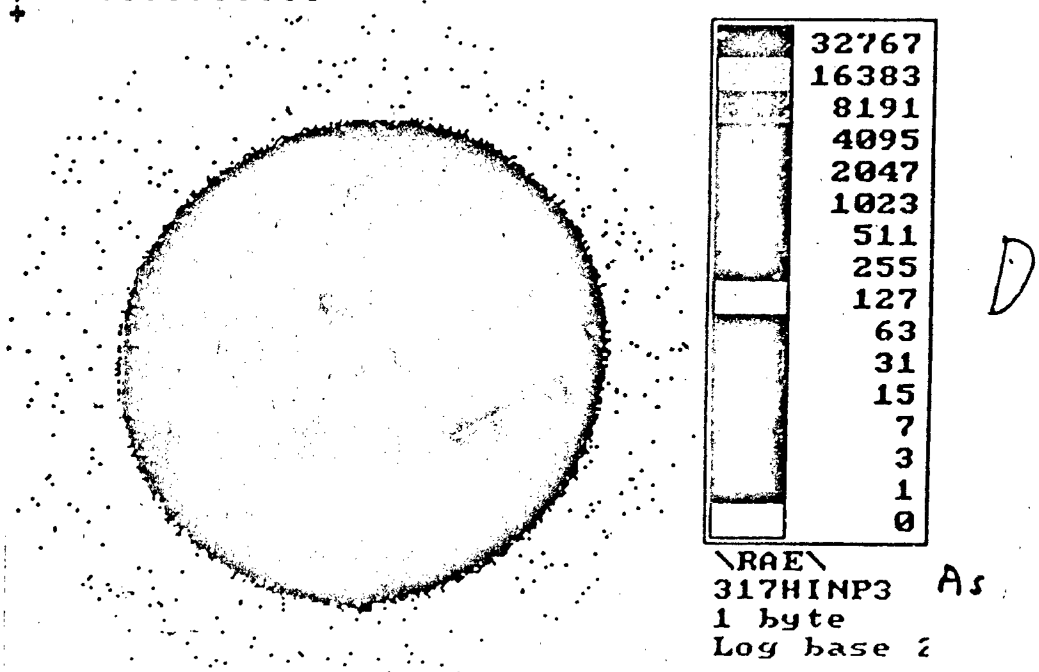
32767
16383
8191
4095
2047
1023
511
255
127
63
31
15
7
3
1
0
D
\RAE\
317HINP3
1 byte
Log base 2
As

A

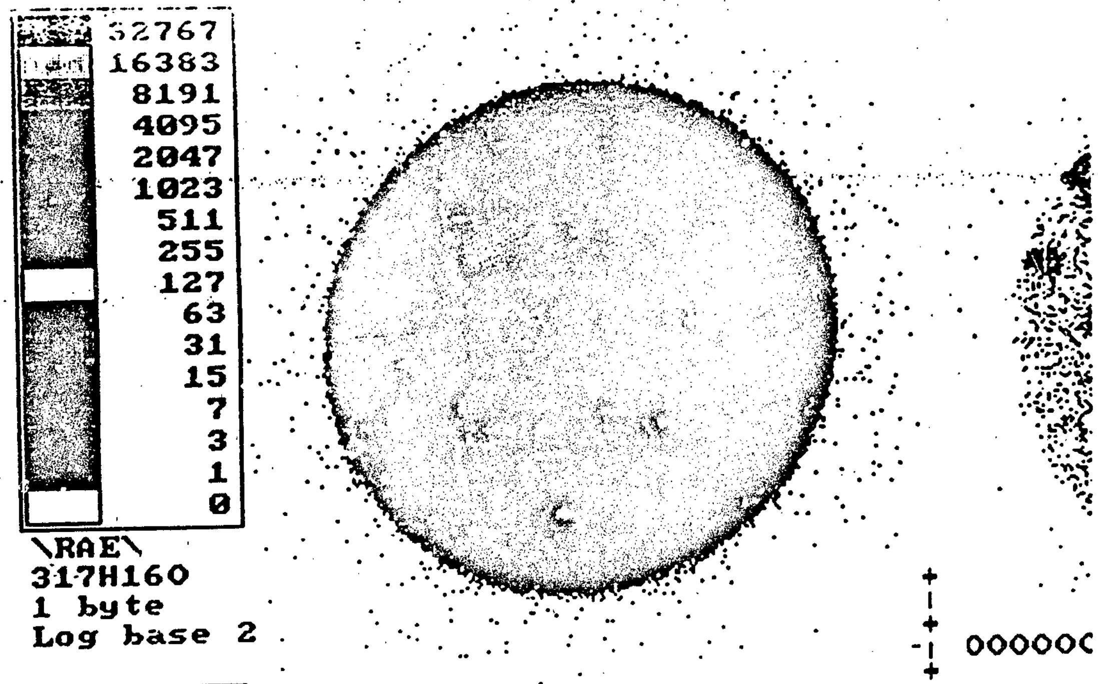
32767
16383
8191
4095
2047
1023
511
255
127
63
31
15
7
3
1
0
\RAE\
317H160
1 byte
Log base 2

16. 0

B

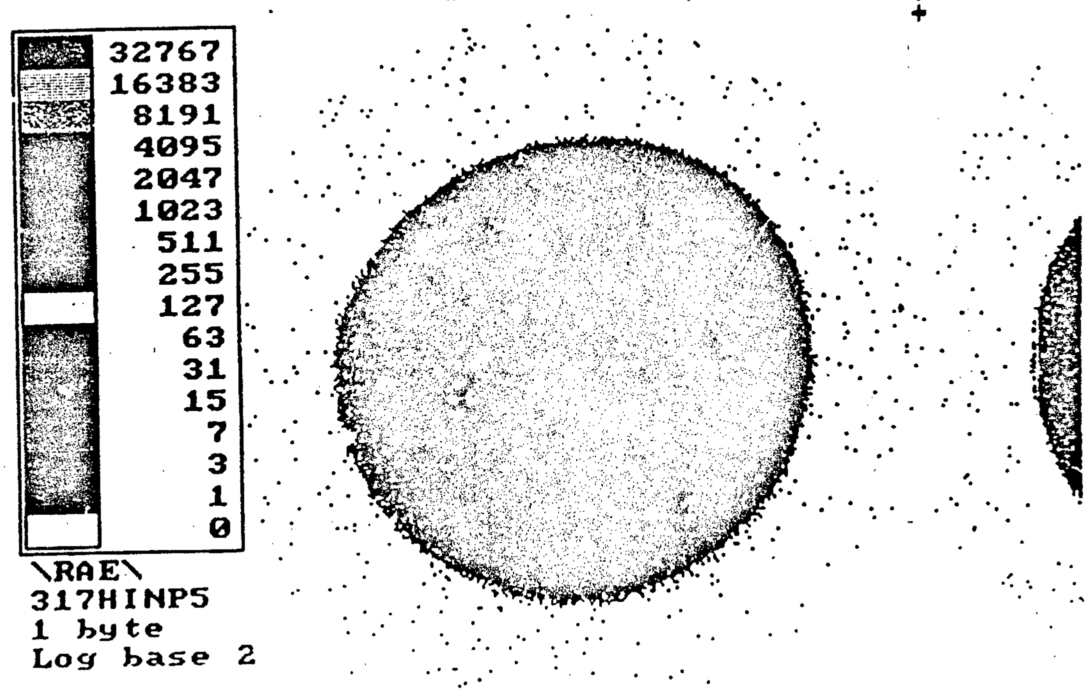
32767
16383
8191
4095
2047
1023
511
255
127
63
31
15
7
3
1
0
\RAE\
317HINP5
1 byte
Log base 2

As

(1)

Fig 3

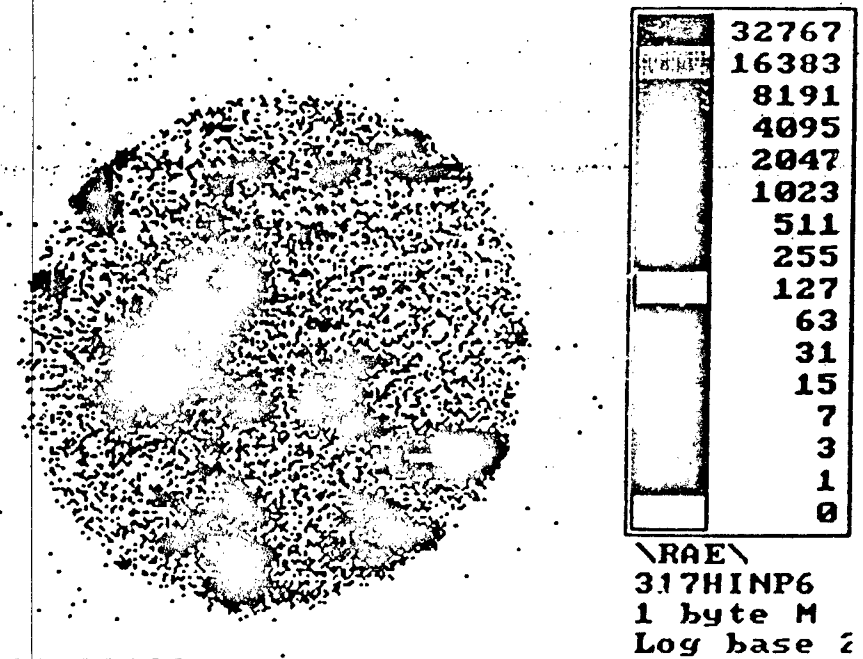

C

A1

0000000000000

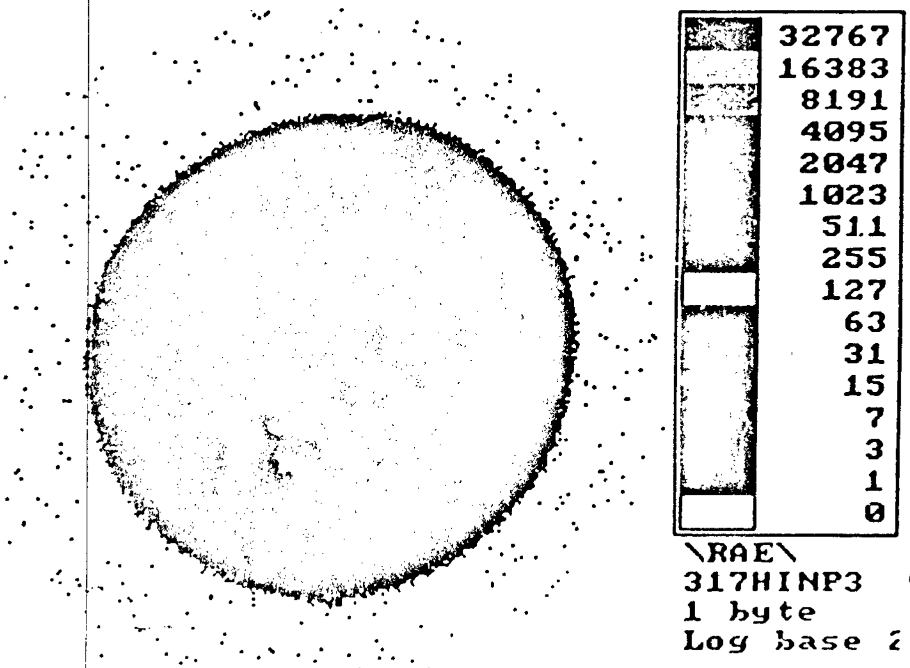

D

As

E

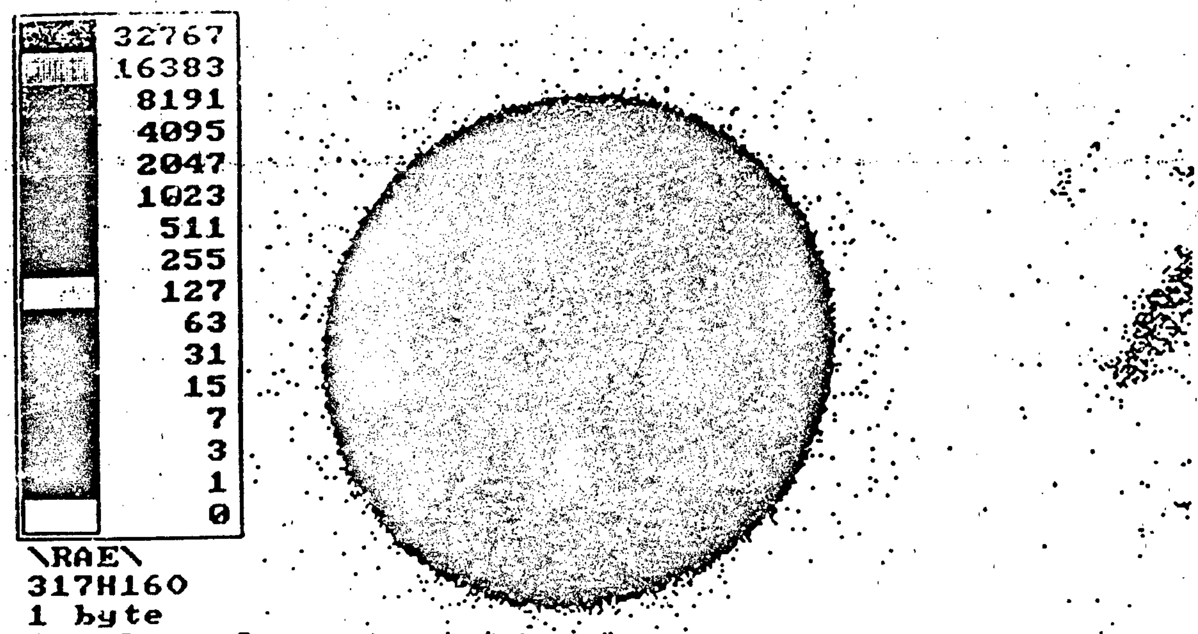

InP surface images

F

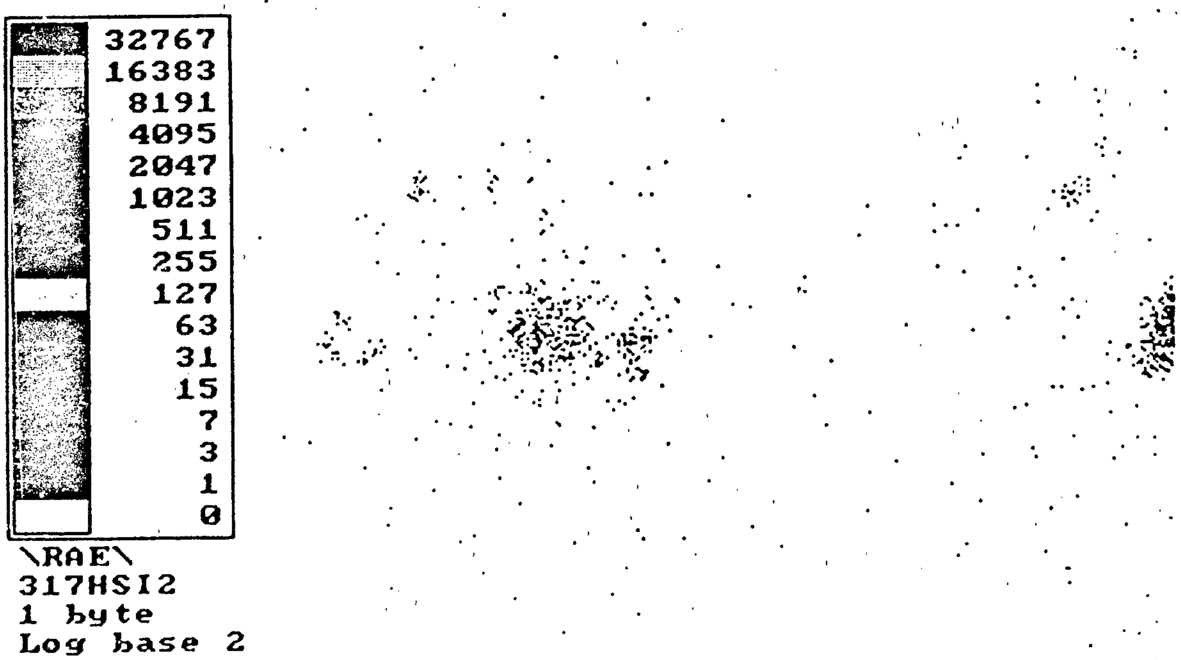

Fig 4

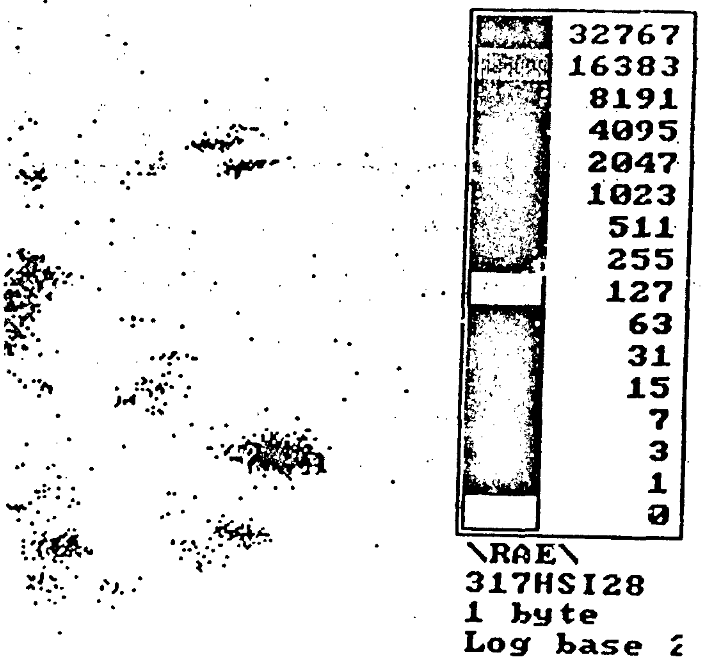
32767
16383
8191
4095
2047
1023
511
255
127
63
31
15
7
3
1
0
\RAE\
317HSI28
1 byte
Log base

G

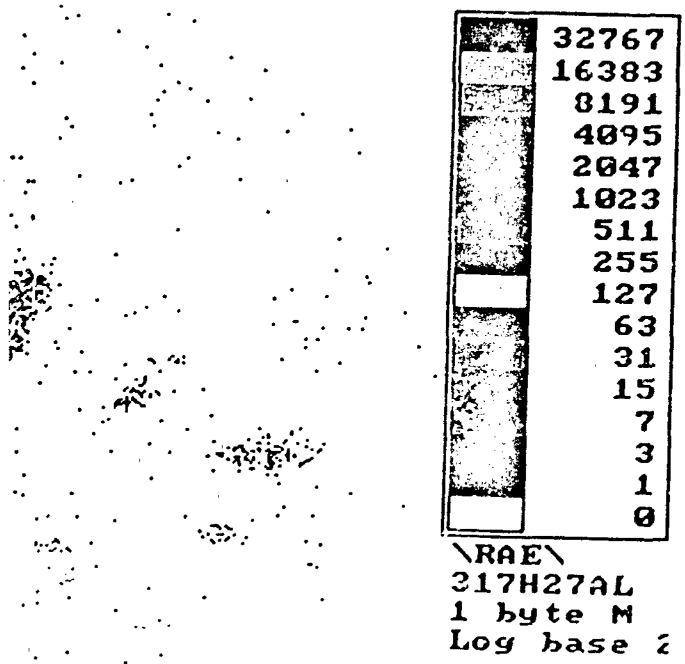
32767
16383
8191
4095
2047
1023
511
255
127
63
31
15
7
3
1
0
\RAE\
317H27AL
1 byte M
Log base

H

SIMS ANALYSIS OF Mg DISTRIBUTION IN Mg IMPLANTED GaAs

1. On 10 February 1987 B. Molnar, Code 6812, submitted a sample of Mg implanted (4.8 MeV, 4.4 x 10^{14} atoms/cm^2) GaAs for analysis by secondary ion mass spectrometry. Of interest was the depth distribution of Mg.

2. The specimen was depth profiled with a CAMECA IMS-300 ion microscope using 5.5 keV O_2^+ ions at a primary current of 2.0 μA. The primary beam was rastered over an area of approximately 500 x 800 μm. In the center of this raster an area of 250 μm in diameter was analyzed. Because of the difference in size between the rastered and analyzed areas, contributions of analyte atoms residing at the crater walls to the detected signal were eliminated. Some details concerning the CAMECA IMS-300 ion microscope are presented in the appendix.

3. Figure 1 shows a depth profile of the sample for mass 24 ($^{24}Mg^+$, $^{12}C^+$) and mass 75 ($^{75}As^+$). The depth scale was determined by total crater depth measurement using a Dectak surface profilometer. As may be seen from the mass 24 background levels the contribution to the total ion signal from $^{12}C^+$ is quite small (approximately 10-20 counts/sec) relative to the peak signal.

4. Appendix:

The CAMECA IMS-300 ion microscope employs an energetic (0-10 keV) primary ion beam (typically O_2^+, Ar^+, or O^-) to analyze solid materials. The interaction of the primary ions with the sample erodes the target surface liberating secondary ions which are subsequently mass analyzed. The instrument design is such that the lateral distribution of the secondary ions is reformed at the detector resulting in a magnified mass analyzed image of the sample surface. This image may be observed visually or recorded on electron sensitive film with a field of view of 250 microns and a lateral resolution of one micron. The ion microscope is also capable of providing a three dimensional characterization of solids by monitoring the secondary ion signal of interest as a function of time. Provided the sputter yield (sputtered atoms/incident ion) is constant (or the layer thicknesses of a heterogeneous sample are known) this time scale may be converted to a depth scale by measurement of the crater depth. Crater depth measurements are normally made in this laboratory by interferometry. Secondary ion mass spectrometry (SIMS) is capable of detecting all elements in the periodic table, with detection limits in the ppm to ppb range. With proper standards, quantification may be performed with accuracies of ~ 10% or less. The instrument is normally operated as a low resolution mass spectrometer (M/M = 300), but may also be operated in a high resolution mode (M/M = ~2500).

GEO-CENTERS, INC.

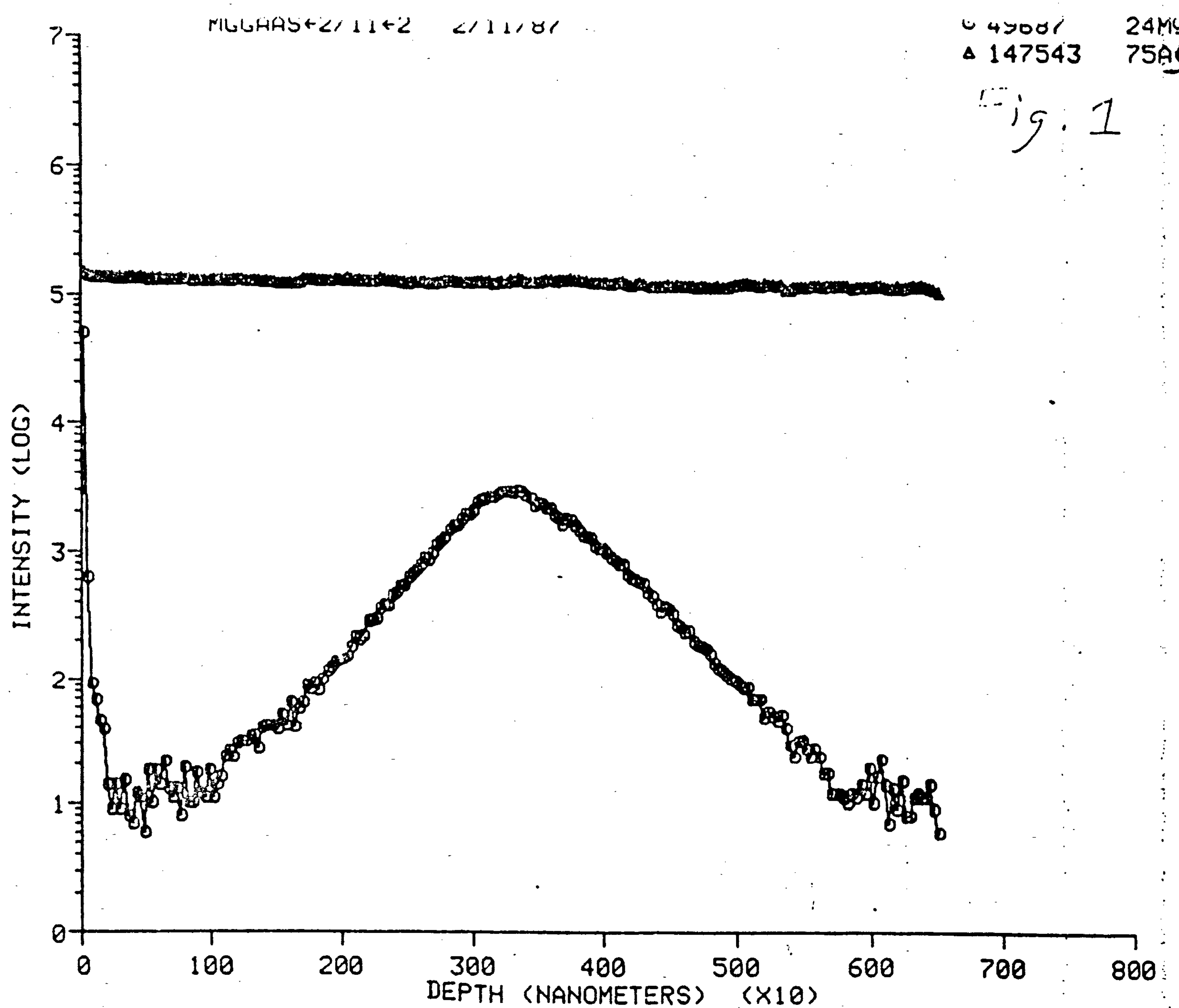
MGGAAS+2/11+2 2/11/87
○ 49687 24Mg
△ 147543 75As
INTENSITY (LOG)
DEPTH (NANOMETERS) (X10)

Fig. 1

DETERMINATION OF As DETECTION LIMIT IN Si

1. On 6 February 1987, B. Molnar Code 6812, submitted a sample of Si implanted with As (10^{15} atoms/cm^2) and Sn (10^{14} atoms/cm^2). Of interest was the detection limit of As in Si for the CAMECA IMS-300.

2. The specimen was depth profiled with a CAMECA IMS-300 ion microscope using 5.5 keV O_2^+ ions at primary currents of 250 and 500 nA. The primary beam was rastered over an area of approximately 500 x 800 μm. In the center of this raster an area of 250 μm in diameter was analyzed. Because of the difference in size between the rastered and analyzed areas, contributions of analyte atoms residing at the crater walls to the detected signal were eliminated. Some details concerning the CAMECA IMS-300 ion microscope are presented in the appendix.

3. The analysis of As in Si is difficult both because of its relatively low ion yield and because of a mass interference from the molecular ion $^{30}Si^{29}Si^{16}O^+$. Fig. 1 shows a depth profile of the sample for mass 30 ($^{30}Si^+$), mass 75 (As^+, $^{30}Si^{29}Si^{16}O^+$), and mass 118 ($^{118}Sn^+$). These high signal levels are mainly due to molecular mass interferences. Because molecular ions have a much narrower kinetic energy distribution than atomic ions (molecular ions which have higher kinetic energy dissociate) the contribution of molecular ions to the total ion signal may be reduced by shifting the energy band pass of the instrument to a higher energy. This, however, also reduces the ion signal due to atomic ions as well, since one is sampling the tail of the kinetic energy distribution and not the peak maximum. Another method is to use high mass resolution to separate the atomic from the molecular species on the basis of their mass defects. The resolution required is not available on the IMS-300. Figs. 2 and 3 show depth profiles of the sample, at primary ion currents of 500 and 250 nA, respectively, under the same conditions as Fig. 1, except that a -23 volt offset has been placed on the secondary accelerating voltage. Again the As implant is not detected. Fig. 4 shows a depth profile obtained at a primary current of 500 nA with a -17 volt secondary accelerating voltage offset. As may be seen at this voltage offset the contributions of molecular interferences is again significant.

Arsenic may also be analyzed as a negative ion. The instrument was focused in the negative secondary ion mode and manually scanned throughout the desired mass ranges. Although peaks were found corresponding to a variety of atomic and molecular ions, the signal levels for As^-, AsO^-, and $AsSi^-$ were not significantly higher than those for the positive ions. This situation could be improved by using a Cs^+ primary ion beam to increase the negative secondary ion yield. This ion source, however, is not currently available at NRL.

Depth profiles of this sample previously performed at the University of Illinois, using oxygen primary ions and high mass resolution, obtained As signal levels in the 10^3 counts/second range. The inability of this instrument to reproduce those results is explained by a study by Wittmaak (1), in which the fractional ion yield of As^+ and As^- from GaAs is studied as a function of the incidence angle of the primary oxygen beam. As the incidence angle is increased the sputtering yield of the substrate is also increased resulting in a decrease in the steady-state surface concentration of oxygen. This decrease in oxygen surface concentration reduces the ion yield enhancement and therefore the total As signal detected. The incidence angle of the IMS-300 is 60° relative to the sample normal, while that of the IMS-3f is 30°. From Wittmaak's data it may be seen that the decrease in the fractional ion yield, between 30° and 60°, of a factor of approximately 10 for As^+ and of approximately 100 for As^-. This effect coupled with the reduced transmission caused by the energy offset would reduce the sensitivity for As to the present level.

In conclusion, the detection limit for As in Si under the present analysis conditions is above the peak concentration of a 10^{15} atoms/cm^2 ion implant (approximately 10^{20} atoms/cm^3).

4. Appendix:

The CAMECA IMS-300 ion microscope employs an energetic (0-10 keV) primary ion beam (typically O_2^+, Ar^+, or O^-) to analyze solid materials. The interaction of the primary ions with the sample erodes the target surface liberating secondary ions which are subsequently mass analyzed. The instrument design is such that the lateral distribution of the secondary ions is reformed at the detector resulting in a magnified mass analyzed image of the sample surface. This image may be observed visually or recorded on electron sensitive film with a field of view of 250 microns and a lateral resolution of one micron. The ion microscope is also capable of providing a three dimensional characterization of solids by monitoring the secondary ion signal of interest as a function of time. Provided the sputter yield (sputtered atoms/incident ion) is constant (or the layer thicknesses of a heterogeneous sample are known) this time scale may be converted to a depth scale by measurement of the crater depth. Crater depth measurements are normally made in this laboratory by interferometry. Secondary ion mass spectrometry (SIMS) is capable of detecting all elements in the periodic table, with detection limits in the ppm to ppb range. With proper standards, quantification may be performed with accuracies of ~ 10% or less. The instrument is normally operated as a low resolution mass spectrometer (M/M = 300), but may also be operated in a high resolution mode (M/M = ~2500).

(1) K. Wittmaak, Wall Chart of SIMS Analysis Data, Atomika, Inc., 1983.

STEVEN HUES

GEO-CENTERS, INC.

Fig. 4

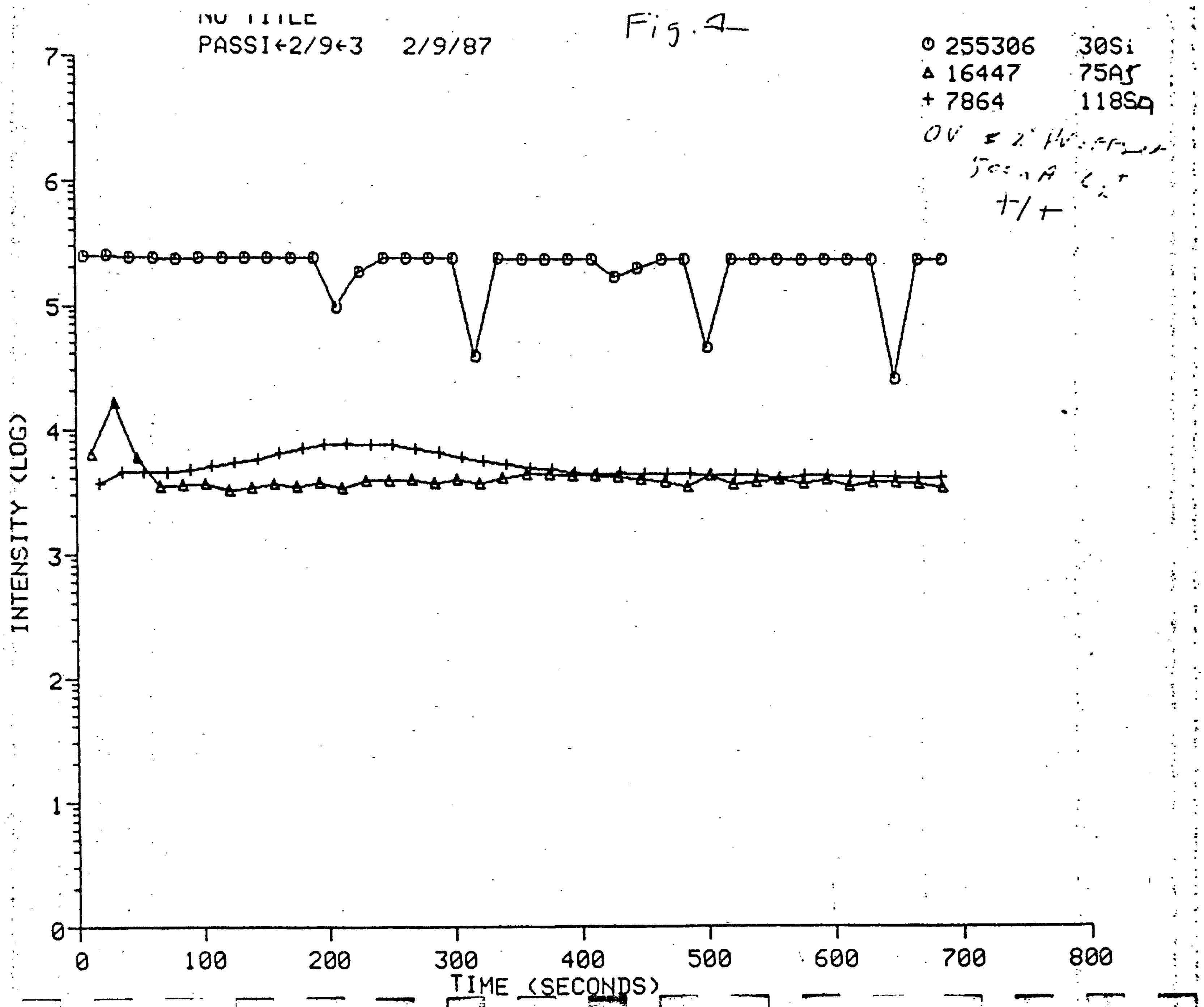

NO TITLE
PASSI←2/9←3 2/9/87
⊙ 255306 30Si
△ 16447 75As
+ 7864 118Sn
INTENSITY (LOG)
TIME (SECONDS)
0
100
200
300
400
500
600
700
800
1
2
3
4
5
6
7

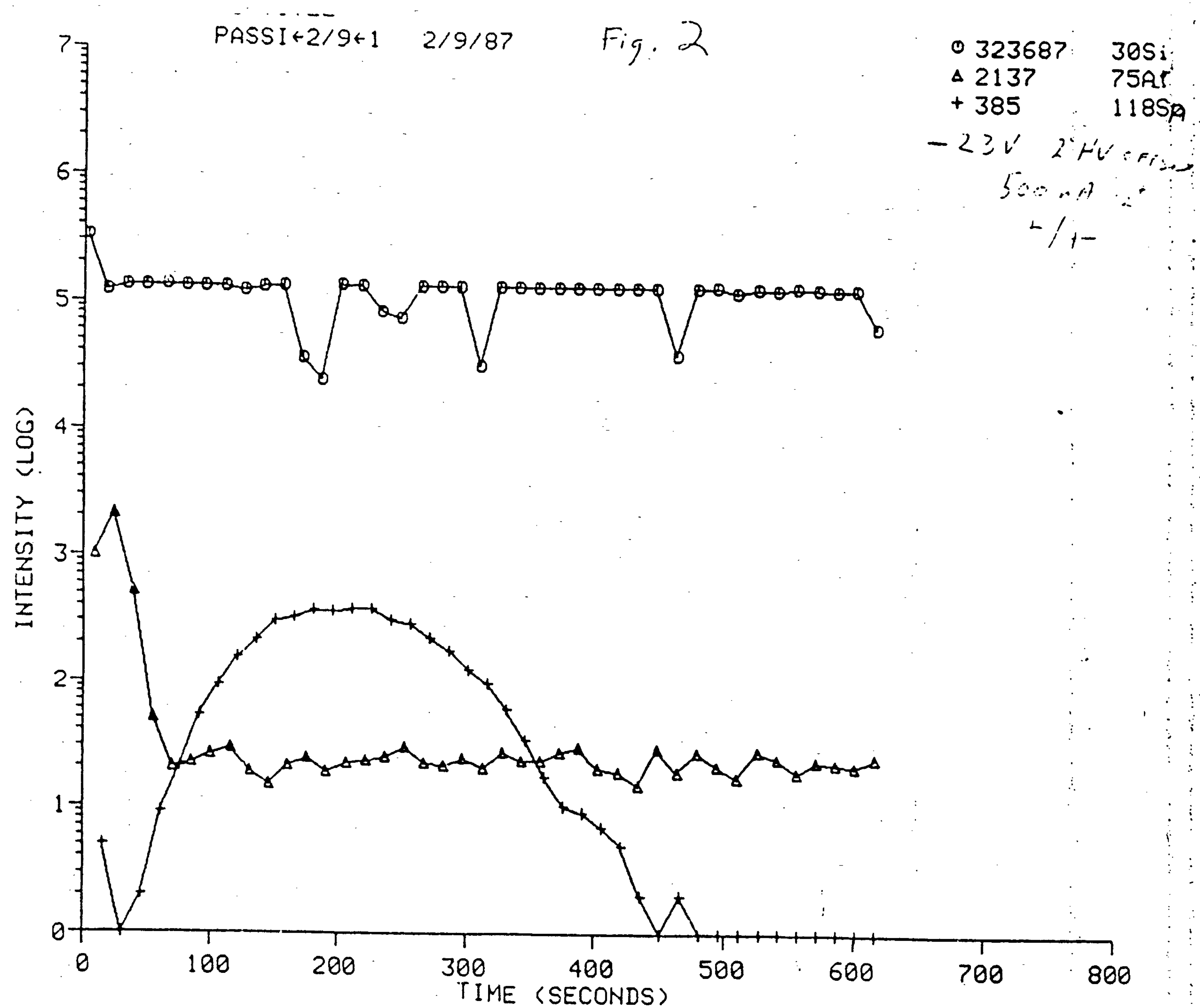

PASSI+2/9+1 2/9/87
Fig. 2
323687 30Si
2137 75As
385 118Sn
INTENSITY (LOG)
TIME (SECONDS)

Fig. 3

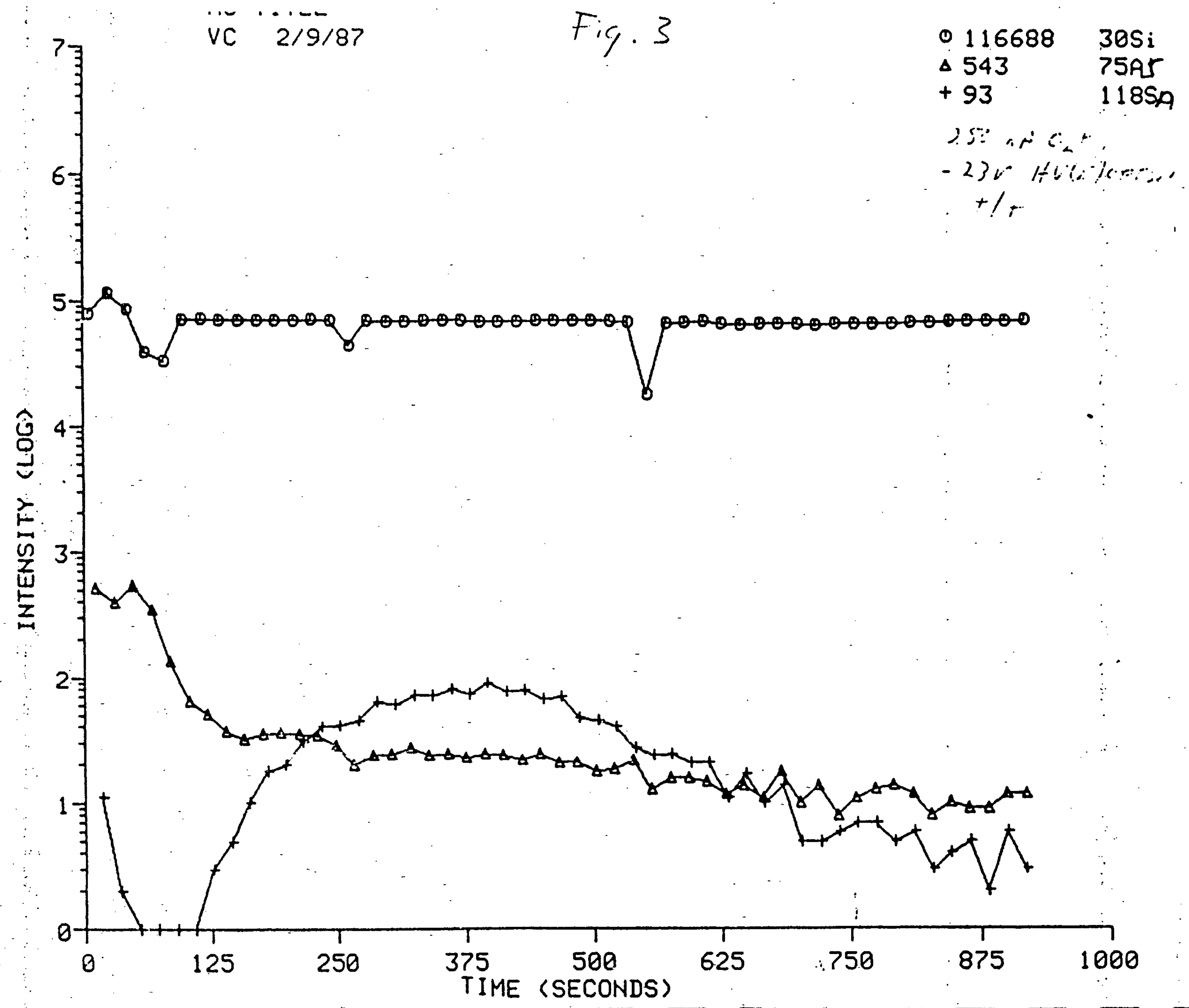

VC 2/9/87
116688 30Si
543 75As
93 118Sn
INTENSITY (LOG)
TIME (SECONDS)

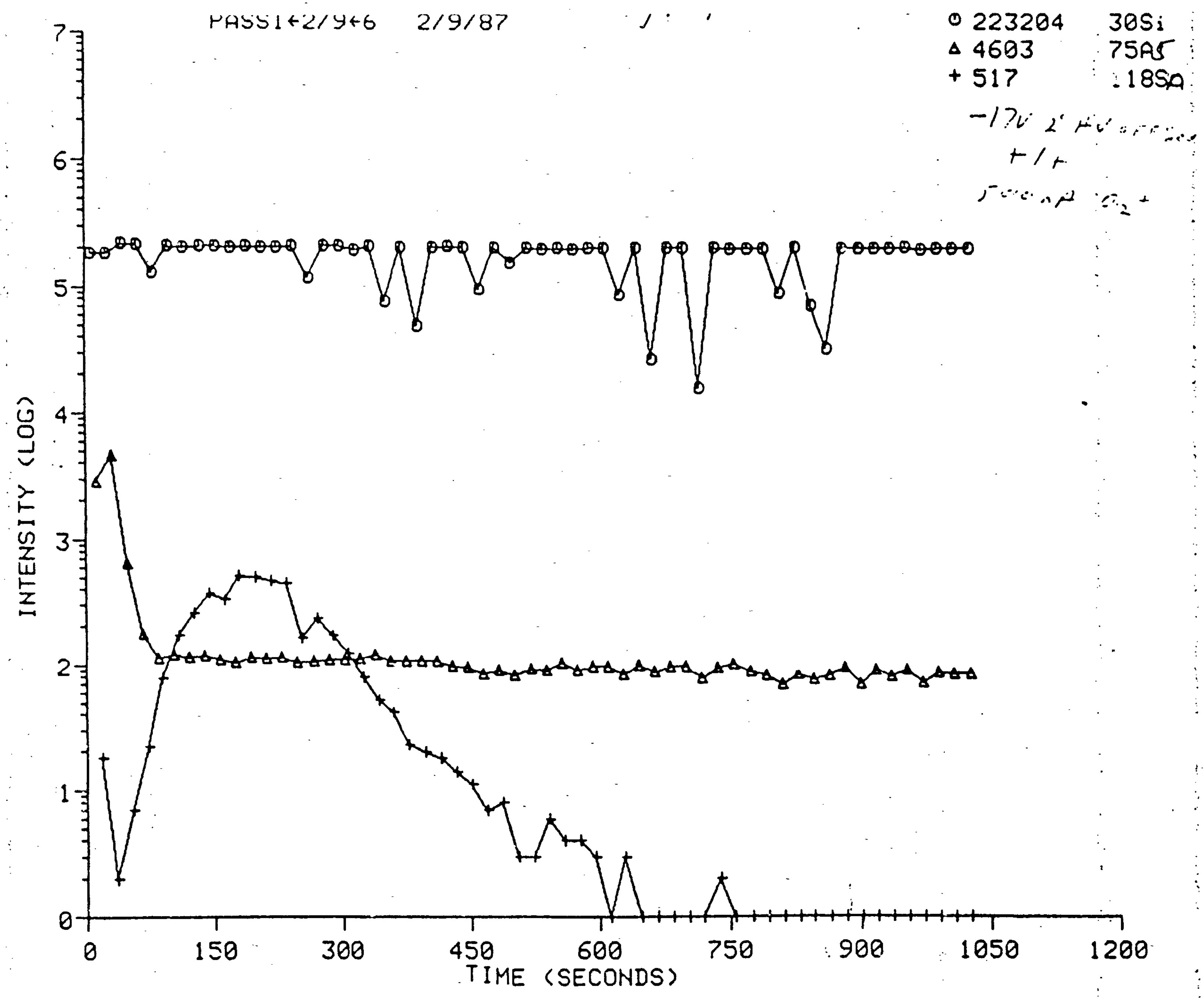

PASS1+2/9+6 2/9/87
⊕ 223204 30Si
△ 4603 75As
+ 517 118Sn
INTENSITY (LOG)
7
6
5
4
3
2
1
0
0
150
300
450
600
750
900
1050
1200
TIME (SECONDS)

SIMS ANALYSIS OF SiC FILMS ON Si

1. On 19 March 1987 B. Molnar, Code 6812, submitted two samples, labeled SiC 511-R and SiCNASA, consisting of SiC films mounted on polycrystalline Si substrates for analysis by secondary ion mass spectrometry. Of interest was the depth distribution of C, Al, and N.

2. The specimen was depth profiled with a CAMECA SMI-300 ion microscope using 5.5 keV O_2^+ ions at a primary current of 2.0 μA. The primary beam was rastered over an area of approximately 500 x 800 μm. In the center of this raster an area of 250 μm in diameter was analyzed. Because of the difference in size between the rastered and analyzed areas contributions of analyte atoms residing at the crater walls to the detected signal were eliminated. Some details concerning the CAMECA IMS-300 ion microscope are presented in the appendix.

3. Figure 1 shows a depth profile of the sample SiC 51-R for mass 12 ($^{12}C^+$),mass 14 ($^{14}N^+$,$^{28}Si^{+2}$), mass 27 ($^{27}Al^+$), and mass 30 ($^{30}Si^+$). The depth scale was established by surface profilometry assuming a uniform sputtering rate throughout the analyzed depth. Fig. 2 shows a comparable depth profile for the sample labeled SiCNASA.

4. Appendix: The CAMECA SMI-300 ion microscope employs an energetic (0-10 keV) primary ion beam (typically O_2^+, Ar^+, or O^-) to analyze solid materials. The interaction of the primary ions with the sample erodes the target surface liberating secondary ions which are subsequently mass analyzed. The instrument design is such that the lateral distribution of the secondary ions is reformed at the detector resulting in a magnified mass-analyzed image of the sample surface. This image may be observed visually or recorded on electron sensitive film with a field of view of 250 microns and a lateral resolution of one micron. The ion microscope is also capable of providing a three dimensional characterization of solids by monitoring the secondary ion signal of interest as a function of time. Provided the sputter yield (sputtered atoms/incident ion) is constant (or the layer thicknesses of a heterogenous sample are known) this time scale may be converted to a depth scale by measurement of the crater depth. Crater depth measurements are normally made in this laboratory by interferometry. Secondary ion mass spectrometry (SIMS) is capable of detecting all elements in the periodic table, with detection limits in the ppm to ppb range. With proper standards, quantification may be performed with accuracies of ~10% or less. The instrument is normally operated as a low resolution mass spectrometer (M/ M =300), but may also be operated in a high resolution mode (M/M =~2500).

STEVEN HUES

GEO-CENTERS, INC.

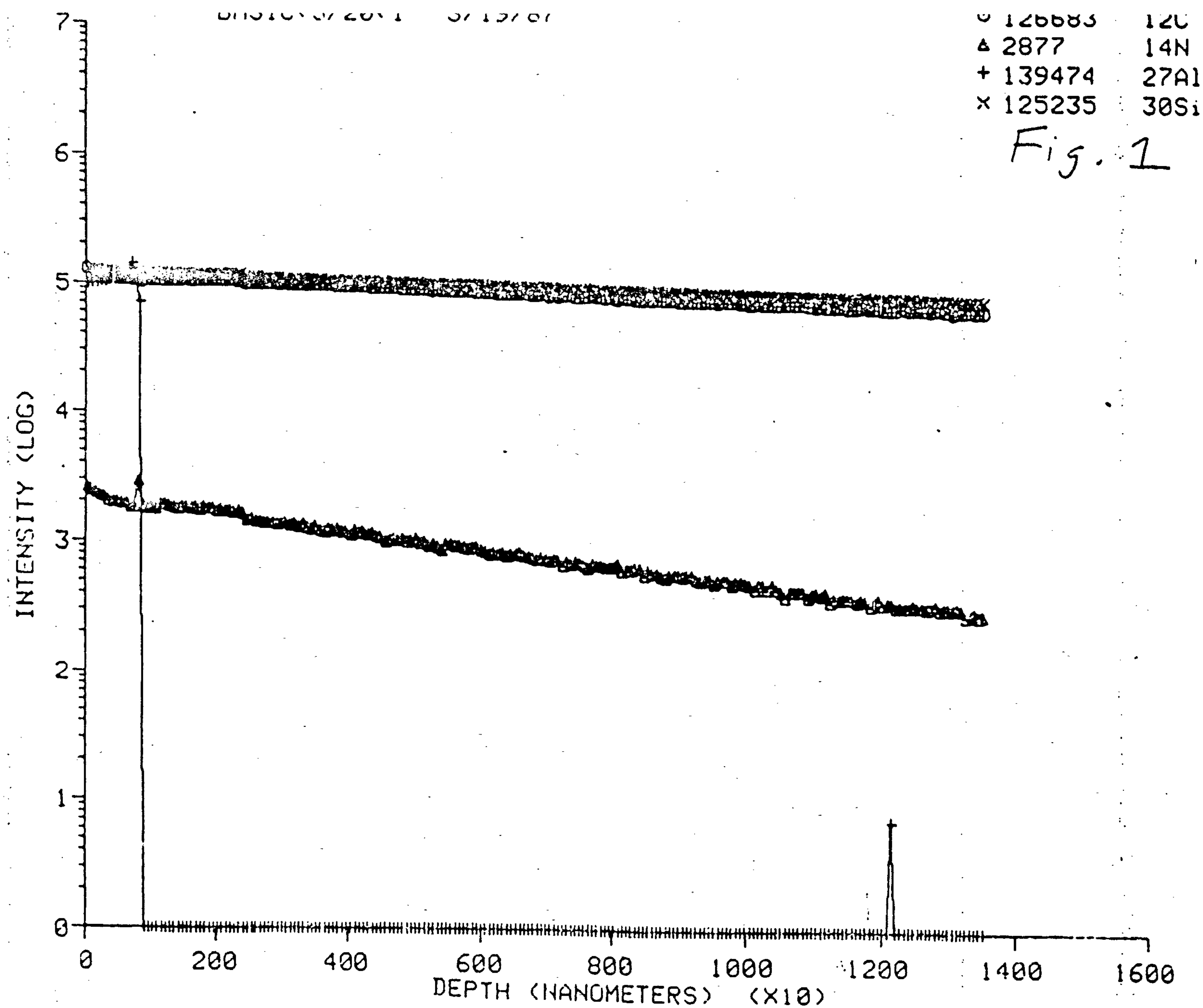

126683 12C
2877 14N
139474 27Al
125235 30Si
INTENSITY (LOG)
DEPTH (NANOMETERS) (X10)
0 1 2 3 4 5 6 7
0 200 400 600 800 1000 1200 1400 1600

Fig. 1

SIMS ANALYSIS OF Be DISTRIBUTION IN MBE GROWN InSb FILMS

1. On 26 May 1987 J. Comas, Code 6823, submitted two samples, labeled 906 and 907, of Be-doped InSb layers grown by MBE on InSb substrates. Of interest was the Be depth distribution in the grown layers.

2. The specimens were depth profiled with a Cameca IMS-300 ion microscope using 5.5 keV O_2^+ ions at a primary current of 200 nA. The primary beam was rastered over an area of approximately 500 x 800 um. In the center of this raster an area of 250 um in diameter was analyzed. Because of the difference in size between the rastered and analyzed area contributions of analyte atoms residing at the crater walls to the detected signal were eliminated. Some details concerning the Cameca IMS-300 ion microscope are presented in the appendix.

3. Depth profiles of samples 906 and 907 for mass 9 ($^{9}Be^+$) and mass 123 ($^{123}Sb^+$) are shown in Figs. 1 and 2 respectively.

4. Appendix:

The Cameca SMI-300 ion microscope employs an energetic (0-10 keV) primary ion beam (typically O_2^+, Ar^+, or O^--) to analyze solid materials. The interaction of the primary ions with the sample erodes the target surface liberating secondary ions which are subsequently mass analyzed. The instrument design is such that the lateral distribution of the secondary ions is reformed at the detector resulting in a magnified mass-analyzed image of the sample surface. This image may be observed visually or recorded on electron sensitive film with a field of view of 250 microns and a lateral resolution of one micron. The ion microscope is also capable of providing a three dimensional characterization of solids by monitoring the secondary ion signal of interest a s function of time. Provided the sputter yield (sputtered atoms/incident ion) is constant (or the layer thicknesses of a heterogenous sample are known) this time scale may be converted to a depth scale by measurement of the crater depth. Crater depth measurements are normally made in this laboratory by interferometry. Secondary ion mass spectrometry (SIMS) is capable of detecting all elements in the periodic table, with detection limits in the ppm to ppb range. With proper standards, quantification may be performed with accuracies of 10% or less. The instruments is normally operated as a low resolution mass spectrometer (M M =300), but may also be operated in a high resolution mode (M /M = 2500).

STEVEN HUES
Code 6177

copy to: R. Colton, Code 6177

GEO-CENTERS, INC.

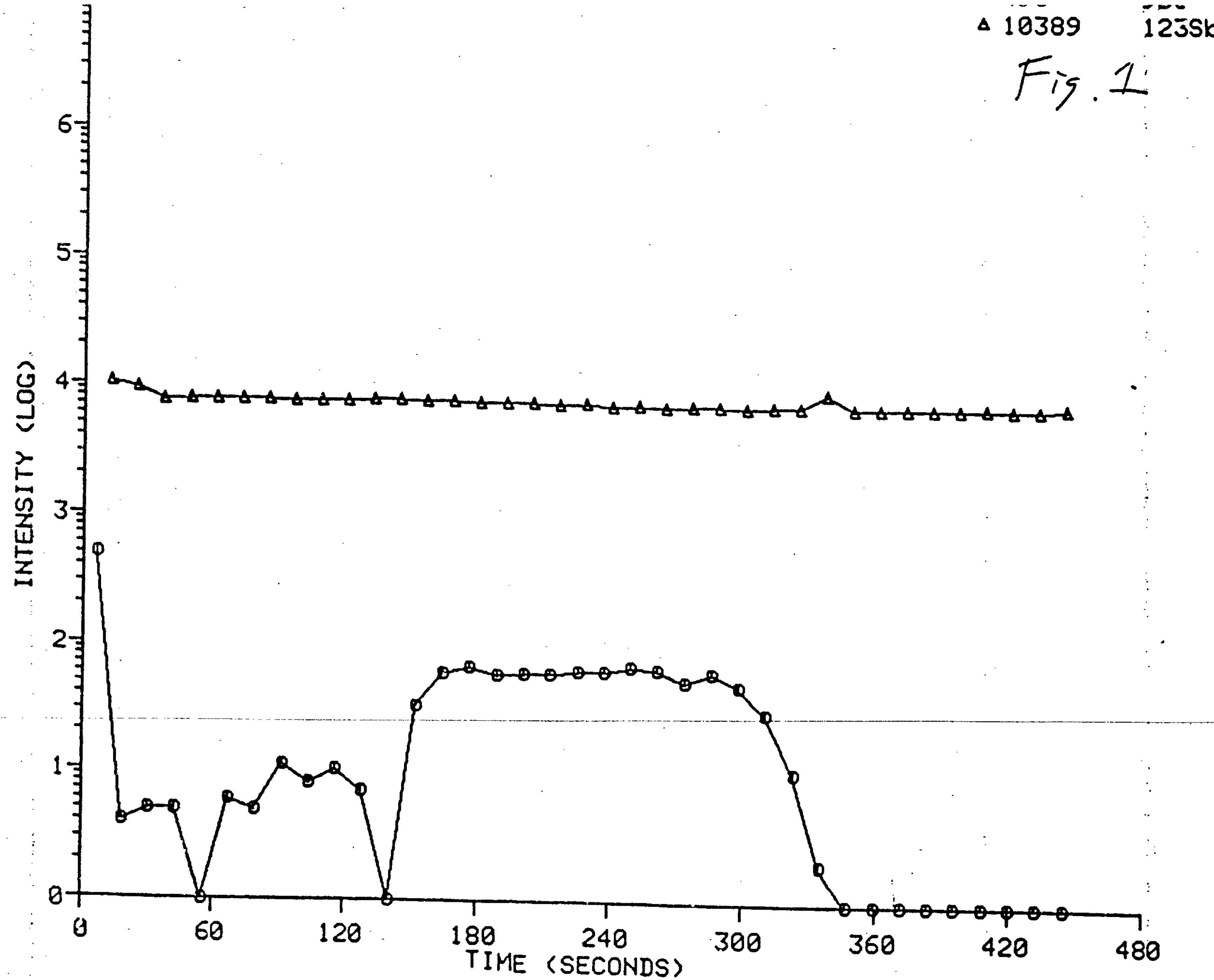

△ 10389
123Sb
6
5
4
3
2
1
0
INTENSITY (LOG)
0
60
120
180
240
300
360
420
480
TIME (SECONDS)

Fig. 1

Fig. 2

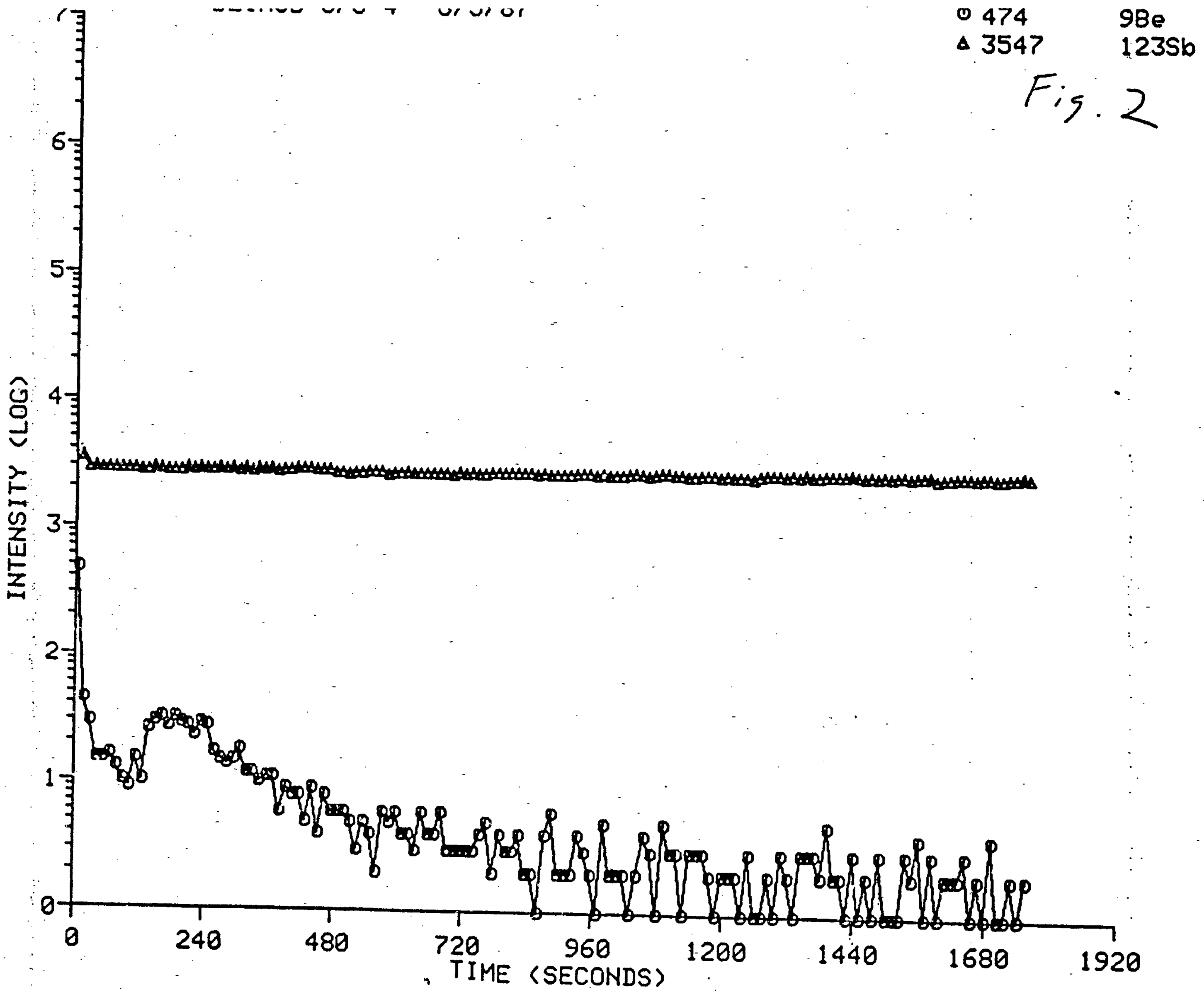

474 9Be
3547 123Sb
INTENSITY (LOG)
0
1
2
3
4
5
6
7
0
240
480
720
960
1200
1440
1680
1920
TIME (SECONDS)

GEO-CENTERS, INC.

SCANNING AUGER IMAGING ANALYSIS OF As IN InP

1. On approximately 5 May 1987 B. Molnar, Code 6812, submitted three samples, labeled 4, 8, and 14 of chemically etched As-doped InP. Structural defects present in the InP had resulted in some areas having relatively rapid etching, producing etch pits in the sample surface. Of interest was whether or not As had preferentially segrated to the defects associated with these etch pits.

2. The analyses were performed using a PHI 660 Scanning Auger Multiprobe. SEM images were obtained using 3 keV primary electrons at a current of -5.5 nA. Auger spectrum were also obtained using 3 keV primary electrons at a current of -1.5 uA. Some details concerning the PHI 660 SAM are presented in the appendix.

3. Photo #1 is a low magnification image of a portion of the surface of sample 8. Labeled within this image are the two etch pits which were analysed. Photo #2 is a higher magnification image of pit #1. An analysis was attempted on the floor of the etch pit, however a useful spectrum could not be obtained due to the insulating nature of the etch pit floor. Auger specta obtained from a spot surrounding the etch pit wall are presented in Figs. 1 and 2. Analysis of pit #2 yielded similar results. Corresponding spectra for a non-pitted area of the sample surface are shown in Figs. 3 and 4. As may be seen there is no observed signal in either set of spectra corresponding to the principal As Auger transition (1228 eV). Analysis of sample 14 also did not detect the presence of As. Based upon these results sample 4 was not analyzed.

4. Appendix:

The PHI 660 Scanning Auger Multiprobe employs an energetic (normally 3 keV) beam of electrons to analyze solid materials. These electrons interact with the sample surface producing secondary electrons by Auger decay. The kinetic energy of the secondary electrons, determined by utilizing a cylindrical mirror analyzer mounted coaxially with the primary electron gun, may be used to identify the atoms under going Auger decay. The intensity of the secondary electron signal may be used as a basis for quantitative analysis with an accuracy of ~10% and a detection limit of 0.1-1 atomic %. This instrument may also be used to prepare Auger maps of a sample in which the contrast of the image is related to the lateral distribution of a specific element on the target surface. The instrument may also be used, in conjunction with a secondary electron detector, as a high resolution secondary electron microscope in order to locate desired surface features and correlate them with ~~those~~ obtained by Auger mapping.

STEVEN HUES

Copy to: R.J. Colton

10903 Indian Head Highway
Fort Washington • Maryland • 20744
(301) 292-1010

BOSTON
WASHINGTON, D.C.
ALBUQUERQUE

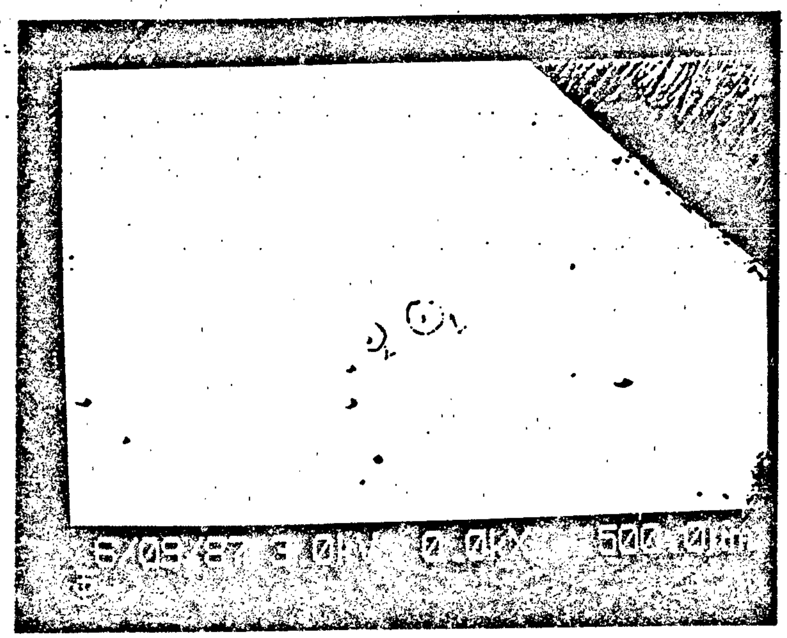

35X

photo #1

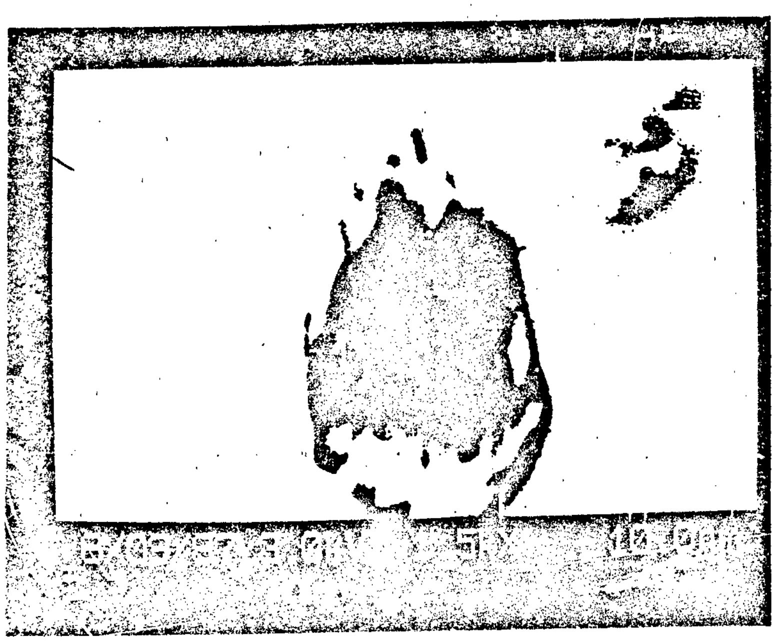

spot #1

Photo #2

Fig #1

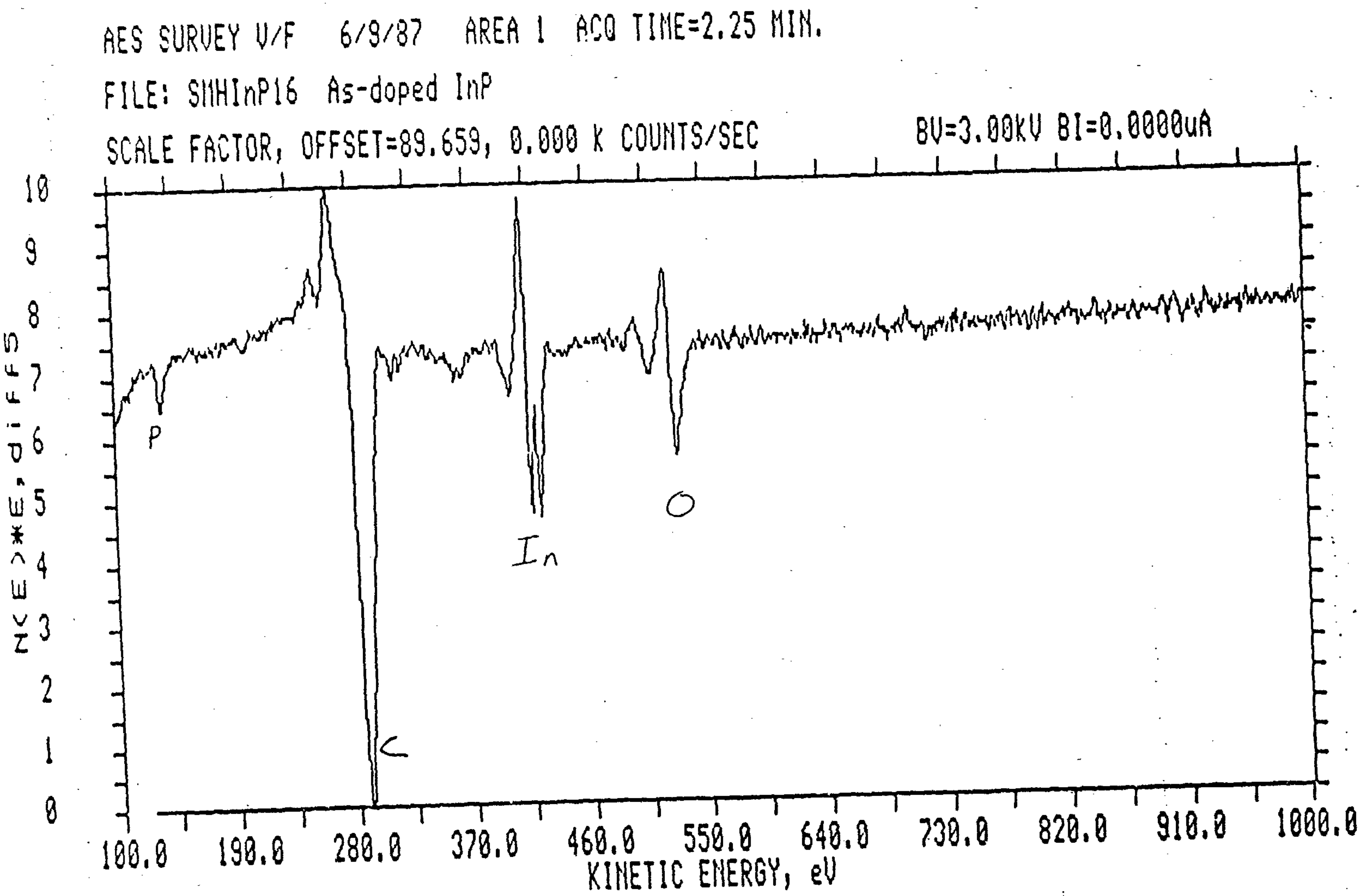
AES SURVEY V/F 6/9/87 AREA 1 ACQ TIME=2.25 MIN.
FILE: SMHInP16 As-doped InP
SCALE FACTOR, OFFSET=89.659, 0.000 K COUNTS/SEC
BV=3.00KV BI=0.0000uA
N(E)*E, diffS
10
9
8
7
6
5
4
3
2
1
0
P
C
In
O
100.0
190.0
280.0
370.0
460.0
550.0
640.0
730.0
820.0
910.0
1000.0
KINETIC ENERGY, eV

Fig. #2

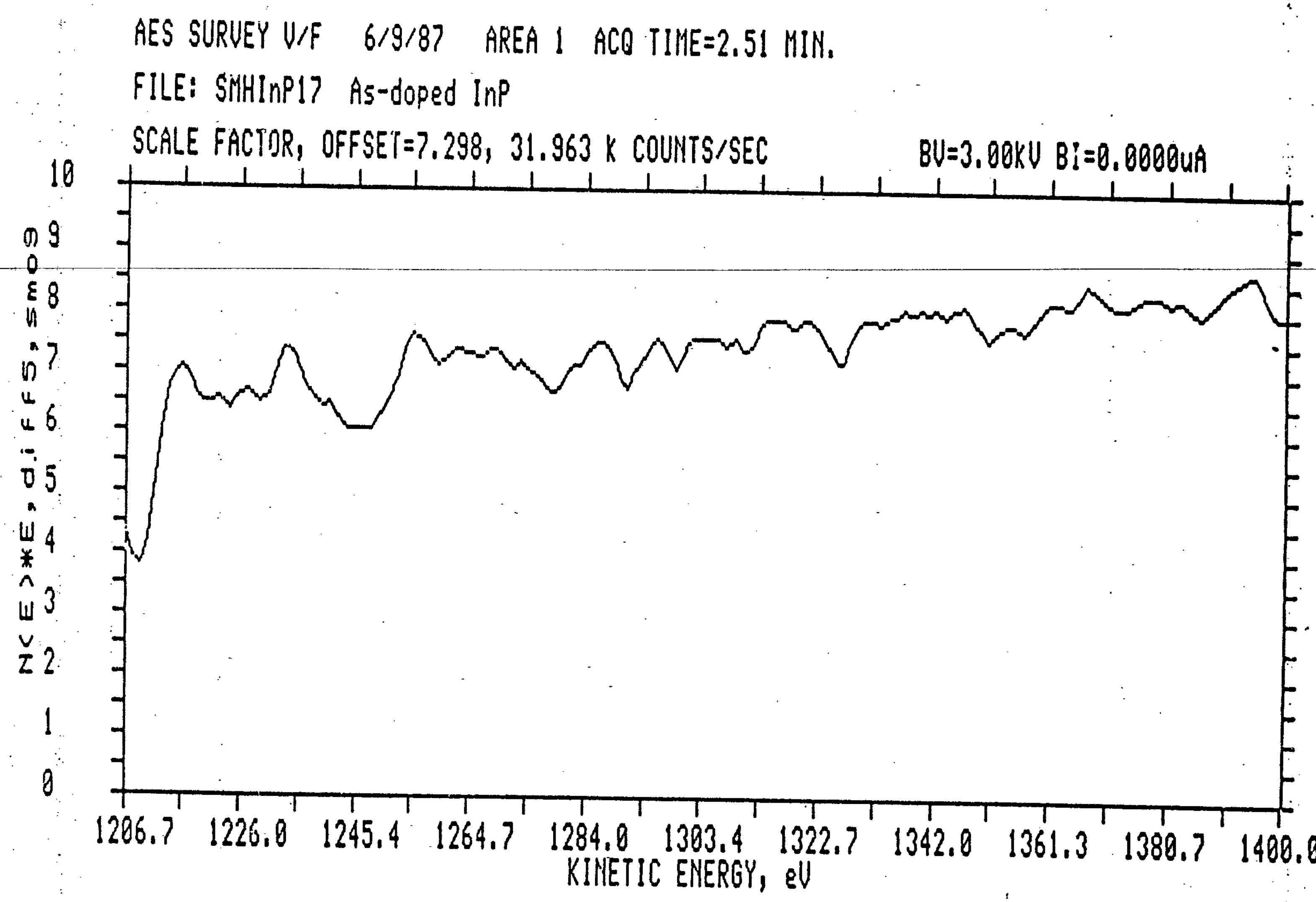
AES SURVEY V/F 6/9/87 AREA 1 ACQ TIME=2.51 MIN.
FILE: SMHInP17 As-doped InP
SCALE FACTOR, OFFSET=7.298, 31.963 k COUNTS/SEC
BV=3.00KV BI=0.0000uA
N(E)*E, diff5, smo9
0
1
2
3
4
5
6
7
8
9
10
1206.7
1226.0
1245.4
1264.7
1284.0
1303.4
1322.7
1342.0
1361.3
1380.7
1400.0
KINETIC ENERGY, eV

Fig. #3

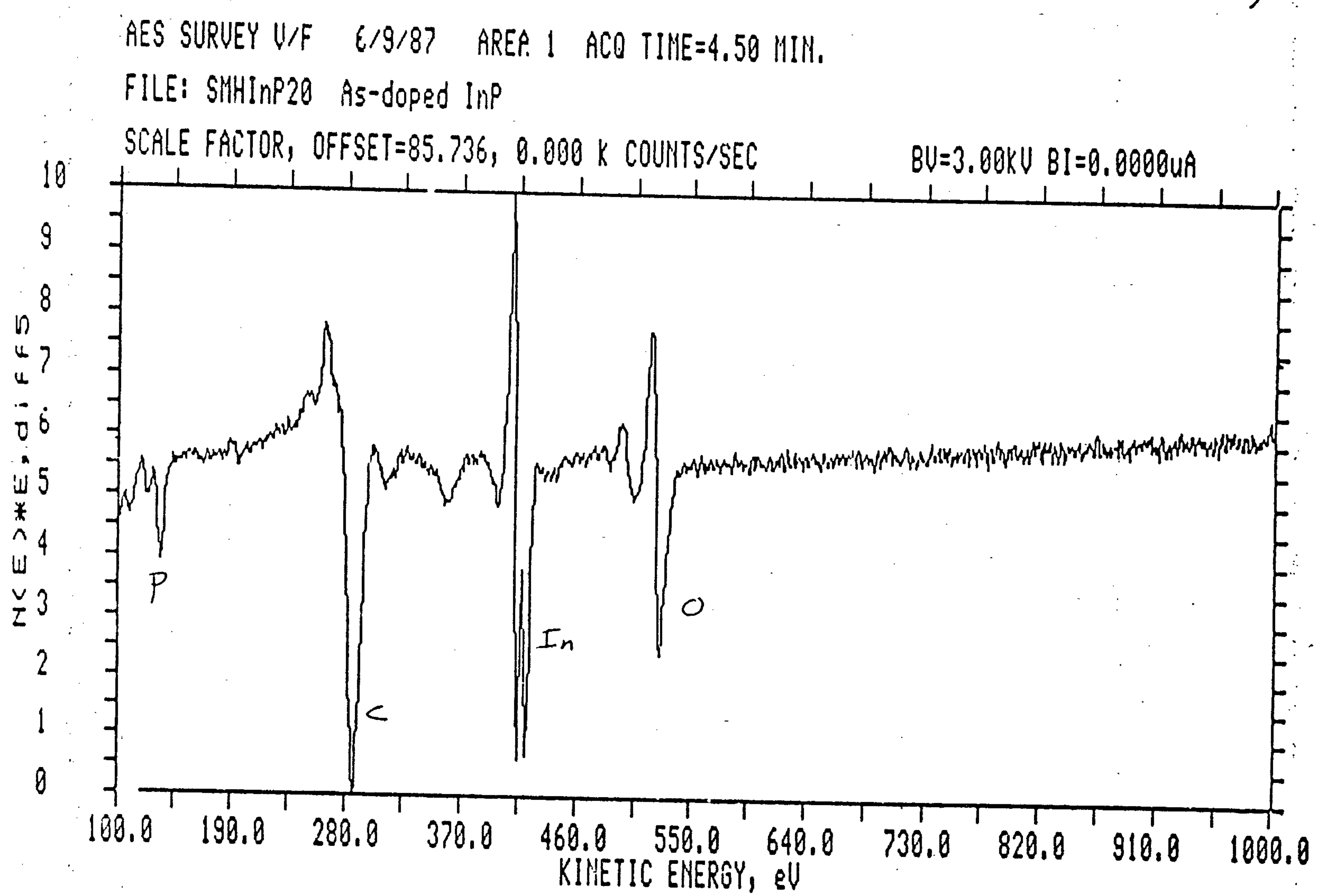
AES SURVEY V/F 6/9/87 AREA 1 ACQ TIME=4.50 MIN.
FILE: SMHInP20 As-doped InP
SCALE FACTOR, OFFSET=85.736, 0.000 k COUNTS/SEC
BV=3.00kV BI=0.0000uA
N(E)*E, diff5
0
1
2
3
4
5
6
7
8
9
10
P
C
In
O
100.0
190.0
280.0
370.0
460.0
550.0
640.0
730.0
820.0
910.0
1000.0
KINETIC ENERGY, eV

Fig. #4

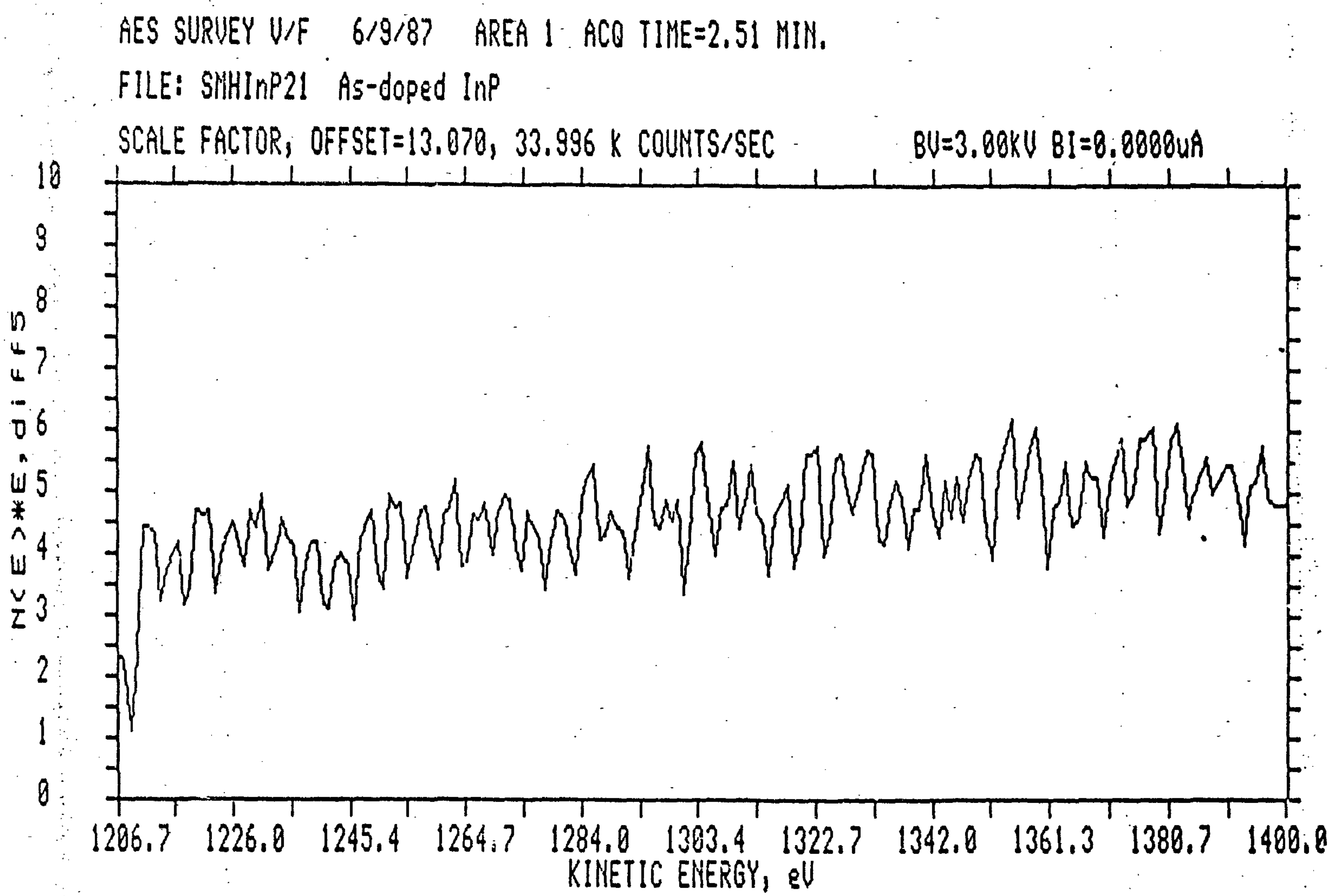

AES SURVEY V/F 6/9/87 AREA 1 ACQ TIME=2.51 MIN.
FILE: SMHInP21 As-doped InP
SCALE FACTOR, OFFSET=13.070, 33.996 k COUNTS/SEC
BV=3.00kV BI=0.0000uA
N(E)*E, diffs
0
1
2
3
4
5
6
7
8
9
10
1206.7
1226.0
1245.4
1264.7
1284.0
1303.4
1322.7
1342.0
1361.3
1380.7
1400.0
KINETIC ENERGY, eV

To: J. Murday

From: S. Hues

Re: Analysis of Mg Flare Powders Submitted By NWSC.

Date: 2 October 1986

NWSC has requested analysis of two samples of Mg powder. Although both samples satisfy current procurement specifications, one sample is difficult to ignite and does not exhibit the desired combustion behavior.

Based on previous analysis performed at NRL (see attached report) it is believed that the failure of the "bad" Mg sample is due to the formation of an excessively thick oxide or hydroxide coating which acts to passivate the surface.

It is proposed to identify the nature of the surface coating on these samples by comparison to known standards of MgO and MgOH using X-Ray Photoelectron Spectroscopy (XPS). Once the identity of the coating is confirmed it will be recommended that the percentage of inactive, i.e. non-metallic, Mg be quantified according to the procedure of Hiller and Stenger (see attached article). Using this method a series of experiments may be performed to determine the maximum allowable inactive Mg content and procurement specifications may be modified accordingly.

Analysis time for the XPS analysis is estimated to be six hours. The atomic absorption analysis for inactive Mg may be performed at NRL, assuming the proper instrumentation is available. However, since an analysis of this type requires considerable set-up time, approximately 8 hours, for the initial analysis with subsequent analyses taking considerably shorter time, it may be more cost-efficient to have this analysis done by an outside analysis firm.

Steven Hues

ANALYSIS OF MAGNESIUM POWDERS

1. Introduction

On 17 April 1986, Dr. D. Ladouceur, NRL Code 6174, returned from a visit to NWC, Crane, Indiana, with two (2) samples of "good" and "bad" magnesium. The samples were provided by Mr. Hank Webster, and we were asked to determine if their chemical compositions differed. Both samples consisted of a fine-mesh powder; the sample labeled "good" was grey in color, while the sample labeled "bad" was grey-brown. Each sample was analyzed by X-ray photoelectron spectroscopy (XPS or ESCA) and by X-ray powder diffraction. (See the appendix for a brief description of XPS.)

2. RESULTS - XPS

The surface composition of the magnesium sample is summarized in Table 1. The major difference between the two specimens appears to be in the thickness of the oxide layer. The "good" specimen clearly shows both metallic and oxide (hydroxide?) chemical states for magnesium, indicating that the oxide layer (presumed to be at the surface) is fairly thin, probably of the order of 30Å. The "bad" specimen, on the other hand, shows only the oxide (hydroxide?) layer and no metallic component. The oxide layer is therefore assumed to be much thicker on the "bad" specimens, probably >100Å.

The exact chemical nature of the surface can be determined by using appropriate standards (e.g., Mg, MgO, $Mg(OH)_2$, Mg CO_3, etc.) or by exposing clean Mg to various oxidizing atmospheres (e.g., O_2, H_2O, air, etc). These experiments can be initiated at your request.

3. Results - X-ray Diffraction

In order to determine if the "bad" specimens had been completely oxidized, we obtained an X-ray powder diffraction pattern of the "good" and "bad" specimens. The diffraction pattern for both the "good" and "bad" specimens were nearly identical and corresponded to the standard pattern for metallic magnesium.

4. Conclusions

While the bulk composition of the "good" and "bad" specimens is mainly magnesium metal, the "bad" specimen has a much thicker oxide (hydroxide?) layer on its surface.

5. Recommendations

The properties of the "bad" specimen could possibly be improved if the oxide layer can be removed or reduced by appropriate chemical means.

Richard J. Colton

Richard J. Colton, Head
Advanced Surface Spectroscopy Section

Robert L. Jones

Robert L. Jones, Head
High Temperature Chemistry Section

6. Appendix

X-ray Photoelectron Spectroscopy (XPS), Surface Science Laboratory, SSX-100-03.

X-ray photoelectron spectroscopy uses the principles of the Einstein photoelectric effect to determine the binding energy of valence and core electrons in solids. The electrons are photoionized by energetic monochromatic x-rays Al Kα (1486.6eV) and are emitted with a mean escape depth of 5-20 Å. Auger electrons also are emitted with x-ray irradiation. The technique is capable of detecting all elements except H and He with a detection limit between 0.1 - 1 atomic percent. Changes in the chemical environment of the element causes a shift in the binding energy of the ejected electrons. These chemical shifts are of the order of 1-10 eV. Empirical formula determinations can be made from height and/or area determinations.

Table 1: Surface Composition of "Good" and "Bad" Magnesium Specimens

Specimen	Element	Binding Energy(eV)[a]	Atomic Percent (%)	Chemical Type
Good	Mg 2s	88.8	12.4	metal
	Mg 2s	90.9	17.3	oxide
	C 1s	284.6	4.5	hydrocarbon
	C 1s	287.1	11.9	
	C 1s	291.5	5.5	carbonate?
	O 1s	531.1	16.5	oxide
	O 1s	533.4	31.9	hydroxide?
Bad	Mg 2s	89.9	32.0	oxide
	C 1s	284.6	4.5	hydrocarbon
	C 1s	286.4	13.1	
	C 1s	290.8	8.1	carbonate?
	O 1s	531.2	15.3	oxide
	O 1s	533.1	27.0	hydroxide?

[a] Binding energies were corrected to the binding energy of $-CH_2$ at 284.6 eV.

›termination of Magnesium Oxide in Finely Divided Magnesium ›tal

Hiller and V. A. Stenger

›ical Laboratories, 574 Building, The Dow Chemical Company, Midland, Mich. 48640

; long been known that magnesium metal and its com- commercial alloys are inert toward aqueous solutions ›romic acid. However, the acid will dissolve magnesium . One of the authors utilized this difference in behavior ›nber of years ago to determine magnesium oxide in ›esium millings or turnings, titrating the free acid re- ›ng after treatment of the metal sample with a standard ›ic acid solution. The volumetric determination of ›ic acid had been studied by Kolthoff and Vogelenzang ›1 and good results had been obtained in the presence ›rium chloride. Recently a more convenient method ›l on the same reactivity difference has been devel- ›in which dissolved magnesium in the chromic acid so- ›is determined by atomic absorption. This made it pos- ›o show that a "blank" on the purest metal available ›ctually due to magnesium in the solution and not to ›tion of chromic acid on the metal. Good agreement is ›ed between these two methods, two other methods ›metric and eudiometric), and also with direct deter- ›ons of oxygen by neutron activation. The new work ›d to improved conditions for leaching, avoiding filtra- ›d saving time in the titration procedure.

›he early years of the magnesium alloy industry, prob- ›rose from inclusions of magnesium oxide in metal ›s. Oxide inclusions affect the bulk properties of the causing embrittlement and loss of tensile strength. ›nior author (VAS) was asked in 1943 to devise a lab- › method for analyzing magnesium samples for their ›content. It was known at the time that chromic acid ›ns would dissolve magnesium oxide without signifi- attacking the metal, and chromates were being used junction with nitric or hydrofluoric acids as corro- ›oofing treatments for magnesium alloy products. upon this solubility difference, a titrimetric method ›veloped in which any loss of acidity upon exposure ›ndard chromic acid solution to a sample of the fine- ›led metal was attributed to reaction of the acid with ›o form magnesium chromate. Use of the method in ›ion with foundry studies led to improved practices ›ng, gas blanketing, and gating which largely elimi- ›xide inclusion problems.

› recently it has become desirable to know the oxide ›, primarily superficial, of magnesium powders used preparation of flares. Military specifications (*1, 2*) › the determination of active magnesium in such ›s, wherein a sample is dissolved with dilute sulfuric ›d the evolved hydrogen is measured in a eudiome- the absence of other metals, this procedure can be ›furnish a measure of the oxide content by differ- ›t the precision is not great and a direct oxide deter- ›n would be preferred. The junior author (TAH) ap- plied the chromic acid treatment procedure successfully to this problem and developed two modifications, in one of which active magnesium is determined by a chelometric titration after removing oxide with chromic acid and dissolving the remaining metal. In the other, magnesium from the dissolved oxide is determined directly by atomic absorption measurement. As the original method was not published, it seems appropriate to describe both that and the modifications at this time.

The titration of chromic acid as a dibasic acid (K_2 = 3.2 × 10^{-7}) was studied long ago by Kolthoff and Vogelenzang (*3*). They arrived at the best results by adding barium chloride shortly before the end point, to precipitate barium chromate and thus, in effect, to change the titration from that of a weak acid to a strong acid. This permitted the observation of a fairly sharp end point instead of a rather vague one at about pH 10. Phenolphthalein was used as indicator and data accurate to within 0.25% were obtained. If the barium salt were added too early in the titration, some dichromate ion would apparently be occluded with the precipitate and the acidity found would be low. Because the transition from dichromate to chromate is slow, a five-minute waiting period was recommended to assure that the end point has actually been reached.

EXPERIMENTAL

Apparatus. The atomic absorption work was done with a Perkin-Elmer Model 303 instrument, using a magnesium hollow cathode tube as the radiation source.

The eudiometer employed in the determination of active magnesium was modified somewhat from that described in the military specification (*2*) to allow for weighing the sample in a small glass cup rather than a paper wad. The cup is designed to be attached with silicone grease to a glass arm which can be rotated, after equilibrium conditions have been reached, to drop the cup and sample into sulfuric acid, liberating hydrogen.

For activation analyses, 6- to 7-gram samples in 7-ml (2-dram) polyethylene vials were exposed to 14-meV neutrons generated in a Texas Nuclear Corporation Cockcraft-Walton type 150-kV positive-ion accelerator. Oxygen was thereby converted to ^{16}N, which has a 7.4-second half-life. The irradiated samples were transferred quickly via a pneumatic tube to a scintillation counter. The apparatus and procedure were approximately the same as described for the analysis of cesium metal by Anders (*4*).

A Beckman Model IR-215 non-dispersive infrared analyzer with a 13.5-cm gas cell was used for the determination of carbon dioxide (in order to allow for correction of the oxygen data obtained by neutron activation analysis, as will be discussed later). The procedure was similar to that of Van Hall and Stenger (*5*) except that, for the analysis of magnesium, the sample was treated with acid in an aeration bottle rather than in a heated tube.

Reagents. The solutions employed were prepared from ACS analytical reagent grade chemicals or from material of the highest purity available. The water used was purified by passing steam condensate through ion exchange resins in a mixed bed.

Chromic acid solution, 5.00 grams CrO_3 per liter (approximately 0.10*N* as an acid).

›Military Specification MIL P-14067 B (MU); Powders, Metal, 10 › 1957.
› Standard MIL-STD-1234, Pyrotechnics; Method 412.1.

(3) I. M. Kolthoff and E. H. Vogelenzang, *Rec. Trav. Chim., Pays-Bas*, 40, 681 (1921).
(4) O. U. Anders, in V. A. Stenger *et al.*, Ed., "Analytical Methods for Impurities in Cesium Metal," Tech. Doc. Rep. No. ML TDR 64-193, Wright-Patterson Air Force Base, Ohio, May 29, 1964, pp 17–30.
(5) C. E. Van Hall and V. A. Stenger, *Anal. Chem.*, 39, 503 (1967).

Table I. Active Magnesium in Samples of Magnesium Chips

Sample	Active magnesium, %	
	Iodimetric method	Chelometric method
MC-305-1	99.0 ± 0.3	99.2 ± 0.2
-2	99.0 ± 0.3	99.0 ± 0.2
-3	99.2 ± 0.3	99.1 ± 0.2
-4	99.0 ± 0.3	99.0 ± 0.2
-5	99.1 ± 0.3	99.0 ± 0.2
MC-511-1	99.0 ± 0.3	99.0 ± 0.2
-2	99.2 ± 0.3	99.1 ± 0.2
-3	99.0 ± 0.3	99.0 ± 0.2
-4	99.0 ± 0.3	99.0 ± 0.2
-5	99.1 ± 0.3	99.2 ± 0.2

[illegible] hydrogen evolution, for here the acid [illegible] would correspond exactly with the metal and oxide in solution.

$$Mg + H_2CrO_4 \longrightarrow MgCrO_4 + H_2 \quad (2)$$

$$MgO + H_2CrO_4 \longrightarrow MgCrO_4 + H_2O \quad (3)$$

Also included in Table II are the results of total oxygen determinations by neutron activation analysis. These analyses were undertaken in an attempt to determine whether the chromic acid methods were revealing all the magnesium oxide in the samples. First indications were that the chemical results might be low. However, the realization that other forms of oxygen might also be present prompted the determination of carbonate by acid attack and infrared analysis. Correction for the oxygen equivalent of the

Table II. Magnesium Oxide Content of Magnesium Chips

Sample	Apparent magnesium oxide, %				
			Neutron activation analysis		
	Acid-base titration	Atomic absorption analysis	From total oxygen	Correction for CO_2	Net MgO
MC-305-1	0.66 ± 0.02	0.65 ± 0.03	0.91	0.20	0.71
-2	0.85 ± 0.01	1.02 ± 0.05	1.16	0.18	0.98
-3	0.99 ± 0.06	0.95 ± 0.05	1.31	0.18	1.13
-4	0.81 ± 0.02	0.91 ± 0.05	1.16	0.15	1.01
-5	0.88 ± 0.03	0.80 ± 0.04	1.28	0.15	1.13
MC-511-1	0.97 ± 0.01	0.84 ± 0.04	1.16	0.29	0.87
-2	0.91 ± 0.02	0.88 ± 0.04	1.01	0.27	0.74
-3	0.88 ± 0.01	0.81 ± 0.04	0.98	0.22	0.76
-4	0.91 ± 0.04	0.83 ± 0.04	1.11	0.21	0.90
-5	0.74 ± 0.01	0.65 ± 0.03	1.08	0.20	0.88
Mean of all samples	0.860	0.834	1.116	0.205	0.911

amples, intended for use in flares, consisted of rounded but irregular pellets generally less than 0.4 mm along their largest axis. They had been analyzed by emission spectrography with the following results: present at about 1 ppm, Cu, Fe, Mn, Ni, Ca; not detectable at a sensitivity of about 1 ppm, Ag, Co, Cr, Pb, Sn, V, Zn, Zr. The indications are hat the samples are quite similar in elemental magnesium ntent and that magnesium oxide by difference would not e expected to exceed 1%. The military specification for active magnesium is 98.0% minimum.

Results of magnesium oxide determinations on the same amples are given in Table II. The data from titrations and tomic absorption measurements represent the means of uplicate determinations (in some cases triplicates), the inges of which are indicated by the plus or minus figures. will be seen that, for at least half the samples, the results f the two methods differ by more than would be anticiated from their precisions. Nevertheless, the overall averges differ by less than 0.03%, the AA results being lower. his comparatively small bias argues against any significnt loss of chromic acid either by adsorption on the magsium metal or by a possible reduction process in which ore chromic acid would be consumed than would correspond to the apparent magnesium oxide dissolved:

$$3Mg + 5H_2CrO_4 \longrightarrow 3MgCrO_4 + 2Cr(OH)_3 + 2H_2O \quad (1)$$

evolved carbon dioxide yielded the data shown in the last column as net MgO. Generally the NAA results are considered to have a relative precision of ±10%. The apparent mean bias of +0.05% MgO for the NAA method over acid-base titration is within this precision range but is probably real. The presence of only 0.022% moisture would cause the NAA results to be high by 0.05% MgO; it would be difficult to determine or remove moisture from an active metal such as magnesium at this low level without affecting the oxide content. Consequently, we feel that chromic acid is effectively reacting with all the oxide in these samples. Additional justification for this view is found in the fact that magnesium has a higher expansion coefficient than magnesium oxide. When hot metal contracts around an oxide particle, it probably develops cracks which later expose the oxide as the metal is milled, turned, or ground. A series of samples turned on a lathe showed no differences due to cutting depths of 0.05 or 0.10 inch (0.127–0.254 cm) when analyzed by the titration method.

A question remains as to the significance of the 0.11% MgO lower limit found in samples analyzed by the earlier titration procedure. The agreement between the methods on samples with higher oxide content indicates that the result is probably real. Analyses of very pure metal by the activation method would be necessary to decide the question.

Barium nitrate solution, 26.0 grams $Ba(NO_3)_2$ per liter (approximately 0.1*M*).

Sodium hydroxide solution, aqueous, 0.10*N*, standardized against potassium hydrogen phthalate.

Chlorophenol red sodium salt, 0.10 gram per 100 ml of water.

Magnesium standard solutions. Weight 2 grams of pure magnesium accurately to within one milligram, dissolve it in 125 ml of 1:4 hydrochloric acid (added slowly) and dilute with water to one liter in a volumetric flask. One milliliter contains 2 milligrams of magnesium. For atomic absorption measurements dilute 50 ml to one liter and dilute 50 ml of that solution to 500 ml. The final solution contains 0.010 mg Mg per ml.

EDTA solution, 40.0 grams ethylenedinitrilotetraacetic acid disodium salt dihydrate per liter (approximately 0.1*M*). Standardize against the standard magnesium solution, 2 mg per ml, as in the chelometric titration procedure.

Buffer solution for pH about 10. Dissolve 65.5 grams of ammonium chloride in 300 ml of water, add 570 ml of concentrated ammonium hydroxide and dilute to one liter with water.

Eriochrome Black T indicator solution. Dissolve 0.8 gram of the powder in a mixture of 40 ml of methanol and 60 ml of triethanolamine.

Sample. The sample may be in the form of finely divided shavings, millings, filings, or powder. To compare various samples of solid metal, they should be milled under the same conditions, preferably in an inert atmosphere. Powders should be of the same mesh size. Generally a one-gram sample is used; if more than one per cent MgO is present, the sample weight should be correspondingly decreased.

Acidimetric Titration Procedure. Place the weighed sample in a 150-ml beaker, add exactly 25 ml of 0.1*N* chromic acid solution from a pipet, and cover with a watch glass. Stir magnetically for 15 minutes with a plastic-coated stirring bar, rinse the cover and bar with 25 ml of water, and add 0.5 ml of chlorophenol red indicator solution. Titrate with 0.1*N* sodium hydroxide to a change from orange to red-orange and add up to 10 ml more of the titrant. Introduce 30 ml of 0.1*M* barium nitrate solution; the mixture should be yellow unless too much sodium hydroxide was added. Continue the titration slowly until the yellow or slightly greenish yellow suspension shows a pink cast. Upon overtitration by a drop or two, the solution becomes a more definite pink which can be confirmed by allowing the precipitate to settle.

Run a blank in the same way. The difference between the sample and blank represents the amount of sodium hydroxide equivalent to chromic acid neutralized by the sample. One ml of 0.1*N* solution represents 2.016 mg of MgO. If the titration difference is more than about 5 ml, the determination should be repeated with a smaller sample.

Chelometric Titration Procedure for Active Magnesium. Place a one-gram sample (weighed to within 0.5 mg) in a 250-ml beaker with a magnetic stirring bar. Add 50 ml of 0.10*N* chromic acid solution, cover the beaker, and stir for 15 minutes. While retaining most of the metal in the beaker, decant the solution through a Gooch crucible with a small moist asbestos pad, under suction. Rinse the metal, beaker, and crucible about six times with water, or until the final washing is colorless. Reserve the filtrate and washings if dissolved magnesium is to be determined by atomic absorption; otherwise they may be discarded.

Transfer the filter pad to the beaker containing the remaining metal. Add 50 ml of water, cover the beaker, and add 1:4 hydrochloric acid in small portions to dissolve the magnesium. Boil the mixture for about a minute, then cool it, transfer to a 500-ml volumetric flask, and dilute to volume. Pipet a 50-ml aliquot into a 500-ml Erlenmeyer flask, add 250 ml of water, 20 ml of pH 10 buffer solution, and 0.5 ml of Eriochrome Black T indicator solution. Titrate with 0.10*M* EDTA solution to a color change from red to blue against a reflected light background. No red color should remain at the end point. Calculate the magnesium content of the sample from the titration volume and the magnesium equivalent of the EDTA solution as found by standardization.

Atomic Absorption Procedure for Magnesium Oxide. Place a one-gram sample in a 150-ml beaker and proceed as in the first paragraph of the preceding method. After obtaining the first filtrate and washings, treat the residual magnesium metal with another 50-ml portion of chromic acid solution and again filter and wash. Dilute each filtrate to 250 ml in a volumetric flask. Prepare a blank on chromic acid filtered through asbestos in the same way.

Pipet a 5-ml aliquot of each sample filtrate for enough to contain 25 to 100 micrograms of Mg) into a 100-ml volumetric flask. Dilute to volume and mix. Adjust the atomic absorption instrument to obtain appropriate sensitivity for the 285.2-nm line of magnesium. Aspirate standards and sample solutions successively into the flame, obtaining the absorbance for each. The blank can be analyzed directly (without dilution) since it is very low in magnesium. Ordinarily no background corrections are necessary. Plot the absorbance vs. concentration of the standards in micrograms per milliliter on linear graph paper. Calculate the concentration of magnesium in each sample solution and the corresponding percentages of magnesium oxide and magnesium they represent in the original sample, correcting for the blank if necessary.

The sum of the magnesium oxide figures obtained in the two extractions is normally used as the content of the sample. However, additional treatments may be made to demonstrate whether additional oxide is dissolved or a constant level of attack upon the metal is reached.

RESULTS AND DISCUSSION

The procedure for titrating excess chromic acid as given above was modified from that of Kolthoff and Vogelenzang (3) in two respects. Barium nitrate was substituted for barium chloride to avoid interference from magnesium metal which is not removed prior to titration. Chloride ion is known to promote the action of chromic acid upon magnesium, whereas nitrate ion does not. This substitution should have no adverse effect on the titration. Chlorophenol red was used in place of phenolphthalein because it seemed more desirable to observe the end-point change at a pH near 7 than at about 9.

The recommended conditions for treating magnesium with chromic acid differ from those originally employed in connection with the titration procedure. Originally two leachings were carried out in a medium porosity glass filter crucible, for ten-minute periods, with occasional stirring with a glass rod. A pretreatment with potassium chromate solution, 5 grams per liter, was given to remove chloride possibly present from fluxes. No pretreatment is needed when chloride is absent. In a test of the ability of 0.1*N* chromic acid to dissolve magnesium oxide under those conditions, with no free metal present, 93.5% of the oxide was found to have reacted during the first leaching and 3.5% more in the second. Under the conditions given in the current procedure, 99% or more was dissolved in one treatment. The improvement is probably due to the more effective stirring and the slight rise in temperature caused by the magnetic stirring apparatus. In these tests, 20-mg portions of pure magnesium oxide, previously ignited at 800 °C, were employed.

No standards of magnesium or its alloys with known oxide content were available at the time of the original study or in the more recent work. However, several hundred samples from experimental and commercial castings were analyzed. These were generally alloys containing six percent aluminum and three percent zinc, equivalent to what is now designated as AZ63 alloy under the ASTM system. Results from 0.11 to 5.3% MgO were obtained. At the lower end of the range the results for duplicate samples were usually reproducible within 0.03% and the castings were of excellent quality. Samples with more than 1% oxide, which were not numerous, showed poorer reproducibility and the metal quality was obviously also poor. No result below 0.11% was found. At the time, it was not known whether this apparent limit represented a true minimum oxide content, adsorption of chromic acid on the metal surface, or reduction of a little chromic acid by active magnesium or another metal. The observation of a green tint near the end point, perhaps from chromium(III) hydroxide, offered some indication of the last possibility.

The chelometric titration procedure has been utilized only for determining active magnesium in powders or chips free from other metals. Table I presents a comparison of chelometric data with those of the eudiometer method. The

INTERFERENCES

Common alloying elements such as aluminum, zinc, and low concentrations (<1%) of manganese do not appear to be dissolved by chromic acid. If any did dissolve, there should be no interference with the atomic absorption method and interference should be minimal in the acid-base titration because these elements would largely be precipitated as hydroxide during the titration, releasing the equivalent quantity of chromic acid which is titrated. Dissolved metals would cause interference with the chelometric method for active magnesium, but procedures for avoiding these interferences are available (6). Any metal capable of yielding hydrogen with sulfuric acid would be counted as magnesium in the eudiometric method.

Magnesium nitride would interfere in the titration method by forming both magnesium and ammonium chromates, and to a lesser extent in AA where only the magnesium equivalent is effective. If the nitride content is determined through hydrolysis followed by any method for ammonia determination (7), corrections can be calculated:

$$Mg_3N_2 + 3H_2O \longrightarrow 3MgO + 2NH_3 \quad (4)$$

(6) F. J. Welcher, "The Analytical Uses of Ethylenediaminetetraacetic Acid," D. Van Nostrand Company, Inc., Princeton, N.J., 1958, pp 111–120, 140.

(7) E. G. Bobalek and S. A. Shrader, *Anal. Chem.*, 17, 551 (1945).

Ordinarily the nitride content of magnesium or its alloys is too small (<0.01%) to cause measurable interference. The same is true of magnesium carbide, which if present would yield soluble magnesium in both methods and might also reduce some chromic acid.

Alloys containing silicon would likely have some of this element combined with magnesium as the silicide, which on treatment with chromic acid would yield soluble magnesium. In practice, however, no serious interference from any of the above-listed possible causes has been encountered in either the titration or AA method.

ACKNOWLEDGMENT

Thanks are expressed to W. R. Kramer and W. B. Crummett for numerous determinations by the titration method, to S. L. Love for atomic absorption analyses, and to G. L. Jewett for neutron activation analyses. The powdered magnesium samples were prepared by the Reade Manufacturing Company, Inc., Metal Powder Division, Lakehurst, N.J.

RECEIVED for review May 15, 1974. Accepted July 22, 1974. Presented at the 167th National Meeting of the American Chemical Society, Los Angeles, Calif., April 1974, at the Symposium of the Division of Analytical Chemistry in honor of I. M. Kolthoff on his 80th birthday.

Studies of Heavy Metal Adsorption by Hydrous Iron and Manganese Oxides

R. Rao Gadde and Herbert A. Laitinen[1]

School of Chemical Sciences, Department of Chemistry, University of Illinois at Urbana-Champaign, Urbana, Ill. 61801

Individual adsorption studies of Pb^{2+}, Cd^{2+}, Zn^{2+}, and Tl^{+} on hydrous iron and manganese oxides are reported. Using pulse polarography to determine the heavy metal ion concentrations before and after adsorption, the effects of hydrogen ion and metal ion concentrations on the adsorption were evaluated. For the divalent ions, the ratio, H^{+} released per heavy metal ion adsorbed was greater than one. Specific adsorption of Pb^{2+}, Zn^{2+}, and Cd^{2+} on hydrous manganese oxide (HMO) and also Pb^{2+} and Cd^{2+} on hydrous ferric oxide (HFO) was observed. Except for Tl^{+} on HMO, which is complicated by a redox process, the adsorption on HFO and HMO followed the order $Pb^{2+} > Zn^{2+} > Cd^{2+} > Tl^{+}$. The adsorption processes are reversible with respect to H^{+} and other adsorbing ions. Adsorption capacities of the order of 0.2 mole heavy metal ion/mole HMO were observed except in the case of lead, which showed much higher adsorption (0.56 mole/mole HMO).

Analytical chemists have studied adsorption of foreign ions on hydrous oxides from the viewpoint of contamination of precipitates as well as the removal of radioactive elements from solution (1–4). In general, a dramatic increase in adsorption is observed with increasing pH and hydrogen ions are released into the solution. The adsorption and, in turn, the release of hydrogen ions is dependent on the surface area of hydrous oxide. In fact, it has been suggested (5–7) that adsorption of zinc ions be used as a measure of the surface area of oxides such as MnO_2, ZrO_2, and SiO_2. Although the displacement of hydrogen ion from the surface is an indication of specific ion exchange adsorption, the number of hydrogen ions released per heavy metal ion adsorbed cannot be taken directly as a measure of the number of binding sites to which the heavy metal is attached. For example, four hydrogen ions are released from a silica sample for each copper(II) ion adsorbed from an ammonium acetate solution (5), presumably because of the involvement of copper amine complexes in the adsorption process.

[1] [illegible] Department of Chemistry, University of Flor[illegible]

(1) I. M. Kolthoff and B. Moskovitz, *J. Phys. Chem.*, 41, 629 (1937).

(2) I. M. Kolthoff and L. B. Overholser, *J. Phys. Chem.*, 43, 767, 909 (1939).

(3) M. H. Kurbatov, G. B. Wood, and J. D. Kurbatov, *J. Phys. Chem.*, 55, 1170 (1951).

(4) J. Korkisch, "Modern Methods for the Separation of Rarer Metal Ions," Pergamon Press, New York, N.Y., 1969.

(5) A. Kozawa, *J. Electrochem. Soc.*, 106, 552 (1959).

(6) A. Kozawa, *J. Inorg. Nucl. Chem.*, 21, 315 (1961).

(7) A. Kozawa, S. C. Paterson, and T. A. Reilly, in "Oxide-Electrolyte Interfaces," R. S. Alwitt, Ed., The Electrochemical Society Inc., Princeton, N.J., 1973, pp 72–90.

APPENDIX C

GEO-CENTERS, INC.

. . . (1987) 175

AN AUTOMATED VAPOR-GENERATION AND DATA COLLECTION INSTRUMENT FOR THE EVALUATION OF CHEMICAL MICROSENSORS

JAY W. GRATE*

Chemistry Division, Naval Research Laboratory, Washington, DC 20375-5000 (U.S.A.)

DAVID S. BALLANTINE, JR

Geo-Centers, Inc., 4710 Auth Place, Suitland, MD 20746 (U.S.A.)

HANK WOHLTJEN

Microsensor Systems, Inc., P.O. Box 90, Fairfax, VA 22030 (U.S.A.)

(Received July 21, 1986; accepted September 18, 1986)

Abstract

An instrument has been built which can generate up to twelve different vapors from bubbler or permeation tube sources. These vapors can be individually selected, diluted to concentrations typically in the range of 1 to 10 000 mg/m^3 volume and delivered at a programmable flow rate to the system output. Mixtures of two vapors can also be easily generated. The system is fully automated using a small personal computer and permits completely unattended operation during elaborate vapor-exposure sequences. Parameters describing the vapor test conditions are automatically stored in the computer disk memory, along with the sensor responses to the test. This instrument has proved to be extremely valuable for rapidly testing prototype chemical sensors.

1. Introduction

The development of any chemical vapor sensor device is not complete until it has been repeatedly exposed to a variety of challenge vapors. These vapors should include those for which the sensor was designed to be sensitive, as well as others that may appear as significant interferences in the environment monitored by the sensor. Furthermore, truly realistic evaluation of the sensor performance requires that the device response be measured while it is exposed to mixtures of the target vapor and interference vapors. However, the generation of several different vapors at precisely known concentrations in various sequences and mixtures is not a trivial problem. The instrument reported here is designed to address this problem.

*Author to whom correspondence should be addressed.

Precise concentrations of individual vapors can be generated by a variety of techniques [1]. Dynamic methods that involve the addition of calibrated amounts of vapor to a flowing stream of carrier gas are generally preferred over static methods, particularly for very dilute vapors. Dynamic methods minimize the effects of wall adsorption on calibration accuracy, and a wide range of concentrations can be prepared by simple manipulation of the gas flow rates.

The instrument reported here is unique in its ability to generate dynamic gas streams of a number of vapors (*i.e.*, 12) from either neat chemical liquid bubblers or calibrated permeation tubes [2]. Moreover, mixtures of low concentration target vapors derived from permeation tubes (typically 1 - 100 mg/m^3) and high concentration interference vapors derived from bubblers (typically 100 - 100 000 mg/m^3) are easily prepared. The gas stream output of the instrument can be switched (under computer control) between the generated vapor stream and clean air so that the zero drift and reversibility of the sensor can be readily observed. Finally, the flow rate of the gas being output to the sensor is regulated to a constant value, regardless of the carrier gas flow rates required to perform the desired dilution. This unusual capability is accomplished using a servo-controlled piezoelectric valve to divert all vapor flow in excess of the amount programmed to be output to the sensor.

Instrument operations are carried out under the control of a microcomputer, and carrier gas flow rates are metered using electronic mass flow regulators. The fully automated character of this instrument affords many advantages including unattended operation during long sequences of tests, reduced operator exposure to toxic chemicals, and improved measurement precision. This system is designed to meet the requirements of a complete chemical vapor sensor research and development program.

2. Description of the instrument

Microcomputer interfacing

The vapor-generation and sensor-evaluation instrument consists of a vapor flow system to generate and deliver vapor streams to the sensor(s), and an Apple IIe microcomputer to control and monitor the vapor flow system. The microcomputer also collects and stores data from the sensor(s)*. The overall system is shown schematically in Fig. 1.

The microcomputer is interfaced with the vapor-generation system and sensors by means of four I/O boards. The IEEE-448 I/O board collects data from a frequency counter, which measures signals from surface acoustic wave (SAW) sensors [3, 4]. This particular I/O board adds great versatility

*Alternatively, sensor data can be collected by a second microcomputer in communication with the first. This configuration is preferred when data must be collected from multiple sensors simultaneously.

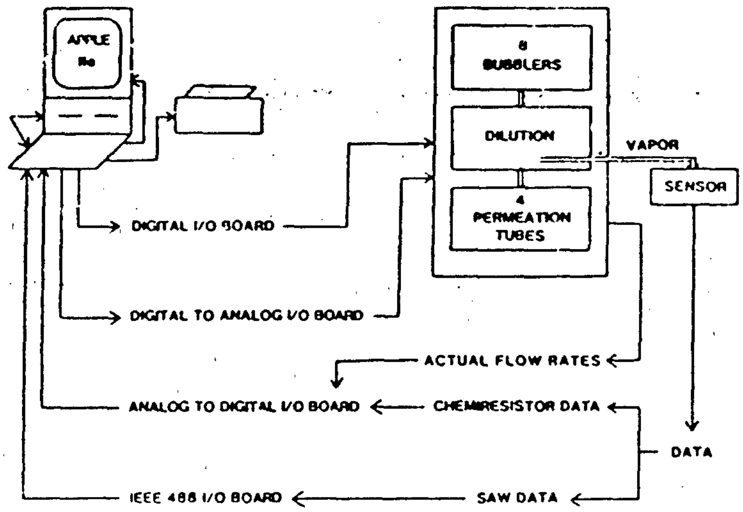

Fig. 1. System interfacing diagram for the vapor-generation instrument.

to the instrument, because other measuring devices such as electrometers can also be interfaced via the IEEE-488 bus. Signals from many types of sensors can therefore be easily monitored. Alternatively, data from any sensor or sensor system whose output is a voltage (*e.g.*, a chemiresistor system [5]) can be collected using the analog to digital I/O board. This board is also used to monitor carrier gas and vapor stream flow rates. Automated control of the vapor flow system is achieved using a digital I/O board, which commands solenoid valves open or closed, and a digital to analog I/O board, which commands mass flow controllers to deliver precise flow rates of carrier gas.

Vapor flow system

The vapor flow system is contained in three boxes: the bubbler box, the permeation tube box and the dilution box. The bubbler and permeation tube boxes are used to generate vapor streams. The dilution box performs several functions: vapor streams are selected from one or more inputs, *e.g.*, from the bubbler and/or permeation tube boxes; the vapor stream or mixture is diluted; either clean carrier gas or diluted vapor stream is output to the sensor. In addition, a flow reduction system within the dilution box regulates the flow rate of gas output to the sensor. The details of the vapor flow system are shown schematically in Fig. 2. The plumbing is constructed using 1/8 inch stainless steel tubing and stainless steel Swagelok fittings.

The bubbler box generates a vapor stream by bubbling a controlled flow rate of carrier gas through a neat chemical liquid. Eight different liquids are contained in separate bubblers, each of which is isolated from the carrier gas loop by a pair of solenoid valves. When a particular bubbler is chosen as the vapor source, its pair of solenoid valves opens, and all other bubbler valves and the bypass valves remain closed. The bypass valves are depicted as

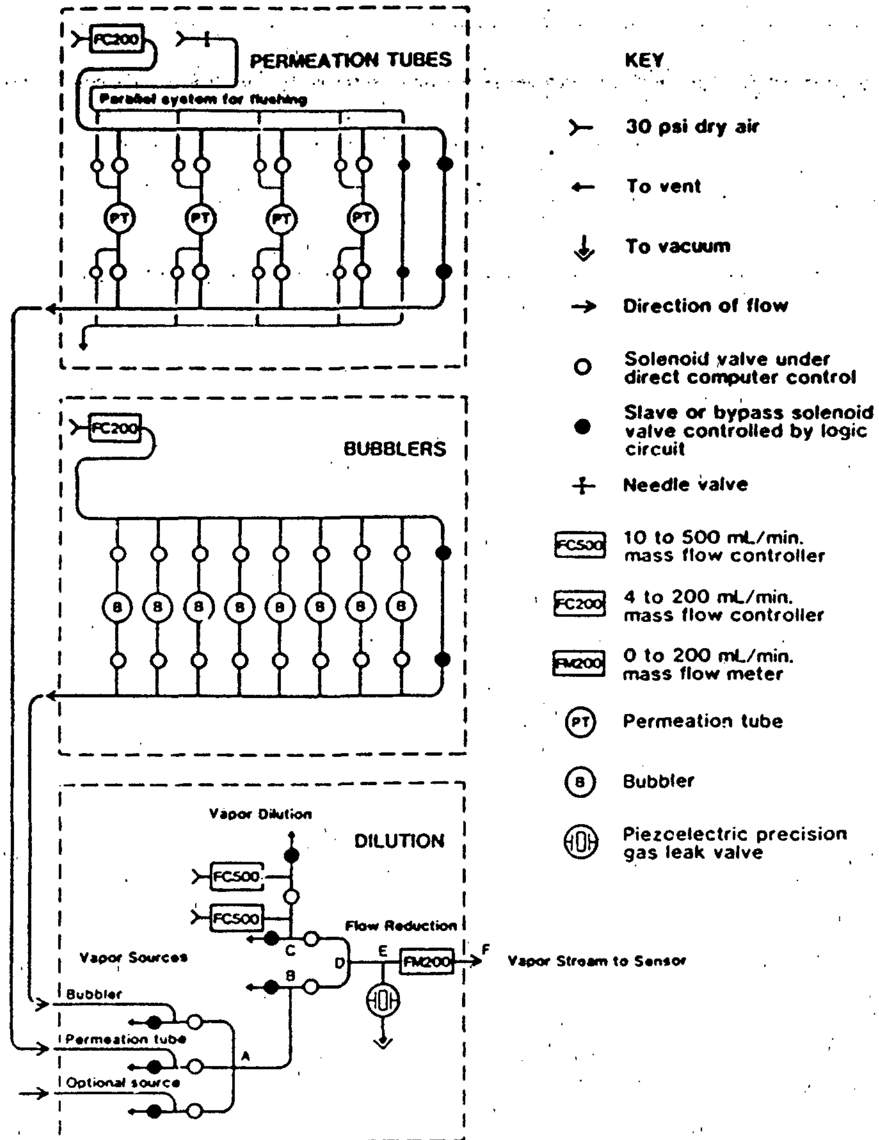

Fig. 2. Vapor stream flow system.

solid circles in Fig. 2 and open to allow flow through the carrier gas loop when none of the bubblers are opened. The flow rate of the carrier gas is regulated by a 4-200 ml/min air mass flow controller (FC200). The bubblers themselves are constructed of 6¾ inch lengths of 2 inch O.D. stainless steel pipe, with 1/8 inch thick stainless steel discs (2 inch diameter) welded to the ends. The top end of each has 1/8 inch stainless steel tubing welded into inlet and outlet holes. The inlet tube extends to 1/2 inch from the bottom and the outlet tube is flush with the inside of the top.

The permeation tube box generates a vapor stream by directing the carrier gas past one of four permeation devices. These devices are closed tubes containing a liquid chemical, which permeates out through a plastic barrier and is swept into the carrier gas [2]. The permeation tubes are contained within chambers constructed of 4 inch hex long nipples (1/2 inch male pipe size) fitted with hex reducing couplings and male connectors on the ends*. Each such assembly is housed in a Dewar flask and maintained at constant temperature by a heating tape and thermocouple.

The flow system within the permeation tube box is similar to that of the bubbler box. Each permeation tube is isolated by a pair of solenoid valves, bypass valves allow flow through the carrier gas loop when no permeation tube is open, and the carrier gas flow is regulated by a 4 - 200 ml/min mass flow controller (FC200). However, a second parallel flow system is also present so that the permeation tube chambers can be flushed to vent when they are not being used to generate a vapor stream for sensor testing. The flushing process assures stable permeation rates by preventing the buildup of high concentrations of vapor within the permeation tube chamber and maintaining a stable concentration gradient across the plastic barrier of the permeation device.

The dilution box contains an arrangement of tubing junctions and solenoid valves, which mixes various gas streams and delivers a gas stream to the sensor at point F in Fig. 2. The output to the sensor can be either clean carrier gas or a vapor stream, and can be switched between the two by opening and closing solenoid valves in carefully planned sequences. Any gas streams not being used as part of the output are vented to a hood.

Clean carrier gas flow within the dilution box is regulated by two 10 - 500 ml/min mass flow controllers. This gas proceeds to the sensor output at F via points C, D and E. Clean carrier gas is used to output clean air, or it is mixed with a vapor stream at point D to output a diluted vapor stream. Initial vapor streams (*i.e.*, prior to their dilution) are supplied by the bubbler and permeation tube boxes and by a third optional input. These can be used singly or mixed, and proceed to the sensor via points A, B, D and E. The configuration of solenoid valves in the dilution box is such that the vapor stream arriving at point B cannot be diluted without sending it to the output at the same time.

The dilution box also contains the flow reduction system, which will be explained separately below. Its function is to maintain the output to the sensor at a constant flow rate, regardless of the total flow of gas required to generate the chosen vapor concentration.

Solenoid valve control

The solenoid valves in the vapor flow system are controlled in two different fashions, depending on their function. Those valves depicted in Fig. 2

---

*Some commercial permeation tubes come equipped with tube fittings and can be incorporated into the system by means of a simple T junction.

with open circles are turned on (opened) at the command of signals sent by the digital I/O board in the microcomputer. These valves are used to select vapor sources and gas streams to be sent toward the sensor. They can be individually opened by an operator at the computer keyboard or by statements in the software used to operate the instrument automatically.

Those solenoid valves depicted by solid circles in Fig. 2 cannot be controlled directly by either the computer keyboard or software. Instead, they are controlled by logic circuits in each box, which read the control signals going to the open circle valves in that box and decide on the proper operation of the corresponding solid circle valves. For example, the bubbler box contains a pair of bypass valves depicted by solid circles. The associated logic circuit has eight inputs, one for each bubbler, and functions as an eight-input NOR gate. The output of this gate commands the bypass valves. If any of the bubblers are open, the bypass is closed; if no bubblers are open, the bypass opens. Similar four-input NOR gates control the bypasses in the permeation tube box.

The solenoid valves in the dilution box are arranged in master/slave pairs on T junctions. The master valves are depicted with open circles and the slave valves are depicted with solid circles in Fig. 2. The gas flow coming into a T junction will exit via either the slave valve (to a vent) or the master valve (toward the sensor), depending on which is open. The logic circuit in the dilution box commands the slave valve to be open when the master valve is closed, and vice versa. The circuit functions by inverting each control signal for a master valve and using the inverted signal to control the corresponding slave valve.

Designing the vapor flow system with bypass and slave valves automatically controlled by logic circuits assures that an open flow path from each flow controller to either the sensor or a vent is always maintained. This avoids no-flow conditions in the flow controllers, and continually flushes clean carrier gas through any part of the system not currently being used to generate a vapor stream. Automatic operation of these valves by hardware allows the operator or programmer to be concerned only with those valves leading toward the sensor.

The solenoid valves (Precision Dynamics, New Britain, CT) are normally closed valves with Kalrez seals on the plungers and ethylene propylene rubber (EPR) O-rings*. These valves are powered by 115 VAC, which is switched on and off by optically-coupled solid-state relays. The relays are commanded by the TTL digital signals discussed above.

Mass flow controllers

The carrier gas is supplied to the vapor flow system as dry air at 30 psi. The pressure of this gas is reduced and its flow regulated by means of air mass flow controllers (Tylan, Carson, CA). These devices contain an air mass

*Some vapors cause standard seal and O-ring materials to swell, which can impair valve function.

flow sensor and an electronically actuated needle valve. The mass flow controller is commanded to a particular flow rate by an 0 - 5 V analog signal, which is proportional to the desired flow rate and the range of the flow controller. For example, a 3.0 V control signal to a FC500 commands a 300 ml/min flow rate. Control signals are generated by the digital to analog I/O board in the microcomputer at the command of an operator at the keyboard or by software. The mass flow controllers also generate a 0 - 5 V analog signal proportional to the actual flow rate measured by their air mass flow sensor. These signals are read by the analog to digital I/O board.

Flow reduction system

The flow reduction system is contained in the dilution box and consists consists of a T junction (labeled E in Fig. 2), a precision piezoelectric gas leak valve (Vacuum Accessories Corp., Bohemia, NY), an air mass flow meter (FM200) and an analog control circuit. This system divides the total mixed gas flow arriving at junction E into two paths. The path from point E to F through the flow meter delivers gas to the sensor. The other path leads to the gas leak valve, which bleeds the remaining flow into vacuum. The degree to which the gas leak valve opens is governed by a 0 - 100 V control signal commanded automatically by the analog circuit. This circuit determines the control signal for the gas leak valve by comparing the signal generated by the mass flow meter (FM200) with a 0 - 5 V analog control signal from the microcomputer (via the digital to analog conversion I/O board). If, for instance, the flow rate to the sensor being measured by the flow meter is greater than the flow being commanded by the microcomputer, then the gas leak valve begins to open more. This diverts more gas flow into vacuum, and results in a reduced flow rate though the flow meter. The flow meter output signal starts going down. When it matches the control signal from the microcomputer, the 0 - 100 V command signal to the gas leak valve stops increasing and the gas leak valve opening remains steady at the position that maintains the commanded flow rate through the flow meter.

3. Instrument operation

Automated sensor evaluation

The overall purpose of this instrument is to evaluate sensor behavior under clean air and under various vapor streams. For each vapor, the sensor must first be observed under clean air to determine its baseline drift. Secondly, the sensor is observed under a vapor stream to determine its response. Finally, the sensor is observed under clean air again to determine its recovery. Usually this cycle is repeated to determine reproducibility, and for each vapor it is desirable to observe response under a range of concentrations. The specific solenoid valve operations necessary to switch the instrument between clean air and vapor stream output will be described separately from the overall process of testing sensors.

Sensor testing is normally carried out using two BASIC programs written specifically for this instrument. These programs are outlined in Table 1. Many instrument functions can be accessed directly by commands entered at the computer keyboard, but this is mainly useful for instrument check out. Sensor testing requires keeping track of numerous instrument functions at once, and this is most reliably accomplished with the aid of software.

TABLE 1

Software for sensor testing

Program 1
1. Update vapor source mass flow rates.
2. Calculate menus of concentration choices for each vapor.
3. User selects vapor/concentrations to be generated.
4. Text file stored on disk for each selection.

Program 2
1. Flush flow system, output clean air.
2. Read first text file.
3. Generate and equilibrate vapor stream, output clean air.
4. Test sensor, output clean air, then vapor, then air.
5. Store data on disk.
6. More experiments?
   No — Flush flow system, output clean air, end.
   Yes — Read next text file.
7. Is the next vapor different?
   No — Adjust dilution air, loop to step 4.
   Yes — Flush flow system, loop to step 3.

The first BASIC program helps the user to plan the sensor exposure experiments. The mass flow of vapor that each installed vapor source generates is displayed and can be updated. This information is combined with information on the dilution capabilities of the instrument in order to produce menus of possible vapor concentrations. A separate menu is created for each vapor. The user then selects vapors and concentrations in the order that the sensor is to be exposed to them.

Once the user has completed his selections, the program begins storing text files on disk. Each of these text files contains an array of variables that will command the vapor flow system to generate the chosen vapor stream at the chosen concentration. Specifically, the values of these variables dictate which solenoid valves will be opened to generate the chosen vapor stream, and what flow rates the mass flow controllers will set in order to dilute to the chosen concentration. In addition, certain variables indicate which solenoid valves must be opened and shut when the vapor flow system output is switched between clean air and vapor.

After the user has selected vapors and concentrations and stored text files on disk using program 1, sensor testing can proceed using program 2.

This program operates the instrument and performs the experiments (*i.e.*, vapor/concentration) contained in the text files. The program begins operation by opening solenoid valves in a configuration that will flush the entire system (excluding individual bubblers) with clean air. The initial instrument output is also clean air. The first text file is read and the chosen vapor stream is generated and sent to vent. The program does not begin a sensor testing sequence until the vapor stream has equilibrated for twenty minutes. Then sensor data collection begins and the instrument output is switched between clean air and vapor stream at programmed intervals. The results are displayed graphically on the computer monitor. At the completion of the experiment, the test conditions and the sensor response data are stored on disk, the graphics are dumped to the printer, and the next text file is read from disk. If the next vapor is different from that of the previous experiment, the system is flushed with clean air for ten minutes before generating and equilibrating the new vapor stream. If the next vapor is the same but at a different concentration, then the flow rates are adjusted for the new concentration and the experiment proceeds. The cycle of reading the experiment from disk, performing the experiment and saving the data on disk is repeated until all the experiments have been completed. The system is then flushed with clean air until the operator shuts it down.

Clean air and vapor output operations

Following the detailed switching operations of the vapor flow system will require reference to Fig. 2. All solenoid valves depicted by open circles should be assumed to be closed unless indicated otherwise, with the bypass and slave valves operating automatically. The flow controllers are delivering a commanded flow rate of air to their respective carrier gas pathways, and the flow reduction system is automatically maintaining the output of the dilution box at the commanded flow rate.

(1) *Vapor stream generation.* When a particular bubbler contains the chosen vapor, its corresponding pair of solenoid valves is opened. The carrier gas passes through the bubbler and delivers the resulting vapor stream to a T junction in the dilution box. The master solenoid valve on this T junction is opened so that the vapor stream proceeds through junctions at A and B and exits to vent via the slave valve on junction B. This configuration is maintained for at least twenty minutes to equilibrate the vapor source and tubing wall surfaces and achieve a stable, reproducible mass flow of vapor. A vapor stream is generated this way when the first text file is read. The bubbler (or other vapor source) is not closed again until a subsequent text file that requires a different vapor is read.

(2) *Set up dilution and output clean air.* Most of the time the output of this instrument is clean air, which comes from one or both of the FC500s in the dilution box. All of this air proceeds via junctions C and D to E. The flow reduction system then sends the commanded amount to the output at F and diverts the rest via the gas leak valve. When a text file is read, the flow

of air from the FC500 is adjusted to the levels that will be required when the vapor stream is diluted and output.

(3) *Switch to vapor stream output.* The vapor stream is output or 'switched on' by opening the master valve at junction B. This stream proceeds via D and E to the output at F, possibly mixing with dilution air at D. If the vapor stream is not to be diluted at D, then the master valve on junction C is closed at the same time that the master valve on junction B is opened. Switching solenoid valves open and closed at C and D clearly has the potential to change the total volumetric flow rate arriving at junction E in the flow reduction system. Such a change would force the flow reduction system to adjust the opening of the gas leak valve in order to maintain the constant commanded output flow rate. However, such adjustment can be avoided by simultaneously reducing the clean air flow when the vapor stream flow is switched on, as outlined below.

When the vapor stream is to be output in undiluted form, the air used for clean air output comes entirely from the FC500 closest to junction C. (The master solenoid closest to the farther FC500 is closed and its flow exits to a vent.) The flow rate of this air has been set to match the flow rate of the vapor stream arriving at B (and exiting to vent). Clean air output is switched to undiluted vapor stream output by opening the master valve at B and closing the master valve at C. The flow rate arriving at E is unchanged and the flow reduction system makes no adjustments.

If the vapor stream is to be diluted, but with less than 500 ml/min of air, then the FC500 farthest from C is set to match the vapor stream flow rate. The FC500 closest to C is set to provide all the air required to dilute the vapor stream to the chosen concentration. During clean air output the air from both FC500s proceeds from C to E. When the vapor is switched on, the flow from the FC500 farthest from C is switched off (to vent) by closing its master solenoid valve. The flow rate arriving at E is therefore unchanged.

When the vapor stream is diluted with greater than 500 ml/min of air, then the combined flow rate from both the FC500 flow controllers is set to the flow of air needed for the dilution. This flow always proceeds from C via D to E. Clean air is switched to dilute vapor stream by simply opening the master valve at B. The flow reduction system must readjust the gas leak valve in this case because this switching mechanism increases the flow rate arriving at E. However, this flow rate increase is small compared to the amount of dilution air flow already being diverted by the flow reduction system, and the required adjustment in the gas leak valve is minor.

(4) *Switch back to clean air output.* To return the system to clean air output, the solenoid valves are simply returned to their configuration prior to switching the vapor stream on. This requires closing the master solenoid at B and possibly opening another solenoid valve to compensate with more air flow. Note that switching the output between clean air and vapor while a sensor is being tested is accomplished solely by the opening and closing of solenoid valves. The commands to the mass flow controllers are not changed during the course of an experiment.

(5) *Change vapor or concentration for the next experiment.* If the vapor for the next experiment is the same but at a different concentration, then the commanded flow rates to the flow controllers are changed to provide the required dilution. The next experiment can then proceed. If the vapor is to be changed, then the previous vapor source is closed and the system is flushed for ten minutes before opening and equilibrating the next vapor stream.

4. Instrument precision and range

Vapor concentrations

The concentrations of the vapor streams output by the instrument are calculated by dividing the vapor mass flow rate by the total volumetric flow rate of the gas containing the vapor:

$$\text{concentration} = \frac{\text{vapor mass flow rate}}{\text{total volumetric flow rate}} \tag{1}$$

The uncertainty in the vapor concentrations therefore depends on the uncertainties in the vapor mass flow rates and the volumetric flow rates of carrier gas.

The mass flow rate of a permeation tube is dependent on the area, thickness, and material of the permeation barrier, and is independent of the carrier gas flow rate. These devices are conveniently calibrated by determining their mass loss as a function of time at the thermostatted temperature. Successive determinations on Teflon permeation tubes produced in-house gave uncertainties of less than 10%. Commercial permeation tubes purchased already calibrated are rated at 5% uncertainty.

The mass flow rate of a bubbler depends on the vapor pressure of the liquid, the degree to which the carrier gas becomes saturated with the vapor and the flow rate of the carrier gas. The use of electronic mass flow controllers in this instrument assures that the carrier gas flow rate will be constant regardless of changes in downstream flow conditions. The degree of saturation depends on the efficiency of the bubbler and the amount of liquid it contains. These variables can be controlled by good bubbler design and maintenance.

Bubblers were calibrated by passing their effluent into a charcoal filter to trap the vapor quantitatively, and measuring the mass increase of the trap. This procedure was carried out with the bubblers installed in the instrument at ambient temperatures with a carrier gas flow rate of 39 ml/min. Mass flow rates were stable after fifteen minutes of bubbling. Successive determinations resulted in mass flow rates with uncertainties of less than 6%.

It should be noted that simply estimating the mass flow rate of a bubbler from published vapor pressures and the ideal gas law is unreliable. Such estimates can vary from gravimetrically determined values by as much as 30%. Estimated values were sometimes less than gravimetric values, indicating that the difference between observed and estimated values is not due to a failure to saturate the carrier gas.

The total volumetric flow rate of the gas containing the vapor is equal to the sum of the carrier gas flow rates of those flow controllers contributing to the total flow, plus the volume of the vapor itself. For dilute vapor streams, the volume of the vapor is negligible. The uncertainty in the carrier gas flow rate is then determined by the flow controllers, which are accurate to 1% of full-scale flow, *e.g.*, 5 ml/min for an FC500 (and repeatable to 0.2% of full scale). The percentage uncertainty in total flow of carrier gas is, therefore, the least when the number of flow controllers contributing to the total flow is minimized and when low-flow conditions are avoided through any of those flow controllers (especially FC500s).

Clearly, the uncertainty in the total volumetric flow rate will vary depending on the particular dilution being performed. When a given concentration can be achieved by more than one method of dilution, the most precise method is used. For example, diluting the mass flow from a permeation tube with an increasing amount of volumetric flow from the permeation tube FC200 (up to 200 ml/min) is more precise than diluting 39 ml/min of flow from the permeation tube box with additional volumetric flow from an FC500 in the dilution box.

As noted earlier, vapor/concentration experiments are planned by the user with the help of program 1. This program provides the user with menus of concentration choices for each vapor. Each choice represents a particular procedure for diluting the vapor stream, which was designed to accomplish the dilution in the most precise manner available. One set of procedures was developed for diluting mass flow from permeation tubes, and a different set of procedures was developed for bubblers. For any particular permeation tube, for instance, the mass flow of that permeation tube is divided by the total flow of carrier gas generated by each dilution procedure, and this produces the menu of concentrations. Table 2 provides an example of the dilution information associated with selected menu choices for permeation tubes. An actual menu would include a column of vapor concentrations calculated according to eqn. (1).

Sixteen menu choices are available for permeation tubes, each choice being approximately 80% of the concentration of the choice before it. These range from the concentration of an initial vapor stream, which enters the dilution box and is output to the sensor with no further dilution, to the most dilute stream the instrument can produce. Concentrations relative to that of an initial vapor stream are given in the Fractional concentration column. The instrument can dilute permeation tube vapor streams to 3.3% of their initial concentration. The uncertainty in the total volumetric flow rate is the greatest (5%) for an undiluted vapor stream and least (1%) at maximum dilution. The uncertainty in the output vapor concentration calculated according to eqn. (1) is the sum of the mass flow rate uncertainty (5 - 10%) and the total volumetric flow rate uncertainty (1 - 5%). Permeation tube vapor stream concentrations are therefore known to ±6 to 15%.

TABLE 2

Selected permeation tube dilution menu choices

Menu choice #	Flow controller flow rates (ml/min)			Total volumetric flow rate[a] (ml/min)	Fractional concentration[b]
	FC200[c]	FC500	FC500		
1	39 ± 2	0[d]	0	39 ± 5.1%	1.000
2	48 ± 2	0	0	48 ± 4.1%	0.805
4	77 ± 2	0	0	77 ± 2.6%	0.509
8	195 ± 2	0	0	195 ± 1.0%	0.200
12	200 ± 2	254 ± 5	0	454 ± 1.5%	0.086
16	200 ± 2	500 ± 5	500 ± 5	1200 ± 1.0%	0.033

[a]The sum of the volumetric flow rates from all contributing flow controllers.
[b]Fractional concentration relative to the concentration when the mass flow is carried by 39 ml/min of carrier gas.
[c]FC200 in the permeation tube box. Flow from the FC200 in the bubbler box is not used to dilute permeation tube vapors.
[d]Zeros indicate that this flow controller does not contribute flow or uncertainty to the total flow.

The bubbler menu is set up similarly. However, the maximum dilution for a bubbler is somewhat less, because the carrier gas flow in the bubbler must be constant to deliver a constant mass flow of vapor. Therefore, the FC200 in the bubbler box always contributes 39 ml/min of carrier gas, and all further dilution flow comes from the FC500s. The maximum dilution is into 1039 ml/min of carrier gas, giving a fractional concentration of only 0.038 relative to the concentration of the initial bubbler vapor stream.

The uncertainty in the total volumetric flow rate is 5% for undiluted bubbler vapor stream, and then increases sharply when volumetric flow from an FC500 is added to the 39 ml/min from the FC200. The menu does not allow the user to choose concentrations with high uncertainties. The first diluted choice given is to 40% of the initial vapor stream, with an uncertainty of 7%, the largest uncertainty of any choice on either menu. The uncertainty is below 5% for bubbler dilution choices below 25% of the initial concentration, and is near 1% at maximum dilution. Combining the 6% uncertainty in the bubbler mass flow rates with the 1 - 7% uncertainties in volumetric flow rates gives concentrations (eqn. (1)) known to ±7 to 13%.

However, bubbler vapor streams are not always so dilute that the total volumetric flow rate of gas containing the vapor can be determined simply from the volumetric flow rate of the carrier gas. The volume of the vapor itself must be considered for volatile liquids whose vapor is not diluted by a large volume of carrier gas. For example, isooctane with a gravimetrically-determined mass flow rate of 0.014 g/min will contribute a volumetric flow rate of 3 ml/min at 25 °C and 1 atm, based on an ideal gas law conversion. Addition of 3 ml/min to the 39 ml/min of carrier gas of an undiluted vapor stream gives a total volumetric flow rate of 42 ml/min. The calculated vapor concentration is 8% too high if the vapor volumetric flow is not added to the carrier gas volumetric flow in the denominator of eqn. (1).

Flow reduction system

The flow reduction system takes the diluted vapor stream and splits the volumetric flow into two paths, one of which goes to the sensor. This process does not change the concentration of the vapor stream or the precision with which it is known. The accuracy of the volumetric flow rate output to the sensor is dependent on a number of factors, including the accuracy of the flow measurement by the mass flow meter (FM200, ±2 ml/min) and minor uncorrected offsets in the analog circuit that controls the system. In practice, actual flow rate output is generally within 5% of the commanded output, 39 ml/min.

The magnitude of the volumetric flow that the flow reduction system can divert via the gas leak valve is dependent on how it is configured. With 1/16 inch stainless steel tubing from the T junction (E on Fig. 2) to the flow meter and a single gas leak valve installed, the flow reduction system can reduce up to 800 ml/min arriving at E to 39 ml/min output at F. With two gas leak valves placed in parallel by having a cross at E instead of a T junction, and 1/8 inch stainless steel tubing from the cross to the flow meter, flow rates in excess of 1200 ml/min arriving at E can be reduced to 39 ml/min output at F.

It was stated in Section 3 that the flow reduction system need not adjust the opening of the gas leak valve when the system output is switched from clean air to vapor, provided that the volumetric flow of air arriving at point E is not changed. This is the case when the vapor stream is either undiluted, or is diluted by less than 500 ml/min of air. Nevertheless, the flow reduction system does sometimes make adjustments under these conditions. This adjustment occurs because the mass flow meter in the flow reduction system is calibrated for dry air, and gives an erroneous reading when high concentrations of a vapor with thermal properties differing from those of air are sent through it. The flow reduction system automatically adjusts the gas leak valve so that the reading from the flow meter will return to the desired value, even though that reading is mis-stating the actual flow. This error becomes negligible when the vapor stream is dilute.

5. Conclusion

The instrument described here has proved to be extremely valuable in conducting chemical sensor research. Sensor coating materials can now be rapidly screened against a range of chemical vapors. The capability of generating mutliple concentrations of a single vapor and maintaining a constant flow rate to the sensor regardless of the dilution required to achieve the desired concentration allows calibration curves to be determined very conveniently. Extended sequences of tests involving target vapors at low concentrations, potential interferents at high concentrations and mixtures of two vapors can be automaticaaly executed to critically evaluate prototype sensors. Testing sequences requiring days of continuous operation can be routinely conducted. The generation of sensor data sets of sufficient size for the application of pattern recognition techniques is a readily manageable task. A matrix of surface acoustic wave sensor data, which was collected with this instrument and analyzed by pattern recognition techniques, has recently been reported [4]. This type of instrument should be useful to all those who must test and evaluate chemical sensors.

Acknowledgements

The support of the U.S. Army Chemical Research Development and Engineering Center, Aberdeen Proving Grounds, MD, is gratefully acknowledged. The research was performed at the Naval Research Laboratory, Washington, D.C.

References

1 R. S. Barratt, The preparation of standard gas mixtures. a review, *Analyst (London) 106* (1981) 817 - 849.
2 J. Namiesnik, Permeation devices for the preparation of standard gaseous mixtures, *Chromatographia, 17* (1983) 47 - 48, and refs. therein
3 H. Wohltjen, Mechanism of operation and design considerations for surface acoustic wave device vapor sensors, *Sensors and Actuators, 5* (1984) 307 - 325.
4 D. S. Ballantine, Jr., S. L. Rose, J. W. Grate and H. Wohltjen, Correlation of surface acoustic wave device coating responses with solubility properties and chemical structure using pattern recognition, *Anal. Chem., 58* (1986) 3058 - 3066.
5 H. Wohltjen, W. R. Barger, A. W. Snow and N. L. Jarvis, A vapor-sensitive chemiresistor fabricated with planar microelectrodes and a Langmuir Blodgett organic semiconductor film, *IEEE Trans. Electron Devices, ED-32* (1985) 1170 - 1174.

Biographies

Jay W. Grate is a Research Chemist at the U.S. Naval Research Laboratory. After completing his undergraduate education (B.A. in chemistry, 1978) at Rollins College, he went on to the University of California, San Diego as a National Science Foundation Pre-doctoral Fellow. His Ph.D. degree (chemistry), which he completed in 1983, was based on studies in organometallic and bio-inorganic chemistry. From 1983 to 1984 he conducted post-doctoral research on the organometallic chemistry of the lanthanides at the University of California, Irvine. Since joining NRL in 1984, his work has addressed several areas of chemical sensor research, including the use of sorptive materials, semiconductive coatings and Langmuir–Blodgett films for vapor sensing, and the development of automated instrumentation for sensor evaluation.

David S. Ballantine, Jr. was born on Long Island, NY in 1955. He received a B.S. from the College of William and Mary in 1977, and a Ph.D. in analytical chemistry from the University of Maryland, College Park Campus, in 1983. He has been employed by Geo-Centers, Inc. as a research chemist at the NRL facility in Washington, D.C. since 1984. His current research involves investigating vapor/coating interactions using SAW devices, and the testing and development of SAW devices as chemical sensors.

Hank Wohltjen was born in Staten Island, NY on July 20, 1950. He received a B.S. in chemistry in 1972 and a B.S. in engineering science (electrical) in 1974, both from the City University of New York, and a Ph.D. in chemistry from the Virginia Polytechnic Institute, Blacksburg, VA. His dissertation research was in the area of surface acoustic wave chemical sensors. From 1978 to 1980 he was an IBM postdoctoral fellow in the electron beam lithography group at the Thomas J. Watson Research Laboratory, and during this period was also employed in the New Devices group at IBM's research laboratory in Zurich, Switzerland. He joined the U.S. Naval Research Laboratory as a research chemist in 1981 and initiated research in the area of chemical microsensors based on surface acoustic wave devices, organic semiconductors and optical waveguides. In 1985 he founded Microsensor Systems, Inc., an organization dedicated to research and development of chemical microsensor instrumentation.

Reprinted from Analytical Chemistry, 1986, 58, 2883.

Optical Waveguide Humidity Detector

David S. Ballantine*

Geo-Centers, Inc., Suitland, Maryland 20746

Hank Wohltjen

Microsensor Systems, Inc., P.O. Box 90, Fairfax, Virginia 22030

The relative humidity of ambient air can have a significant impact on many physical and chemical processes of industrial interest (*1-5*). As a result, research toward the development of sensitive and reliable humidity sensors has increased. Current developments have centered around either electronic devices (e.g., moisture-sensitive resistors, capacitors, or conductive cells), or colorimetric devices. The electronic sensors exhibit sensitivity to temperature as well as humidity, whereas colorimetric reagents, such as metal salts of Co^{2+}, Cu^{2+}, or V^{5+}, are highly selective for moisture with little or no temperature dependence. These colorimetric reagents are usually suspended in gels or in adsorbent paper. The extent of hydration is determined by visual inspections, which are highly subjective and nonquantitative.

The use of colorimetric reagents coated on an optical waveguide has been demonstrated (*6*). Such devices have the advantage of higher sensitivity and quantitative precision compared to visual methods. The use of an optical fiber sensor for humidity measurements has been described by Russell and Fletcher (*7*). They employed a cobalt chloride/gelatin film on a silica optical fiber as the humidity probe. These probes were attached to an optical system consisting of a visible light monochromator and a photodetector. While this system was useful in demonstrating the applicability of optical devices as humidity sensors, it is not practical for field applications.

In this work we describe an optical waveguide humidity sensor that also uses a cobalt chloride/polymer film. It utilizes small, inexpensive optical components that enhance the practical nature of the device for use in the field, or for other applications requiring a portable detector. Experimental results and response characteristics are presented, and possible improvements of the devices are discussed.

THEORY

The optical waveguide is related to internal reflection spectroscopy, which has been described in detail by Harrick (*8*). It takes advantage of the fact that light will propagate through a medium (i.e., a glass rod or optical fiber) by internal reflection. The lightwave can interact with a second material which is in contact with the reflecting surface of this medium. The degree of interaction is related to the angle and wavelength of the incident light and the refractive indexes of the two media.

If the refractive indexes of the waveguide and the coating material are nearly equal, then the lightwave is not reflected at the glass/film interface, but travels unimpeded into the film (see Figure 1). The lightwave would then be reflected at the film/air interface. If light is absorbed as it passes through the film, then the waveguide can be used for spectroscopic analyses. The more reflections that occur, the greater the degree of interaction of the lightwave with the film. The sensitivity of the device is thus a function of the length and thickness of the waveguide.

EXPERIMENTAL SECTION

A. Device Components. The waveguide humidity detector consists of an optical waveguide coated with a reagent/polymer film, a light source, a photodetector, and an associated electronics package.

The light sources used in this study were light emitting diodes (LEDs). They are relatively inexpensive, and commercially available in four spectral ranges (red, orange, yellow, green). Phototransistors were used as photodetectors. Like the LEDs, they are suitable for use in a small device, are relatively inexpensive, and commercially available. The spectral response of the phototransistors used in this study drops off dramatically below 600 nm, so only the red (660 nm) and orange (635 nm) LEDs were used as light sources.

The waveguide consisted of a thin-walled glass capillary tube (~1.1 mm o.d. × 90 mm long; 0.2 mm thick wall). One end of these capillary tubes was rounded off, which aided in focusing the transmitted light onto the phototransistor. Clear plastic rods were used to manufacture optical couplers that were bored to accommodate the individual components (see Figure 2). These couplers held the optical components in a rigid, reproducible geometry which eliminated the need to strictly control the wavelength or angle of incident light. In addition, these couplers enhanced the transmission of light from the LED to the waveguide, and from the waveguide to the phototransistor. Cells to hold the waveguide were fashioned out of plastic rods that were

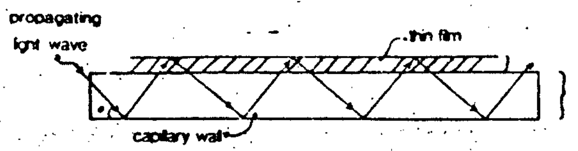

Figure 1. Diagram illustrating the interaction of an internally reflected lightwave with a thin film coated on the surface of a glass capillary waveguide.

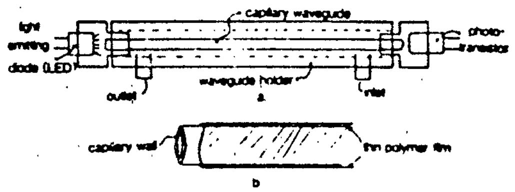

Figure 2. Diagram of the components comprising the optical waveguide detector.

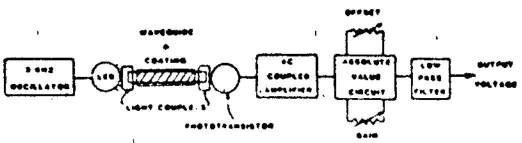

Figure 3. System diagram for the optical waveguide humidity detector.

bored to hold the optical components. These cells have a very small dead volume and were painted black to prevent the introduction of stray light.

The electronics package (Figure 3) consists of a modulated LED power source and signal processor which amplifies, demodulates and filters the phototransistor voltage. A 3-Hz RC timed, astable multivibrator circuit is used to pulse modulate the LED. Modulation of the light source is essential for reducing the effects of temperature drift in the phototransistor dark current. Without modulation, small variations in phototransistor temperature would produce unacceptable variations in the base line signal. The phototransistor signal was amplified by using an ac coupled op-amp and fed into an absolute value circuit and low pass filter which provided a dc voltage level proportional to the intensity of light striking the phototransistor. Small variations in light intensity produced by changes in the waveguide coating characteristics produced very easily measured changes in the output voltage of the electronics system. The system also was equipped with offset and gain controls to permit output signal adjustment to 0% and 100% transmittance conditions.

B. Reagent Films. The colorimetric reagent selected for testing with this device was $CoCl_2{\cdot}6H_2O$. The anhydrous salt ($CoCl_2$) is blue and exhibits a strong absorption peak between 600 and 750 nm. When hydrated, the absorption peak shifts to 500 nm, characteristic of the $CoCl_2{\cdot}6H_2O$ complex. This behavior is completely reversible and is well suited for probing with LEDs that produce 635–660 nm wavelengths of light.

Since the anhydrous cobalt chloride is a crystalline salt that does not readily adhere to the surface of the waveguide, it was suspended and immobilized in a poly(vinylpyrrolidone) (PVP) film. The PVP film has a refractive index of 1.53 (9), which is slightly greater than that of the soda lime glass waveguide (n_D = 1.49). Under these conditions, light would travel unimpeded through the glass/film interface and be reflected at the film/air interface. In addition, PVP is optically transparent in the wavelength region used for this study.

We were interested in determining the effect of various film parameters on the device response. For this reason, solutions were prepared in acetone/H_2O that contained varying concentrations of $CoCl_2{\cdot}6H_2O$ (from 30 mg/mL to 230 mg/mL). Known weights of poly(vinylpyrrolidone) (PVP) were then added to these solutions to produce solutions containing 0.75–3.0% (w/w) of PVP. In addition, solutions of just $CoCl_2{\cdot}6H_2O$ and just PVP were prepared to examine the effect of each component on the overall response.

Prior to coating with reagent/polymer films, the waveguides were etched for 5 min in a buffered, dilute HF solution. Reagent films were then applied using one of two different methods.

Table I. Film Reagent Concentrations and Reponse Characteristics

film label	[$CoCl_2{\cdot}6H_2O$], mg/mL	% PVP (w/w)	100% T, mV	response time, s
AB 1	133	2.0	1900	57
AB 2	161	1.5	1200	51
AB 4	168	0.75	850	47
AB 5	67	1.0	825	49
AB 6	230	0.86	1210	70
AB 10	100	1.0	1250	52
AB 12	100	1.0	1720	47
AB 17	200[a]	1.5	3560	170
AB 18	200[b]	1.5	2450	88
DIP 1	30	1.0	2430	66
DIP 10	100	1.0	1710	52

[a] Thick. [b] Thin.

The first method involved dip-coating the waveguides by immersing them in a solution and slowly withdrawing them. As the solvent was evaporated with a heat gun, a light blue film of $CoCl_2$/PVP was deposited on the surface of the waveguides. The second method involved using an air brush to spray a light mist of reagent/solvent on the waveguide surface, which was then dried using a heat gun. The films produced by dip coating were thicker, and contained areas of high $CoCl_2$ concentrations, indicated by spots of darker blue color. Air brush films were generally thinner and more evenly distributed. Waveguides coated with these films were exposed to varying concentrations of water vapor at 22 °C. The introduction of water vapor to the cell, and the acquisition of response data were controlled by the computer system described below.

C. Analytical System. A gas handling system was designed and constructed to control the introduction of vapor and/or diluting air to the sensor. Flow rates of water-saturated air and dry air were controlled with variable rotameters. Introduction of clean, dry air or water-saturated air to the sensor was controlled by solenoid valves which had been interfaced to an Apple IIe microcomputer via the I/O game-controller. The percent relative humidity of water-saturated air was assumed to be ~95% when calculating the relative humidity of diluted vapor streams.

Voltage data from the phototransistor were collected by the Apple II via an A/D converter card. Voltage vs. time data were plotted by using our own data acquisition program.

Before data were collected, a waveguide was inserted into the holder assembly, the LED was turned off, and the zero adjustments were made. The LED was then turned on, and the null adjustment was used to produce an output voltage just greater than 0 V. The device was then ready for testing.

RESULTS AND DISCUSSION

Response characteristics and film properties are listed in Table I. Individual films are identified as air-brushed films (AB) or dipped films (DIP). Examples of typical humidity reponse curves are given in Figure 4. In general, the response follows an S-shaped curve, with percent transmission increasing rapidly in the range of 60–85% relative humidity (RH), and then gradually leveling off as 100% RH is approached. This behavior holds true for all $CoCl_2$/PVP films.

Films of PVP alone exhibited no significant response to water vapor. It appears that the polymer film serves two purposes; first, it acts as a binder to ensure long life and good contact between the reagent film and the waveguide surfaces, and second, it acts as a protective, semipermeable membrane to regulate the introduction of water vapor to reagent. Films containing $CoCl_2$ alone exhibited poor adherence to the waveguide surface. Signal losses were noted, which may be the result of light scattering off $CoCl_2$ crystals.

To determine the effect of film variables on response, response times were determined for each film and are summarized in Table I. These response times represent the time required for the device response to level off at a maximum

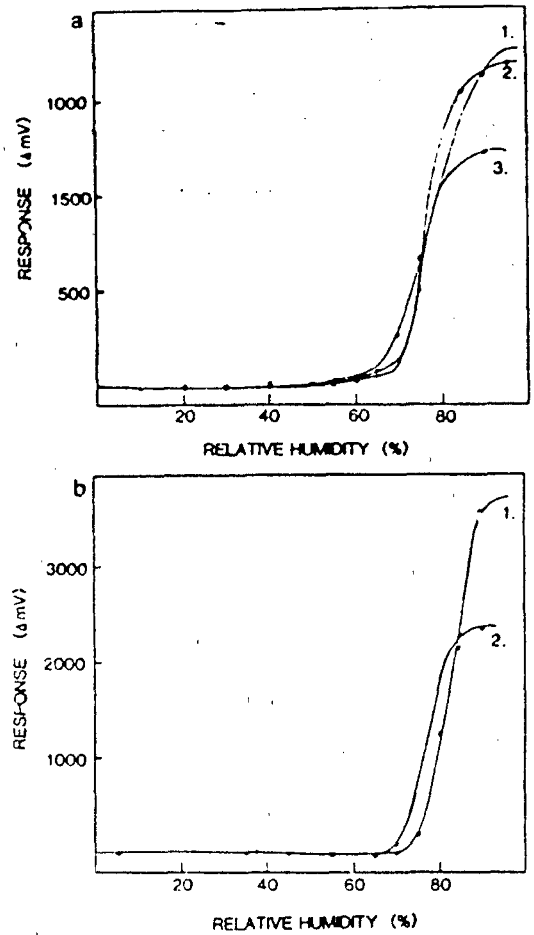

Figure 4. These S-shaped curves are typical of the waveguide device response (ΔmV) vs. percent relative humidity (% RH). (a) Films prepared from solutions of 100 mg/mL $CoCl_2$ and 1.0% PVP. Curves are for the following films: (1) DIP 10; (2) AB 12; (3) AB 10. (b) Films prepared from solutions of 200 mg/mL $CoCl_2$ and 1.5% PVP. Curves are for the following films: (1) AB 17; (2) AB 18

value upon exposure to an air stream of 95% RH. The two variables examined were film thickness and cobalt chloride concentration.

To determine the effects of film thickness, response times for films prepared from the same solution were compared. Figure 4a shows response curves for three (3) films prepared from a solution 100 mg/mL of cobalt chloride and 1.0% (w/w) of PVP. Figure 4b shows response curves for two films prepared from a solution of 200 mg/mL cobalt chloride and 1.5% PVP. It is worth noting that while the maximum signals vary, the relative shapes of these curves are very similar.

Since the films in each case were prepared from the same respective solutions, any difference in response times should be due to difference in film thickness. A qualitative assessment of relative film thicknesses can be made by comparing maximum signals (100% T); thicker film containing more $CoCl_2$ would exhibit a larger difference between 0% and 100% T.

For the three films represented in Figure 4a, no appreciable difference in response times is observed, even though the maximum signals differ by 30%. For the films represented in Figure 4b, however, there is an obvious increase in response time with film thickness. The data also indicate some dependence of response time on $CoCl_2$ concentration for some films but this effect is not as strongly indicated as the effect of film thickness.

The dependence of response time on film thickness is readily explained, in that it takes longer for a thick film to become saturated and reach equilibrium with water vapor than for a thin film. For films with high concentrations of cobalt chloride, it is possible that microcrystals of the metal salt have formed within the film. Such microcrystals may be responsible for the increased response times observed for some films containing high concentrations of $CoCl_2$.

CONCLUSIONS

The waveguide humidity sensor presented here exhibits very good sensitivity in the range of 60–95% RH. The general response data follow an S-shaped curve, and are comparable to the results obtained by Russell and Fletcher. Our results indicate that the portable, inexpensive device described here can be used to obtain reliable humidity measurements.

Before the device can be utilized as a throw-away device, better agreement between individual waveguides is necessary. This involves applying uniform, reproducible films on individual capillary waveguides. The device could then be developed as is for use in specific cases where the desired humidity levels are within the range of good response.

Further development of the reagent/polymer film may extend the region of reliable response of the present device. Such film development could include the use of polymer/copolymer films of different hygroscopicity (e.g., poly(vinyl alcohol) (PVA) or poly(styrenesulfonic acid) (PSSA), or combinations of different metal salts as reagents.

In addition, some form of temperature monitoring or control would be desirable to facilitate conversions from parts per million (H_2O) to percent relative humidity and vice versa.

ACKNOWLEDGMENT

Work was performed in the Chemistry Division, Code 6170, Naval Research Laboratory, Washington, DC 20375-5000.

Registry No. $CoCl_2$, 7646-79-9.

LITERATURE CITED

(1) Meade, K. E.; Auerback, I; and Erickson, R. H. *Org. Coat. Plast. Chem.* 1981, *44*, 336–342.
(2) Alfred, R. E.; Roylance, D. K. *J. Mater. Sci.* 1983, *18*, 652–656.
(3) McMurray, P. H.; Wilson, J. C. *J. Geophys. Res.* 1983, *88*, 5101–5108.
(4) Ferron, G. A. *J. Aerosol Sci.* 1977, *8*, 251–267.
(5) Tanto, J.; Ambrus, A; and Visi, E. *Pestic. Chem.: Hum. Welfare Environ., Proc. Int. Congr. Pestic. Chem., 5th, 1982* 1983, *4*, 129–134.
(6) Giuliani, J. F.; Wohltjen, H.; Jarvis, N. L. *Opt. Lett.* 1983, *8*, 54–56.
(7) Russell, A. P.; Fletcher, K. S. *Anal. Chim. Acta* 1985, *170*, 209–216.
(8) Harrick, N. J. *Internal Reflection Spectroscopy*; Interscience: New York, 1967.
(9) *Polymer Handbook*; Bandrup, J., Immergut, E. H., Eds.; Wiley: New York, 1974; pp 111–243.

RECEIVED for review August 27, 1985. Resubmitted May 30, 1986. Accepted June 10, 1986. This research was supported in part by USAFSAM, San Antonio, TX 78235.

Reprinted from Analytical Chemistry, 1986, 58, 3058.

Correlation of Surface Acoustic Wave Device Coating Responses with Solubility Properties and Chemical Structure Using Pattern Recognition

David S. Ballantine, Jr.

Geo-Centers, Inc., 4710 Auth Place, Suitland, Maryland 20746

Susan L. Rose and Jay W. Grate*

Chemistry Division, Naval Research Laboratory, Washington, D.C. 20375-5000

Hank Wohltjen

Microsensor Systems, Inc., P.O. Box 90, Fairfax, Virginia 22030

Twelve surface acoustic wave device coatings were exposed to 11 chemical vapors and responses were correlated with solubility properties and coating structure to determine possible vapor/coating interaction mechanisms. Hydrogen bonding ability is implicated as a significant vapor/coating interaction mechanism. Pattern recognition schemes applied to the preliminary data aided in solubility property/response correlations. Principal component analysis demonstrated good separation of different classes of chemical vapors tested. Hierarchical clustering provided additional evidence of the correlations between solubility properties and the observed clustering. In addition, pattern recognition methods were used to determine potential selectivity of an array detector using these coatings. Learning techniques show that one-fourth of the sensor can adequately separate compounds of interest from chemically similar interferences.

Surface acoustic wave (SAW) devices exhibit great potential as small, very sensitive chemical sensors. The principles of operation have been described in detail (*1*), but they are essentially mass-sensitive detectors. They consist of a set of interdigital transducers that have been microfabricated onto the surface of a piezoelectric crystals. When placed in an oscillator circuit, an acoustic Rayliegh wave is generated on the surface of the crystal. The characteristic resonant frequency of the device is dependent on transducer geometry and the Raleigh wave velocity. Small mass changes or elastic modulus changes on the surface perturb the wave velocity and are readily observed as shifts in this resonant frequency. The extreme sensitivity of these devices makes them attractive as potential gas sensors. The 112-MHz dual SAW devices routinely used in our laboratory, for example, have a theoretical sensitivity of >17 Hz/(ng/cm^2). Considering that the active area of the device covers 0.17 cm^2 and assuming a signal to noise ratio of 3, this sensitivity results in a minimum detectability of about 0.2 ng (*1*).

The ultimate performance of a SAW device as a chemical sensor is critically dependent on the sensitivity and selectivity of the adsorbent coating applied to the surface of the piezoelectric crystal. However, no systematic investigation of adsorbent coatings on SAW devices has yet been reported, and references to responses of specific SAW coatings to specific vapors are few in number (2-5). The most closely related sensor technology is the bulk piezoelectric crystal sensor, which has been reviewed (6). Coatings exhibiting selectivity to specific vapors have been identified in some cases, but many coatings have been of ill-defined composition and, until recently, selection has been largely empirical (6-11). It is therefore essential to identify coatings for SAW devices which respond to vapors of interest and to develop a rationale for the selection or design of such coatings.

The development of adsorbent coatings alone may not be sufficient for some applications of these devices. It is unlikely that any given material possesses sufficient selectivity to permit accurate detection and identification of a single chemical vapor of interest in the presence of multiple, unknown interferences. A promising approach to this type of analytical problem is the use of pattern recognition techniques in conjunction with an array of sensors of varying selectivity. This approach has been applied to vapor response data from electrochemical sensors (12) and to the selection of coatings for piezoelectric crystal sensors (7).

Pattern recognition techniques, as applied to sensor data, can be described as follows. The sensors encode chemical information about the vapor in numerical form. Each sensor defines an axis in a multidimensional space. Vapors can be represented as points positioned in this space according to sensor responses. Vapors that produce similar responses from the set of coatings will tend to cluster near one another in space. Pattern recognition uses multivariate statistics and numerical analysis to investigate such clustering and to elucidate relationships in multidimensional data sets without human bias. In addition, the method can reduce interference effects and improve selectivity in analytical measurements.

In this study, we have generated a large data base consisting of the responses of 12 SAW coatings to 11 vapors at various concentrations, and we have analyzed these data by using pattern recognition techniques. Our objectives were 2-fold. First, we wished to gather sufficient data to investigate and possibly identify the types of vapor/coating interactions responsible for the observed SAW devices responses. Pattern recognition techniques assisted in this effort by clustering vapors with similar response patterns and by identifying similarities between coatings based on responses to vapors. Secondly, we wished to determine the ability of pattern recognition techniques in conjunction with SAW sensors to discriminate between vapors of interest and chemically similar interferences. Such discrimination is necessary for an array detector to be practical and effective.

EXPERIMENTAL SECTION

Materials. Solvents for vapor stream generation were commercial materials of 99.99% purity, except diethyl sulfide (98%, Aldrich) and dimethyl methylphosphonate (97%, Aldrich). These materials are listed in Table I.

The following coating materials were obtained from Aldrich: abietic acid, octadecyl vinyl ether/maleic anhydride copolymer, poly(epichlorohydrin), *cis*-poly(isoprene), and acrylonitrile/butadiene copolymer (0.45/0.55). Poly(vinylpyrrolidone) and OV210 were purchased from Alltech. The two polyphosphazines are proprietary materials and were obtained courtesy of Ethyl Corp. Poly(ethylene maleate) was prepared as described by Snow and Wohltjen (2). Poly(amidoxime) was prepared by reaction of the acrylonitrile/butadiene copolymer (Aldrich) with hydroxylamine. Subsequent IR analysis indicated a nitrile to amidoxime ratio of 0.38/0.07 (13). Fluoropolyol was prepared using methods described by O'Rear et al. (14). These materials and their structures are given in Table II.

Analytical System. The 112-MHz dual SAW delay lines used in this study were fabricated photolithographically on polished S-T Quartz substrates (1 cm × 1 cm × 0.08 cm thick). The electrodes were made of gold (100 Å thick) deposited onto titanium (about 200 Å thick) to provide adhesion. Each electrode array consisted of 50 "finger" pairs with each electrode 7 μm wide and spaced 7 μm from the next finger. The electrode arrays had an aperture of 0.224 cm. The devices were clamped into a Teflon holder using small pressure clips and screws. A lid attached to this holder was fitted with inlet and outlet tubes to provide a vapor flow path. The two delay lines used in this system were connected as shown in Figure 1.

Table I. Test Vapors and Solubility Parameters

	π^*	β	α
Permeation Tubes, Class 1			
methanesulfonyl fluoride (MSF)			
N,N-dimethylacetamide (DMAC)	0.88	0.76	0.0
dimethyl methylphosphonate (DMMP)[a]		(0.81)	(0)
Bubblers, Class 2			
1,2-dichloroethane (DCE)	0.81	0.00	0.0
water	1.09	0.18	1.17
isooctane (ISO)[a]	(0.0)	(0.0)	(0.0)
toluene (TOL)	0.54	0.11	0.0
diethyl sulfide (DES)[a]	0.36	0.28	0.0
tributyl phosphate (TBP)[a]	0.65	0.77	0.0
2-butanone (BTN)	0.67	0.48	0.0
1-butanol (BTL)	0.47	0.88	0.79

[a] These values are unpublished data from Abraham (25). Values in table for DMMP are taken from a similar compound, DEP; values for isooctane are taken from 2,4-dimethylpentane.

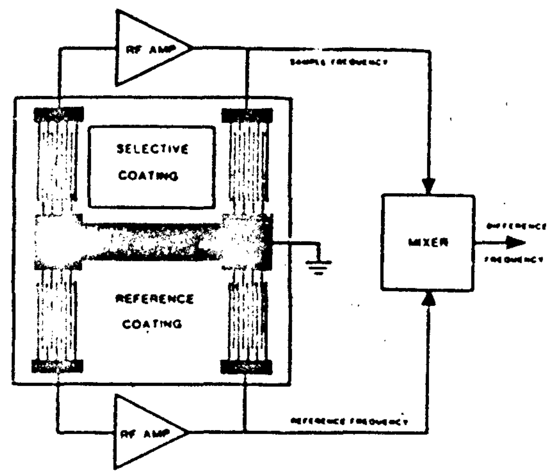

Figure 1. 112-MHz SAW device and associated electronic circuit diagram.

Dilute solutions of the coating materials were prepared in volatile solvents, usually chloroform, tetrahydrofuran, or a methanol/chloroform mixture. To make chemical sensors, one delay line was coated with the material under investigation using an airbrush. Coating deposition produced frequency shifts of 75–200 kHz, which were recorded and used as a measure of film thickness for normalization and comparison of data (1).

The uncoated delay line acted as a reference oscillator to provide compensation for ambient temperature and pressure fluctuations. Each delay line was connected to a TRW 2820 wide band rf amplifier to provide the amplification required for oscillation to occur. The frequencies obtained from each oscillator were mixed in a double balance mixer (Mini Circuits Labs SRA-1) to provide the low-frequency differences signal which was measured. Frequency measurements were made with a Systron-Donner frequency counter, Model 6042A. The frequency counter was interfaced to an Apple IIe microcomputer via an IEEE 488 bus and interface card.

Vapor Generation System. Vapor streams were generated with an automated gas handler system interface with an Apple IIe microcomputer. Plumbing connections were made by using

Table II. Coating Materials and Structures

COATING	STRUCTURES	HYDROGEN BOND ACCEPTOR–DONOR (% OF TOTAL)
POLY (ETHYLENE MALEATE) (PEM)	$[\text{-O-C(=O)-CH=CH-C(=O)-O-CH}_2\text{-CH}_2\text{-}]$	CARBONYL (HBA)-20% O-LINKAGE (wHBA)-11%
OCTADECYL VINYL ETHER/ MALEIC ANHYDRIDE COPOLYMER (OVERMAC)	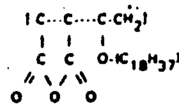	CARBONYL (HBA)-14% O-LINKAGE (wHBA)-8%
POLYVINYLPYRROLIDONE (PVP)	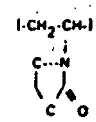	CARBONYL (HBA)-25% N (HBA)-13%
ACRYLONITRILE/ BUTADIENE COPOLYMER (PBAN)	$[\text{-CH}_2\text{-CH=CH-CH}]_{55}[\text{CH}_2\text{-CH}_2\text{-}]_{45}$, with C≡N on CH	NITRILE (HBA)-22%
POLY (AMIDOXIME) (PAOX)	C≡N $[\text{-CH}_2\text{-CH=CH-CH}_2\text{-}]_{(55)}$ $\text{-}[\text{-CH}_2\text{-CH-}]_{(38)}$, with C≡N on CH $\text{-}[\text{-CH}_2\text{-CH-}]_{(07)}$, with $\text{H}_2\text{N-C=N-OH}$ on CH	NITRILE (HBA)-19% AMIDOXIME (HBA-D)-3%
POLY (EPICHLOROHYDRIN) (PECH)	$[\text{-O-CH}_2\text{-CH-}]$, with CH_2Cl on CH	O-LINKAGE (wHBA)-17%
ABIETIC ACID (ABACD)	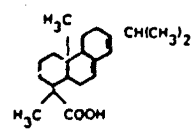	CARBOXYL (HBA-D)-15%
OV210	$[\text{-Si-O-}]$, with CH_3 and $\text{CH(CH}_3\text{CF}_3)$ on Si	O-LINKAGE (wHBA)-10%
FLUOROPOLYOL (FPOL)	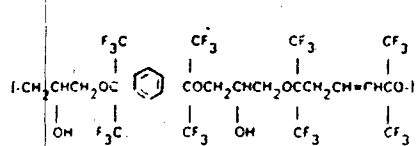	HYDROXYL (HBA-D)-4%
POLY (ISOPRENE) (PIP)	$[\text{-C-CH=C-CH}_2\text{-}]$, with CH_3 on C	NONE (NHB)
POLYPHOSPHAZINES (PPZN1, PPZN2)	----	----

$^1/_8$-in. stainless steel or nickel tubing. The carrier gas was compressed air that was dried by passage through Drierite. Flow rates were controlled with mass flow controllers (Tylan).

Individual vapor streams were generated from one of up to eight bubblers, or one of up to four permeation tubes. Air flow to bubblers was maintained at 39 mL/min, while flow rates to permeation tubes varied from 39 to 200 mL/min, depending on the desired concentration. Additional air for dilution could be added downstream, up to a total volumetric flow of 1200 mL/min. Based on the accuracy of the mass flow controllers, the uncertainties in the total volumetric flow rates were 1.7%. A constant system output of 39 mL/min to the sensor was maintained by a piezoelectric precision gas leak valve. This system will be described in more detail elsewhere (15).

The bubblers consisted of stainless steel vessels containing approximately 100 mL of solvent, with inlet and outlet tubes of $^1/_8$-in. stainless steel tubing. Vapor mass flow rates were determined by adsorbing the vapor output onto clean, dried charcoal traps. The traps were weighed after 15–20 min collection periods, and mass flows were determined. Two traps in series were periodically used to check for breakthrough. Multiple successive determinations resulted in calculated mass flow (in mg/min) with errors of less than 6%.

A calibrated permeation tube containing methanesulfonyl fluoride was purchased from G.C. Industries (Chatsworth, CA). Permeation tubes containing 1-3 mL of dimethyl methylphosphonate or *N,N*-dimethylacetamide were prepared using 1-$1^1/_2$ in. lengths of Teflon heatshrink tubing ($^3/_8$ in. i.d., Cole-Parmer) capped at both ends with Teflon rods. These tubes were stored in a desiccator for 1-3 weeks and then calibrated at operational temperatures (DMMP, 50 °C; DMAC, 25 °C). The tubes were weighed every 2-3 days until constant permeation rates (in µg/min) were obtained. Permeation rates had errors of less than 10%.

Data Collection and Analysis. During coating testing, the difference frequency output of the sensor was recorded every 2 s at 1 Hz resolution. In a typical experiment, the sensor was exposed to air for 1 min to establish a base line response. This was followed by repeated exposures of vapor/air/vapor/air, with each exposure of 2-min duration.

Each of the 12 coatings was exposed to 11 chemical vapors. Each vapor was run at four different concentrations, with two experiments (four vapor exposures) at each concentration. Frequency shifts caused by these vapor exposures were determined by integrating the area under the signal peak and averaging over the number of data points collected. An equilibration time of 20 min was scheduled at the beginning of each new vapor to allow the vapor stream to achieve equilibrium. At the completion of the experiments for a given vapor, the gas handler system was flushed with clean air for 10 min.

Pattern Recognition. Since dividing the sensor responses by concentration is not possible for a field instrument measuring unknowns, it is important for each sensor to be exposed to the same concentrations, and to apply a closure method (such as pattern normalization) to the results. The data were collected on individual sensors rather than an array. As a result, the sensor data for a given vapor were not always collected at the same concentration for each sensor. To get the same concentrations for each vapor across a pattern vector, responses for some sensors were interpolated from the calibration curves. For most of the 11 vapors, average frequency shifts were determined for two experiments at each of three concentrations. Only two concentrations resulted in satisfactory responses for MSF, while all four concentrations of DMMP were consistent for all of the sensors tested. These response values, or descriptors, for the 11 vapors formed a 66 × 12 data matrix. Each row in the matrix is a pattern vector, representing responses of the 12 coatings to a given vapor/concentration experiment.

These data were then analyzed on a VAX 11-750 using pattern recognition routines included in ADAPT (16). The pattern vectors were normalized using pattern normalization methods described previously (12). The normalization procedure removes the effects of concentration and the sensitivity of one vapor relative to another. This is necessary to obtain the maximum amount of chemical information from vapors that give only weak responses. Each descriptor for a given coating was then autoscaled to a mean of zero and a standard deviation of unity. Although autoscaling alters the actual values of the sensor responses, it does not alter the number of features or the basic geometry of the clustering (16).

Multiple linear regression was used to investigate the uniqueness of each sensor while testing for collinearities which could cause numerical instabilities in the analysis. After the set of sensor responses was checked for collinearities, pattern recognition techniques for display and mapping, clustering, and classification were implemented.

Because it is impossible to imagine the data points clustering in *n*-dimensional space, a display method was used to transform the data into two-dimensional space for easier visualization. The Karhunen–Loeve transformation finds the axes in the data space that account for the major portion of the variance while maintaining the least amount of error. A correlation matrix for the stored data set is computed and the eigenvalues and eigenvectors are then extracted. The two-principal-component plot presents the plane that best represents the data (17). For display purposes, a nonlinear mapping routine is used to separate vapors that overlap when projected onto this plane but are separated in the multidimensional space. The nonlinear mapping routine transforms a set of points from *n*-space to two-space by maintaining the simularities between the points. It does this by minimizing an error function (18).

Clustering techniques, which are unsupervised learning techniques because the routines are given only the data and not the class membership of the points, group compounds together according to some criterion. By examination of the different clustering results, a clearer insight is gained into the actual clustering in *n*-space (17). ADAPT includes a variety of agglomerative hierarchial clustering routines which group the data by progressively fusing them into subsets, two at a time, until the entire group of patterns is a single set. The routines maintain a particular within-group homogeneity, depending on the criterion and the fusing strategy used. Three dissimilarity metrics were used: (a) Euclidean distance squared, (b) Euclidean distance, and (c) Canberra distance. The fusing strategies investigated were (a) nearest neighbor, (b) median, (c) average, and (d) flexible fusion. Resulting data are displayed in dendrograms (19).

Classification methods, which are also considered supervised learning techniques because they are given both the data and the correct classification results, generate mathematical functions to described the clustering. There are two basic modes of operation for classification methods: (a) parametric, and (b) nonparametric. Parametric techniques use statistical information based on the underlying data to define the boundaries of the clusters. Their performance is based on the assumption made concerning the statistical characteristics of the data. The nonparametric techniques use mathematics to define the area between the clusters. The primary parametric programs used in these studies are Bayes linear and quadratic (17), while the nonparametric routines were the perception (17) and adaptive least-squares (ALS) (20).

To achieve the best classification results, each sensor response is multiplied by a constant so that the contribution of each sensor is weighted. The vector that is generated is called a weight vector. The routine iteratively updates the weight vector, and a decision surface can be located between the classes. The weight vector for a linear decision surface can be generated by one classifier, stored, and then used subsequently in another classifier. Weight vectors can be improved by passing them between classifiers.

Learning techniques are used to train the algorithm on the correct classification results. A discriminant function is found that separates one class from another. The width of the function is a measure of the separation. Feature selection is used to reduce the number of sensors to the smallest set while maintaining good classification results (14). One feature selection method randomly removes vapors from the data set for each analysis in multiple applications of the perception algorithm. As each vapor is removed, the variance in the weight vector is determined. If the observed variance is large, then the information from the corresponding sensor does not contribute significantly to the observed separation of classes.

RESULTS

Vapors used during this study are given in Table I. These vapors were chosen to represent a variety of structural and functional groups. In addition, we were specifically interested in coatings that would be sensitive to toxic organophosphorus compounds. The set of vapors contains three vapors selected as simulants of these materials. Methanesulfonyl fluoride is an irreversible enzyme inhibitor and, as such, exhibits biological activity similar to the organophosphorus insecticides (21). Dimethylacetamide has solubility properties that are similar to these materials, as indicated by the solubility pa-

Table III. Normalized Vapor Responses (10^{-3} Hz/(ppm/kHz))

vapors	PEM	OVEMAC	PVP	PBAN	PAOX	PECH	ABACD	FPOL	PIP	OV210	PPZN1	PPZN2
	coatings											
MSF	240	78	44	160	130	0.0	96	390	21	0.0	30	37
DMAC	650	60	0.0	38	290	210	39	1360	15.6	6.4	19	130
DMMP	6500	460	40	450	830	550	590	15800	230	204	310	990
DCE	4.2	0.9	2.0	3.4	4.2	3.0	3.3	2.4	2.5	0.4	0.5	0.9
water	2.8	1.3	4.8	0.3	0.4	0.6	0.4	0.2	0.09	0.2	0.2	0.7
ISO	0.7	0.6	0.13	0.4	0.4	0.4	1.9	0.4	1.7	0.3	0.0	0.4
TOL	3.8	1.3	0.7	3.9	4.8	3.9	9.4	0.12	3.7	0.6	0.5	1.4
DES	4.4	1.3	0.4	3.4	4.0	4.1	8.7	3.0	3.7	0.5	0.4	1.7
TBP	24	3.6	33	6.4	17	7.2	13.8	13	0.08	29	3.7	
BTN	3.6	0.5	0.5	1.8	1.9	2.0	2.2	5.0	0.54	0.3	1.3	1.9
BTL	11	2.7	11	3.4	8.9	2.6	18	8.0	1.0	0.7	0.9	1.1

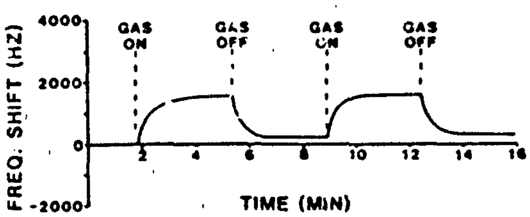

Figure 2. Typical SAW device reversible response.

rameter values in Table I. Dimethyl methylphosphonate (DMMP) is structurally similar to many of the organophosphorus pesticides. These three vapors are grouped together and labeled class 1 vapors. The remaining vapors are called class 2 and represent a very general set of potential interferences. Note that tributyl phosphate is also an organophosphorus compound. It has been included in class 2 specifically to test the ability of the coatings and pattern recognition techniques to distinguish between chemically similar compounds. Included in the table are solvatochromic parameters, which are a scale for comparing the solubility properties of these vapors (22, 23). These parameters are a measure of the dipolarity/polarizability (π^*), hydrogen bond donor acidity (α), and hydrogen bond acceptor basicity (β). The ranges of values in the tables are evidence of the generality of the set of selected vapors. No data are available directly for DMMP or isooctane. Values in the table for DMMP are based on values for a similar compound, dimethyl ethylphosphonate (DMEP). Values for isooctane are based on values for 2,4-dimethylpentane. These parameters will be correlated with observed response behavior in the discussion section.

Adsorbent coatings exhibited good response times, usually reaching 90% of total response within 1 min. At high vapor concentrations, the response time was more a function of the system dead volume than of the coating response behavior. At lower concentrations, however, responses may have been affected by longer equilibration time between vapor and coating, or by adsorption of vapor onto tubing walls. Upon removal of the vapor stream, a rapid return to stable baseline was usually observed. A typical response is shown in Figure 2. Reversible responses were observed for all vapor/coating pairs given in Table III. Frequency shift data were used to generate calibration curves. The slopes of these curves in Hz/ppm (vapor), were then normalized by dividing by the film thickness (in kHz). Normalized responses are presented in Table III.

Coating materials and their structures are given in Table II. Because we were interested in detecting organophosphorus compounds, coatings were selected based on preliminary tests that indicated a sensitivity to DMMP. Coating sensitivities to other vapors in this study were not known, and extreme selectivities to DMMP and other class 1 vapors were not

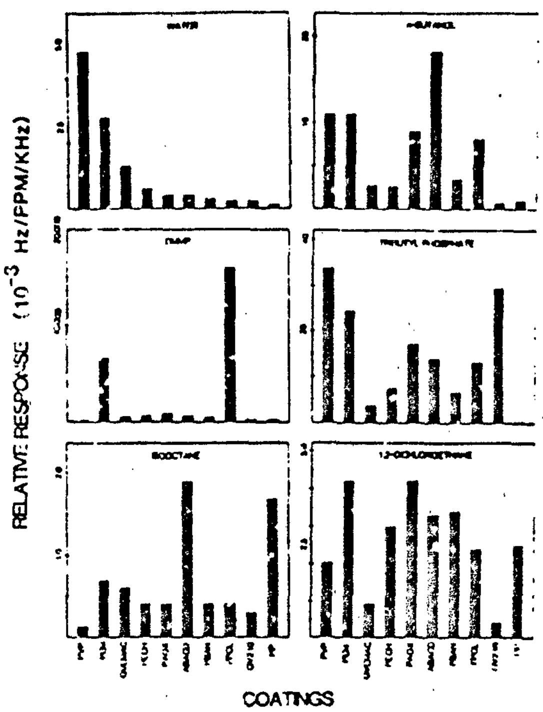

Figure 3. Bar graphs showing relative response patterns of 10 coatings to specific vapors.

suspected. In general, most of the coatings were more sensitive to class 1 than to class 2 vapors and exhibited particularly good sensitivity to DMMP. Poly(ethylene maleate) and fluoropolyol were the most sensitive coatings for detecting DMMP and other class 1 vapors. The response of fluoropolyol to DMMP was the response of greatest magnitude in the entire data set and was at least 2000 times greater than its response to any class 2 vapor. The coating that was least sensitive to DMMP was poly(vinylpyrrolidone). While it was the most sensitive coating for water, its response to water was still 10 times less than its response to DMMP.

Noise levels of 10–15 Hz are associated with the SAW devices. Assuming a S/N ratio of 3, the minimum detected signal is 45 Hz. For a 100-kHz film of fluoropolyol, for example, this translates into detection limits of 0.03 ppm for DMMP and <2000 ppm for water. For a 100-kHz film of poly(vinylpyrrolidone), these detection limits are 11 ppm and 100 ppm, respectively.

Individual bar graphs showing the relative responses of the 12 coatings to six of the vapors are shown in Figure 3. For display, responses are normalized to the coating with the greatest responses, while the scale of actual response (in

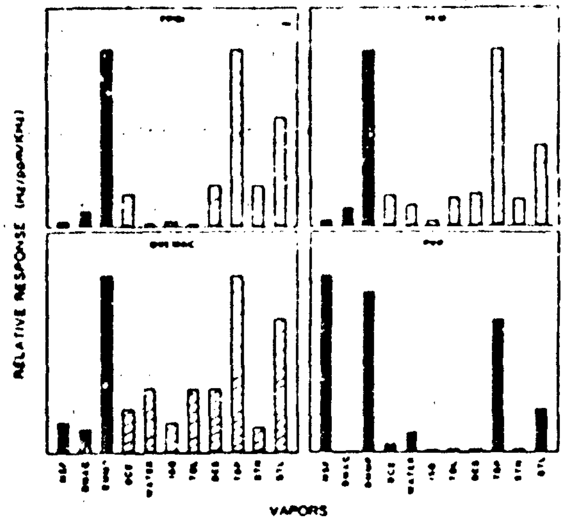

Figure 4. Bar graphs showing relative response patterns of four coatings normalized to class 1 vapors (solid bars) and class 2 vapors (parallel striped bars).

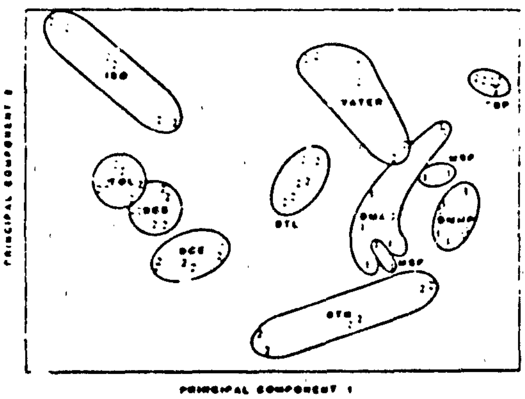

Figure 5. Principal component plot using results from all 12 coatings.

Hz/(ppm/kHz) is given on the y axis. Similarly, bar graphs showing the responses of four of the coatings to all 11 vapors are shown in Figure 4. The solid bars shown are all normalized to the vapor eliciting the highest response. In most cases, the class 2 vapors elicited much lower responses than class 1 vapors. For this reason, the response patterns for these vapors are not easily seen when plotted on the same scale as the class 1 vapors. To display the relative responses of the class 2 vapors on the same graph, the class 2 vapors were normalized to the highest class 2 response. Bars have been superimposed in Figure 4 to show the response pattern of the normalized class 2 vapors.

Pattern Recognition. The multiple linear regression results indicate that the correlation between sensors is not strong, so individual coatings could not be eliminated on the basis of redundancy. According to eigenanalysis, ten sensors account for 99% of the variance, indicating that at least two of the sensors can be removed without reducing the separation between compounds. The first two principal components from the Karhunen-Loeve transformation were used to initialized the nonlinear mapping routine. The resulting plot is shown in Figure 5. Class 1 and class 2 compounds are labeled on the plot with a 1 or a 2, respectively. It is clear that responses for individual vapors tend to cluster in discrete sectors of space with well-defined boundaries. In addition, class 1 vapors tend to cluster near one other. Vapors cluster in n-space based on similarities in response patterns. These clusters may indicate

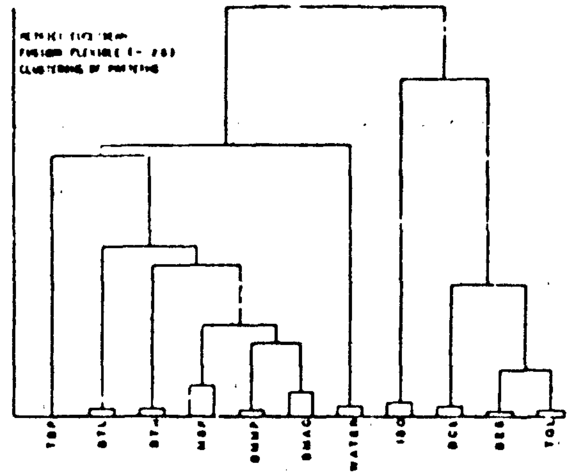

Figure 6. Typically hierarchical cluster results of all the vapors based on all 12 coatings (Euclidean distance metric with flexible fusion).

Table IV. Weight Vector Components for Four Best Coatings

coating	weight vector value	no. wrong class 1	no. wrong class 2	% recognition
		[illegible]	0	100
OVEMAC	−0.06783	3	1	93.9
PEM	0.11633	2	8	84.9
PVP	−0.80966	18	0	72.7
FPOL	0.20978	14	6	69.7

similarities in vapor/coating interaction mechanisms for these vapors.

Hierarchical cluster analysis produce similar results for each metric. The fusion methods, however, produced different groupings. Flexible fusion was selected for display because it is space conserving and does not change the relationships between the groups of data (24). The dendrogram resulting from hierarchical cluster analysis on one third of the data set is shown in Figure 6. The original matrix was reduced to simplify visualization. Results from the second experiment of the two highest concentrations were selected. The y axis of the dendrogram is a measure of the dissimilarity of response patterns for given vapors. Thus, diethyl sulfide and toluene exhibit very similar response patterns, and the lines representing the response patterns for these vapors converge very low on the y axis of the dendrogram. Conversely, the lines for water and isooctane do not converge, indicating very dissimilar response patterns.

Similarities and dissimilarities in the coating were examined by applying cluster analysis on the transpose of the 66 × 12 matrix. Since no structural information was available for the polyphosphazine coatings, information derived from these coatings is of limited value. Disregarding the response data for these coatings, cluster analysis was also applied to the transpose of the resulting 66 × 10 matrix. These results are displayed in Figure 7.

By use of classification routines and feature selection to reduce the sensors with the most variance, four coatings were found that could separate class 1 from class 2 vapors. These were poly(ethylene maleate), fluoropolyol, octadecyl vinyl ether/maleic anhydride copolymer, and poly(vinylpyrrolidone). The hyperplane between the two classes can be given a dead zone (or a width of 1000 times the normal width produced by the routines), which indicates that the classes are well separated. With all four coatings, 100%

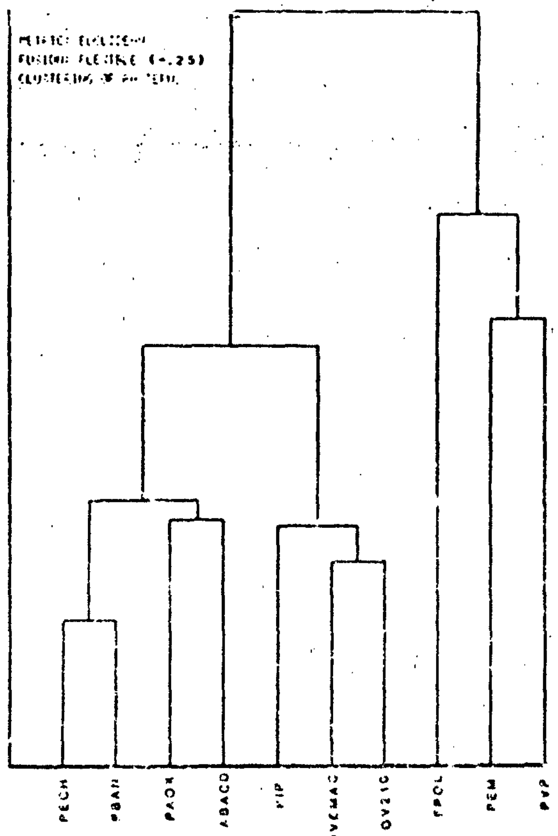

Figure 7. Typical hierarchical cluster results of coatings based on responses to 11 vapors (Euclidean distance metric with flexible fusion).

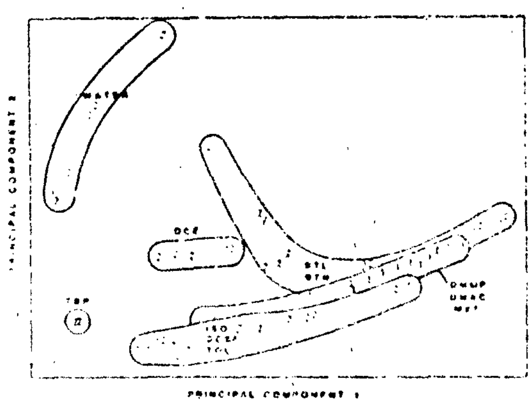

Figure 8. Principal component plot using results from the four best coatings: PEM, FPOL, PVP, OVEMAC.

recognition of vapors as class 1 or class 2 is possible. Eliminating octadecyl vinyl ether/maleic anhydride copolymer decreases this to 94%, which still represents reasonably good discrimination. The weight vectors for these coating are given in Table IV. Of these coatings, fluoropolyiol and poly(vinylpyrrolidone) are most important for the correct classification of class 1 vapors, while poly(ethylene maleate) is important for class 2 vapors.

The nonlinear mapping plot from the two principal components using these four coatings is shown in Figure 8. While the cluster spaces for some of the vapors appear to overlap the boundary for class 1 compounds is still well defined. The dendrogram produced by Euclidean metrics and flexible fusion for these coatings is given in Figure 9. Class 1 compounds

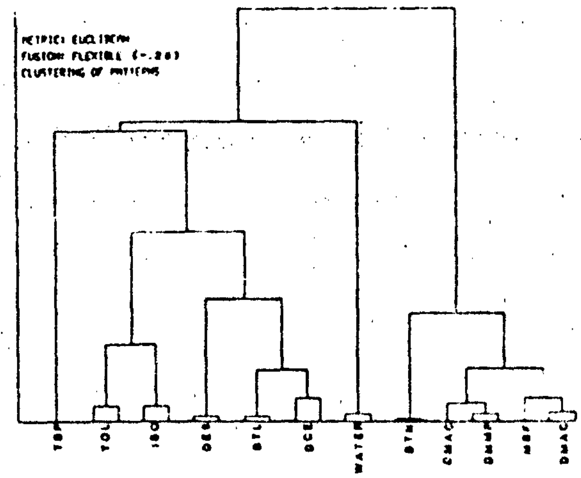

Figure 9. Typical hierarchical cluster results of the vapors for the best four coatings (Euclidean distance metric with flexible fusion).

are clustered very closely, and except for butanone, are well separated from the interference vapors.

DISCUSSION

In the course of discussing these results we will attempt to develop a rationale to be used in future coating design and/or selection. The solvatochromic parameters in Table I represent a relative scale for comparing solubility properties of the vapors. The values in the table are for bulk solutions and do not describe all possible solubility interactions. For the purposes of the discussion they represent a reasonable first approximation of the solubility properties of these materials. By correlating observed responses with these parameters, we hope to identify the vapor/coating interaction mechanisms that are responsible for our results.

Since no quantitative scale is available to characterize the solubility properties of the coating materials, qualitative estimates of relative hydrogen bond acceptor (HBA) and hydrogen bond donor (HBD) strengths were made based on the weight percentages of HBA and HBD functional groups in their structure. These percentages are reported in Table II. Materials lacking any hydrogen bonding functional groups were labeled non hydrogen bonding (NHB). All these materials are polymers with the exception of abietic acid, which is a crystalline organic material. Since no structural information was available for the polyphosphazines, results for these coatings will not be included in the discussions of structure/response correlations.

The vapor/coating interaction could be modeled as the dissolution of a solute vapor in a solvent coating. It is reasonable to model the coatings as a solvent phase since all the polymers were employed above their glass transition temperatures. The response should be determined by solubility interactions, e.g., dipole-dipole and hydrogen bond interactions. The data set as a whole indicates that the solubility properties represented by the parameters in Table I are important in determining SAW device responses. The six vapors whose response patterns are illustrated by the bar graphs in Figure 3 are representative of various classes of vapors, based on solubility properties. Water is a strong HBD and a weak HBA; 1-butanol is both HBD and HBA; DMMP and tributyl phosphate are HBA but not HBD; isooctane is a NHB vapor with little or no dipolarity/polarizability; and dichloroethane is a NHB vapor with significant dipolarity/polarizability. The bar graphs in Figure 3 show that vapors with different solubility properties elicited different coating response patterns. Vapors with similar solubility properties, such as DMMP, dimethylacetamide, and 2-butanone have more similar response patterns (see data in Table III). DMMP and tributyl phosphate, however, have easily distinguishable response patterns but have a similar solubility properties. Closer examination shows that this is primarily due to poly(vinylpyrrolidone), fluoropolyol, and OV210. While the overall response of the remaining coatings is still more sensitive to DMMP, the general response pattern of these coatings is more similar.

The reason for which all the coatings were most sensitive to DMMP is not clear. Examination of the solubility parameters in Table I indicates that DMMP is not exceptional in its hydrogen bonding ability. Therefore, the extremely high response of these coatings to DMMP must be due to some solubility property that has not been characterized in Table I, such as its dipolarity/polarizability, or to a fortuitous combination of solubility properties.

The noted differences observed between DMMP and tributyl phosphate are also likely due to differences in a solubility parameter that is not examined here. Structurally, these vapors differ in size, with tributyl phosphate containing large alkyl groups that may significantly affect its solubility in certain materials.

Hierarchical cluster analysis provides a more systematic determination of the similarity or dissimilarity of the various vapors, as determined by SAW sensor responses. The resulting dendrogram in Figure 6 sorts the vapors in a manner that is consistent with their solubility properties. Starting from the top of the plot and working down (toward increasing similarity), the NHB vapors on the right are separated from the HBA and HBD vapors on the left. Isooctane is separated from the other NHB vapors, a result consistent with the unique character of isooctane as indicated in Table I. It is the only vapor with near zero dipolarity/polarizability. The NHB vapors with significant dipolarity/polarizability (1,2-dichloroethane, toluene, and diethyl sulfide) are more similar to one another than they are to isooctane or the HBA and HBD vapors. In this cluster, dichloroethane stands out in the dendrogram and in Table I as the NHB vapor with the greatest dipolarity/polarizability.

Among the HBA and HBD vapors on the left of the dendrogram, water is the least similar to any other vapors. Accordingly, water is seen in Table I to have extremely highly dipolarity/polarizability. It is also unusual in its relatively high HBD character. The other HBD vapor, 1-butanol, has significantly greater HBA character and less dipolarity/polarizability than water and is shown in the dendrogram to be more similar to the other HBA vapors. In general, the HBA vapors cluster together, with DMMP and dimethylacetamide being the most similar. These results demonstrate that the solubility properties in Table I should be considered as important factors affecting SAW sensor responses.

Exceptions to these general trends must also be considered. For example, methanesulfonyl fluoride clusters with the other HBA vapors, but it is a weak HBA vapor and may be more similar to that of diethyl sulfide, a NHB vapor. Similarly, tributyl phosphate does not cluster as closely to DMMP as [illegible] be expected based on the fact that both are organo[illegible] compounds with similar HBA strength. [illegible] therefore, emphasize the importance of [illegible] to the solubility properties in Table I.

[illegible] coating properties and structures in deter[illegible] be fully determined by these [illegible] will be influenced by a mixture of [illegible] various structural features such as [illegible] aliphatic side chains, and hetero atomic [illegible] difficult to determine [illegible] relevant solubility [illegible] of these coatings have not yet been identified.

We can, however, explore the role of hydrogen bonding interactions by using the relative scale of HBA and HBD strengths in Table II. With the exception of poly(isoprene), all of the coatings contain heteroatoms capable of accepting hydrogen bonds. HBA strength should be significant for those coatings containing carbonyls of nitrogen-containing groups. Weaker HBA strength is expected for those coatings containing only ether linkages. Three of the coatings also contain HBD groups (fluoropolyol, poly(amidoxime), and abietic acid). Water and butanol are the only HBD vapors in our data set. Of these, trends in the response to water vapor are most likely due to HBA strength of the coatings because water has stronger HBD than HBA strength and has no aliphatic character. For this reason, coatings were listed on the x axis of Figure 3 in order of decreasing response to water.

The results in Figure 3 show that the relative coating responses to water tend to follow the relative HBA strengths estimated from the weight percentages of the HBA functional groups in the coating structures. This confirms that hydrogen bonding interactions are important and justifies consideration of the simple scale in Table II. While water also has considerable dipolarity/polarizability properties, the data indicate no correlation with polarity. Nonpolar isooctane does not exhibit a trend opposite to that exhibited by water nor does polarizable dichloroethane follow any apparent trend. The other HBD vapor, 1-butanol, exhibits a different response pattern. This may be due to greater HBA strength and more organic character relative to water.

On the low end of this scale, poly(isoprene) is the only NHB vapor coating in this study. It exhibits a much larger response to the NHB vapor isooctane than any other coating, with the exception of abietic acid. In addition, the responses of poly(isoprene) to other NHB vapors (dichloroethane, toluene, and diethyl sulfide) are larger than for the HBA and HBD vapors in class 2. In general, the other coatings exhibit higher responses to class 2 HBA vapors, particularly TBP and butanol, than to the NHB vapors.

The bar graphs in Figure 4 and the data in Table III indicate that all the coatings, except poly(vinylpyrrolidone), have a fundamental similarity. They are more sensitive to class 1 than to class 2 vapors. Cluster analysis helps to more clearly identify similarities and dissimilarities among the coatings. In the dendrogram in Figure 7, fluoropolyol, poly(ethylene maleate), and PVP stand out as being most dissimilar to other coatings and also dissimilar to one another. These results can be related to the data by examining the bar graphs in Figure 3. Relative to the other coatings, fluoropolyol has very strong response to DMMP, a weak response to water, and average responses to tributyl phosphate and isooctane. Poly(ethylene maleate) exhibits strong response to DMMP, water, and tributyl phosphate, and an average response to isooctane. Poly(vinylpyrrolidone) has strong responses to water and tributyl phosphate, but gives the weakest responses to DMMP and isooctane. In relating the dendrogram results to structure it is worth noting that poly(vinylpyrrolidone) may be the most basic of the coatings in the data set. Poly(ethylene maleate) may be the most polar, since it has polar groups in the backbone and no side chains. Fluoropolyol is distinctive in its combination of structural features, such as fluoroaliphatic, aromatic, ether, and hydroxyl groups.

[illegible] among the coatings are shown in the dendrogram by the clustering of poly(isoprene), octadecyl vinyl [illegible] anhydride copolymer, and [illegible]. These all have substantial hydrophobic character. The cluster containing [illegible](epichlorohydrin), abietic acid, acrylonitrile-butadiene [illegible] and poly(amidoxime) [illegible] is a modification of the acrylonitrile-butadiene copolymer. The modification created a small percentage

(0.07) of HBD groups. As a result, poly(amidoxime) clusters slightly closer to abietic acid, which also has HBD groups, than to its parent polymer. A previous study of 27 coating materials on piezoelectric sensors demonstrated that clustering of these materials may be influenced by structural similarities (7). Fewer coatings were used in our data set, and the coatings employed were structurally more diverse. As a result, such clustering is not as evident.

CONCLUSIONS

The solubility properties considered in this paper were systematically demonstrated to be important factors in determining SAW sensor responses. The exceptions noted indicate the limitations of using bulk solution values in describing dilute solutions and also indicate that additional properties not yet considered may also exert some influence. Solubility properties currently provide the best rationale for selecting or designing coatings for specific applications. A more detailed investigation of the relationship between structure and observed solubility properties would also facilitate the selection and design processes.

Pattern recognition techniques were valuable in extracting information regarding vapor/coating interactions from this multidimensional data set. In addition, it is clear that the combination of multiple sensor arrays of coated SAW devices and appropriate pattern recognition software will provide a sensor system that can be selective as well as sensitive for a broad spectrum of compounds.

ACKNOWLEDGMENT

The authors wish to thank the following persons for their efforts: Peter Jurs for his guidance in the pattern recognition work; Arthur Snow and James Griffith of the NRL Polymeric Materials Branch, NRL, for supplying us with much of the coating materials and related structures; and M. J. Kamlet and Michael Abraham for much informative discussion. Research was performed at Naval Research Laboratory, Washington, DC.

Registry No. MSF, 558-25-8; DMAC, 127-19-5; DMMP, 756-79-6; DCE, 107-06-2; ISO, 540-84-1; TOL, 108-88-3; DES, 352-93-2; TBP, 126-73-8; BTN, 78-93-3; BTL, 71-36-3; PEM, 25949-13-7; OVERMAC, 28214-64-4, PVP, 9003-39-8, PBAN, 9003-18-3, PAOX, 103496-60-2; PECH, 24969-06-0; ABACD, 514-10-3; FPOL, 104051-33-4; PIP, 9003-31-0; H_2O, 7732-18-5.

LITERATURE CITED

(1) Wohltjen, H. *Sens. Actuators* **1984**, *5*, 307.
(2) Snow A.; Wohltjen, H. *Anal. Chem.* **1981**, *56*, 1411.
(3) Bryant, A.; Poirer, M.; Riley, G.; Lee, D. L.; Vetelino, J. F. *Sens. Actuators* **1983**, *4*, 105.
(4) D'Amico, A.; Palma, A.; Verona, E. *Sens. Actuators* **1982/1983**, *3*, 31.
(5) Chuang, C. T.; White, R. M.; Bernstein, J. J. *IEEE Electron. Device Lett.* **1982**, *3*(6), 145.
(6) Alder, J. F.; McCallum, J. J. *Analyst (London)* **1983**, *108*, 1169.
(7) Carey, W. P.; Beebe, K. R.; Kowalski, B. R.; Illman, D. L.; Hirschfeld, T. *Anal. Chem.* **1986**, *58*, 149.
(8) Fog, H. M.; Rietz, B. *Anal. Chem.* **1985**, *57*, 2634.
(9) Morrison, R.; Guilbault, G. *Anal. Chem.* **1985**, *57*, 2342.
(10) Guilbault, G.; Kristoff, J.; Owen, D. *Anal. Chem.* **1985**, *57*, 1754.
(11) Kindlund, A.; Sundgren, H.; Lundstrom, I. *Sens. Actuators* **1984**, *6*, 1.
(12) Stetter, J.; Jurs, P. C.; Rose, S. L. *Anal. Chem.* **1986**, *58*, 860.
(13) Jarvis, N. L.; Lint, J.; Snow, A. W.; Wohltjen, H. Proceedings of the 1983 Scientific Conference on Chemical Defense Research; CRDC-SP-84014; Dimmick, R. L.; Rausa, M., Eds. U.S. Army, 1984; pp 45–53; NTIS, ADB-09086L.
(14) O'Rear, J. G.; Griffith, J. R.; Reines, S. A. *J. Paint. Technol.* **1971**, *43*(552), 113.
(15) Grate, J. W.; Ballantine, D. S., Jr.; Wohltjen, H. *Sens. Actuators*, in press.
(16) Stuper, A. J.; Brugger, W. E.; Jurs, P. C. *Computer Assisted Studies of Chemical Structure and Biological Function*; Wiley-Science: New York, 1979.
(17) Tou, J. T.; Gonzalez, R. C. *Pattern Recognition Principles*; Addison-Wesley: Redding, MA, 1974.
(18) Beech, G. *Fortran IV in Chemistry*; Wiley: New York, 1975.
(19) Massart, D. L.; Kaufman, L. *The Interpretation of Analytical Chemical Data by Use of Cluster Analysis*; Wiley: New York, 1983.
(20) Moriguchi, I.; Komatsu, K.; Matsushita, Y. *J. Med. Chem.* **1980**, *23*, 20.
(21) Dafforn, A.; Neenan, J. P.; Ash, C. E.; Betts, L.; Finke, J. M.; Garman, J. A.; Rao, M.; Walsh, K.; Williams, R. R. *Biochem. Biophys. Res. Commun.* **1982**, *104*, 597.
(22) Kamlet, M. J.; Taft, R. W. *Acta Chem. Scand., Ser. B* **1985**, *B39*, 611.
(23) Kamlet, M. J.; Abboud, J. M.; Abraham, M. H.; Taft, R. W. *J. Org. Chem.* **1983**, *48*, 2877.
(24) Williams, W. T.; Lance, G. N. In *Statistical Methods for Digital Computers*; Enslein, K., Ralston, A., Wilf, R., Ed.; Wiley-Interscience: New York, 1975.
(25) Abraham, M. H., personal communication.

Received for review April 15, 1986. Accepted June 19, 1986. The authors gratefully acknowledge the support of the coatings testing work by Army/CRDC, Aberdeen Proving Ground, MD (61-1633), and of the pattern recognition work by Brad Rikke, HQ AMD/RDSX, Brooks Air Force Base, TX (MIPR 86-0005).

Trace Chemical Vapor Detection Using SAW Delay Line Oscillators

HANK WOHLTJEN, MEMBER, IEEE, ARTHUR W. SNOW, WILLIAM R. BARGER, AND DAVID S. BALLANTINE

Abstract—**The resonant frequencies of SAW delay line oscillators are shown to be very sensitive to the presence of thin organic films that are deposited onto the delay line surface. Theory suggests that the sensitivity of the SAW device to mass loading depends on the square of the resonant frequency. This dependence has been studied experimentally using devices resonating at 31, 52, and 112 MHz that were coated with organic films of precisely controlled composition and thickness. The mass sensitivity of SAW oscillators can be exploited to make very sensitive chemical sensors if an appropriate sorptive coating is applied to the device. Results obtained from a SAW delay line oscillator operating at 290 MHz (the highest frequency SAW chemical sensor reported to date) suggest that the rapid detection of organic vapors at concentrations substantially below 100 parts per billion (by volume) is readily achievable.**

Introduction

Chemical detectors based on SAW devices have been the focus of growing interest since the first studies were reported in 1979 [1]-[9] SAW chemical microsensors are very attractive because of their small size, ruggedness, and sensitivity. Numerous applications of SAW chemical microsensors to problems in environmental monitoring, chemical process control, and clinical analysis are being investigated. In all cases the SAW device is coated with a thin film that is capable of interacting with the chemical of interest through physical absorption, adsorption, or other chemical bonding mechanisms. The nature of this interaction determines the sensitivity, selectivity, and operational reversibility of the sensor.

The purpose of this study was two-fold. First, theoretical considerations predict that SAW oscillators should exhibit a sensitivity to changes in coating mass density that depends on the square of the unperturbed resonant frequency of the SAW device. If the square relationship holds then as frequency gets higher (and device size gets smaller) the sensitivity will increase. Experimental confirmation of this relationship was necessary to allow the accurate design and modeling of chemical detection instruments. The second purpose of this study was to investigate the performance of a very-high-frequency (290 MHz) SAW chemical sensor. We believe that this is the highest frequency SAW vapor sensor studied up to this date.

Theoretical Response of SAW Vapor Sensors

The signal provided by a SAW oscillator vapor sensor can be described by the following theoretically derived relationship (5):

$$\Delta f = (k_1 + k_2) f_0^2 h\rho' - k_2 f_0^2 h \left(\frac{4\mu'}{V_r^2} \left(\frac{\lambda' + \mu'}{\lambda' + 2\mu'} \right) \right) \tag{1}$$

where Δf is the SAW oscillator frequency change produced by the coating, k_1 and k_2 are material constants for the piezoelectric substrate, f_0 is the unperturbed resonant frequency of the SAW oscillator, h is the coating thickness, ρ' is the coating density, μ' is the shear modulus, λ' is the first Lamè constant of the coating, and V_r is the Rayleigh wave velocity in the piezoelectric substrate (3158 m/s for ST-quartz). This relationship assumes that the SAW device coating is isotropic, nonconducting, and nonpiezoelectric. Furthermore, the relationship is valid only for very thin films (e.g., less than 0.2 percent of the acoustic wavelength thick). For thicker films, (1) can only provide estimates of the signal magnitude. When organic coatings are employed, it is often found that the second term of (1) is negligible because the shear elastic modulus of the coating μ' is small compared to the stiffness of the SAW device. Under these conditions, (1) reduces to

$$\Delta f = (k_1 + k_2) f_0^2 h\rho'. \tag{2}$$

For Y-X quartz SAW devices, $k_1 = -9.33 \times 10^{-8}$ m^2 · s/kg and $k_2 = -4.16 \times 10^{-8}$ m^2 · s/kg. (Material constants for ST-quartz have not been published but are believed to be similar to those of Y-X quartz. Work is being conducted to calculate the values for ST-quartz and will be published elsewhere.) The product of the coating thickness h and its density ρ' is the mass per unit area on the device surface. Equation (2) predicts that the signal obtained from a given mass loading ($h\rho'$ product) will increase with the square of the operating frequency of the SAW oscillator. Furthermore, operating frequency determines the size of the device since it imposes size require-

Manuscript received March 17, 1986; revised September 23, 1985.

H. Wohltjen is with Microsensor Systems, Inc., P.O. Box 90, Fairfax, VA 22030, USA.

A. W. Snow and W. R. Barger are with Chemistry Division, Code 6170, US Naval Research Laboratory, Washington, DC 20375, USA.

D. S. Ballantine is with Geo-Centers, Inc., 4710 Auth Pl., Suitland, MD 20746, USA.

IEEE Log Number 8612197.

ments on the interdigital-electrodes used to generate the Rayleigh surface wave. As the operating frequency increases, the device area (and cost) decreases. Higher operating frequencies permit thinner coatings to be employed with a corresponding improvement in response time since vapor diffusion and equilibration with the coating will be more rapid. Higher operating frequencies also result in greater baseline noise, which hinders detection at the lowest concentrations. All of these considerations result in a set of scaling laws [9] that can offer guidance in predicting the ultimate performance capabilities of SAW vapor sensor technology. The key assumption in these predictions is that the sensitivity increases with the square of the frequency. Preliminary studies indicated that this theoretical model was valid [5]. Nevertheless, further studies were conducted to provide additional substantiating evidence of the model's accuracy.

Experimental Techniques

Resonant Frequency versus Film Thickness Study

In order to verify the preceding theoretical model, experiments were conducted on devices operating at frequencies of 31, 52, and 112 MHz. Devices designed for 290 MHz operation were not included in the study because the device package made it impossible to coat these devices using the Langmuir-Blodgett (L-B) technique. In this series of experiments, the frequency shift produced by different mass loadings applied to the SAW oscillator was measured.

1) SAW Device Configuration: The 31-, 52-, and 112-MHz SAW delay lines used in this study were all fabricated on *ST*-quartz. Gold electrode metallization was used. The interdigital transducers (IDT) consisted of 50 finger pairs having one-quarter-wavelength finger widths and spacings. The acoustic aperture of the IDT was a uniform 80 wavelengths in all cases. The center-to-center spacing between the IDT's was different for each device. On the 112 MHz device the IDT's were separated by 0.7392 cm (i.e., 264 wavelengths); at 52 MHz the separation was 1 cm (i.e., 166 wavelengths); and the 31 MHz device had an IDT separation of 3.5 cm (i.e., 350 wavelengths).

Each SAW device was mounted in a plastic holder fabricated with a slot into which the device could fit. Electrical connections were made using screws, threaded into the plastic holder, that pressed small gold clips against the large gold bus bars of the IDT's. This arrangement permitted the SAW devices to be removed and cleaned for reuse.

The RF electronic system for the 31-, 52-, and 112-MHz SAW delay line oscillators consisted of a TRW model CA2820 wideband RF amplifier with series tuning inductors connected between the input and output IDT's of the delay line. The experimental system is shown in Fig. 1.

2) Film Deposition Technique: A highly reproducible mass loading on each device was obtained from coatings of various thicknesses of an organic material deposited by the Langmuir–Blodgett technique. The coating material was a 1 : 1 mole ratio mixture of stearyl alcohol and copper tetracumylphenoxy phthalocyanine. This material and the L-B monolayer film transfer technique are described in greater detail elsewhere [10]. The material was chosen because its monolayer and multilayer film properties have been carefully studied in our laboratory. In general, the L-B film transfer technique requires a film material capable of forming a compressible film, one molecule thick, on the surface of ultra-clean water in a shallow trough. The mixed film used in this experiments has a complex structure that includes aggregates of the phthalocyanine. Compression of this film, by slowly sweeping a barrier across the water surface, causes it to become structurally ordered at the air–water interface. With the appropriate film material and substrate, dipping of the substrate into the trough allows one layer to be transferred with each pass through the air–water interface. Thus films of precisely known thickness can be deposited. The ability to control the film thickness with precision permits a highly reproducible mass loading to be applied to the SAW device. The entire surface of all devices was covered with the film.

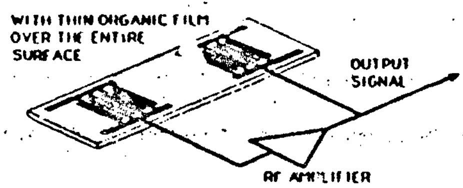

Fig. 1. SAW delay line oscillator configuration used to make frequency shift measurements under various Langmuir-Blodgett film mass loadings.

3) Experimental Procedure: Resonant frequencies were measured on a Fluke model 1910A digital frequency counter connected to the RF amplifier output of the delay line oscillator. Coatings were applied to the devices, which were then connected to the RF electronics for measurement of the resonant frequency. Then with the device still connected to the electronics, the coating was removed using a Q-tip soaked with a solvent (such as, chloroform) that could dissolve the coating. When the device was clean and dry, the resonant frequency was again measured. The difference between the clean and coated resonant frequencies was recorded as the frequency shift produced by the coating. It was expected that the same number of layers of coating would produce correspondingly greater frequency shifts as the device frequency was increased from 31 to 52 MHz and then to 112 MHz.

290-MHz Dual SAW Vapor Sensor Performance Demonstration

A second group of experiments was performed with the 290 MHz SAW device to demonstrate its performance in detecting organic vapors.

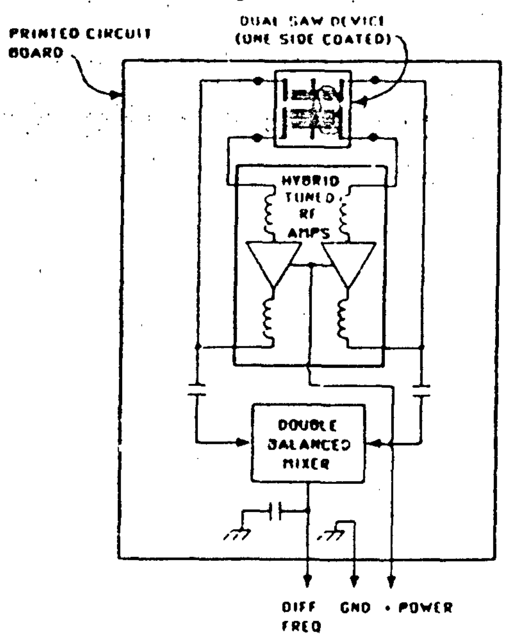

Fig. 2. Dual SAW delay line configuration used with 290-MHz vapor sensor.

SAW Device Configuration

A dual-SAW-delay-line oscillator configuration was chosen for the vapor sensor. In this design, two SAW delay lines are fabricated on the same *ST*-quartz substrate. One delay line is coated with the chemically selective film and the other is left uncoated. The frequencies of the two delay line oscillators are mixed to provide a frequency equal to the difference of the two oscillator frequencies (Fig. 2). This scheme helps to compensate for SAW frequency drifts caused by ambient temperature and pressure fluctuations. Furthermore, the difference frequency is much lower than the frequency of the oscillators themselves (e.g., several hundred kHz versus 290 MHz). This permits SAW vapor response measurements using inexpensive, digital counter circuitry.

The 290-MHz dual SAW device had an input transducer with 100 finger pairs of gold interdigital electrodes spaced ten wavelengths from an output transducer having 75 finger pairs. Each IDT had an acoustic aperture of 88 wavelengths. This arrangement was selected to provide a reasonably high resonant Q and minimal insertion loss from the coating. Overall size of the chip is 0.61 × 0.33 cm. The active area of each SAW delay line is approximately 0.02 square centimeters.

The SAW device was mounted in a conventional microelectronic eight-pin gold flat package in which the internal volume was less than 60 μl. The device was held in the package using epoxy. Electrical connections were wire-bonded from the device to the package connecting leads. The conventional gold lid of the device package was replaced with a piece of Lucite fitted with two $\frac{1}{16}$-inch stainless steel vapor inlet and outlet tubes. This lid was held onto the top of the device using a small C-clamp.

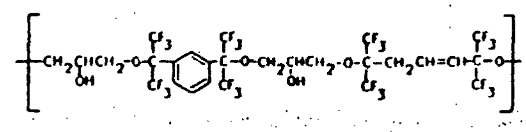

Fig. 3. Chemical structure of fluoropolyol coating used to demonstrate performance of 290-MHz SAW vapor sensor.

Hybrid technology was employed in the supporting RF electronic system. The two RF amplifiers required to power the dual-SAW-delay-line oscillators were contained in a 24-pin dual inline package. Each RF amplifier was of a simple single-transistor tuned circuit design. Chip resistors, capacitors and transistors were used along with chip inductors. The dual SAW device and RF module were connected together on a small printed circuit board to form a complete vapor sensor subsystem. Electrical power and output signal connections are made to this board. In addition, the mixer used in this device is mounted on the board external to the RF module. The mixer is a passive device (Mini-Circuits Lab, double balanced mixer, TFM-2). The total volume occupied by the sensor system is less than 1 in^3.

Selective Coating Deposition

SAW devices rely on a surface mass change to cause a shift in their resonant frequencies. A selective coating must therefore behave as a "sponge" in which the mass is increased by the vapor to be detected. The coating must exhibit a number of characteristics including chemical stability, adhesion to the device surface, permeability, and specificity to the vapors to be detected. A number of selective coatings have been studied for use with bulk wave quartz crystal gas sensors and are appropriate for use with SAW devices [11], [12]. In this investigation, a fluoroepoxy prepolymer, dubbed *fluoropolyol*, was used to evaluated the response of the 290-MHz SAW vapor sensor. It is an oligomeric material that is soluble in a number of organic solvents including chloroform. Prior investigations with this material at the Naval Research Laboratory showed that it possessed many desirable properties as a vapor absorbent coating. The material was synthesized and provided by Dr. Jim Griffith of the NRL Polymeric Materials Branch. Fig. 3 shows the structure fluoropolyol.

The technique selected to deposit this material onto the SAW device was air brushing. Other techniques such as LB dipping or spin casting could not be employed because the 290-MHz SAW devices were packaged and wire-bonded prior to coating. This made application of a uniform coating impossible. The only other method available was solvent evaporation in which a small drop of a dilute solution of coating in a volatile solvent is deposited onto the device surface and allowed to dry. This technique requires great care since the active area to be coated was only about 2 mm^2 in size.

The coating was applied by spraying through a small mask positioned over the active area of the delay line to be coated. A dilute solution of fluoropolyol in chloroform approximately 0.1 percent by weight was used. Compressed air was used as the propellant. The spray was adjusted to provide a barely visible deposit on a clean glass plate when sprayed from a distance of 3 in for 15 s. This spray was then used to coat the device from a distance of 6 in while the difference frequency was monitored with an oscilloscope and frequency counter. Multiple short bursts of the spray onto the device surface resulted in a coating that produced a total frequency shift of 260 kHz. Using (2), the average film thickness deposited is calculated to be approximately 240 Å (assuming uniform device coverage and a film density of 1 g/cm^3). The device was allowed to sit in clean, dry air for about 12 h prior to testing.

Measurement Apparatus

Exposure of the fluoropolyol coated SAW device to various vapor challenges was performed using a fully automatic vapor generating system designed and built at NRL. The system was capable of generating low concentrations of vapor (e.g., 0.1–10 ppm) using thermostatted and gravimetrically calibrated permeation tubes. Higher vapor concentrations (e.g., 100–10 000 ppm) could be generated using gravimetrically calibrated bubblers. Vapor streams from both the bubblers and permeation tubes could be diluted using precise computer-operated mass-flow controllers. Dry air was used as a carrier gas and the outlet of the system was at ambient pressure. All tubing in the system was stainless steel to minimize corrosion and wall adsorption. The flow rate of vapor presented to the sensor was computer controlled and programmable. Vapor generation and acquisition of sensor resonse data were performed with an APPLE IIe computer. The SAW sensor signal from the RF module was fed into a Systron-Donner model 6042 digital frequency counter that communicated to the computer via an IEEE-488 interface bus.

Experimental Procedure

One low-concentration target vapor (dimethyl acetamide; generated using a permeation tube) and eight high concentration interference vapors (dichloro ethane, water, toluene, isooctane, diethyl sulfide, tributyl phosphate, 2-butanone, and 1-butanol which were generated using bubblers) were used to test the SAW sensor. All experiments were conducted at room temperature with a carrier gas flow rate of 39 cm^3/min. The sensor was exposed repeatedly to clean air carrier and then to air contaminated with each vapor. The difference between the SAW frequencies measured during clean air and contaminated air exposure was used to determine the magnitude of sensor response. Data were obtained at four different concentrations for each of the vapors investigated.

RESULTS

Frequency Shift Versus Film Thickness Studies

Each layer of the L-B film used in this study is known to produce a mass loading of 570 ± 20 ng/cm^2 based on

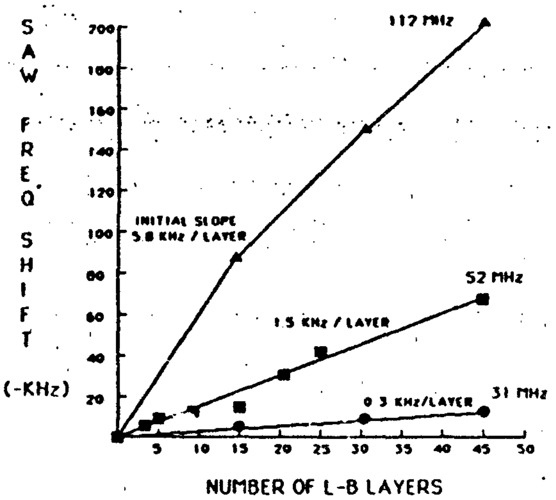

Fig. 4. Experimental frequency shifts obtained from various mass loadings on 31-, 52-, and 112-MHz SAW delay line oscillators.

TABLE I
THEORETICAL AND EXPERIMENTAL SAW OSCILLATOR SENSITIVITY TO L-B FILM MASS LOADING

SAW Frequency (MHz)	Theory (2) (kHz/Layer)	Experiment (kHz/Layer)
31	0.74	0.3
52	2.08	1.5
112	9.65	5.8

experimentally measured molecular areas [13], [14]. This value represents the product of film thickness and density and can be used in conjunction with (2) to predict the frequency shift expected by the mass loading only. The experimental results are presented in Fig. 4. Table I compares the experimental results with those predicted theoretically by (2). The dependence of device mass sensitivity on operating frequency is strong. There is a significant and systematic quantitative discrepancy between the experimental values and those predicted using a theory which neglects elastic effects in the film. Inspection of (1), which includes elastic effects, reveals that if the shear elastic modulus of the organic coating is not negligibly small, then the observed frequency shift will be diminished from that expected for mass loading alone. Unfortunately, values for the shear elastic modulus of the LB film used in this study are not known. Assuming that the discrepancy between experiment and theory is due entirely to elastic effects, one can use (1) to estimate that the L-B film had a shear elastic modulus in the range of 0.8 to 1.6×10^{10} N/m^2. Such values are higher than one might expect for an organic material [15]. They are, however, not unreasonable considering that most organic materials are viscoelastic and can exhibit a range of elastic moduli that can be large particularly as the measurement frequency is increased.

The primary purpose of these mass-loading experiments was to study the dependence of SAW device mass

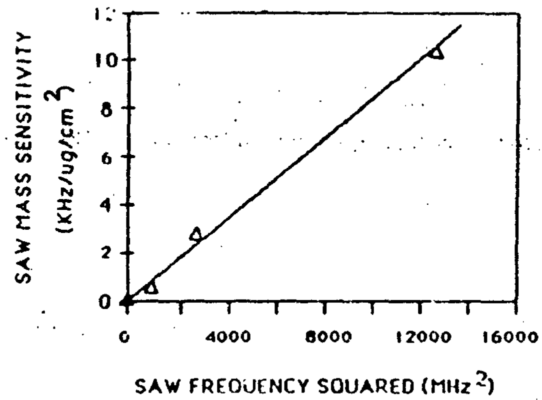

Fig. 5. SAW oscillator mass sensitivity plotted as function of operating frequency squared.

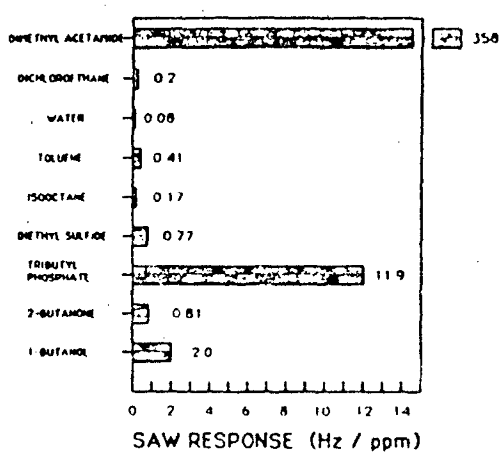

Fig. 6. Summary of 290-MHz dual SAW vapor sensor responses to various test vapors.

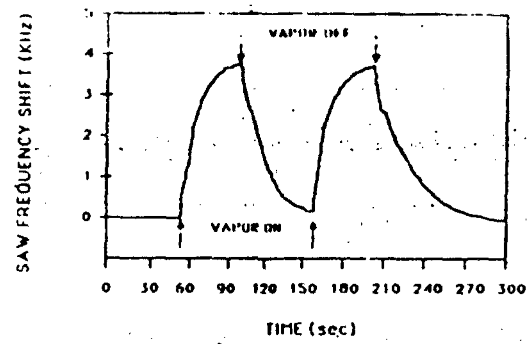

Fig. 7. Typical response of fluoropolyol coated 290 MHz SAW device exposed to consecutive pulses of 7.3 ppm of dimethyl acetamide (DMAC) in clean dry air.

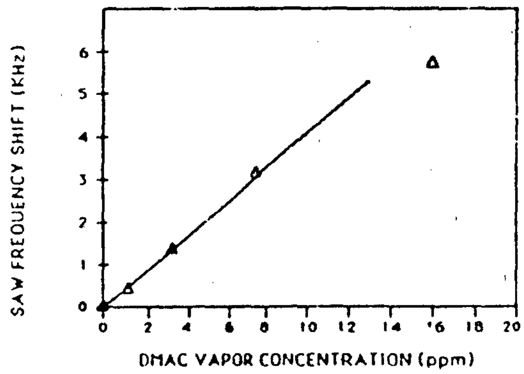

Fig. 8. 290-MHz dual SAW resonant frequency shift as function of DMAC vapor concentration.

sensitivity as a function of operating frequency. The mass sensitivity, expressed in kilohertz per microgram per square centimeter is plotted as a function of operating frequency squared in Fig. 5. The dependence of sensitivity on the square of the operating frequency is evident.

Chemical Vapor Responses

A summary of the vapor exposure data is illustrated graphically in Fig. 6. The responses are expressed in terms of SAW frequency shift (Hertz) per part per million of vapor concentration and represent the slopes obtained from a linear least squares fit of replicate data sets of sensor response to four concentrations of vapor. The actual vapor concentrations used were in the range of 1–16 ppm for dimethyl acetamide (DMAC), 5–30 ppm for tributyl phosphate and 200–4000 ppm for the remaining vapors. The results show that fluoropolyol exhibits the highest sensitivity for dimethyl acetamide (358 Hz/ppm) and the lowest sensitivity for water (0.08 Hz/ppm), isooctane (0.17 Hz/ppm), and dichloroethane (0.2 Hz/ppm). Solubility considerations allow this behavior to be predicted, at least qualitatively. Fluorinated compounds like fluoropolyol are quite hydrophobic and are not likely to accomodate very much water in the polymer. Similarly, fluoropolyol is expected to be an excellent hydrogen bond acid that should interact strongly with a hydrogen bond base like dimethyl acetamide. It is clear that the coating is not uniquely selective for any of the vapors tested. Nevertheless, the fluoropolyol is still more than 30 times more sensitive to DMAC than to tributyl phosphate, the worst interferent. The selectivity against water vapor is very good with the fluoropolyol responding about 4400 times more strongly to DMAC than to water.

Fig. 7 shows a typical response profile obtained from two consecutive 45 s on-off exposures to 7.8 ppm (by volume) of DMAC in clean and dry air. The results illustrated in Fig. 7 are quite typical and could be repeatedly duplicated after a complete series of vapor exposures had been performed. The baseline frequency of the sensor did exhibit slow drift that was believed to be related to thermal effects. In a laboratory environment with no sensor temperature control, the baseline frequency drift was typically less than 1 kHz per hour. A calibration curve for DMAC is shown in Fig. 8. The response is quite linear at low concentrations and decreases at higher concentrations. This behavior is quite typical. At a DMAC concentration of 1.3 ppm, the sensor is providing a signal of almost 500 Hz with a baseline noise level of less than 30 Hz. From (2) it is possible to calculate that a mass change of approximately 90 pg has been detected. This small amount of material is, nonetheless, able to produce a signal-to-noise ratio of more than 16 to 1. A vapor concentration detection limit of about 0.1 ppm can be estimated from these results. The study represents the first attempt at vapor detection using the 290 MHz SAW sensor. Further improvements to the system which reduce the noise or increase the signal will yield still lower detection limits.

The observed response time of the 290 MHz dual SAW sensor is less than 30 s and is probably limited by the ability of the vapor generator to switch vapor streams and establish equilibrium, rather than by the response time of the sensor itself. If the response time is limited solely by the rate of diffusion into the coating, then one expects to observe a very rapid response. Fickian diffusion coefficients for organic vapors and polymers are typically in the range of 10^{-8} cm^2/s. For a polymer film that is 1000 Å thick, a vapor diffusion time of about 5 ms is expected. As film thicknesses decrease, the sensor response time is expected to decrease greatly. This is due to the fact that the time for diffusion to occur is inversely proportional to square of the coating thickness. In practice there are numerous factors (such as boundary layer transport rates) besides simple diffusion into a coating that are quite significant in determining the response time of the sensor. Nevertheless, substantial improvements in response times are observed as the operating frequency is increased since progressively thinner films are employed.

Conclusion

The L-B monolayer film transfer technique has been used successfully for producing precise surface mass loadings on SAW devices. The experiments described here have clearly demonstrated that SAW device mass sensitivity increases as a square function of the device resonant frequency. This has important implications in the design of practical vapor sensors since this dependence defines the physical scaling laws exhibited by the device. Experimental results also show that the elastic properties of the LB coating have a strong effect on the Rayleigh wave velocity since the observed frequency shifts cannot be explained by mass changes alone.

A 290-MHz dual-SAW-delay-line oscillator and a hybrid RF electronics module has been demonstrated that can rapidly detect trace organic vapors at concentrations below 1 ppm. This is the highest frequency SAW vapor sensor reported to date. While the selectivity obtained using the fluoropolyol coating was not ideal, it is likely that such selectivity will prove to be adequate for many practical applications, particularly when an array of sensor devices can be employed. An array of SAW devices, each having a different selective coating is being developed at NRL in conjunction with a computerized pattern recognition algorithm that can evaluate the array sensor response pattern and determine if an environmental hazard exists. High-frequency SAW devices are very attractive for array sensor applications because of their small size, ruggedness, and the fact that multiple devices can be fabricated on the same substrate.

Prior experience with SAW delay line oscillators has shown that the magnitude of the baseline noise is typically around one part in 10^7 of the resonant frequency. The noise performance of the coated 290 MHz device fell within this predicted range (i.e., about 30 Hz rms measured over a 10-s interval). Strongest responses were obtained when the sensor was exposed to DMAC, a compound for which the fluoropolyol was expected to be sensitive based on solubility considerations. A detection limit of about 0.1 ppm of DMAC is estimated for the present device. Modest improvements in coating technology (i.e., materials and methods of application) along with modest reductions in baseline frequency noise should permit the routine detection of a number of organic vapors at concentrations below the ten part per billion range.

Acknowledgment

The authors are grateful to their colleagues at NRL, particularly Dr. Jim Griffith of the NRL Polymeric Materials Branch for providing the fluoropolyol coating material used in this study, Mr. Mark Klusty for applying the L-B coatings, Dr. Jay W. Grate for his assistance in developing the vapor generation apparatus, Dr. James Murday of NRL and Mr. Thomas O'Shea and Mr. Robert Kindel of SAWTEK, Orlando, FL, for helpful discussions in the course of this work.

References

[1] H. Wohltjen and R. E. Dessy, "Surface acoustic wave probe for chemical analysis. Parts I–III," *Analytical Chem.*, vol. 5, no. 9, pp. 1458–1475, 1979.

[2] A. Bryant, D. L. Lee, and J. F. Vetelino, "A surface acoustic wave gas detector," in *Proc. IEEE 1981 Ultrason. Symp.*, pp. 171–174.

[3] C. T. Chuang, R. M. White, J. J. Bernstein, "A thin membrane surface acoustic wave vapor sensing device," *Electron. Dev. Lett.*, vol. EDL-3, no. 6, pp. 145–148, 1982.

[4] A. D'Amico, A. Palma, and E. Verona, "Surface acoustic wave hydrogen sensor," *Sensors and Actuators*, pp. 31–39, 1982/1983.

[5] H. Wohltjen, "Mechanism of operation and design considerations for surface acoustic wave vapor sensors," *Sensors and Actuators*, pp. 307–325, 1984.

[6] A. Snow and H. Wohltjen, "Poly(ethylene maleate)-cyclopentadiene: A model reactive polymer-vapor system for evaluation of a SAW microsensor," *Analytical Chem.*, vol. 56, no. 8, pp. 1411–1416, 1984.

[7] S. J. Martin, K. S. Schweizer, S. S. Schwartz, and R. L. Gunshor, "Vapor sensing by means of a ZnO-on-Si surface acoustic wave resonator," in *Proc. 1984 IEEE Ultrason. Symp.*

[8] A. W. Barendsz *et al.* "A SAW-chemosensor for NO_2 gas-concentration measurement," in *Proc. 1985 IEEE Ultrason. Symp.*

[9] H. Wohltjen, A. Snow, and D. Ballantine, "The selective detection of vapors using surface acoustic wave devices," in *Proc. 1985 Int. Conf. Solid State Sensors and Actuators*, IEEE cat. no. CH2127-9/85/0000-0066, pp. 66–70.

[10] H. Wohltjen, W. R. Barger, A. W. Snow, and N. L. Jarvis, "A vapor sensitive chemiresistor fabricated with planar microelectrodes and a Langmuir-Blodgett organic semiconductor film," *IEEE Trans. Electron. Dev.*, vol. ED-32, pp. 1170–1174, July 1985.

[11] J. Hlavay and G. G. Guilbault, "Applications of the piezoelectric crystal detector in analytical chemistry," *Analytical Chem.*, vol. 49, no. 13, pp. 1890–1898, 1977.

[12] J. F. Alder and J. J. McCallum, "Piezoelectric crystals for mass and chemical measurements," *The Analyst*, vol. 108, pp. 1291, 1169–1189, 1983.

[13] W. R. Barger, US Naval Res. Lab. Washington, DC, unpublished results, 1985.
[14] W. R. Barger, A. W. Snow, H. Wohltjen, and N. L. Jarvis, "Derivatives of phthalocyanine prepared for deposition as thin films by the Langmuir-Blodgett technique," *Thin Solid Films*, vol. 133, pp. 197-206, 1985.
[15] W. P. Mason, *Physical Acoustics and the Properties of Solids*. New York: Van Nostrand, 1958, p. 17.

Hank Wohltjen (S'74-M'78) was born in Staten Island, NY, on July 20, 1950. He received the B.S. degree in chemistry in 1972 and the B.S. degree in engineering science (electrical) in 1974, both from the City University of New York, and the Ph.D. in chemistry from the Virginia Polytechnic Institute, Blacksburg.

His dissertation research was in the area of surface acoustic wave chemical sensors. From 1978 to 1980 he was an IBM postdoctoral fellow in the electron beam lithography group at the Thomas J. Watson Research Laboratory. During this period he was also employed in the New Devices group at IBM's research laboratory in Zurich, Switzerland. He joined the US Naval Research Laboratory as a research chemist in 1981 and initiated research in the area of chemical microsensors based on surface acoustic wave devices, organic semiconductors, and optical waveguides. In 1985 he founded Microsensor Systems, Inc., an organization dedicated to research and development of chemical microsensor instrumentation.

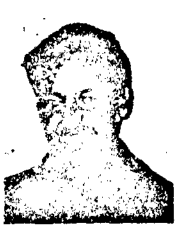

Arthur W. Snow was born in Adak, AK, on January 10, 1949. He received the B.S. degree in chemistry from the Michigan State University, East Lansing, in 1971 and the Ph.D. degree from the City University of New York in 1977.

He was with the American Cyanamid Company for a year before joining the Naval Research Laboratory in 1978 as a Research Chemist. He also has been teaching polymer chemistry at the Catholic University of America, Washington, as an Adjunct Professor since 1980. His research interests are in the areas of synthesis and characterization of highly unsaturated polymers and of conjugated macrocyclic compounds.

William R. Barger was born in Baltimore, MD, on November 9, 1942. He received the B.S. and Ph.D. degrees in 1967 and 1985, respectively, from the University of Maryland, College Park.

In 1967, he was employed as a research chemist in the Chemical Oceanography Branch of the Naval Research Laboratory (NRL), where he studied the effects of organic monolayer films in the environment and sought practical applications for monolayer forming chemicals such as control of oil spills, control of mosquitos, and improved Navy dye markers. Analysis of trace quantities of surface-active compounds in the atmosphere and in natural water bodies was a major area of interest. From 1980 to 1982 as a member of the Environmental Chemistry Branch of NRL his interests turned to trace gas analysis in air and water. He joined the microsensor research group in the NRL Surface Chemistry Branch in 1982, where his primary interest is in the development of practical gas sensing chemiresistors which depend on multimolecular coating films deposited one monolayer at a time by the Langmuir-Blodgett technique.

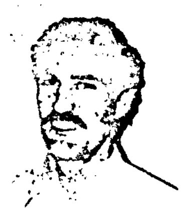

David S. Ballantine was born on Long Island, NY in 1955. He received the B.S. degree from the College of William and Mary in 1977 and the Ph.D. degree in analytical chemistry from the University of Maryland, College Park, in 1983.

He is a Research Chemist with Geo-Centers, Inc. at the US Naval Research Laboratory facility in Washington, DC, since 1984. His current research involves investigating vapor/coating interactions using SAW devices and the testing and development of SAW devices as chemical sensors.

Naval Research Laboratory
Washington, DC 20375-5000

NRL Memorandum Report 6024

Relationship of Surface Acoustic Wave Vapor Sensor Responses to Thermodynamic Parameters for Gas Solubility: Polymer/Gas Partition Coefficients for Fluoropolyol

J. W. GRATE AND A. SNOW

Surface Chemistry Branch
Chemistry Division

D. S. BALLANTINE

GEO Centers, Inc.
Fort Washington, MD 20744

H. WOHLTJEN

Microsensors Systems Inc.
Fairfax, VA 22030

M. H. ABRAHAM, A. R. MCGILL AND P. SASSON

University of Surrey
Guildford Surrey GU2 5XH
United Kingdom

July 29, 1987

SECURITY CLASSIFICATION OF THIS PAGE

REPORT DOCUMENTATION PAGE

1a. REPORT SECURITY CLASSIFICATION UNCLASSIFIED	1b. RESTRICTIVE MARKINGS
2a. SECURITY CLASSIFICATION AUTHORITY 2b. DECLASSIFICATION / DOWNGRADING SCHEDULE	3. DISTRIBUTION / AVAILABILITY OF REPORT Approved for public release; distribution unlimited.
4. PERFORMING ORGANIZATION REPORT NUMBER(S) NRL Memorandum Report 6024	5. MONITORING ORGANIZATION REPORT NUMBER(S)
6a. NAME OF PERFORMING ORGANIZATION Naval Research Laboratory 6b. OFFICE SYMBOL (If applicable) Code 6170	7a. NAME OF MONITORING ORGANIZATION
6c. ADDRESS (City, State, and ZIP Code) Washington, DC 20375-5000	7b. ADDRESS (City, State, and ZIP Code)
8a. NAME OF FUNDING / SPONSORING ORGANIZATION Chemical Research Development & Engineering Ctr. 8b. OFFICE SYMBOL (If applicable) CRDEC	9. PROCUREMENT INSTRUMENT IDENTIFICATION NUMBER
8c. ADDRESS (City, State, and ZIP Code) Aberdeen Proving Ground Aberdeen, MD 21010-5423	10. SOURCE OF FUNDING NUMBERS PROGRAM ELEMENT NO. / PROJECT NO. / TASK NO. / WORK UNIT ACCESSION NO. DN180-445

11. TITLE (Include Security Classification)
Relationship of Surface Acoustic Wave Vapor Sensor Responses to Thermodynamic Parameters for Gas Solubility: Polymer/Gas Partition Coefficients for Fluoropolyol

12. PERSONAL AUTHOR(S)
(See page ii)

13a. TYPE OF REPORT	13b. TIME COVERED	14. DATE OF REPORT (Year, Month, Day)	15. PAGE COUNT
Memorandum	FROM ______ TO ______	1987 July 29	50

16. SUPPLEMENTARY NOTATION
*GEO Center, Inc., Ft. Washington, MD 20744, **Microsensors Systems, Inc., Fairfax, VA 22030
***University of Surrey, Guildford, Surrey GU2 5XH, United Kingdom

17. COSATI CODES

FIELD	GROUP	SUB-GROUP

18. SUBJECT TERMS (Continue on reverse if necessary and identify by block number)
Surface acoustic wave; Vapor sensor; Fluoropolyol; SAW; Partition coefficient; Microsensor; Gas liquid chromatography

19. ABSTRACT (Continue on reverse if necessary and identify by block number)

Surface acoustic wave (SAW) devices coated with a thin film of a stationary phase sense chemical vapors in the gas phase by detecting the mass of the vapor which distributes into the stationary phase. This distribution can be described by the partition coefficient, which gives the ratio of the concentration of the vapor in the stationary phase to the concentration of the vapor in the gas phase. An equation is presented which allows partition coefficients to be calculated from SAW vapor sensor frequency shifts. Partition coefficients for nine vapors into SAW coating "fluoropolyol" have been determined by this method, using both 112 MHz and 158 MHz SAW devices. Partition coefficients have also been determined independently by GLC and the results are in good agreement. The relationship between SAW frequency shifts and partition coefficients allows SAW sensor responses to be predicted if the partition coefficient has been measured by GLC, or if the partition coefficient can be estimated by various correlation methods being developed.

20. DISTRIBUTION / AVAILABILITY OF ABSTRACT ☒ UNCLASSIFIED/UNLIMITED ☐ SAME AS RPT ☐ DTIC USERS	21. ABSTRACT SECURITY CLASSIFICATION UNCLASSIFIED
22a. NAME OF RESPONSIBLE INDIVIDUAL Jay W. Grate	22b. TELEPHONE (Include Area Code) (202) 767-2536 22c. OFFICE SYMBOL Code 6170

DD FORM 1473, 84 MAR — 83 APR edition may be used until exhausted. All other editions are obsolete.

SECURITY CLASSIFICATION OF THIS PAGE

12. PERSONAL AUTHOR(S)

Grate, Jay W., Snow, Arthur, Ballantine, David S.,* Wohltjen, Hank,** Abraham,***
Michael H., McGill,*** Andrew R., Sasson,*** Pnina

CONTENTS

INTRODUCTION 1

EXPERIMENTAL 5
- Materials 5
- 112 MHz SAW Device 5
- 158 MHz SAW Device 6
- Vapor Sensor Coating 7
- Vapor Stream Generation 8
- Sensor Response Data Collection 8
- Gas Liquid Chromatography (GLC) 10

RESULTS 11
- Equation Relation SAW Frequency Shift to Partition Coefficient 11
- Relationship to Thermodynamic Parameters for Gas Solubility 14
- K Values Determined from SAW Vapor Sensor Frequency Shifts 15
- K Values Determined by GLC Measurements 28

DISCUSSION 30

CONCLUSIONS 38

ACKNOWLEDGMENTS 39

REFERENCES 40

APPENDIX 42

RELATIONSHIP OF SURFACE ACOUSTIC WAVE VAPOR SENSOR RESPONSES TO THERMODYNAMIC PARAMETERS FOR GAS SOLUBILITY: POLYMER/GAS PARTITION COEFFICIENTS FOR FLUOROPOLYOL

INTRODUCTION

The use of surface acoustic wave (SAW) devices for sensing chemical vapors in the gas phase was first reported in 1979,[1] and has since been investigated by several groups.[2-10] SAW devices function by generating mechanical Rayleigh surface waves on a thin slab of a piezoelectric material (such as quartz) and oscillate at a characteristic resonant frequency when placed in an oscillator circuit with an rf amplifier.[6] The oscillator frequency is measurably altered by small changes in mass or elastic modulus at the surface of the SAW device. Vapor sensitivity is typically achieved by coating the device surface with a thin film of a stationary phase which will selectively absorb and concentrate the target vapor. Vapor sorption increases the mass of the surface film and a shift in the oscillator frequency is observed. SAW devices offer many advantages as chemical sensors including small size, low cost, ruggedness, and high sensitivity. A further advantage is the potential for these devices to be adapted to a variety of gas phase analytical problems by strategic design or selection of coating material. Full realization of this potential will require methods to quantify, understand, and finally to predict the vapor/coating interactions responsible for vapor sorption.

Manuscript approved April 29, 1987

The change in oscillator frequency, Δf_s, observed when a bare SAW device is coated with an isotropic, non piezoelectric, thin film has been described by equation (1).[6]

$$\Delta f_S = (k_1+k_2)\, F^2 h\rho - k_2 F^2 h \left(\frac{4\mu}{V_r^2} \left(\frac{\lambda + \mu}{\lambda + 2\mu} \right) \right) \quad (1)$$

k_1 and k_2 are material constants for the piezoelectric substrate; F is unperturbed resonant frequency of the SAW oscillator, which is determined by the geometry of the interdigital transducers fabricated onto the surface; h is the coating thickness; ρ is the coating density; μ and λ are the shear modulus and Lame constants of the coating; and V_r is the Rayleigh wave velocity in the piezoelectric substrate. The second term in this equation depends on the mechanical properties of the film, and is often negligible for soft organic materials. If the mechanical properties are negligible, then equation (1) reduces to equation (2), which describes the perturbation in frequency caused by the mass of the applied film[6] ($h\rho$ is simply the mass per unit area of the film). This treatment assumes 100% coverage of the device active area.

$$\Delta f_s = (k_1 + k_2) F^2 h\rho \quad (2)$$

Similarly, the frequency shift observed when the coated SAW device is exposed to a vapor provides a measure of the mass of the vapor absorbed.

Sorption of ambient vapor into the SAW device coating until equilibrium is reached represents a partitioning of the solute vapor between the gas phase and the stationary phase. This process is illustrated in Figure 1. The distribution can be quantified by a partition coefficient, K, which gives the ratio of the concentration of the vapor in the stationary phase, C_s, to the concentration of the vapor in the vapor phase, C_v (equation 3).

$$K = \frac{C_s}{C_v} \tag{3}$$

An equation is derived herein which allows K to be calculated directly from observed SAW vapor sensor frequency shifts. This conversion provides a standardized method of normalizing empirical SAW data, and does so in a way that provides information about the vapor/coating equilibrium.

In this study we examine in detail the absorption of vapors into a soft polymeric material referred to as "fluoropolyol". This material was chosen on the basis of a prior study where several diverse stationary phases were applied to SAW devices and exposed to a range of chemical vapors.[3] The fluoropolyol-coated sensor gave some of the highest responses observed. We now present vapor response data for fluoropolyol coated onto both 112 and 158 MHZ SAW devices. These data have been used to calculate partition coefficients for each vapor into fluoropolyol. Partition coefficients for the same vapors into fluoropolyol were

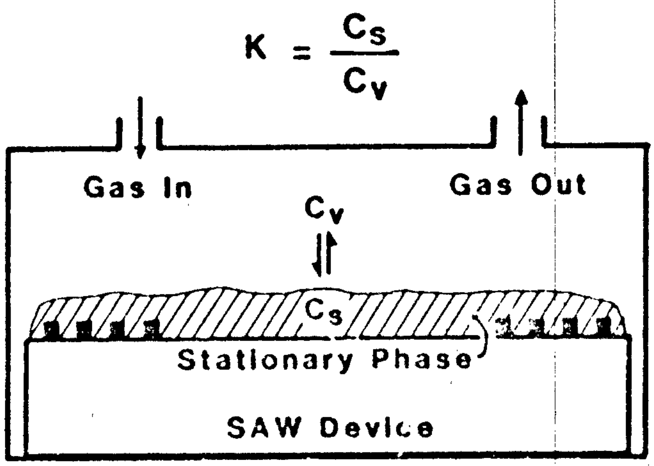

Figure 1. The distribution of vapor between the gas phase and the stationary phase which is quantified by the partition coefficient, K.

also determined independently by gas-liquid chromatographic (GLC) measurements. The values resulting from these two different techniques are in good agreement.

These results demonstrate that the mechanism of action of a coated SAW device is the same as that of GLC, i.e., reversible absorption of the vapor in the gas phase into the stationary phase. This confirms the solubility model for the interaction of vapors with the SAW coating; i.e. the solute vapor dissolves and distributes into the solvent stationary phase. Finally, the correlation between SAW vapor sensor responses and GLC partition coefficients creates a means for predicting SAW sensor behavior. Thus, if GLC partition coefficients are available from experimental measurement, or can be reliably predicted, then SAW vapor sensor responses can also be predicted.

EXPERIMENTAL

Materials. The fluoropolyol used in these studies was synthesized and provided by Dr. Jim Griffith of the Naval Research Laboratory Polymeric Materials Branch. These types of materials are prepared by methods described by O'Rear et. al.[11] The density of the fluoropolyol could not be determined using a density bottle or a pycnometer because of its high viscosity. Instead, a bulb with a vertical calibrated stem was weighed before and after being filled with fluoropolyol. On leaving the device in a thermostat, the polymer gradually settled and the volume reading was then taken. The results at various temperatures are as follows: T(°C),ρ(g ml^{-1}); 25, 1.6530; 40, 1.6322; 60, 1.6044; 90, 1.5629. The glass transition temperature of fluoropolyol is 10°C.

The liquid solvents used to generate vapor streams were commercial materials of greater than 99% purity, except diethyl sulfide (98%, Aldrich) and dimethyl methylphosphonate (DMMP) (97%, Aldrich). The solutes used in the GLC measurements were also commercial materials used as received; the GLC method does not require highly purified compounds.

<u>112 MHz SAW Device</u>. The 112 MHz dual SAW delay line sensors (Microsensor Systems, Inc. part number SD-112-B) were fabricated photolithographically using gold electrode metallization onto polished ST cut quartz substrates (1 cm x 1 cm x 0.08 cm thick). Each interdigital transducer (IDT) consisted of 50 finger pairs having one quarter wavelength finger widths and spacings (7 microns) and an 80 wavelength (.2240 cm) acoustic aperture. The IDT's were separated by 264 wavelengths (0.7392 cm). These 112 MHz SAW devices differ from those described previously[3] in having a separate ground contact for each IDT. Electrical contacts from the RF electronics to the IDT contact pads were made by mounting the device in a plastic box with small gold-plated clips and screws. The lid to the box was equipped with two stainless steel tubes for the vapor stream inlet and outlet.

Each delay line was connected to a TRW model CA2820 wideband RF amplifier to provide the amplification necessary for oscillation to occur. The frequencies obtained from each oscillator were mixed in a double balanced mixer (Mini Circuits Labs SRA-1) to provide a low frequency difference signal between the two delay lines on the device.

158 MHz SAW Device

The 158 MHz dual SAW devices used in this study (Microsensor Systems, Inc. part number SD-158-A) were also fabricated on ST cut quartz substrates. The two delay lines were lithographically patterned onto a chip that was approximately 0.5 cm square. This chip was epoxied onto a conventional gold plated, 12 pin, TO-8 style integrated circuit package and electrical connections were made from the SAW interdigital electrodes by means of ultrasonically welded 1 mil gold wires. After coating the device, the device was covered and sealed by a nickel plated lid with two 1/16 inch stainless steel tubes for vapor flow. The input interdigital transducer for each SAW device consisted of 75 pairs of electrodes with each pair repeated at 20 micron intervals (i.e. an acoustic wavelength of 20 microns). The acoustic aperture was 70 wavelengths (i.e. 0.1400 cm). The output interdigital transducer was spaced 10 wavelengths (i.e. 0.0200 cm) from the input transducer and consisted of 100 pairs of electrodes also having each pair repeated at 20 micron intervals. The edges of the quartz substrate beyond the ends of the delay lines were cut 5° out of parallel with the IDT fingers to eliminate triple transit echos. Coatings applied to the device covered the entire surface of the electrodes as well as the space in between electrodes.

Vapor Sensor Coating. Vapor sensors were prepared by coating one delay line with a thin film of fluoropolyol. The uncoated delay line served as a reference oscillator to provide temperature and pressure compensation. The coating was applied by spraying a dilute solution of fluoropolyol in chloroform through a small mask positioned to shield the reference delay line. The spray was generated with an airbrush using compressed air as the propellant. The difference frequency of the device was monitored until the desired amount of coating had been applied.

The two 112 MHz sensors reported herein were coated with 106 and 104 KHz of film respectively. The first was coated and stored overnight in ambient air prior to vapor testing. The second was annealed for one hour at 110°C and stored overnight in ambient air prior to vapor testing. After the first round of vapor testing, these devices were stored for two months in ambient air and then tested again.

The 158 MHz SAW device was coated with 207 KHz of film and stored for one week at room temperature prior to vapor testing.

Vapor stream generation. Vapor streams were generated from gravimetrically calibrated permeation tubes or gravimetrically calibrated bubblers using an automated vapor-generation instrument described in reference 12. This instrument generates selected vapor streams, dilutes them, and delivers a programmable flow rate of either clean carrier gas or the diluted vapor stream to the sensor. The instrument is controlled with an Apple IIe computer.

For these studies the carrier gas was dry air delivered to the sensor at ambient pressure. Dimethyl methylphosphonate and N,N-dimethylacetamide vapor streams were generated using permeation tubes and the remaining vapor streams were generated from bubblers. The flow rate of vapor stream to the sensor was 100mL/min.

In between collecting the first data sets on the 112 MHz devices and collecting the aged data set on the 112 MHz devices, the handling of permeation tubes was changed in a manner which appears to affect the concentrations generated. The 158 MHz data were also collected after this change. In the first data set permeation tube chambers were flushed for one hour prior to vapor testing to remove accumulated vapor. Normally the chambers were closed. This procedure was changed so that the chambers are continually flushed, 24 hours a day, assuring equilibrium conditions in each chamber at all times.

Vapor concentrations are calculated from the mass flow of the permeation tube as measured under equilibrium conditions. If one hour of flushing did not assure equilibrium conditions and remove buildup of vapor in the chamber or on the chamber walls, then the delivered concentrations may have been higher than the concentrations assigned based on the mass flow rates determined from the weight loss of the permeation tube. This would result in higher apparent frequency shifts and K_{saw} values. The log K values reported for DMMP and DMAC prior to continual permeation tube flushing are in parentheses in the tables.

Sensor response data collection. The difference frequency from the SAW sensor was monitored using a Systron-Donner model 6042A frequency counter or with a Phillips PM6674 frequency counter. The data were transferred over an IEEE-488 bus to an Apple IIe computer. This computer was in communication with the computer controlling vapor stream flows so that data collection and vapor stream operations were synchronized. The frequency data were collected at 1 Hz resolution. The difference in the frequency before the sensor was exposed to the vapor stream (i.e. the sensor is under clean dry air) and after the sensor has reached a stable equilibrium response to the vapor stream gives the frequency shift caused by the vapor.

The observed frequency shifts were used to calculate a partition coefficient for each vapor exposure. However, frequency shifts of less than 100-200 Hz were generally omitted from subsequent calculations so that K values were determined only from sensor responses with high signal to noise ratios.

Gas liquid chromatography (GLC). Fluoropolyol-gas partition coefficients, defined by equation 3, were obtained by GLC using fluoropolyol as the stationary phase. Absolute values of K (denoted by us previously as L)[13] were obtained essentially as described before,[13] using glass columns 1.5 m long containing a 4% loading of fluoropolyol on chromosorb GAW, with helium as the carrier gas and a thermal conductivity detector. Corrections for the pressure drop across the column were made as described (see equations 4-6 in ref. 13), and corrections for gas imperfections (equation 7 in ref. 13) were also carried out. However, the latter were trivial. Two series of measurements, at 298°K and at 333°K, with alcohols as the standard solutes were carried out: results are in Table VI. Values of K for water were also obtained. A variety of solutes were then examined at both 298°K and 333°K, using a flame ionization detector, and relative values of K were converted to absolute values, using the known absolute values of the standard compounds, exactly as described before.[13]

RESULTS

Equation Relating SAW Frequency Shift to Partition Coefficient

The derivation of an equation relating SAW frequency shifts directly to partition coefficients begins with equation (2), which gives the frequency shift caused by a thin film on the SAW surface. The product of the factors h (film thickness in m) and ρ (film density in kg m^{-3}) in this equation is simply the mass per unit area.[6] Therefore the frequency shift in Hz, Δf_s caused by application of the thin film coating onto the bare SAW device can be expressed as in equation (4).

$$\Delta f_s = \frac{(k_1+k_2)F^2 m_s}{A} \qquad (4)$$

The variable m_s is the mass of the coating in kg and A is the coated area in m^2. The frequency shift in Hz, Δf_v, caused by absorption of the vapor into the coating can be expressed similarly as in equation (5).

$$\Delta f_v = \frac{(k_1+k_2)F^2 m_v}{A} \tag{5}$$

The variable m_v is the mass of the vapor in the stationary phase coating. Division of equation (5) by equation (4) and rearranging gives equation (6).

$$\Delta f_v = \Delta f_s \frac{m_v}{m_s} \tag{6}$$

The mass of the vapor in the stationary phase coating is the factor of greatest interest. It can be related to the concentration of the vapor in the stationary phase C_s, in grams per liter, by equation (7).

$$C_s = \frac{m_v}{V_s\ (.001\ \mathrm{kg\ g^{-1}})} \tag{7}$$

V_s is the volume of the stationary phase in liters. Now, substitution of (7) into (3) and rearranging gives (8).

$$m_v = K\, C_v V_s\ (.001\ \mathrm{kg\ g^{-1}}) \tag{8}$$

C_v is the concentration of the vapor in the gas phase in grams per liter. Finally, substitution of (8) into (6) relates Δf_v to K as shown in equation (9).

$$\Delta f_v = \frac{\Delta f_s \, K \, C_v V_s \, (.001 \text{ kg g}^{-1})}{m_s} \quad (9)$$

This result can be further simplified by noting that V_s/m_s is the reciprocal of the density, ρ, of the stationary phase. If Δf_s is converted from Hz to KHz, the .001 conversion factor cancels out. The final result is equation (10):

$$\Delta f_v = \frac{\Delta f_s \, C_v \, K}{\rho} \quad (10)$$

Δf_v = vapor frequency shift ;in Hz

Δf_s = coating frequency shift in KHz

ρ = coating density in kg L^{-1} (= g mL^{-1})

C_v = vapor concentration in the gas phase in g L^{-1}

K = partition coefficient

The assumptions inherent in equation (10) are that the SAW device functions as a mass sensor (mechanical effects are negligible) and that the observed mass change is due to partitioning of the vapor between the gas phase and the stationary phase coating. In this regard, the equation represents a solubility model, i.e. dissolution of the solute vapor into the solvent stationary phase. The partition coefficient, K, can be readily calculated since all the remaining terms are known. Δf_s is determined when the vapor sensitive coating of density ρ is applied to the bare SAW device. Δf_v is measured when the sensor is exposed to a calibrated vapor stream of concentration C_v. The units of C_v, g L^{-1}, are appropriate since dynamic vapor streams are typically prepared by diluting a measured mass flow (g min^{-1}) into a known volumetric flow (L min^{-1}) of carrier gas.[12]

One additional assumption is made in the substitution of the reciprocal of the stationary phase density, ρ, for V_s/m_s in equation (9). Following the derivation closely it is seen that m_s is the mass of the stationary phase, whereas V_s is the volume of the stationary phase when an equilibrium quantity of vapor has been absorbed. This volume is therefore assumed to be equal to the volume of the stationary phase itself. So long as the mass loading of the stationary phase by vapor is low, as it will be for low vapor concentrations or weakly sorbed vapors, this assumption is reasonable. In addition, the density of the material applied as a thin film is taken to be the same as the density of the bulk material.

Relationship to Thermodynamic Parameters for Gas Solubility

Equation (3) is a standard equation for the expression of gas solubility in a liquid at a constant temperature. The limiting value of the partition coefficient at low concentration may be defined as

$$K^{\circ} = \left(\frac{C_s}{C_v}\right)_{C\to 0} \qquad (11)$$

and under normal gas chromatographic conditions, derived values of the gas-liquid partition coefficient may be taken as identical to K°. It should be pointed out that K° is the same as the Ostwald solubility coefficient, L°, defined exactly as in equation (11). Hence if equation (10) is applied to the detection of gases or vapors at low partial pressures, the constant K should represent K°(or L°).

The Henry's constant for absorption of a gas in a liquid at again limiting concentration or partial pressure, is defined as

$$K^H = \left(\frac{P_v}{X_s}\right)_{P_v \to 0} \qquad (12)$$

where P_v is the solute partial pressure and X_s the solute mole fraction in the liquid phase. Since K^H and K° are related through equation (13), it is easy to derive an equation that connects Δf_v and K^H.

$$K^H = RT\rho / M_s K^\circ \qquad (13)$$

However, such an equation will be rigorously true only for liquid stationary phases whose molecular weight, M_s, is known. In the present context, using polymeric stationary phases, the relationship is of little value.

K values Determined from SAW Vapor Sensor Frequency Shifts. Vapor response data were collected using 112 or 158 MHz SAW dual delay line sensors with one delay line coated with a thin film of fluoropolyol. These devices are shown schematically in Figures 2 and 3. The chemical structure of fluoropolyol is shown in Figure 4. Coating a delay line with a thin film causes its frequency of oscillation to decrease in accordance with equation (2). The magnitude of this decrease provides a measure of the amount of coating applied.[6] For example, 112 MHz SAW devices are typically coated with sufficient material to produce a 100 KHz frequency decrease in the coated delay line. Using equation (2), the 1.653 g mL^{-1} density of fluoropolyol, and values of -9.33×10^{-8} and -4.16×10^{8} m^2 sec kg^{1} for k_1 and k_2,[6] the estimated average thickness of a 100 KHz film of fluoropolyol on a 112 MHz SAW device is 36 nm. Given that the active area of the device is 0.17 cm^2, this corresponds to about 1 μg of material on the active surface. Similarly, a 158 MHz device with 200 KHz of fluoropolyol has an average coating thickness of 36 nm.

When a SAW vapor sensor under clean air is exposed to air containing a vapor to which it is sensitive, the frequency of the coated delay line shifts from its baseline value to a still lower frequency. This causes the measured difference frequency between the coated and uncoated delay lines to increase. A typical response curve for two successive vapor exposures is shown in Figure 5.

For most of the vapors at the concentrations employed in these studies, the frequency shifts were less than a few thousand Hz on the 112 MHz sensors. For water and isooctane, the highest shifts were less than one thousand Hz. For strongly sorbed

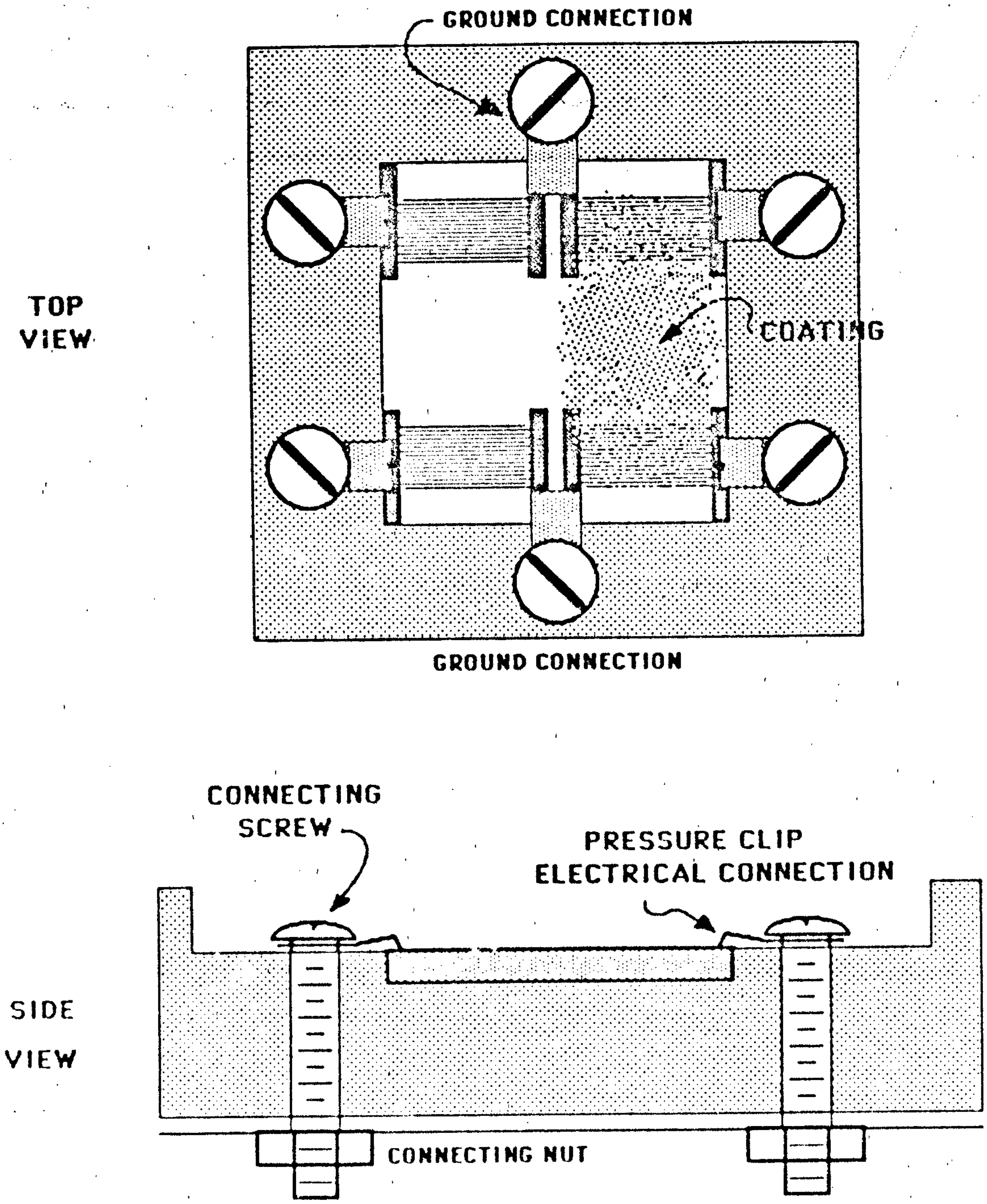

Figure 2. Schematic diagram of a coated 112 MHz dual SAW delay line contained in a plastic box with electrical connections made by screws and pressure clips.

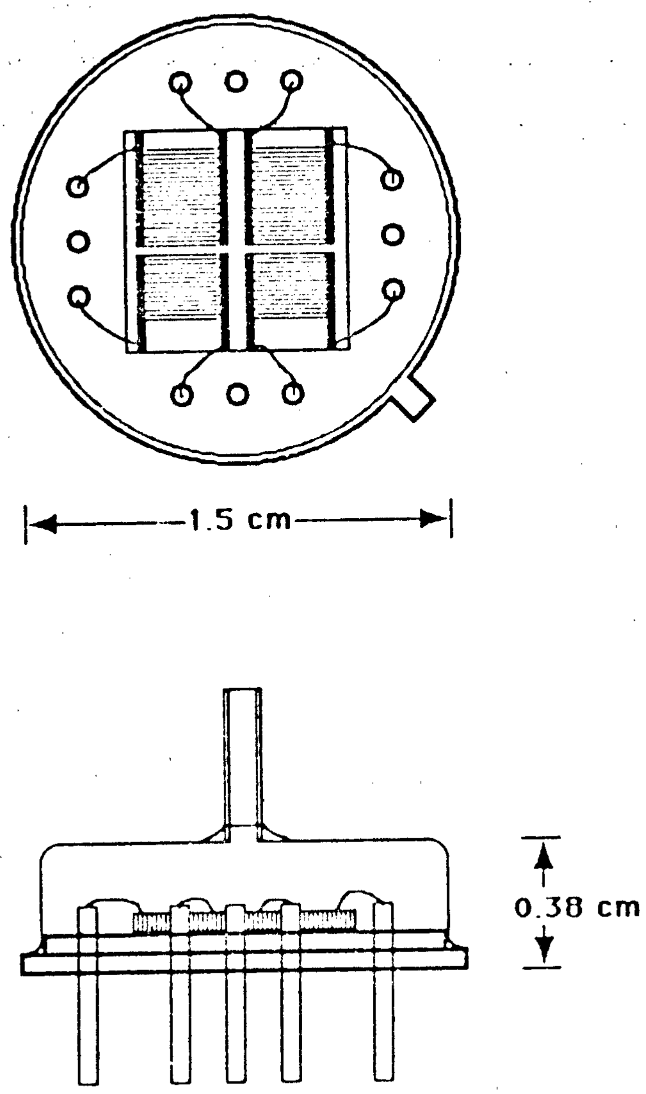

Figure 3. Schematic diagram of a 150 MHz dual SAW delay line mounted on a TO-8 style package with wire-bonded electrical connections.

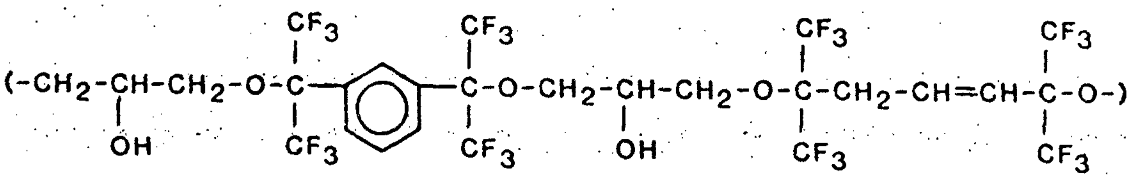

Figure 4. The structure of fluoropolyol.

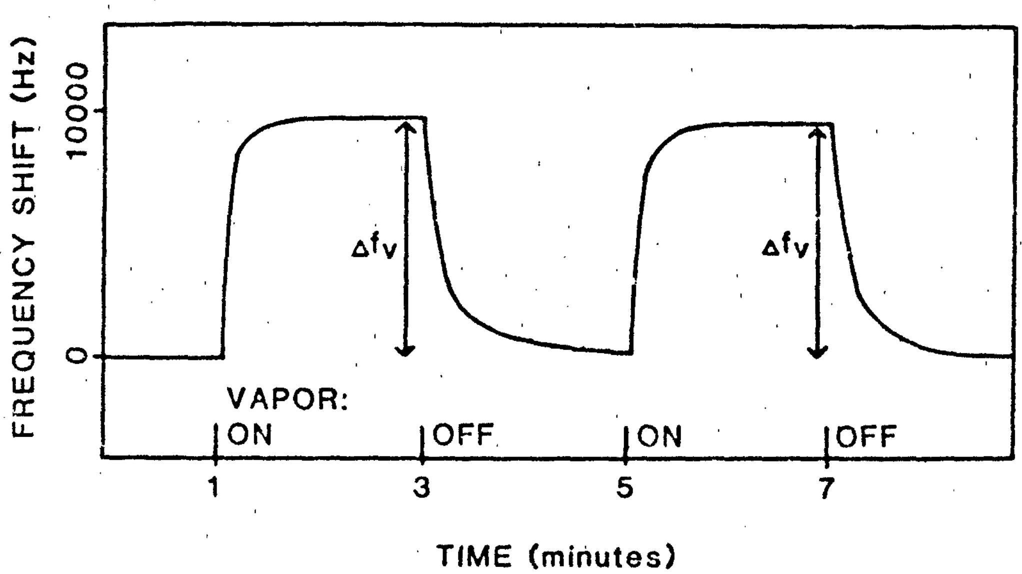

Figure 5. Response curve from two successive exposures of the 158 MHz SAW sensor to N,N-dimethylacetamide at .000057 g L^{-1} gas phase concentration.

vapors such as dimethyl methylphosphonate (DMMP) frequency shifts as high as five to ten thousand Hz were observed. Similarly, shifts for 2-butanone, whose vapor phase concentration was very high, ranged up to ten thousand Hz. Vapor induced frequency shifts on the order of a few thousand Hz or less are much smaller than the one hundred thousand Hz of fluoropolyol coating on the 112 MHz devices. This demonstrates that the mass loading of the coating by vapor is small, and validates the use of the density term in equation (10).

The two 112 MHz sensors prepared for this study were coated with 106 and 104 KHz of fluoropolyol, and tested against vapor simultaneously by connecting them to the vapor stream in series. Testing began one day after coating the devices, and was repeated two months later to see if aging influenced sensor responses. These two devices differed slightly in their handling between coating and vapor testing. The device with 106 KHz of fluoropolyol was simply stored under ambient air at room temperature. The film on the second device, however, was annealed at 110°C for one hour, and then stored under ambient conditions. For the two months in between vapor testing, these devices were both stored under ambient conditions.

The 158 MHz device was coated with 207 KHz of film and tested a week later. In between coating and testing the device was stored under ambient conditions. The frequency shifts observed for the 158 MHz sensor were typically twice those observed for the corresponding vapor exposures on the 112 MHz sensors. This is due to the presence of twice the amount (in

KHz) of fluoropolyol on this sensor compared to the 112 MHz sensors. These results are in accordance with the linear dependence of Δf_v on Δf_s as expressed in equation (10).

For each vapor exposure, a partition coefficient was calculated from the observed frequency shift using equation (10). These values will be referred to as SAW partition coefficients and denoted K_{SAW}. The logarithms of the K_{SAW} values for a given vapor were then averaged. Average log K_{SAW} values are reported in Tables I through V for fluoropolyol on a 112 MHz device one day after coating, annealed fluoropolyol on a 112 MHz device one day after coating, fluoropolyol on a 112 MHz device two months after coating, annealed fluoropolyol on a 112 MHz device two months after coating, and fluoropolyol on a 158 MHz device one week after coating. Also reported with each log K_{SAW} value are the standard deviation (S), the number of vapor exposures used to determine K_{SAW} values (N), the number of different concentrations for each vapor (#), and the vapor concentration range. These tables represent nearly 900 measurements of SAW frequency shifts.

For the vapors and concentrations examined in this study, the frequency shifts observed increased linearly with vapor concentration, and K_{SAW} values were independent of vapor concentration. This is in accordance with the relationships expressed in equation (10). Graphically this corresponds to a linear calibration curve of SAW response vs. concentration whose slope is dependent on a constant partition coefficient.

Table I. Average Log K_{SAW} Values for 106 KHz of Fluoropolyol on a 112 MHz SAW Device One Day After Coating Application

VAPOR	Log K_{SAW}	S[a]	N[b]	#[c]	Concentration Range, g/l	
DMMP	(6.56)[d]	.15	38	7	3.59E-6	2.63E-5
N,N-Dimethylacetamide	(6.30)	.05	40	7	7.47E-6	5.47E-5
1,2-Dichloroethane	2.52	.06	16	4	.0182	.124
Toluene	2.74	.06	16	4	.00625	.0434
Isooctane	2.11	.06	8	2	.0454	.0914
Diethyl sulfide	2.82	.05	16	4	.00797	.0552
2-Butanone	3.12	.02	16	4	.0145	.0986
Water	3.04	.04	8	2	.00271	.00550
1-Butanol	3.20	.03	12	3	.00205	.00815

[a] S = standard deviation
[b] N = number of measurements
[c] # = number of different concentrations
[d] values in parantheses are less certain. See experimental section.

Table II. Average Log K_{SAW} Values for 104 KHz of Annealed Fluoropolyol on a 112 MHz SAW Device One Day After Coating Application

VAPOR	Log K_{SAW}	S^a	N^b	$\#^c$	Concentration Range, g/l	
DMMP	(6.36)[d]	.07	40	7	3.59E-6	2.63E-5
N,N-Dimethylacetamide	(6.10)	.08	40	7	7.47E-6	5.47E-5
1,2-Dichloroethane	2.30	.06	16	4	.0182	.124
Toluene	2.62	.05	16	4	.00625	.0434
Isooctane	2.00	.04	8	2	.0454	.0914
Diethyl sulfide	2.65	.10	16	4	.00797	.0552
2-Butanone	2.98	.02	16	4	.0145	.0986
Water	2.49	.11	8	2	.00271	.00550
1-Butanol	3.16	.02	12	3	.00205	.00815

[a] S = standard deviation
[b] N = number of measurements
[c] # = number of different concentrations
[d] values in parentheses are less certain. See experimental section.

Table III. Average Log K_{SAW} Values for 106 KHz of Fluoropolyol on a 112 MHz SAW Device Two Months After Device Coating

VAPOR	Log K_{SAW}	S[a]	N[b]	#[c]	Concentration Range, g/l	
DMMP	5.69	.05	36	6	6.83E-5	1.59E-4
N,N-Dimethylacetamide	5.50	.06	44	7	1.38E-5	1.01E-4
1,2-Dichloroethane	2.33	.08	16	4	.0182	.151
Toluene	2.65	.09	16	4	.00731	.0652
Isooctane	1.88	.05	12	3	.0454	.137
Diethyl sulfide	2.72	.06	16	4	.00933	.0828
2-Butanone	3.12	.09	16	4	.0169	.146
Water	2.91	.05	12	3	.00271	.00827
1-Butanol	3.25	.[illegible]2	16	4	.00136	.0123

[a]S = standard deviation
[b]N = number of measurements
[c]# = number of different concentrations

Table IV. Average Log K_{SAW} Values for 104 KHz of Annealed Fluoropolyol on a 112 MHz SAW Device Two Months After Coating Application

VAPOR	Log K_{SAW}	S^a	N^b	#^{c}	Concentration Range, g/l	
DMMP	5.60	.04	36	6	5.15E-5	1.59E-4
N,N-Dimethylacetamide	5.39	.04	40	7	1.30E-5	1.01E-4
1,2-Dichloroethane	2.20	.06	16	4	.0182	.151
Toluene	2.50	.08	16	4	.00731	.0652
Isooctane	1.70	.03	12	3	.0454	.137
Diethyl sulfide	2.62	.08	16	4	.00933	.0828
2-Butanone	3.00	.06	16	4	.0169	.146
Water	2.84	.07	12	3	.00271	.00827
1-Butanol	3.10	.01	12	3	.00401	.0123

[a]S = standard deviation
[b]N = number of measurements
[c]# = number of different concentrations

Table V. Average Log KSAW Values for 207 KHz of Fluoropolyol on a 150 MHz SAW Device One Week After Coating Application

VAPOR	Log K_{SAW}	s^a	N^b	#[c]	Concentration Range, g/l	
DMMP[d]	6.02	.15	54	7	4.86E-5	3.56E-4
N,N-Dimethylacetamide	6.05	.07	47	7	1.26E-5	1.18E-4
1,2-Dichloroethane	2.59	.03	16	4	.0182	.124
Toluene	2.93	.06	15	4	.00625	.0434
Isooctane	2.16	.09	16	4	.0132	.0914
Diethyl sulfide	3.10	.05	16	4	.00797	.0552
2-Butanone	3.52	.06	16	4	.0145	.0986
Water	3.11	.06	15	4	7.88E-4	.00550
1-Butanol	3.68	.05	16	4	.00116	.00815

[a] s = standard deviation
[b] N = number of measurements
[c] # = number of different concentrations

[d] Log K values for DMMP showed a systematic decrease with increasing vapor concentration i.e. the calibration curve was not linear.

Alternatively stated, the sorption isotherms were linear in the concentration ranges examined. The principle exception to this rule was DMMP on the 158 MHz device. A slight decrease in K_{SAW} with increasing concentration was observed in this data set.

The reproducibility of a given SAW sensor tested one day after coating and again two months after coating was good, and aging appeared to have little effect. Average log K_{SAW} values had standard deviations up to about 0.1 log K units, whereas the differences between values from one day to two months were generally 0 to 0.2 log K units. Variations for water and isooctane were somewhat greater, but these are vapors to which fluoropolyol is not very sensitive at the vapor concentrations generated.

Data from device to device showed some systematic variations. In testing both one and two months after coating, the 112 MHz SAW device n the annealed film was about 0.1 to 0.2 log K units less sensitive than the unannealed film on a 112 MHz device. (The data for water were anomalous.) This systematic variation is small, and may or may not be an effect of annealing the film. The log K_{SAW} values determined from the data collected on the 158 MHz device are systematically higher than those from 112 MHz device data by about 0.4 log K units. Systematic variations from device to device could be most easily explained by errors in the measurement of the coating material applied, or by differences in the temperatures at which the sensors were operating during testing. Temperature effects will be further discussed below.

Table VI. Absolute Values of K Determined by GLC.[a]

Solute	298°K	333°K
Methanol	579.6 ± 11.7 (7)	170.0 ± 1.4 (3)
Ethanol	728.2 ± 12.7 (6)	246.4 ± 6.0 (3)
1-Propanol	2174.8 ± 22.0 (5)	445.9 ± 2.6 (3)
1-Butanol	6975.2 ± 37.1 (4)	961.2 ± 4.5 (5)
1-Pentanol		2035.8 ± 34.4 (5)
1-Hexanol		4203.8 ± 14.0 (5)

a Standard deviations are given. The values in parenthesis are the number of determinations.

Log K_{GLC} and log K_{SAW} values for nine solute vapors are compared in Table VII with vapors in order of decreasing log K_{SAW}. All of the GLC values refer to 298°K, either by direct measurement, or via equation (14) as described above. In one additional case, diethyl sulfide, the log K_{GLC} value was estimated from various correlations we have constructed using solvatochromic parameters. With the exception of this estimated value, the order of decreasing log K values is identical for the SAW and GLC measurements. Indeed, there is good agreement between all but the highest log K values, such that the SAW sensor frequency shifts could be estimated using K_{GLC} values and equation (10). The general trend of the highest Log K vapors (DMMP and dimethylacetamide) having larger SAW responses than the other vapors could also be predicted from K_{GLC}, but not accurately. In these cases, the error in Log K_{GLC} values will be larger than usual, but certainly not so large to account for the differences in Table VII.

DISCUSSION

The experimental conditions for measuring partition coefficients with a SAW device are somewhat different than those for GLC measurements. SAW measurements, for instance, are carried out at finite vapor concentrations while the GLC measurement usually refers to infinite dilution. In addition, the SAW measurements reported here were conducted at ambient temperatures, while the GLC measurements were rigorously thermostatted. Finally, the calculation of K_{SAW} assumes that

Table VII. Comparison of Log K_{SAW} and Log K_{GLC} Values

VAPORS		
Dimethyl methylphosphonate	5.77	7.53[c]
N,N-Dimethylacetamide	5.65	7.29[c]
1-Butanol	3.24	3.66
2-butanone	3.15	3.48[c]
Water	2.88	2.89
Diethyl sulfide	2.78	2.54[d]
Toluene	2.69	2.64[c]
1,2-Dichloroethane	2.39	1.94[c]
Isooctane	1.97	1.22

a These values are averages of those in Table I-V, excluding values which are in parentheses.

b At 298°K.

c Determined from values measured at 333°K and corrected to 298°K with equation (9).

d Estimated value using a correlation equation.

the vapor causes the sensor to respond based on mass effects alone; if mechanical effects become significant for a particular vapor/coating interaction, then the calculated K_{SAW} will be altered proportionately. One or more of the above factors may be responsible for differences in the precise values of log K_{SAW} and log K_{GLC} shown in Table VII. In this regard, the standard deviations reported with the log K_{SAW} values in Tables I-V represent the variation of the measurement about some value which may or may not be the same as the fluoropolyol/gas partition coefficient at infinite dilution.

The influence of temperature on partition coefficients deserves some attention. It is well known from GLC that increasing temperature causes smaller retention volumes and lower partition coefficients. Consequently a SAW sensor will become less sensitive as temperature increases. The extent of this effect for fluoropolyol is now experimentally defined by the results in Table VI and equation (14). Precise thermostatting of a SAW device to fractions of a degree is clearly not critical, but changes of five to ten degrees will influence sensor response and reproducibility, especially for strongly sorbed vapors.

In practice, an unthermostatted sensor may change temperature because of changing ambient conditions, or because the electronics package containing the sensor generates heat. In our experience, the system containing the 158 MHz SAW sensors heats up to the 35 to 40° range, while temperatures as high as [illegible] have been measured in the 112 MHz SAW sensors systems we have used. The worst case effect of these temperatures can be illustrated for DMMP, with log K_{GLC} = 7.5 at 298°K. From equation (14) it is estimated that log K at 40°C will be 6.7, and at 55°C only 5.9. These higher temperature estimates are closer to the results observed experimentally for the SAW sensors. The effect is much less severe for vapors with lower K values. Thus, a log K of 3.0 at 298°C becomes 2.8 at 40°C and 2.6 at 55°C. The influence of temperature on K values and the higher operating temperatures of our sensors may explain the discrepancy observed between log K_{GLC} and log K_{SAW} for strongly sorbed vapors (DMMP and dimethylacetamide), while less strongly sorbed vapors are in better agreement. In addition, temperature effects may also contribute to the higher K values observed for the 158 MHz sensor compared to the 112 MHz sensors.

The overall correlation between K_{GLC} and K_{SAW} values clearly shows that partition coefficients are a useful concept for thinking about SAW sensor behavior (see also references 3 and 7). Indeed, the calculation of K_{SAW} values by equation (10) provides a standardized method of normalizing empirical SAW data which also provides information about the magnitude of the vapor/coating interaction. We have previously normalized our data by dividing the sensor response by the ppm of vapor in the gas phase and the KHz of coating.[3] Normalization to yield a partition coefficient, K_{SAW}, is very similar, and requires only that the vapor concentration be expressed in g liter^{-1}, and that the density of the stationary phase coating be factored out, according to equation (10). Expressing vapor concentration in the international convention of mg m^3 instead of g $liter^{-1}$ requires only a simple conversion factor of 10^6.

The correlation between K_{GLC} and K_{SAW} is important because it demonstrates experimentally that relative retention times for various vapors on a GLC column with a given stationary phase should be a reliable indicator of the relative sensitivity of a similarly coated SAW sensor to these vapors. This requires, of course, that the GLC measurement and SAW device operation be at the same temperature. On a more quantitative level, if absolute K_{GLC} values are determined, then estimates for actual SAW sensor frequency shifts can be made using equation (10). Finally, a clear relationship between SAW sensor responses and K_{GLC} values means that methods developed to predict K_{GLC} values will also be useful in predicting SAW sensor responses.

The correlation between the K_{GLC} and K_{SAW} values also provides important confirmation of the general operating principles of coated SAW chemical sensors. The functioning of the device primarily as a mass sensor is confirmed because mass sensitivity was a fundamental assumption of the equation used to calculate the K_{SAW} values. In addition, the concept of reversible partitioning of the vapor between the gas phase and the stationary phase is clearly demonstrated. Since partitioning represents the dissolution of a solute vapor into a solvent stationary phase, the solubility model for SAW coating/vapor interactions is confirmed, and solubility interactions are indicated as important factors in determining sensor responses.[3]

A simple examination of the order of the partition coefficients determined in this study further illustrates the importance of solubility properties (Table VII). The lowest K values are those of isooctane, a solute which is not dipolar or polarizable, and which cannot accept or donate hydrogen bonds. Solutes which are more polarizable, such as dichloroethane, toluene, and diethyl sulfide have greater K values than isooctane. However, these solutes are still incapable of hydrogen bonding. The top of the list contains exclusively those solutes which can accept and/or donate hydrogen bonds.

A further influence on the order of vapor sorption is the saturation vapor pressure of the solute, P_v°. Values of K_{GLC} are proportional to solute adjusted retention times. All other things being equal, solutes of low P_v° values will be eluted after more volatile solutes, and hence in general will have larger K_{GLC} values and will give rise to larger Δf_v values in equation (10). Experimentally, this result is seen in the high frequency shifts and K values seen for DMMP. This solute has a vapor pressure of less than 1 Torr at room temperature.

Solubility interactions can be placed on a more quantitative scale by the use of solvatochromic parameters, which describe the dipolar and hydrogen bonding properties of the solute vapors.[14,15] Such parameters are available for a wide range of vapors, but similar parameters are not yet available for very many coating materials. The challenges, therefore, are to characterize the solubility properties of polymeric stationary phases, and ultimately to be able to predict partition coefficients for any vapor with any characterized phase. Methodologies to accomplish this are being developed using equations of the general form shown in equation (15).[16]

$$\log K = \text{constant} + s\pi^* + a\,\alpha + b\,\beta + l\,\log L^{16} \quad (15)$$

In this equation, the parameters π^*, α, β, and $\log L^{16}$ characterize the solute vapor. The first three measure the dipolarity, hydrogen bond donor acidity, and hydrogen bond acceptor basicity, respectively. L^{16} is the Ostwald solubility coefficient (partition coefficient) of the solute vapor on hexadecane at 25°C. The coefficients s, a, b, and l are determined by multiple regression analysis and characterize the stationary phase. For example, b, as the coefficient for solute hydrogen bond acceptor basicity, provides a measure of the stationary phase hydrogen bond donor acidity. For any particular stationary phase/vapor interaction, evaluation of the individual terms (such as $b\beta$) and comparison of their magnitudes allows the relative strengths of various solubility interactions to be sorted out and examined.

The complex structure of fluoropolyol provides an interesting test case for these methods. This polymer contains a variety of functionalities which provide polarizability, dipolarity, hydrogen bond acceptor sites, and hydrogen bond donor sites. But the structure alone does not allow precise predictions of which interactions will be most important in determining the sorption of a particular vapor. Full characterization of fluoropolyol by GLC measurements and equations of the form in (15) is in progress, and we hope to report on this work soon. In addition, various other polymeric stationary phases which have been useful as SAW sensor coatings are being examined. Once the coefficients for a given phase have been determined, then it will be possible to evaluate solublity interactions and to predict K values for all vapors for which the relevant solute parameters are known. Then, via equation (10), it will be possible to predict the responses of a SAW vapor sensor to the same set of vapors.

Finally, it is anticipated that specific vapor/coating interactions may be encountered where mass effects alone do not adequately account for SAW sensor response. In such cases, mechanical effects (e.g. stiffening or softening of the surface coating by penetrant vapor) will be implicated, and the relationship between the actual coating/gas partition coefficient and SAW frequency shift will not be so simple as that expressed in equation (10). However, equation (10) will allow the frequency shift due to mass effects alone to be estimated if the partition coefficient has been measured by GLC or if it can be predicted from solubility parameters. It will then be possible to estimate the mechanical effect from the difference between the observed frequency shift and the frequency shift due to mass effects calculated from equation (10). Therefore, equation (10) will be useful for predicting SAW sensor responses when mass effects predominate, and in sorting out mass and mechanical effects when mass changes alone do not account for observed behavior.

CONCLUSIONS

An equation has been derived which relates SAW vapor sensor frequency shifts directly to partition coefficients. This equation has been validated by a comparison and correlation of partition coefficients determined independently by SAW vapor sensor responses and GLC measurements. This correlation also confirms mass sensitivity as the principle mechanism of vapor sensitivity for fluoropolyol-coated vapor sensors, and reversible sorption as the mechanism of vapor/coating interaction. Solubility properties such as dipolarity and hydrogen bonding are indicated as important factors in determining the extent of vapor sorption. The saturation vapor pressure of the solute vapor also influences sorption. The direct relationship between SAW sensor response and partition coefficients provides an avenue for predicting SAW sensor response from measured GLC partition coefficients. Partition coefficients predicted from solute vapor solvatochromic parameters and correlation equations characterizing the solvent stationary phase are also expected to be useful for predicting SAW sensor responses.

ACKNOWLEDGEMENTS

The authors acknowledge M.J. Kamlet for many useful discussions on solubility interactions.

This work was supported by the U.S. Army, CRDEC, Aberdeen Proving Ground, MD, and the U.S. Navy, Naval Surface Weapons Center, Dahlgren, VA and the Office of Naval Technology.

REFERENCES

1. Wohltjen, H.; Dessy, R.E., Anal. Chem., 1979, 51, 1458-1475.

2. Wohltjen, H.; Snow, A.W.; Barger, W.R.; Ballantine, D.S., IEEE Trans. Ultrason., Ferroelectrics, Freq. Contr., in press.

3. Ballantine, D.S.; Rose, S.L.; Grate, J.W.; Wohltjen, H., Anal. Chem., 1986, 58, 3058-3066.

4. Wohltjen, H.; Snow, A.; Ballantine, D., Proc. of the Int. Conf. on Solid State Sensors and Actuators - Transducers '85, Philadelphia, PA, June 11-14, 1985, IEEE Cat. No. CH2127-9/85/0000-0066, pp 66-70.

5. Venema, A.; Nieuwkoop, E.; Vellekoop, M.J.; Nieuwenhuizen, M.S.; Barendsz, A.W., Sens. Actuators, 1986, 10, 47-64

6. Wohltjen, H. Sens. Actuators, 1984, 5, 307.

7. Snow, A.; Wohltjen, H. Anal. Chem., 1984, 56, 1411.

8. Bryant, A.; Poirier, M.; Riley, G; Lee, D.L.; Vetelino, J.F., Sens. Actuators, 1983, 4, 105.

9. D'Amico, A.; Palma, A.; Verona, E., Sens. Actuators, 1982/1983, 3, 31.

10. Chuang, C.T.; White, R.M.; Bernstein, J.J., IEEE Electron, Device Lett., 1982, 3(6), 145.

11. O'Rear, J.G.; Griffith, J.R.; Reines, S.A., J. Paint. Technol., 1971, 43(552), 113.

12. Grate, J.W.; Ballantine, D.S., Jr.; Wohltjen, H., Sens. Actuators, 1987, 11, 173-188.

13. Abraham, M.H.; Grellier, P.L.; McGill, R.A., J. Chem. Soc. Perkin Trans. I, in press.

14. Kamlet, M.J.,; Taft, R.W., Acta Chem. Scand., Ser. B, 1985, B39, 611, and references therein.

15. Kamlet, M.J.; Abboud, J.M.; Abraham, M.H.; Taft, R.W., J. Org. Chem., 1983, 48, 2877.

16. Abraham, M.H.; Grellier, P.L.; McGill, R.A.; Doherty, R.M.; Kamlet, M.J.; Hall, T.M.; Taft, R.W.; Carr, P.W.; Koros, W.J., Polymer, in press.

APPENDIX

Relationships to Henry's Law Constants and Activity Coefficients

The Henry's Law constant, K^H, is defined as the ratio of the partial pressure of the solute vapor in the gas phase, P_V, to the mole fraction of the solute vapor in the liquid phase (equation 16).

$$K^H = \frac{P_V}{x_S} \tag{16}$$

This law applies to the limiting case of dilute solutions, where x_S approaches zero. Activity coefficients, γ, are defined according to equation (17), and K^H and γ are related by equation (18).

$$P_V = \gamma\, x_S P_V^{\circ} \tag{17}$$

$$K^H = \gamma\, P_V^{\circ} \tag{18}$$

P_V° is the saturation vapor pressure of the vapor at the experimental temperature.

Both K^H and γ can be related to the partition coefficient, K, if additional assumptions are made. SAW frequency shifts can then be calculated as well. If the vapor is assumed to behave ideally in the gas phase, then P_V (in atm.) is simply related to C_V (in g liter^{-1}) by equation (19).

$$P_V = \frac{C_V RT}{M_V} \tag{19}$$

M_V is the molecular weight of vapor. The ratio of the moles of solute vapor in the stationary phase to the moles of solvent molecules in the stationary phase can be determined from C_s using the density of the stationary phase and its molecular weight, ρ and M_s, respectively. For the case of very dilute solutions. the mole fraction of the vapor in the stationary phase, x_s, will be nearly equivalent to their mole ratio, i.e. the moles of solute vapor is much less than the moles of solvent. The mole fraction can be expressed as in equation (20).

$$x_S \cong \frac{C_S \quad M_S \quad (.001 \text{ kg g}^{-1})}{M_V \ \rho} \qquad (20)$$

Finally, division of equation (19) by equation (20) gives the Henry's law constant as defined in equation (16). Substitution of the definition of K (equation 3) and rearranging then relates K^H to K in equation (21).

$$K = \frac{1}{K^H} \quad \frac{R\ T\ \rho}{M_S\ (.001 \text{ kg/g})} \qquad (21)$$

Similarly, K and γ are related by equation (22)

$$K = \frac{1}{\gamma} \quad \frac{R\ T\ \rho}{P_V^{\circ}\ M_S\ (.001 \text{ kg/g})} \qquad (22)$$

Equations (21) and (22) can easily be substituted into equation (9) so that SAW sensor frequency shifts can be calculated if K^H or γ is known for the interaction between the vapor and the stationary phase coating at a relevant temperature and vapor concentration. By using equation (19) as well as equations (9) and (22), Δf_V is related to γ by equation (23).

$$\Delta f_V = \Delta f_S \frac{P_V}{P_V^\circ} \frac{M_V}{M_S} \frac{1}{\gamma} \qquad (23)$$

Equation (23) differs from equation (10) in several ways. The density term and the assumptions associated with it in equation (10) have been cancelled out of equation (23). The most convenient units for Δf_S in equation (23) are Hz and the equation is expressed in this form. The vapor concentration in the vapor phase is expressed in partial pressure. However, equation (23) is rigorously correct only for liquid stationary phases whose molecular weight is known. It is awkward for polymeric stationary phases. Moreover, activity coefficients refer primarily to the interaction between the liquid vapor and the liquid stationary phase, while we are [illegible] interested in the equilibrium between the gaseous vapor and the liquid stationary phase.

The terms in equation (23) show that SAW frequency shifts (Δf_V) will increase with decreasing saturation vapor pressure (P_V°) of the solute vapor. This result is consistent with the known increases in GLC retention times and partition coefficients with P_V°. Equation (23) also suggests that the molecular weight of the stationary phase (M_S) will influence Δf_V. However, changes in M_S are cancelled out by corresponding changes in γ because γ depends on molar volume. Thus, GLC experiments have demonstrated that retention volumes (and therefore partition coefficients) show little change with variations in stationary phase molecular weight.

Naval Research Laboratory

Washington, DC 20375-5000 NRL Memorandum Report 5865 October 6, 1986

USAF/NRL Surface Acoustic Wave Vapor Sensor Program

D. BALLANTINE, A. SNOW, M. KLUSTY,
G. CHINGAS, AND H. WOHLTJEN

Surface Chemistry Branch
Chemistry Division

SECURITY CLASSIFICATION OF THIS PAGE

REPORT DOCUMENTATION PAGE

1a. REPORT SECURITY CLASSIFICATION: UNCLASSIFIED

1b. RESTRICTIVE MARKINGS

2a. SECURITY CLASSIFICATION AUTHORITY

2b. DECLASSIFICATION / DOWNGRADING SCHEDULE

3. DISTRIBUTION / AVAILABILITY OF REPORT: Approved for public release; distribution unlimited.

4. PERFORMING ORGANIZATION REPORT NUMBER(S): NRL Memorandum Report 5865

5. MONITORING ORGANIZATION REPORT NUMBER(S)

6a. NAME OF PERFORMING ORGANIZATION: Naval Research Laboratory

6b. OFFICE SYMBOL (If applicable): Code 6170

7a. NAME OF MONITORING ORGANIZATION

6c. ADDRESS (City, State, and ZIP Code): Washington, DC 20375-5000

7b. ADDRESS (City, State, and ZIP Code)

8a. NAME OF FUNDING / SPONSORING ORGANIZATION: U.S. Air Force

8b. OFFICE SYMBOL (If applicable)

9. PROCUREMENT INSTRUMENT IDENTIFICATION NUMBER

8c. ADDRESS (City, State, and ZIP Code): Brooks AFB
San Antonio, TX 78235

10. SOURCE OF FUNDING NUMBERS

PROGRAM ELEMENT NO	PROJECT NO	TASK NO	WORK UNIT ACCESSION NO
			DN155-131

11. TITLE (Include Security Classification): USAF/NRL Surface Acoustic Wave Vapor Sensor Program

12. PERSONAL AUTHOR(S): Ballantine, D., Snow, A., Klusty, M., Chingas, G., and Wohltjen, H.

13a. TYPE OF REPORT: Interim

13b. TIME COVERED: FROM 6/84 TO 8/85

14. DATE OF REPORT (Year, Month, Day): 1986 October 6

15. PAGE COUNT: 23

16. SUPPLEMENTARY NOTATION

17. COSATI CODES

FIELD	GROUP	SUB GROUP

18. SUBJECT TERMS (Continue on reverse if necessary and identify by block number)

Surface acoustic wave device (SAW)
Chemical microsensors
Chemiresistors
CHEMFETs
Microdielectrometers

19. ABSTRACT (Continue on reverse if necessary and identify by block number)

A sensitive, inexpensive chemical microsensor is described that is capable of meeting performance requirements for DoD applications. Experimentally obtained frequency shifts for known mass loading compare favorably with theoretically predicted mass sensitivities for the 31, 52 and 112 MHz surface acoustic wave (SAW) devices. The 300 MHz SAW device exhibits a frequency stability of better than 1 part in 10^7, as well as good temperature and pressure stability under ambient conditions. Response times were generally less than 10 sec. When coated with a fluoroepoxy pre-polymer this device exhibited a calculated detection limit of 0.04 mg/m^3 for DMMP.

20. DISTRIBUTION / AVAILABILITY OF ABSTRACT: ☒ UNCLASSIFIED/UNLIMITED ☐ SAME AS RPT. ☐ DTIC USERS

21. ABSTRACT SECURITY CLASSIFICATION: UNCLASSIFIED

22a. NAME OF RESPONSIBLE INDIVIDUAL: J. S. Murday

22b. TELEPHONE (Include Area Code): (202) 767-3550

22c. OFFICE SYMBOL: Code 6170

DD FORM 1473, 84 MAR — 83 APR edition may be used until exhausted. All other editions are obsolete.

SECURITY CLASSIFICATION OF THIS PAGE

*U.S. Government Printing Office: 1985-407-947

CONTENTS

BACKGROUND 1

THEORETICAL SCALING LAWS FOR SAW VAPOR SENSORS 3

EXPERIMENTAL INVESTIGATION OF SCALING BEHAVIOR 5

300 MHz SAW VAPOR SENSOR SYSTEM DESCRIPTION 8

SAW COATING PROCEDURE 12

EXPERIMENTAL INVESTIGATION OF VAPOR RESPONSE 13

CONCLUSION 18

REFERENCES 19

USAF/NRL SURFACE ACOUSTIC WAVE VAPOR SENSOR PROGRAM

BACKGROUND

The detection and identification of hazardous chemicals is an important problem. Numerous technologies presently exist for monitoring chemical threats but few are capable of meeting the extremely difficult performance requirements of the Department of Defense. These requirements include small size, ruggedness, automatic operation, sensitivity, selectivity, long shelf life, and minimal maintenance.

Recent advances in microelectronic technology have spawned a new generation of sensor devices all based on planar microfabrication techniques. These sensors are small "chip" size devices which have many of the characteristic features (e.g. manufactuarable, solid state, electronic output) that have been used to great advantage by the microelectronics community. Chemical microsensors have emerged which offer great potential for monitoring hazardous materials. Among these are CHEMFETs, Microdielectrometers, MIS diodes, Chemiresistors, and Surface Acoustic Wave (SAW) devices. All of these devices require a chemically selective coating to permit the detection of the chemical agent of interest. At the beginning of this USAF/AMD sponsored R&D program, the only chemical microsensor technology which was known to possess (at least theoretically) the required sensitivity for detecting war gases at or near miosis levels was the SAW device. Furthermore, several years of work had been spent (with U.S. Army CRDC support) developing coatings for this device which offered selectivity to organophosphorus compounds typically encountered in nerve gas formulations. As a result, the SAW device was selected as the most promising candidate microsensor for development into a DOD suitable chemical agent monitor.

The emphasis of the USAF/AMD program at NRL has been on the engineering of very high frequency (i.e. 300 MHz) SAW sensor devices and hybrid microelectronic support electronics. It was felt that the development of such a system would accomplish several objectives in a fashion which was complementary to other SAW research programs being

Manuscript approved July 17, 1986.

conducted by NRL with U.S. Army funding. First, the system would allow the lead time for engineering of a complete prototype instrument to be shortened since the engineering development work on the USAF SAW sensor subsystem could be conducted in parrallel with more fundamental U.S. Army coating development work. In this way, advanced sensor devices would be available at or near the same time that optimized selective coatings were available. Second, fabrication of a breadboard 300 MHz sensor device would allow potential problems to be identified early in the program. This approach would allow a proof of concept demonstration prior to initiation of a major development program.

The principle by which a SAW vapor sensor operates is conceptually quite simple. The surface acoustic Rayleigh wave is generated on a very small polished slab of a piezolelectric material (e.g. quartz) with an interdigital electrode array which is lithographically patterned on the surface at each end of the device. When the electrode is excited with a radio frequency voltage, a Rayleigh wave is generated which travels across the device surface until it is "received" by the electrode at the other end. The Rayleigh wave has most of its energy constrained to the surface of the device and thus interacts very strongly with any material which is in contact with the surface (e.g. a chemically absorbent coating). Changes in mass or mechanical modulus of the coating produce corresponding changes in the Rayleigh wave velocity. The most common configuration for a SAW vapor sensor is that of a delay line oscillator in which the RF voltage output of one electrode is amplified and fed into the other electrode. In this way the device resonates at a frequency determined by the Rayleigh wave velocity and the electrode spacing. If the mass of the chemically selective coating is altered, then this changes the wave velocity which is measured as a shift in resonant frequency of the device.

The SAW vapor sensor is clearly quite similar to bulk wave piezoelectric quartz crystal sensor such as that originally described by King (1) and subsequently investigated extensively by Guilbault et.al. (2). Both devices respond to mass changes of coating deposited on the device surface. However, SAW devices possess several distinct advantages including substantially higher sensitivity (owing to the much greater device operating frequencies which are possible with SAW), smaller size, greater ease of coating, and improved ruggedness. Direct comparisons of SAW and bulk wave quartz crystal vapor sensors have been conducted by Vetelino et. al. who observed significantly larger signals using SAW devices (3). Other workers have reported on the mechanism of SAW vapor sensor response and model coating studies (4,5).

THEORETICAL SCALING LAWS FOR SAW VAPOR SENSORS

The signal provided by a SAW oscillator vapor sensor can be described by the following theoretical equation (4):

$$\Delta f = (k_1 + k_2) f_0^2 \ h \rho' - k_2 f_0^2 \ h \left(\frac{4\mu'}{V_r^2} \left(\frac{\lambda' + \mu'}{\lambda' + 2\mu'} \right) \right) \quad (1)$$

where Δf is the SAW oscillator frequency change produced by the vapor absorbed into the coating, k_1 and k_2 are material constants for the piezoelectric substrate, f_0 is the unperturbed resonant frequency of the SAW oscillator, h is the coating thickness, ρ' is the coating density, μ' is the shear modulus and λ' is the Lame' constant of the coating, and V_r is the Rayleigh wave velocity in the piezoelectric substrate (3159 m/sec for Y-X Quartz). This relationship assumes that the SAW device coating is isotropic and non-piezoelectric. Furthermore, the relationship is valid only for very thin films (e.g. less than 0.2% of the acoustic wavelength thick). For thicker films, equation 1 can only provide estimates of the signal magnitude. When organic coatings are employed, it is often found that the second term of equation 1 is negligible because the shear elastic modulus of the coating (μ') is small compared to the square of the Rayleigh wave velocity (V_r). Under these conditions, equation 1 reduces to:

$$\Delta f = (k_1 + k_2) f_0^2 \ h \rho' \quad (2)$$

For Y-X Quartz SAW devices, $k_1 = -9.33 \times 10^{-8}\ m^2 \cdot sec/kg$ and $k_2 = -4.16 \times 10^{-8}\ m^2 \cdot sec/kg$. The product of the coating thickness (h) and its density (ρ') is the mass per unit area on the device surface. Equation 2 predicts that the signal obtained from a given mass loading ($h \rho'$ product) will increase with the square of the operating frequency of the SAW oscillator. Furthermore, operating frequency determines the size of the device since it imposes size requirements on the interdigital electrodes used to generate the Rayleigh surface wave. As the operating frequency increases, the device area (and cost) decreases. Higher operating frequencies permit thinner coatings to be employed with a corresponding improvement in response time since vapor diffusion into the coating will be quicker.

Higher operating frequencies also result in greater baseline noise which hinders detection at the lowest concentrations. All of these considerations result in a set of scaling laws (detailed in reference 6) which can offer guidance in predicting the ultimate performance capabilities of SAW vapor sensor technology. The key assumption in these predictions is that the sensitivity increases with the square of the frequency. Preliminary studies indicated that this theoretical model was valid (4). Nevertheless, additional studies were performed to provide additional substantiating evidence of the model's accuracy.

Experimental Investigation of Scaling Behavior

In order to verify the preceeding theoretical model a series of experiments were conducted on devices operating at frequencies of 31, 52, and 112 MHz. In these experiments, the frequency shift produced by different mass loadings applied to the SAW oscillator was measured. A highly reproducible mass loading on each device was obtained from coatings of various thicknesses deposited by the Langmuir- Blodgett (L-B) technique. Devices designed for 300 MHz operation were not included in the study because the device package made it impossible to coat these devices using the Langmuir-Blodgett technique. Coatings were applied to the devices and then connected to the RF electronics in order to measure the resonant frequency of the coated device. Then, with the device still connected to the electronics, the coating was removed using a Q-tip soaked with solvent for the coating. When the device was clean and dry, the resonant frequency was again measured. The difference between the clean and coated resonant frequencies was recorded as the frequency shift produced by the coating. It was expected that the same number of layers of coating would produce correspondingly greater frequency shifts as the device frequency was increased from 31 to 52 and then 112 MHz. The results of this investigation are presented in figure 1. The strong dependence of sensitivity (defined as the slope of the frequency shift vs number of layers) is clearly evident. The theoretical model would predict that these slopes should increase in the ratio of 1 : 2.8 : 12.8 as the measurement frequency is increased from 31 to 52 to 112 MHz. The experimentally measured slope increase in the ratio of 1 : 5 : 19 which suggests that the sensitivity increases even more with frequency than one would anticipated from the theory.

In addition to improved sensitivity, higher operating frequencies also afford faster response times since thinner coatings are employed. A 31 MHz and 112 MHz SAW device were coated with the same material (Poly(ethylene maleate)) to a thickness which provided similar sensitivities to DMMP vapor. When exposed to 2 ppm of DMMP, the 31 MHz device required more than 1000 seconds to reach equilibrium. The 112 MHz device required less than 100 seconds. Preliminary results with a 300 MHz SAW device, having a different coating than that used in the 31 and 112 MHz studies, have revealed response times of less than 10 seconds. In fact, reponse times this small are probably determined by the speed with which the challenge gas mixture can be made rather than by the

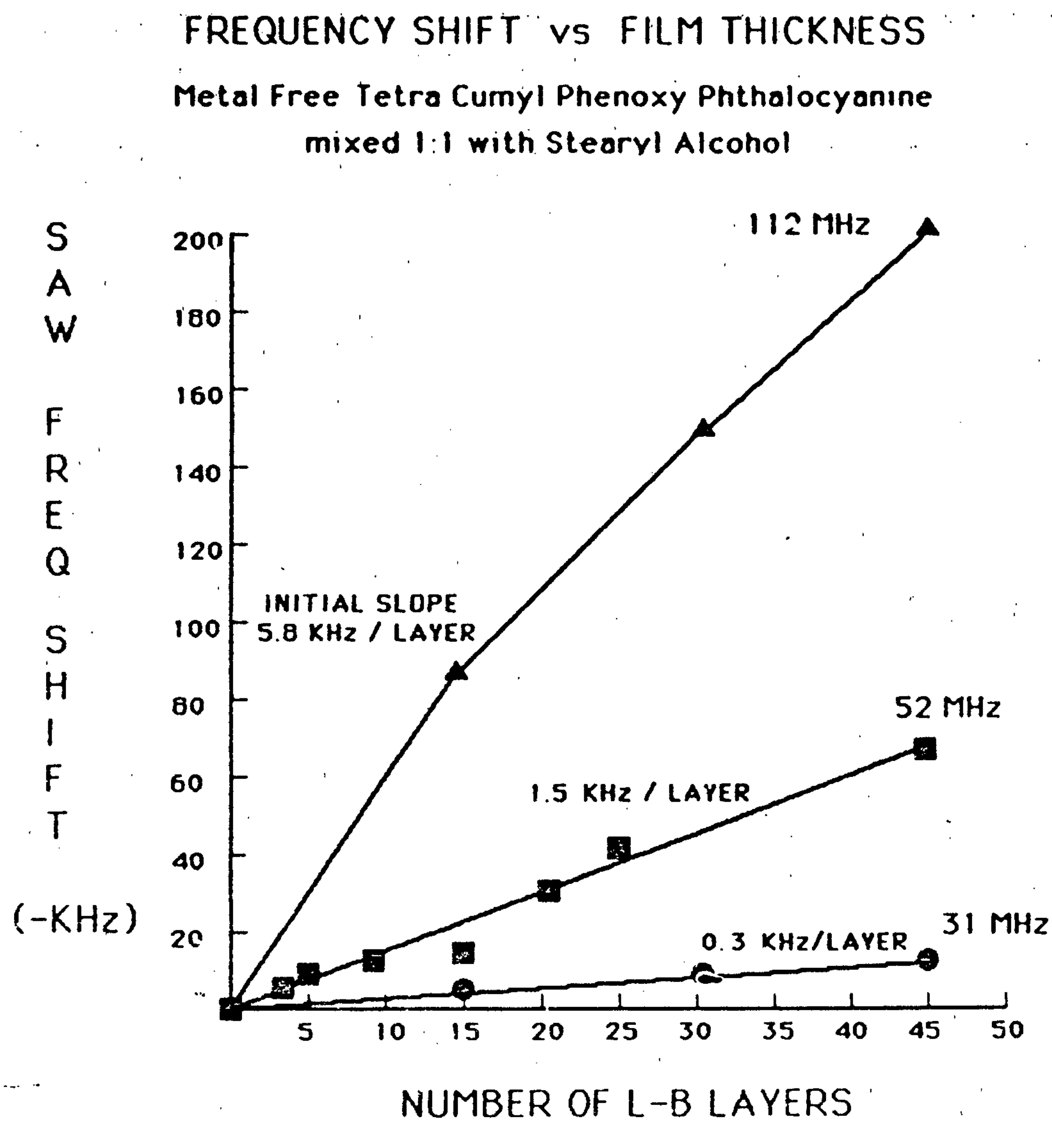

Fig. 1 — Experimental frequency shifts obtained from various mass loadings measured with 31, 52, and 112 MHz SAW oscillators

response time of the sensor itself. If the response time is limited solely by the rate of diffusion into the coating, then one expects to observe an inverse fourth power dependence of reponse time on operating frequency. This is due to the fact that the time for diffusion to occur is related to the inverse square of the coating thickness and the coating thickness required to provide a given vapor sensitivity is related to the inverse square of the operating frequency. In practice this inverse fourth power dependence is not observed, probably because other factors besides simple diffusion into a coating are involved. Nevertheless, substantial improvements in response times are observed as the operating frequency is increased.

300 MHz SAW Vapor Sensor System Description

The objective of this work was to design the highest frequency SAW vapor sensor ever studied. A frequency of 300 MHz was selected as a suitable target frequency since it was possible to fabricate SAW devices at this frequency using optical lithographic tools. Devices at significantly higher frequencies (e.g. 600 MHz and above) usually require more exotic fabrication technologies such as X-ray or E-beam lithography. Theory indicated that a 300 MHz device would offer substantial improvements in sensitivity, size, and response time over previous SAW vapor sensor devices.

A dual SAW delay line oscillator configuration was chosen for the vapor sensor. In this design, two SAW delay lines are fabricated on the same substrate. One delay line is coated with the chemically selective film and the other is left uncoated. The frequencies of the two delay line oscillators are mixed to provide a frequency equal to the difference of the two oscillator frequencies. In this way, frequency drifts caused by ambient temperature and pressure fluctuations experienced by the SAW device are compensated. Furthermore, the difference frequency is much lower (e.g. several hundred KHz) than the frequency of the oscillators themselves (i.e. 300 MHz). This makes it much easier to measure the SAW vapor response using inexpensive, digital counter circuitry. The actual design of the 300 MHz dual SAW vapor sensor device is illustrated in figure 2. The "chip" is fabricated on ST-Quartz using gold metallization on top of a thin adhesion layer of titanium. The electrode configuration was selected to provide high resonant Q and minimal insertion loss from the coating. Overall size of the chip is 240 X 130 mils (6 X 3.3 mm). The active area of each SAW delay line is approximately 2 square millimeters. The SAW device is mounted in a conventional microelectronic 8 pin gold flat package whose internal volume is less than 60 microliters. The device is held in the package using epoxy and electrical connections are wire bonded from the device to the package connecting leads. The SAW delay line was fabricated to NRL specifications by SAWTEK, Inc. Orlando, Florida (P/N 851210). The conventional gold lid of the device package was replaced with a piece of Lucite fitted with two, 1/16 inch stainless steel vapor inlet and outlet tubes. This lid was held onto the top of the device using a small C-clamp.

The high frequency of this sensor required a new approach toward the fabrication of not only the SAW device but also the supporting electronics.

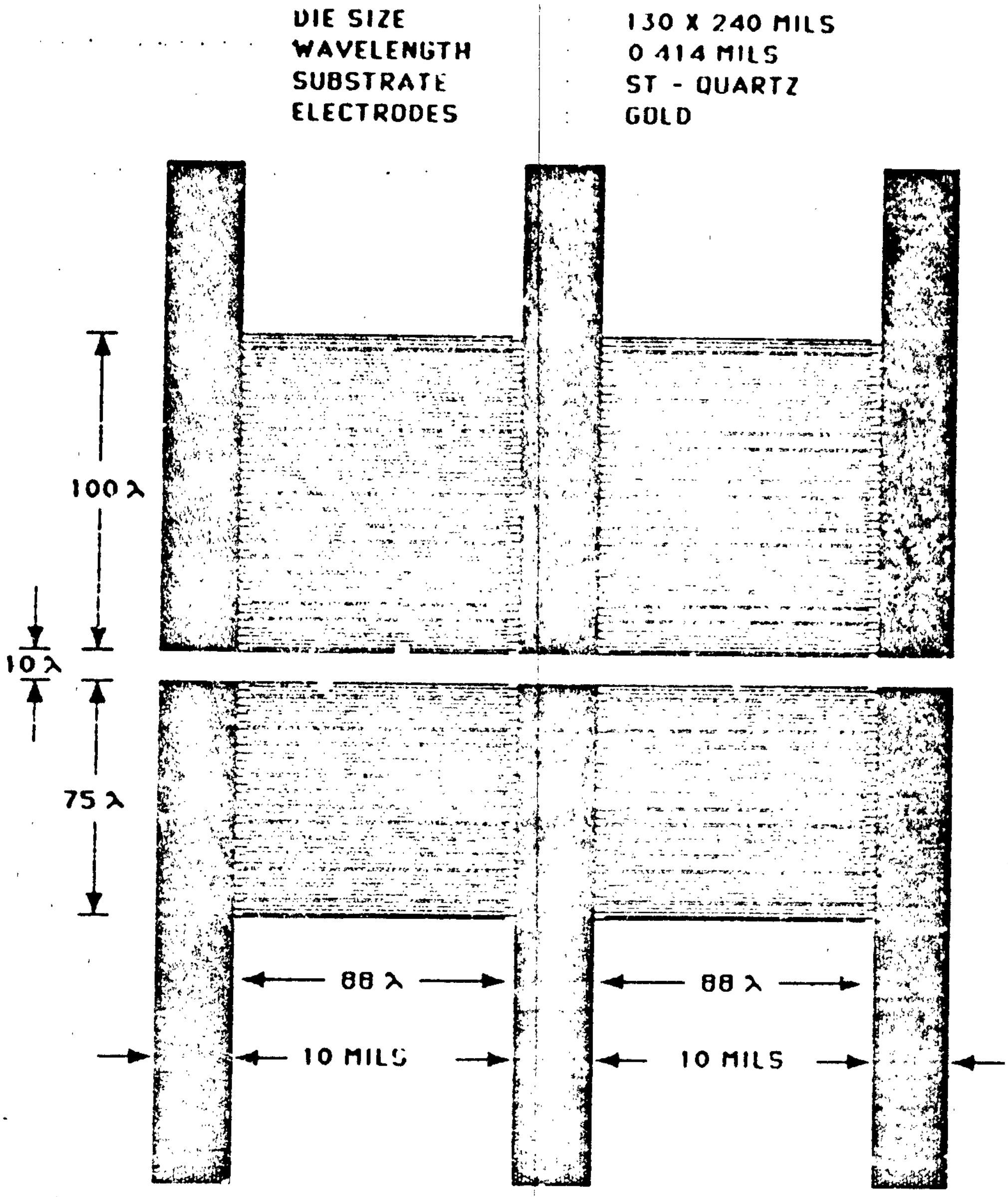

Fig. 2 — NRL 300 MHz dual SAW device

In order to improve stability and reliability and to reduce the size of the supporting electronics, hybrid fabrication technology was employed. The two RF amplifiers required to power the dual SAW delay line oscillators were contained in a 24 pin dual inline package. Each RF amplifier was a simple single transistor, tuned circuit design. Chip resistors, capacitors and transistors were used along with novel chip inductors microfabricated on glass. The final design consumed less than 500 mW of power and provided more than 20 db of gain at 300 MHz. The RF module can be reconfigured (i.e. tuned) to operate at other frequencies besides 300 MHz. The Dual 300 MHz SAW RF Module was fabricated to NRL specifications by SAWTEK, Inc. Orlando, Florida (P/N 852008).

The dual SAW device and RF module were connected together on a small printed circuit board to form a complete vapor sensor subsystem as shown in figure 3. Electrical power and output signal connections are made to this P.C. board. In addition, the mixer used in this device is mounted on the board external to the RF module. The mixer is a passive device (Mini-Circuits Lab, double balanced mixer, TFM-2) which could be incorporated into the RF module in future designs. The total volume occupied by the sensor system was less than 1 cubic inch.

The electrical performance of the complete dual SAW vapor sensor module proved to be quite acceptable. Power consumption (less than 1/2 Watt) was substantially below the 1 Watt design goal. The actual, uncoated, resonant frequency of the device was 290 MHz. A frequency stability of 1 part in 10^7 measured over a 1 second interval was desired. The actual system (uncoated) was stable to better than 9 parts in 10^8. This translates into a baseline noise level of less than 30 Hertz. Significant improvements in the stability of the oscillator may be possible through redesign of the SAW device. The present design utilized a common ground bus for the two delay lines. This common ground was found to cause some cross talk between the two oscillators thereby degrading the frequency stability.

The stability of the system to pressure fluctuations appeared to be good. Increasing the pressure on the device by about 0.1 atmospheres produced frequency variations of less than 4 KHz. Temperature stability of the system under normal room temperature fluctuations was very good. However, when a more aggressive temperature test was made (i.e. a 600 degree heat gun placed 3 feet away which made the system too hot to touch), large frequency changes (e.g. 100 KHz) were observed. While it was not possible in a quick test to determine unambiguously the source of the drift, it appeared that the RF module was the most likely culprit. Small phase shifts caused by changes in temperature of capacitors or inductors could easily explain the observed temperature sensitivity. More attention to this problem will be required in future designs which must operate over the full MIL-SPEC temperature range.

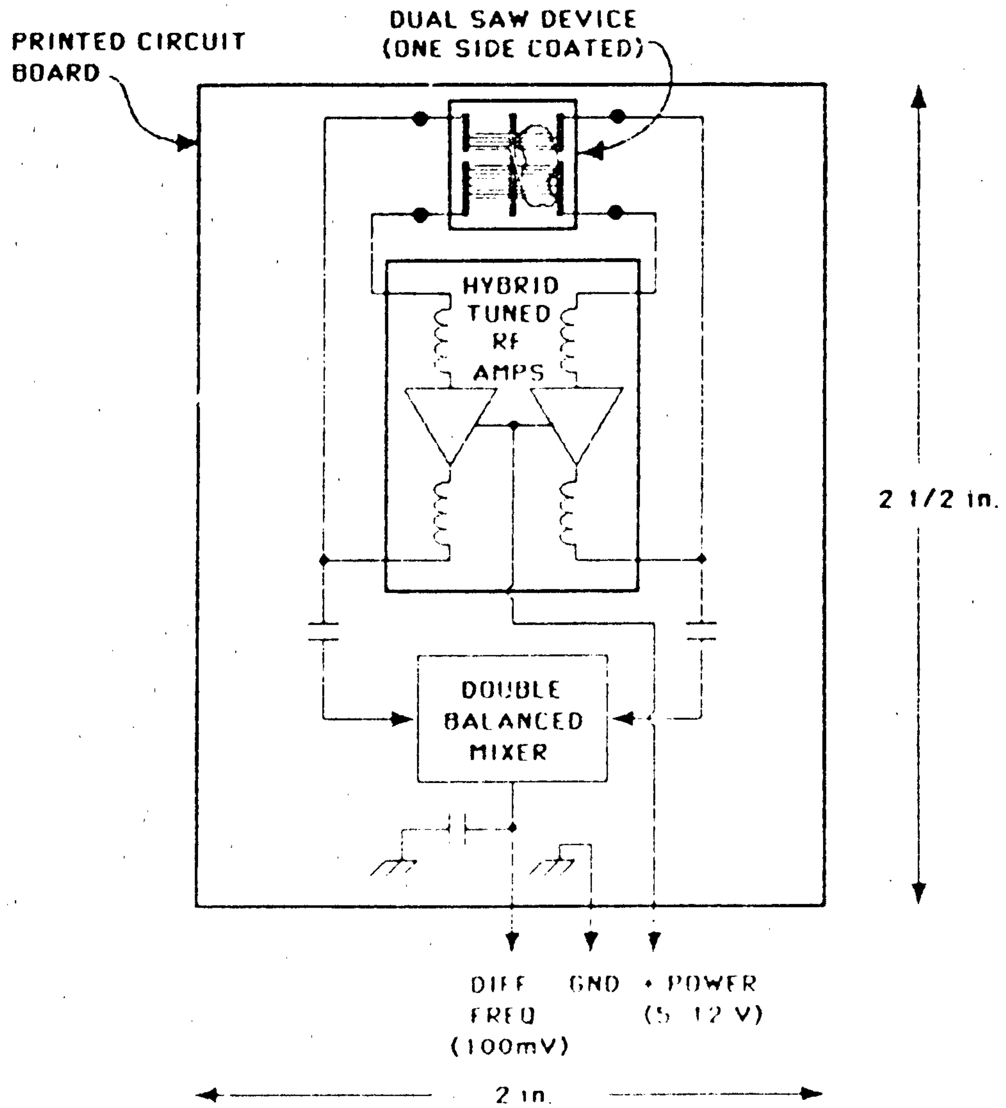

Fig. 3 — NRL 300 MHz dual SAW vapor sensor system

SAW Coating Procedure

Results of SAW vapor sensor tests conducted at 31 and 112 MHz revealed that one of the best coatings for detecting G-agent simulants (such as DMMP) was a fluoroepoxy pre-polymer provided by Dr. Jim Griffith of NRL's polymer materials branch. This compound, dubbed "fluoro polyol" has been demonstrated to detect GB and GD and was used to evaluated the response of the 300 MHz SAW vapor sensor. It is an oligomeric material which is soluble in a number of organic solvents including chloroform. The structure of the material is shown below:

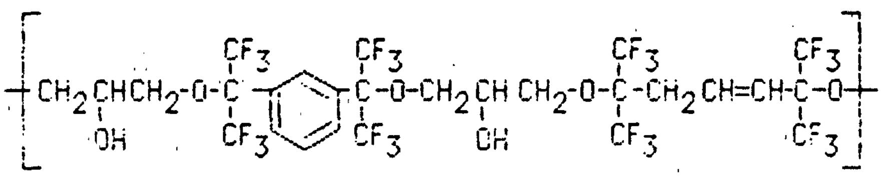

NRL's "Fluoro polyol"

The technique selected to deposit this material onto the SAW device was air brushing. Other techniques such as Langmuir-Blodgett dipping or spin casting could not be employed because the devices were packaged and wire bonded. This would make application of a uniform coating impossible. The only other method available was solvent evaporation in which a small drop of a dilute solution of coating in a volatile solvent is deposited onto the device surface and allowed to dry. This technique requires great care since the active area to be coated was only about 2 square millimeters in size.

Coating application was accomplished by spraying through a small mask positioned over the active area of the delay line to be coated. A dilute solution of approximately 0.1% by weight of fluoro polyol in chloroform was used. Compressed air was used as the propellant. The spray was adjusted to provide a barely visible deposit on a clean glass plate when sprayed from a distance of 3 inches for 15 seconds. This spray was then used to coat the device from a distance of 6 inches while the difference frequency was monitored with an oscilloscope and frequency counter. Mulyiple short bursts of the spray onto the device surface resulted in a coating which produced a total frequency shift of 260 KHz. The device was allowed to sit in clean, dry air for about 12 hours prior to testing.

Experimental Investigation of Vapor Response

Exposure of the fluoro polyol coated SAW device to simulant and interferent vapor challenges was performed using a fully automatic vapor generating system designed and built at NRL. The system is capable of generating low concentrations of vapor (e.g. 0.1 - 10 ppm simulants) using thermostatted, gravimetrically calibrated, permeation tubes. Higher vapor concentrations (e.g. 100 - 10,000 ppm interferences) can be generated using gravimetrically calibrated bubblers. Vapor streams from both the bubblers and permeation tubes can be diluted using precise, computer operated, mass flow controllers. Dry air is used as a carrier gas and the outlet of the system is at ambient pressure. All tubing in the system is stainless steel to minimize corrosion and wall adsorbtion. The flow rate of vapor presented to the sensor is computer controlled and programmable. Vapor generation and acquisition of sensor response data is performed with an APPLE IIe computer. The SAW sensor signal from the RF module is fed into a Systron-Donner frequency counter which communicates to the computer via an IEEE 488 interface bus.

Four low concentration vapors (ammonia, methane sulfonyl fluoride, dimethyl acetamide, and dimethyl methyl phosphonate; generated using permeation tubes) and eight high concentration vapors (dichloro ethane, water, toluene, isooctane, diethyl sulfide, tributyl phosphate, 2-butanone, and 1-butanol; generated using bubblers) were used to test the SAW sensor. The sensor was exposed repeatedly to clean air carrier and then to air contaminated with a particular vapor. The difference between the SAW frequencies measured during clean air and contaminated air exposure was used to determine the magnitude of sensor response. Data were obtained at four different concentrations for each of the vapors investigated.

A summary of the vapor exposure data is illustrated graphically in figures 4 and 5. The responses are expressed in Hertz per part per million of vapor concentration. The results show a very high degree of selectivity for the simulants (i.e. DMMP, DMAC, and MSF) as opposed to the interferents. The largest interferent (besides ammonia) is tributyl phosphate which is the interferent most closely related to DMMP. However, the fluoropolyol is still more than 150 times more sensitive to DMMP than to tributyl phosphate. The selectivity against water vapor is really excellent with the fluoro polyol responding more than 20,000 times more strongly to DMMP than to water.

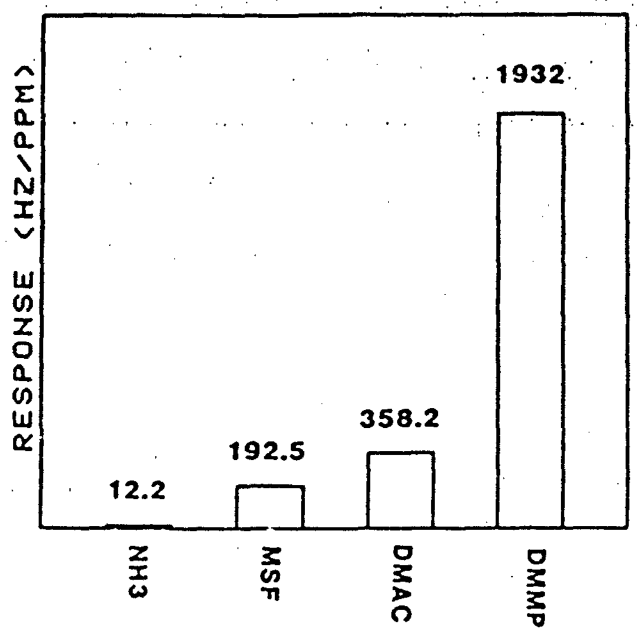

Fig. 4 — Summary of SAW responses to simulant vapors

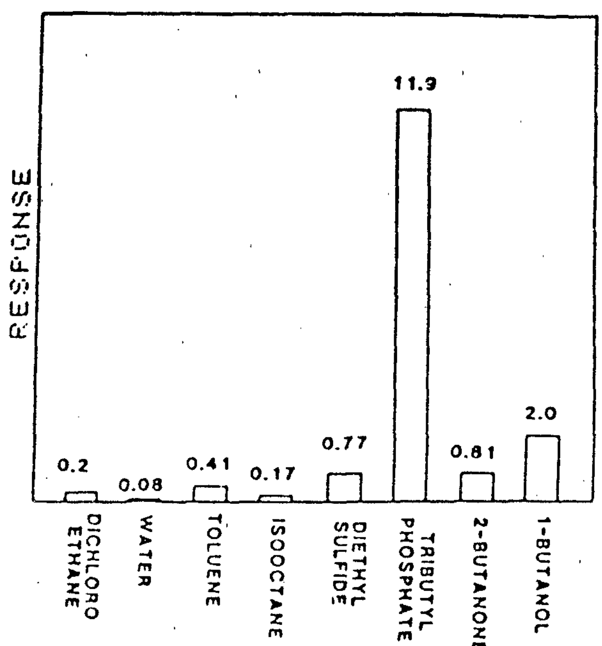

Fig. 5 — Summary of SAW responses to interference vapors

Figure 6 shows a typical response curve obtained from an exposure to 0.5 ppm (about 2 mg/m^3) of DMMP. The results are very good. Response time is less than 10 seconds and is probably limited by the ability of the vapor generator to switch vapor streams and establish equilibrium. At this concentration, the sensor is providing a signal of more than 5 KHz with a baseline noise level of less than 30 Hz. This is a signal to noise ratio of more than 150 to 1. A conservative estimate of the detection limit based on these results is 0.04 mg/m^3 assuming a detection threshold signal to noise ratio of 3 to 1. These results represent the first attempt at vapor detection using the 300 MHz SAW sensor. Further improvements to the system which reduce the noise or increase the signal will yield still lower detection limits.

A calibration curve for DMMP is shown in figure 7. Calibration curves for other vapors tested and raw data from the vapor exposure experiments is contained in the Appendix.

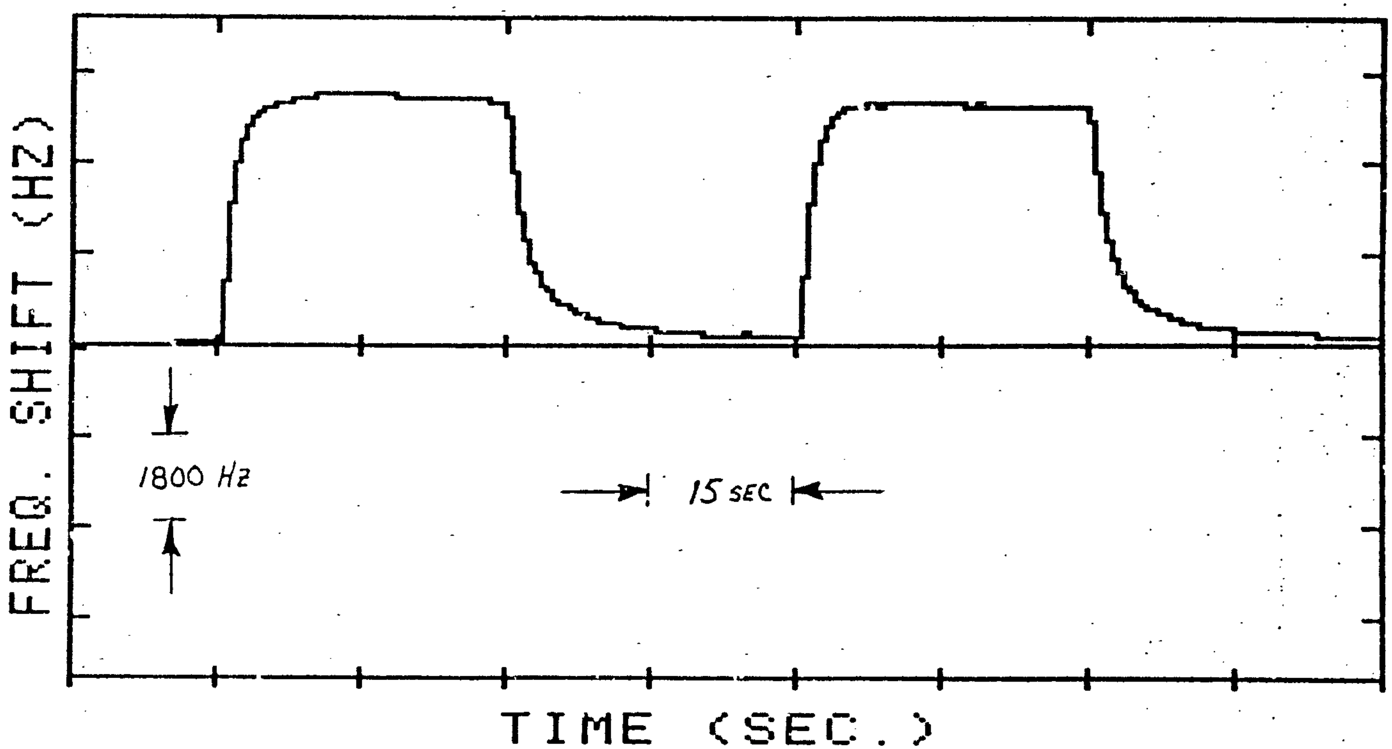

Fig. 6 — Typical response of a fluoro polyol coated 300 MHz SAW device exposed to consecutive pulses of 0.5 ppm DMMP in air

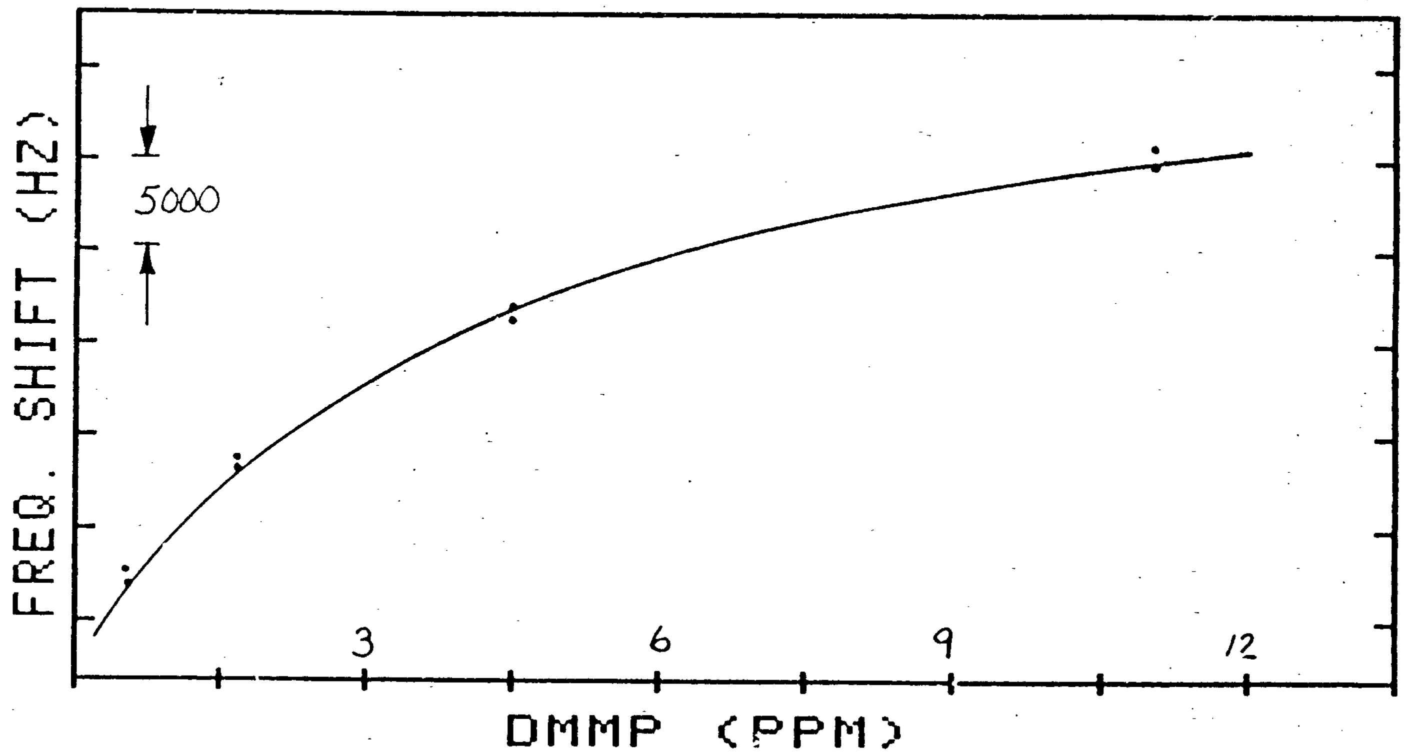

Fig. 7 — Calibration curve for fluoro polyol coated 300 MHz SAW device exposed to various concentrations of DMMP in air

CONCLUSION

The experiments described here have demonstrated the validity of a theoretical response model developed at NRL which predicts a SAW device sensitivity which increases with the square of the frequency.

A 290 MHz dual SAW delay line oscillator and a hybrid RF electronics module has been designed, fabricated, and tested. The electrical performance of the device met or exceeded the design targets. Further attention should be paid to the areas of baseline noise reduction, temperature drift compensation of the RF electronics, and improved packaging of the SAW device.

An oligomeric fluorinated pre-polymer material developed at NRL, "fluoro polyol" was selected as the coating to be used in evaluating the SAW vapor sensor response. This compound has been shown to detect GB and GD with slightly less sensitivity than that measured with DMMP. The material is soluble in chloroform and was applied to the active area of the SAW device using a spraying technique.

The vapor responses measured during the preliminary study were very good. Response times were usually less than 10 seconds and it is believed that this time is determined not by the SAW sensor, but by the vapor generation apparatus. The magnitude of the baseline noise fell within the predicted limits as did the magnitude of the vapor responses. Strongest responses were obtained when the sensor was exposed to DMMP. A detection limit of less than 0.04 mg/m^3 is estimated for the present device. Very modest improvements in coating technology (i.e. materials and methods of application) along with modest reductions in baseline noise should permit the selective detection of organophosphorus compounds at concentrations below 0.01 mg/m^3.

REFERENCES

1. W. King Jr., Analytical Chemistry, 36, 1964, pp 1735-1739.

2. J. Hlavay, and G.G. Guilbault, "Applications of the Piezoelectric Crystal Detector in Analytical Chemistry", Analytical Chemistry, 49(13), 1977, pp1890-1898.

   J. F. Alder, and J.J. McCallum, "Piezoelectric Crystals for Mass and Chemical Measurements", The Analyst, 108 (1291) 1983, pp 1169-1189.

3. A. Bryant, D.L. Lee, and J.F. Vetelino, "A Surface Acoustic Wave Gas Detector", Proc. IEEE 1981 Ultrasonics Symposium, pp 171-174.

4. H. Wohltjen, "Mechanism of Operation and Design Considerations for Surface Acoustic Wave Vapor Sensors", Sensors and Actuators, 1984, pp 307-325, volume 5.

5. A. Snow, and H. Wohltjen, "Poly(ethylene maleate) - Cyclopentadiene: A Model Reactive Polymer-Vapor System for Evaluation of a SAW Microsensor", Analytical Chemistry, 56(8), 1984, pp 1411-1416.

6. H. Wohltjen, A. Snow, and D. Ballantine, "The Selective Detection of Vapors Using Surface Acoustic Wave Devices", Proc. of the Int. Conf. on Solid State Sensors and Actuators - Transducers '85, Philadelphia PA, June 11-14, 1985, IEEE Cat. No. CH2127-9/85/0000-0066, pp 66-70.

APPENDIX D

GEO-CENTERS, INC.

THE DYNAMIC BEHAVIOR OF WATER ON ACTIVATED CARBON

D.K. Friday[1], J.J. Mahle[2], G.O. Wood[3]

ABSTRACT

Water is present, usually in relatively large concentrations, in almost all military air purification systems. This work develops an approach to predict the dynamic behavior of water on an activated carbon adsorbent. Although water is the only adsorbate considered, the approach may easily be extended to treat filtration systems with multicomponent challenges.

Water isotherms were measured for BPL carbon at 25C and 35C and a correlation was developed using an expression introduced by Dubinin. The isotherm correlation was incorporated into a non-isothermal mathematical model used to predict the uptake rate and breakthrough behavior of water. Breakthrough experiments were performed using the following initial bed and feed conditions: (1) 50% RH feed to a dry bed, (2) 80% RH feed to a bed equilibrated at 50% RH, and (3) 80% RH feed to a dry bed. The model predictions compare quite favorably to the experimentally measured values.

INTRODUCTION

It is important to understand the behavior of water for two reasons; (1) it can adversely effect filter performance against challenges of light gases (e.g. cyanogen chloride) and (2) the transient behavior of water by itself can result in adverse behavior. This work develops a mathematical model to describe the dynamic behavior of water vapor challenging a bed of activated carbon. Experiments are performed to measure the adsorption equilibrium of water and the results are correlated using a function suggested by Dubinin for water adsorbed onto activated carbon. Three breakthrough experiments are

1. GEO-CENTERS, INC., 10903 Indian Head Hwy, Ft. Washington, MD 20744

2. Air Purification Branch, Research Directorate, CRDEC

3. Los Alamos National Laboratory, Los Alamos, New Mexico

UNCLASSIFIED

performed which result in three different types of waves. The characteristics of each wave type and their impact on filter performance are discussed.

MATHEMATICAL MODEL --- MATERIAL AND ENERGY BALANCES

The following mathematical development is found in several previous works (1,2,3). A more detailed description of the assumptions and the physical meaning and evaluation of the parameters can be found in these references.

Dimensionless material and energy balances for a cylindrical fixed-bed adsorber with an external mass transfer controlling resistance and no radial gradients in temperature and concentration are:

Material Balance

$$\rho_b \frac{\partial q}{\partial \tau} + \frac{\partial (v^* c)}{\partial \zeta} = 0 \qquad (1)$$

Energy Balance

$$\rho_b \frac{\partial h_s}{\partial \tau} + \frac{\partial (v^* \rho_f h_f)}{\partial \zeta} = -U' \Delta T \qquad (2)$$

Rate Expression

$$\rho_b \frac{dq}{d\tau} = (k_v a)' \cdot (c - c^*) \qquad (3)$$

where the stationary-phase and fluid-phase enthalpies, h_s and h_f, respectively are defined in Reference 1. The two rate parameters, U' and $(k_v a)'$ are defined as

$$U' = \frac{2UL}{\epsilon v r_i} \qquad (4) \qquad\qquad (k_v a)' = \frac{k_v a L}{\epsilon v} \qquad (5)$$

Equation 3 describes the rate at which material is transferred from the passing vapor stream to the surface of the carbon. It assumes a linear driving force (4) where c* is the vapor phase concentration at the surface of the particle. The value of $k_v{}^*a$ can be calculated a priori using a Sherwood number correlation (5) to determine k_v and an appropriate value for the surface area per volume, a.

Equations 1, 2, and 3 can be reduced to a set of ordinary differential equations using a stage model approach (1,6,7). In this work, the resulting ordinary differential equations are solved using a Runge-Kutta fourth order integration algorithm with twenty stages.

EXPERIMENTS

Adsorption Equilibria for Water on Activated Carbon

Figure 1 shows the results for water adsorption isotherms measured for BPL 25 and 35C. It has been suggested by Dubinin (8) that a function of the form,

$$RH = \frac{q}{K1\ (K2 + q)\ (1 - K3\ q)} \tag{6}$$

may be used to correlate adsorption data measured for water on activated carbons. The solid line appearing in Figure 1 is the best fit of the parameters K1, K2, and K3 to the data using the a least squares criteria on RH.

The procedure used to measure these data is given by Mahle et al. (9). Also, as shown by the measurements of Mahle et al., the isotherms for water on ASC carbon deviate only slightly from those presented here for water adsorbed on BPL carbon. Therefore, the breakthrough results reported here for BPL carbon are very similar to behavior expected for ASC carbon. (This laboratory has conducted breakthrough experiments using ASC carbons and found the results to be similar to BPL).

Note the water isotherm has both unfavorable (concave up) and favorable (concave down) regions. The experimental conditions were chosen to illustrate the significance of each of these regions. The next section will discuss those results.

Breakthrough Experiments

Apparatus and Procedure -- The apparatus used for the breakthrough experiments is shown in Figure 2. Air, used as the carrier gas, passes through a molecular sieve dryer and a carbon filter to remove water and organics. The main metering valve is used to regulate the flow, 5 lit/min for experiments 1 and 2 and 10 lit/min for experiment 3. After the clean air passes through the flowmeter, a portion of the stream passes through a saturated water bath. The desired relative humidity is achieved in the following manner. The metering valve and the bypass valve are set such that the ratio of their flows produces a relative humidity near the desired value. The humidity analyzer and controller (EE&G 911 Digital Humidity Analyzer) measures the relative humidity of the feed stream based on the temperature of the feed stream. If the relative humidity is below the setpoint, the water bath heater is activated. Since, it is a simple on-off controller with no cooling action, the initial setting of the bypass flow must produce a lower than desired RH. The humidified air flows through the carbon bed and the effluent relative humidity is measured by a second EE&G humidity analyzer.

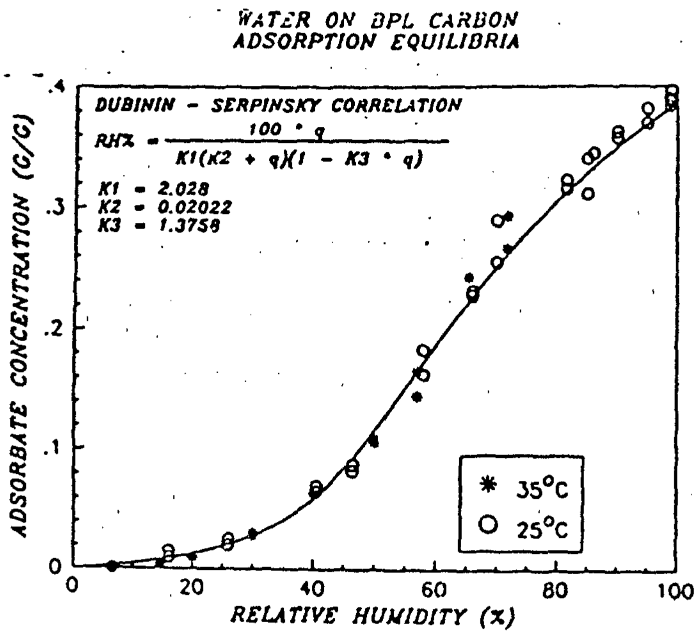

Figure 1

FIGURE 2

SCHEMATIC OF BREAKTHROUGH APPARATUS

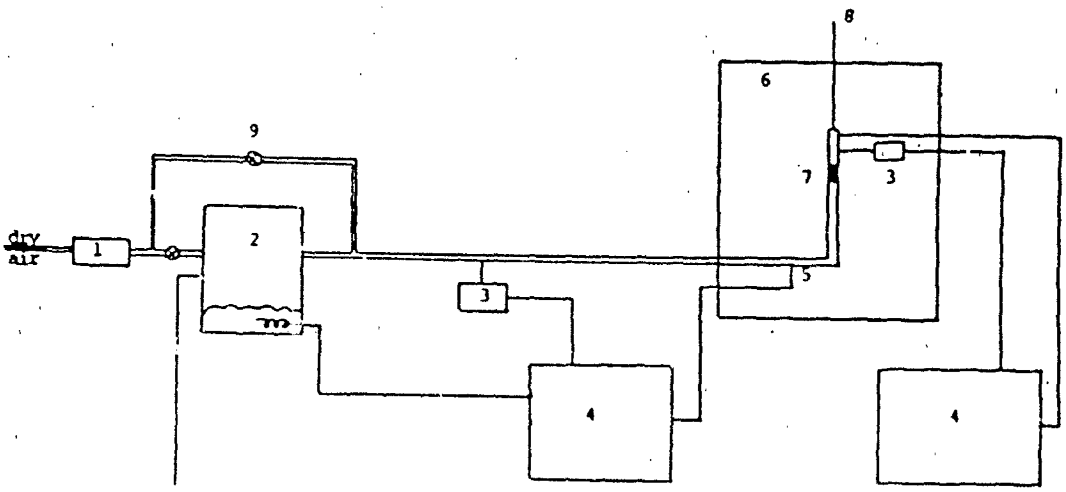

1. Flow meter
2. Water bath
3. Humidity Sensor
4. Humidity Analyzer and Controller
5. Temperature probe
6. Controlled Temperature Chamber
7. Carbon Bed
8. Effluent Air
9. By-pass Valve

UNCLASSIFIED

Breakthrough Results --- The breakthrough concentration and temperature were measured using the following feed and initial bed conditions:

1. 50% RH feed to a clean bed
2. 80% RH feed to a bed equilibrated at 50% RH
3. 80% RH feed to a clean bed

These conditions were chosen to illustrate the three different wave types that can be formed in an adsorption bed. Rhee et al. in their equilibrium theory analysis (10), describe the three wave types as: (1) gradual, (2) abrupt and (3) combined . The important features of each will be discussed as each experiment is analyzed.

Table 1 contains the constant parameters for each experiment. Table 2 is a summary of the operating conditions for each experiment.

TABLE 1. SYSTEM CONSTANTS

ρ_b = 480 kg/m^3
c_f = 1.04 kJ/kg K
c_s = 2.7 kJ/kg K
c_a = .075 kJ/mol K
k_v = Reference (5)

a = 3400 m^{-1}
d_p = 0.001 m (particle diameter)
U = 0.093 kJ/m^{2}K s
T_{ref} = 298
λ_d = 40.68 kJ/mol
d_b = 0.0415 m (bed diameter)

TABLE 2. BREAKTHROUGH EXPERIMENTS

Experiment	Feed		Initial Bed Condition			v	T_{amb}
	RH%	T(K)	RH(%)	T(K)	Carbon dry (g)	(m/sec)	(K)
1	50	298	0	297.5	23.96	.0616	297.5
2	80	297	50	297	23.96	.0616	297
3	80	298	0	298	25.85	.123	298

Experiment 1. Figure 3 shows the breakthrough results for a challenge of 50% RH air to an initially dry bed. The effluent RH and temperature are plotted as a function of time. The symbols represent the experimental values and the solid lines are the predictions of the mathematical model. The conditions for this experiment were selected to show the effluent concentration response when the isotherm is unfavorable (see Figure 1 between 0 and 50% RH).

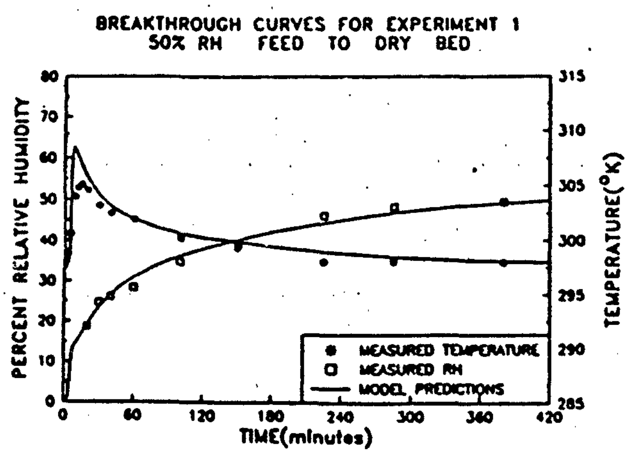

Figure 3.

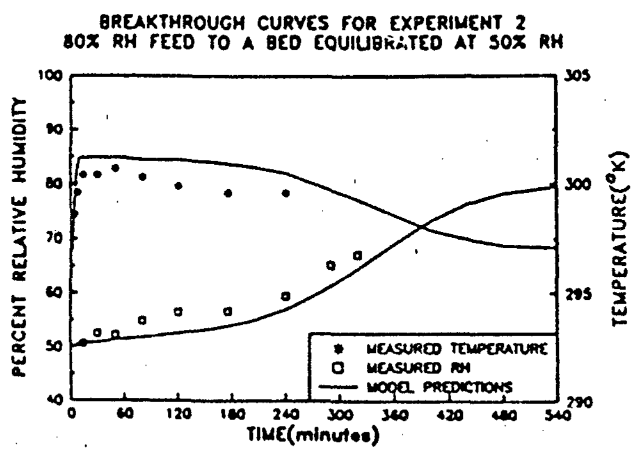

Figure 4

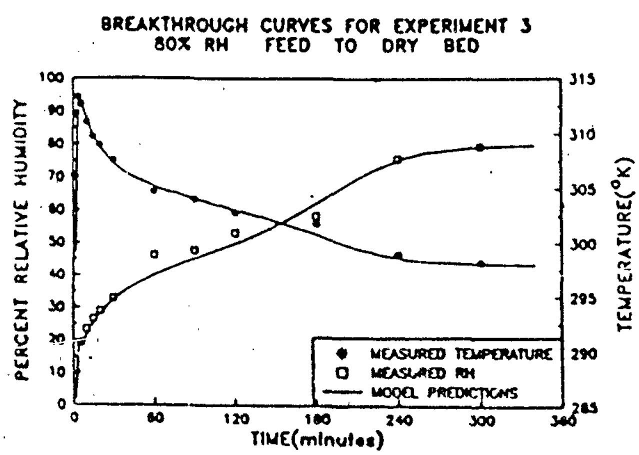

Figure 5

UNCLASSIFIED

The effluent RH versus time curve is typical of a gradual wave. The through curve is concave downward to the time axis. After a short period of time, an appreciable percentage of the feed concentration is seen in the effluent (about 20% RH).

The temperature response is also typical of a gradual wave. The temperature quickly rises to a maximum temperature (in this case about 305K) and then falls back gradually to the feed temperature. Note the temperature rise for this experiment was approximately 8K.

Experiment 2. Referring back to Figure 1, notice that the water isotherm is favorable between 50% and 80% RH. This is the situation for most adsorbates, in particular the standard nerve agents, thus one would expect an S-shaped breakthrough curve. Figure 4 shows the results of an 80% RH feed to a bed initially equilibrated at 50% RH. Although not very sharp, the breakthrough behavior does follow an S-shaped pattern.

This type of wave is called an abrupt wave or a constant pattern wave. This means that at a certain distance into the bed, the shape of the concentration front does not change as the wave is transmitted down the bed. The temperature profile is also interesting. Typically, when an adsorbate if fed to a clean bed, a pure thermal wave (i.e., no associated concentration wave) is produced. The thermal waves usually moves much faster through the bed than the concentration front, therefore, adsorption takes place at the higher plateau temperature. Figure 4 clearly depicts this phenomenon. The thermal wave is through the bed in about ten minutes while the concentration wave does not start to leave the bed until about three hours. Note also that the change in temperature is only about 5K.

Experiment 3. Figure 5 shows the breakthrough data measured for 80% RH feed to a clean bed. The effluent RH as a function of time shows the characteristics of a combined wave. This type of wave possess at least one abrupt and one gradual section. For this experiment, the first section of the wave is gradual and the last section is abrupt. Notice that the resulting breakthrough curves of both temperature and RH are essentially a combination of the breakthroughs of experiment 1 and experiment 2. The only difference is the higher flow rate (10 lit/min as opposed to 5 lit/min).

The temperature rise in this experiment was 15K. There are two points important points to make. First, the temperature rise is relatively independent of the feed temperature and flow conditions. Therefore, the heat generated from adsorbing water cannot be the cause of a filter fire. Second, a soldier wearing a gas mask may experience some discomfort as the temperature rises, which could be of concern especially in a stressful situation.

In general, the model predictions and the experimental results are in agreement. Notice that Experiment 3 seems to give the best agreement. This is due in large part to several improvements in the experimental procedure, which include better temperature and RH control procedures.

UNCLASSIFIED

CONCLUSIONS

1. The three types of waves that can be formed in and passed through [illegible] adsorption are demonstrated both mathematically and experimentally.

2. The mathematical model seems to fairly represent the breakthrough behavior using correlated equilibrium data and _a priori_ calculated rate parameters.

3. The heat generated by the adsorption of water is not nearly high enough to ignite a bed. However, the temperature rise could be significant enough to be of concern to a soldier in a stressful situation.

REFERENCES

1. Friday, D.K. and LeVan, M.D., "Solute Condensation in Adsorption Beds During Thermal Regeneration:, AIChE J., 28, 86 (1982).

2. Friday, D.K. and LeVan, M.D., "Thermal Regeneration of Adsorption Beds. Equilibrium Theory for Solute Condensation", AIChE J., 30, 679 (1984).

3. Friday, D.K. and LeVan, "Hot Purge Gas Regeneration of Adsorption Beds with Solute Condensation:Experimental Studies", AIChE J., 31, 1322 (1985).

4. Vermeulen, T. et al., "Adsorption and Ion Exchange", Chemical Engineers Handbook, 6th Edition, McGraw-Hill, New York, Section 16 (1984).

5. Petrovic, L.J. and Thodos, G., "Mass Transfer in the Flow of Gases Through Packed Beds", Ind. Eng. Chem. Fund, 7, 274 (1968).

6. Rodigrues, A.E. and Beira, E.C., "Staged Approach of Percolation Processes", AIChE J., 25, 416 (1979).

7. Ikeda, K., "Performance of the Nonisothermal Fixed-Bed Adsorption Column with Nonlinear Isotherms", Chem. Eng. Sci., 34, 941 (1979).

8. Dubinin, M.M., "Isotherm Equation for Water Vapor Adsorption by Microporous Carbonaceous Adsorbents", Carbon, 19, 402, (1981).

9. Mahle, J.J., Wood, G.O., Friday, D.K., "Vapor Phase Equilibria of Water on Activated Carbon", Proceedings of the 1987 Conference on Chemical Defense Research, U.S. Army CRDEC, APG, MD, November 1987.

10. Rhee, H.K., Aris, R., and Amundson, N.R., "First Order Partial Differential Equations: Volume I. Theory and Application of Single Equations", Prentice-Hall, Englewood Cliffs, N.J., 1986.

VAPOR PHASE EQUILIBRIA [illegible] ON ACTIVATED CARBONS

John J. Mahle[1], David K. Friday[2], and Gerry O. Wood[3]

ABSTRACT

Vapor phase adsorption of water accompanies almost all military applications of activated carbons. Capillary condensation is primarily responsible for the adsorption of water vapor on activated carbons. Capillary condensation produces a hysteresis phenomena. The desorption side of the hysteresis loop can be used to predict pore volume distribution from the Kelvin equation. Studies of the water vapor equilibria on a variety of activated carbons have been used to obtain an understanding of the capacity and temperature dependence of the adsorption. Models to correlate water vapor adsorption and multicomponent adsorption with water as a constituent have been examined. The pore volume distributions as determined from water adsorption were the same as those from nitrogen isotherms. It is proposed that water vapor adsorption be determined in lieu of nitrogen adsorption, because the former provides valuable phase equilibria data as well as a means of characterizing the pore volume distribution on activated carbons.

INTRODUCTION

Water adsorption on activated carbons is important because water vapor is always present in the atmosphere and because the behavior of water adsorption provides information about the structure of the carbon. Water adsorption on several carbons is examined together with the implications of water's unique behavior.

Adsorption equilibria can be characterized by isotherms which relate the amount adsorbed to the fluid phase concentration. The shape of the isotherm can reveal much information about the mechanism of adsorption.

The equilibrium isotherm of water is characterized by hysteresis which is an irreversibility between adsorption and desorption. The presence of hysteresis in the water isotherm and the lack of hysteresis for organic vapor isotherms indicates that a different mechanism is involved for water adsorption than for adsorption of organic vapors on activated carbons.

---

[1]Air Purification Branch, Research Directorate, CRDEC

[2]GEO-CENTERS, INC., 10903 Indian Head Hwy, Ft. Washington, MD 20744

[3]Los Alamos National Laboratory, Los Alamos, New Mexico

Organic vapors adsorb by wetting the surface of the carbon and filling the pores at a reduced vapor pressure due to favorable van der Waals interactions. In water adsorption, the pores are filled sequentially according to the capillary condensation mechanism as described by the Kelvin equation:

$$r = \frac{-2\,\sigma \cos\Theta\, V}{RT\,\ln(p/p_o)}$$

r - Pore Radius (Angstroms)
σ - Surface Tension (dynes/cm)
V - Molar Volume (cc/mole)
Θ - Contact Angle
T - Temperature (K)
p/p_o - Relative Pressure
R - Gas Constant

The reason that adsorption differs from desorption is not fully understood. Everett (1) describes the various theories of adsorption hysteresis. One of the most widely accepted theories is the so called "ink bottle" theory which suggests that small pore radii constrict the path between larger pores. Thus the larger pores cannot empty until the relative pressure has reached that corresponding to the radius of the smallest pores, which constrict that volume of adsorbate.

Several researchers (2-7) have studied water adsorption on activated carbons. They suggested that the water isotherm which exhibits hysteresis due to capillary condensation could be used to study the pore volume distribution of activated carbon. They showed that the micropore size distribution predicted using the Kelvin equation and the water isotherms gave the same values as were given by the more widely accepted method of Barrett et al. (8). The latter method correlated the pore distribution to the desorption side of the nitrogen isotherm.

The most recent studies of water adsorption have centered on developing an isotherm correlation of water. Dubinin et al. (9) published an isotherm correlation which is derived from a proposed surface reaction mechanism between the water and surface oxide sites. This is a three parameter model that could correlate the shape of the isotherm. This isotherm lacks an explicit temperature dependence and the physical significance of the parameters has not been verified. More recently Sircar (10) proposed a isotherm correlation which accounts for capillary condensation through the Kelvin equation and pore volume distribution parameters. This correlation is conceptually simple but difficult to evaluate analytically. Neither of these correlations provides a complete description of water adsorption equilibria on activated carbons because they ignore the presence of hysteresis.

EXPERIMENTAL

The equilibrium loading of water on the activated carbon samples was measured as a function of the relative humidity and temperature. A schematic of the apparatus is presented in Figure 1. The adsorbed concentration was recorded as the grams of adsorbed water per gram of dry carbon.

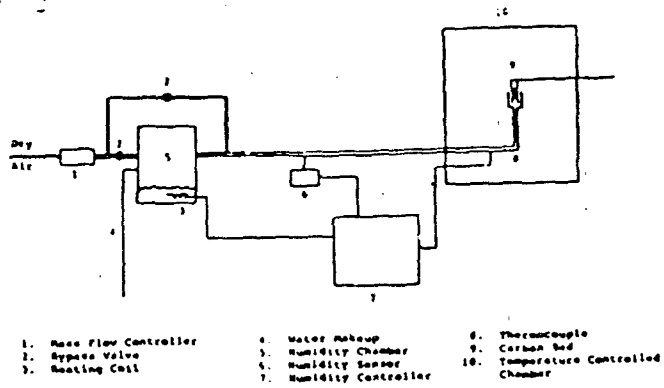

Figure 1

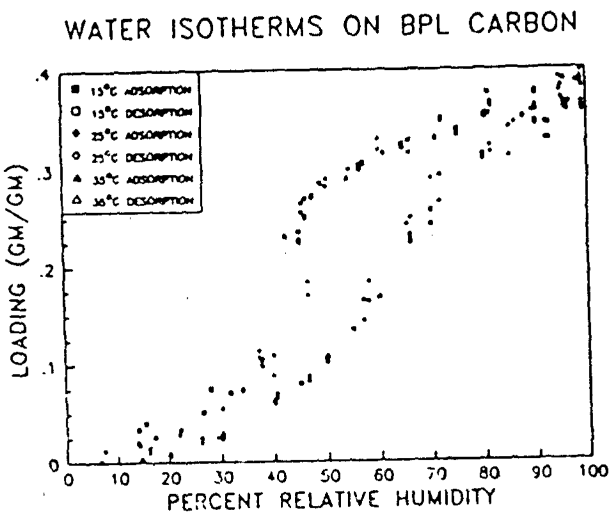

Figure 2

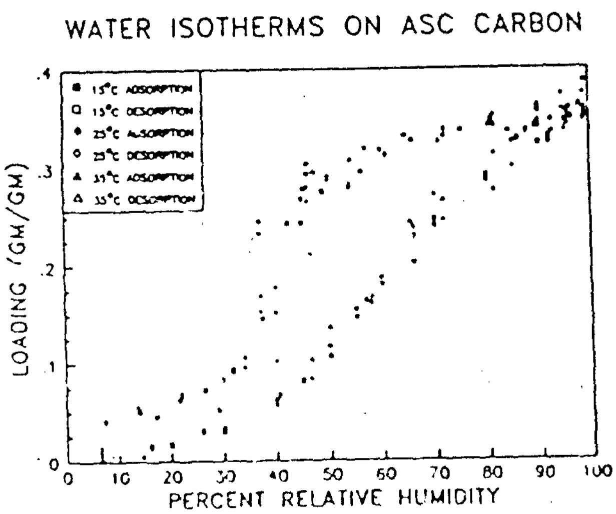

Figure 3

UNCLASSIFIED

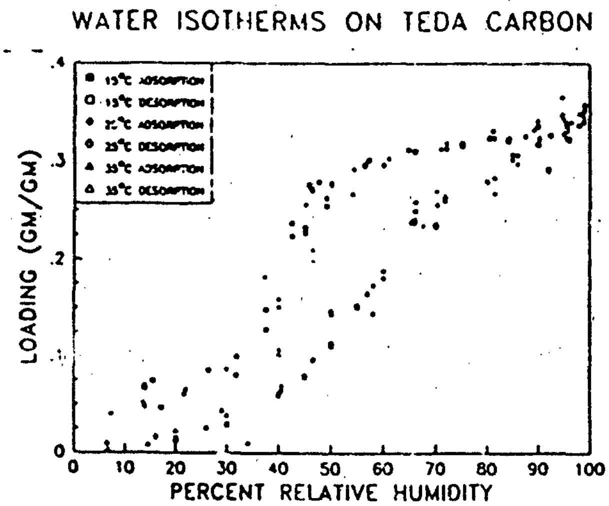

Figure 4

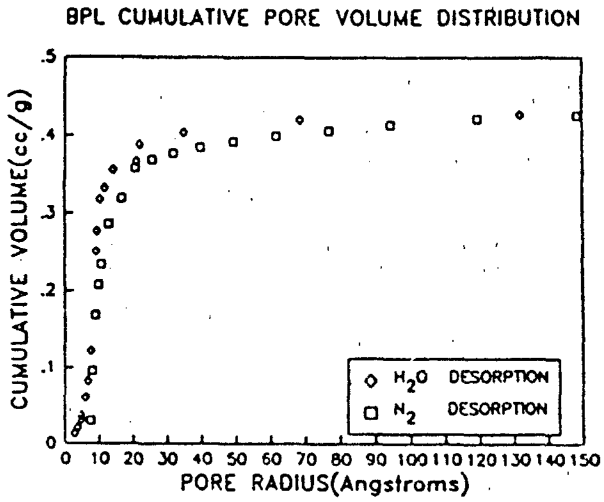

Figure 5

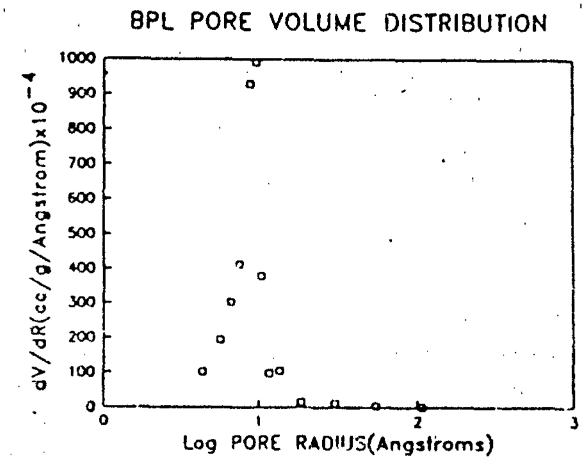

Figure 6

UNCLASSIFIED

The feed air was conditioned by first drying it on a molecular sieve adsorbent and then passing it over a water bath. Low humidity air was obtained using a bypass line. Higher humidities were obtained using the feedback controller which activated a heating element in the water bath when the sensor reading dropped below the setpoint.

The humidified air was drawn over the carbon samples using a vacuum line. The constant temperature chamber was used to equilibrate the feed air and carbon.

Three carbon samples were studied. BPL an unimpregnated activated carbon, ASC an activated carbon similar to BPL which was impregnated with copper, silver, and chromium salts, and ASC-TEDA an ASC carbon which was also treated with triethylene diamine. All three carbon were manufactured by Calgon Inc.

RESULTS AND DISCUSSION

The equilibrium isotherms of water vapor on BPL, ASC and ASC-TEDA are shown in Figures (2-4). Both adsorption and desorption data are presented for each carbon at three temperatures 15, 25 and 35^{o} C. The saturation loading on each carbon sample shows some scatter due to condensation at the highest relative humidities.

The fluid phase concentration is plotted as percent relative humidity in order to be able to compare the adsorption at different temperatures. The hysteresis loop appears to close slightly as the temperature is increased for all three carbons. If the heat of adsorption followed the same temperature dependence as the heat of condensation the isotherms when plotted on an RH scale would overlay each other at each temperature. Since this is not the case the model of water adsorption should incorporate an explicit temperature dependence to account for this.

The hysteresis, which is characteristic of water adsorption on activated carbons, is present in each sample at each temperature. The desorption side of the hysteresis loop maintains a high loading down to 45% RH where the loading drops off dramatically. The implication of this is that once the carbon is saturated with water it would take prolonged exposure to air with a relative humidity below 40% to desorb a substantial amount of water. The lower closure point of the BPL carbon occurs at approximately 20% RH. The lower closure point of the hysteresis loop for the impregnated carbons, ASC and ASC-TEDA is never reached. This is probably due to solution effects of the water with the impregnants. The residual loading on these samples was eliminated by drying them overnight. This indicates that the residual amount is desorbed but it requires a great deal of energy, such that under ambient conditions once an initial adsorption of water has occurred there will always be some water loaded on the impregnated carbons. This would significant is any study of hydrolysis on these carbons.

The desorption side of the water isotherm can be used to predict the pore volume distribution of the carbon samples. The method used here was the same as Juhola et al. (2) as discussed earlier. Here the adsorbate properties are summarized in Table 1. The pore volume distribution of BPL carbon was also measured using the nitrogen isotherm desorption method of Barrett et al. (8). This was performed on an automated Digisorb 2600 manufactured by Micromeritics Inc. (11). The cumulative pore size distributions from each method is shown in Figure 5. The agreement between these two distributions indicates that the water isotherm can be used to correlate pore volume distributions of carbons.

TABLE 1

Properties of Water for Kelvin Equation

Surface Tension	71.97 dynes/cm
Molar Volume	20.0 cc/mole
Contact Angle - cos θ	0.62

The methods just described for determining pore size distributions are effective for pores up to 200 Å. According to these methods the pore in BPL are centered around 9 Å in radius as shown in Figure 6. Results from nitrogen desorption on impregnated carbons were not available. However, the similarity between the water isotherms of BPL, ASC and ASC-TEDA indicates that the pore size distributions of the impregnated carbons do not differ much from that of the BPL in the micropore range. The difference in the isotherms of BPL, ASC, and ASC-TEDA are most pronounced at the higher relative humidities. Figures 2-4 indicate that the isotherms are essentially the same below about 70% RH. This indicates that the micropore size distribution would be the same for these carbons while the macropore volume is reduced by the presence of the impregnants.

A knowledge of the pore size distribution is important in order to compare the relative performance of various adsorbents. It can give an indication of the ease with which an adsorbent can be impregnated. It can also be used to assess the potential mass transfer resistances of an adsorbent. A distribution of pores whose radii are very small may result in an adsorbent which would selectively adsorb only very small molecules. The water isotherm thus provides a basis to evaluate this very important information, the pore size distribution, for activated carbon adsorbents. The technique requires very few calculations and very limited equipment.

As stated earlier a comprehensive model has not been developed which correctly accounts for all the observed behavior in the isotherms of water adsorbed on activated carbon. Although the Dubinin-Serpinsky equation (9) does correlate individual isotherms it does not account for hysteresis. In addition the fact that the BPL isotherm returns to zero loading at low RH indicates that a proposed surface reaction is not a feasible explanation for the observed adsorption behavior. The Sircar isotherm (10) incorporates a dependence on the Kelvin equation which appears to be valid for water adsorption on carbon. Further work seems justified in an attempt to incorporate into this model the effect of hysteresis.

The only available literature on multicomponent vapor adsorption with water and organic constituents was by Okazaki et al. (12). They proposed a model which accounted for water adsorption through the Kelvin equation and the pore volume distribution. Their model requires solubility parameters for the organic and the water. This type of approach seems well grounded for a further development of a multicomponent system of water and toxic vapors. The presence of adsorbed water must influence the adsorption of toxic vapors either through displacement, or solution, or reaction effects. Therefore a single component water adsorption isotherm on an activated carbon is the basis for the study of the multicomponent case because it provides information about the pore volume distribution and to the amount of water adsorbed.

CONCLUSIONS

Water isotherms on activated carbons are characterized by hysteresis. The presence of water hysteresis must be consiiered in the development of a multicomponent adsorption theory for carbon adsorbents. The hysteresis is also significant in that it can provide information about the pore size distribution of the carbon.

REFERENCES

1. Everett, D.H., "Adsorption Hysteresis", The Solid Gas Interface, ed. E. Alison Flood, New York, Marcel Dekker, (1967).

2. Juhola, A.J., "Palumbo, A.J., and Smith, S.B., JACS, 74, 61, (1952).

3. Juhola, A.J., and Wiig, E.O., JACS, 71, 2069, (1949).

4. Wiig, E.O., and Juhola, A.J., JACS, 71, 561, (1949).

5. McDermott, H.L., and Arnell, J.C., Canadian J. Chem., 30, 177, (1952).

6. McDermott, H.L., and Tuck, M.G.M., Canadian J. Research, 28B, 292, (1950).

7. McDermott, H.L., and Arnell, J.C., J. Phys. Chem., 58, 492, (1954).

8. Barrett, E.P., Joyner, L.G., and Halenda, P.P., JACS, 73, 373, (1951).

9. Dubinin, M.M. and Serpinsky, V.V., Carbon 19, 402, (1981).

10. Sircar, S., Carbon, 25(1), 39, (1987).

11. Henderson, P., Personal Communication, June 1987.

12. Okazaki, M., Tamon, H. and Taei, R., J. Chem. Eng. Japan, 11, 209, (1978).

THE LEVAN EQUATION ISOTHERMS FOR CW-AGENT ADSORPTION ON ACTIVATED CARBON

David K. Friday, GEO-CENTERS, and John B. Opfell[1],
Garrett AiResearch

Abstract: The empirical equation proposed by Hacskaylo and LeVan[2] for adsorption isotherms has several advantages for dynamic-model applications involving chemical warfare (CW) agents. It facilitates reliable extrapolation of equilibrium adsorption data to conditions outside the ranges of partial pressures and temperatures explored. It passes through the point where the adsorbate partial pressure and loading on the sorbent are both zero. And it converges to Henry's Law as the adsorbate partial pressure approaches zero and to the Antoine vapor-pressure equation at the loading corresponding to complete saturation of the sorbent. Isosteric heat of adsorption predicted by this equation has the same temperature dependence as the adsorbate's heat of vaporization. This equation contains six empirically determined coefficients, three of which are calculated from the adsorbate's vapor pressure-temperature relationship. The values of these coefficients have been calculated for the CW agents AC, CK, and CG.

INTRODUCTION

The adsorption phase equilibrium relationships (isotherms) are required to accurately predict the performance of a carbon filter designed to protect personnel from toxic-chemical challenges. There is an overall lack of single-component CW-agent isotherm data that has been measured, and studies that have been conducted frequently use concentrations an order of magnitude greater than the projected challenge concentrations, which are at the very most 30 mg/m^3. Moreover, no reliable multicomponent phase equilibria have been measured for any CW agent and water system. Experimentally determined isotherm data, both single- and multicomponent, for CW agents are required in order to design reliable protection systems based on carbon adsorbents. An appropriate tool to correctly interpolate and correlate these data is also required.

The LeVan equation possesses several characteristics that make it an appropriate tool:

(1) It reduces to Henry's Law at low loadings. This feature makes the correlation much more reliable for interpolating between measured isotherm data points involving concentrations of CW agent in air. Concentrations military protective systems are expected to encounter are generally below those for which adsorbate loading on the sorbent can be reliably measured.

(2) It performs well in interpolating data for CW agents presenting the greatest challenge to carbon-based protective systems.

(3) It predicts within an order of magnitude the adsorption behavior of vapors of closely homologous substances provided the Antoine equation parameters for both substances are available.

The Dubinin-Radushkevich (D-R) and the Dubinin-Astakhov (D-A) equations (given below) are commonly used to correlate and interpolate isotherm data.

$$\ln(p) = D - (E/T)\sqrt{\ln(Wo/w)} \qquad \text{(D-R)} \qquad (1)$$

$$\ln(p) = D - (E/T^{2/n})(\ln(Wo/w))^{1/n} \qquad \text{(D-A)} \qquad (2)$$

where D = empirically determined coefficient
E = empirically determined coefficient
n = empirically determined coefficient
p = adsorbate partial pressure, torr
T = absolute temperature, kelvin
w = adsorbate loading, cc liquid per g sorbent
Wo = pore volume, cc

The Dubinin-Radushkevich equation (Equation 1), in particular, has been used in several studies pertaining to military air purification devices. It has, however, two significant weaknesses. First, it is thermodynamically inconsistent at low loadings in that it predicts an infinite value for heat of adsorption and a deviation from Henry's Law. Second, it frequently predicts different micropore volumes for different adsorbates on the same sorbent.

ANALYSIS

The LeVan equation has been shown[2] to be superior to the D-R and the D-A (Equation 2) equations for several organic vapors. In each instance the two-parameter version of the LeVan equation fits the data as well or better (by the least-squares criterion) than does the D-A equation which has three adjustable parameters. This is an indication that the LeVan equation may provide a better functional representation of the adsorption behavior than does either the D-R or the D-A equation.

In the evaluation of pressure-swing (PSA) and temperature-swing (TSA) adsorbers for air purification, the design-limiting vapor (or vapors, e. g., water and CK) must be identified and the equilibrium adsorption data (isotherms) for them must be measured and correlated. The LeVan equation is an appropriate correlating equation. The correlation is essential in evaluation of alternative sorbents and in choosing the most appropriate simulant vapors.

The LeVan equation, Equation (3), relates the partial pressure of an adsorbate to the adsorbate loading and the absolute temperature of the sorbent-adsorbate system. It is the Antoine equation with the coefficients adjusted to reflect adsorbate loading. It is exactly the Antoine equation when the adsorbate loading is Wo; i. e., the sorbent is "saturated."

$$\ln(p) = A' - B'/(C' + t) \qquad (3)$$

where A' = $2.3025 \times A + \ln (w/Wo)$

A = Antoine equation coefficient, log torr

B' = $2.3025 \times B + b \times (1 - W/Wo)$

B = Antoine equation coefficient, °C-log torr

b = LeVan equation coefficient, °C-ln torr

C' = $C + c \times (1 - w/Wo)$

C = Antoine equation coefficient, °C-log torr

c = LeVan equation coefficient, °C

p = adsorbate partial pressure, torr

t = temperature, °C

w = adsorbate loading, cc liquid adsorbate per g sorbent

Wo = LeVan equation coefficient, cc liquid adsorbate per g sorbent

The LeVan equation has six empirical coefficients. All six can be evaluated simultaneously, of course, by fitting the equation to six data points or by use of a least-square algorithm on the data set for the particular adsorbate-sorbent pair. The Antoine equation coefficients A, B, and C, however, can be determined from adsorbate vapor-pressure data alone and this approach was used to obtain the coefficient values reported in Table 1. Moreover, the coefficient c was assigned the value 0.0 to obtain the two-coefficient form of the LeVan equation.

RESULTS

Table 1 presents Antoine equation coefficient values for the CW agents CK, CG, and AC. How these values can vary with the range of temperature represented in the data set used to obtain them is illustrated by the values presented for CG and AC. (The numbers under "Source" identify the appropriate references.)

TABLE 1

Values of the Antoine Equation Coefficients for Several CW Agents

CW Agent	Temperature Range, °C	A	B	C	Source
CK (cyanogen chloride)	-76.7 to 13.1	6.85736	850.01	200.655	3
CG (phosgene)	-92.9 to 57.2	7.06793	1033.74	239.157	3
CG (phosgene)	-68 to 68	6.84297	941.25	230.0	4
AC (hydrogen cyanide)	-71 to 25.9	6.1370	672.17	180.527	3
AC (hydrogen cyanide)	-40 to 70	7.29761	1206.79	247.532	4

Values for the LeVan equation coefficients for CK, CG, and AC are presented in Table 2. Values for A, B, and C were taken from Table 1.

Values for coefficients b and Wo were calculated from the experimental data through minimizing the sum of the squares of the differences between the observed and predicted values of the logarithm of the equilibrium partial pressure of the adsorbate over the sorbent. Other criteria might have been used, of course, but for extrapolating the available experimentally determined information to the low partial pressures of interest in engineering a CW protection system, the criterion used is an appropriate one. Using the differences between predicted and observed values of ln (p)

TABLE 2

Values of the LeVan Equation Coefficients for Several CW Agents

CW Agent	Wo	A	B	C	b	c
CK (cyanogen chloride)	0.509	6.35736	850.01	200.655	1091	0.0
CG (phosgene)	0.549	6.84297	941.25	230.0	1704	0.0
AC (hydrogen cyanide)	0.511	7.29761	1206.79	247.532	745	0.0

Values assumed for adsorbed-phase densities were: CK, 1.186; CG, 1.392; AC, 0.687 g/cc.

Only the 22.2°C data points were used in evaluating b and Wo for AC.

weights the data at the lower values of partial pressure more heavily in determining the coefficient values than does using the differences in p.

Figure 1 shows the experimental data for CK reported by Reucroft and Chiou[5] and the curve representing the least-squares fit of the LeVan equation to this data. Figure 1 shows the LeVan equation to reasonably represent the experimental data over the range of adsorbate partial pressure explored. It also shows the partial pressures explored in the experiments are nearly all above the range of interest in designing devices to protect personnel from CW agents. Military tube tests, for example, use 1.2 torr (4 mg/liter) as the partial pressure of CK in the feed stream to a protective device under evaluation and 0.0024 torr (0.008 mg/liter) as the breakthrough partial pressure in the adsorber effluent. These test conditions point to the need for isotherm relationships that can be used reliably to extrapolate below the range of partial pressure explored in experiments.

Figure 2 shows the experimental data for CG reported by Reucroft and Chiou[6] and the curve representing the least-square fit of the LeVan equation to this data.

Figure 3 shows the experimental data for AC reported by Reucroft and Freeman[7]. The solid curve represents the least-squares fit of the LeVan equation to the 22.2°C data points only. The agreement between the 22.2°C data points and the curve is acceptable.

The ability of the two-coefficient LeVan equation to correctly represent the temperature dependence is tested by using the 22.2°C values for the coefficients b and Wo in predicting the isotherms for the other temperatures for which experimental data was reported. The agreement between the predicted values of partial pressure and those reported by Reucroft and Freeman is very good, even up to 120.4°C when the AC loading is above 0.02 cc liquid per g carbon. Below this value of loading the agreement deteriorates substantially. Why? In the absence of low-loading data and confirming experimental investigations, one can only speculate. Possibly the two-coefficient form of the LeVan equation is not sufficiently flexible to capture the relationship between loading and partial pressure at very low loadings. On the other hand, accurate measurement of loading at very low values of loading is difficult. Possibly the leveling of the experimentally determined isotherms is an artifact; Henry's Law requires the isotherm to approach an asymptote having a positive slope. Clearly the LeVan equation curves do this. Resolution of the disagreement between the experimental data and the LeVan equation predictions must await additional experimental data.

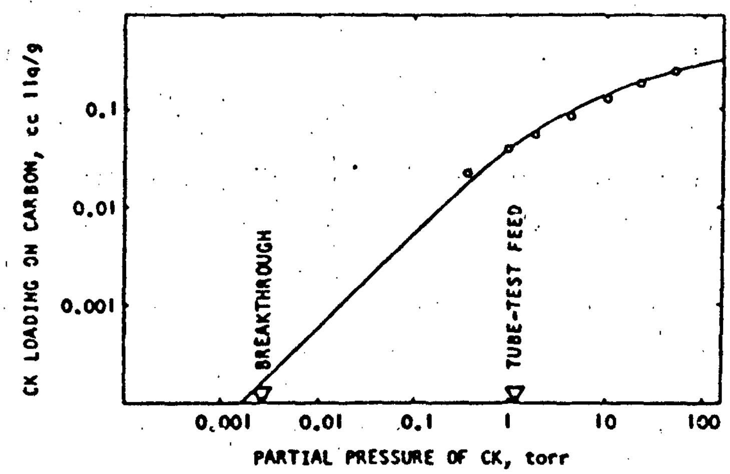

Figure 1. Adsorption of CK on BPL Activated Carbon at 23°C

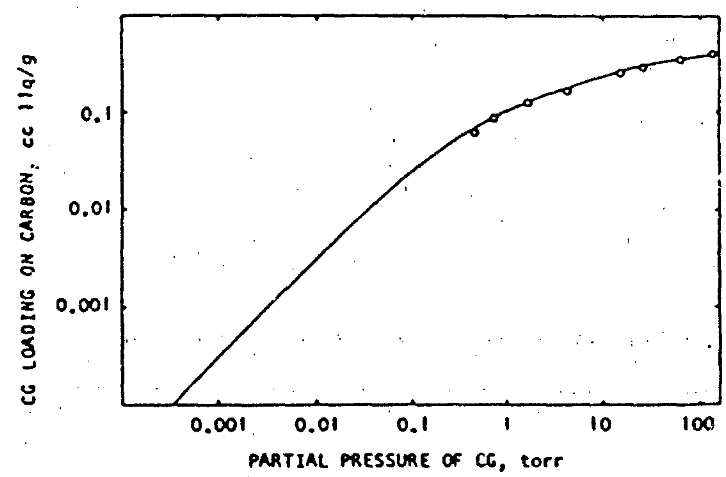

Figure 2. Adsorption of CG on BPL Activated Carbon at 25°C

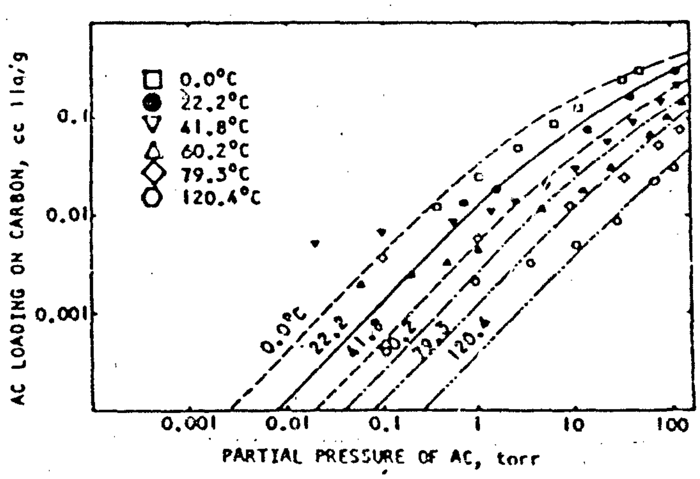

Figure 3. Adsorption of AC on BPL Activated Carbon at Several Temperatures

The values of Wo for each correlation are in the range one would expect for BPL carbon (i. e. 0.5 to 0.6 cc liquid per g of carbon). The differences in the values may arise from the difficulty of determining the adsorbed-phase density. The adsorbed-phase density, for example, has a temperature dependency and the density of the adsorbed phase may be considerably different from the adsorbate's liquid-phase density at the same temperature and pressure.

CONCLUSIONS

1. The LeVan equation appears to be a reasonable correlation for the CW-agent vapors considered.
2. More data from experimental measurement is needed to better assess the efficacy of the correlation, especially at lower values of partial pressure.
3. The particular advantage in using the LeVan equation for extrapolating experimental data is that the predicted isotherms do not intersect between zero loading and the experimental data if the Antoine equation values are used for the coefficients A, B, and C.
4. The LeVan equation provides a reasonable tool for small extrapolation of data on one isotherm to other temperatures.
5. It may prove possible to use the LeVan equation with coefficients b and Wo determined from data on a homologous compound in predicting reliably the equilibrium adsorption behavior of a relatively volatile substance. The prediction of the behavior of one blood agent from the LeVan equation coefficients b and Wo for another, however, is not reliable.

ACKNOWLEDGEMENT

This work was supported by CRDEC and by Garrett AiResearch. John J. Mahle of CRDEC and Lori Woodward of Garrett AiResearch helped with the computation of the coefficients reported.

REFERENCES

1. Garrett AiResearch, 2525 West 190th Street, Torrance, California 90504-6099.
2. Hacskaylo, J. J., and M. D. LeVan, 1985. "Correlation of Adsorption Equilibrium Data Using a Modified Antoine Equation: A New Approach for Pore-Filling Models," Langmuir 1, 97.
3. Green, D. W., 1984. Perry's Chemical Engineers' Handbook, New York: McGraw-Hill.
4. Lange, N. A., 1967. Handbook of Chemistry, Revised Tenth Edition, New York: McGraw-Hill.
5. Reucroft, P. J., and C. T. Chiou, 1975. "Gas Adsorption by Activated and Impregnated Carbons," Quarterly Status Report No. 6 (for July-October 1975) on Edgewood Arsenal Contract EC-CR-76036.
6. Reucroft, P. J., and C. T. Chiou, 1975. "Gas Adsorption by Activated and Impregnated Carbons," Quarterly Status Report No. 4 (for January-April 1975) on Edgewood Arsenal Contract EC-CR-75020.
7. Reucroft, P. J. and G. B. Freeman, 1977. "Gas Adsorption by Activated and Impregnated Carbons," Quarterly Status Report (for July-October 1977) on Edgewood Arsenal Contract ARCSL-CR-78024.

THE BREAKTHROUGH BEHAVIOR OF A LIGHT GAS IN A FIXED-BED ADSORPTIVE REACTOR

David K. Friday, GEO-CENTERS INC.
Prospect Square Building
10903 Indian Head Highway
Ft. Washington, MD 20744

ABSTRACT

The adsorption and subsequent chemical reaction of cyanogen chloride on impregnated, activated carbon is studied. The system is considered to be isothermal and at a constant relative humidity of 80%. A material balance is written which includes a reaction rate based on the adsorbed phase concentration of cyanogen chloride and the concentration of the impregnant material. Two mass transfer resistances are included : (1) external mass transfer from the passing vapor stream to the surface of the carbon particle, and (2) internal mass transfer describing the rate at which material is transported from the adsorption site to the reaction site. Breakthrough times measured using different flow rates, bed depths and particle sizes compare favorably with model predictions.

INTRODUCTION

Adsorption coupled with chemical reaction is a phenomenon that finds applications in several areas. Several investigators (1-4) have studied systems where chromatographic reactors are used to determine reaction rate constants or achieve higher levels of separation than is possible with a simple adsorption bed. Others (5,6) have examined systems where it is desired to remove pollutants from contaminated water streams.

Mathematical analyses of systems where physical adsorption is coupled with chemical reaction fall into two areas. The first investigations were conducted using chromatographic columns and include the work of Magee (3) who assumed a linear adsorption isotherm and a simple reversible reaction,

$$A \rightleftharpoons B + C$$

where the forward and reverse reaction rates are expressed in terms of the vapor phase concentrations. Gore (4) modified this approach by writing the reaction rates as functions of the adsorbed phase concentrations. Chu and Tsang (7) extended the treatment of Magee by introducing a Langmuir-Hinshelwood kinetic model to account for competitive adsorption.

The second major area of investigation has involved using an equilibrium theory approach to develop the appropriate material balances. It is assumed that mass transfer resistances and dispersion forces are not important so that the resulting partial differential equations may be solved using the method of characteristics. Rhee *et al.* (8) developed solutions to problems where several different reaction mechanisms were considered and either Langmuir or Freundlich adsorption isotherms were used. Other workers (9,10) have followed a similar approach and have compared equilibrium theory solutions to measured breakthrough curves. The equilibrium theory approach can be used to identify the type of transitions that may be formed (gradual, abrupt, combined) and to calculate the speed of the stoichiometric centers of these transitions.

Most of the earlier studies of chromatographic systems have assumed linear isotherm relationships, reaction rates governed by the mobile phase concentrations and fast mass transfer rates. This work will extend the previous chromatographic studies by considering a nonlinear adsorption isotherm and a reaction rate based on the adsorbed phase concentration. In addition, both an external film resistance and an internal particle resistance is included. Measured breakthrough times for cyanogen chloride on activated, impregnated carbon are used to evaluate model parameters. The predicted breakthrough curves are compared with the equilibrium theory solution using a time invariant first order reaction to demonstrate the effects of a second order reaction rate and mass transfer resistances.

MATHEMATICAL DEVELOPMENT

The fixed-bed adsorptive reactor consists of a cylindrical bed of activated carbon treated with reactive metal salts (ASC Whetlerite (11) . The reactor is assumed to operate isothermally. For fixed-bed adsorption systems involving gases at low and moderate pressures, the accumulation in the vapor phase may be neglected. It is assumed the vapor phase is ideal, there is negligible pressure drop through the bed, the effect of composition on the vapor phase density and velocity is small, and that there is plug flow with no axial dispersion. The resulting overall material balances may be written as

$$\rho_b\,(\partial q/\partial t) + \epsilon\, v\,(\partial c/\partial z) = -\,R_i(q,M) \qquad (1)$$

$$\rho_b\,(\partial M/\partial t) = -\,\alpha\; R_i(q,M) \qquad (2)$$

where α is the stoichiometric coefficient for the chemical reaction between the adsorbate and the impregnant. The metal impregnant remains in the stationary phase and the reaction products do not change the adsorption equlibria or affect the material balance.

Because the breakthrough behavior at relatively low effluent concentrations is considered (below 0.5% of the feed concentration), it is important to include an external mass transfer resistance in the model. A film resistance is represented by a traditional linear driving force approximation with reaction rate included as,

$$\rho_b\,(\partial q/\partial t) = k_v a\,(c - c^*) - R_i(q,M) \qquad (3)$$

Since the chemical reaction takes place in the adsorbed phase, it is important to include an internal mass transfer resistance. There are two basic approaches that researchers have taken when modelling solid phase resistances. Distributed parameter models used to represent macropore and/or micropore diffusion control express the adsorption rate as a partial differential equation with c and q as the dependent variables and the radial position within the particle as the independent variable. However, distributed parameter models when coupled with the material balances make the resulting set of differential equations more difficult to solve and frequently still retain a loading-dependent diffusivity. A second approach is to represent the solid phase resistance using a lumped parameter model with a linear driving force approximation. This may be expressed as,

$$\rho_b (\partial q/\partial t) = k_p a (q^* - q) - R_i(q,M) \tag{4}$$

where $k_p a$ is the internal mass transfer coefficient. Ruthven (12) assesses the validity of this approximation by saying "the simple linearized model is a useful engineering approximation for unfavorable, linear or moderately favorable isotherms". Therefore, for systems involving light gases on activated carbon which normally exhibit linear to moderately favorable adsorption equlibria, one would expect Equation (4) to be a reasonable approximation.

According to Glueckauf (13,14), $k_p a$ is a function of the adsorbent particle diameter, d_p, given by the equation,

$$k_p a = 60\ D_p\ /\ (d_p)^2 \tag{5}$$

where D_p is the average particle diffusivity.

EXPERIMENTAL SYSTEM

It is desired to remove small amounts of cyanogen chloride from a humid air stream to produce breathable air. To accomplish this, a fixed bed of activated, impregnated carbon is used to adsorb and then subsequently react with the cyangen chloride. This system is considered to be isothermal and at a constant relative humidity of 80%. The reaction rate is assumed to be second order in the adsorbed phase concentration of cyanogen chloride and metal concentration. Therefore, R_i may be defined as,

$$K_i = k_i\,[q]\,[M] \qquad (6)$$

It has been determined in a previous study (15) that the stoichiometric coefficient, α, for the reaction of cyanogen chloride with the metal impregnant is about 1/5. The governing material balance and rate equations are solved using a staged model approach (16). For the results to be presented, forty stages are used.

In addition to the material balances and rate expressions, the adsorption phase equilibria for cyanogen chloride on ASC carbon at 80% relative humidity is required. Reucroft *et al.* (11) measured the quantity of adsorbed cyanogen chloride as a function of the vapor phase concentration at a constant relative humidity of 80%. The temperature of the study was ambient (22-25C). A Langmuir isotherm was used to correlate the data and the resulting equation is given below.

$$q^* = q_{sat}\, K\, c^* / (1 + K\, c^*) \qquad (7)$$

The parameters K and q_{sat} were determined using a least squares best fit of the measured data of Reucroft.

There are two sources for the experimental data which will be presented. The breakthrough time as a function of bed depth at four velocities was measured by Morrison (17) and the breakthrough time as a function of bed depth for three different particle sizes was measured by Puhala (18). The breakthrough time is established as the time for a specified concentration of cyanogen chloride to appear in the effluent. The conditions used by Morrison and Puhala are given below.

Initial Condition = a bed of activated , impregnated carbon in equilibrium with uncontaminated air at a relative humidity of 80%

Feed Condition = air at 80% relative humidity, contaminated with 0.065 mol/m^3 of cyanogen chloride

Breakthrough Concentration = 1.3×10^{-4} mol/m^3

Bed Diameter = 2.0 cm

Temperature = ambient (21C-25C)

ANALYSIS AND DISCUSSION

Shown in Figure 1 are the breakthrough times for different bed depths and velocities. The symbols are the measured data of Morrison (17) and the lines are the model results using the conditions given above and the parameter values given below.

k_va = 105, 143, 188, 263 (for 5.9, 9.6, 14.7, 24.8 cm/s, respectively)
$D_p = 2.0 \times 10^{-3}$ cm^2/s
$d_p = 1.0 \times 10^{-3}$ m
$k_1 = 4.33 \times 10^{-6}$ m^3/mol s

The values for D_p and k_1 were obtained using a value for D_p in the range suggested by Costa *et al.* (19) for light gases on activated carbon and picking the value of k_1 to give the best fit to the data. The Ranz-Marshall (20) correlation for mass transfer to a packed bed of non-porous particles was used to calculate k_va. The results indicate that the model with the appropriate values of k_1 and D_p accurately describes the behavior of cyanogen chloride on ASC carbon over the range of conditions tested. The model results presented in the following discussion are generated using the values for k_1 and D_p given above.

Figure 2 shows the predicted breakthrough times and the measured breakthrough times versus bed depth using three different particle sizes. The superficial velocity for these tests was 9.6 cm/s . The results indicate a stronger particle size dependence than the model predicts. (The model was run with a large value for k_pa and the predicted curves are closer together.) The difference between the predicted and actual results may be caused by several factors. One possibility is that D_p is smaller than 0.002, making the particle resistance more dominant. However, this is unlikely for two reasons. First, it is well known that there is efficient solid phase transport in activated carbons due to the well developed marcopore structure. Second, a smaller D_p was tried, but the data measured for Figure 1 could not be well represented with any value of k_1 and the prediction for Figure 2 does not get appreciably better (the curve for the 12-16 mesh size falls well below the actual data).

Figure 3 shows the predicted effluent concentrations of cyanogen chloride as a function of time using three different bed depths. The parameter values used to generate these results were the same as the Figure 1 results at 9.6 cm/s. The effluent concentrations are plotted on a log scale to show more clearly the breakthrough behavior at low concentrations. The top dotted line indicates the feed concentration and the bottom dotted line is the breakthrough concentration. If one follows the breakthrough concentration line across the graph, the points where it intersects the breakthrough curves correspond to the breakthrough times plotted in Figure 1. Figure 3 not only provides an interesting picture of the breakthrough behavior of cyanogen chloride at the low concentrations , it also shows the effect of a time dependent reaction rate. In previous studies (8-10), using an equilibrium theory approach, the chemical reaction rate has been assumed to be first order and time invariant. Therefore, once a steady state is achieved, (i.e., the initial abrupt concentration transition leaves the bed) the effluent concentration does not change with time and the breakthrough curves are parallel to the time axis. However, as Figure 3 clearly shows, there is a second transition (as indicated by the severe change in the slope of the breakthrough curve) that moves through the bed at a speed governed by the change in the second order reaction rate and mass transfer resistances.

Figure 4 shows the same predicted breakthrough curves for the 2-cm and 3-cm beds shown in Figure 3 along with the breakthrough curves of identical systems without chemical reaction (i.e., $k_1 = 0$). A comparison of breakthrough curves presented in Figure 4 with those predicted by an equilibrium theory analysis can provide some insight into the system performance. Equilibrium theory with a time invariant reaction rate would predict a vertical line at a time corresponding to the stoichiometric center of the transition which would extend to a concentration determined by the rate constant. Once that plateau concentration was achieved, the breakthrough curve would simply be a horizontal line. One can see that the initial breakthrough is not vertical as a result of the mass transfer resistances and the breakthrough curve at longer times has a finite slope as a result of the slowing reaction rate. Consider the breakthrough curve of the 2-cm bed without chemical reaction and the 2-cm bed with chemical reaction. The abrupt transition one would expect from a favorable isotherm passes through the bed but is attenuated and slowed down. But once this front is through the bed (about 2-4 minutes) , the second transition for the reactive system becomes more obvious.

The application of the fixed-bed adsorptive reactor model presented here is limited to systems where bed depths are small and velocities are relatively high. The model has been derived to treat light gases and is especially well suited to handle cases where very low breakthrough concentrations are considered. If one would want to model adsorptive reactor systems with deeper beds, then an axial dispersion and/or channeling term would need to be included.

The temperature effects and the transient effect of water have been neglected because the system is assumed to operate at a constant relative humidity and relatively small contaminant concentrations are considered. If one would want to examine the performance at different relative humidities, then a multicomponent isotherm for cyanogen chloride and water would be required. In addition, one would have to include an energy balance if large changes in relative humidity and/or larger feed concentrations (heat of reaction can become significant) are considered.

NOTATION

c^*	= vapor phase concentration at the adsorbent surface	mol/m^3
c	= bulk vapor phase concentration	mol/m^3
D_p	= average particle diffusivity	cm^2/s
d_p	= particle diameter	m
K	= Langmuir isotherm constant	m^3/mol
k_1	= reaction rate constant	$m^3/mol\ s$
k_pa	= internal (particle) mass transfer coefficient	s^{-1}
k_va	= external mass transfer coefficient	s^{-1}
M	= impregnant concentration	mol/kg
q^*	= adsorbed phase concentration in equilibrium with c^*	mol/kg
q	= average adsorbed phase concentration	mol/kg
q_{sat}	= Langmuir isotherm saturation capacity	mol/kg
R_i	= overall reaction rate	$mol/m^3\ s$
t	= time	s
v	= interstitial velocity	m/s
z	= axial distance	m
ϵ	= bed void fraction	
ρ_b	= adsorbent density	kg/m^3
α	= stoichiometric reaction coefficient	

REFERENCES

1. Grob, R. and J. Leasure , *J.Chromatogr.* , 197 (1980) 129.

2. Langer, S. , Yurchak, J. and J. Patton , *Ind. Eng. Chem.*, 61 (1969) 11.

3. Magee, E. M. , *Ind. Eng. Chem. Fundam.* , 2 (1963) 32.

4. Gore, F. E. , *Ind. Eng. Chem. Process Des. Dev.* , 6 (1967) 10.

5. Lowry, J. and C. Burkhead, *J. Water Pollut. Control Fed.* , 52 (1980) 389.

6. Andrews, G. and C. Tien , *AIChE J.* , 27 (1981) 396.

7. Chu, C. and L. Tsang , *Ind. Eng. Chem. Process Des. Dev.* , 10 (1971) 47.

8. Rhee , H. K., Aris, R. and N. R. Amundson, "First Order Partial Differential Equations : Volume I. Theory and Applications of Single Equations", Prentice Hall , 1986.

9. Loureiro, J. , Costa, C. and A. Rodrigues, *Chem. Eng. J.* , 27 (1983) 135.

10. Schweich, D. , Villermaux, J. and M. Sardin , *AIChE. J.* , 26 (1980) 477.

11. Reucroft, P. J. , Freeman, G. B. and P. B. Rao , *Carbon* , 21 No.3 (1983) 171.

12. Ruthven , D. M. , "Principles of Adsorption and Adsorption Processes", Wiley-Interscience, 1984.

13. Glueckauf, E. and J. E. Coates, *J. Chem. Soc.* (1947) 1315.

14. Glueckauf, E. , *Trans. Faraday Soc.* , 51 (1955) 1540.

15. Grabenstetter, R. J. and F. E. Blaut, Summary Technical Report Of the NDRC, Division 9 , Chapter 4. (1946) 40.

16. Friday, D. K. and M. D. LeVan , *AIChE J.* , 28 (1982) 86.

17. Morrison, R. W. , unpublished data.

18. Puhala, R. J. , CRDEC Technical Report Number ARCSL-TR-79021 April 1979.

19. Ranz, W. E. and W. R. Marshall, *Chem. Eng. Prog.* , 48 (1952) 173.

20. Costa, E., Calleja, G. and F. Domingo, *AIChE J.* , 31 (1985) 982.

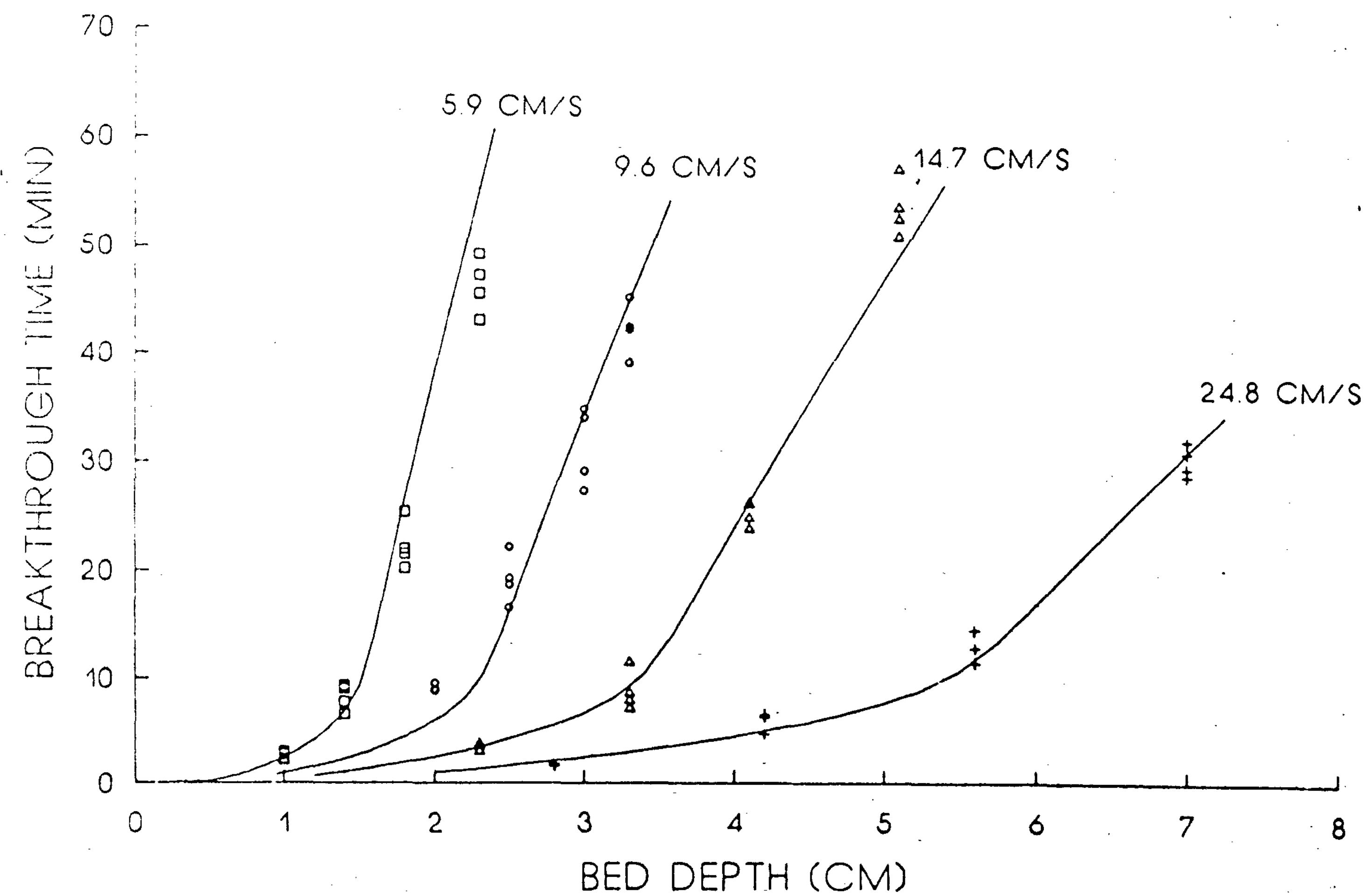

FIGURE 1. PREDICTED BREAKTHROUGH TIMES (LINES) AND MEASURED BREAKTHROUGH TIMES (SYMBOLS) AS A FUNCTION OF BED DEPTH AND VELOCITY

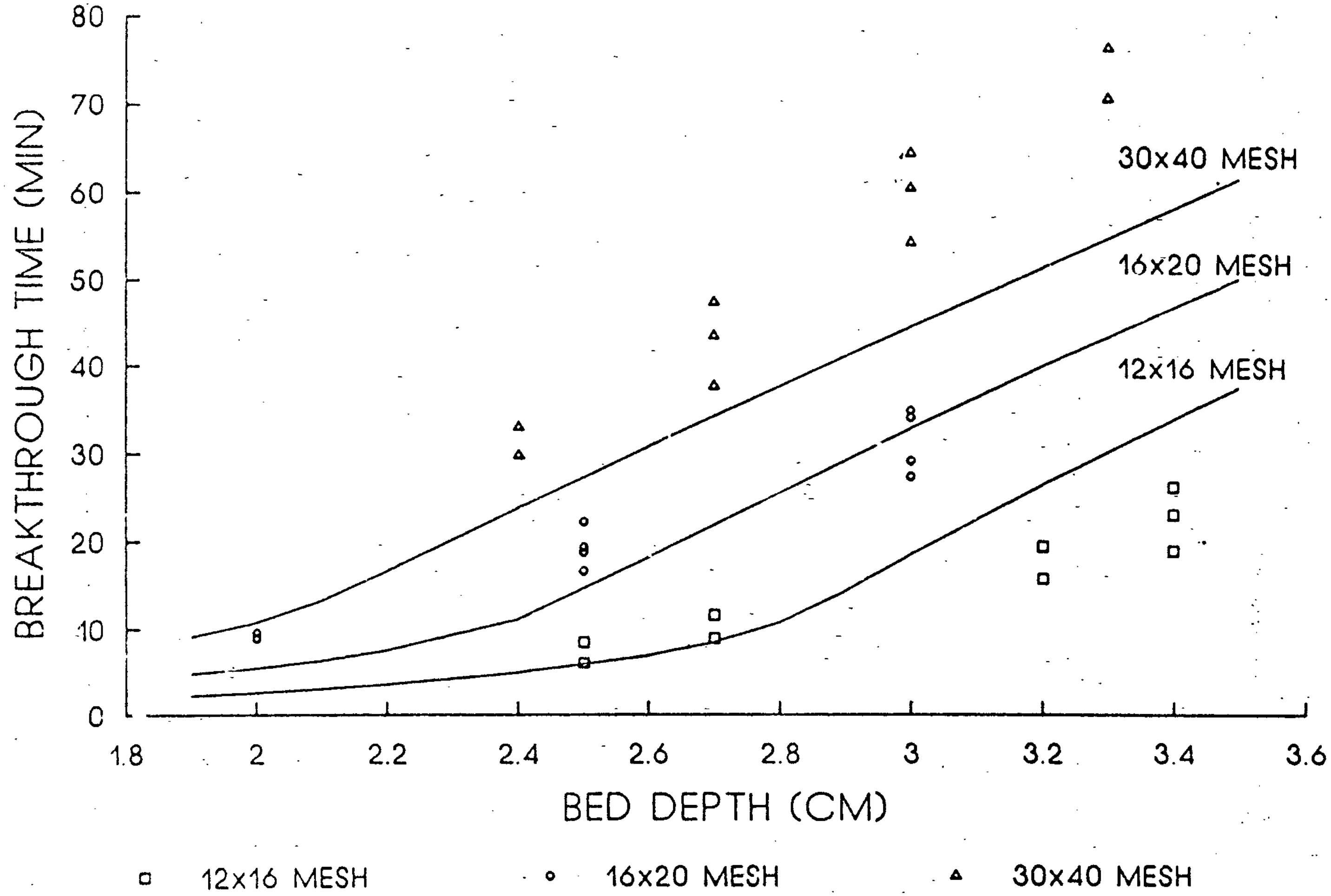

FIGURE 2. MODEL PREDICTIONS (LINES) AND MEASURED DATA (SYMBOLS) AT A VELOCITY OF 9.6 CM/S USING THREE DIFFERENT PARTICLE SIZES

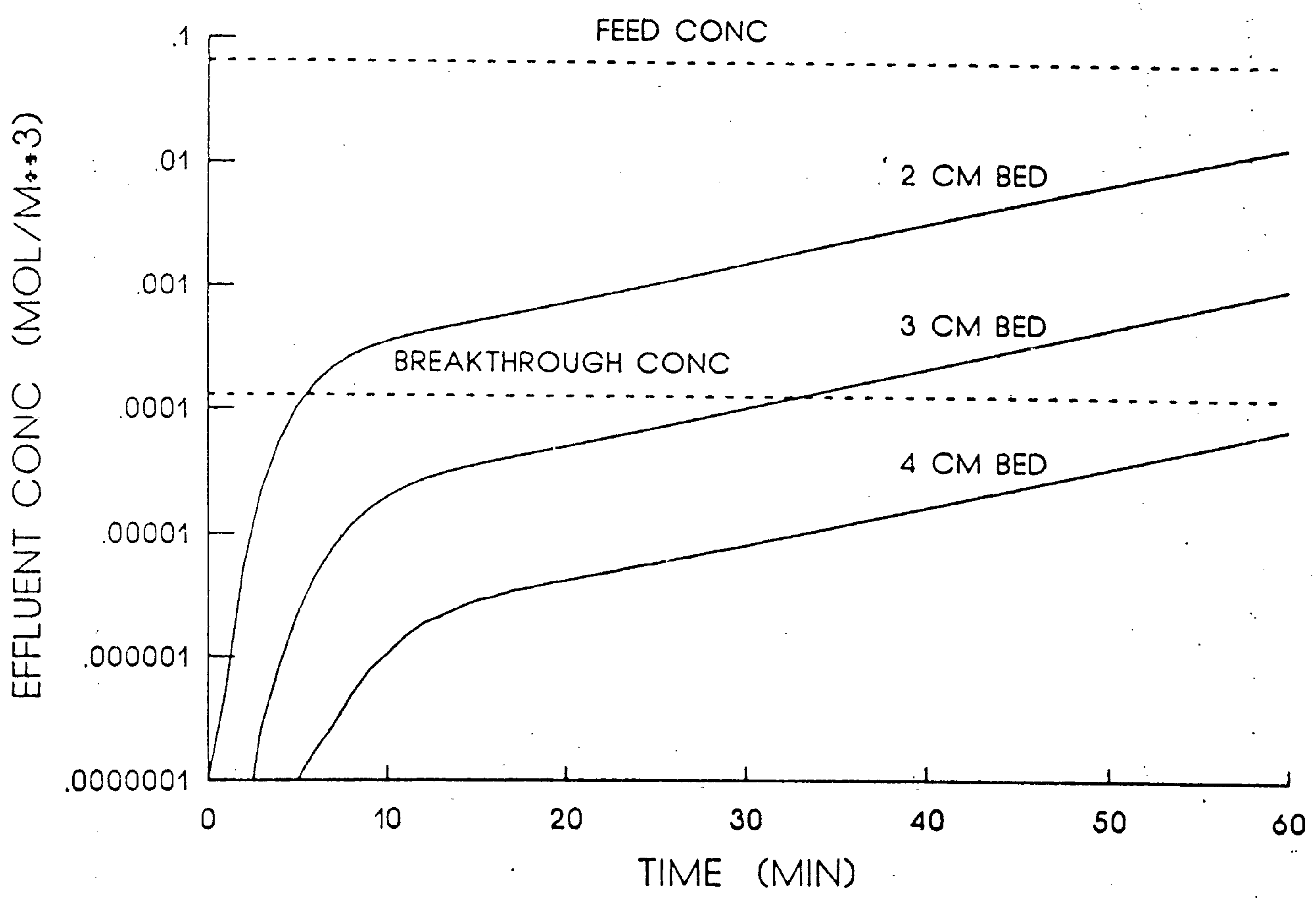

FIGURE 3. PREDICTED BREAKTHROUGH CURVES FOR THREE BED DEPTHS (VELOCITY = 9.6 CM/S)

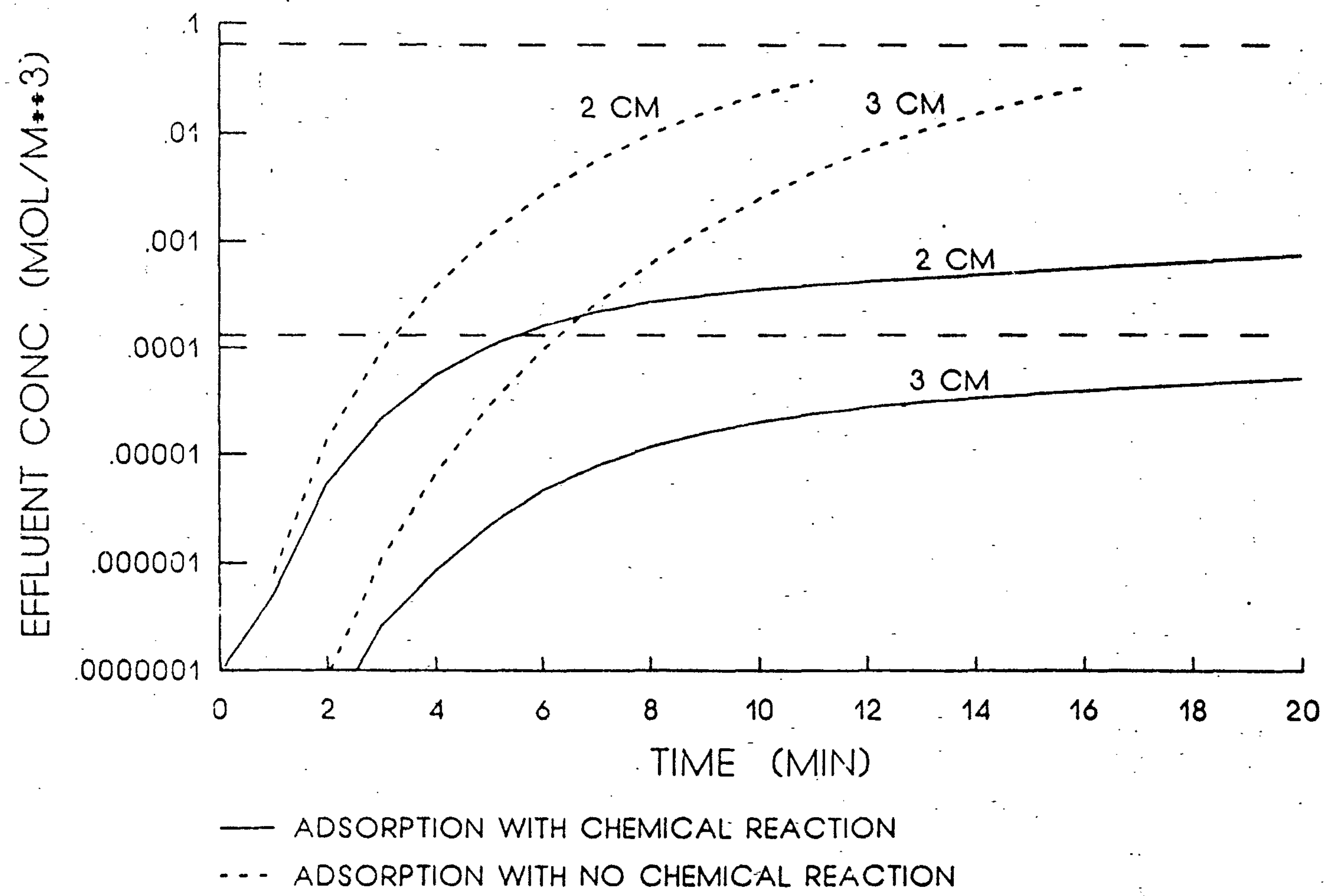

FIGURE 4. BREAKTHROUGH CURVES FOR REACTIVE AND NON-REACTIVE SYSTEMS USING TWO BED DEPTHS (9.6 CM/S)

A FAST SELF-MODELLING CURVE-RESOLUTION METHOD FOR TIME RESOLVED MASS SPECTRAL DATA

by

W. Windig* and S. Liebman
GEO-CENTERS INC.**
Prospect Square Building
Suite 502
10903 Indian Head Highway
Ft. Washington, MD 20744

and

A.P. Snyder and M. Wasserman
U.S. Army Chemical Research,
Development and Engineering Center
SMCCR-RSL
Aberdeen Proving Ground
Maryland 21010-5423

** Mailing address:
U.S. Army Chemical Research, Development and Engineering Center
SMCCR-RSL
Aberdeen Proving Ground
Maryland 21010-5423

BRIEF

A rapid method for self-modelling curve-resolution is presented. The method can be used in a continuous or on-line mode. Examples are given of overlapping GC-MS data of a mixture of three amines and time resolved mass spectral data of a biopolymer mixture and a Group A *Streptococcus* organism.

ABSTRACT

A rapid self-modelling curve-resolution method for time resolved mass spectral data is described. The method is much simpler and thus faster than factor analysis based methods. Examples are given of the application of this technique to an unresolved GC-MS data set of a mixture of dicyclohexylamine, diphenylamine and dibenzylamine and time resolved mass spectral data sets of a biopolymer mixture and a Group A Streptococcus organism which were obtained by oxidative pyrolysis atmospheric pressure ionization mass spectrometry. The method can be applied in a continuous ('on-line') mode , which is demonstrated on the overlapping GC-MS data.

INTRODUCTION

Most of the modern self-modelling curve-resolution methods are based on the use of factor analysis (1-19). Factor analysis is well suited for curve-resolution procedures because of the noise reduction that can be obtained by the use of the proper number of factors (20) and the ability to find 'pure masses', i.e. masses that have an intensity for only one of the components of the mixture under consideration (2,5,9).

Although factor analysis is presently the state-of-the-art approach for self-modelling curve-resolution, problems arise when applied to complex mass spectral data, such as that resulting from pyrolysis mass spectrometry. There is no established way to determine the proper number of factors. Error indicator functions such as those developed by Malinowski (20) are not applicable to information such as pyrolysis data. Furthermore, noisy peaks behave like pure masses, and therefore, the latter must be confirmed by independent methods, e.g. by checking if a pure mass axis shows a correlated behavior with other masses that are more or less characteristic for a particular component (21).

The above problems that are inherent in factor analysis necessarily yield a time-consuming process for which an experienced operator is required. A rapid method with minimal or no operator interaction would make self-modelling curve-resolution more accessible for general use. Also, an approach for analyte detection in a continuous mode would be desirable , e.g. for process monitoring with a mass spectrometer.

A method is described for self-modelling curve-resolution that uses a simpler and faster algorithm than that of factor analysis and yields time resolved component curves and spectra of the pure components. For obtaining the spectra of the pure components a method is described that does not require the knowledge of all the components in the mixture, which is in contrast to pure mass methods.

MATERIALS AND METHODS

Gas Chromatography Mass Spectrometry

Samples of dibenzylamine, diphenylamine and dicyclohexylamine were obtained from commercial sources and used as received. The samples were diluted in methanol and syringe-injected in 0.1 ul aliquots for analysis on a DB-5, 30m x 0.25mm fused silica capillary column contained in a Hewlett-Packard 5985B GC-MS system. Conditions were chosen in order to obtain co-eluting peaks of the three selected amines in approximately equal amounts with methanol as the solvent. Reference spectra for each of the amines were obtained in separate analyses. Typical experimental conditions were: 1-2 ml/min helium carrier, 200 C isothermal oven for 2-3 min, then isothermal at 300 C.Total ion currents were recorded with standard electron impact conditions; source temperature 200 C, electron energy 70 eV, 300 uA emission current with a 33-500 mass scan range.

Mass Spectrometry

The biopolymer mixture was prepared from DNA, glycogen (GLY) and bovine serum albumin (BSA) (Sigma, D-2251, G-0885 and A-9647, respectively). 1.0 mg/0.1 ml solutions were prepared for each biopolymer with distilled, deionized water as well as one solution containing 1.0 mg/0.1 ml of each biopolymer.

A Group A strain of Streptococcus bacteria was obtained as a gift from Alvin Fox from the University of South Carolina. A 1.0mg/0.1ml suspension in distilled deionized water was made and sonicated for 30 s. Muramic acid (Sigma M-2503), in a water solution (1.0mg/0.1ml) was prepared.

Twenty ug (2 ul) of each sample was applied to a Chemical Data System pyroprobe platinum filament, and the probe was connected to a Chemical Data Systems Micro-Extended Pyroprobe pyrolysis power supply. The solvent was evaporated by flash heating the ribbon to 100 C for 20 s prior to analysis. Oxidative pyrolysis of the samples was conducted at 300 C/min with a final set temperature of 600 C and the total heating time was two minutes. Pyrolyzate transfer from the heating zone to the Atmospheric Pressure Chemical Ionization (APCI) source and subsequent removal was effected by an air flow through the probe in combination with an 8 mm presure difference between the ion source cannister and ambient obtained by the exhaust motor of the mass spectrometer. The configuration of the platinum ribbon probe interfaced to the APCI source was identical to that of a pyroprobe quartz tube assembly (22). The ion source exhaust motor was necessary in order to return the Total Ion Current (TIC) to the background level within the two minutes analysis time. The mass spectral analysis was started after the first minute of the temperature program, since no TIC increase was observed before that and a subsequent one minute data collection was performed.

Mass spectral analysis was performed on a Sciex TAGA 6000 APCI triple quadrupole mass spectrometer. The analysis conditions were: mass range scanned m/z 74 to 200 at a mass scan speed of approximately 1 spectrum/second. This resulted in 54 spectra for a 1 minute analysis period. Daughter ion analysis was performed with the central quadrupole in the rf-only mode and the pressure of the argon collision gas was 6.0×10^{-5} torr.

RESULTS AND DISCUSSION

In order to demonstrate the data analysis procedure, a simulated data set of three components with an overlapping temporal response was used. The behavior in time of the individual components and their resulting TIC is presented in Figure 1a. A clear evolution of the three components is not observed in the TIC. If the peak widths of the TIC-curves of each of the three components would be narrower, the presence of three components could be observed in the total ion current plot. A mathematical way to achieve this is to square the intensities of the three separate components. This is demonstrated with the simulated data set in Figure 1b. If the desired result is not reached after squaring the values, the process can be continued by multiplying the data set by itself again, resulting in the fourth power of the data set.

GC-MS data set

The partially resolved GC-MS data set as presented in the inset of Figure 2a was used as a model for the self modelling curve resolution approach by smoothing the chromatogram to produce an unresolved chromatogram (Figure 2a). This was achieved by applying smoothing equation 1a four times to the chromatographic data.

$$S^{*}_{t} = .25 * S_{t-1} + .5 * S_{t} + .25 * S_{t+1} \quad \text{for } t = 2, m-1 \qquad \text{eq. 1a}$$

where S^*_t is the smoothed spectrum at time t, S_t is the unsmoothed spectrum at time t and m is the total number of spectra. For the first and last spectrum, the following smoothing formulae were used:

$$S^*_1 = .67 * S_1 + .33 * S_2 \qquad \text{eq. 1b}$$

$$S^*_m = .33 * S_{m-1} + .67 * S_m \qquad \text{eq. 1c}$$

As can be seen in Figure 2a, the TIC curve does not show a clear presence of three components. The approach described above to resolve the overlapping behavior of the components can be adapted for this data set as follows:

The behavior of a mass that is typical for dicyclohexylamine will show a similar behavior in time as the dicyclohexylamine component. The same is true for masses that are typical for the other two components. Therefore squaring the intensities of these variables results in a narrowing of the component curves comprising the TIC and, consequently, produces a temporal separation of the individual components. Other masses that have contributions from more than one component will produce less of an overall separation effect, however they will contribute to the temporal separation of overlapping components as long as they are biased to one component or non-overlapping components, e.g. the first and third component of the data set under consideration.

Before applying the squaring procedure to the data set, the mass variables are scaled, in order to yield features of equal contributions by giving them equal vector length (20). This is important in order to prevent dominance in the data set of high intensity mass spectral peaks. This is especially true for pyrolysis mass spectra, since high intensity peaks often represent non-characteristic fragments (23).

In mathematical terms the scaling procedure is the following:

The original matrix D (size s*m), where s is the number of spectra and m is the number of mass variables, is transformed to matrix $D^{\#}$ by:

$$D^{\#} = D\,B \qquad \text{eq. 2a}$$

$$b_{jj} = \left(\sum_{i=1}^{s} d_{ij}^{2} \right)^{-1/2} \qquad \text{eq. 2b}$$

The scaling procedure in equation 2 has a disadvantage in that indiscriminate, low intensity features are treated the same way as peaks characteristic to a particular component. In order to avoid this undesirable effect, mass vectors with a length less than 10 % of the maximum length were eliminated. The combination of scaling the data, followed by calculating the second, fourth or higher power and the TIC of the obtained data will be called the Scaled Power TIC method, abbreviated SP-TIC.

Application of the scaling procedure on the GC-MS data set is presented in Figure 2b and does not change the overlapping behavior of the three components. The result of squaring the scaled intensities is given in Figure 2c, and the presence of the three components becomes clear. Squaring the data again, resulting in the fourth power of the scaled intensities, indicates a clear presence of the three components as can be deduced from Figure 2d.

The mass spectra of the pure components are given in Figure

3a-c . The spectra at the local maxima in Figure 2d, which have a maximum contribution of the components dicyclohexylamine, diphenylamine and dibenzylamine, respectively (spectrum numbers 6, 10 and 15), are given in Figure 3d-f.

Comparison of the mass spectrum of pure dicyclohexylamine (Figure 3a) with that of maximum dicyclohexylamine content in the GC-MS data(Figure 3d), shows a minor contribution of the diphenylamine (e.g. m/z 169, Figure 3b) and dibenzylamine (e.g. m/z 91, Figure 3c) components. The spectrum at the local maximum assigned to diphenylamine (Figure 3e) shows clear contributions of dicyclohexylamine (e.g. m/z 138, Figure 3a) and dibenzylamine (e.g. m/z 91, Figure 3c). Finally, the spectrum at the third local maximum of Figure 2d, assigned to dibenzylamine (Figure 3f), shows some overlap when compared to the spectra of the other two components. Dicyclohexylamine is clearly represented by m/z 138 and a minor contribution from m/z 169 indicates the presence of diphenylamine.

The overlap between the spectra indicated that a further procedure is necessary in order to produce the mass spectra of the individual components with no contributions from the other components. In order to achieve this, the knowledge of 'pure masses' is desirable. Although pure masses have a limited meaning for complex data, it is the only way to calculate the spectra of the pure components.

A pure mass is defined as the mass with the highest (length-scaled) intensity in a particular component peak after applying the SP-TIC method (Fig 2d). The pure masses for dicyclohexylamine, diphenylamine and dibenzylamine were found to be m/z 55, m/z 169 and m/z 106, respectively. The validity of each of the pure masses was confirmed by determining if they had a high intensity in their immediate neighbouring mass spectra as well as a minimal intensity in the spectra at the other maxima. As can be seen, the procedure for pure mass assignment to a particular component does not always agree with assignments made by visual inspection of the pure spectra.

Once the pure masses of the three components are obtained, the spectra of the pure components can be calculated as follows.

Matrix A (Table I) presents the three pure masses from the three spectra of the local maxima in Figure 2d.

Pure masses (by definition) are only found in one component of a mixture. The relatively small intensities in the off-diagonal elements of matrix A indicate overlap between the components. The pure mass concept provides a relatively simple way to calculate a component's pure mass spectrum. A transformation matrix B is required that, when applied on matrix A, results in a matrix that has intensities only on the diagonal. If the identity matrix is chosen for this latter matrix, matrix B is simply the inverse of A, as can be deduced from equation 3.

$$BA = I \qquad \text{eq. 3}$$

Application of the inverse of A on the complete mass spectra (i.e from the original unscaled data matrix) at the local maximum of each component (Figure 3d-f) results in the resolved mass spectra (Figure 3g-i), respectively. The mathematically extracted spectra are almost identical to the separate compounds (Figs. 3a-c). This procedure is in principle the same as used for factor analysis-based mixture analysis approaches (20,21)

The time-resolved envelope of the three components can be obtained either by using the pure masses or by expressing every mass spectrum in terms of the extracted spectra of the pure components. Since the extracted spectra are based on the pure masses, they are in principle no better than the pure masses. Therefore, the extracted pure masses were used, which simplifies the mathematical procedure and increases the speed of the algorithm. The intensities of the pure masses need to be scaled, in order to reconstruct the original TIC:

$$AF = T \qquad \text{eq. 4}$$

where A is the matrix of the pure mass spectra of size n*n, where n is the number of components in the mixture. The matrix F, size n*1 scales the intensities of the pure masses in such a way that they represent the intensity of the pure components. T, size 1*n, represents the original total ion current of the spectra under consideration (i.e. 6, 10 and 15 in Figure 2d)

The solution of the unknown matrix F is:

$$F=A^{-1}T \qquad \text{eq. 5}$$

Since A^{-1} is known from the pure spectra calculations, it is simply a matter of multiplication of matrices. The plot of the extracted component curves and the reconstructed TIC calculated from these curves (TIC*) are shown in Figure 4. The original smoothed TIC (Fig. 2a) is observed to closely track the reconstructed TIC*.

Biopolymer mixture

The next example is based on the oxidative pyrolysis of a mixture of DNA, glycogen (GLY) and a protein, bovine serum albumin (BSA), followed by mass spectral analysis. These biopolymers have been the subject of several other Py-APCI-MS studies (24, 25). In a previous pyrolysis study, it was determined that DNA evolves in time before GLY, which in turn evolves before BSA (19). In Figure 5a the TIC of the one-time smoothed data set is presented. Although some structure is present in this curve, it does not give a clear indication of three components. Resolving curves such as the one given in Figure 5a by the derivative procedure does not produce a reliable resolution of the component curves because of the noisy character (not shown). The results of the SP-TIC method (fourth power) are presented in Figure 5b and the maxima assigned to the three components have been indicated by their respective mass spectrum numbers. In spite of the presence of three components in the sample, more than three local maxima can be observed, e.g. there are two local maxima in the region assigned to the BSA profile. Since replicate analyses appeared to be reproducible after similar mathematical treatments, the split maximum was studied more closely. Both local maxima were caused by mass intensities that could be assigned to BSA (Figure 6c). Differences between the two maxima were apparently represented by a slight domination of mass intensities representing aliphatic fragments in the first maximum and of aromatic mass peaks in the second maximum. The conclusion was that the behavior of BSA could be attributed to the complex nature of its pyrolysis over time. This phenomenon was also observed with the protein component in the time-resolved data analysis of the Streptococcus sample discussed below. It is interesting to note that protein has shown a complex behavior in several pyrolysis studies (26, 27). For the present discussion, the BSA maximum will be considered on the basis of spectrum number 21.

As observed in Figure 5b, there is also a minor fourth maximum, indicated by a *. Mass spectral analysis indicates a secondary volatilization of condensed products on the glass wall of the probe. Therefore, this maximum was not used in the data processing.

The spectra at the local maxima of Figure 5b, i.e. spectra numbers 6, 12, 21, produce differences in comparison to the spectra of the pure components, which cannot be explained by a simple temporal overlap. For example, a comparison of the mass spectrum of pure DNA (Figure 6a) with the mass spectrum with the maximum DNA content in the time resolved mixture data set (Figure 6d) shows that m/z 127 is almost absent in the latter spectrum. This phemomenon clearly indicates that the analysis of a mixture is not always the simple sum of the analyses of the separate components and is especially important for ionization under atmospheric pressure circumstances (28). This information was confirmed with m/z 127 daughter ion mass spectra of DNA, GLY and the biopolymer mixture. The m/z 127 daughter spectrum of the biopolymer mixture essentially yielded only the characteristic GLY m/z 127 spectrum (not shown). A clear, reproducible difference of the relative intensity of m/z 136 is also observed.

A comparison of the GLY model spectrum with the spectrum with the highest GLY content in the biopolymer mixture data (number 12), Figure 6b and 6e, respectively, again provide a different peak distribution. For example, the presence of m/z 144 and 162 (Fig 6e) in the extracted spectrum rather than m/z 145 and 163 (Figure 6b), respectively, might indicate a charge transfer mechanism rather than protonation. The presence of m/z 136 very likely indicates an overlap with DNA. Finally, the model spectrum of BSA and the spectrum with the maximum BSA concentration in the data file (number 21), Figure 6c and 6f, respectively, show some differences, e.g. the m/z values 115 and 129 are low in intensity in the spectrum presented in Figure 6f. The origin of these peaks is unclear, however, their absence in the extracted mass spectrum provides an indication of their relatively low proton affinity as compared to the pyrolysis products of the DNA and GLY biopolymers. The spectrum with the maximum BSA content in the file also shows some peaks that indicate an overlap with the evolution of GLY, e.g. m/z 127, 134 and 144. The minor amount of m/z 136 might indicate an overlap with the DNA component.

The pure masses for this data set were m/z 136, 127 and 113 for DNA, GLY and BSA, respectively. The mathematically extracted spectra are presented in Figure 6g-i. The mass spectra of DNA and GLY do not show significant differences, when compared to the spectra in Figure 6d and 6e, respectively, except for the absence of m/z 136 in the GLY spectrum. Minor differences are observed in a comparison of the BSA mass spectra (Figure 6f and 6i). The influence of GLY, represented by m/z 99, 117 and 127 is virtually absent, although a small amount of m/z 134 and 144 is still present. From the single ion currents of these masses, it appeared that they indeed showed a more gradual decrease in time during the last part of the heating program than other masses typical for GLY. One has to keep in mind that programmed heating of a biopolymer does not result in a simple, concurrent evolution of all masses , but that there are also complex degradative reactions involved, which can affect the different masses of one component to different degrees, e.g the double maxima for the BSA component (Figure 5b).

The reconstruction of the TIC's of the three separate components, represented by their pure masses, is shown in Figure 7. The reconstructed TIC portrays some differences when compared to the original TIC (Figure 5a), which are probably due to the noise reduction obtained by reconstructing the total ion current from a three-dimensional event rather than using all the information in the data set.

Group A Streptococcus.

The SP-TIC procedure was applied on the smoothed data of the pyrolysis of a Group A Streptrococcus strain (Figure 8a), which has been the subject of a number of GC and GC-MS pyrolysis studies (29-31). Subjects of this complexity provide a considerable challenge to the SP-TIC approach. Analytical pyrolysis mass spectrometry studies generally rely on the single spectrum resulting from signal averaging all the spectra obtained during the pyrolyzate production (23). From such a single spectrum it is not possible to obtain information on (classes of) separate components in a self-modelling way, i.e. without using reference spectra. The results of the SP-TIC method (fourth power) on the Streptococcus sample are presented in Figure 8b. As was observed in the biopolymer mixture analysis, the region assigned to protein (spectra 31 to 34 in Figure 8b) shows two maxima. Since the mathematically extracted mass spectra and the spectra at the local maxima of Figure 8a did not differ significantly, an analysis of the mathematically extracted spectra will suffice (Figure 9a-c).

The choice of model compounds for this complex 'mixture' is indeed a challenge. Since the presence of muramic acid in this organism is well documented in the literature (32,33) it was selected as a model compound. The mathematically extracted spectrum of the first maximum (Fig 9a) indeed shows the presence of peaks typical for muramic acid, i.e. m/z 90 and 108, as can be deduced from its model spectrum in Figure 9d. This was confirmed by daughter ion spectra of m/z 90 and 108 in both muramic acid and the Group A Streptococcus organism. The daughter ion spectrum of m/z 90 in both cases produced essentially identical spectra (not shown). The m/z 108 MS-MS spectrum from the organism, produced the same m/z distribution and intensity pattern as muramic acid along with a few other signatures, the latter presumably representing other compounds contributing to m/z 108 (not shown). The presence of m/z 136 might originate from nucleic acid-like materials.

The extracted spectrum (Figure 9b) associated with the second maximum (spectrum number 23, Figure 8b) presents a complex pattern, which contain some peak series that might be related with hexoses, e.g. m/z 96, 98, 102 and 126 in an unprotonated form. The presence of m/z 115 and 129 possibly is an indication of the presence of fatty acids. The third maximum shows similarities with a protein pattern, e.g. m/z 80, 84, 86, 113 and 153 (also see Figure 6c). In addition a peak series with m/z 111, 125 and 139 is observed, which might be indicative for the presence of aminosugars, often present in capsular polysaccharides (23,34,35). Systematic studies by MS-MS and/or GC-MS with the appropriate model compounds are warranted for a more complete accounting of structure/peak assignments.

The reconstruction of the TIC's of the separate components and the reconstructed TIC* is given in Figure 10. The TIC* shows differences with the original TIC from Figure 8a, which is very likely due to noise reduction by reconstructing the data from the three components. An additional indication for this is the fact that the TIC of the scaled data (not shown) is relatively similar to the reconstructed TIC*.

Continuous mode or on-line analysis application.

Self-modelling curve-resolution such as the SP-TIC method appears to have a number of potential applications when applied in a continuous mode. For example the method can apply to monitoring applications of spectral methods, or for 'on-line' data analysis of GC-MS data. The following outlines the self modelling-curve resolution method in a continuous analysis mode.

a) After obtaining n spectra (n is odd), t_1, t_2, t_3, ...t_n, the SP-TIC (fourth power) is calculated. In order to simplify the example, the value of 9 is assigned to n, based on the actual value which will be used below. The obtained TIC values are labeled $a_{1,1}$, ... $a_{9,1}$.
The central data point of the obtained values, i.e. $a_{5,1}$, is used as the first data point for the continuous data analysis mode: C_1.

b) After the next measurement has been made, the data analysis procedure is applied on the last 9 spectra, i.e. t_2 - t_{10}, which yields the data points $a_{2,2}$ - $a_{10,2}$. The central point of these numbers, i.e. $a_{6,2}$ cannot be used directly for the continuous data analysis mode, because the length scaling is different for different data sets.
A correction for the different mass vector lengths can be made by scaling the data in such a way that the intensity of a continuous data point is the same as in the analysis of the next series, so

the scaling requires that $a_{5,2}$ has the same value as C1 (which equals $a_{5,1}$. The scaling factor required to do this results in the calculations of the continuous data points as given in Table II.

c) The same procedure as described under b) is repeated for every measured spectrum.

In mathematical terms, the procedure does the following.

For the first point:

$$C_1 = a_{(.5n + .5)} \qquad \text{eq. 6a}$$

and for all the other points:

$$C_i = C_{(i-1)} * a_{(.5n - .5 + i),\, i} \,/\, a_{(.5n - 1.5 + i)} \qquad \text{eq. 6a}$$

where C_i is the TIC for the continuous data analysis mode and $a_{i,j}$ is the result of scaling and fourth power calculation on the spectra with the numbers i, (i + n - 1), where n is the number of continuous data points and is of an odd value.

The length of the vectors can be calculated in an efficient way in a continuous data analysis mode by adjusting the length of the previous calculation by extracting the contribution of the first spectrum of the previous calculation and adding the contribution of the newly obtained data point.

This process was applied on the GC-MS data shown in Figure 2a. A window of 9 spectra appeared to give satisfactory results for this data set. Because of the use of a window of 9 spectra, the number of points calculated for the curve (Table II) would miss the first and last four data points of the curve in Figure 2d. In order to obtain the same number of data points for the continuous mode, four spectra were added in front of the data set, i.e. a quadruplicate set of the original first mass spectrum.

Similarly, four spectra were added to the end of the data set by appending the last spectrum four more times. The curve (Figure 11) is similar to the results obtained when the data analysis procedure is applied on the whole data set (Figure 2d).

For the mathematical extraction of the spectra, the best approach is to use the spectra at the local maxima in Figure 11, because it is these spectra that have the maximum contributions of the respective components. In a continuous mode, this is not possible, since the 'future' maximum is not yet known. It appeared, however, that it was still possible to use the spectral calculation procedure given by equation 3. For the local maximum at spectrum # 10 (Figure 11), for example, the spectra 6-14 were used in the calculation of the data point C10 (see Table II). Application of the equations 3-5 on the pure masses of the mass spectra 6, 10 and 14, resulted in mathematically extracted spectra (not shown) highly similar to the ones presented in Figure 3g-i.

Since speed can play an important role for on-line applications, a simpler, faster approach for resolving the overlapping spectra is presented. The procedure simply uses the data on which the resolved TIC-curve is based, i.e. the scaled fourth power data. The applied scaling procedure, however, produces a spectrum that is difficult to analyze from a chemical point of view. Masses that are known to have a high intensity for a certain component will have the same intensity as masses that have a low intensity when they are both typical for the component. This problem can be solved by simply back-transforming the data (36). This means that the reverse process of eq. 2 has to be done, i.e. multiplying the scaled (fourth power) intensities by their respective lengths:

$$S = S^{\#} B^{-1} \qquad \text{eq. 7}$$

where $S^{\#}$ is an (row) array with the scaled fourth power spectrum to be back-transformed and is S the back-transformed spectrum. The result of this procedure applied on the spectrum with the highest overlap, i.e. spectrum number 10, see Figure 3e, is given in Figure 12. As can be seen, the diphenylamine extracted spectrum shows some overlap with the other two components, i.e. m/z 56, 138 represent dicyclohexylamine and m/z 91, 106 represent dibenzylamine. However, the mathematically extracted spectrum shows only a minor contribution of dicyclohexylamine and dibenzylamine, when compared to the mass spectrum number 10 (Figure 3e).

CONCLUSION

From the results presented above it appears that self modelling curve resolution can be accomplished by much simpler ways than factor analysis based methods. Although no direct comparisons have been done between the two methods, indications are that the method is one to two orders of magnitude faster than factor analysis based methods. Another important feature of the SP-TIC approach is that it can be used in a countinous mode. Extension of this method with an algorithm that finds the maxima and checks if the maxima describe different chemical components (by checking the singularity of matrix A), could produce a fully automated approach, which will be a subject for further research in this laboratory.

There are curve resolution problems in the SP-TIC method that can be obviated by factor analysis. The SP-TIC requires that the components have a different maximum in time. This is not required for factor analysis, as long as the shape of the curves of the components is different. It is also perceived that the SP-TIC approach can be used to provide an estimate of the dimension of the data set (i.e the number of maxima) prior to factor analysis.

ACKNOWLEDGEMENTS

Mark Jones and Christine Houseknecht are acknowledged for their assistance with the data analysis.

FIGURE CAPTIONS

Figure 1.

a) A simulated overlapping evolution of three components, A, B and C, results in a total signal that does not show the presence of three processes. b) After squaring the intensities of the three components, the total signal shows the presence of the three processes. The intensities are expressed as a percentage of the maximum total signal.

Figure 2. a) The total ion current (TIC) of a smoothed GC-MS trace. There is no clear indication of the presence of three components in the mixture analyzed. The inset represents the unsmoothed, partially resolved data set.

b) The TIC after the mass variables were scaled to make the length of all mass vectors in the data set equal.

c) The TIC resulting from the squaring of the scaled mass intensities, the presence of three components becomes visible.

d) The TIC resulting from the fourth power of the scaled mass intensities; the maxima assigned to the three components are clearly visible; spectrum number 6 represents dicylohexylamine, 10 represents diphenylamine and 15 represents dibenzylamine.

Figure 3. Model spectra of the three components, dicyclohexylamine, diphenylamine and dibenzylamine, are presented in 3a-c, respectively.

The spectra at the local maxima in the plot given in Figure 2d, which have the highest amount of the above three components, are presented in d-f. Overlap is obvious in 3d.

The mathematically extracted spectra,calculated on the basis of the spectra in 3d-f, are given in 3g-h. It is obvious that these spectra are similar to the spectra of the model components.

Figure 4. The plot of the evolution of the three separate components, represented by their pure masses, after the proper scaling and the resulting TIC (solid line).

Figure 5. a) The total ion current resulting from oxidative pyrolysis of DNA, GLY and BSA. There is a clear overlap between the signals of the three components.
b) The TIC resulting from the fourth power of the scaled mass intensities, the three components are clearly visible.

Figure 6. Model spectra of DNA, BLY and BSA are presented in 6a-c, respectively.
The spectra at the local maxima in the plot given in Figure 5b, which have the highest amount of the three biopolymers, are presented in d-f. Overlap between BSA and GLY can be observed.
The mathematically extracted spectra,calculated on the basis of the spectra given in 6d-f, are given in 6g-h. The presence of GLY in the BSA component (Figure 6f) became less pronounced.

Figure 7. The plot of the evolution of the three separate components, represented by their pure masses, and the resulting TIC.

Figure 8. a) The TIC from oxidative pyrolysis of a group A Streptococcus organism.
b) The TIC resulting from the fourth power of the scaled mass intensities. Three processes can be distinguished. The maximum indicated by a * is the result of secondary volatilization of pyrolysis products condensed on the glass wall of the probe.

Figure 9. The mathematically extracted spectra of each local maximum are shown (a-c) together with a model spectrum of muramic acid (Figure 9d). The mathematically extracted spectra did not differ significantly from the spectra at the local maxima indicated in Figure 8b.

Figure 10. The plot of the evolution of the three separate components, represented by their pure masses, and their resulting TIC.

Figure 11. The TIC curve of the GC-MS data (Figure 2a), scaled and raised to the fourth power resulting from a continuous analysis mode.

Figure 12. The mathematically extracted spectrum from applying the SP-TIC continuous mode on the GC-MS data in Figure 11. This spectrum is calculated by back-transforming the (length-scaled) spectrum number 10 by multiplying the mass intensities by their respective lengths. Compare with Figure 3e and 3h.

m/z	55	169	106
Spectrum #			
6	.1329	.0670	.0305
10	.0387	.3148	.1270
15	.0068	.0207	.3376

Table I: Contents of matrix A.

ORIGINAL DATA	TIC OF SCALED FOURTH POWER DATA OF SEQUENCE 1- 9	2-10	3-11	4-12	....	
t_1	$a_{1,1}$					
t_2	$a_{2,1}$	$a_{2,2}$				
t_3	$a_{3,1}$	$a_{3,2}$	$a_{3,3}$			
t_4	$a_{4,1}$	$a_{4,2}$	$a_{4,3}$	$a_{..}$		
t_5	$a_{5,1}$	$a_{5,2}$	$a_{5,3}$	$a_{..}$	$a_{..}$	
t_6	$a_{6,1}$	$a_{6,2}$	$a_{6,3}$			
t_7	$a_{7,1}$	$a_{7,2}$	$a_{7,3}$			
t_8	$a_{8,1}$	$a_{8,2}$	$a_{8,3}$			
t_9	$a_{9,1}$	$a_{9,2}$	$a_{9,3}$			
t_{10}		$a_{10,2}$	$a_{10,3}$			
t_{11}			$a_{11,3}$	$a_{..}$	$a_{..}$	$a_{..}$
t_{12}				$a_{..}$	$a_{..}$	$a_{..}$
$t_{..}$					$a_{..}$	$a_{..}$
t_m						

$C1 = a_{5,1}$

$C2 = C1 * a_{6,2} / a_{5,2}$

$C3 = C2 * a_{7,2} / a_{6,2}$

Table II. Calculation scheme for continuous curve resolution.

REFERENCES

(1) Lawton, W.H.; Sylvestre, A.S., Technometrics, 1971, 13, 617-633.

(2) Knorr, F.H.; Futrell, J.H., Anal. Chem., 1979, 51, 1236-1241.

(3) Jie-Hsung Chen;Lian-Pin Hwang, Anal. Chim. Acta, 1981, 133, 271-281.

(4) Sharaf, M.A.; Kowalski, B.R., Anal. Chem., 1981, 53, 518-522.

(5) Malinowski, E.R., Anal. Chim. Act., 1982, 134, 129-137.

(6) Sharaf, M.A.; Kowalski, R.K., Anal. Chem., 1982, 54, 1291-1296.

(7) Gillette, P.C.; Lando, B.L.; Koenib, J.L., Anal. Chem., 1983, 55, 630-633.

(8) Osten, D.W.; Kowalski, B.R., Anal. Chem., 1984, 56, 991-995.

(9) Malinowski, E.R., Anal. Chem., 1984, 56, 778-781.

(10) Vandeginste, B.; Essers, R.; Bosman, T.; Reijnen, J.;, Kateman, G., Anal. Chem., 1985, 57, 971-985.

(11) Borgen, O.S; Kowalski, B.R., Anal. Chim. Acta, 1985, 174, 1-26.

(12) Ramos, L.S.; Burger, J.E.; Kowalski, B.R.,

Anal. Chem., 1985, 57, 2620-2625.

(13) King, M.D.; King, G.S.,
Anal. Chem. 1985, 57, 1049-1056.

(14) P. J. Gemperline,
Anal. Chem, 1986, 58, 2656-2668.

(15) Lacey, F.L.,
Anal. Chem., 1986, 58, 1404-1410.

(16) Sharaf, M.A.,
Anal. Chem., 1986, 58, 3084-3091.

(17) Windig W.; Chakravarty T.; Richards, J.M.; Meuzelaar H.L.C.,
Anal. Chim. Act., 1986, 191, 205-218.

(18) Lindberg, W.L.; Ohman, J.,
Anal. Chem., 1986, 58, 299-303.

(19) Windig, W.; Jakab, E.; Richards, J.M.; Meuzelaar, H.L.C.,
Anal. Chem., 1987, 59, 317-323.

(20) Malinowski, E.R.; Howery, D.G.,
Factor Analysis in Chemistry
Willey-Interscience: New York, 1980.

(21) W. Windig, W.H. McClennen and H.L.C. Meuzelaar,
Chemometrics and Intelligent Laboratory Systems, 1987, 1, 151-165.

(22) Liebman, S.A.; Snyder, A.P.; Kremer, J.H.; Reutter, D.J.,
Schroeder, M.A.; Fifer, R.A.,
J. Anal. Appl. Pyrol., 1987, 12, 83-95.

(23) Meuzelaar, H.L.C.; Haverkamp, J; Hileman, F.D., "Pyrolysis Mass Spectrometry of Recent and Fossil Biomaterials; Compendium and Atlas"; Elsevier: Amsterdam, 1982.

(24) Snyder, A.P.; Kremer, J.H.; Meuzelaar, H.L.C.; Windig, W., Taghizadeh, K. Anal. Chem., 1987, 59, 1945-1951.

(25) Snyder, A.P.; Kremer, J.H.; Meuzelaar, H.L.C.; Windig, W., J. Anal. Appl. Pyrol., 1988, accepted for publication.

(26) Van de Meent, D.; De Leeuw, J.W.; Schenck, P.A.; Windig, W., Haverkamp, J. J. Anal. Appl. Pyrol., 2, (1982), 133-142.

(27) Windig, W.; Meuzelaar, H.L.C.; Haws, B.A.; Campbell, W.F., Asay, K.H. J. Anal. Appl. Pyrol., 1983, 2, 183-198.

(28) Vandiver, V.J.; Leasure, C.S.; Eiceman, G.A., Int. J. Mass Spectrom. Ion Processes, 1985, 66, 223-238.

(29) Elliot, T.R.; Rogers, A.H.; Haverkamp, J.R.; Groothuis, D., Forensic Sci. Int., 1984, 26, 131-137.

(30) Eudy, L.W., Walla, M.D.; Hudson, J.R.; Morgan, S.L., J. Anal. Appl. Pyrol., 1985, 7, 231-247.

(31) Smith, C.S.; Morgan, S.L.; Parks, C.D.; Fox, A.; Pritchard, D.G., Anal. Chem., 1987, 59, 1410-1413.

(32) de Cueninck, B.J.; Shockman, G.D.; Swenson, R.M., Infection and Immunity, 1982, 35, 572-582.

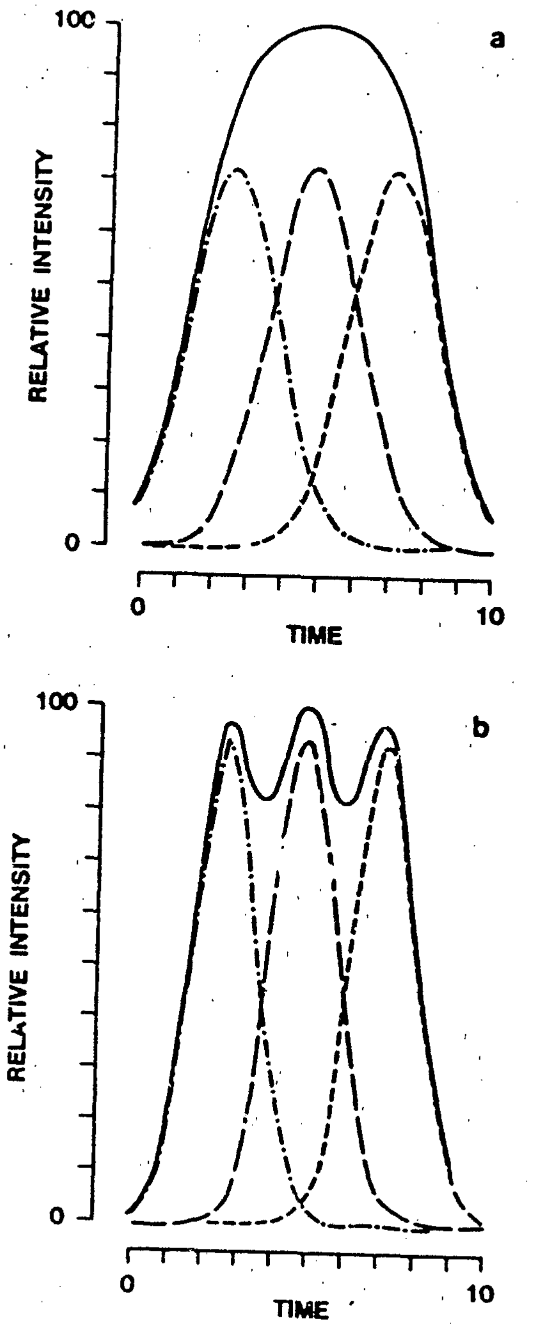

100
a
RELATIVE INTENSITY
0
0
10
TIME
100
b
RELATIVE INTENSITY
0
0
10
TIME

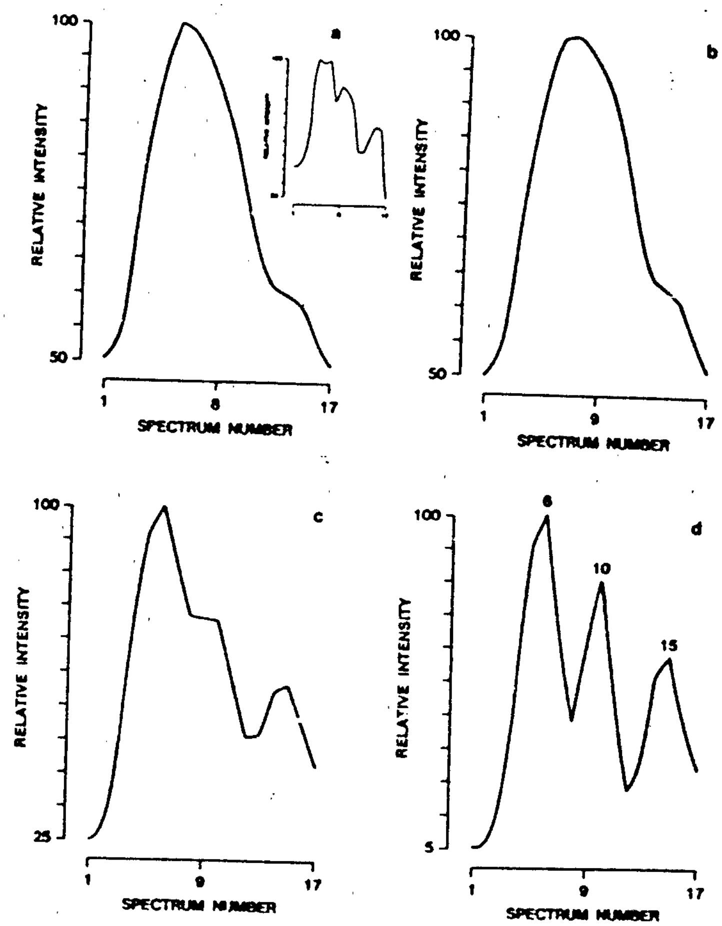
a
b
c
d
100
50
25
5
RELATIVE INTENSITY
SPECTRUM NUMBER
1
8
9
17
6
10
15

SFC/GC system concerning detection of extractables from the SFE/SFD/SFR module. In addition to the well-established flame ionization detector (FID) and conventional uv-vis flow cells, new advances in fiber optics led to feasibility runs to assess the potential of fiber optic monitors (FOM). Results of these runs indicate significant FOM applications for the analytical and process SF field, based on pioneering work at Lawrence Livermore Laboratories and at the Center for Process Analytical Chemistry, University of Washington (6).

Basic capabilities of the SFC/GC system are common to modern instrumentation used in trace organic analysis; e.g., the microprocessor-based unit has five coprocessors that permit highly controlled operational parameters, data acquisition, and interactive display. Moreover, in addition to embedded intelligence of the SFC/GC system operation, the extension of applied AI (7,8) is reported with new development of a proprietary CCS expert system network, microEXMAT. This capability provides the researcher with a problem-solving guide for the system, including analytical strategy, instrument configuration, method development, data analysis, and interpretation. The applied AI development involves a decision structure outlined for four expert systems within the microEXMAT network using an implicit linking mechanism.

These advances in integrated hardware/software systems are demonstrated in applications that require specialty treatments, such as thermally sensitive materials (propellants, foods, pharmaceuticals, etc. (9) as well as synthetic fiber studies; SFD analyses of environmental air samples using charcoal sorbents; and SFR analysis of reaction mechanisms/degradation. This combined sample processing, on-line analysis, and data manipulation system using applied AI within a highly automated environment illustrates "the Integrated Intelligent Instrument" or (I^3) approach (10) (Figure 1a). Applications of these interfaced units within the SFC/GC system are shown for analytical problem-solving in environmental and material sciences.

EXPERIMENTAL:

Materials: Fiber samples were obtained from a manufacturer developing specialty treatments for product and process (QC/QA) applications. Charcoal samples were obtained in environmental air sampling protocols and analyzed in different portions of the sorbent bed. Propellants and energetic material, RDX, were supplied as a test series of formulated propellants and prepared for research at the Ballistics Research Laboratories, Aberdeen Proving Ground, by Leo Asoaka, Naval Ordnance Station, Indian Head, MD. All ingredients were available individually for direct comparison to the formulated product. The matrix binder, hydroxy-terminated polybutadiene, was formulated with all ingredients in Formulation #1, except RDX; Formulation #2, with 40% by weight RDX, and Formulation #3, 80% RDX. The boron catalyst is that referred to in previous studies of RDX thermal degradation (11,12).

Instrumentation: The SF instrument configured for SFE, SFD, and SFR is manufactured by Computer Chemical Systems (CCS), Avondale, PA as the Model 5000 SFC/GC with 301A to 103B SFE options and equipped with dual FID units. Exploratory studies with an FOM system operating in the visible spectral regions from 400 nm to 750 nm were conducted in cooperation with Guided Wave, Inc., El Dorado Hills, CA, and Prochem Scientific, McClure, PA. The FOM was interfaced in the transmission-absorbance configuration to a CCS Model 5000 using the SFE module to monitor food grade dyes in oils as they were extracted in the CO_2 mobile fluid at 1400 psi, room temperature, and also at 100°C.

Figure 1 schematically outlines the basic hardware/software features and the general experimental arrangement. The SFC separations were performed with a 100 x 1 mm microbore 3 micron C-8 column (Keystone Scientific, State College, PA) using a linear pressure program (200 psi/2 min, 300 psi/min to 6000 psi/10 min). This pressure program is superimposed on the SFC printout, seen typically in Figure 2. A column oven temperature program of 50°C/5 min, 20°C/min to 180°C/10 min was also used. One FID monitored the extraction unit with a restriction permitting ca. 6 ml/min CO_2 flow in the 2000 psi range. The other FID recorded the column effluent using a similar restrictor arrangement.

RESULTS AND DISCUSSION

SFE Mode: Figure 2 presents the results when approximately 1-2 mg of formulated propellants 1, 2, and 3 were extracted at 3000 psi CO_2 at 100°C and monitored with the on-line FID. Variations in the extraction profiles indicate the conditions were sufficient for the SFE of RDX and other ingredients from the formulations. Additionally, forty minutes into the extraction, timed sampling for SFC analysis took place as shown for each of the propellants. Compositional variations are indicated among the three extracted formulations.

Further study of the matrix polymer itself was conducted, since sample homogeneity was of interest. Samples from two regions of the same processed bulk polymer were examined under identical conditions to give the SFE profiles seen in Figure 3. The major profiles are similar for the two samples, but a significant difference is noted at the beginning of the extraction profiles, as well as variations in the composition of the extractables when examined with the timed SFC analyses. Because of the sensitivity of the SFE process to mass transfer effects (13), it appears that changes in the viscoelastic properties of the bulk polymer (cross-link density, variations in prepolymer content, etc.) and/or the presence of residuals from the polymerization process are responsible.

Although the on-line FID monitor provided excellent sensitivity for these SFE profile determinations, an opportunity was presented to test other on-line monitors that provide nondestructive spectral or functional group information. Advances in fiber optics (14) were thus assessed in a brief, but important series of runs using stainless steel probes interfaced at the exit of the SFE module. These bundled fiber probes with sapphire windows were connected to a Guided Wave monochrometer operating in the visible spectral region, 400 nm to 750 nm. The on-line monitoring of a blue dye in olive oil solubilized by the CO_2 mobile fluid at 1400 psi was recorded showing an absorbance maximum at 640-50 nm. This feasibility series provided the first indication that fiber optic monitoring could be successful in SFE studies. Since FOM systems are commercially available for other spectral ranges (uv/nir/ir), extension to fiber optic multiple monitoring (FOM^2) is anticipated in the SFE and SFE-ACCUMULATOR configurations, of particular significance when modifiers are used in the CO_2 mobile phase. Previous interfacing to FTIR (15) MS (16), and MS/MS (17) units by numerous workers thus permits encoding applications/methods of interfaced intelligent detectors (I^2D) into microEXMAT.

SFE-ACCUMULATOR MODE: Fiber samples (30 mg) that had been treated with various additives were placed in the SFE module. Extraction in the SFE module was conducted at 4500 psi for 20 min with a CO_2 mobile fluid with the unit interfaced via a restrictor to the on-line accumulator. Desorption (at 150°C) of the trapped extractables was followed by automated transfer into the on-line SFC to provide the patterns shown in Figure 4. Excellent comparisons were made of the fibers, A and B, differing in their specialty treatments which involved oil and wax additives. Such analyses are useful in developing new treatment processes, as well as in QC/QA operations.

SFD-ACCUMULATOR MODE: Charcoal sorbent beds were used in typical air sampling experiments to trap complex hydrocarbon vapor mixtures. The control charcoal had been specially treated to improve performance and was needed for comparison to the loaded samples. Since emphasis is now on surface desorption via the SF CO_2 mobile fluid, the extractor served as a desorption chamber at 300 psi and 100°C for 100-200 mg charcoal samples with the results given in Figure 4. The control charcoal showed low-level desorption (x4 attenuation) relative to the loaded samples (x8). The two differentially loaded charcoals also showed variations in SFD profiles and in composition of the desorbed species by timed SFC analyses. However, SFC analyses of this hydrocarbon mixture were not as informative as well-established conventional GC capillary separations. Therefore, the SFC/GC system was operated in the SFD-ACCUMULATOR-GC configuration to compare the composition of the two desorption mixtures with a 15 m x .025mm DB-5 bonded capillary fused silica column (Figure 5). It is evident that the hydrocarbon distributions are significantly different, as were anticipated for these selected samples. Hence, the use of SFD for environmental analyses was demonstrated, following the reports of researchers at Battelle Northwest Laboratories (18) and at Research Triangle Institute (19).

SFR Mode: Analysis of the energetic nitramine, RDX, was conducted at 2000 psi near its melting/decomposition point, 205°C and the results are shown in Figure 6. Sampling at 20 minutes into the reactive SF treatment showed important difference in degradation product distributions at 200°C and at 250°C. The presence of boron catalyst, of interest because of its effect on propellant burn rate, showed further effects in the complex RDX decomposition. These results are of significance in the detailed research of nitramine thermal decomposition mechanisms that have been reported extensively and are covered in a comprehensive review by Fifer (20). More fundamental SF reaction chemistry has been reported by Klein et al. (21a), by Dooley and Knopf (21b), and Metzger et al. (21c).

APPLIED AI: As is evident from the above experimental studies, numerous configurations are needed to obtain relevant information from diverse sample types, forms, and amounts. The basic SFC/GC may be operated in several different modes, depending on the nature of the problem statement and the sample involved. To guide researchers as to general strategies and specific configurations that may be useful, an expert system network, microEXMAT, has been outlined which presently consists of four linked expert systems: strategy or problem statement, experimental configuration, method development, and data analysis. Illustrations are shown of the initial decision structure setup for (a) experimental configuration and (b) method development, with typical rules from a knowledge base that is being developed for (b) (Figure 7a,b,c).

The ability to encode information gleaned from applications, literature references, research insights, and other heuristics specific to the SF field can be invaluable to analysts. These aspects of our research make use of existing software packages and, in some cases, newly written software as well. For example, multivariate statistics software is commercially available from Guided Wave for data analysis with their fiber optics systems. Integration of these packages into the CCS microEXMAT extends the intelligent instrument concept to detection systems external to the SFC/GC unit. And, since the FOM near-infrared (NIR) and mid-IR probes are available (14c,d), an expert system to aid NIR spectral interpretation, NIRI, is being developed within the microEXMAT format to demonstrate the versatility of applied AI.

SUMMARY:

Description of the I^3 approach has been given with specific emphasis on the highly automated SFC/GC system for process and analytical studies that require the unique attributes of supercritical fluid technology. Varied sample processing modes may combine SF technology with thermal or reactive treatments, so that SF extraction and desorption processes may be assessed, as well as chemical reactions. Advantages of both on-line SFC and capillary GC separations were shown in appropriate situations, using the wealth of established GC technology wherever possible. On-line monitoring has been demonstrated with a conventional FID operating simultaneously with a prototype nondestructive FOM setup at the exit of an SFE unit.

Importantly, these research results have shown examples of SFE-SFC, SFE-ACCUMULATOR-SFC, SFD-ACCUMULATOR-Capillary GC, and SFR-SFC in analytical regimes not readily studied by other methods. Applications were made with samples of significance to industrial R&D, QC/QA, environmental, forensic and material sciences. The interplay of applied AI with these specific instrumental configurations and methods has led to a proprietary expert system network, microEXMAT, that is being developed for the SF analytical and process field. Future effort will be to establish the I^3 approach in SF technology.

REFERENCES:

1. Pyrolysis and GC in Polymer Analysis, Liebman and Levy, Eds., Marcel Dekker, Inc., NY, 1985.
2. (a) E.J. Levy, et al. American Lab, August 1987, "Advanced Supercritical Fluid Systems".

   (b) S. Yocklovich, S. Lurcott, S. O'Neill, E.J. Levy, Workshop on SFC, Salt Lake City, Utah, January, 1988, "Supercritical Extraction-Chromatography Applications".
3. (a) D.R. Gere, Science 222, 253-260 (1983).

   (b) D.R. Gere, R. Board, D. McDanigill, Anal. Chem. 54, 726 (1982).

(c) H.E. Schwartz, P.J. Barthel, S.E. Moring, H.H. Lauer, LC GC, 5, 14-22 (1987). "Packed vs. Capillary Column for SFC: Theoretical Considerations".

(d) C.M. White and R.K. Houck, J. High Resol. Chromat. & Chrom. Comm., 8, 4-17 (1985), "Review: Supercritical Fluid Chromatography and Some Applications".

4. (a) L.G. Randall, in "Chem. Eng. at Supercritical Fluid Conditions", Paulaitis, Penninger, Gray, Davidson, Eds., Ann Arbor Sci., Ann Arbor, MI (1983), Chapter 24, "Analysis of Dense Gas (Supercritical) Systems".

(b) Anon., Anal. Chem. 59, 619A (1987).

(c) L.S. Ettre, J. High Resol. Chrom. & Chrom. Comm. 10, 636-40 (1987). Editorial, "Is Capillary Gas Chromatography Actually Supercritical Fluid Chromatography?"

(d) L.S. Ettre, 195th Nat. Mtg., ACS, Toronto, Canada, June, 1988, Ana. Div. paper no. 99, "Recent History of High-Resolution Chromatography".

5. (a) W.G. Engelhart, A.G. Gargus, Amer. Lab, 31-32 (Feb 1988), "SFE for Automated Sample Preparation".

(b) C.S. Elsbend, D.K. Mohanty, J.E. McGrath, P.M. Gallagher, V.J. Krukonis, Polym. Preprints, 28, No. 2, 399-400 (1987); ACS, New Orleans, LA Mtg, (Aug 1987), "Synthesis and SFE Studies on Amino propyl Terminated Polysiloxanes".

6. J.B. Callis, D.L. Illman, B.R. Kowalski, Anal. Chem. 59, 624A (1987), "Process Analytical Chemistry".

7. S.A. Liebman, P.J. Duff, M.A. Schroeder, R.A. Fifer, and A.M. Harper, in Artificial Intelligence Applications in Chemistry, ACS Sympos. Series 306, Pierce and Hohne, Eds., Amer. Chem. Soc., Washington, DC, 1986, p. 365-384.

8. A.M. Harper, S.A. Liebman, J. Res. NBS, Spec. Publ., 90, No. 6 (Nov-Dec 1985) 453-464. "Intelligent Instrumentation", Proc. of Chemometrics Workshop, Gaithersburg, MD, May 1985.

9. S.A. Liebman, R.A. Fifer, F. Shaw, A.M. Harper, "Propellant Characterization Using Supercritical Fluid Extraction-Chromatography in an Expert System Network", to be published in J. Hazardous Materials.

10. E.J. Levy et al., Pittsburgh Conference, Atlantic City, NJ 1987, and New Orleans, 1988.

11. S.A. Liebman et al., J. Hazardous Materials, 13, 51-56 (1986). "Degradation Profile of Propellant Systems with Analytical Pyrolysis/Concentrator/GC Technology".

12. S.A. Liebman, A.P. Snyder, J.H. Kremer, D.J. Reutter, M.A. Schroeder, R.A. Fifer, J. Anal. Applied Pyrolysis, 12, 83-95 (1987) "Time-Resolved Analytical Pyrolysis Studies on Nitramine Decomposition with a Triple Quadrupole Mass Spectrometer System".

13. (a) Supercritical Fluid Extraction, M. McHugh and V. Krukonis, Eds., Butterworths, Boston, 1986.

(b) Chemical Engineering Supercritical Fluid Conditions, Paulaitis, Penninger, Gray, and Davidson, Eds., Ann Arbor Science, MI, 1983.

14. (a) R. Schirmer, A.G. Gargus, Amer. Lab. 18, 30 (1986), "Application of Remote Chemical Sensing Using Fiber Optics and UV/VIS/NIR Spectroscopy".

(b) S. Foulk, A.G. Gargus, Amer. Lab. 19, 52 (1987), "Fiber Optic Spectroscopy and Multivariate Analysis for In-Situ Chemical Monitoring".

(c) D.A.C. Compton, S.L. Hill, N.A. Wright, et al., Pittsburgh Conference, New Orleans, 1988, paper o. 882. "In-situ FT-IR Analysis of Samples Using a Mid-Infrared Transmitting Fiber Optic Probe".

(d) P.C. Schultz and M.G. Drexhage, Ibid., no. 499, "Preparation, Properties, and Uses of Mid-IR Fiber Optics".

15. K.H. Shafer, S.L. Pentoney, P.R. Griffiths, Anal. Chem. 58, 58-64 (1986). "SFC-FTIR with Automatic DRIFT Interface".

16. (a) R.D. Smith, H.R. Udseth, Ibid. 59, 13-15 (1987) "MS with Direct SF Injection".

17. J.D. Henion, L. Weidolf, E.d. Lee, T.R. Covey, Proc. 35th ASMS Conf. on MS, May 24-29, 1987, Denver, CO., "Determination of Anabolic Steroids by API SFC-MS and SFC-MS Using Packed Columns".

18. B.W. Wright, C.W. Wright, R.W. Gale, R.D. Smith, Anal. Chem. 59, 38-44 (1987). "Analytical SFE of Adsorbent Materials."

19. J.H. Raymer, E.D. Pel_izzarri, Anal. Chem. 59, 1043 and

2069 (1987) "Toxic Compound Recoveries..." and "Desorption Characteristics of Four Polyimide Sorbent...".

20. R.A. Fifer, in Fundamentals of Solid Propellant Combustion, M. Summerfield and K. Kuo, Eds., Progress Aeronautics & Aeronatics Series, AIAA, Vol. 90, 1984, Chapter 4., "Chemistry of Nitrate Esters and Nitramine Propellants".

21. (a) S.H. Townsend, M.A. Abraham, G.L. Huppert, M.T. Klein, S.C. Paspek, Ind. Eng. Chem. Res. 27, 143-149 (1988). "Solvent Effects During Reactions in Supercritical Water".

(b) K.M. Dooley, F.C. Knopf, Ibid., 26, 1910-1916 (1987). "Oxidation Catalysis in an SF Medium".

(c) J.O. Metzger, J. Hartmanns, D. Malwitz, P. Koll, Ref. 13b, Chapter 26, 515. "Thermal Organic Reactions in SF Supercritical Fluids".

ACKNOWLEDGEMENTS:

We gratefully acknowledge the cooperative efforts of A. Greg Gargus (Prochem Scientific), Dr. Roger Schirmer (Guided Wave, Inc.), T. Novak (U.S. Army Chemical Research, Development and Engineering Center) and V. Henderson (Geo-Centers, Inc.). Continued collaboration with Dr. R.A. Fifer is appreciated.

INTEGRATED INTELLIGENT INSTRUMENTS (I^3)

AUTOMATED/INTERFACED

- SAMPLE PROCESSING
- MONITORING/ SAMPLING
- ACCUMULATOR/PREP SCALE
- SEPARATION
- DETECTION/IDENTIFICATION
- DATA ANALYSIS/CHEMOMETRICS
- APPLIED AI

Figure 1a

Figure 1b

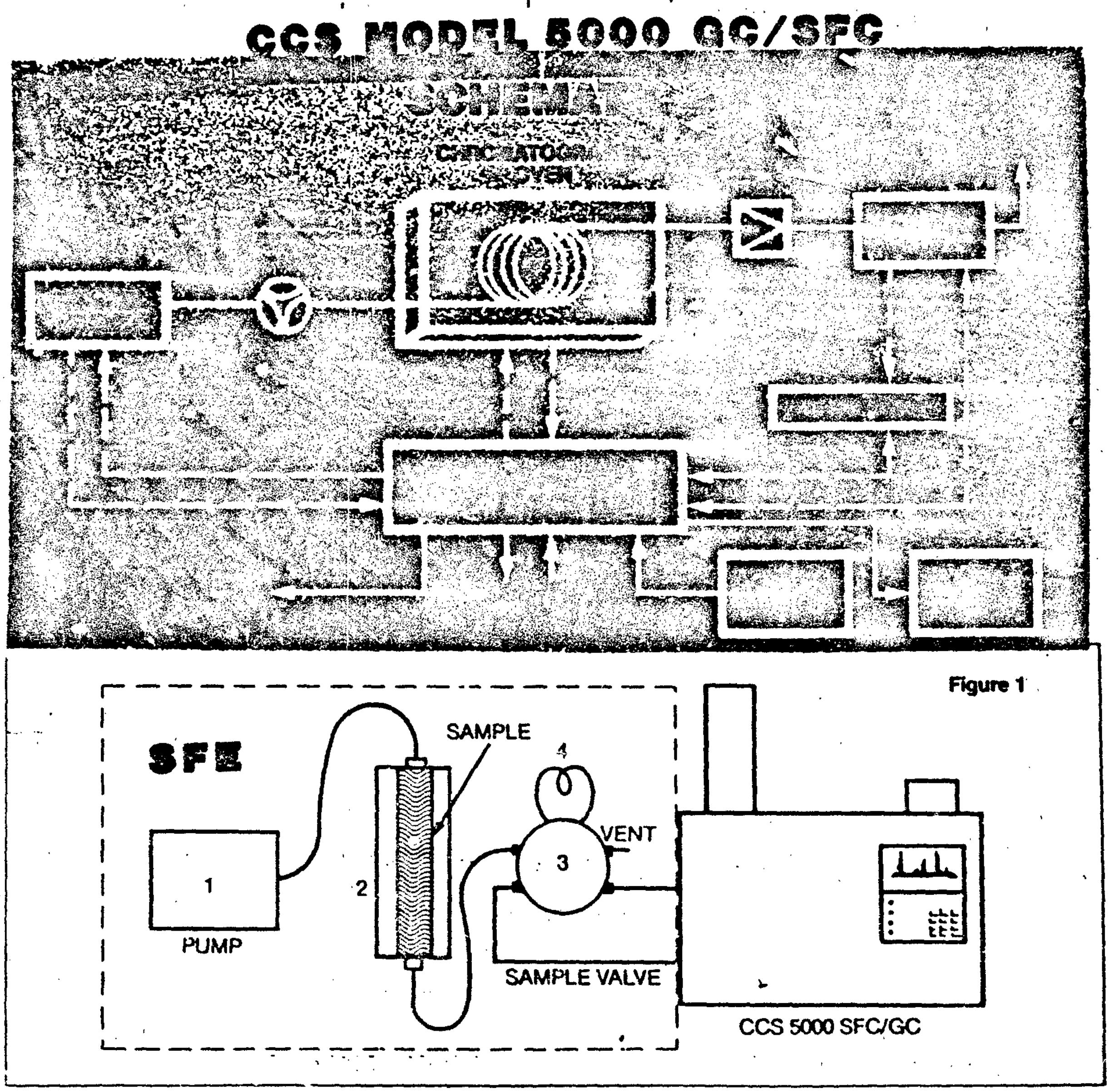

Figure 1

Figure 2

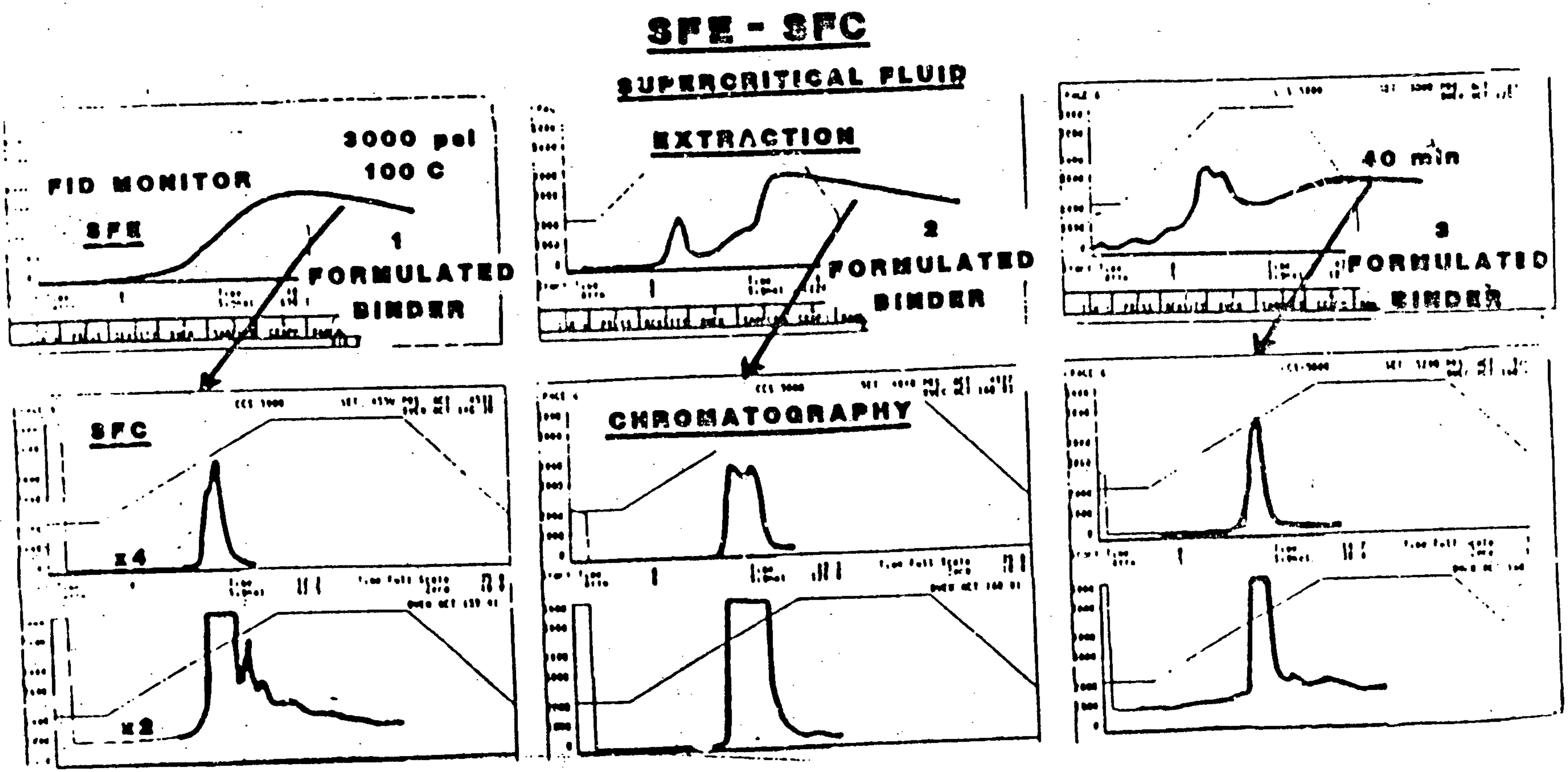

SFE - SFC
SUPERCRITICAL FLUID
EXTRACTION
CHROMATOGRAPHY
3000 psi
100 C
FID MONITOR
SFE
1
FORMULATED
BINDER
2
FORMULATED
BINDER
40 min
3
FORMULATED
BINDER
SFC
x4
x2

Figure 3

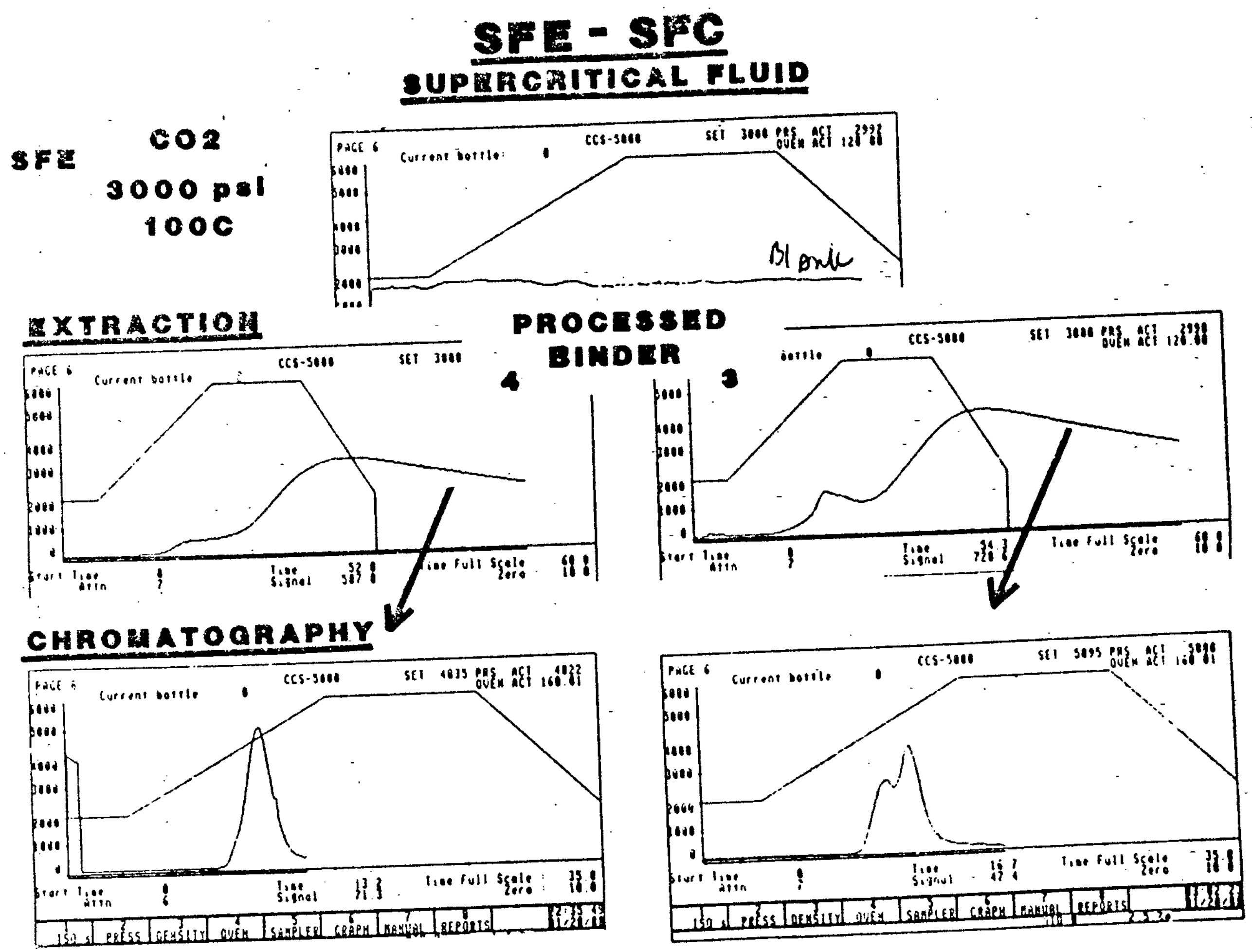
SFE - SFC
SUPERCRITICAL FLUID
SFE
CO2
3000 psi
100C
Blank
EXTRACTION
PROCESSED
BINDER
4
3
CHROMATOGRAPHY

Figure 4a

30 mg [redacted] FIBER A

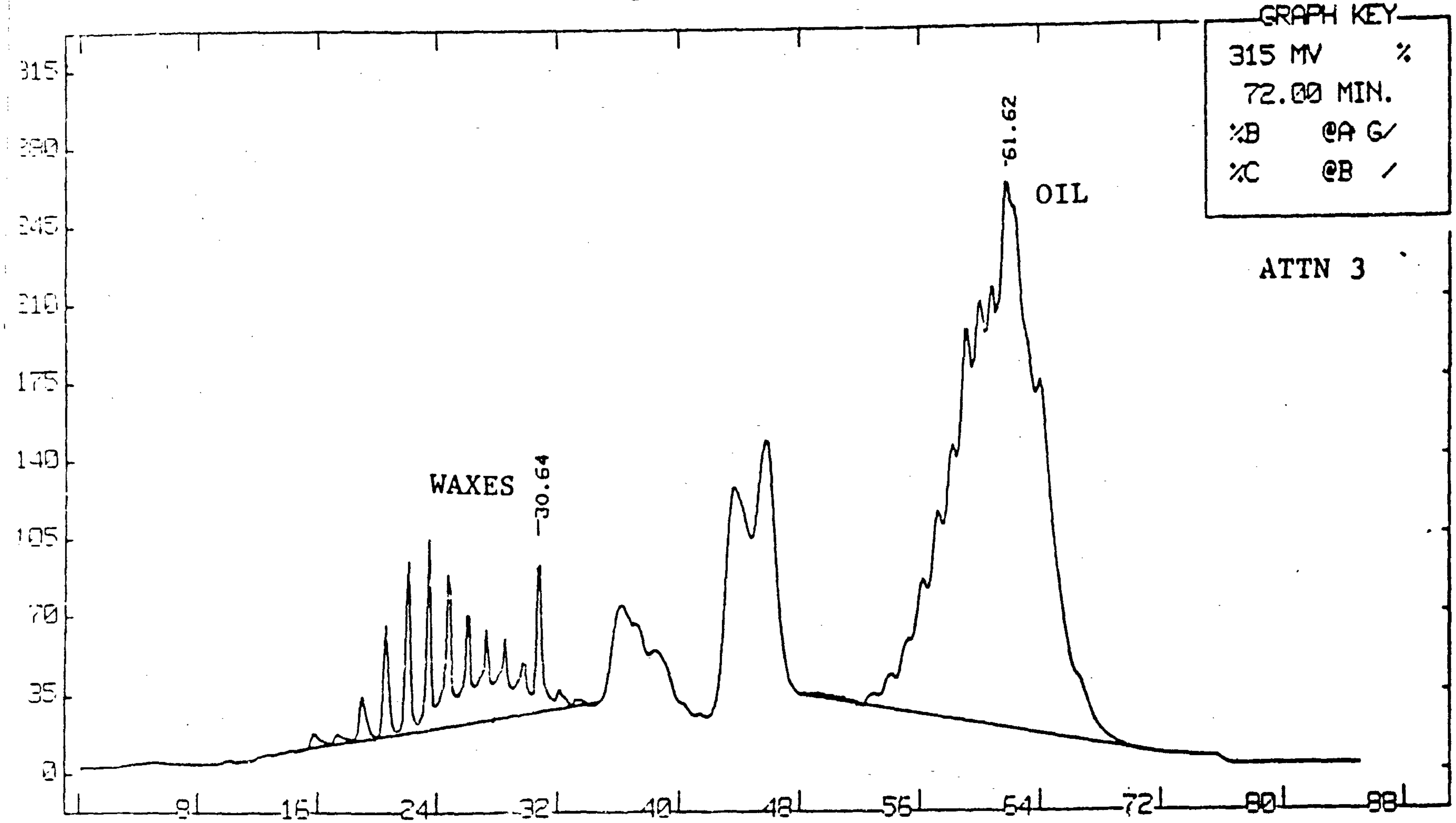

30 mg [redacted] FIBER B

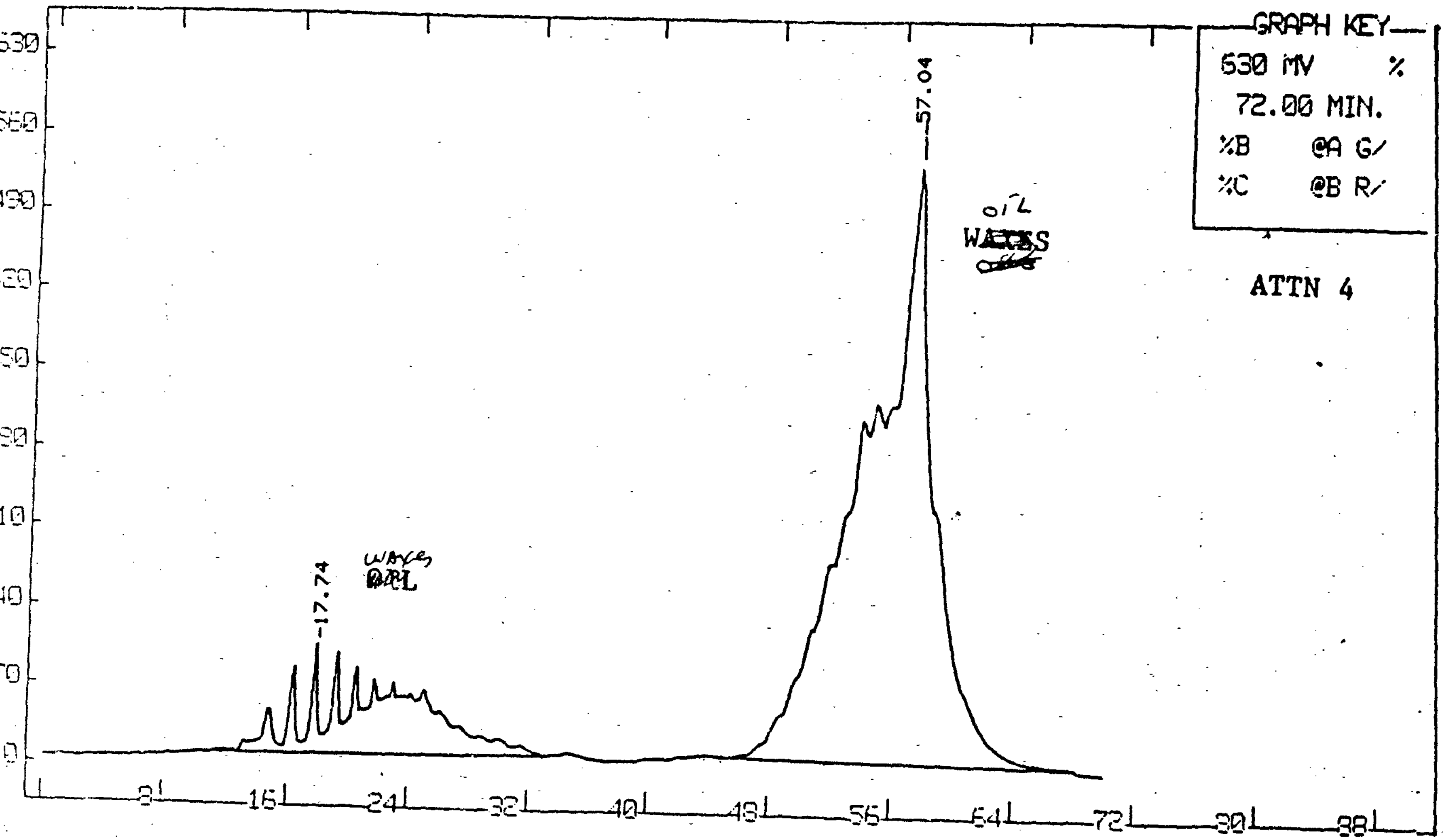

Figure 4b

Figure 5

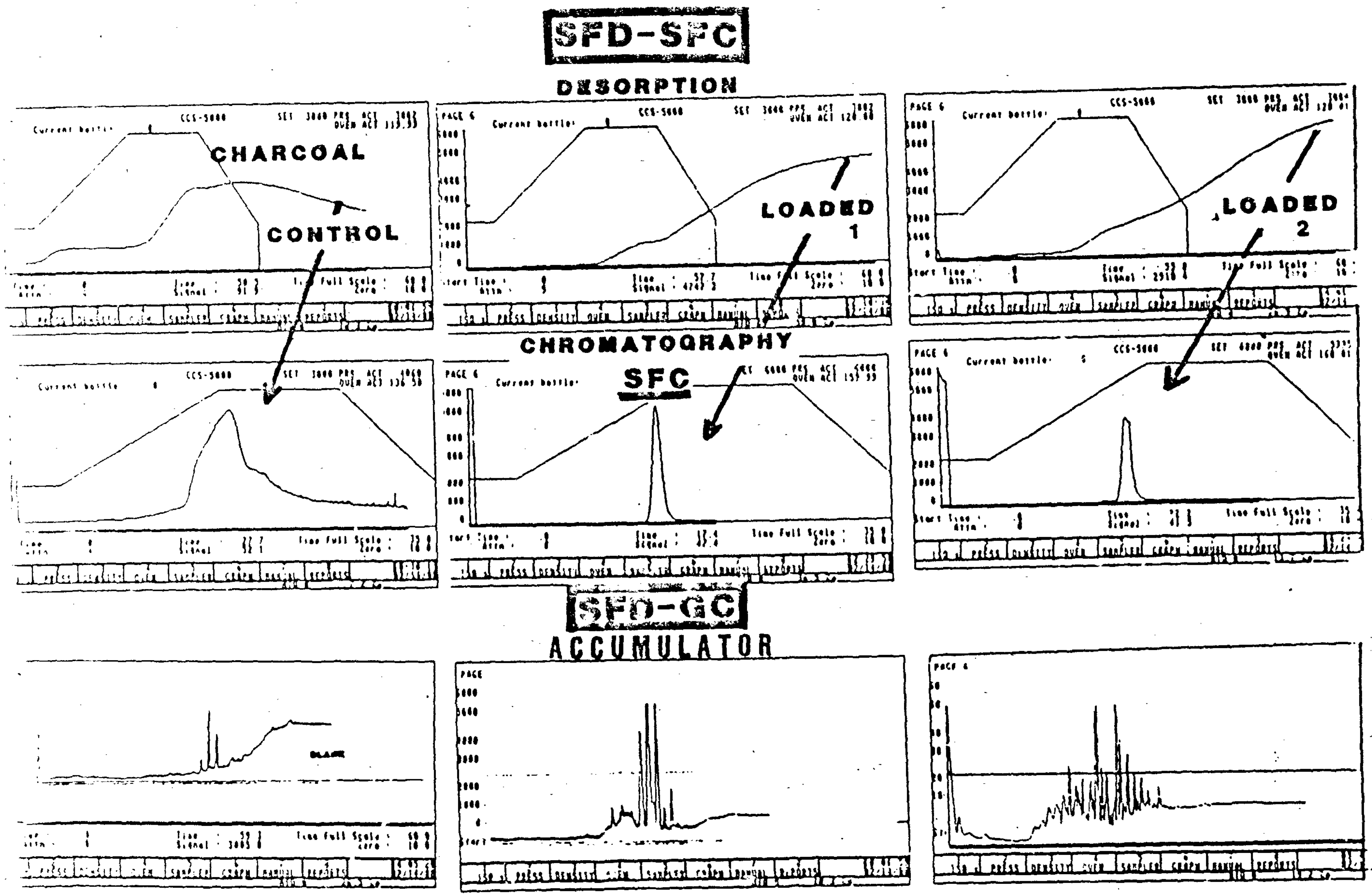
SFD-SFC
DESORPTION
CHARCOAL
CONTROL
LOADED
1
LOADED
2
CHROMATOGRAPHY
SFC
SFD-GC
ACCUMULATOR

Figure 6

SUPERCRITICAL FLUID REACTION

SFR–SFC

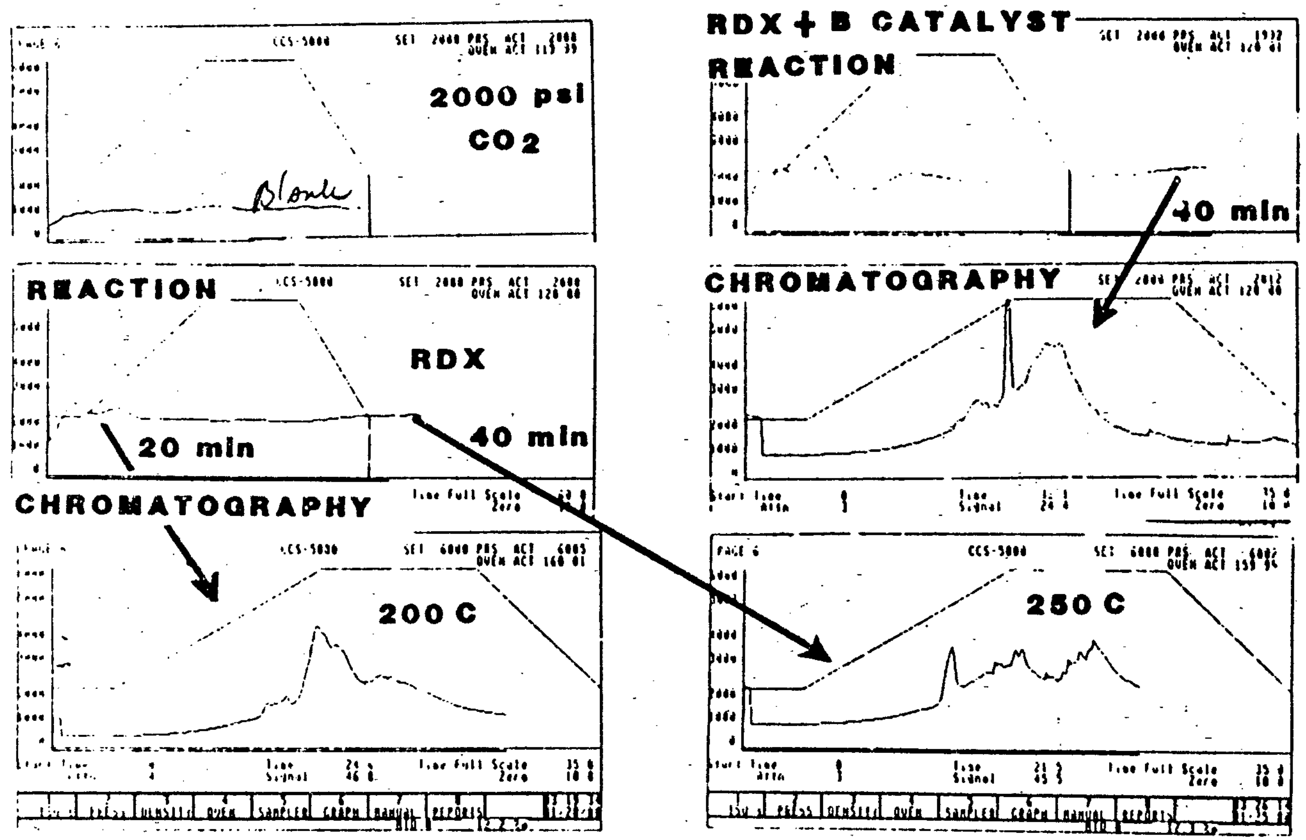

"EXCONFIG"

CHOICES =

DIRECT INJECTION CONFIG A
DHS/PYROLYSIS GC B
EXTRACTION C
DESORPTION D
REACTION E
HIGH TEMP/PRESSURE HYPERGC F
SF FLOW UNIT G
FOM^2/MI^2D

FACTOR = 1 <u>SAMPLE PROCESSING</u>

DIRECT INJECTION
DHS/PYROLYSIS
EXTRACTION
DESORPTION
REACTION
HIGH TEMP/HIGH PRESSURE

2 <u>CONCENTRATOR</u>

MACRO - PREP TRAP
MACRO - QUANTITATION
MICRO - TRACE

3 <u>MOBIL FLUID</u>

SF/CO_2

MODIFIED CO_2

$He/N_2/AIR$

4 <u>CHROMATOGRAPHY</u>

GC (PACKED, CAPILLARY)

SFC (PACKED, MICROBORE, CAPILLARY)

HYPERGC (PACKED, MICROBORE, CAPILLARY)

5 <u>DETECTION</u>

FID, NPD, PID

UV, FTIR, MS, MS-MS

FOM^2 (UV, VIS, NIR, IR)

MI^2D ($SF-FOM^2-GC$)
($SF-FOM^2-GC/MS$)
($SF-FOM^2-MS/MS$)

Figure 7a

DECISION STRUCTURE FOR THE EXPERT SYSTEM "METHOD DEVELOPMENT"

DECISION;

METHOD INFO
CHOICES:

- SFE/SFD/SFR
- SFC/HYPERGC/GC
- SF THEORY
- REVERSE MICELLE/MICROEMUL
- POLAR/IONIC COMPOUNDS
- OLIGOMERS, POLYMERS
- SAMPLE PROCESSING
- EXPERIMENTAL DESIGN

FACTORS;

(1) EXPERIMENTAL CONFIG

- DIRECT INJECT A
- DHS/PYROLYSIS B
- EXTRACTION C
- DESORPTION D
- REACTION E
- HIGH TEMP/HIGH PRESSURE F
- SF FLOW UNIT G

(2) SAMPLE TYPE
TYPE OF VALUES: UNORDERED DESCRIPTIVE PHRASES
VALUES:

- CHEM GROUP 1
- CHEM GROUP 2
- CHEM GROUP 3
- CHEM GROUP 4

(3) SF MOBILE PHASE
TYPE OF VALUES; UNORDERED DESCRIPTIVE PHRASES
VALUES:

- CO_2
- HEXANE
- PROPYLENE
- PROPANE
- SF_6
- N_2O
- NH_3
- SO_2
- REVERSE MICELLE

(4) MODIFIER/COSOLVENT
TYPE OF VALUES: UNORDERED DESCRIPTIVE PHRASES
VALUES:

- MEOH
- ACETONE
- N-OCTANE

(5) EXPERIMENTAL DESIGN

- FRACTIONAL FACTORIAL (2^k)
- BOX-BEHNKEN (3^5)

Figure 7c

KNOWLEDGE BASE FOR THE EXPERT SYSTEM "METHOD DEVELOPMENT"

RULE 7

IF:

SAMPLE	IS CHEM TYPE 1
SYSTEM	IS SFC CONFIG U
MOBILE PHASE	IS REVERSE MICELLE
COLUMN	IS MICROBORE
PROCEDURE	IS #1
SOURCE REF	IS R.W. GALE, J.L. FULTON, R.D. SMITH

THEN:

METHOD INFO	IS REVERSE MICELLE/MICROEMUL (100)

RULE 8

IF:

SAMPLE	IS CHEM TYPE 2
SYSTEM	IS SF FLOW UNIT
MOBILE PHASE	IS CO2
MODIFIER/COSOLVENT	IS MEOH
PROCEDURE	IS #2
SOURCE REF	IS IND. ENG. CHEM. RES. 26,56 (1987)

THEN:

METHOD INFO	IS SF THEORY (100)

RULE 9

IF:

SAMPLE	IS CHEM TYPE 2
SYSTEM	IS SF FLOW UNIT
MOBILE PHASE	IS CO2
MODIFIER/COSOLVENT	IS MEOH
PROCEDURE	IS #2
SOURCE REF	IS J.M. DOBBS, J.M. WONG, R.J. LAHIERE, K.P. JOHNSTON

THEN:

METHOD INFO	IS SF THEORY (100)

RULE 10

IF:

SAMPLE	IS CHEM TYPE 2
SYSTEM	IS SF FLOW UNIT
MOBILE PHASE	IS CO2
MODIFIER/COSOLVENT	IS ACETONE
PROCEDURE	IS #2
SOURCE REF	IS IND. ENG. CHEM. RES. 26,56 (1987)

THEN:

METHOD INFO	IS SF THEORY (100)

RULE 11

IF:

SAMPLE	IS CHEM TYPE 1
SYSTEM	IS SFC CONFIG U
MOBILE PHASE	IS HEXANE/AOT/WATER
PROCEDURE	IS #1
SOURCE REF	IS ANAL. CHEM., 59, 1977 (1987)

THEN:

METHOD INFO	IS REVERSE MICELLE/MICROEMUL (100)

CHARACTERIZATION OF CYCLOTRIMETHYLENETRINITRAMINE (RDX) BY N,H ISOTOPE ANALYSES WITH PYROLYSIS ATMOSPHERIC PRESSURE IONIZATION TANDEM MASS SPECTROMETRY

A. Peter Snyder, U.S. Army Chemical Research, Development and Engineering Center, SMCCR-RSL, Aberdeen Proving Ground, Maryland 21Ø1Ø-5423

Johannes H. Kremer, Wehrwissenschaftliche Dienststelle der Bundeswehr fur ABC-Schutz, Humboldtstrasze, D3Ø42 Munster, FRG

Shirley A. Liebman*, GEO-CENTERS, INC., 1Ø9Ø3 Indian Head Highway, Ft. Washington, MD 2Ø744 (*Mailing Address: GEO-CENTERS, INC., c/o U.S. Army Chemical Research, Development and Engineering Center, SMCCR-RSL, Aberdeen Proving Ground, Maryland 21Ø1Ø-5423

Michael A. Schroeder and Robert A. Fifer, Ballistic Research Laboratory, Aberdeen Proving Ground, Maryland 21ØØ5-5Ø66

Please send correspondence to:

Commander
U.S. Army Chemical Research, Development and Engineering Center
ATTN: SMCCR-RSL/A. Peter Snyder
Aberdeen Proving Ground, Maryland 21Ø1Ø-5423

Abstract

Pyrolysis - atmospheric pressure chemical ionization was used to study the thermal decomposition of the energetic material cyclotrimethylenetrinitramine (RDX) and characterization of the individual molecular ion products was accomplished by tandem mass spectrometry. The analysis was aided with pyrolysis mass spectra of the ^{15}N- and perdeuterated RDX isotopes, and molecular formulae were derived for the m/z 46, 60, 74, 75, 85 and 98 molecular ions in the RDX pyrolysis-mass spectrum. Equivalent fragments between the daughter ion mass spectra of the unlabeled and labeled RDX were determined in order to define a structure for each pyrolysis feature. Daughter ion mass spectra of pure, reference compounds confirmed the identity of five of the six molecular ions. Perdeuterated RDX analyses provided evidence that m/z 74 and 75 are N,N-dimethylformamide and N-nitrosodimethylamine, respectively, rather than the currently accepted structures of nitroformimine and its protonated form, respectively. m/z 46, 60 and 85 were identified as the protonated forms of formamide, N-methylformamide and dimethylaminoacetonitrile, respectively.

Key Words:

Pyrolysis, atmospheric pressure chemical ionization, tandem mass spectrometry, RDX, propellants, isotope analysis, cyclotrimethylenetrinitramine, explosives, daughter ion analysis, nitramines, decomposition, mass spectrometry.

INTRODUCTION

Reaction rates and chemical mechanisms are two key topics that are fundamental to an understanding of the ignition/combustion process and product distribution of compounds used in propellants and explosives. Even more important are questions that address the thermodynamics, kinetic parameters and catalytic influences on the rate and end-product distributions in the ignition, combustion and detonation of solid propellants[1]. A structural analysis of the key fragments and intermediates resulting from the controlled heating of energetic compounds can yield important information relative to the understanding and enhancement of thermal processes. For this purpose, analytical pyrolysis/concentrator-gas chromatography was used to generate nitramine thermal decomposition profiles[2-4]. Furthermore, a large body of information exists on decomposition products of nitramines in the form of molecular formulae obtained by accurate mass measurements with high resolution mass spectrometers[5-8]. However, few studies can be found that have produced direct, unambiguous analyses that delineate the structural identities of the end products.

Two compounds which are commonly used as ingredients in explosives and propellants are the nitramines cyclotrimethylenetrinitramine (RDX) and cyclotetranitramine (HMX). The former compound was chosen as a model for a structural analysis of the product molecular ions produced under oxidative pyrolysis, atmospheric pressure chemical ionization

(Py-APCI) conditions.

Perdeuterated and ^{15}N-RDX were used in isotopic analyses of the key RDX mass spectral features, as well as collision-induced dissociation of the molecular ion products for comparison to daughter ion mass spectra of pure standard compounds. Some of the RDX Py-APCI mass spectral features can be found in the Py-mass spectrometry literature for a number of important propellants ingredients[5-12].

RESULTS AND DISCUSSION

Molecular Formulae by isotope analyses

Figure 1a presents the Py-APCI mass spectra and structure of RDX. Molecular formulae and structural interpretations of the individual features in the Py-APCI mass spectrum of RDX are indeed formidable challenges. Therefore, isotopic analyses were performed in order to provide information to characterize each of the separate mass spectral features. Figure 1b,c depict the Py-mass spectra of (^{1}H, ^{15}N)-RDX and (^{2}H, ^{14}N)-RDX, respectively. Note that Figures 1a,b show six main molecular ion features, but the perdeuterated RDX mass spectrum has only five main features. Table 1 summarizes the equivalent features for each of the RDX isotopes. For example, m/z 46 in Fig. 1a is observed as the m/z 47 ion in both ^{15}N and deuterium RDX isotopes, indicating that the m/z 46 feature contains one nitrogen and one hydrogen atom that originate from RDX. An m/z 74 analysis (Fig. 1 and Table 1) shows that it contains one nitrogen and seven hydrogen atoms, and a similar treatment with m/z 75 yields two nitrogen and six hydrogen atoms that originated from RDX.

Isotope analysis of each molecular ion from RDX produced a CHNO working formula (first column in Table 2) highlighting the number of hydrogen and nitrogen atoms that must be a part of the molecular ion and derived from RDX. The table of different CHNO molecular formulae for a given mass found in Silverstein et al.[9] was consulted for a tentative match to each of the six main features in the Py-APCI mass spectra. None of the molecular formulae in Silverstein et al.[9] contained HN combinations equivalent to the working formulae in Table 2 for each respective mass. Therefore, it was proposed that some of the RDX features were actually protonated forms of the working formulae. The protonated working formulae are listed in Table 2 and indeed, from Silverstein's tables[9], m/z 74, 75, 85 and 98 each had only one molecular formula consisting of the respective number of RDX-derived hydrogen and nitrogen atoms with an extra proton. With this information, the number of carbon and oxygen atoms were automatically known for each formula, and the protonated molecular formulae for m/z 74, 75, 85 and 98 can be found in the last column of Table 2. However, m/z 46 and 60 did not result in similar analyses, hence, the formula that had the least number of hydrogen atoms over that from the protonated working formula of the respective feature was chosen as a tentative molecular formula. These analyses of m/z 46 and 60 produced formulae of $[CH_3NO]H^+$ and $[C_2H_5NO]H^+$, respectively. Structural analysis of the six Py-APCI mass spectral features from RDX are detailed in the following discussion.

m/z 46

The perdeuterated RDX isotope mass spectrum (Figure 1c) portrays a negligible amount of the m/z 46 feature. This leads to the elimination of nitrogen dioxide (NO_2) as a candidate for m/z 46 (Fig. 1a) in the positive ion mode. Furthermore, m/z 46 contains not only a nitrogen but also one hydrogen originating from RDX as is evident from the m/z 46 shift to m/z 47. It is well documented[6-8, 12] that heating of RDX produces NO_2 under many different conditions and an intense m/z 46 feature has been observed in the negative ion mode under Py-APCI conditions (data not shown).

In the daughter ion spectra for m/z 46 and 47 (Fig. 2), it appears that m/z 18, 28 and 29 in the unlabeled compound (Fig. 2a) result in m/z 19, 29 and 29, respectively, for both ^{15}N and ^{2}H isotopes of RDX (Fig. 2b,c). No oxygen or carbon atom can be part of the m/z 18 feature because of the one amu shift from m/z 18 to m/z 19 in both isotopes. This leads to the conclusion that NH_4^+ is the only possible structure, because (a) the nitrogen and one hydrogen atom originate from RDX and (b) the other hydrogens must originate from the ion source. The 28 amu fragment increases by one amu for both RDX isotope species which suggests the $[CNH]H^+$ and/or $[HCN]H^+$ ions, where one proton originates from RDX and the other is an ion source proton. The m/z 29 ion in Fig. 2a is observed to remain at m/z 29 in both isotope daughter ion mass spectra

(Fig. 2b,c) and can be represented by the $[COH]^+$ fragment, where the liberated carbon monoxide is associated with a source proton. From this analysis, two possible structures with a molecular formula of CH_4NO can be considered: a protonated isocyanic acid derivative, $[OCNH_3]H^+$, or protonated formamide, $[HC(O)NH_2]H^+$.

Figure 2d shows the daughter ion mass spectrum of protonated formamide. In a comparison of Fig. 2a and Fig. 2d, protonated formamide is indeed the m/z 46 feature in the Py-mass spectrum of RDX. A paradox exists, because the proton (Fig. 1a) and deuterium (Fig. 1c) isotope analyses indicate only one RDX-derived hydrogen, while formamide contains three inherent protons. Possible explanations for this observation are that (1) free radical hydrogen atom reactions could occur in the melt and/or gas phase and (2) formation of HCN from RDX pyrolysis followed by hydrolysis with atmospheric/RDX decomposition-derived water and subsequent protonation in the ion source.

m/z 60

An analysis of the daughter ion spectra of the m/z 60 molecular ion from RDX and its isotopes (Fig. 3a-c) reveals key fragments for this ion. A methyl function is obvious and m/z 28 consists of one nitrogen and one hydrogen from RDX (Fig. 3d). The m/z 28 fragment appears to be $[HCN]H^+$ where one hydrogen comes from RDX and the other is a source proton. The m/z 42 daughter ion feature contains one nitrogen and four hydrogen atoms from the RDX molecule (Fig. 3d), and the

$[H_3CN(H)C]^{+\cdot}$ and $[CH_3NCH]^{+\cdot}$ fragments appear to be logical candidates. A consistant 18 amu difference appears between each respective primary molecular ion and highest mass daughter fragment, i.e., 60 - 42 (Fig. 3a), 61 - 43 (Fig. 3b), and 64 - 46 (Fig. 3c) and strongly suggests the presence of an oxygen atom. Possible candidates for m/z 60 can be $[H_3CNHC(O)H]H^+$, $[H_3CNCH]^{+\cdot}H_2O$ or a mixture of the two. Figure 3e shows the daughter ion mass spectrum from protonated N-methylformamide. A comparison of Figs. 3a and e shows that m/z 60 is indeed protonated N-methylformamide, $[H_3CNHC(O)H]H^+$. An explanation can be invoked for the presence of the two extra hydrogen atoms that is similar to that of the m/z 46 analysis.

<u>m/z 74</u>

Figure 4a-c presents the m/z 74 daughter ion mass spectra of RDX and its isotopes. Because of the one amu proximity of m/z 74 and 75 (Fig. 1a), daughter ion spectra of both species were obtained where the calibration of the m/z 73, $[H_2O]_4H^+$, reagent ion produced a baseline-to-baseline profile from m/z 72.5 to 73.5 and a peak width at half-height of 0.7 amu. This procedure minimized daughter ion contribution of m/z 75 to the mass spectrum of m/z 74 and vice versa. The molecular formula of $[C_3H_7NO]H^+$ (Table 2) reveals that it is a protonated ion containing one nitrogen and one oxygen atom and seven hydrogen atoms originating from RDX. This molecular ion contains one more hydrogen than the RDX molecule itself which strongly suggests intermolecular interactions in the melt state as well as reduction chemistry taking place during decomposition.

Figure 4d summarizes the daughter fragment ion distribution in Fig. 4a-c, and it is clear that at least one methyl moiety is present. An m/z 30 analysis tentatively indicates a $[H_3CN]H^+$ moiety, and m/z 42 appears to be a $[H_3CNCH]^{+\cdot}$ fragment. Protonated carbon monoxide can account for the m/z 29 fragment (Fig. 4a-c). The m/z 46 feature appears to have one nitrogen (Fig. 4d), however, the ^{2}H-RDX mass spectral interpretation of this fragment is unclear (Fig. 4c). Figure 1c and Table 1 show that both m/z 74 and 75 in the unlabeled compound produce an m/z 81 feature in the perdeuterated sample. Therefore, structural interpretations of the unlabeled RDX m/z 74 and 75 species based on the perdeuterated derivative were interpreted with caution because of the two different m/z 81 molecular ions contributing to the same daughter ion mass spectrum (Fig. 4c). The $[H_3CCHNO]^{+\cdot}$ or $[H_3CNCHO]^{+\cdot}$ structures can account for the m/z 58 fragment while ether and hydroxy structural fragments were rejected.

Possible structures for m/z 74 include N-oxide compounds such as $[H_3CN(O)CHCH_3]^{+\cdot}$ or $[H_3CN(O)CH_2CH_3]^{+\cdot}$. However, because of the inherent charge on the former species, a source proton would not bind to it, and this interpretation would leave the molecular ion at m/z 73. The latter compound would be expected to yield an intense m/z 29 ethyl daughter ion fragment since NO is a good leaving group. The daughter ion mass spectrum of protonated N,N-di-methylformamide

$[(H_3C)_2NC(O)H]H^+$ (Fig. 4e) shows a satisfactory relationship with that of Fig. 4a. Note that the m/z 74 ion is indeed composed of an m/z 73 molecular ion with an ion source proton attached to it (Table 2).

m/z 75

Figure 5a,b presents the m/z 75 and 77 daughter ion mass spectra of ^{14}N- and ^{15}N-RDX, respectively, and the isotope fragment analysis (Fig. 5c). The perdeuterated-RDX mass spectrum of m/z 81 was already presented in Figure 4c. Relatively few daughter ion fragments are observed as compared to m/z 74. A methyl group is present, an m/z 43 analysis reveals $[NCHNH_2]^{+\cdot}$, $[HNCNH_2]^{+\cdot}$ and $[H_3CNN]^{+\cdot}$ as possible structures (Fig. 5c), and the features in the vicinity of m/z 30 were neglected due to their low abundance. The m/z 58 fragment could be represented by the $[H_3CNCHNH_2]^{+\cdot}$, $[H_3CNHCNH_2]^{+\cdot}$ and $[(CH_3)_2NN]^{+\cdot}$ structures, and the remaining 17 amu (to produce m/z 75) can come from an oxygen and ion source proton. Structures that best satisfy the daughter ion mass spectral information are $[H_3CN(O)CHNH_2]H^+$, $[H_3CNHC(O)NH_2]H^+$ and $[(CH_3)_2NNO]H^{+\cdot}$. An m/z 75 daughter ion mass spectrum of protonated N-nitroso-dimethylamine $[(H_3C)_2NNO]H^+$ (Fig. 5d) was identical to that of m/z 75 in RDX (Fig. 5a). This structure is similar to that for m/z 74, with the formyl group being replaced by an NO group.

m/z 85

The molecular formula as proposed in Table 2 is unusual in that it contains one carbon and two hydrogen atoms more than the RDX molecule itself (Fig. 1a inset). The daughter ion mass spectra of m/z 85 and the corresponding isotopic molecular ions are presented in Fig. 6a-c. Figure 6d presents an analysis of each of the fragment ions in terms of equivalent, respective fragments for the unlabeled and labeled molecular ions.

At least one methyl group is observed and m/z 30 appears to be a $[H_3CN]H^+$ moiety with an ion source proton (Fig. 6d). m/z 44 contains one nitrogen and five RDX-derived hydrogen atoms and appears to be any one of a number of fragments with a chemical formula of $[C_2H_5N]H^+$. m/z 45 contains one nitrogen and six RDX-derived hydrogen atoms with structural permutations having the $[C_2H_6N]H^+$ chemical formula. m/z 69 (Fig. 6a) contains two nitrogens and only four hydrogens derived from RDX and is 16 amu apart from the molecular ion. This difference suggests an oxygen atom, however, this atom is not found in the protonated molecular formula (Table 2). Alternative sources of the 16 amu loss are either a methyl group and source proton or an NH group with a source proton, $[NH]H^+$. With the aid of the isotopic analyses, a small suite of compounds was selected, and their daughter ion mass spectra were obtained. Protonated dimethylaminoacetonitrile, $[(CH_3)_2NCH_2CN]H^+$ (Fig. 6e) produced a better match with Fig. 6a than that of the other test compounds. Note that

$(CH_3)_2NCH_2CN$ has one carbon and two hydrogen atoms more than RDX itself. This indicates that its formation is the result of intermolecular reactions among primary products and implies that reduction reactions are involved.

m/z 98

The molecular ion $[C_3H_3N_3O]H^+$ (Table 2) consists of only three RDX-derived hydrogen atoms and strongly suggests a high degree of unsaturation in the molecule. Figure 7a-c presents the daughter ion mass spectra of m/z 98 and its nitrogen and hydrogen m/z 101 isotope equivalents. The methyl group is not observed, and m/z 28 appears to be protonated hydrogen cyanide as shown by the fragment analyses in Fig. 7d. A structural analysis of the minor m/z 16 feature suggests the $[NH]H^+$ group. m/z 44 is most likely protonated cyanic acid, $[HOCN]H^+$ or the isomeric structure $[HCNO]H^+$, and m/z 54, in consideration of the structure of RDX, can be the $[NCHNCH]^{+\cdot}$ fragment. Seventeen amu added to the m/z 54 fragment would yield m/z 71 suggesting an oxygen/proton combination. Possible structures for this fragment can be $[CHNCHNO]H^+$, $[CHN(O)CHN]H^+$, $[NCHNCHO]H^+$ or $[NCH(O)NCH]H^+$ where the oxygen atom is located on an internal or external carbon or nitrogen atom.

To the best of the authors' knowledge, coupounds with the chemical formula $C_3H_3N_3O$ are not commercially available, and therefore Fig. 7e,f presents two possible structures that best fit the isotope fragment analyses of m/z 98. Figure 7e is a protonated triazine-N-oxide and Fig. 7f represents an equivalent structure except that the oxygen is situated on a carbon atom. An inter- or intramolecular oxidation reaction could take place on the RDX molecule which would lead to the proposed structures. The latter structure is a more attractive candidate in that it could act as a direct intermediate in the formation of the m/z 46 and 60 formamide-derived products.

Low vs. Atmospheric Pressure Thermal Products of RDX

The chemical formulae and structural identities of the m/z 46, 74, 75, 85 and 98 features generated under Py-APCI conditions are in contrast with many of the experimental findings in the literature.[5-7,9-12,14-22] Sample conditions such as field desorption[5] and direct insertion and solids probes with water, methane and isobutane chemical ionization (CI)[6,7,9,11,23-26] and electron ionization (EI)[6,7,10,11] have yielded an m/z 74 feature that with accurate mass measurement (AMM) corresponds to $[CH_2N_2O_2]^{+\cdot}$. In the above studies, nitroformimine, $[CH_2NNO_2]^{+\cdot}$, was proposed as the compound, and this species was also observed with infrared multiphoton dissociation of an RDX molecular beam.[27] AMM of m/z 75 produced a chemical formula of $[H_3CN_2O_2]^+$, and this species was rationalized as protonated nitroformimine. Spangler et al.[14] have shown that with flash evaporation of RDX on a solids probe in a heated atmospheric pressure ionization source, a mass-identified ion mobility peak was found for m/z 75, and the authors assumed the identity of the ion was protonated nitroformimine. In the present report, however, under similar pyrolysis and ionization conditions, tandem mass spectrometry isotope analyses yielded the formamine and nitrosoamine derivatives for m/z 74 and 75, respectively.

EI and CI ($\sim$ 1 torr) AMM have shown that m/z 46 and 85 are represented by the NO_2^+[6,7] and triazine ($C_3H_7N_3$),[2,6] respectively. In this study, atmospheric pressure thermolysis of RDX also yielded these mass spectral features, however their identities are different in that protonated formamide and protonated dimethylaminoacetonitrile are responsible for the m/z 46 and 85 features, respectively. In addition to Py-APCI, pyrolysis of RDX under EI conditions[6,7,10,22] has also produced the m/z 98 feature with an AMM-derived chemical formula of $[C_3H_4N_3O]^{+\cdot}$. A structural determination of m/z 98, however, is less definitive in that only protonated triazine oxide (Fig. 7e) has been proposed in the literature while the Py-APCI daughter ion analysis tends to support the carbon-oxygen analogue in Fig. 7f.

These observations strongly suggest either (a) that a different chemical mechanism or additional chemical steps take place in the decomposition of RDX when it is thermally treated under atmospheric pressure conditions as opposed to the low pressure conditions ($\leq$ 1 torr) used for mass spectral analyses of RDX and/or (b) previous studies were not robust in design to distinguish between the assumed structures and those found in the present study because of the absence of perdeuterated-nitramine analyses.

CONCLUSIONS

Analytical pyrolysis-APCI was used to impose selected temperature and pressure conditions for the oxidative degradation of the energetic material RDX. Structural characterization of the pyrolysis products was achieved using ^{15}N- and ^{2}H-RDX with triple quadrupole mass spectrometer instrumentation. Py-APCI tandem mass spectrometry revealed important insights into the decomposition of RDX under the selected experimental conditions. The combination of pyrolysis-atmospheric pressure ionization triple quadrupole techniques with isotopically-tagged samples was shown to be a powerful tool for structural elucidations and provided structural assignments that had not been reported in the previously cited mass spectrometric studies of RDX decomposition.

EXPERIMENTAL

A Sciex (Toronto, Canada) TAGA 6000 atmospheric pressure chemical ionization (APCI) triple quadrupole mass spectrometer was used as the analyzer and detector for mass spectra collection. Background methods and general operating procedures for an APCI-mass spectrometer system have been discussed by Dawson, et al.,[28,29] and the operating conditions for the present study can be found elsewhere.
Normal operating pressure in the conventional mass analyzer

mode was 2.5 - 3.0 x 10^{-6} torr, and all daughter ion analyses were obtained with a 6.0 x 10^{-5} torr pressure of argon collision gas.

Pyrolysis of the solid samples was conducted with a Pyroprobe Model 122 controller (Chemical Data Systems, Oxford, PA), with the platinum coil desorption probe. Pyrolysis was conducted with the temperature ramp (risetime) in the off position and the final set temperature was 360°C. All runs used ca. 0.5 - 1.0 mg of powdered sample positioned in a quartz tube with quartz wool. The tube was placed into the desorption probe, and the latter was inserted into the ion source of the mass spectrometer. Details and a schematic of this interface are presented elsewhere[3]. All pyrolysis experiments were performed with an 80 ml/min air flow from a compressed air cylinder (MG Industries, Valley Forge, PA). Samples of ^{15}N-RDX and perdeuterated (^{2}H)-RDX were obtained as gifts from S. Bulusu, Armament Research and Development Center, Dover, NJ. In preliminary experiments, all RDX samples were observed to contain acetone (m/z 59) in the pyrolysis mass spectra, and therefore they were vacuum-dried for one week to eliminate the solvent. Formamide, N,N-dimethylformamide, N-nitrosodimethylamine and dimethylaminoacetonitrile were obtained from Aldrich Chemical Co., Inc., Milwaukee, Wisconsin, and N-methylformamide was obtained from Eastman, Rochester, NY in high purity, and all were used without further purification. Mass spectral analysis of these liquid compounds were obtained by direct vapor sampling.

Acknowledgement

We thank Ms. Linda Jarvis for the preparation and editing of the manuscript.

FIGURE CAPTIONS

1. Pyrolysis-APCI mass spectra of (a) RDX, (b) ^{15}N-RDX, and (c) ^{2}H-RDX. The structure of RDX is shown as an inset in Figure 1a.

2. Pyrolysis-APCI daughter ion mass spectra of (a) m/z 46, RDX, (b) m/z 47, ^{15}N-RDX, (c) m/z 47, ^{2}H-RDX, (d) m/z 46, protonated formamide.

3. Pyrolysis-APCI daughter ion mass spectra of (a) m/z 60, RDX, (b) m/z 61, ^{15}N-RDX, (c) m/z 64, ^{2}H-RDX, (e) m/z 60, protonated N-methylformamide. Figure 3d presents the m/z value for each major, unlabeled RDX daughter ion fragment and its equivalent fragment in the nitrogen (N) and hydrogen (H)-labeled RDX iostope.

4. Pyrolysis-APCI daughter ion mass spectra of (a) m/z 74, RDX, (b) m/z 75, ^{15}N-RDX, (c) m/z 31, ^{2}H-RDX, (e) m/z 74, protonated N,N-dimethylformamide. Refer to Fig. 3d for explanation of Fig. 4d. (*) unclear m/z assignment.

5. Pyrolysis-APCI daughter ion mass spectra of (a) m/z 75, RDX, (b) m/z 77, ^{15}N-RDX, (d) m/z 75, protonated N-nitrosodimethylamine. Refer to Fig. 3d for explanation of Fig. 5c.

6. Pyrolysis-APCI daughter ion mass spectra of (a) m/z 85, RDX, (b) m/z 87, ^{15}N-RDX, (c) m/z 93, ^{2}H-RDX, (e) m/z 85, protonated dimethylaminoacetonitrile. Refer to Fig. 3d for explanation of Fig. 6d.

7. Pyrolysis-APCI daughter ion mass spectra of (a) m/z 98, RDX, (b) m/z 101, ^{15}N-RDX, (c) m/z 101, ^{2}H-RDX. Refer to

Fig. 3d for explanation of Fig. 7d. (e),(f), possible structures for m/z 98, RDX.

TABLE 1.

PRIMARY PY-APCI MASS SPECTRAL FEATURES FOR RDX AND CORRESPONDING SIGNATURES FOR THE ^{15}N- and ^{2}H-RDX ISOTOPES (SEE FIGURE 1).

RDX Isotope	m/z					
^{14}N, ^{1}H	46	60	74	75	85	98
^{15}N, ^{1}H	47	61	75	77	87	101
^{14}N, ^{2}H	47	64	81	81	93	101

TABLE 2.

DETERMINATION OF THE MOLECULAR FORMULA FOR EACH MOLECULAR ION IN THE RDX PY-APCI MASS SPECTRUM (FIGURE 1a)

m/z	working formula[a]	protonated working formula[b]	molecular formula[c]
46	C_nHNO_x	$C_nH_2NO_x$	$[CH_3NO]H^+$
60	$C_nH_4NO_x$	$C_nH_5NO_x$	$[C_2H_5NO]H^+$
74	$C_nH_7NO_x$	$C_nH_8NO_x$	$[C_3H_7NO]H^+$
75	$C_nH_6N_2O_x$	$C_nH_7N_2O_x$	$[C_2H_6N_2O]H^+$
85	$C_nH_8N_2O_x$	$C_nH_9N_2O_x$	$[C_4H_8N_2]H^+$
98	$C_nH_3N_3O_x$	$C_nH_4N_3O_x$	$[C_3H_3N_3O]H^+$

[a]Derived from the isotope analysis in Table 1. The n and x subscripts are not necessarily the same values for each m/z.

[b]Protonated form of the working (isotope-derived) formula.

[c]Molecular formulae were derived by matching the protonated formula with each respective list of possible CHNO molecular formulae for a given m/z in reference 9.

REFERENCES

1. R.A. Fifer, in Fundamentals of Solid Propellant Combustion, Vol. 90, Progress in Astronautics and Aeronautics Series, ed. by K.K. Kuo and M. Summerfield, pp. 201-237, American Institute of Aeronautics and Astronautics, Inc., New York (1984).

2. S.A. Liebman, P.J. Duff, K.D. Fickie, M.A. Schroeder and R.A. Fifer, J. Hazardous Materials 13, 37 (1986).

3. S.A. Liebman, A.P. Snyder, J.H. Kremer, D.J. Reutter, M.A. Schroeder and R.A. Fifer, J. Anal. Appl. Pyrolysis 12, 83 (1987).

4. S.A. Liebman and T.P. Wampler, in Pyrolysis and GC in Polymer Analysis, E.J. Levy and S.A. Liebman, eds., Chapter 3, Marcel Dekker, New York (1985).

5. H.-R. Schulten and W.D. Lehmann, Anal. Chim. Acta 93, 19 (1977).

6. J. Yinon, D.J. Harvan and J.R. Hass, Org. Mass Spectrom. 17, 321 (1982).

7. J. Yinon, Mass Spectrom. Rev. 1, 257 (1982).

8. S. Bulusu and T. Axenrod, Org. Mass Spectrom. 14, 585 (1979).

9. J. Yinon, Biomed. Mass Spectrom, 1, 393 (1974).

10. J. Stahls, J. Chem. Soc., Faraday Trans. Part 1, 67, 1768 (1971).

11. P. Vouros, B.A. Petersen, L. Colwell, B.L. Karger and H. Harris, Anal. Chem. 49, 1039 (1977).

12. M.A. Schroeder, Report No. AD-A159325, Ballistic Research Laboratory, Aberdeen Proving Ground, Maryland (1985).

13. R.M. Silverstein, G.C. Bassler and T.C. Morrill. Spectrometric Identification of Organic Compounds, John Wiley and Sons, New York (1974).

14. G.E. Spangler, J.P. Carrico and S.H. Kim, in Proceedings of the International Symposium on the Analysis and Detection of Explosives, pp. 267-282, FBI Academy, Quantico, Virginia (1983).

15. M.A. Schroeder, Report No. AD-A160543, Ballistic Research Laboratory, Aberdeen Proving Ground, Maryland (1985).

16. M.A. Schroeder, in Proc. 15th Joint Army-Navy-NASA-Air Force (JANNAF) Combustion Mtg, Vol II, pp. 17-34, Chemical Propulsion Information Agency (CPIA) Pub. No. 308, Rhode Island (1979).

17. M.A. Schroeder, in Proc. 21st JANNAF Combustion Mtg, Vol. II, pp. 595-614, CPIA Pub. 412, Rhode Island (1984).

18. J.N. Bradley, A.K. Butler, W.D. Capey and J.R. Gilbert, J. Chem. Soc., Faraday Trans., Part 1, 73, 1789 (1977).

19. B.B. Goshgarian, Report No. AD-BO32275L, Air Force Rocket Propulsion Laboratory, Edwards Air Force Base, California (1978).

20. M. Farber and R.D. Srivastava, Chem. Phys. Lett. 64, 307 (1979).

21. S. Bulusu, Org. Mass. Spectrom. 3, 13 (1970).

22. R. Behrens, Jr., in Proc. 23rd JANNAF Combustion Mtg., Vol. I, pp. 231-239, CPIA Pub. No. 457, Rhode Island (1986).

23. S. Zitrin and J. Yinon, Adv. Mass. Spectrom. Biochem. Med. 1, 369 (1976).

24. C.T. Pate and M.H. Mach, Int. J. Mass Spectrom. Ion Phys. 26, 267 (1978).

25. R.G. Gillis, M.J. Lacey and J.S. Shannon, Org. Mass Spectrom. 9, 359 (1974).

26. S. Zitrin, Org. Mass Spectrom. 17, 74 (1982).

27. X. Zhao, E.J. Hintsa and Y.T. Lee, J. Chem. Phys. 88, 801 (1988).

28. P.H. Dawson, J.B. French, J.A. Buckley, D.J. Douglas and D. Simmons, Org. Mass Spectrom. 17, 205 (1982).

29. P.H. Dawson, J.B. French, J.A. Buckley, D.J. Douglas and D. Simmons, ibid, p. 212.

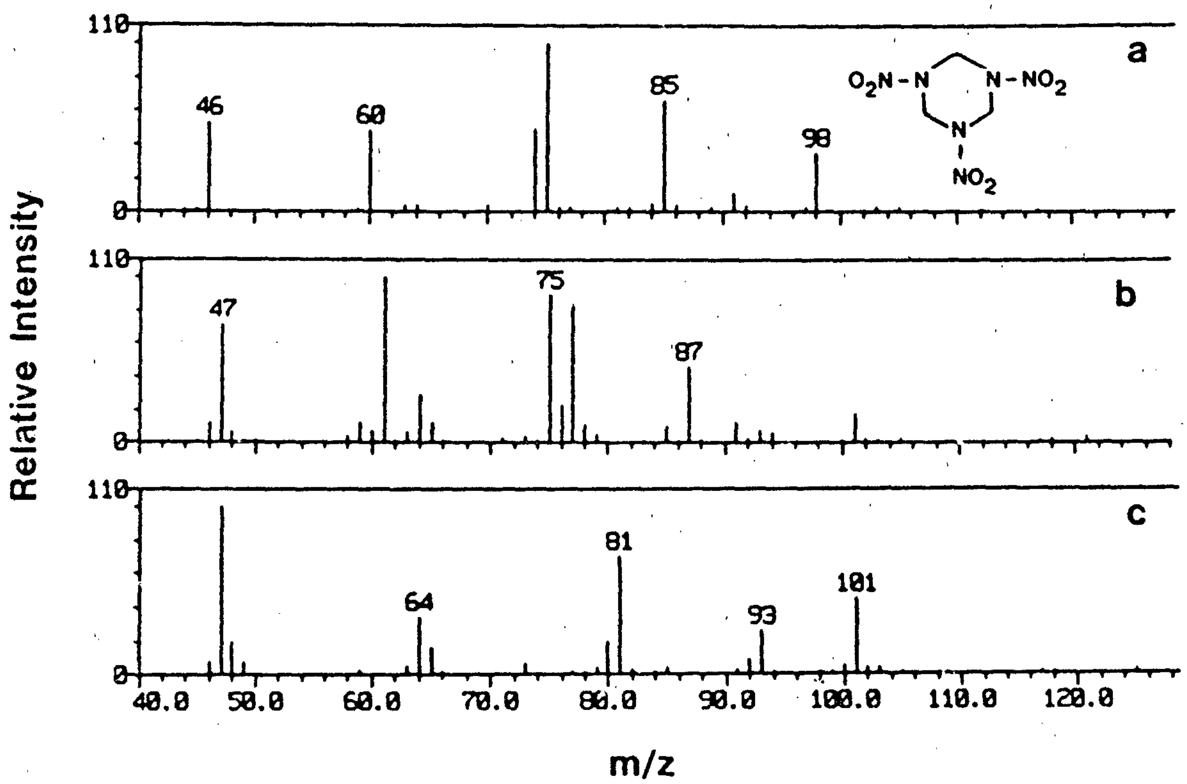

110
0
a
46
60
85
98
O_2N-N N-NO_2 N NO_2
b
47
75
87
c
64
81
93
101
40.0
50.0
60.0
70.0
80.0
90.0
100.0
110.0
120.0
Relative Intensity
m/z

FIG. 1

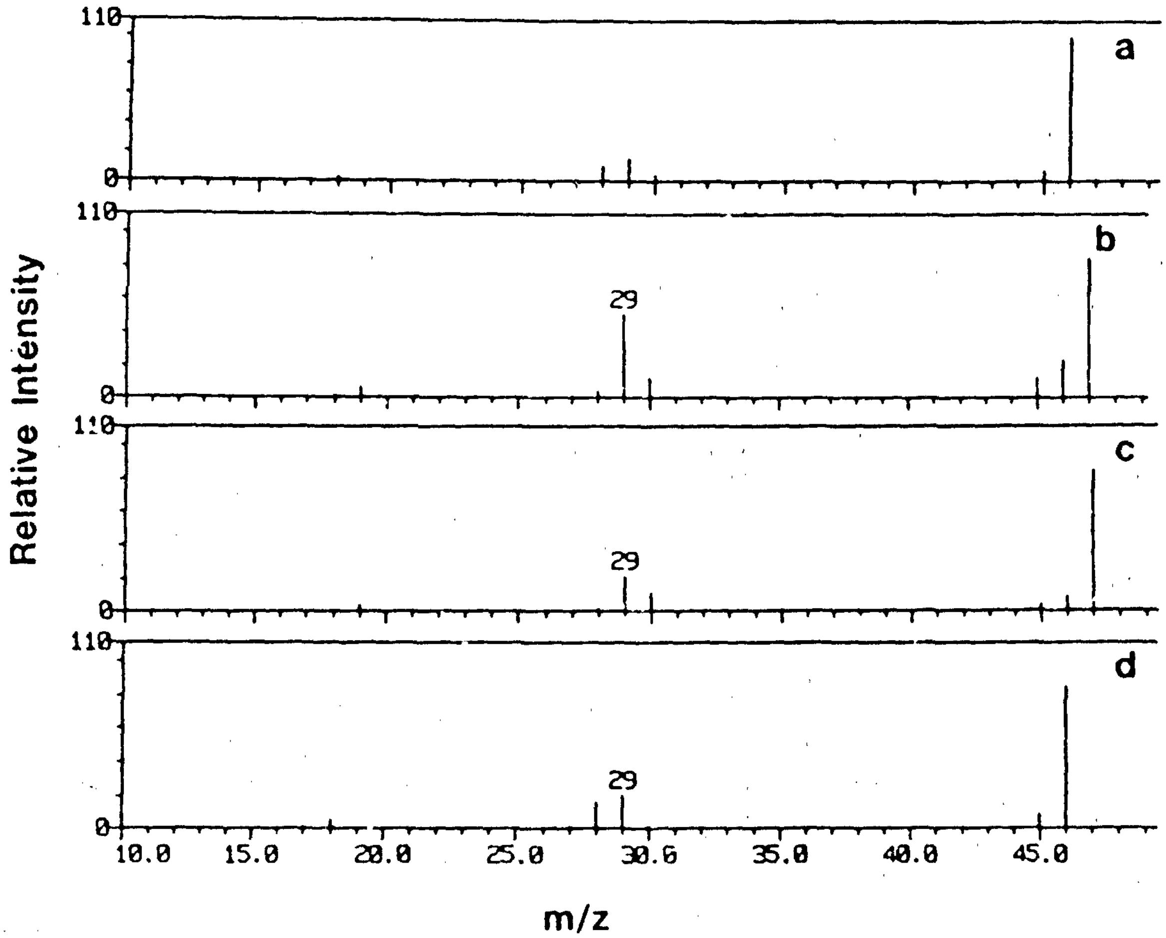
110
0
a
b
c
d
29
Relative Intensity
10.0
15.0
20.0
25.0
30.0
35.0
40.0
45.0
m/z

FIG. 2

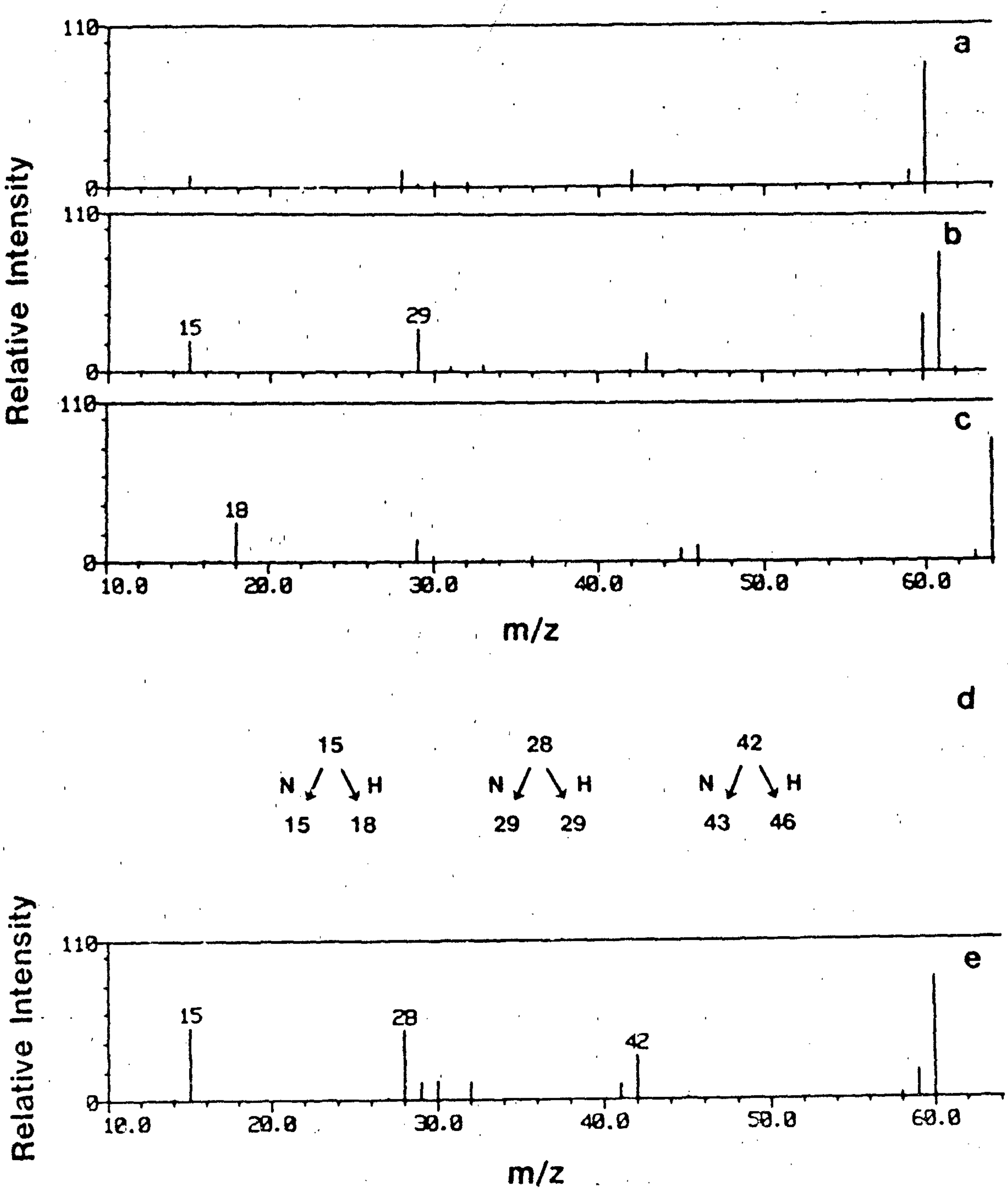
110
0
a
b
c
15
29
18
Relative Intensity
10.0
20.0
30.0
40.0
50.0
60.0
m/z
d
15
N
H
15
18
28
N
H
29
29
42
N
H
43
46
e
15
28
42
Relative Intensity
m/z

FIG 3

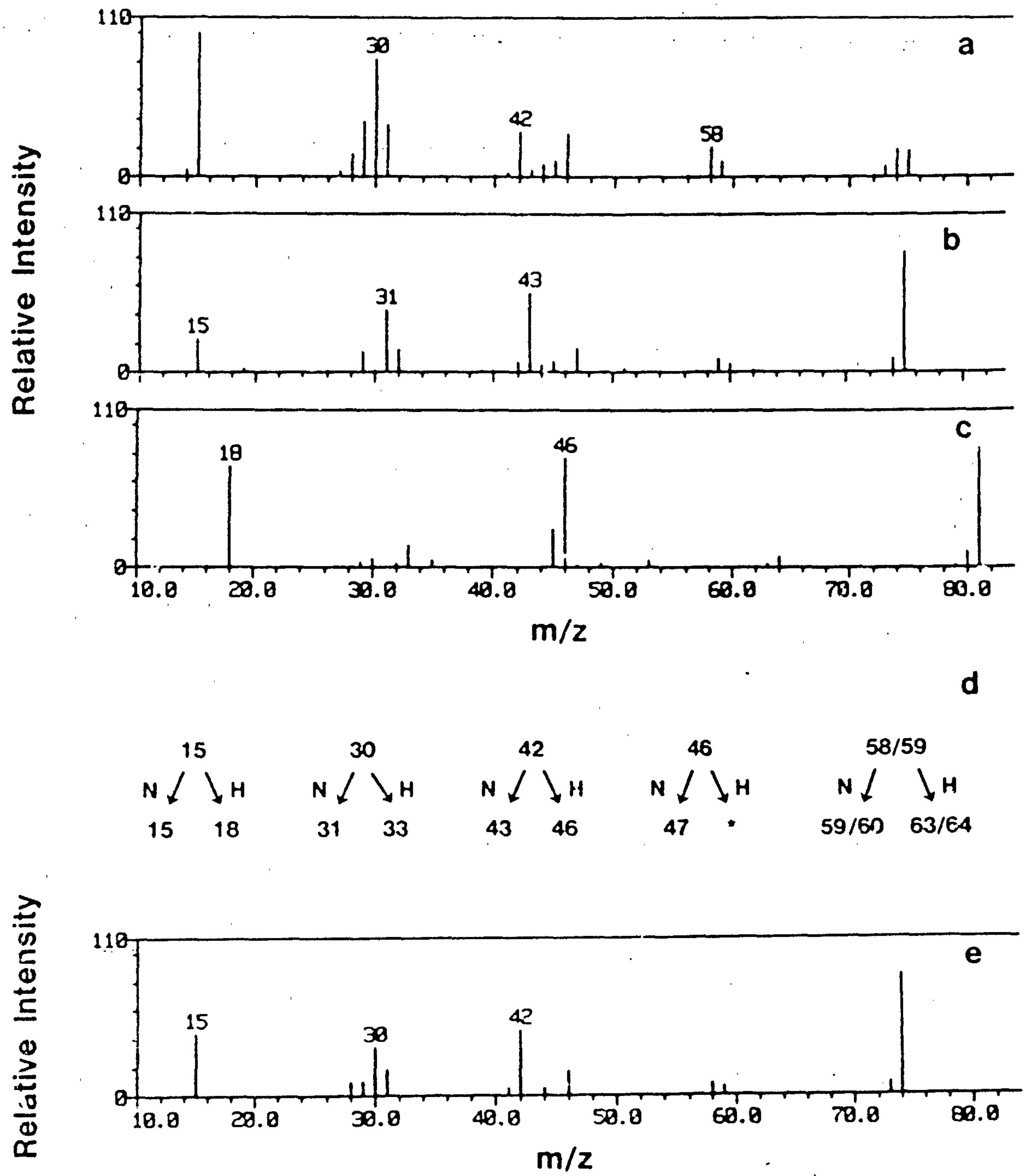
Relative Intensity
110
0
30
42
58
a
b
15
31
43
c
18
46
10.0
20.0
30.0
40.0
50.0
60.0
70.0
80.0
m/z
d
15
N
H
18
30
31
33
42
43
46
47
*
58/59
59/60
63/64
e

FIG. 4

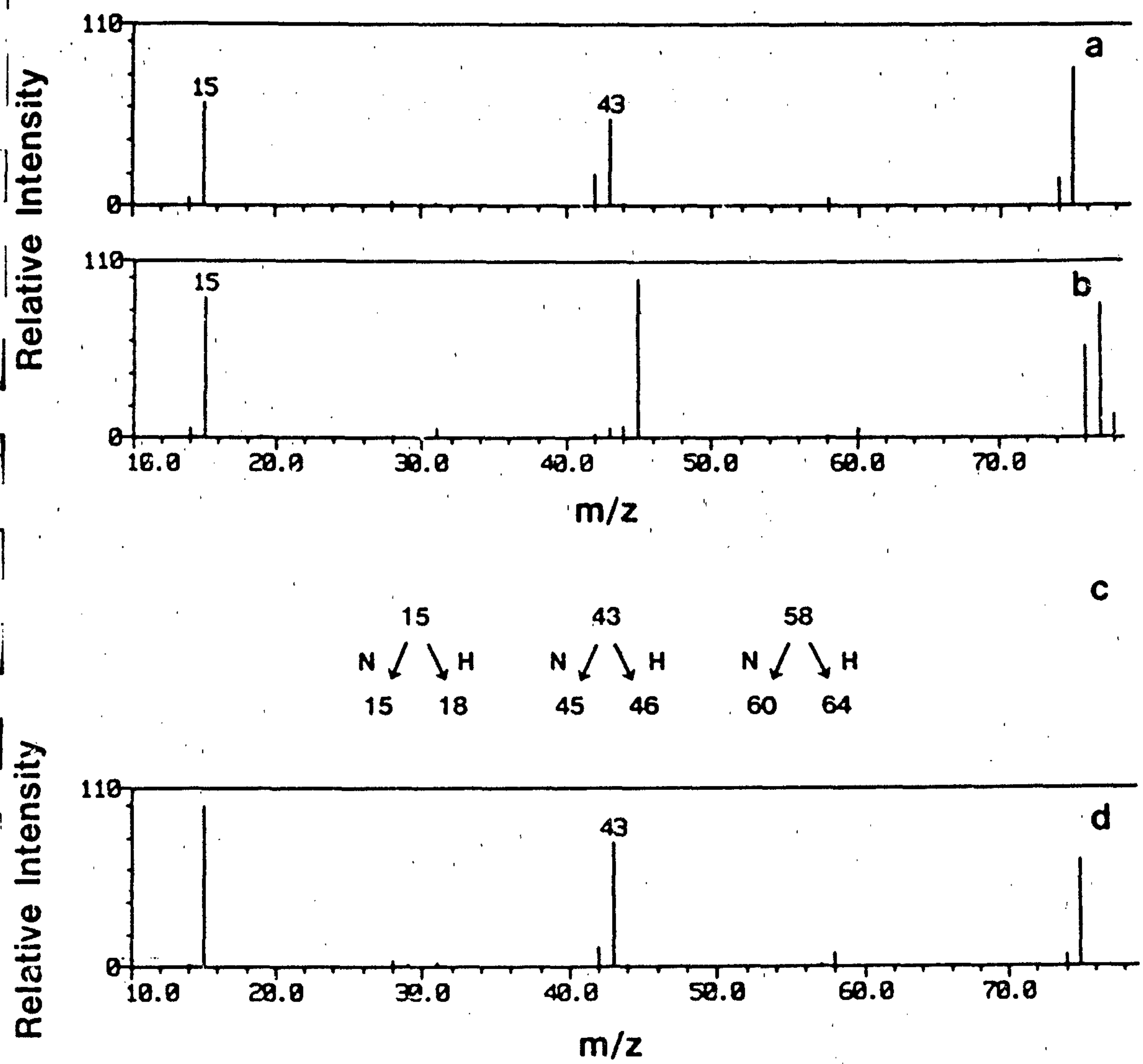

Relative Intensity
110
0
15
43
a
b
10.0
20.0
30.0
40.0
50.0
60.0
70.0
m/z
c
15
N
H
15
18
43
N
H
45
46
58
N
H
60
64
Relative Intensity
110
0
43
d
10.0
20.0
30.0
40.0
50.0
60.0
70.0
m/z

FIG 5

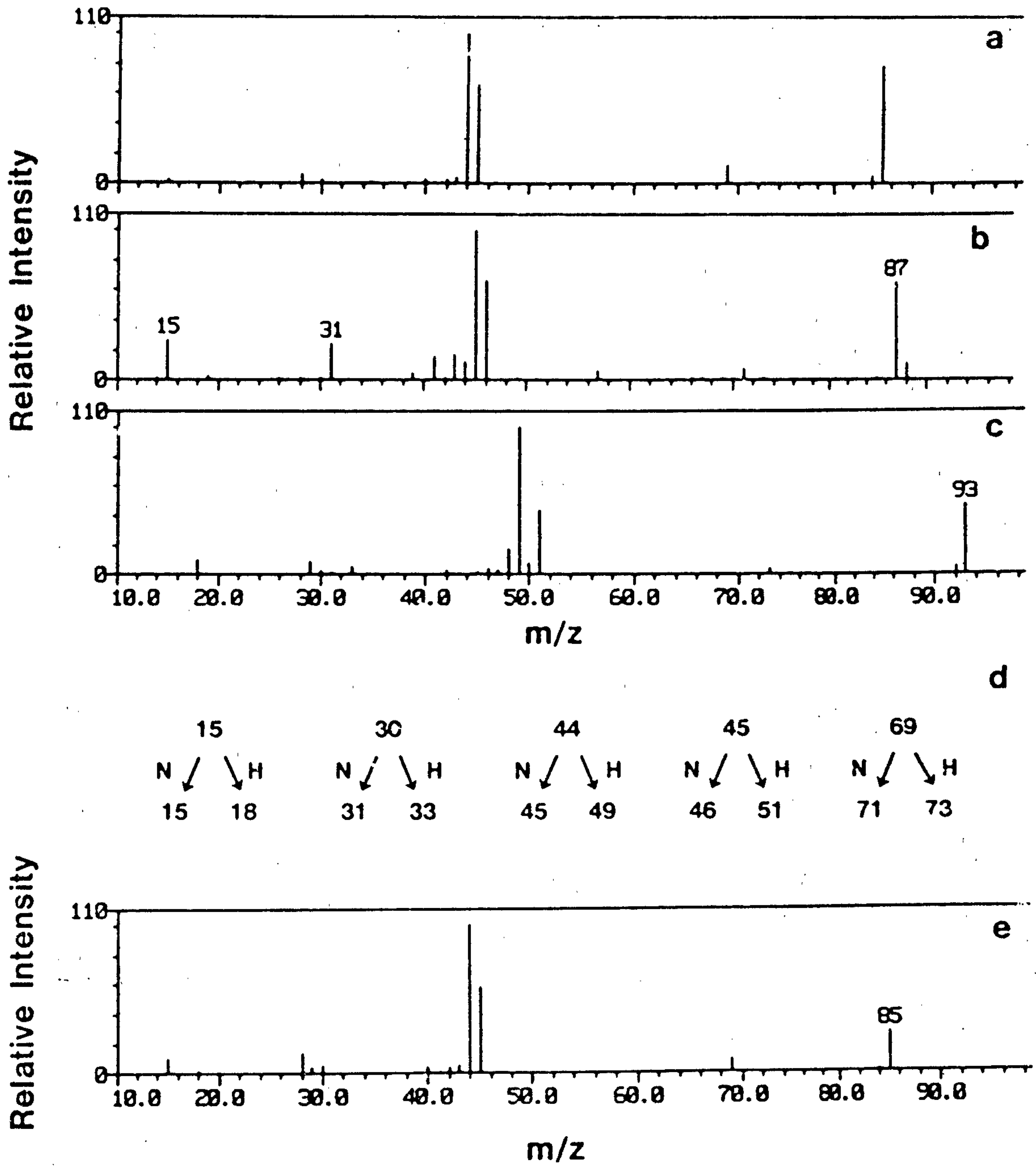

110
0
a
b
15
31
87
c
93
Relative Intensity
10.0
20.0
30.0
40.0
50.0
60.0
70.0
80.0
90.0
m/z
d
15
N H
15 18
30
N H
31 33
44
N H
45 49
45
N H
46 51
69
N H
71 73
e
85

FIG 6

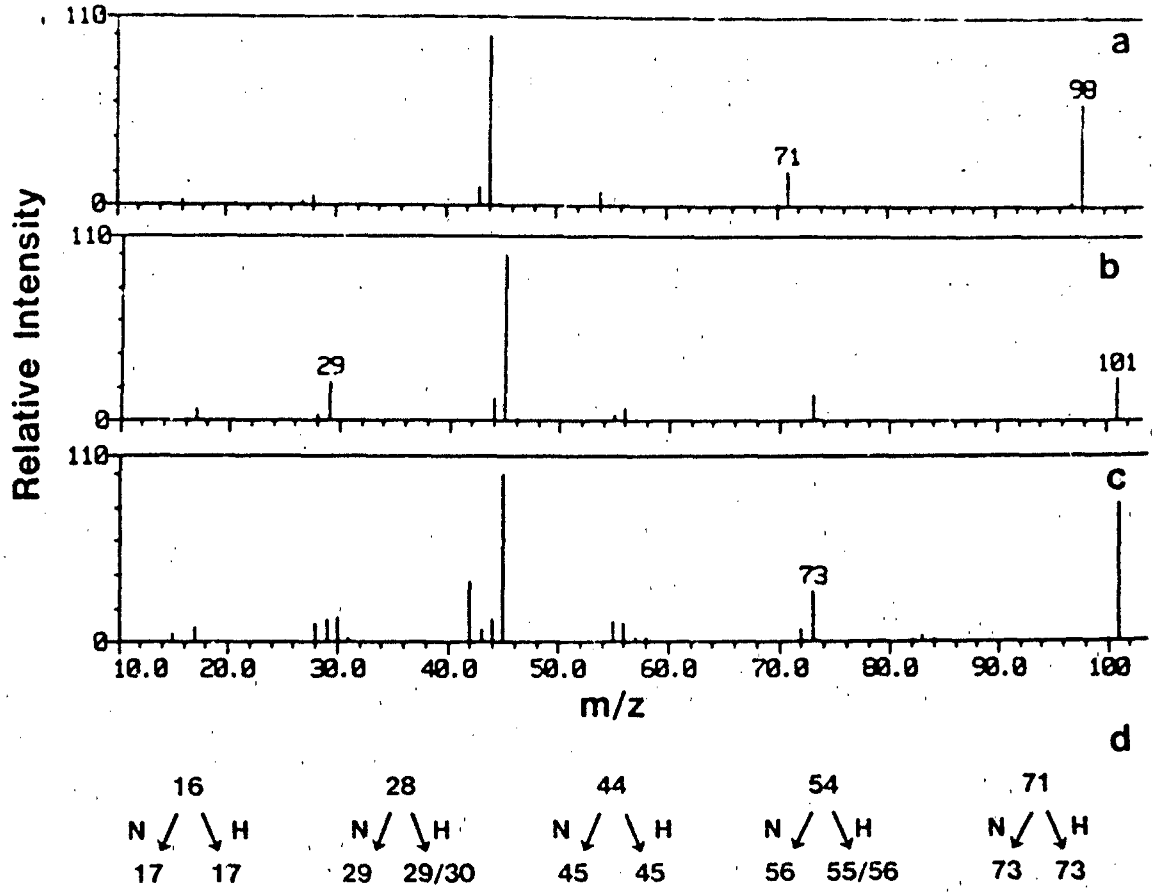

Relative Intensity
110
0
a
98
71
b
29
101
c
73
10.0
20.0
30.0
40.0
50.0
60.0
70.0
80.0
90.0
100
m/z
d
16
N H
17 17
28
N H
29 29/30
44
N H
45 45
54
N H
56 55/56
71
N H
73 73

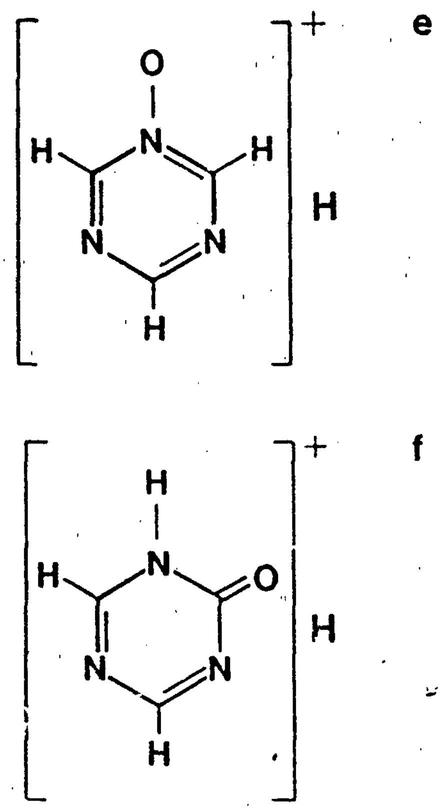

e
+
O
N
H
H
N
N
H
H
f
+
H
N
H
O
N
N
H
H

FIG. 7

PAPER FOR SUBMISSION TO J. ANALYTICAL AND APPLIED PYROLYSIS
PRESENTED IN PART AT FACSS MTG., ST. LOUIS

TIME-RESOLVED ANALYTICAL PYROLYSIS STUDIES OF NITRAMINE DECOMPOSITION WITH A TRIPLE QUADRUPOLE MS/MS SYSTEM

S.A. Liebman, GEO-CENTERS, INC., U.S. Army Chemical Research, Development and Engineering Center, Aberdeen Proving Ground, Maryland 21010-5423
A.P. Snyder, J.H. Kremer, D.J. Reutter, U.S. Army Chemical Research, Development and Engineering Center, Aberdeen Proving Ground, Maryland 21010-5423
M. Schroeder, R.A. Fiter, Ballistic Research Laboratory, Aberdeen Proving Ground, Maryland 21010-5423

SUMMARY

An energetic nitramine, RDX, has been studied over selected thermal ranges and environments with a pyrolysis unit interfaced to an atmospheric pressure chemical ionization (APCI) tandem mass spectrometer (MS/MS) system. Programmed and pulsed thermolytic degradation conditions under oxidative and non-oxidative atmospheres resulted in complex product distributions. Use of selected boron-containing compounds gave evidence of catalytic activity in the RDX degradation. Identification by daughter-ion MS/MS analysis was attempted for key volatiles of m/z 46, 60, 74, 75, 85, 97, 98, and 103. An integrated thermal degradation profile of RDX was thus probed by monitoring the volatile products as they were generated during slow programmed heating (60°C/min) from ambient to temperatures near the RDX melting/decomposition region (190-220°C). Implications of enhanced nitramine performance are suggested.

INTRODUCTION

Extensive literature is available for the study of nitramine degradation (1,2), and in particular, RDX (cyclotrimethylenetrinitramine) (3,4). However, the early experimental work was conducted under a multiplicity of conditions that make it difficult to delineate the fundamental stages in nitramine degradation. The present work was focused on careful thermal processing of small amounts (mg) of RDX under a wide range of heating rates, final temperatures, dynamic/static atmospheres, and in the presence/absence of potential catalysts. The use of analytical pyrolysis has developed extensively over the past two decades (5) with time-resolved analyses being reported using on-line gas chromatography (GC), Fourier Transform Infrared (FTIR) and Mass Spectral systems. Real-time monitoring by the APCI MS/MS system permitted sensitive detection and, in several cases, distinct identification of the volatile species.

A majority of studies have shown that RDX thermally decomposes to give NO_2, formaldehyde, CO_2, N_2O, and several postulated ring-scission fragments, none of which have been satisfactorily identified. Whether the initial step is an $N-NO_2$ bond scission (leading to NO_2) or C-N bond cleavage (leading to CH_2O and N_2O) has not been determined. ESR studies by Beyer et al. (6a) and recent experiments at the Naval Research Laboratory have produced evidence (6b-d) showing that definite free radicals were produced in early thermal decomposition, one of which was consistent with a spectrum of NO_2. Other ESR patterns with complex hyperfine structure were also produced both in solution and solid state decomposition treatments.

EXPERIMENTAL

A. Samples of RDX were obtained by recrystallization from acetone, vacuum dried, and were ground to a fine powder (unsieved) of ca. 100 mesh. Boron-containing compounds were supplied from proprietary sources, Ta_2O_5 from Aldrich Chemical Company, and TaH_2 from private sources. Mixtures were 75% RDX physically mixed with 25% additive. All runs used ca. 1-2 mg powdered sample placed in the quartz tube of the Pyroprobe in the usual manner.

B. Thermal processing of samples was conducted with a Pyroprobe® Model 122 (Chemical Data Systems, Oxford, PA). Many series of pulse pyrolyses were conducted, at the fastest risetime (75 °C/ms) to varied final temperatures (from 200 °C at several intervals to 1000 °C). Programmed pyrolyses were conducted at controlled ramp rates of 60, 120, or 300 °C/min to varied final temperatures in the above range. The most informative rate, 60 °C/min, was used to compare product distributions under air or N_2 atmospheres with varied additives.

Interfacing the Pyroprobe to the MS/MS system was accomplished by inserting the Pyroprobe Pt coil probe into a glass tube fitted with positioning rings to ensure a uniform gas flow over the sample region during thermal treatments. The end of the Pyroprobe coil was positioned within the glass tube such that the end of the coil was about 1.0 cm from the corona discharge needle tip in the MS inlet. Figure 1 shows a schematic of the sample probe and its relative position in the ion source.

C. A Sciex TAGA(TM) 6000 APCI triple quadrupole MS/MS system was operated in the MS mode for total and selected ion monitoring (7). Basic references for the instrumentation and methods are noted elsewhere (8, 9). Additionally, important selected parent ions generated in the thermal processing stage were selected for Ar collision-induced-dissociation (CID) and examination was made of the daughter-ion spectra for structural information. A complete description of the TAGA® operating conditions will be published elsewhere (10).

Each series of data were preceded by a reference run of RDX to verify full instrumental reproducibility limits.

RESULTS AND DISCUSSION

RDX Thermolysis

Based on numerous runs under the experimental conditions noted to be important from an earlier Box-Behnken experimental design (11), the threshold temperature region for programmed thermolysis was chosen as 250^{o}C. The most informative rate was determined to be 60^{o}C/min. and both inert (N_2) and oxidative (air) atmospheres were used in the study. Holding the sample at the 250^{o}C final temperature for one minute was also a selected parameter for the series based on comparative runs.

Figure 2 shows the time-resolved analytical pyrolysis results from thermally processing RDX under air at 60^{o}C/min to 250^{o}C with a one minute hold. Volatile products detected under these conditions are found at m/z 44, 46, 60, 74, 75, 82, 85, and 98 (Figure 2). The earliest detected feature, 46 is noted along with m/z 98 (both slightly under 8.0 minutes). Peaks at 60, 74, 75, and 85 are detected in significant amounts just after 8.2 minutes, while only small levels of 44 and 82 are seen.

Figure 3 shows the generation and decay profiles of these selected species when the programmed thermal treatment was conducted under N_2. A slight delay in appearance of m/z 46 was noted (ca. 8.2 min compared to ca. 7.8 min under air), as well as a steeper initial rate of evolution. Both atmospheres produced a similar rate of decay. Hence, a slight overall delay in volatile product evolution was noted under the inert atmosphere relative to the oxidative one. This is further supported by a comparison of the times for the total ion maxima; 9.2 min for N_2, and 8.7 under air (Figure 4).

RDX Thermolysis with Borohydride Additives:

The influence of added borohydride ("B Catalyst") on RDX thermolysis is also shown in Figures 2-4. Evolution of m/z 46 (NO_2) is not kinetically and/or thermodynamically favorable in the presence of B catalyst, relative to the amount detected with RDX alone under the same experimental conditions (Figure 2). The amount of m/z 44 is somewhat increased, m/z 60 decreased, and m/z 74 is essentially unaffected by the presence of borohydride additive.

Furthermore, m/z 75 and 85 are generated in a similar, rapid manner under programmed pyrolysis in both uncatalyzed and borohydride-catalyzed situations. However, a major change on the evolution of mass 98 is detected when B catalyst is present (Figure 2). The ring-intact amine oxide, identified by its MS/MS daughter-ion spectrum (Figure 5) is detected as one of the first and major volatile thermal fragments in uncatalyzed RDX decomposition; however, it is low in abundance when B catalyst is present. Figure 4 shows the total ion current (TIC) recorded of RDX alone and with borohydride (under N_2). The latter shows a significant earlier time to maximum ion current (9.2 min to 8.2 min).

Thus, under programmed oxidative pyrolysis (6^{0}/min to 250^{0}C, 1 min hold), the absence of both NO_2 and the ring-intact m/z 98, when the borohydride additive is mixed with RDX, are important experimental observations toward understanding its thermal degradation mechanism.

To ensure that a true catalytic effect was being monitored rather than an artifact of the experimental processes, identical runs were conducted with non-boron inorganic additives. Both selected and total ion monitoring were recorded as above. Figure 6 shows the total ion current recorded for the TaH_2 and Ta_2O_5 additives, respectively, in these runs. Likewise, Ta_2O_5 presence showed only minor variations relative to that observed with RDX itself or with the TaH_2 additive. A duplicate TaH_2 run is shown for comparison.

These data confirm that physical processes such as thermal transport and dilution effects are not dominant in these RDX decompositions. Rather, the borohydride additive shows genuine chemical interactions that change the kinetics and mechanism of RDX thermal decomposition. The nature of these changes is similar to those produced when RDX is subjected to a higher final temperature and faster heating rates. Figure 7 shows the comparison of SIM profiles for RDX heated at m/z 60^{0}C/min to 360^{0}C with and without the B catalyst, with SIM for 75, 82, 85, 98 shown for reference when programmed to 250^{0}C. Hence, catalytic activity is evidenced by a higher "effective" temperature when by RDX is thermally processed with B catalyst.

Volatile Product Identification

As noted above, the key set of volatile products from RDX thermolysis was characterized by examination of their daughter-ion spectra. Figure 5 shows the recorded MS/MS of key RDX volatiles patterns. Final confirmations are in progress for m/z 60, 75, and 85 identifications while the interpretation of the CID fragmentation pattern of the m/z 98 product appears to be the triazine oxide, $C_3H_3N_3O$. Additionally, GC-FTIR data obtained in earlier studies support the triazine oxide structure (12). Interpretation of the daughter-ion spectra of the other key volatile products of RDX decomposition is in progress. A more definitive characterization of the full thermal decomposition of RDX will be reported elsewhere (10).

CONCLUSIONS

These experimental studies with an integrated analytical pyrolysis APCI MS/MS system have permitted a unique opportunity to monitor the detailed thermal degradation of RDX. The results may be interpreted towards better understanding the complex chemical interactions in the early stages of RDX thermolysis (11). An understanding of the role of the physical state(s) (solid, melt, vapor) involved in the thermal region near the RDX melting point of 205°C has not been attempted in these studies. However, use of controlled thermal programming at a relatively slow (60°C/min) rate resulted in a time-resolved analysis of some of the major initial volatile thermal fragments evolved under oxidative and nonoxidative conditions. The role of borohydride additives is seen to be significant in the early stages of RDX decomposition and supports earlier work on their effects reported in larger-scale studies (13).

ACKNOWLEDGEMENT

We appreciate the critical comments and suggestions by Dr. R. A. Yost, University of Florida.

REFERENCES

1. R.A. Fifer, "Chemistry of Nitrate Ester and Nitramine Propellants", Chapter 4 in Fundamental of Combustion of Solid Propellants, M. Summerfield and K. Kuo, Eds., Progress in Astronautics and Aeronautics Series, Vol. 90, AIAA, 1984.
2. M.A. Schroeder, 19th JANNAF Combustion Mtg., Greenbelt, MD, CPIA Publ. 366, Vol I, Oct. 1982 and references therein.
3. J. Stals, Rev. Pure Appl. Chem. 20 (1970) 1768.
4. J.N. Bradley, A.K. Butler, W.D. Capey, J.R. Gilbert, JK Chem. Soc. Faraday Trans. 73, (1977), 1789.
5. S.A. Liebman, E.J. Levy, Eds., Pyrolysis and GC in Polymer Analysis, Marcel Dekker, Inc., NY, 1985.
6. (a) C.U. Morgan, R.A. Beyer, Combustion and Flame, 36 (1979) 99 (b) M.D. Pace, J. Energetic Materials, in press, (c) M.D. Pace, B.S. Holmes, J. Magnetic Resonance 52 (1983), 143. (d) M.D. Pace, A.D. Britt, W.B. Monitz, J. Energetic Materials, (1983), 141; 367.
7. Sciex, Inc., Toronto, Canada.
8. H. Kambara, Y. Mitsui, I. Kanomata, Anal. Chem., 51 (1979) 1447.
9. D.I. Carroll, I. Dzidic, E.C. Horning, R.N. Stillwell, Appl. Spectroscopy Revs, 17 (1981) "Atmospheric Pressure Ionization Mass Spectrometry".
10. A.P. Snyder, J.H. Kremer, M.A. Schroeder, R.A. Fifer, S.A. Liebman, Anal. Chem. to be submitted.
11. S.A. Liebman, P.J. Duff, K.D. Fickie, M.S. Schroeder, R.A. Fifer, J. Hazardous Materials, 13 (1986) 51.

12. P.J. Duff, S.A. Liebman, R.A. Fifer, Pittsburgh Conf. Anal. Chem. & Spectros., Atlantic City, NJ 1985.
13. R.A. Fifer, J.E. Cole, "Catalysts for Nitramine Propellants", U.S. Patent 4,379,007.

FIGURE LEGENDS

1. Schematic of the Pyroprobe® - Ion Source of the APCI MS/MS TAGA™ 6000 System.

(a) Pyroprobe

(b) Sample positioned in quartz tube of Coil Pyroprobe (insert)

(c) air/N_2 inlet flow (80 ml/min)

(d) N_2 plenum gas flow inlet (400 ml/min)

(e) static exhaust

(f) interface plate

(g) needle-corona discharge region

2. (a) Time-Resolved Analytical Pyrolysis-APCI MS/MS of RDX under air, 60 °C/min to 250 °C, 1 min hold. M/z 44, 46, 60, 74, 75, 82, 85, 98 are presented in the Selected Ion Monitoring (SIM) mode (b) with Borohydride Additive.

3. Time-Resolved Analytical Pyrolysis-APCI MS/MS of RDX under nitrogen, 60 °C/min to 250 °C, 1 min hold. M/z 46, 60, 74, 75, 82, 85, 98 are presented in the Selected Ion Monitoring (SIM) mode. M/z 75, 82, 85, 98 from RDX under air are shown for comparison.

4. Total Ion Monitoring of RDX alone (N_2) with Borohydride Additive (air). All at 60 °C/min to 250 °C, 1 min hold, except the lower spectrum, run at 60 °C/min to 350 °C, 1 min hold.

5. Positive Ion Daughter Spectra of the Parent m/z 60, 75, 85, and 98 species.

6. Time-Resolved Analytical Pyrolysis-APCI MS/MS of RDX under air with Borohydride Additive, 60 °C/min to 250 °C, 1 min hold. M/z 44, 46, 60, 74, 75, 82, 85, 98 are presented in the Selected Ion Monitoring (SIM) mode.

7. Time-Resolved Analytical Pyrolysis-APCI MS/MS of RDX under air, 60 °C/min to 360 °C, 1 min hold. Comparison (with and without B Additive) of m/z 75, 82, 85 and 98 profiles are shown from programmed runs to 250 °C.

CID FRAGMENTATION SCHEME

Interpretation of Daughter-Ion Spectrum for Mass 98

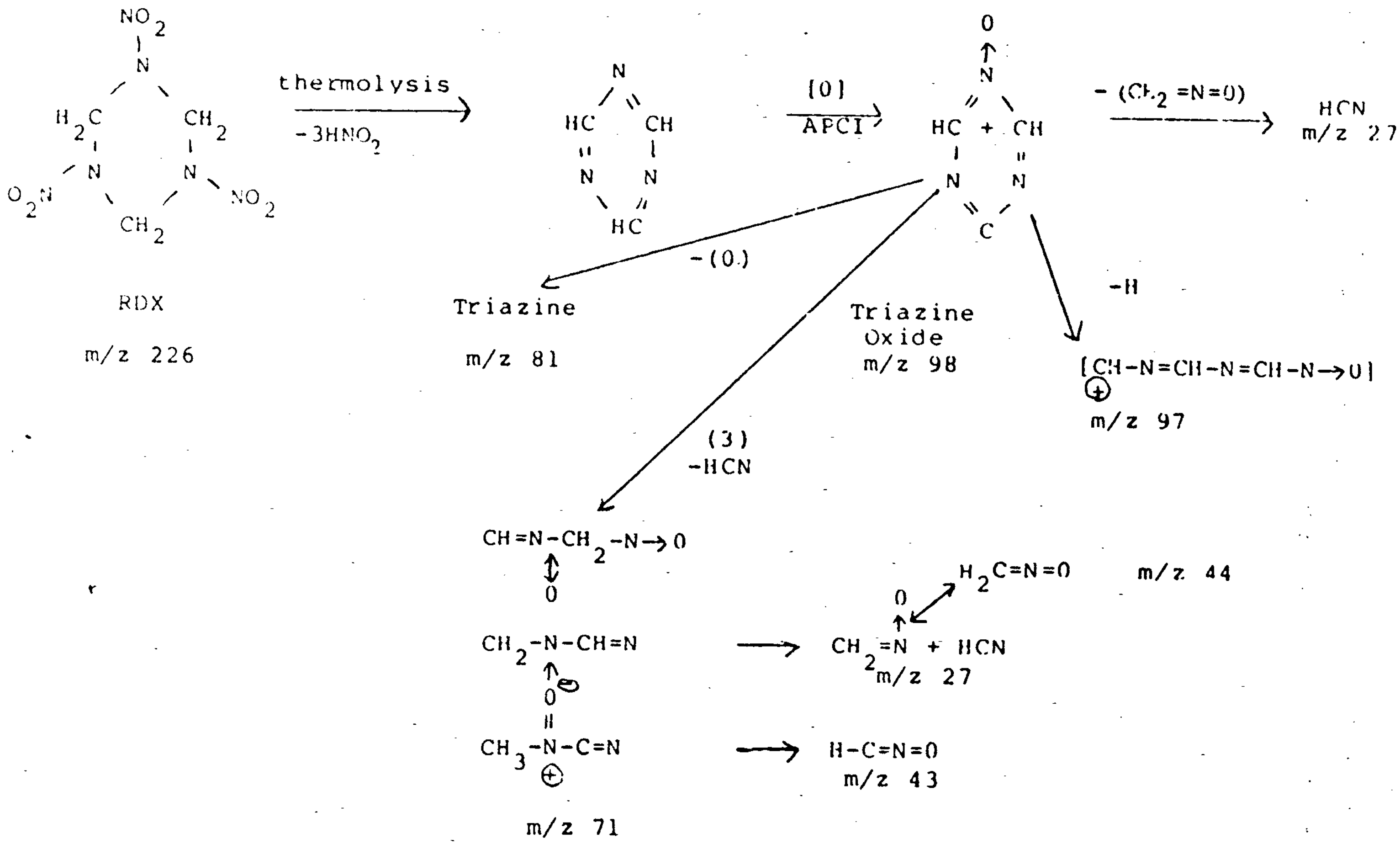

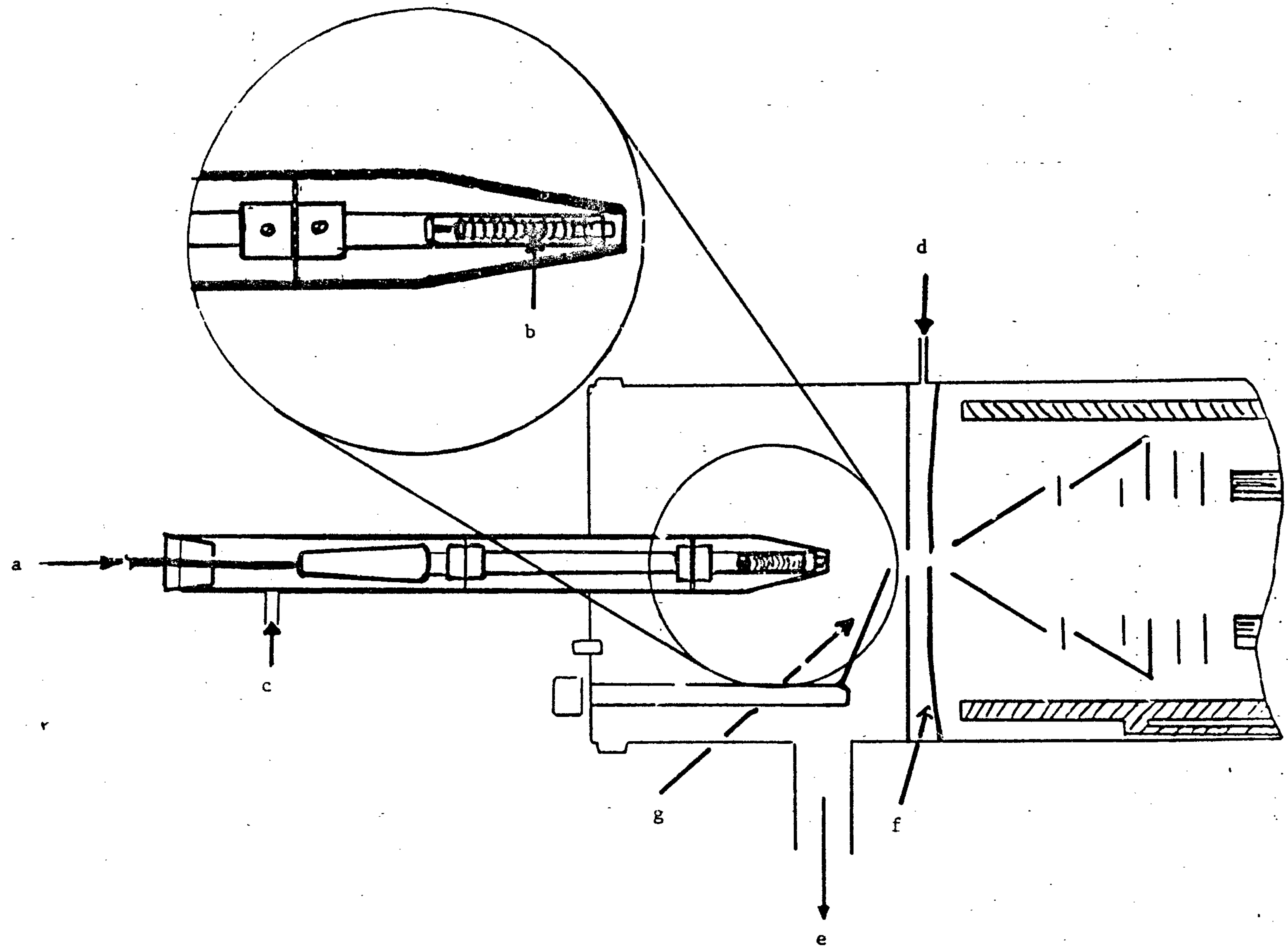

a
b
c
d
e
f
g

TIME-RESOLVED ANALYTICAL PYROLYSIS APCI MS/MS

SELECTED ION MONITORING

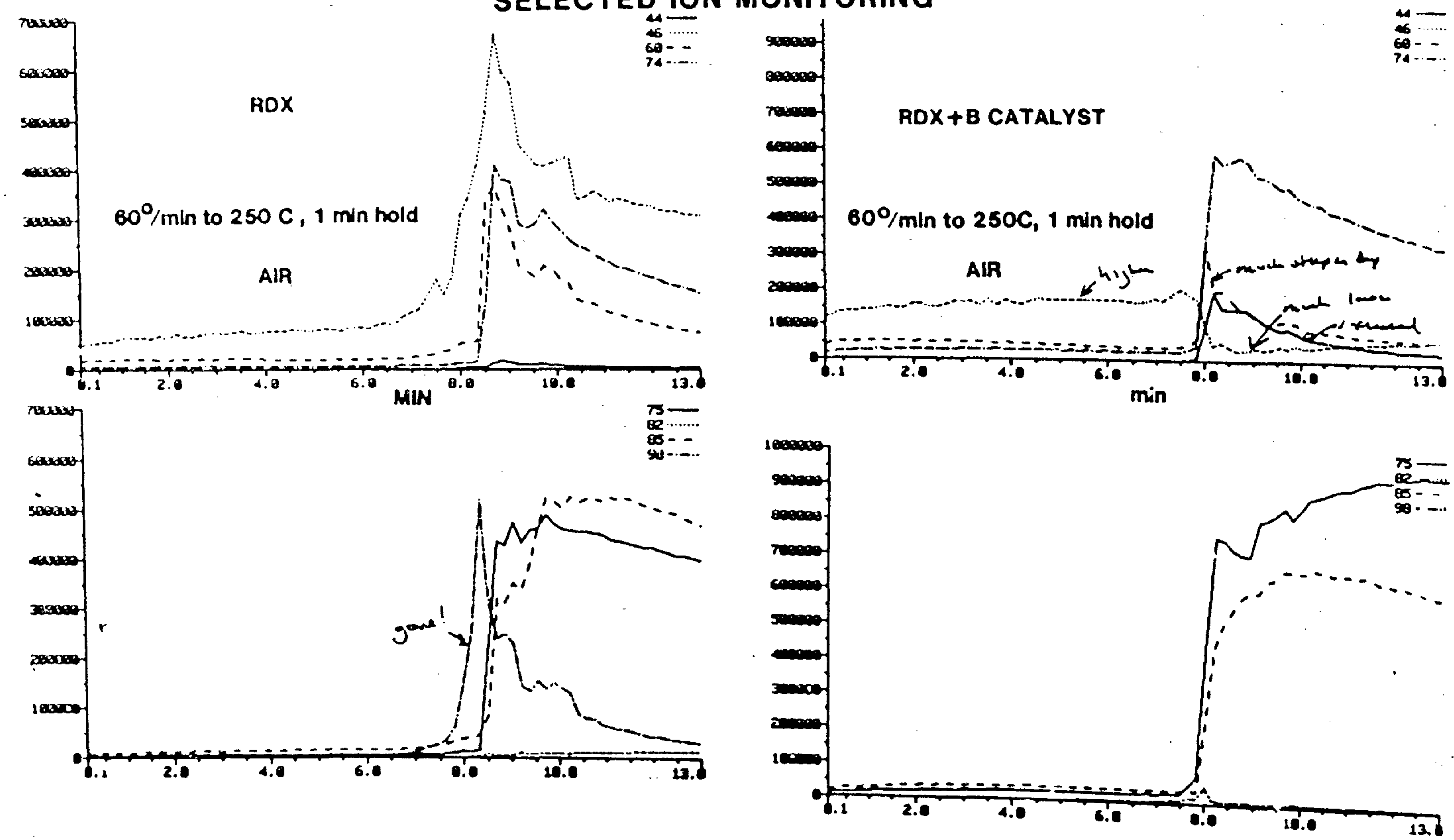

TIME-RESOLVED ANALYTICAL PYROLYSIS APCI MS/MS

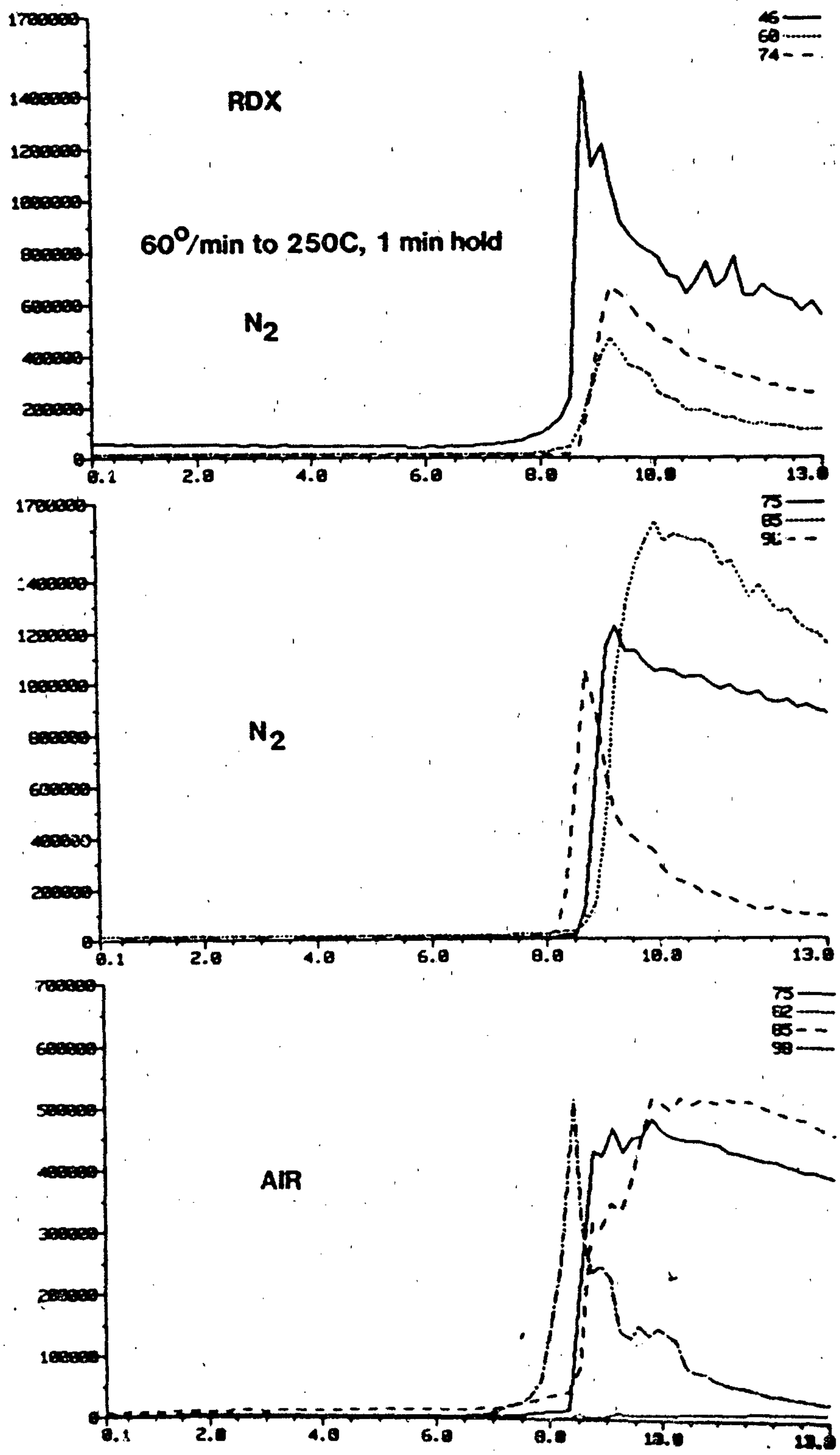

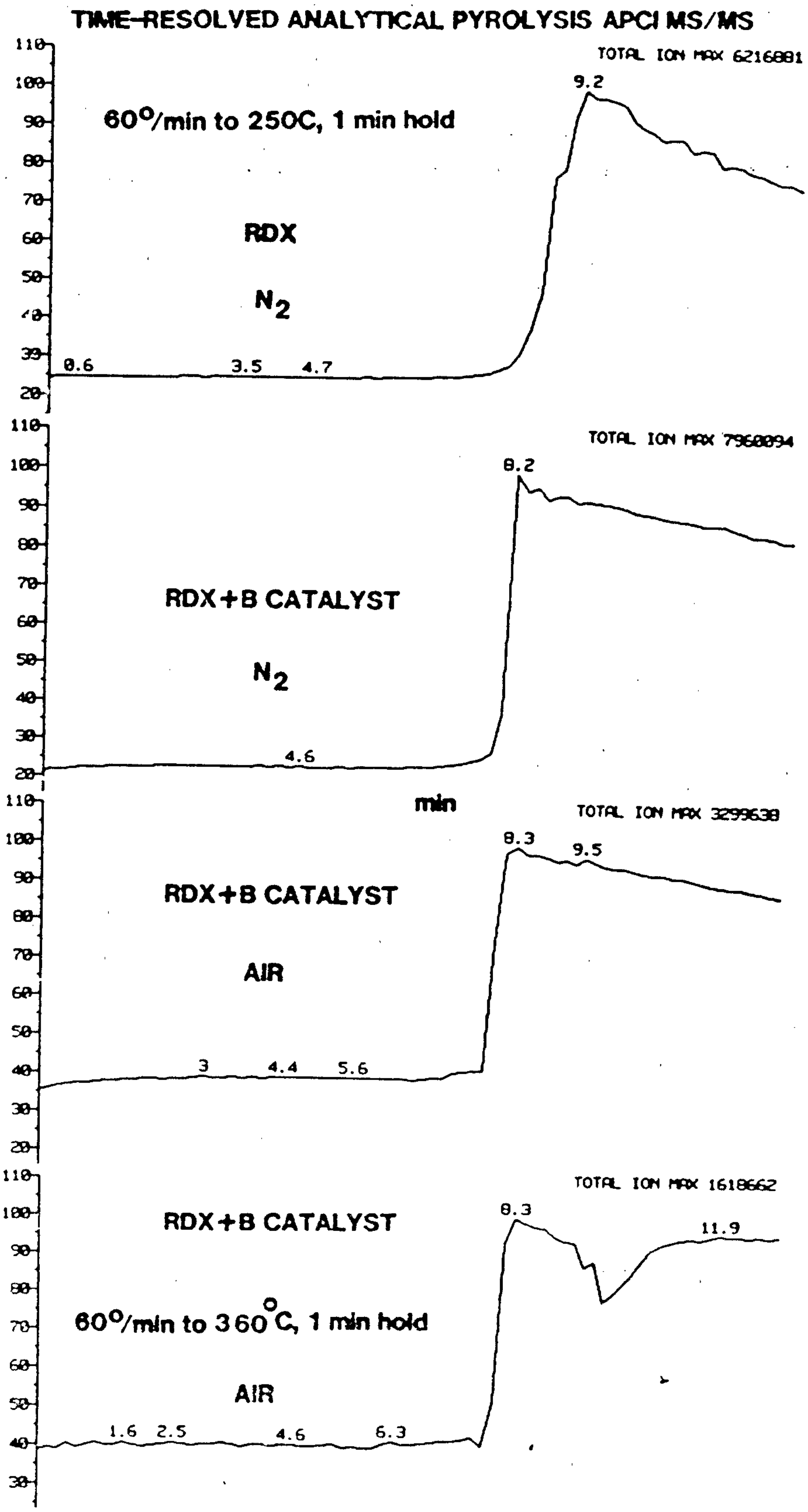
TIME-RESOLVED ANALYTICAL PYROLYSIS APCI MS/MS
TOTAL ION MAX 6216881
60°/min to 250C, 1 min hold
RDX
N2
9.2
0.6
3.5
4.7
TOTAL ION MAX 7960094
RDX+B CATALYST
N2
8.2
4.6
min
TOTAL ION MAX 3299638
RDX+B CATALYST
AIR
8.3
9.5
3
4.4
5.6
TOTAL ION MAX 1618662
RDX+B CATALYST
60°/min to 360°C, 1 min hold
AIR
8.3
11.9
1.6
2.5
4.6
6.3

TRIPLE QUADRUPOLE MS/MS
DAUGHTER-ION SPECTRUM OF PARENT IONS

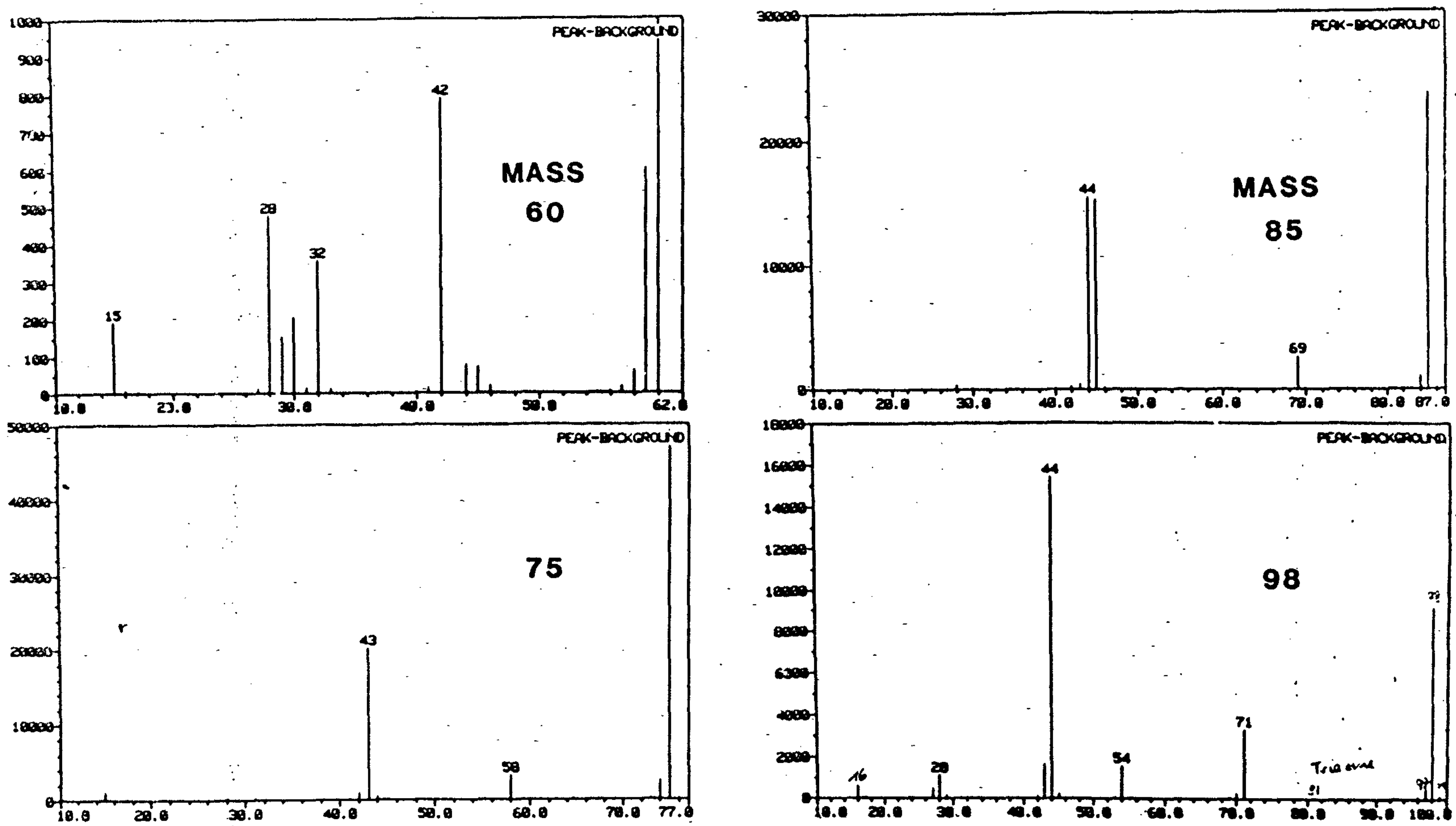

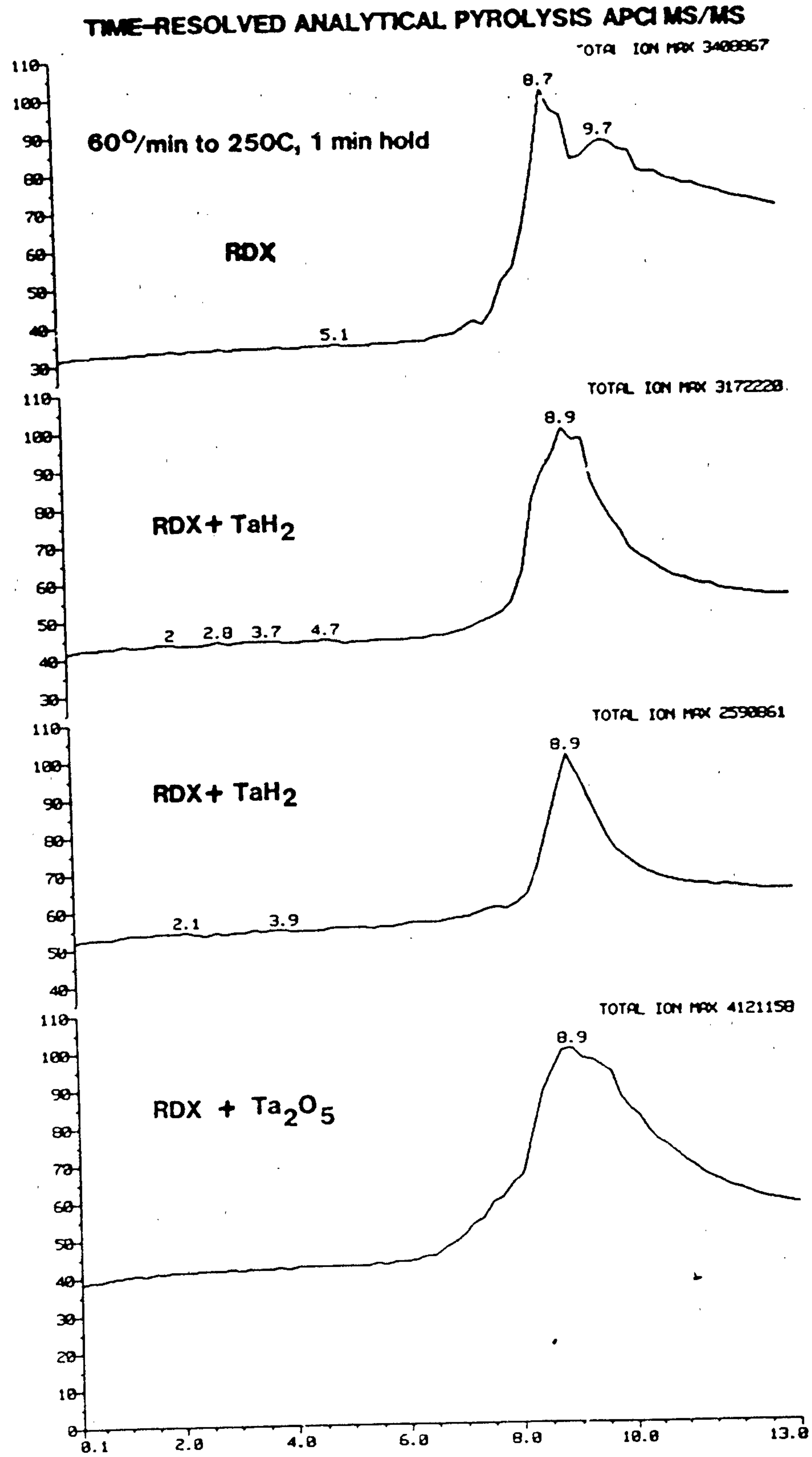

TIME-RESOLVED ANALYTICAL PYROLYSIS APCI MS/MS
TOTAL ION MAX 3408867
60°/min to 250C, 1 min hold
RDX
8.7
9.7
5.1
TOTAL ION MAX 3172228
RDX + TaH2
8.9
2
2.8
3.7
4.7
TOTAL ION MAX 2590861
RDX + TaH2
8.9
2.1
3.9
TOTAL ION MAX 4121158
RDX + Ta2O5
8.9
0.1
2.0
4.0
6.0
8.0
10.0
13.0

Capabilities of the subroutine sets of EXMATH include the following:

1. Preprocessing: variable scaling, variable selection, weighting, distance and similarity, and correlation.

2. Data Manipulation: editing of variables, transposing of data matrices, redefining categories or properties, merging and splitting of datafiles.

3. Classification: linear discriminant analysis, principle component analysis, nonlinear mapping, and nearest neighbors analysis.

4. Factor Analysis: loading extraction, factor scores, factor rotation, and canonical correlation analysis.

EXMATH is the first version of a multivariate pattern recognition system designed to operate under the direction of an expert system driver. It has in common with other statistical packages, a set of mathematical and statistical subroutines which, when operated in proper sequence, produces standard data analysis procedures, such as discriminant analysis and factor analysis. Figure 1 schematically illustrates an application for (a) discriminant analysis and (b) canonical correlation analysis.

It differs from other software packages in being invisible to the user under the expert system decision-making operation. In other words, once in the expert system mode, the user can ask questions about data relationships, but is given no options in the math formulation used to study the data for those relationships. While such a design may lack versatility exercised by data analysis experts, it brings to a facility unique expertise into the problem-solving situation. EXMATH is designed to operate as an expert subsystem within a larger expert system network, EXMAT, as outlined in Figure 2. If certain applications arise wherein the decisions are not the best, changes in parameters are sent to a second-level driver to change the basis of the decision; e.g., in the eigenvector routine, the basis of determination of the rank of the matrix is the average eigenvalue, but the soft-ware is already in place for using several other criteria instead of that one. Therefore, these subroutines in many cases may be considered evolutionary in the same sense that the expert system is evolutionary.

B. EXDBM

A database management system, EXDBM, was created for incorporation into the EXMAT network for material characterization. The DBM system is comprised of four distinct components. The first component manages the transfer of chemical data from the laboratory instruments into the knowledge base of the database management system. A second component sets up the rules for generation of the databases from the database library in response to the problem statement. A third component translates the rules and uses them to search the library for the appropriate data vectors and builds the data matrix for input into the EXMATH expert system. A fourth component is an interactive editor for updating the knowledge base on the samples, listing information about samples and databases, and for correcting any mistakes which might have occurred during data transfer. EXDBM may operate within an expert system shell, receiving generation rules from the (TIMM) shell or, in an interactive mode, receiving generation rules from the user. Programming had begun on HP9000/500 series UNIX system and was transferred to a VAX/780 and finally to the CRDEC microVAXII. The programs are essentially machine independent when the computer system has a FORTRAN 77 compiler with downward (to IV) compatability. Because of the extensive use of character arrays which are 20 characters by 9999 elements, the system requires approximately 1.5 Mb of memory on a 32 bit processor. Extensive use is made of the inquire (file, exist) function of the VMS F77 compiler.

The relational database management expert system thus has been completed and incorporated into the REASON library of the TIMM shell. Sample relationships exist as metric production rules for chemometric analysis. These relational definitions form a knowledge base for matrix generation rather than for direct sample relationships. Therefore, determination of sample sets which satisfy a defined relationship can be instantaneously updated from the knowledge base as new data are acquired. Hence, EXDBM is operational as a stand-alone interactive program for data management tasks as well as a database generator for numerical methods operating as one of the networked expert systems within the TIMM REASON library.

Additionally, operation of the expert system for pattern recognition, EXMATH, was modified to network with both the TIMM REASON library and with EXDBM. EXMATH, when operating with increased intelligence now is driven by TIMM decision rules for chemometric analysis and by EXDBM data decisions. EXMATH receives file names containing TIMM rules for algorithm generation and the EXDBM data matrix. This information serves as factor values for the decision making process of the pattern recognition expert system. Hence, the feasibiltiy of knowledge base sharing and integrated decision-making between TIMM expert systems in the EXMAT network and chemometric expert systems in EXMATH was shown successfully at CRDEC (Figure 2). Crucial to the interaction is a smart database management capability, EXDBM, which understands the requirements of pattern recognition matrices.

SUMMARY

The goal of the software development phase has been achieved: to develop a capability for material characterization within an AI format that encompasses both the requirements of chemical instrumental analysis and of chemometric algorithms for data processing and decision-making. The design is one which encorporates commercial expert system shell technology (TIMM) with in-house developed expert systems (EXMAT, EXDBM, EXMATH) for instrumental data management and chemometric analysis. The algorithms in this prototype system are those found useful for chemical pattern recognition with wide potential use, including model formulation and prediction in the chemical sensor area. Thus, using knowledge bases from TIMM expert systems, decisions that are important to selection of samples for chemometric analysis and to appropriate analytical algorithms, can be deduced as a result of queries made to the chemist and to the database management expert system. This prototype development validates the concept of applied AI having significant impact in the field of instrumental analytical chemistry. Expertise from analysts and chemometricians is now encoded into an AI system designed with extensive symbolic and numeric computing capabilities for problem-solving applications. Development of the knowledge bases will now proceed within the EXMAT, EXDBM, and EXMATH design format.

REFERENCES

1. Naval Weapons Center, Code 3851, China Lake, CA 93555.

2. U.S. Army Chemical Research, Development and Engineering Center, Aberdeen Proving Ground, MD 21010-5423.

3. GEO-CENTERS, INC., Prospect Square Building, 10903 Indian Head Highway, Ft. Washington, MD 20744.

4. A.M. Harper, S.A. Liebman, J. Res. NBS, Special Publ., Nov-Dec, 90 (1985) "Intelligent Instrumentation".

5. S.A. Liebman, P.J. Duff, M.A. Schroeder, R.A. Fifer, A.M. Harper, in ASC Sympos. Series No. 306, Pierce and Hohne, Eds., Amer. Chem. Soc., Washington, DC, 1986, p. 365-384, "Concerted Organic Analysis of Materials and Expert System Development".

(a) **EXMATH HEURISTIC DESIGN**

EXAMPLE-ALGORITHM BUILDING-EXSPDS

PURPOSE- EMULATION OF SPSS PROCEDURE FOR
DISCRIMINANT ANALYSIS

- USED IN ANALYSIS OF VARIANCE MODE
- PRODUCES DATA MAPPING OF SPACE OF SAMPLE REPLICATE VARIATION ABOUT SAMPLE MEANS

OPERATION- INSPECTS INPUT DATA FOR
(1) PRIOR PREPROCESSING
(2) NECESSITY OF RANK REDUCTION PRIOR TO ANALYSIS

- SCALES DATA IF NEEDED
- PERFORMS FACTOR ANALYSIS REDUCTION IF NEEDED
- COMPUTES SAMPLE MEANS AND ARRANGES DATA AS A TRAINING SET OF MEAN VECTORS AND TEST SET OF REPLICATE VECTORS
- PROJECTS BY FACTOR ANALYSIS OF MEAN VECTORS
- REPRODUCES VARIABLE WEIGHTS FOR PROJECTION AND FURTHER ANALYSIS

(b) **CANONICAL CORRELATION**

EXTRACTION OF INFORMATION FROM
MULTIPLE ANALYTICAL TECHNIQUES

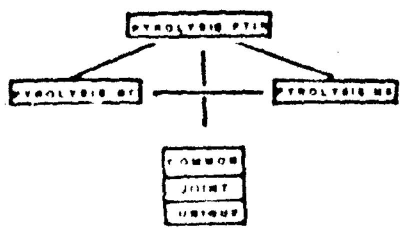

ALGORITHM EXTRACTS INFORMATION BASED ON
THE SQUARE CORRELATION BETWEEN N DATA MATRICES
(CARROLL'S TECHNIQUE)

FIGURE 1

OPERATIONAL OUTLINE

TIMM AI SHELL

EXMAT

DECISION RULES FOR CHEMOMETRICS

EXDBM

DATA DECISIONS

EXMATH

FILE NAMES WITH RULES FOR ALGORITHM GENERATION AND EXDBM DATA MATRIX SERVE AS FACTOR VALUES FOR DECISION-MAKING

RESULT

CLASSIFICATION OF GROUPS I,II, III AMINE SALTS USING APPLIED AI

Figure 2

ANALYTE DETECTION AND IDENTIFICATION IN COMPLEX MATRICES BY PYROLYSIS-ATMOSPHERIC PRESSURE CHEMICAL IONIZATION-TANDEM MASS SPECTROMETRY

A. Peter Snyder*, U.S. Army Chemical Research, Development and Engineering Center, Aberdeen Proving Ground, Maryland 21010-5423

Shirley A. Liebman, GEO-CENTERS, INC., Mailing Address: U.S. Army Chemical Research, Development and Engineering Center, Aberdeen Proving Ground, Maryland 21010-5423

Richard A. Yost, Department of Chemistry, University of Florida, Gainesville, Florida 32611

Please send correspondence to:

Dr. A. Peter Snyder
U.S. Army Chemical Research, Development and Engineering Center
SMCCR-RSL
Aberdeen Proving Ground, Maryland 21010-5423
301-671-2416

Brief

Pyrolysis-atmospheric pressure ionization-tandem mass spectrometry is used for explosive, drug and pesticide detection in solid commercial and munition formulations.

ABSTRACT

Pyrolysis-atmospheric pressure chemical ionization-tandem mass spectrometry was investigated for its potential in characterizing analytes of interest in solid formulations with essentially no sample preprocessing. Experimental logistics are convenient in that 0.5 mg amounts of the formulation, e.g., - powders, shavings and tablet scrapings, are placed directly into the heating device. The energetic nitramine RDX, in a propellant formulation was found to produce a distinct mass spectral pattern with no polymer binder/filler interference. Aspirin and caffeine were detected in over-the-counter drug tablets, and the dichlorvos phosphate pesticide was identified with and without heating in a commercial pesticide strip.

Characterization of analytes in complex, solid samples is a subject which has been addressed by a number of analytical techniques for a wide variety of applications. Quality control and assurance (QA/QC) in manufacturing processes, forensics and environmental and biomedical assays are a few of the representative areas which take advantage of methods that extract information from a particular substance of interest in a solid formulation. The degree of qualitative and quantitative sample information, sample turnover rate, sensitivity and selectivity are a few of the important criteria when considering a technique for a particular sample analysis. Selectivity is generally a prime concern since, depending on the analysis technique, the polymer/matrix formulation could interfere and/or obscure the presence of the compound of interest unless some sample preprocessing (e.g. - extraction or chromatographic separation) is performed.

Trade-offs among the above requirements normally occur and result in an enhancement of certain desirable features (e.g. - figures of merit) at the expense of others (e.g. - experimental logistics or data analysis methods). Field desorption mass spectrometry has been shown to produce the molecular ion and high molecular weight fragments of the nitramine RDX with no interference from the stearic acid formulation (1). Fast atom bombardment of an untreated sliver of an infant pacifier known to contain the di(2-ethylhexyl) phthalate plasticizer placed on a target with thioglycerol produced intense signals for the phthalate compound (2). Hieftje et al. (3) have shown that near-infrared reflectance and cluster analysis of whole, untreated and unopened allergy/cold remedy tablets could be successfully used for the detection of altered tablet products along with an approximate concentration determination of the adulterant. Sample signatures were observed that indicated differences from a reference database with adulterants such as ferric oxide, aluminum metal, arsenic trioxide, sodium fluoride and cyanide. Related to this method is near infrared spectroscopy. The technique is convenient in that samples can be analyzed without pretreatment, and it can provide qualitative and quantitative information (4). Forensic methods generally use water and/or solvent wash procedures for bomb/explosive, post-blast debris with subsequent chemical spot tests prior to analytical interrogation techniques such as ion chromatography, high pressure liquid chromatography (HPLC), gas chromatography/mass spectrometry (5,6) and pyrolysis (Py)-GC/MS (7).

Other methods can produce an accurate measure of analyte concentration in a formulation at the expense of sample processing methods such as crushing, extracting, filtering and concentrating. Oftentimes, pH values must be adjusted along with the addition of reagents to effect a more convenient detection of the analyte. These sample processing methods are essential in the analysis of commercial drug tablet formulations with the HPLC (8,9), liquid chromatography (10), micellar electrokinetic capillary chromatography (11) and conventional UV-VIS spectrophotometry (12) analytical methods.

Atmospheric pressure ionization (API) of vaporized, solid compounds has been shown recently to provide relatively convenient experimental logistics in terms of minimal sample preprocessing and convenient sample introduction for spectrometer systems. API is inherently selective (i.e. - analyte proton affinity or ionization threshold) which can provide a distinct advantage in the analysis of a particular compound when interferential substances are present. Laser desorption (LD) and ionization of solid, polycyclic aromatic hydrocarbons (13) and API-LD of pure biological and drug compounds (14) have been performed with ion mobility spectrometry. Pyrolysis-atmospheric pressure chemical ionization (Py-APCI) mass spectrometry has been shown to provide characteristic mass spectral information on pure biopolymers (15), biopolymers in the presence of a salt matrix (16), and the nitramine RDX (17). The present discussion explores the relative merits of Py-APCI-tandem mass spectrometry (MS/MS) for the detection and identification of pesticide and drug analytes in commercial formulations and a nitramine in a propellant formulation.

EXPERIMENTAL SECTION

A Sciex (Toronto, Canada) TAGA 6000 atmospheric pressure chemical ionization (APCI) triple quadrupole mass spectrometer was used as the analyzer; the mass spectrometry conditions for the present study are as previously reported (15). Normal operating pressure in the conventional MS mode was typically $2.5\text{-}3.0 \times 10^{-6}$ torr in the analyzer with a nitrogen curtain gas; all daughter ion (MS/MS) analyses were obtained with argon collision gas at an analyzer pressure of 6.0×10^{-5} torr and a collision energy of approximately 65 eV.

Three different types of solid samples were analyzed. The No-Pest Strip (Spectrum Group Inc., Jacksonville, FL) was used for investigation of the pesticide 2,2-dichlorovinyl-dimethylphosphate(dichlorvos); Anacin (Whitehall Laboratories, Inc., New York) and Extra-Strength Bufferin (ESB) (Bristol-Meyers Co., New York) analgesic tablets were investigated for the presence of aspirin (2-acetylsalicylic acid) and caffeine. Anacin contains 400 mg and 22 mg of aspirin and caffeine per tablet, respectively, and Bufferin contains 324 mg of aspirin per tablet. Pure caffeine and aspirin standards were obtained from Eastman Chemicals, Rochester, NY and Chem Service, Media, PA, respectively. A U.S. Army formulated propellant (HTPBX) was tested for the presence of cyclotrimethylenetrinitramine (RDX). The formulation (HTPBX) consists of an hydroxyterminated polybutadiene (HTPB) base matrix with prepolymers and additives and is 40% by weight RDX. Pure RDX and HTPBX were obtained from the Ballistic Research Laboratory, Aberdeen Proving Ground, MD. RDX samples were found to contain acetone in the pyrolysis mass therefore, were vacuum-dried for one week to eliminate the solvent.

Pyrolysis of the solid samples was conducted with a Pyroprobe Model 122 controller from Chemical Data Systems, Inc., Oxford, PA, with a platinum coil desorption probe. Pyrolysis was conducted with the temperature ramp (risetime) in the off position and a final set temperature of 500°C. All runs used ca. 0.5 mg of sample positioned in a quartz tube with quartz wool. The tube was placed in the desorption probe, and the latter was inserted into the ion source of the mass spectrometer. Details and a schematic of the interface are presented elsewhere (17). All pyrolyses were performed with a 170 ml/min air flow over the pyrolysis region from a compressed air cylinder (MG Industries, Valley Forge, PA), and the ion source exhaust motor was turned on during the experiments in order to obtain a one minute baseline-to-baseline total ion current.

RESULTS AND DISCUSSION

The ability of oxidative pyrolysis-APCI mass spectrometry to detect and identify a compound of interest in a complex matrix depends on a number of processes. In addition to mass spectrometry performance characteristics, critical conditions must be met in the pyrolysis event and ionization processes. The thermal treatment must produce either the intact compound of interest, characteristic and informative analyte fragment species, or a combination of the two with minimal interaction effects from the matrix and matrix pyrolyzate. Once the sample has been pyrolyzed to gaseous products, they must be transferred from the pyrolysis zone to the ionization source rapidly. Noncatalytic, heated surfaces should be used to prevent prevent secondary reaction and/or product condensation. Another important consideration for adequate analyte detection is that the neutral molecular and/or fragment species must be able to compete effectively for the available protons in the ion source relative to that of the matrix pyrolyzate. These aspects, fundamental to Py-APCI-mass spectrometry and Py-APCI-tandem mass spectrometry were investigated in the detection and identification of propellant, drug and pesticide analytes in three different solid matrix formulations.

Propellant Formulation. Figure 1a presents the Py-APCI mass spectra of pure RDX. Under oxidative pyrolysis conditions, the protonated molecular ion was not detected; however, a series of fragments were observed at m/z 46, 60, 74 75, 85 and 98. Analyses of deuterium and ^{15}N isotope-labeled RDX provided the necessary information for structural elucidation of each of the ions (18). With the exception of the m/z 98 ion, all are observed in the Py-APCI mass spectrum of the formulated propellant (Figure 1b). Figure 1c shows the Py-APCI mass spectrum of the HTPB binder. Comparison of Figures 1b and c shows that the binder produces minimal background in the detection of the RDX analyte.

Daughter ion MS/MS analysis was used to confirm the identities of the main ions in the HTPBX formulation mass spectrum (Figure 1b). Figure 2a, c, e, g, and Figure 2b, d, f, h represent the daughter ion spectra of m/z 46, 60, 75 and 85 for the pure and formulated RDX, respectively. For each respective pair of daughter ion mass spectra, a satisfactory relationship is observed. The same conclusion was also reached in a comparison of the m/z 74 RDX and HTPBX daughter ion mass spectra (data not shown). With the exception of m/z 85, APCI of the HTPB produces minimal abundance of the major ions corresponding to RDX. Figure 2i shows that the m/z 85 parent ion in Figure 1c produced from HTPB is significantly different from that produced from RDX. Therefore, despite the absence of the protonated molecular ion of RDX and m/z 98 in the Py-APCI mass spectrum of the formulated propellant, sufficient mass spectral information is retained for the detection of presence and identification of RDX.

Commercial Drug Formulations. Two over-the-counter analgesics, Anacin and Extra-Strength Bufferin were examined for the detection and identification of the pharmaceutical analytes contained in the solid formulations. Figure 3a,b present the Py-APCI mass spectra of pure aspirin (2-acetyl-salicylic acid) and caffeine, respectively. A low intensity protonated molecular ion (m/z 181) is observed for aspirin in Figure 3a, while intense ions are observed for the dehydrated (m/z 163) and deacetylated (m/z 121) aspirin species. Schulten and Beckey (19) have shown that with field desorption mass spectrometry, only the m/z 180 molecular and m/z 181 protonated molecular ions are observed.

In contrast, negligible fragmentation occurs in Py-APCI of caffeine, in that only the protonated molecular ion (m/z 195) is present in Figure 3b. Figures 3c,d show the Py-APCI mass spectra of Anacin and Extra-Strength Bufferin, respectively. In both formulations, the mass spectral pattern of aspirin ions is obvious, while the MH^+ ion of caffeine (m/z 195) is prominent in Anacin (Figure 3c) but minor in Extra-Strength Bufferin (which does not contain caffeine) (Figure 3d). Confirmation of these assignments can be found in the daughter ion spectra in Figure 4a-l. The daughter ion spectra of m/z 121, 163 and 181 of aspirin provide a satisfactory match with their respective counterparts in the two drug formulations (Figure 4a-i). The daughter ion mass spectra of m/z 195 (Figure 4j-l) show that identical fragmentation patterns are observed from pure caffeine and Anacin, while the daughter ion mass spectrum of the small ion at m/z 195 (Figure 4l) in the Py-APCI mass spectrum of Extra-Strength Bufferin (Figure 3d) does not resemble the daughter spectra for caffeine.

A typical Anacin tablet contains approximately 400 mg of aspirin and 22 mg of caffeine, yet caffeine produces a significantly greater response for MH^+ than does aspirin in the Anacin Py-APCI mass spectrum in Figure 3c. This arises from the different proton affinities of the two compounds; and combination (dry, solid mixture) of the pure aspirin and caffeine compounds, in the same 400:22 ratio, respectively, produced a similar intensity distribution (data not shown) to that of Figure 3c. Under these experimental conditions, the Py-APCI-MS/MS results for caffeine in the pure and matrix forms are similar with those observed in other thermal treatment methods. Py-field ionization (FI) and Curie-point pyrolysis-gas chromatography-FI mass spectrometry (20) produced the m/z 194 molecular ion of caffeine from the pure and ground roasted coffee product forms. Caffeine was also analyzed for its presence in a urine sample by direct insertion probe APCI-tandem mass spectrometry (21). After the caffeine was separated from the urine by thin-layer chromatography, the silica spot containing the caffeine was scraped from the plate and placed directly on the probe. Thermal desorption of the silica-caffeine sample resulted in a clear, protonated caffeine signal at m/z 195. The daughter ion spectrum confirming its identity with that of the pure standard (21) was essentially the same as the Py-APCI-daughter ion spectrum in Figure 4j.

Commercial Pesticide Strip. Depending upon the analyte of interest and its vapor pressure, pyrolysis of a solid formulation for analyte detection is not always necessary for an APCI-mass spectrometric analysis. For example, the Spectrum No-Pest Strip was investigated for the presence of dichlorvos. By merely holding the polyvinylchloride-based strip in front of the APCI ion source, the protonated molecular ion (m/z 221) and its chlorine isotopic peaks at m/z 223 and 225 were observed (Figure 5a). The intense ions at m/z 109 and 127 represent $[(CH_3CO)_2PO]^{+\cdot}$ and $[(H_3CO)_2PO_2H]H^+$ fragment ion species, respectively, as observed by direct probe, methane CI tandem mass spectrometry (22).

Pyrolysis of a small portion of the No-Pest Strip yields the same ions (Figure 5b) as that of Figure 5a except with a significant difference in ion intensity distribution. The increased abundance of m/z 109 and 127 relative to the dichlorvos MH^+ ions in the pyrolysis mass spectrum indicates that these ions can arise not only from APCI fragmentation, but also from ionization products of pyrolysis of dichlorvos. The m/z 141 ion apparently arises from pyrolysis of dichlorvos or other components in the strip. Because of the straightforward detection of the phosphate pesticide in Figure 5a, daughter ion analyses were deemed unnecessary. Indeed, pyrolysis is not desirable in this instance (Figure 5b), because even though the analyte ions are present, a significant loss in the dichlorvos MH^+ relative ion abundances is observed.

CONCLUSION

Analytical pyrolysis-APCI-tandem mass spectrometry has been shown to provide an attractive set of experimental conditions for the detection of targeted analytes in complex solid formulations. The ease of sample introduction and an ion source that is selective to compounds with high proton affinity highlight the technique. The method requires only minimal sample preprocessing, and complex matrices may be investigated with APCI-mass spectrometry from a controlled thermal treatment to determine the presence of analyte(s) of interest. Analytical pyrolysis-APCI of analytes in complex matrices produced protonated molecular ions, characteristic fragment ions or a combination of both.

ACKNOWLEDGEMENT

We thank Linda Jarvis for the preparation and editing of the manuscript and Robert A. Fifer and Michael A. Schroeder for providing us with RDX and formulated RDX propellant.

LITERATURE CITED

(1) Schulten, H.-R.; Lehmann, W.D. Anal. Chim. Acta 1977, 93, 19-31.

(2) O. Lay, Jr., J.; Miller, B.J. Anal. Chem. 1987, 59, 1323A-1325A.

(3) Lodder, R.A.; Selby, M.; Hieftje, G.M. Anal. Chem. 1987, 59, 1921-1930.

(4) Saferstein, R. Pyrolysis and GC in Polymer Analysis, 1985, E.J. Levy and S.A. Liebman, eds., Marcel Dekker, NY, Chapter 7.

(5) Rudolph, T.L.; Bender, E.C. Proc. Intl. Symp. on the Analysis and Detection of Explosives 1983, The Federal Bureau of Investigation, Quantico, VA, p. 71-78.

(6) Fine, D.H.; Yu, W.C.; Goff, E.U. ibid, p. 169-179.

(7) Clancy, P. Am. Lab. 1988, 20, 176-189.

(8) El-Gizawy, S.M.; N. Ahmed, A.-El-H.; Analyst 1987, 112, 867-869.

(9) Al-Kaysi, H.N.; Sheikh Salem, M.A.; Anal. Lett., 1987, 20, 1451-1466.

(10) Krieger, D.J. J. Assoc. Off. Anal. Chem. 1987, 70, 212-214.

(11) Fujiwara, S.; Honda, S. Anal. Chem. 1987, 59, 2773-2776.

(12) Tan, H.S.I.; Salvador, G.C. Anal. Chim. Acta 1986, 188, 295-300.

(13) Eiceman, G.A.; Anderson, G.K.; Danen, W.C.; Ferris, M.J.; Tiee, J.J. Anal. Lett. 1988, in press.

(14) Kolaitis, L.; Lubman, D.M. Anal. Chem. 1986, 58, 2137-2142.

(15) Snyder, A.P.; Kremer, J.H.; Meuzelaar, H.L.C.; Windig, W.; Taghizadeh, K. Anal. Chem. 1987, 59, 1945-1951.

(16) Snyder, A.P.; Kremer, J.H.; Meuzelaar, H.L.C.; Windig, W.; J. Anal. Appl. Pyrolysis 1988, 13, 77-88.

(17) Liebman, S.A.; Snyder, A.P.; Kremer, J.H.; Reutter, D.J.; Schroeder, M.A.; Fifer, R.A. J. Anal. Appl. Pyrolysis 1987, 12, 83-95.

(18) Snyder, A.P.; Kremer, J.H.; Liebman, S.A.; Schroeder, M.A.; Fifer, R.A. Submitted to Org. Mass Spectrom. 1988.

(19) Schulten, H.-R.; Beckey, H.D. Adv. Mass Spectrom. 1974, 6, 499-507.

(20) Schulten, H.-R.; Halket, J.M. Org. Mass Spectrom. 1986, 21, 613-622.

(21) Henion, J.; Maylin, G.A.; Thomson, B.A. J. Chromatog. 1983, 271, 107-124.

(22) Hummel, S.V.; Yost, R.A. Org. Mass Spectrom. 1986, 21, 785-791.

FIGURE CAPTIONS

1. Py-APCI mass spectra of (a) pure RDX; (b) HTPBX formulation; (c) HTPB binder.
2. Py-APCI daughter ion mass spectra of m/z 46: (a) RDX; (b) HTPBX; m/z 60: (c) RDX; (d) HTPBX; m/z 75: (e) RDX; (f) HTPBX; m/z 85: (g) RDX; (h) HTPBX; (i) HTPB binder without RDX.
3. Py-APCI mass spectra of (a) pure aspirin; (b) pure caffeine; (c) Anacin; (d) Extra-Strength Bufferin.
4. Py-APCI daughter ion mass spectra of m/z 121: (a) aspirin; (b) Anacin; (c) Extra-Strength Bufferin; m/z 163: (d) aspirin; (e) Anacin; (f) Extra-Strength Bufferin; m/z 181: (g) aspirin; (h) Anacin; (i) Extra-Strength Bufferin; m/z 195: (j) caffeine; (k) Anacin; (l) Extra-Strength Bufferin.
5. APCI-mass spectra of the Spectrum No-Pest Strip (a) without and (b) with pyrolysis sample introduction.

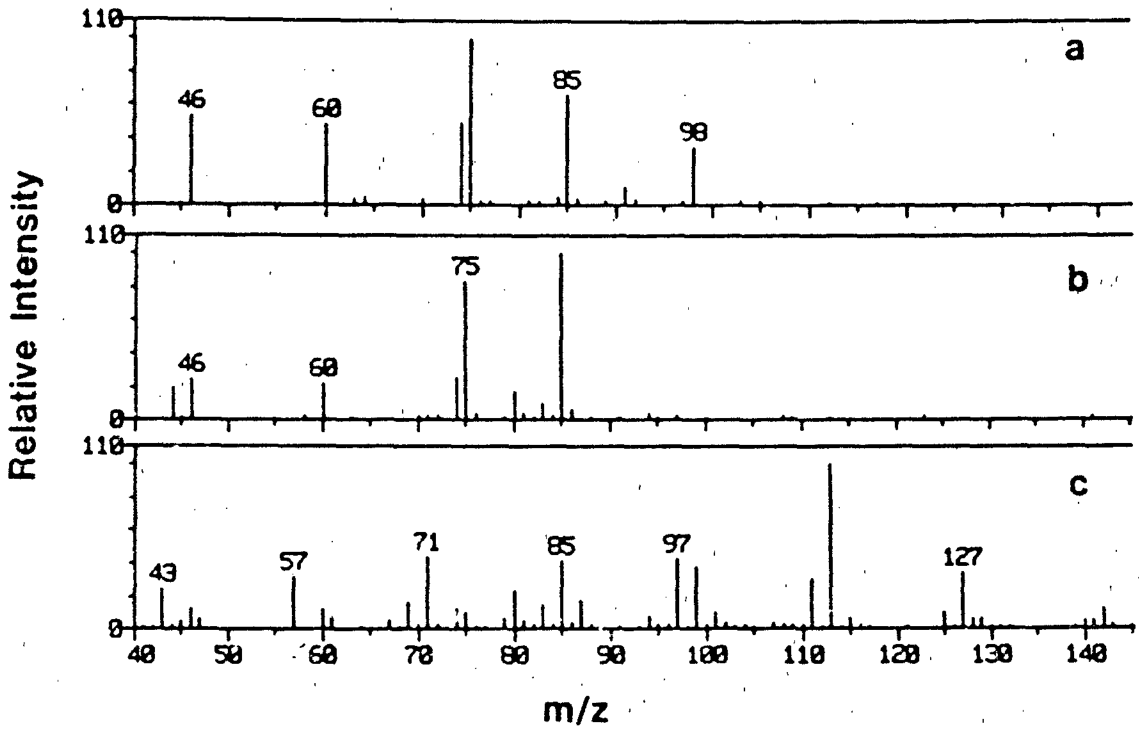

Relative Intensity
110
0
a
46
60
85
98
b
75
46
60
c
43
57
71
85
97
127
40
50
60
70
80
90
100
110
120
130
140
m/z

FIG. 1

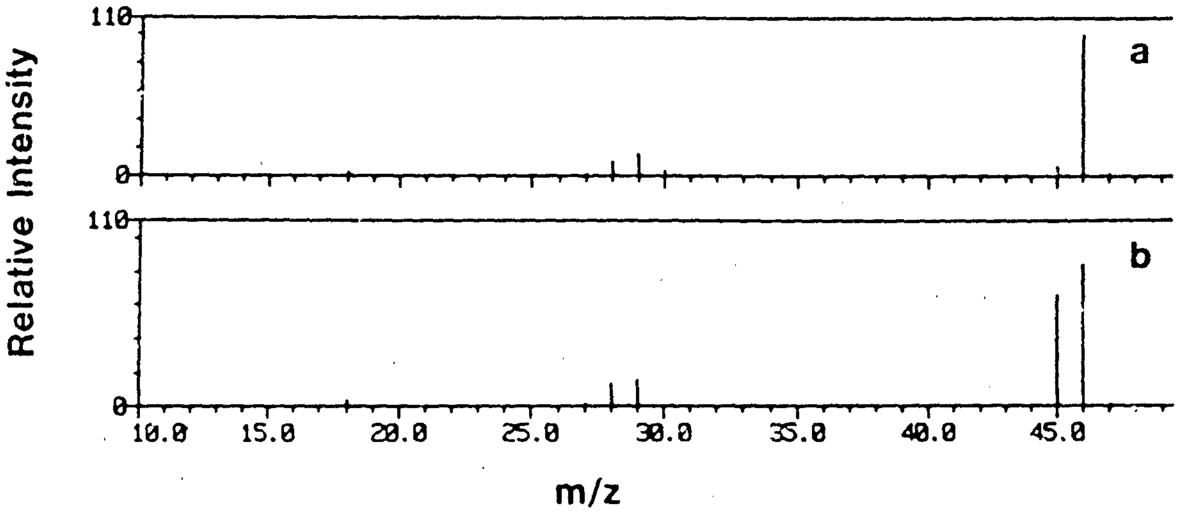

110
0
110
0
Relative Intensity
a
b
10.0
15.0
20.0
25.0
30.0
35.0
40.0
45.0
m/z

FIG 2,

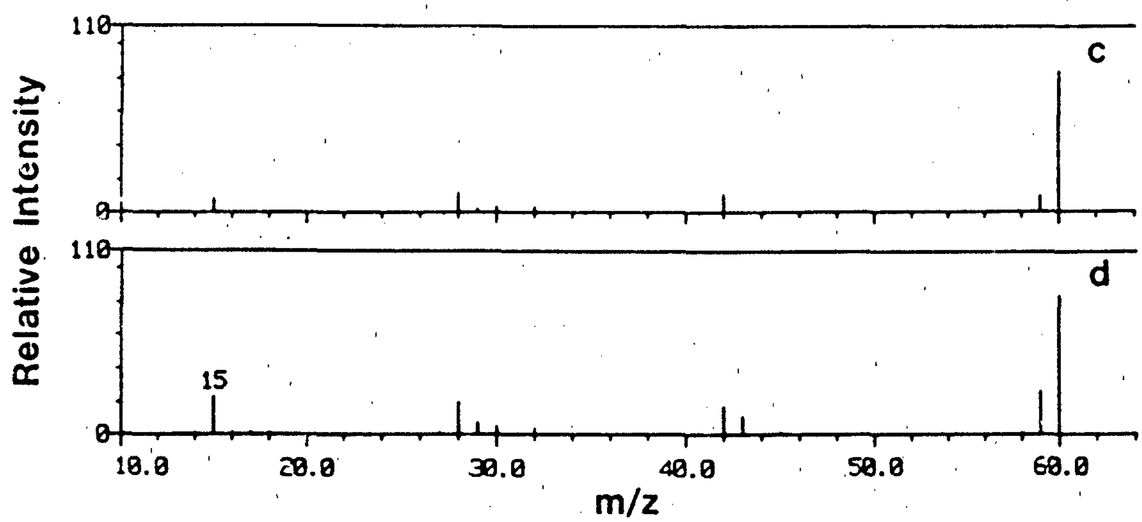

Relative Intensity
110
0
c
110
0
d
15
10.0
20.0
30.0
40.0
50.0
60.0
m/z

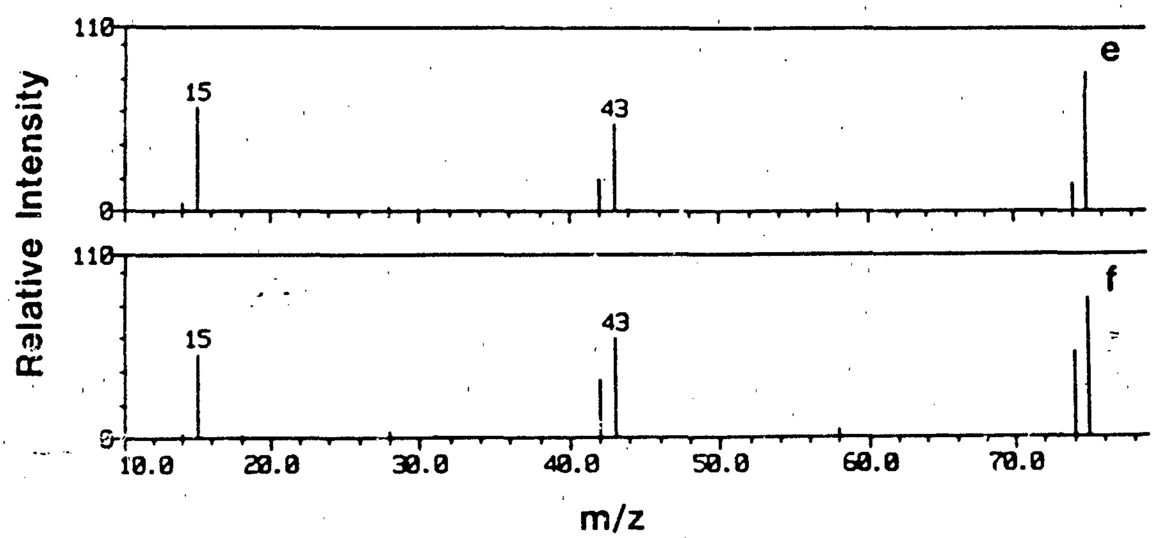

Relative Intensity
110
0
e
15
43
110
0
f
15
43
10.0
20.0
30.0
40.0
50.0
60.0
70.0
m/z

FIG. 2

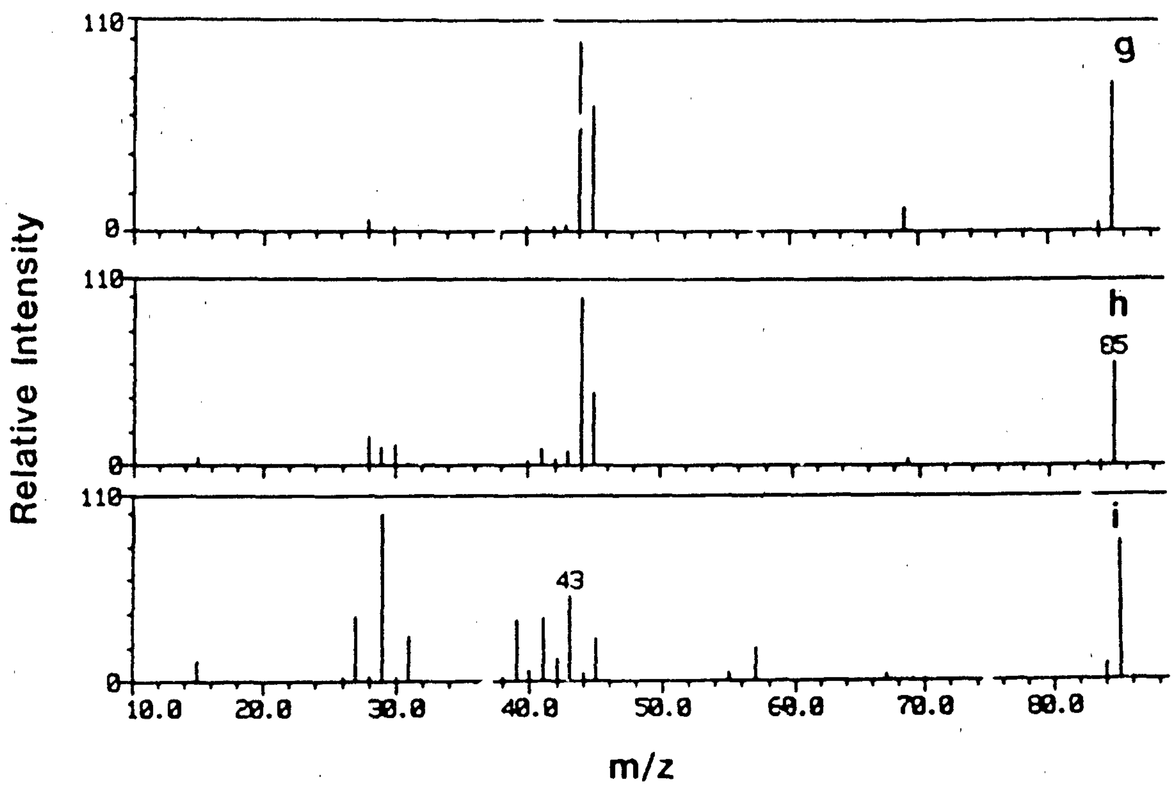

110
0
g
h
85
i
43
10.0
20.0
30.0
40.0
50.0
60.0
70.0
80.0
Relative Intensity
m/z

FIG. 2

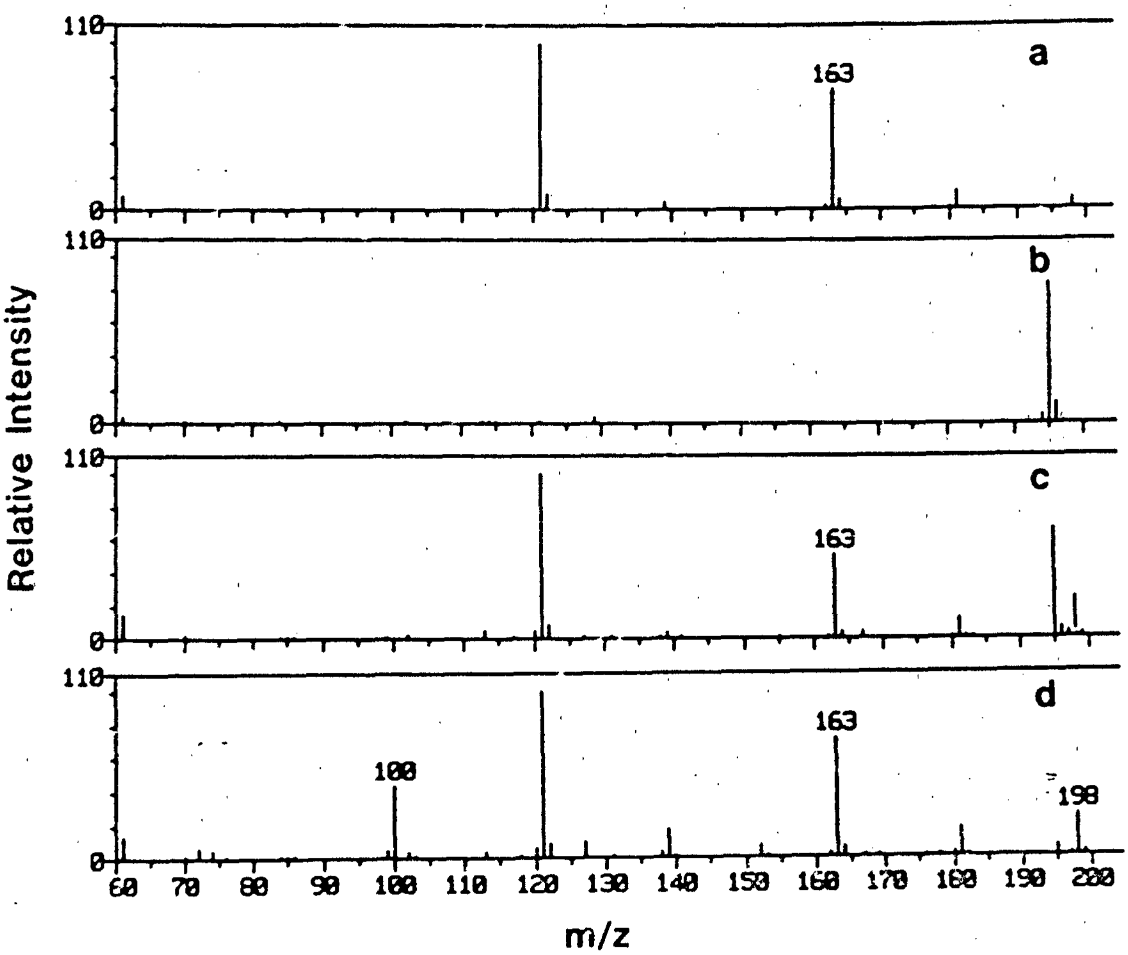

Relative Intensity
110
0
a
163
b
c
163
d
100
163
198
60
70
80
90
100
110
120
130
140
150
160
170
180
190
200
m/z

FIG. 3

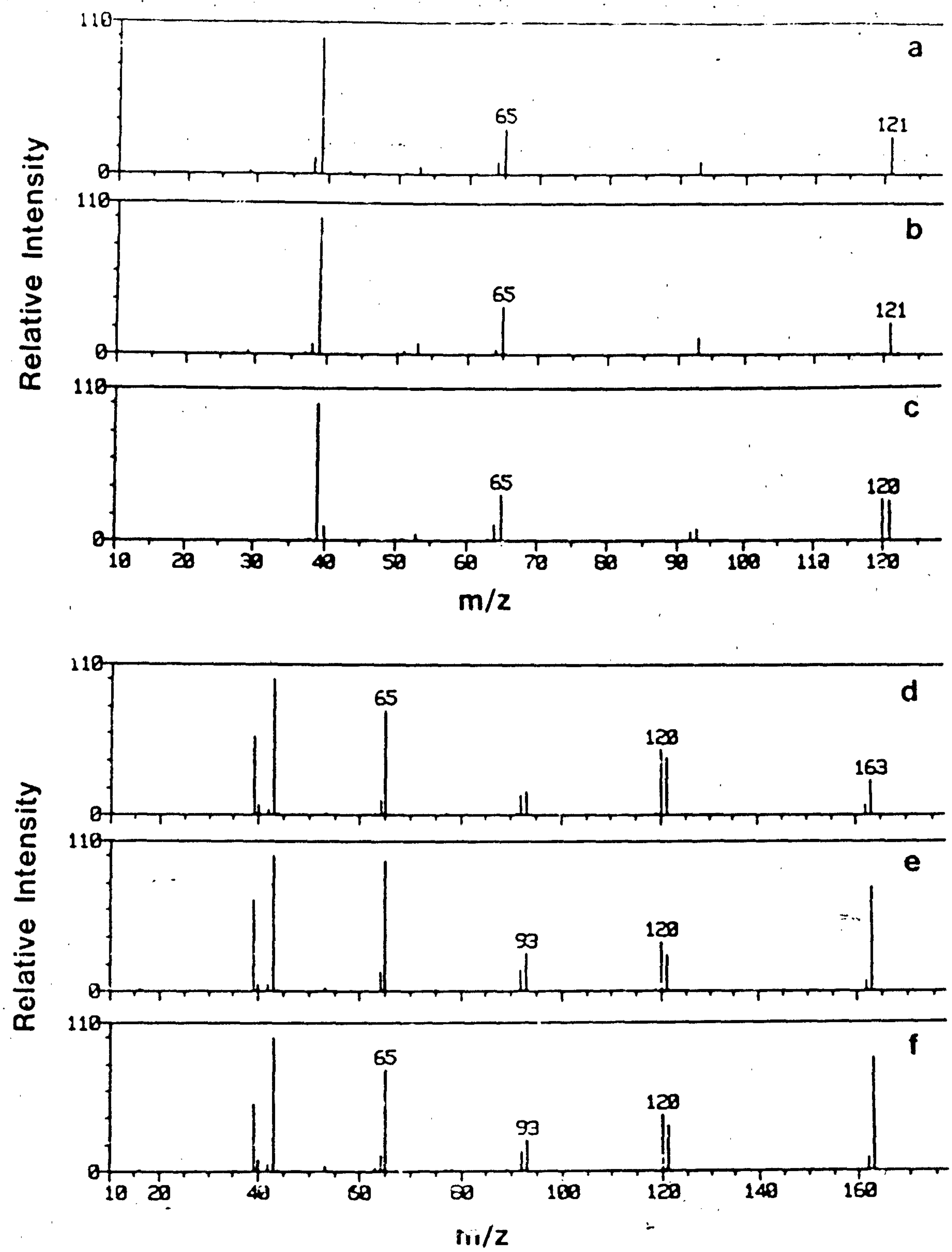

110
0
Relative Intensity
a
65
121
b
65
121
c
65
120
10 20 30 40 50 60 70 80 90 100 110 120
m/z
d
65
120
163
e
93
120
f
65
93
120
10 20 40 60 80 100 120 140 160
m/z

FIG. 4

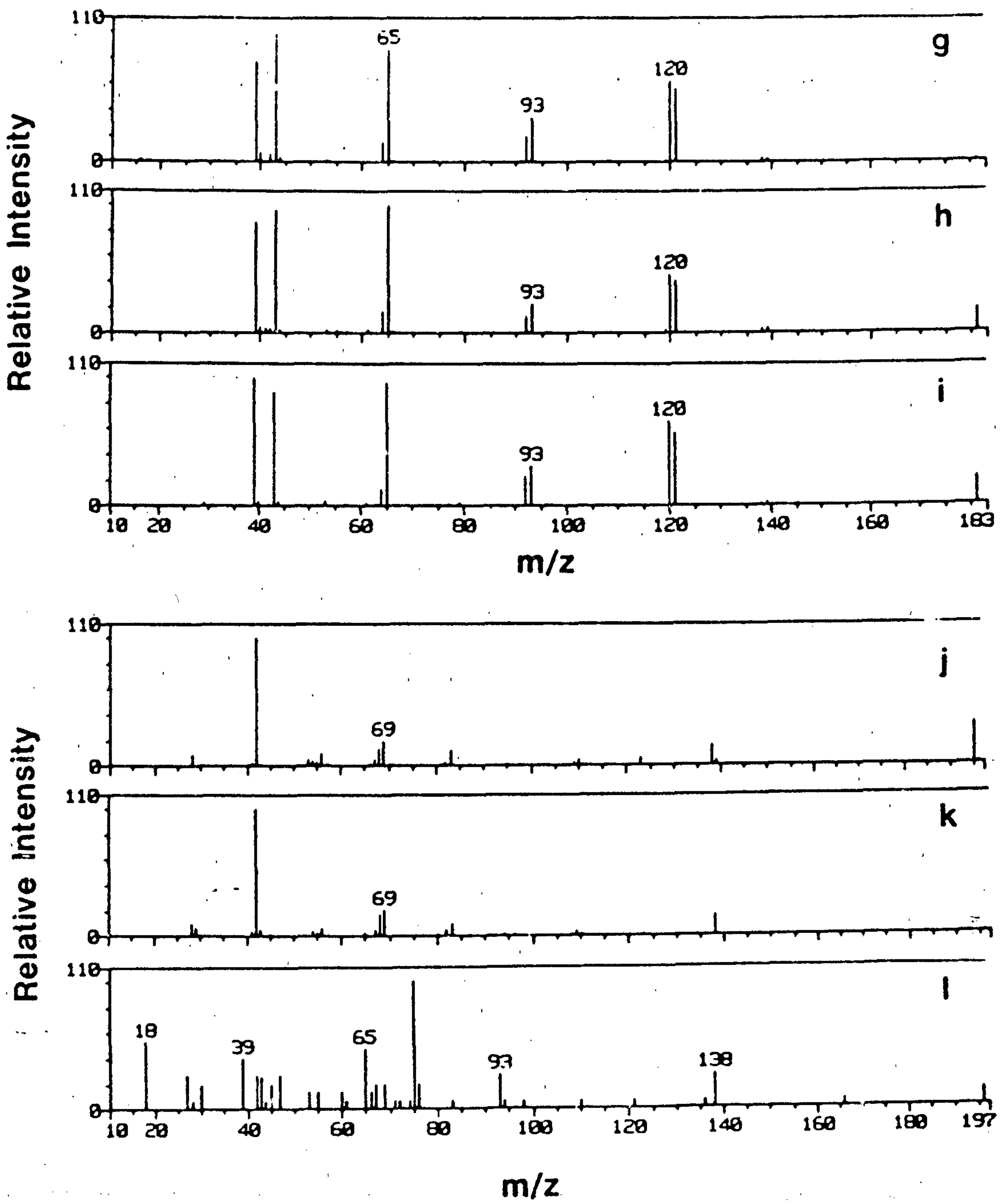

110
0
65
93
120
g
h
i
10
20
40
60
80
100
140
160
183
Relative Intensity
m/z
j
k
l
69
18
39
138
180
197

FIG. 4

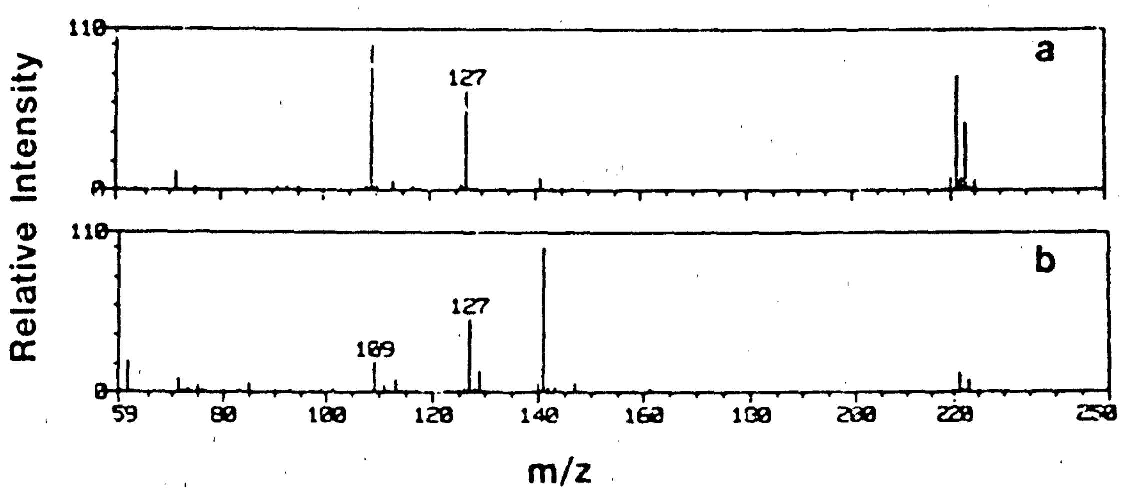

110
0
a
127
110
0
b
109
127
59
80
100
120
140
160
180
200
220
250
Relative Intensity
m/z

FIG. 5

MECHANICAL TESTING OF TRANSLUCENT POLYMERIC MATERIALS FOR CORRELATION TO CHEMICAL RESISTANCE BEHAVIOR: SURVEY OF CURRENT LITERATURE, EQUIPMENT/METHODS, AND APPLICATIONS

TASK 003

S.A. Liebman, Ph.D.
GEO-CENTERS, INC.
Senior Scientist

December 1, 1987

REPORT DOCUMENTATION PAGE

Approved for public release; distribution is unlimited.

6a. NAME OF PERFORMING ORGANIZATION: GEO-CENTERS, INC.	6b. OFFICE SYMBOL (If applicable)
7a. NAME OF MONITORING ORGANIZATION	
6c. ADDRESS (City, State, and ZIP Code): 7 Wells Avenue, Newton Centre, MA 02159	7b. ADDRESS (City, State, and ZIP Code)
8a. NAME OF FUNDING/SPONSORING ORGANIZATION: CRDEC	8b. OFFICE SYMBOL (If applicable)
9. PROCUREMENT INSTRUMENT IDENTIFICATION NUMBER: DAAA15-87-D-0007-0002	
8c. ADDRESS (City, State, and ZIP Code): Aberdeen Proving Ground, MD 21010-5423	10. SOURCE OF FUNDING NUMBERS: PROGRAM ELEMENT NO / PROJECT NO / TASK NO / WORK UNIT ACCESSION NO

11. TITLE (Include Security Classification)
Chemical Agent Simulants for Testing Transparent Materials

12. PERSONAL AUTHOR(S) Lewis, Randall E.; Liebman, Shirley A.; Isaacson, Louis; Grasso, Paul; Sarver, Emory W.

13a. TYPE OF REPORT	13b. TIME COVERED	14. DATE OF REPORT (Year, Month, Day)	15. PAGE COUNT
Contractor	FROM 87Sep TO 88Jan	1988 April	

16. SUPPLEMENTARY NOTATION
COR: J. Pistritto, SMCCR-RSC-C, (301) 671-2443

17. COSATI CODES

FIELD	GROUP	SUB-GROUP
15	06	03

18. SUBJECT TERMS (Continue on reverse if necessary and identify by block number)
Transparent polymeric materials; CW agents; Polycarbonate; Cast polymethylmethacrylate; Stretched polymethylmethacrylate (cont on reverse)

19. ABSTRACT (Continue on reverse if necessary and identify by block number)

Transparent polymeric materials undergo physical changes when exposed to CW agents. The object of this task was to: 1) select candidate liquids to simulate GB, VX and HD effects (three each) and 2) perform three point bend tests to determine critical strain values for cracking/crazing for simulant/transparent polymer materials combinations. The critical strain tests were accomplished using ASTM method D790-80 for stress crazing. The method was modified and enhanced to detect stress crazing via changes in reflection/diffraction patterns produced with a helium-neon (He-Ne) laser. Four transparent polymer materials were tested; namely, as cast polymethyl methacrylate (PMMA), biaxially stretched PMMA, polycarbonate and polyurethane GAC-590. The critical strain values obtained for the simulant/polymer combinations are presented as a four by nine map that allows easy comparisons as a function of material or simulant. Comparison with actual agent data is possible using this four by nine map.

20. DISTRIBUTION/AVAILABILITY OF ABSTRACT: ☒ UNCLASSIFIED/UNLIMITED ☐ SAME AS RPT ☐ DTIC USERS	21. ABSTRACT SECURITY CLASSIFICATION: UNCLASSIFIED
22a. NAME OF RESPONSIBLE INDIVIDUAL: Sandra J. Johnson	22b. TELEPHONE (Include Area Code): (301) 671-2914 — 22c. OFFICE SYMBOL: SMCCR-SPS-T

DD FORM 1473, 84 MAR — 83 APR edition may be used until exhausted. All other editions are obsolete.

SECURITY CLASSIFICATION OF THIS PAGE
UNCLASSIFIED

ABSTRACT

The submitted survey includes six major areas of information focused on mechanical and chemical characterization of plastics, specifically those transparent/translucent materials for aerospace/military uses, such as windshields, canopies, lens coatings. Appendix I contains coverage of the fundamentals of plastics testing and chemical analysis from major sources in the field, including tabulation of current mechanical and instrumental chemical methods, their advantages and limitations. Appendices II - VI cover basic literature and information on specific polymer testing, materials science, coatings technology; research institutes, services/courses/meetings; mechanical test equipment (destructive methods and nondestructive methods); chemical analytical instruments/methods; and background information on materials commonly used in the denoted applications.

This compilation serves (a) to identify the major activities and concerns in the field of plastics mechanochemistry and (b) to provide a basis for a comprehensive assessment of chemical and mechanical behavior of new materials in military applications of importance to CRDEC.

I. INTRODUCTION:

This literature survey was performed for the purpose of defining the mechanical testing procedures generally followed for QC/QA testing by manufacturers of translucent engineering plastics, used primarily in aircraft canopies, windshields, lenses, vision, and weapons systems. Although the selected screening tool, ASTM 484, will be used for the test maerials involved, it is significant to be aware of other hardware/software testing procedures currently developing. Evaluation of chemical/environmental test methods for plastics is one of the more difficult, less understood areas, and hence no widely acceptable standard (mil or industry) has been found. However, existance of an ASTM Subcommittee, F7.08 for Transparent Aerospace Materials, should aid the field.

Furthermore, correlation of these chemical resistance/mechanical data to in-field performance behavior is even less defined. Predictive use of static/dynamic mechanical tests, before and after exposure to the chemicals of concern, requires careful sample preparation (surfaces, internal stress maps, etc.), realistic chemical exposure parameters (concentrations, time, temperature, etc.), mode of application (wicking, fogging, droplets, etc.), and careful simulation of the anticipated stress loads that will provide meaningful data in a reasonable time frame. For purposes of this review, limitations of test materials to common polymer systems compounded for such applications in windshields/lenses, etc., puts a focus on polycarbonates, polyacrylics, polyurethanes, and specialty glass, as well as film coatings applied to these transparent/translucent materials.

Likewise, selection of chemical species of concern in this study indicates potentially severe interaction with typically formulated materials within and joining such polymeric/composite structures. Polymer matrices undergo such a wide range of swelling, dissolution, permeation, reaction and degradation on exposure to common environmental stresses (erosion, thermal, photolytic, hydrolytic, radiolytic) that a major percentage of industrial R&D is devoted to the proper formulation packages to ensure short and long-term stability of the in-field product. Thus, exposure to hazardous, chemically reactive, and powerful solvent delivery systems pose significant problems when combined with normal environmental concerns. Common consumer products that must maintain proper wear/abrasion/anti-soiling/discoloration characteristics for bulk and surface coatings may contain up to 20-25 ingredients carefully formulated to achieve design performance limits. Effects on translucent/transparent materials, as measured by absorption, transmission, hazemeters, etc. are added parameters to those of standard stress-induced crazing/cracking, impact, and vibration tests. At best, there are difficult tests to interpret and quantify, but serve for screening assessments. Additionally, transmission or modulation of the electromagnetic frequency spectrum (UV-VIS-IR-far-IR-microwave-rf) requires advanced coating/application technology with new formulation problems.

II. DISCUSSION:

The above all point to the difficulties involved in "normal" environmental/chemical resistance tests and translation to predictive capability from aging, weathering, or chemical exposures. If, therefore, selection of chemical delivery systems of concern can be made with reasonable confidence and combined with appropriate mechanical static/dynamic testing, a major accomplishment will be achieved. Product manufacturers will have a standard/guideline to formulate for predictive exposures. If, however, inadequate or inappropriate selection of simulants/test methods result and are included in governmental/mil specs, a major, serious problem will develop.

Because of these factors, basic understanding of the physical/chemical phenomena that are involved in the test procedures must be established concurrently. The need for fundamental knowledge of engineering plastics behavior is critical as design criteria are developed. The composites, adhesives, and structural polymers industry has recognized this need (spurred by the Challenger loss) and the current literature listed in the Appendices attest to this situation. National Centers for Excellence and focused academic/research institutes are listed for many of these materials-oriented fundamental research/development areas. Industrial technical centers have focused on these aspects related to their specific product needs. A list of pertinent references and general approach of industrial researchers in chemical/mechanical field is in Appendix. Indeed, the role of Nondestructive Testing (NDT) is of increasing significance and interaction with the Center for Nondestructive Evaluation at Johns Hopkins is assured.

The active ASTM committee F-7 on Aerospace and Aircraft maintains eight subcommittees, including a specific one, 7.08, for transparent enclosures and materials. A recent meeting in Texas is included in the Appendix for the most timely, specific coverage in this area. Furthermore, inclusion of the article from Modern Plastics Encyclopedia 1986-1987 "Selecting Plastics for Chemical Resistance" provides one of the best, clear and comprehensive evaluations of fundamental concerns (mechanism of chemical attack, critical conditions in chemical resistance testing, interpretation of data and typical environmental/stress-crack resistance tables for acrylics, polycarbonates, and polyimides). CRDEC/GEO-CENTERS representation on this subcommittee (and on the 7.02 Propellant Technology) will ensure timely, significant information flow for research program development.

III. INSTRUMENTATION:

a. Manufacturers of instrumented mechanical testing have responded to the above need for improved hardware/software with which to study engineering plastics. The automated systems and accompanying software provides a major improvement to the mechanical testing community. Industrial researchers now probe fundamental and practical regimes of polymer structure-property relationships with improved data-gathering and interpretation capabilities. However, proper experimental design focused on a given problem is still fundamental to the valid data generation and interpretation of the method. Applied polymer science requires such multivariate analytical capabilities at both the mechanical testing level, as well as in the chemical/physical research level.

For these reasons, Appendixes in this survey covering these resources list the advantages and disadvantages of commercially available polymer testing equipment.

b. Additionally, the analytical chemistry instrumentation appropriate to these studies and available at CRDEC include the full range of spectral, chromatographic, thermal, and microscopy tools. In conjunction to other projects, incorporation of a mechanical testing/chemical resistance program into the CRDEC artificial intelligence (AI) network, EXMAT, would be relevant and direct. The acknowledged reference in this regard is the monograph by Kaeble, "Computer-Aided Design of Composites", wherein the need to study structure-function by pragmatic methods based on fatigue and fracture mechanics is clearly applied to the complementary tools of the analytical chemist.

In the propellant field, researchers at BRL have undertaken such a program with newly installed dynamic mechanical testing equipment (MTS, Inc.) to correlate with combustion/physicochemical analyses on the formulated propellant systems. Additionally, by extending the initial AI effort (that led to the CRDEC capability), BRL has reported developing an expert system to aid in propellant formulation. This will enable expertise in the propellant formulation field to be encoded and provide guidelines to design performance criteria from experimental data. The viscoelastic behavior of polymer binders in these materials dominate the macromechanics just as in structural engineering systems, such as the transparent/translucent materials. Hence, instrumentation and interpretive expertise will focus on BRL's unique requirements within those polymeric systems.

IV. Summary:

A most basic theme is acknowledged by material scientists:

Physical property behavior of polymers is based on their detailed microstructure and processing variables or stated otherwise: microstructure/micromechanics dictate macromechanics/macrobehavior. Knowledge of polymer microstructure/viscoelasticity and composition is thus obtained with test/analytical instruments and integrated into predictive behavior scenarios. A most useful reference, "Plastics Polymer Science and Technology, M. Baijal, Ed., Wiley, NY, 1982, is recommended reading for all researchers getting involved in the polymer structure-property testing field. Selected portions are included in this survey from several chapters but the most pertinent is that on Environmental Resistance. Professor Rudy Deanin, Lowell University (Lowell, MA) is highly recommended as the most preeminent polymer specialist in this area. Additionally, SAMPE, SPI, SPE and other groups involved in plastics technology are basic reference sources. The complexity of the problem and the magnitude of the consequences as new plastics are developed for specialty uses demand no less than such a comprehensive approach. This survey brings together information reflecting this philosophy and emphasizes the need for expedient, pragmatic evaluation of the field. While focused on chemical/mechanical testing of transparent/translucent materials, extension of the compiled information to modern plastics/composites technology is obvious.

APPENDICES

I. Fundamentals of Plastics Testing and Analysis

   A. ASTM F7.08 Aerospace Transparent Enclosures and Materials

   B. Computer-Aided Design of Polymers and Composites

   C. Plastics Polymer Science and Technology

   D. Handbook of Plastics Technology

   E. Polymer Characterization

   F. Toughness and Brittleness of Plastics

   G. Pyrolysis and GC in Polymer Analysis

   H. Modern Plastics Encyclopedia 1986-87 Testing; Chemical Resistance

   I. Composite Failure Analysis

   J. The Fracturing of Glass

   K. Polymer Critical Surface Tensions

   L. Surface Activity at Organic Liquid

   M. Air Interfaces

   N. Immersional Wetting of Solid Surfaces

   O. Attractive Forces at Interfaces

II. Literature References on Polymer Testing, Fracture Mechanics, and Fatigue; Material Sciences, Coatings, Composites

III. Research Institutes, Courses, Seminars and Services for Polymer Technology

   A. Univ. Delaware, Center for Composite Materials

   B. Johns Hopkins University, Center for Nondestructive Evaluation

   C. Amer. Institute of Aeronautics and Astronautics - Technical Information Service

D. Automated Material Testing - Fatique Technology, Inc.

E. Testing and Training Services - Strainoptic Technologies, Inc.

F. Analytical Services, Air Products and Chemicals, Inc.

G. Miscellaneous Seminars, etc.

IV. Mechanical Test Equipment for Plastics

A. Destructive

1. Standard Tests - Celanese
2. Sintech
3. Tinius Olsen
4. MTS, Inc
5. Applied Test Systems, Inc.
6. Instron
7. Laboratory Microsystems, Inc.
8. Dynatup - General Research Corp.
9. Rheometrics
10. Polymer Laboratories
11. Haake Buchler Instruments
12. Sangamo Schlumberger
13. C.W. Brabender Instruments
14. Fatigue Dynamics, Inc.

B. Non-Destructive

1. Hydrostatic and X-ray (US XFS)
2. Liquid Penetrant
3. Acoustic Emission
4. Photoelastic/Shadow Moire

5. SPATE Dynamic Stress by Thermal Emission

6. Ultrasonics

7. Holograms, Pulsed Laser Interferometry

V. Analytical Methods/Instruments

A. IR, NIR, NMR Spectroscopy

B. ESCA/SEM/TEM

C. Thermal Analysis

D. Dynamic Headspace, Pyrolysis GC, Inverse GC

E. Video Thermography

F. Image Analysis/Microscopy

VI. Materials

Polycarbonates, Polyurethanes, Polyacrylics, etc.

PERSONAL CONTACTS/REFERENCES

ASTM F-7 Committee Aerospace Materials

*Nelson Gould, NV Pro (Lockheed) 818-847-2282

ASTM D-2Ø Plastics
(Chm, R.B. Waller, Bell Labs, Holmdel, NJ Ø7733)
J.A. Blair, DuPont, PPD, Wilmington, DE

Dennis Riddle, Chris Thole, Grumman Aircraft,
Chairman, ASTM Subcom. 7.Ø8 516-575-26Ø4
*Task Force, Hostile Environ/Crazing/Stress Weathering
Malcolm Kelly AF 513-255-6Ø24

GE (LEXAN)
M.D. Bertolucci, Mgr. Lexan 812-838-761Ø
Bill McNally, QA Mgr, (Blend) Valox Line x 7569
*Randy Reed 812-838-78Ø4, Solvent Resistance
Dr. Don McGrand - Research/Tests/etc.
Rich Rische, 413-448-465Ø (AI Expert System)
Jim Rieke, Dow Chemical (Midland, MI) 517-636-4252
Polymer Mechanical Testing and Chemical Resistance
Dr. Dan Scola, United Technologies (E. Hartford, CT)
2Ø3-727-7268
Dr. Paul Frayer, Dartco Mgr, (August, GA) Composites, Rigid
Rod Polymers, 4Ø4-79Ø-31ØØ
Jim Peraro, Rockwell International (Troy, MI)
Composites, Coatings
Dr. Tom Santosusso, Lord Corp. (Erie, PA), 313-435-12Ø1
Coatings
Vickie Sholtes, Boeing Vectol (Phila, PA) 215-591-2581
Composites
*Jim Tillman, Owens-Illinois, (Toledo, OH) 419-247-7Ø47
Glass Resins
re: Bob Fogerty (Goodyear Aerospace) Coatings
Optical Technologies (NY) & PPG/Scott Aviation, Oregon
Lance Teten, TEXSTAR, 214-647-1366
V.O. Brinkman (Douglas Aircraft) Long Beach, CA
Don Chapin, Sierracin, CA 818-362-6711 (Video
Thermography)
PPG, Resins and Coatings Div., and Glass Div, Phys.
Testing/Res
Bill Englebert, Mgr., 412-665-8796 (Huntsville, AL)
*Bill Heidish, Dir. R&D, 2Ø5-539-2975 (859-25ØØ Factory)

APPENDIX E

GEO-CENTERS, INC.

CARYSPEC

A FORTRAN 77 Program For
Spectral Data Acquisition And Control Of
The Varian CARY 2390 UV–VIS–NIR Spectrophotometer

Robert A. Binstead,
GEO–CENTERS, Inc.,
10903 Indian Head Highway,
Fort Washington, MD. 20744

and

John C. Cooper,
Chemistry Division,
Naval Research Laboratory,
4555 Overlook Avenue,
Washington, D.C. 20375–5000

CONTENTS

Section	Description	Page
INTRODUCTION		1
IMPLEMENTATION		
1.0	Hardware Interface	2
1.1	System Handshaking	2
1.2	Instrument Commands Format	3
1.3	Instrument Commands Summary	7
1.4	Real Time Transmission Data Format	9
1.5	Illegal Parameter Changes	10
SOFTWARE DESCRIPTION		
2.0	Purpose Of CARYSPEC	11
2.1	Language Features Of CARYSPEC	11
2.2	Structure Of CARYSPEC	12
2.3	BLOCK DATA	22
2.4	SUBROUTINES	24
2.5	FUNCTIONS	31

... cont'd

Section	Description	Page
PROGRAM CODE		
3.0	Source Code Availability	31
3.1	Variable Names And Usage	31
3.2	Program Listing	36

LIST OF TABLES

TABLE	Description	Page
I	ASCII Codes For Touch Panel Keys	6
II	Data File Format	21
III	Glossary Of Integer Variables	32
IV	Glossary Of Real Variables	33
V	Glossary Of Character Variables	34

CARYSPEC

A FORTRAN 77 Program For Spectral Data Acquisition And Control Of The Varian CARY 2390 UV-VIS-NIR Spectrophotometer

INTRODUCTION

The CARY 2300 and 2400 series spectrophotometers are high quality, microprocessor controlled analytical instruments intended for measurements of the UV-Visible and Near IR absorption spectra of solids, liquids and gases. When equipped with an optional IEEE-488 standard interface these instruments and their accessories are programmable by an external computer system enabling acquisition of spectral measurements in digital form. This document describes a fully tested FORTRAN 77 program, CARYSPEC, designed for *single scan* acquisition of spectra from a CARY 2390 instrument using a Hewlett-Packard 1000 minicomputer running the multi-user CI shell and RTE-6/VM operating system. The program uses very few machine specific functions and could be modified easily to run on other host systems supporting the IEEE-488 interface standard.

CARYSPEC implements a large subset of the programmable instrument control functions of the CARY 2390 spectrophotometer in a menu driven format closely resembling the menu displays on the instrument. Therefore, no special training is required for users already familiar with operation of the instrument. Indeed, operation from a computer console has proven to be more convenient than using the clumsy keypad on the instrument. The control functions implemented reproduce the facilities of the spectrophotometer's Instrument Settings, Baseline Setup, Lamp and Detector Modes and Accessory Setup menus, as well as a number of single keypad functions. The program *does not support* the statistics calculation modes, rapid scan setup keys or the automatic sequencer operation for repetitive scans. The latter mode, although useful, is not compatible with reliable IEEE-488 data transmission. A future version of the program may implement this feature using the the single scan mode of CARYSPEC with automatic data file storage and system clock control of the timing of successive scans.

CARYSPEC is a moderately large program and will not run in a single 32K word segment of the Hewlett-Packard 1000 minicomputer. The program has been segmented to run in 5 memory resident nodes of the HP 1000 using the Multi Level Segmentation utility programs SGMTR and MLLDR. The program requires an 83K word memory partition, including 40K words of Extended Memory Addressing (EMA) space for data arrays.

IMPLEMENTATION

1.0 Hardware Interface:

The IEEE-488 interface for the HP 1000 system is implemented with an HP 59310B interface card which utilizes 4 Logical Unit (LU) addresses in the system. The LU addresses are dependent on the computer system and are defined by the system generation. The interface card used by the program, CARYSPEC, occupies LU addresses 35-38 corresponding to card addresses 0-3. Address 0 is a special addressing mode which allows access to low level IEEE-488 bus command sequences for any device number. Addresses 1-3 are predefined automatic READ/WRITE channels which select device numbers 1-3 on the bus. CARYSPEC uses automatic device addressing from channel 3 (LU 38) and consequently the device address of the CARY 2390 has been set to 3. Physical connection between the computer and spectrophotometer consists of 5 metres of IEEE-488 standard cabling. Reliable data transmission was obtained with cable lengths up to 9 metres. With 13 metres of cable commands sent to the CARY 2390 were accepted but data transmissions from the CARY 2390 spectrophotometer were corrupted owing to the limited drive capability of the MC3447L bus transceivers in the CARY 2390. The bus was found to be totally inoperative with a cable length of 17 metres.

1.1 System Handshaking:

The IEEE-488 subsystem of the HP 1000 is operated by the RTE driver DVA37 configured for ASCII Data Record mode. This mode sends and expects to receive an End Of Record (EOR) with data transmission in the form of a Carriage Return/Line Feed (CR/LF) sequence, though Line Feed alone is sufficient. The CARY 2390 accepts commands in this format automatically. However, the instrument must be instructed to send data with the CR/LF trailer using the command "@@20", sent as a series of ASCII characters to the instrument. This is the first instrument command in the program CARYSPEC and instructs the CARY 2390 both to insert CR before LF on transmissions and to turn off check sum error detection. Therefore, all commands to the instrument end with a check sum byte of zero. Correctly operating IEEE-488 systems do not quire check sum error detection. During real time spectral data transmission the CARY spectrophotometer is the active talker on the bus. The End Of Record character for this mode has been specified as a Line Feed in CARYSPEC - this works without a CR, as expected for IEEE-488 handshaking. Termination of real time transmission is effected by the active controller via a bus level routine which sends the ASCII codes for UNTALK/UNLISTEN.

1.2 Instrument Commands Format:

Programmable control of the CARY 2300-2400 series spectrophotometers has been implemented by Varian Instruments with a series of *single character* commands in ASCII code, most being accompanied by following characters to select a particular setting for the command selected. The instrument generates similar reply messages to most commands and these character strings must be read by the controller before sending further commands.

Varian's documentation defines the command structure as a sequence of [ASCII] characters in the following format (blanks added for clarity):

[LDI] [MI] [MD] [MQ] [CSM] [EOI]

where,

[LDI] = Logical Device Identifier

ASCII representation of the talk address of the sender - the value is ignored but some character must be sent as a place holder. {NOTE: The correct character for the bus controller at address 0 is "@"}.

[MI] = Message Identifier

ASCII character C, P or N used to indicate the message type as Command, Positive reply or Negative Reply. {NOTE: This character field is actually INVALID within a command - 'C' will cause a system reset if used}.

[MD] = Message Descriptor

ASCII character which specifies the actual command to be executed.

[MQ] = Message Qualifier

A string of characters used to set one or more variables or operating modes.

[CSM] = Check sum

The binary sum of all characters in a particular message – this is always the "0" character since checksum mode is turned off normally.

[EOI] = End Or Identify (actually End Of Record)

A linefeed character is specified as the terminator character to end data transmissions. {NOTE: This is appended automatically by most IEEE-488 drivers during handshaking.}

The [MI] field given in the message structure above is actually invalid within a command and must not be used – otherwise command 'C', system reset, will be executed followed by a bus hang up on the trailing unused command characters. However, the [MI] field is valid in the reply messages from the instrument.

The correct COMMAND format is given by the following fields:

[LDI] [MD] [MQ] [CSM] [LF]

EXAMPLE: Send the Record Trailer Set-up Command '@'

```
      Command='@@20'
      WRITE (UNIT=38,FMT=10) Command
10    FORMAT (A4)
      READ (UNIT=38,FMT=20) Reply
20    FORMAT (A64)
```

where,

@ = [LDI] address of bus controller
@ = [MD] command for record trailer set-up command
2 = [MQ] value to select no check sum (bit 1 = 0), insert CR before LF
0 = [CSM] check sum (off)
LF is sent automatically with WRITE command

All instrument commands sent to the CARY 2390 by an external computer comprise a sequence of ASCII data characters as far as the IEEE-488 bus is concerned. The details of the handshaking, with talk and listen addresses, are transparent to high level languages such as this implementation of FORTRAN 77 where such details are handled automatically by the device driver – in this case DVA37. Unfortunately, Varian Instruments chose to document the software control of the 2300 series instruments for a particular dialect of BASIC used in their proprietary controller, a model DS-15 data station, which appears to operate in a purely binary mode on the IEEE-488 bus. Thus, their examples of the message structure include a line feed character appended to the actual data command message. Furthermore, they confuse this End Of Record character (EOR) with the title of the End Or Identify handshake line of the IEEE-488 bus. The trailing line feed character is omitted from all instrument commands in the program CARYSPEC, this terminator being supplied automatically by the HP 1000 driver routine using the standard FORTRAN output command, WRITE.

While the reply messages generated by the CARY spectrophotometer must be read, only a few require testing for negative replies in a correctly structured program. CARYSPEC utilizes tight error trapping for inappropriate combinations of instrument parameters, diminishing the need for extensive use of the error message numbers from the instrument. In fact, only the Baseline Set Up subroutine checks for a negative reply and even that is probably superfluous since illegal combinations of operating modes are trapped before calling this routine. Such internal errror trapping provides a smoother user interface compared with taking corrective action after rejection of bad commands by the instrument.

The full range of instrument commands and their reply formats are summarized below in Section 1.3. Some commands can be accessed only using the 'D' command to mimic key pad presses on the instrument. These often involve sequences of key presses to implement a single function. Table I contains the ASCII codes required to send Key Pad entries with the 'D' command. However, full familiarity with the instrument is required to use these effectively. For example, the Baseline Set Up procedure could be implemented by sending a large number of Key Pad sequences but a more efficient means is the 'J' command which includes all of the requested baseline parameters in a single string.

TABLE I

ASCII Codes For Touch Panel Keys

KEY	DECIMAL	ASCII
0	48	'0'
1	49	'1'
2	50	'2'
3	51	'3'
4	52	'4'
5	53	'5'
6	54	'6'
7	55	'7'
8	56	'8'
9	57	'9'
.	58	':'
CLEAR	59	';'
CHANGE	60	'<'
ENTER	61	'='
ABS vs WLNGTH	64	'@'
ABS vs TIME	65	'A'
SEL WLNGTHS	66	'B'
INSTR SETTINGS	67	'C'
LAMPS & DETECTORS	68	'D'
AUTO OP	69	'E'
ACCRY SETTINGS	70	'F'
CALC MODE	71	'G'
BASLN SETUP	72	'H'
TEST FUNCTION	73	'I'
GOTO WLNGTH	74	'J'
LOCK	75	'K'
START	80	'P'
STOP	81	'Q'
RESUME	82	'R'
STANDBY	83	'S'
READY	84	'T'
AUTO BALANCE	85	'U'
CASSETTE	88	'X'
PRINT	89	'Y'
RIGHT CURSOR	104	'h'
LEFT CURSOR	105	'i'
MANUAL SCAN +	106	'j'
MANUAL SCAN -	107	'k'

1.3 Instrument Commands Summary:

'A' Lock or Unlock Keyboard

Command - '@AX0' where X - 0,1 (Unlock, Lock)

Reply - '#PAX0'

'B' Status Request

Command - '@B0'

Reply - '#PB[*data*]0' 5 bytes of *data* are returned

'C' System Reset

Command - '@C0'

No Reply

'D' Activate A Touch Panel Key

Command - '@DX0' where X - ASCII code for Key

Reply - '#PDX0'

Reply - '#NDX0'

'E' Dump Parameter Table

Command - '@E0'

Reply - '#PE[*no. of data bytes*][*data*]0'

'F' Accessory ON/OFF Control

Command - '@FXY0' where X - 0,1 (Turn Off, On)

where Y - Accessory Number

Reply - '#PFXY00' where 0 before CSM - no error

Reply - '#NFXY[*error no.*]0'

'G' Return Value Of Parameter Or Variable

Command - '@G1Y0' Y - Index Number Of Parameter

Reply - '#PG1Y[*string length*][*string*]0'

Command - '@G2Y0' Y - Index Number Of Variable

Reply - '#PG2Y[*value*]0'

Reply - '#NGXY[*error no.*]0' for X - 1,2

'H' Change Value Of A Parameter

Command - '@HXY0' — where X - Parameter Number

where Y - Required Index Value

Reply - '#PHXYZ0' — where Z - New Index Value

Reply - '#NXY[*error no.*]0'

'I' Change Value Of A Variable

Command - '@IX[*number*]!0' — where X - Variable Number

Reply - '#PIX0'

Reply - '#NIX[*error no.*]0'

'J' Set Up A Baseline

Command - '@J[*value 1*]!...[*value 9*]!0'

Reply - '#PJ00' — where 0 before CSM - no error

Reply - '#NJ[*error no.*]0'

'K' Request Real Time Data Transmission

Command - '@K1Y0' — Interval mode

Command - '@K3Y[*interval*]!0' — Continuous mode

where Y - 0-3 specifies delimiter (0, LF, CR, &)

Reply - '#[*data*]!...[*data*]![EOR]#...

Reply - '#NKXY[*error no.*]0' — where X - 1,3 (mode)

'L' Display Message On Line 4 Of C.R.T.

Command - '@L1[*message*]0'

Command - '@L00' — Turn Off Message Display

Reply - '#PL0' — No Negative Reply

'M' Accessory Mode Set Up

Command - '@MX[*value*]!0' — where X - Parameter Number

Reply - '#PMX00' — where 0 before CSM - no error

Reply - '#NMX[*error no.*]0'

'@' Record Trailer Set Up

Command - '@@Y0' — where Y - 0-3 (2 for CR/LF)

No reply

1.4 Real Time Transmission Data Format:

The 'K' command selects one of two real time transmission modes with the CARY spectrophotometer as the active talker on the bus. The continuous mode transmits data at the frequency of the instrument's chopper motor (15 Hz at line frequeny = 60 Hz) in an abbreviated format of Ordinate and Abscissa. The more useful mode, as used in CARYSPEC, is the programmed interval mode which transmits 9 instrument measurements. This increases the overhead for each datum but the extra string processing time has been found to be insignificant for the HP 1000 system. CARYSPEC limits the choice of scan speed and wavelength interval for a maximum transmission rate of 5 Hz. This modest rate is determined by the interrupt service times of the multi-user operating system rather than program processing speed.

The data format for the programmed interval mode varies with the choice of Ordinate and Abscissa modes for the CARY 2390. The data acquisition subroutine ACQUIRE within CARYSPEC supports all 6 choices of Ordinate mode and the 4 choices of Abscissa. However, the main portion of CARYSPEC rejects any choices other than Absorbance or Transmittance *vs* Wavelength which send data in the following formats:

A typical record for Absorbance *vs* Wavelength: (59 characters)

```
#   0.0012! 2000.00!1!01!128! 2000.00!     0.0!  28.72!-199.83!
```

A typical record for Transmittance *vs* Wavelength: (58 characters)

```
# 100.06! 2000.00!1!01!128! 2000.00!     0.0!  28.72!-199.73!
```

These fields correspond to Ordinate, Abscissa, Cell #, Cycle #, Sample #, Wavelength, Time, Temperature and Gel Scanner Distance. Transmissions from the CARY 2390 are read left-justified into a CHARACTER variable dimensioned to length 64. This is sufficient for all operating modes and makes ACQUIRE a general purpose subroutine for use in other programs. Since the record format is fixed for each choice of Ordinate and Abscissa there is no need to search the data strings for the '!' delimiters. CARYSPEC begins substring extraction at character position 2 and uses arrays XOFF(I) and YOFF(J) to determine the offsets for the first two data fields. The remaining substrings are fixed length and their boundaries are calculated from the sum of the lengths of the first two data fields.

1.5 Illegal Parameter Changes:

Several instrument parameters have been masked off from changes by an external computer, so becoming READ ONLY. The slit height parameters #22 & #26 are not programmable since the slit height is a manual adjustment. The Baseline parameters also are intended to be READ ONLY in order to prevent overwriting the descriptors for a current baseline. Hence, parameters #23 – #26 are updated only when a new Baseline request is sent using the 'J' command. The Baseline status parameter #37 has limited accessibility and can be turned ON or OFF only. CARYSPEC also allows parameter #37 to be set to the RECORD and ON/SETUP states by issuing Key Pad sequences with the 'D' command. However, CARYSPEC does not use these settings to actually record the Baseline. The settings are used only to transfer setup information between the instrument and baseline menu parameters for users accustomed to this feature.

Unfortunately, two setup parameters, DERIV TEMP RANGE (#11) and TEMP ZERO (#13), have also been masked off making it difficult to control the CARY in some operating modes. However, it was discovered that the DERIV TEMP RANGE can be set by using parameter #10, the DERIV RANGE settings for Absorbance and %T. Thus, parameter #11 appears to be an internal table only. Special action has to be taken in selecting the derivative range settings since only the 1,5,10 sequence is valid while a 1,2,5,10 sequence can be selected. CARYSPEC includes an INDEX array variable which holds the valid indices for the derivative modes. This allows derivative spectra to be drawn while the external computer acquires the raw measurements. While CARYSPEC does not allow acquisition with TEMPERATURE as the Ordinate or Abscissa, the functionality of the Temperature setup modes is preserved with one exception. The TEMP ZERO parameter can not be set from the external computer and only the range can be selected from CARYSPEC. Since this is not a feature required for CARYSPEC no attempt has been made to issue a Key Pad sequence for TEMP ZERO.

The CARY 2390 also masks off the %T offset variable (#10) when the 200 %T range is selected. This appears to be designed so that only a 0–200 %T range can be selected. However, if a non–zero offset has already been set for another scale then selection of the 200 %T range will not result in a 0–200 %T scale – it will have the old offset. This illegal mode can be reset by changing to another range and setting the offset to zero before selecting the 200 %T range again.

SOFTWARE DESCRIPTION

2.0 Purpose Of CARYSPEC:

The collection of spectrophotometric data in digitized form provides both a permanent means of storage and the ability to perform more sophisticated analysis. While the instrument obtains spectral measurements as absorbance *vs* wavelength (nm), plotting programs can rescale the raw data into more meaningful units such as molar absorptivity *vs* wavenumber (cm^{-1}). Techniques such as difference spectroscopy no longer need to be performed in real time since data files can be manipulated easily to achieve this function by scaling and subtraction. Noise can be removed from single scan spectra using least squares smoothing while similar functions can be used to generate derivative spectra which are more accurate than those produced in real time by the CARY 2300–2400 series spectrophotometers on their internal pen recorders. Such benefits make it worthwhile to develop software for data transfer between the CARY spectrophotometer and an external computer system, in this case a Hewlett–Packard 1000 minicomputer running the CI shell and RTE–6/VM operating system.

2.1 Language Features Of CARYSPEC:

The program CARYSPEC was written in FORTRAN 77 since this language provides the most complete set of interface and control functions available on the HP · 1000. The communication between FORTRAN 77 and the IEEE–488 interface to the CARY 2390 spectrophotometer is completely transparent and standard READ/WRITE statements control the operation of the instrument and the collection of data transmitted by the CARY. Therefore, the program is portable, with some minor alterations, between systems supporting the FORTRAN 77 language and IEEE–488 Input/Output. CARYSPEC uses three machine specific function calls requiring substitution to run on a different host system. The first is CALL FFRCL(79) which changes the free field record length from the default value of 72 to 79. This is used to provide more column space on the console display screen. The second is a call to read the system clock to provide calibrated delay loops. Thus the operation of SUBROUTINE Wait(DELAY) and FUNCTION Time(I) would need to be altered. The third is CALL ABRT(35,3) which terminates transmission from the CARY by sending UNTALK/UNLISTEN on the IEEE–488 bus. Syntactical differences also appear between various versions of FORTRAN 77, particularly in the READ/WRITE statements. CARYSPEC uses the format READ (1,...) and WRITE (1,...) for the user's console (defined as LU·1) while Microsoft's compiler uses an * to denote the console unit.

2.2 Structure Of CARYSPEC:

CARYSPEC comprises a large main program unit containing most of the console menu displays, block data for named COMMON variables and a number of subroutines that perform string processing, input validation and communication with the CARY 2390 spectrophotometer. The main program is responsible for all the logic flow and the subroutines execute specific support tasks, which are summarized below:

The main program unit of CARYSPEC comprises 9 distinct segments of code to carry out the the functions of instrument setup, spectral data acquisition and disk file data storage. The code fragments appear under the following assigned labels: MENU, SPECTRUM, BASELINE, ADVANCED, INSTRUMENT, LAMP, ACCESSORY, STORE and EXIT.

MAIN PROGRAM

MENU:

This is the first and main control menu of the program, selecting entry to the remaining instrument control menus, data acquisition, storage and exit routines. The choices are as follows:

'A'.....Acquire Spectrum

This selection branches to label SPECTRUM and performs logical tests for the presence of a valid Baseline in the CARY, valid choices of Abscissa/Ordinate modes and the presence of an unstored spectrum in memory before proceeding with data acquisition. If there is no valid Baseline information in memory the program will branch to label BASELINE. If the Abscissa/Ordinate settings are inappropriate the program will branch to label INSTRUMENT.

'B'.....Baseline Setup

This selection branches to label BASELINE which reads the current instrument settings and presents the pertinent Baseline parameters in a menu arrangement similar to the equivalent display on the CARY. The user can alter these selections but most will not take effect unless a new Baseline scan is recorded on exit from this menu. Otherwise, an exit is made to the main MENU with the instrument baseline settings intact, a feature of the CARY which prevents inadvertent alterations to the parameters describing the current instrument Baseline.

'I'.....Instrument Settings

This selection branches to label INSTRUMENT, reads the current instrument settings and presents the most important in a menu arrangement similar to the equivalent display on the CARY. The user may alter these instrument settings and any changes are implemented immediately by the instrument. If such changes affect the quality of the Baseline matching for a subsequent acquisition scan then the changes will be overridden automatically, if possible. Otherwise, the user will be directed to record a new Baseline scan with the altered settings, followed by acquisition of the spectrum. In most cases the automatic matching routines will take effect to provide a smooth user interface.

'L'.....Lamps/Detectors/Accessories

This selection branches to label ADVANCED and reads the current instrument settings and presents a number of menu selections for subsidiary functions and operating modes of the CARY. Selection '1' branches to label LAMP and presents a menu which lists the status of the lamp and detector modes, which then may be altered. Selection '2' branches to label ACCESSORY and presents a menu which lists the status of the temperature and printer accessories, which then may be setup as desired. Selection '3' for automatic operations is not yet supported.

'S'.....Store File On Disk

This selection branches to label STORE and prompts the user for entry of pertinent file information before saving a data file to disk. This routine includes standard error checking for File Exists, File Open and disk transfer errors. The user is returned to the main MENU on exit.

'X'.....Exit

This selection braches to label EXIT and checks for the presence of an unstored spectrum which causes a prompt for confirmation before proceeding. The user then has the option of setting the CARY to standby mode, if desired, before the program stops.

SPECTRUM:

This portion of CARYSPEC controls the acquisition of a spectrum from the CARY 2390 spectrophotometer. On entry, this code will check important instrument parameters and status variables and perform conditional branches to BASELINE, INSTRUMENT or MENU if the conditions outlined above are not satisfied. A successful entry will display a reques for the wavelength scan limits, which default to the Baseline scan range. New limits may be chosen and are validated for the range 185–3152 nm. {The limits may exceed the Baseline range but this will cause a subsequent call to SUBROUTINE Bline with the new limits and current instrument settings before returning to the data acquisition loop.}

The remaining entry required is the step size interval (0.01–5 nm) during the scan. The instrument is capable of 0.01 nm steps in the UV–VIS region or 0.04 nm in the Near IR. No restrictions are placed on the user in this regard but it is *strongly recommended* that sensible units be chosen, *e.g.* .1, .2, .25, .5 nm. The program will reject combinations of scan rate and step size which would result in the data rate exceeding 5 Hz. This restriction is a result of the rather slow multi–user environment of the HP 1000 rather than a processing speed problem. Either scan rate or step size may be altered to meet this condition. Finally, the wavelength range and step size are used to check the number of data points for the scan. If the request exceeds 10001 points the user is prompted for a new step size.

After satisfying the basic conditions above the program will perform a number of checks on the current operating conditions of the CARY 2390 to determine whether these will match the conditions for the Baseline scan. Mismatched settings of SBW (nm) and GAIN will be reset automatically to smooth over some instrument peculiarities. Other mismatches are assumed to be operator requirements and result in a prompt to record a new Baseline scan. The user may either proceed or abort this operation and return to the main MENU to take corrective action.

Successful traversal of all the matching checks will present a listing of scan parameters and a prompt to Start or Abort the scan. Aborting will return the user to the main MENU and restore the parameter strings describing any previous spectrum in memory. Starting will position the monochromator to the starting wavelength and prompt for Print to Screen during the scan – removal of this I/O overhead helps prevent missed data with several users on the HP 1000. The remainder of the acquisition is automatic, returning to the main MENU after completion.

BASELINE:

The current instrument Baseline parameters are read on entry to this section of CARYSPEC for display in a menu format similar to the Baseline Setup menu on the instrument. This code is responsible for the selection of all relevant parameters for a new Baseline scan. However, since most of these parameters are masked from direct changes by the computer, via SUBROUTINE Select, a number of inappropriate combinations are tested for after each new selection is made. These tests reset the bad parameter requests to the most appropriate selection thereby eliminating the rejection of any parameters in subsequent calls to SUBROUTINE Bline. After validation of the Baseline parameters the program tests whether the operating mode at the start of the scan will be AUTO GAIN (MODE = 1) or AUTO SLIT (MODE = 2). The integer variable MODE then controls the logical operation of the remainder of the program and SUBROUTINE Bline where choices between SBW and GAIN settings are important for determining or controlling the operation of the CARY 2390.

A special exit is made from the BASELINE code for setting the instrument GAIN level if the requested value exceeds the current setting by more than a factor of 10, which can result in misbeaviour of the slit servo system of the CARY 2390. A sudden, large increase in GAIN should just send the instrument closer to zero slit width. However, on *this* CARY 2390, at least, the slit width can overshoot through zero and continue to fully open the slits with high gain, seriously imperilling the detectors! To prevent such a disaster the program will select AUTO SLIT mode and branch to line 490, which is part of the INSTRUMENT code fragment. This subsection resets the current instrument GAIN in factors of 10 until it matches the new Baseline request. The logical variable TRANSFER controls the exit from this routine back to BASELINE.

On exit from the Baseline Setup menu the user may either record a new Baseline or return to the main MENU. Both options read the current instrument parameters before returning to MENU, keeping the program updated. This is performed by re-using part of the code at the start of the BASELINE fragment under the control of logical variable TRANSFER. If a new Baseline is recorded the program will monitor the instrument until completion of the procedure and then issue an AUTO BALANCE command to zero the instrument on the reference material. Subsequent data acquired via the SPECTRUM fragment will therefore produce baseline corrected spectra.

ADVANCED:

This portion of CARYSPEC presents a small menu of subsidiary instrument setup functions that may need to be changed occasionally. The selection are:

'1'.....LAMPS & DETECTORS

This selection will display a further menu which lists the current status of the LAMP POWER, LAMP SELECT and DETECTOR SELECT modes. Normally, both lamps are ON and the lamps and detectors are in AUTO SELECT mode. These settings can be changed to increase the working wavelength range for the individual lamps or detectors. {NOTE: Individual selection of a lamp or detector prevents lamp or detector changes and thereby prevents coverage of part of the wavelength range accessible with AUTO SELECT modes.}

'2'.....ACCESSORY SETTINGS

This selection allows the user to turn on and setup two installed accessories, the TEMPERATURE READOUT and the thermal PRINTER. On entry to this routine both accessories are commanded to an OFF status. If a positive reply is received from the CARY that parameter is reset to ON. If the TEMPERATURE accessory is selected and turned ON a small menu is presented for selection of the TEMPERATURE RANGE. If the PRINTER option is selected and turned ON a subsidiary menu is presented to select the operating mode and interval step size for printer output. The modes supported are Wavelength, Time and Temperature. However, CARYSPEC only acquires data in Wavelength mode.

'3'.....AUTO OPERATIONS

This selection is intended for future expansion for automatic repetitive scans. Currently, it prints an error message and returns for another selection.

'X'.....EXIT TO MENU

This entry returns to the main MENU.

INSTRUMENT:

This section of CARYSPEC reads the current wavelength and instrument settings from the CARY and presents the most important functions in a menu format that is very similar to the equivalent display on the instrument. Changes made from this menu are executed by the CARY 2390 immediately. The selections are:

'0' .....WAVELENGTH

This selection allows the monochromator to be repositioned to any valid wavelength for the current selections of Lamp and Detector modes.

'1' .....ORDINATE

Only Absorbance, %T and Temperature are selectable from this menu. However, CARYSPEC will not allow Temperature as a valid ordinate during scans.

'2' .....ABSCISSA

Wavelength, Time and Temperature are selectable from this menu. However, CARYSPEC only allows Wavelength as a valid abscissa during scans.

'3' .....SCAN RATE

The scan rate must be chosen in combination with spectral bandwidth and filter period for accurate recording of bandshape. There is a particular difficulty in the 650 nm region where a Wood's anomaly causes poor baseline correction. The scan rate should not exceed 1 nm/sec per SBW (nm) per second period.

'4' .....CHART DISPLAY

The chart recorder may be used on any setting during data acquisition.

'5' .....REFERENCE MODE

The instrument is normally used in AUTO SELECT mode to allow full wavelength coverage with both lamps and both detectors. However, AUTO GAIN and AUTO SLIT modes may also be used for wavelength scans. The working range for these depends on the detector mode selected. AUTO GAIN may be used above 800 nm with the PM Tube if the UV/VIS detector modes is selected. AUTO SLIT mode can be used for the full instrument range (185-3152 nm). The reference mode for data acquisition must match that used for the Baseline scan. SINGLE BEAM mode is not valid for wavelength scans and is intended only for instrument adjustments.

'6' .....SBW (nm), GAIN

This selection allows setting of *either* the SBW or GAIN depending on whether the CARY is operating in AUTO GAIN or AUTO SLIT mode at the current wavelength. The actual operating mode for AUTO SELECT reference mode is determined by the wavelength and detector select mode. These are checked by CARYSPEC to determine the correct prompt and instrument command.

'7' .....PEN FUNCTION

The pen operates independently of the raw spectrophotometric data sent via the IEEE-488 bus to an external computer and may operate in any valid mode during data acquisition. The Ordinate choice determines which modes are valid and inappropriate selections are masked by CARYSPEC. However, it is perfectly feasible to draw a second derivative spectrum while acquiring data via the IEEE-488 bus.

'8' .....PEN LIMITS

This selection allows for setting the range and offset for all valid Ordinate modes. The NORMAL mode pen limits are selected via the Parameter and Variables Tables. The %T mode has a minor bug for the 200 %T scale. If a previous choice has set a non zero offset this will not be correctly reset to 0 %T as expected since the $\%T_{zero}$ variable is masked off by the CARY on the 200 %T scale. Similarly, the Temperature zero offset parameter *can not be changed* by an external computer, though the setting *is read* by CARYSPEC. A non-zero offset entered from the instrument keypad will be displayed but only the range can be set by CARYSPEC. The Derivative and Log(Abs) mode limits are handled by parameter table selection with special handling of the indexing to prevent use of invalid settings in the CARY firmware table.

'9' .....RESPONSE TIME (sec)

This selection allows the filter period to be set to 0.5, 1, 3 or 10 seconds.
During the recording of a Baseline the period should be set to 0.5 seconds for maximum fidelity in the 650 nm region where there is a Wood's anomaly. Failure to observe the scan rate, filter period and SBW limitations will results in improper baseline corrections. Higher period settings can be used on subsequent spectra with little prejudicial effect.

'10'.....BEAM INTERCHANGE

This selection allows the front and rear light beam paths to be interchanged between the sample and reference channels for special applications, such as the diffuse reflectance accessory.

'11'.....SLIT HEIGHT

This selection is not valid - it is a READ ONLY parameter for the manual slit height setting.

'X' .....EXIT Instrument Menu

This selection performs a return to the main MENU.

LAMP:

This subsidiary menu reads and reports the current status of the lamp and detector operating modes. The selections are:

'1' .....LAMP POWER

Normally, the instrument is operated with this parameter set to BOTH ON enabling the complete wavelength range to be covered. However, the UV or VIR/NIR selections may be made to prolong the life of a lamp. CARYSPEC *does not* automatically turn on lamps as required for a particular scan.

'2' .....LAMP SELECT

For complete coverage of the wavelength range 185-3152 nm this parameter must be in the AUTO select mode, which will result in a lamp change at 340 nm. The range covered by the individual lamps may be extended - up to 400 nm for the D_2 lamp (UV) and down to 270 nm for the tungsten lamp (VIS/NIR). However, no lamp change will then be made. CARYSPEC provides error checking for the latter two modes to prevent positioning the monochromator outside the valid wavelength limits since this would result in the instrument turning OFF the current baseline. Recovery from such a state involves repositioning the monochromator and using the ON/SETUP selection for Baseline Status in the Baseline Setup menu.

'3' .....EXIT TO MENU

This selection returns to the ADVANCED menu.

ACCESSORY:

The CARY 2390 has two installed accessories programmable by an external computer. The selections are:

'1' .....TEMPERATURE READOUT

This selection should normally be turned ON so that subsequent data files are stored with the correct temperature (a reading of 2.55 is passed by the CARY with the accessory OFF). If this selection is made and turned ON a further menu will be presented for selection of the temperature range. This only affects the pen scaling with TEMPERATURE as the Ordinate or Abscissa – not valid modes for data acquisition in CARYSPEC. Thus, selecting 100 degrees is recommended.

'2' .....PRINTER

This selection allows the user to setup the thermal strip printer to provide instrument readings at selected intervals during a scan (1 point/sec max.). While the selections include WAVELENGTH, TIME and TEMPERATURE the latter two are not valid scan modes in CARYSPEC.

STORE:

This portion of CARYSPEC provides the data file storage routine. On entry to this code CARYSPEC checks that a spectrum has been acquired and has not yet been stored. Otherwise, the program returns to the main MENU. After this validation the program will present a series of prompts for Filename and Directory information, which are then used to build a Pathname and to check that such a file does not already exist in the specified directory. If the filename is valid the user will be prompted for the LABEL, DATE, CONCENTRATION (M) and PATHLENGTH (cm) file descriptors followed by disk file storage. The data file is stored in the following format given in Table II.

EXIT:

This final portion of CARYSPEC checks that any spectrum in memory has been stored and prompts for confirmation before allowing the user to terminate the program. On exit the user may elect to set the CARY 2390 to standby mode if no further spectra will be acquired.

TABLE II

Data File Format

Line	File Variables	Format Type [a]
1	TITLE	CHARACTER (A72)
2	DATE	CHARACTER (A8)
3	XMIN,XMAX,XSTEP,CONC,PATH	REAL (*)
4	ORD,ABSC,CELL,CYCLE,SAMPLE, WAVE,TIMER,TEMP,DIST	REAL (*)
5	J,K,NARRAY	INTEGER (I3,I3,I6)
6–54	PARAM(I)	INTEGER (I2)
55	VARIABLE(I)	REAL (*)
56–*l*	Y(I)	REAL (*)
l–eof	X(I)	REAL (*)

a: (*) indicates free field format

2.3 BLOCK DATA:

All COMMON variables used by CARYSPEC are held in named COMMON blocks and initialized in BLOCK DATA immediately following the main program unit. The compiler directive /NOALLOCATE/ is used to ensure that only one block of memory is set aside during the multi-level segmentation of CARYSPEC. The variables contained within the COMMON blocks are listed below:

/MODE/ Contains COMMON INTEGER variables

NDATA Number of data points in a scan
Value set in main program
Value used in SUBROUTINE Acquire
Value stored in NARRAY in main program for disk data file

XMODE Specifies abscissa mode for selecting length of data field
Value set in main program
Value used in SUBROUTINE Acquire as index for local array XOFF

YMODE Specifies ordinate mode for selecting length of data field
Value set in main program
Value used in SUBROUTINE Acquire as index for local array YOFF

/CARY/ Contains COMMON REAL variables

ORD, ABSC, CELL, CYCLE, SAMPLE, WAVE, TIMER, TEMP, DIST
Values correspond to the 9 instrument readings sent during scan
Values set in SUBROUTINE Acquire
Values used in main program
Values stored in disk data file

/IP/ Contains COMMON INTEGER arrays

NPAR Specifies the number of settings for each instrument parameter
DIMENSION = 49
Values set in BLOCK DATA
Values used by SUBROUTINE Select for changing instrument settings

OFFSET Species the index offset in the parameter table
DIMENSION = 49
Values set in BLOCK DATA
Values used in SUBROUTINE Select for changing instrument settings

/IS/ Contains COMMON CHARACTER string arrays

Pname Specifies the names of instrument parameters for screen display
DIMENSION = (49)*10 characters
Values set in BLOCK DATA
Values used in SUBROUTINE Select

Vname Specifies the names of instrument variables for screen display
DIMENSION = (49)*8 characters
Values set in BLOCK DATA
Values not used in current version (for future use)

2.4 SUBROUTINES:

CARYSPEC uses subroutines to perform specific tasks which, with one exception, are required more than once. Terminate is setup as a subroutine solely for clarity of main program execution. The purpose and calling sequences are listed below:

Acquire(Inc,PRINT,SINGLE,WAVELENGTH)

Performs real time data acquisition from the CARY 2390 in two modes, single point for updating the current monochromator position and scan mode at Inc (nm) steps. COMMON variables XMODE, YMODE and NDATA select the correct data string format for the Abscissa and Ordinate modes selected by the main program unit and the number of data points required in the scan. The scan mode stores each Abscissa and Ordinate value in EMA COMMON arrays X and Y. COMMON BLOCK /CARY/ returns the final set of readings to the main program unit for data file storage.

/MODE/	INTEGER XMODE,YMODE,NDATA input variables control acquisition
/CARY/	REAL ORD,ABSC,CELL,CYCLE,SAMPLE,WAVE,TIMER,TEMP,DIST output
/DATA/	REAL arrays X,Y hold Abscissa and Ordinate values for output
Inc	CHARACTER*4 variable input which specifies the interval (nm)
PRINT	LOGICAL variable input which turns screen output on/off during scan
SINGLE	LOGICAL variable input which selects single datum or scan mode
WAVELENGTH	REAL variable output for single datum mode

CALLED BY: Main program unit only
CALLS: SUBROUTINE Val

Bline(WMIN,WMAX,Bdet,Bgain,Blamp,Bperiod,Brate,Bref,Bsbw,Bslit,Bscan,Btime,MATCH,MODE)

Performs a Baseline Setup by sending a list of instrument parameter requests to the CARY 2390. Validation of the instrument settings is performed by the main program unit before calling Bline.

WMIN,WMAX	Wavelength limits passed from main program unit
Bdet	CHARACTER*1 variable input to select detector mode
Bgain	CHARACTER*4 variable input to set gain value
Blamp	CHARACTER*1 variable input to select lamp mode
Bperiod	CHARACTER*1 variable input to select period setting
Brate	CHARACTER*1 variable input to select scan rate setting
Bref	CHARACTER*1 variable input to select reference mode
Bsbw	CHARACTER*4 variable input to set SBW value
Bslit	CHARACTER*1 variable input to match physical slit height
Bscan	CHARACTER*14 variable input for screen display of scan rate
Btime	CHARACTER*14 variable input for screen display of period
MATCH	LOGICAL variable .TRUE. on entry and exit unless scan aborted
MODE	INTEGER variable input to specify AUTO GAIN/SLIT mode

Center(TITLE)

Prints a string on the user console centred within a 72 column line.

TITLE	CHARACTER*72 string, contents set by calling unit

CALLED BY:	Main program unit, SUBROUTINE Select, SUBROUTINE Bline and SUBROUTINE Acquire
CALLS:	None

GOTO(Wlength)

Performs the same function as the Key Pad GO TO WLNGTH on the instrument to enable repositioning of the monochromator to a specified wavelength. Error trapping for illegal or inappropriate settings is performed by the main program unit and no negative reply is tested for.

Wlength	CHARACTER*7 variable input from the main program unit

CALLED BY:	Main program unit only
CALLS:	SUBROUTINE Send, SUBROUTINE Instats
EXTENSION:	LEN(*string*) function, HP extension to FORTRAN 77

Instats(Slew,...,Windex)

Performs a request for current instrument status from the CARY 2390. Slew is used to determine if the monochromator is still in motion. The other variables are not used in this version. No negative reply is issued by the CARY for this command.

Slew,Model,Ncell,Range,Windex

CHARACTER*1 variables passed back to calling unit

CALLED BY:	Main program unit, SUBROUTINE GOTO
CALLS:	None

Limits(MIN,MAX)

Reads entries for the wavelength limits from the user console, swaps the entries if necessary and validates the entries against the instrument limits (185 - 3152 nm). The values are then rounded to whole digits.

MIN,MAX	REAL variables passed back to main program unit
CALLED BY:	Main program unit only
CALLS:	None

Line(N)

Prints a line of '–' characters to the user console N columns wide and centred within a 72 column line.

N	INTEGER variable input from calling unit
CALLED BY:	Main program unit, SUBROUTINE Select, SUBROUTINE Bline and SUBROUTINE Acquire
CALLS:	None

Partable(PARAM)

Performs a request to send the parameter table from the CARY 2390 and processes the reply to update the program's list of current instrument settings held in the integer array PARAM. No negative reply is issued by the CARY for this command.

PARAM	INTEGER array output which holds the instrument parameter settings DIMENSION = 49, values set by CARY and SUBROUTINE Select
CALLED BY:	Main program unit only
CALLS:	None

Select(N,PARAM,Pstr)

Performs selection of available instrument settings for parameter N. Calls SUBROUTINE Send(Command) to set new parameter values. Negative replies are not tested since the parameter table values are read again on return to the main program menus calling Select. A special fix has been added for Derivative modes to use only valid selections from PARAM(11) and Pstr(11).

N	INTEGER input value (1 - 49) representing parameters 0 - 48
PARAM	INTEGER array input of current instrument parameter settings DIMENSION = 49, used to detect special case indexing for Pstr
Pstr	CHARACTER string array containing all selections for parameters DIMENSION = (49,16)*14 characters, 41-49 not used in this version
/IP/	INTEGER arrays NPAR,OFFSET used to select index number for Pstr
/IS/	CHARACTER array Pname containing the names of each parameter DIMENSION = (49)*10
INDEX	INTEGER array of valid index values for Derivative modes DIMENSION = 11, uses local data for indices to PARAM(11)

Send(Command)

Performs an IEEE-488 WRITE to the CARY 2390 to send a string command to the instrument and to read the reply. Negative replies are not checked using this routine. Commands are either validated before calling Send or parameters and variables are read afterwards to check the results from Send.

Command	CHARACTER variable holding an ASCII string command for CARY DIMENSION = variable, set by calling unit.

CALLED BY:	Main program unit, SUBROUTINE Select, SUBROUTINE GOTO
CALLS:	None

Str(VALUE,String,PREC)

Performs a conversion from numeric value to a string number for floating point numbers only with up to 12 digits precision. This is more than required by the CARY 2390.

VALUE	REAL variable input to be processed by the routine
String	CHARACTER*14 string output corresponding to VALUE
PREC	INTEGER variable input to set the rounding precision for string

CALLED BY: Main program unit, SUBROUTINE Bline
CALLS: None

Terminate

Performs an IEEE-488 WRITE to UNTALK the CARY 2390 and terminate real time transmission mode.

CALLED BY: Main program unit only
CALLS: ABRT(35,3) an EXTERNAL class system level routine
This function sends the UNTALK/UNLISTEN characters '_?'

Uppper(Code)

Performs a check for lower case characters in a string of arbitrary length and converts to upper case if necessary.

Code	CHARACTER variable passed into routine and UPPER case on exit DIMENSION = arbitrary, set by calling unit

CALLED BY: Main program unit, SUBROUTINE Bline
CALLS: None

Val(String,VALUE)

Performs a conversion from string to numeric value for a string number containing up to 10 digits. This is more than required by the CARY 2390.

String	CHARACTER string input to be processed by routine DIMENSION = arbitrary, set by calling unit
VALUE	REAL variable output

CALLED BY: Main program unit, SUBROUTINE Vartable, SUBROUTINE Acquire

CALLS: None

Vartable(VARIABLE)

Performs a request to send all 14 instrument variables and processes the replies to update the program's list of current values held in the floating point array VARIABLE. Negative replies from the CARY are not tested in this routine since illegal requests are not issued by Vartable.

VARIABLE	REAL array output which holds the instrument operating variables DIMENSION = 14, values set by CARY and main program unit

CALLED BY: Main program unit only

CALLS: SUBROUTINE Val

Wait(DELAY)

Performs a loop which tests the system clock until DELAY seconds have elapsed. The routine does not make provision for the special case at the transition to 2400 hours.

DELAY	REAL variable holding the value of the delay period in seconds

CALLED BY: Main program unit and SUBROUTINE Bline

CALLS: FUNCTION Time(I)

2.5 FUNCTIONS:

CARYSPEC uses only one function subprogram that makes an EXEC call to read the system time.

Time(I)

Performs an EXEC call to read the system clock and converts the reading to seconds and centiseconds.

I Dummy argument

CALLED BY: SUBROUTINE Wait only
CALLS: EXEC(ICODE,ITIME) system level command

PROGRAM CODE

3.0 Source Code Availability:

The source code for program CARYSPEC is an 83K ASCII text file available on either a Hewlett-Packard cartridge tape or an IBM 360K format floppy disk. All requests should be accompanied by the blank medium desired. A printed copy of the source code is listed below.

3.1 Variable Names And Usage:

A complete listing of the INTEGER, REAL and CHARACTER variables for the MAIN segment of CARYSPEC is given below in Tables III, IV & V, respectively. The subroutines use the same names as the main program for the same variables. Additional variables in the subroutines and simple integers, I-N, are not documented since their usage is rather obvious. The logical variables MATCH, PRINT, SINGLE and TRANSFER are used within the program to control conditional branching. MATCH is related to BLOCK IF tests for matching of the baseline and spectrum parameters. PRINT controls whether data will be printed to the console screen during data acquisition. SINGLE controls the operation of Acquire to update the wavelength. TRANSFER is used for special branching to reuse portions of code.

Table III

Glossary of INTEGER Variables

Name	Description	Value
ACCESSORY	Assigned Label - Accessory Setup Menu	600
ADVANCED	Assigned Label - Subsidiary Functions	350
BASELINE	Assigned Label - Baseline Setup Menu	200
EXIT	Assigned Label - Terminate Program	900
INSTRUMENT	Assigned Label - Read Cary Settings	390
LAMP	Assigned Label - Lamp & Detector Modes	570
MENU	Assigned Label - Main Control Menu	10
PARAMETER	Assigned Label - Instrument Setup Menu	400
SPECTRUM	Assigned Label - Acquire Spectrum	90
STORE	Assigned Label - Store Disk File	700
ASCII	ASCII code for a command output	> 48
MODE	Controls the selection of AUTO GAIN/SLIT	0,1
NARRAY	Number of data points in spectrum - file	1-10001
NCOL	Number of screen columns in menu display	50-70
NDATA	Number of data points in spectrum - Acquire	1-10001
PREC	Precision for rounding function in Str	3,4
XMODE	Selects abscissa data format in Acquire	1
YMODE	Selects ordinate data format in Acquire	1,2
NPAR(49)	Number of settings for each parameter	1-16
OFFSET(49)	Index offset for parameter settings	0-11
PARAM(49)	Instrument operating modes table	1-16

Table IV

Glossary of REAL Variables

Name	Description
ORD	Final ordinate value returned by Acquire
ABSC	Final abscissa value returned by Acquire
CELL	Final cell # value returned by Acquire
CYCLE	Final cycle # value returned by Acquire
SAMPLE	Final sample # value returned by Acquire
WAVE	Final wavelength value returned by Acquire
TIMER	Final time value returned by Acquire
DIST	Final distance value returned by Acquire
BAND	Spectral Bandwidth (nm) - AUTO GAIN mode
CONC	Concentration of sample (M) - file variable
GAIN	Instrument gain - AUTO SLIT mode
NUMBER	General purpose data entry variable
PATH	Pathlength of sample cell (cm) - file variable
PMIN	Pen scale minimum limit
PMAX	Pen scale maximum limit
RATE	Numeric equivalent of scan rate parameter
RATIO	Variable for data rate & slit gain checks
SPECBAND	File variable for SBW (nm) at λ_{min} (nm)
SPECGAIN	File variable for GAIN at λ_{max} (nm)
STEP	Numeric value of step size (nm) interval
WAVELENGTH	Current monochromator position (nm)
WMIN	Requested ending wavelength for scan
WMAX	Requested starting wavelength for scan
XMIN	File variable for WMIN
XMAX	File variable for WMAX
XSTEP	File variable for STEP
ZERO	Pen scale offset variable, %T and Deriv. modes
VARIABLE(14)	Instrument operating conditions table
X(10001)	Wavelength array
Y(10001)	Absorbance or %T array

Table V

Glossary Of CHARACTER Variables

Name	Description
Screen Control:	
BELL	CHAR(7) bell character
CLR*2	Clear screen
DOWN*2	Move cursor down 1 line
ESC	CHAR(27) escape character
HOME*2	Move cursor to upper right corner
UP*2	Move cursor up 1 line
Instrument Status:	
Bdet	Baseline detector mode
Bgain*4	Baseline gain setting
Bgbw*4	Baseline SBW or GAIN, depending on mode
Blamp	Baseline lamp mode
Bmin*4	Baseline ending wavelength
Bmax*4	Baseline starting wavelength
Bperiod	Baseline filter setting
Brate	Baseline scan rate
Bsbw*4	Baseline spectral bandwidth
Bslit	Baseline slit height
Odet	Previous spectrum detector mode
Ogain*4	Previous spectrum gain setting
Olamp	Previous spectrum lamp mode
Omin*4	Previous spectrum ending wavelength
Omax*4	Previous spectrum starting wavelength
Operiod	Previous spectrum filter setting
Orate	Previous spectrum scan rate
Osbw*4	Previous spectrum spectral bandwidth
Oslit	Previous spectrum slit height
Sdet	Spectrum detector mode
Sgain*4	Spectrum gain setting
Slamp	Spectrum lamp mode
Smin*4	Spectrum ending wavelength
Smax*4	Spectrum starting wavelength
Speriod	Spectrum filter setting
Srate	Spectrum scan rate
Ssbw*4	Spectrum spectral bandwidth
Sslit	Spectrum slit height

Instrument Control:

Accon*3	Turn accessory on command
Accoff*3	Turn accessory off command
Autobal*4	Perform auto balance to zero reading
Command*44	String of instrument commands to CARY
CSM	Checksum character for data transmission
Blstat*5	Read baseline status parameter command
Instr*4	Recall instrument setup menu display
Key*2	Press key command
Lock*4	Lock keyboard command
Messon*3	Send message to line 4 of CARY display
Messoff*4	Clear message from CARY display
Par*3	Read parameter command
Parset*2	Change parameter command
Ready*4	Release CARY from standby mode
Response*64	String for reply messages from CARY
Setup*4	Record trailer setup command
Standby*4	Place CARY in standby mode
Start*4	Issue a start command
Stop*4	Issue a stop command
String*14	String to pass data to or from subroutines
Unlock*4	Unlock keyboard command
Var*3	Read variable command
Varset*3	Change variable command

Program Control:

Access(5)*4	Accessory status (OFF, ON)
Astat*10	Auto balance status (OFF, SET)
Bscan*14	Scan rate, Baseline screen output
Bstat*10	Baseline status (OFF, ON, ON/MATCH)
Btime*14	Filter period, Baseline screen output
Code	Menu selection variable
Icode	Parameter setting in ASCII format
Pcode	Parameter number in ASCII format
Pname(49)*10	Table of names for each parameter
Printer(6)*12	Printer operating mode
Pstr(49)*14	Table of names for each parameter setting
Sstat*10	Spectrum status (OFF, ACQUIRED, STORED)
TITLE*72	String to be printed to screen
Vname(14)*8	Table of names for each variable
Wlength*7	Wavelength in ASCII format for GOTO

File Storage:

DATE*8	Date in mm/dd/yy format
Directory*40	Directory pathname
Fname*20	Filename and extension
INITIALS*2	User's initials for extension .Sxx
Name*16	Filename without extension
Outfile*63	Complete pathname for file

```
FTN7X,L
$FILES 0,1                          ! # Setup One Disk I/O File
$ALIAS /MODE/,NOALLOCATE            ! # BLOCK DATA Holds Values Of Named
$ALIAS /CARY/,NOALLOCATE            !   COMMON Variables So Don't Allocate
$ALIAS /IP/,NOALLOCATE              !   Memory For These Here - SGMTR Will
$ALIAS /IS/,NOALLOCATE              !   Create Memory For These As Required
$EMA /DATA/                         ! # Use EMA Space For Large Data Arrays
C
C     ****************************************************************
C
      PROGRAM CARYSPEC
C
C     ****************************************************************
C
C     This Program Is Designed To Control Data Acquisition From The
C     CARY 2390 UV-VIS-NIR Spectrophotometer Via The IEEE-488 Bus:
C
C     The CARY 2390 Is Addessed As Device #3 On The IEEE-488 Bus.
C
C     The HP 1000 Is Configured To Operate The IEEE-488 Bus In ASCII
C     Data Record Mode With Auto Addressing Enabled. The Bus Occupies
C     Logical Unit Addresses 35 - 38 (Device Addresses 0 - 3). LU 38
C     Controls The CARY 2390 And LU 35 Is Used To Issue Bus Commands.
C
C     ----------------------------------------------------------------
C
C
C         AUTHOR:  Dr. Robert A. Binstead,
C                  Chemistry Division, Code 6125,
C                  Naval Research Laboratory,
C                  Washington. D.C. 20375-5000
C
C
C         WRITTEN: December, 1986 - January, 1987
C
C         VERSION: 1.7
C
C         REVISED: March, 1987:
C                              - Modified to store Abscissa (X) array
C                                after Ordinate (Y) values to prevent
C                                data file corruption in the event of
C                                missed data points during multiuser
C                                sessions where the HP 1000 can not
C                                keep up with data transmission rate.
C                  May, 1987:
C                              - Modified MATCHING criteria between
C                                Spectrum & Baseline to omit checks
C                                on Scan Rate & Period. This allows
C                                the Baseline scan to be taken under
C                                conditions for the best correction
C                                of instrumental artifacts.
C                              - On MISMATCHED BASELINE detection the
C                                program will collect a new baseline
C                                with instrument parameters specified
```

```
C                                        for the spectrum except for PERIOD
C                                        and SCAN RATE which revert to those
C                                        for the previous baseline scan.
C                                      - Altered data storage routine to use
C                                        default or specified cartridge #.
C                    June, 1987:
C                                      - Modified Filename convention to match
C                                        the use of Directory Paths in the
C                                        new CI operating system.
C                                      - Segmented the program using SGMTR
C                                        to fit within CI's smaller boundary.
C                    August, 1987:
C                                      - Eliminated INQUIRE statement for FILE
C                                        EXISTS or FILE OPEN check since this
C                                        caused a memory protect error in the
C                                        segmented versions if the filename
C                                        was already in use. These checks are
C                                        made using the IOSTAT number returned
C                                        by the OPEN statement instead.
C                    November,1987:
C                                      - Altered updating of Variables Table
C                                        so that SBW at Smin and GAIN at Smax
C                                        are stored in Data File.
C                    January, 1988:
C                                      - Placed All COMMON Variables In Named
C                                        COMMON Blocks To Prevent Them From
C                                        Being Re-initialized On Calls To Other
C                                        Nodes Of The Multi-Level Segmentation.
C                                      - Explicitly Specified Allocation Of
C                                        BLOCK DATA memory Using NOALLOCATE
C                                        Compiler Directives.
C                                      - Eliminated Overwriting Of Data File
C                                        Variables By The Wavelength Reading
C                                        Routine. The CALL To Acquire Has
C                                        Been Augmented To Bypass The Usual
C                                        Spectral COMMON Variables in /CARY/.
C                    February,1988:
C                                      - Removed Single Beam Operation Since
C                                        The Cary Cannot Acquire A Baseline
C                                        In This Operating Mode.
C                                      - Added Tight Checking For Improper
C                                        Combinations Of Baseline Detector,
C                                        Lamp and Reference Mode Requests.
C                                      - Revised AUTO GAIN vs AUTO SLIT Mode
C                                        Selection In Baseline And Instrument
C                                        Setup Menus To Utilize Detector Mode
C                                        Under AUTO SELECT Reference Selection.
C                                      - Added Automatic Adjustment Of SBW And
C                                        GAIN Before Scan To Match Baseline.
```

```
C
C        MODES:    All Abscissa & Ordinate Modes (SUBROUTINES)
C                  Absorbance or %T vs Wavelength (PROGRAM only)
C
C        MEMORY:   28,000 Words (Max.PATH) + 40,000 Words EMA (DATA)
C                   3,000 Words (MSEG)     + 5 Memory Resident Nodes
C                         - 83 Page Partition Required -
C
C        SEGMENT:  This Program Is Too Large To Run Under CI On The
C                  HP 1000 - It Must Be Segmented Using SGMTR And
C                  MLLDR Loader - A CMD Transfer File SEGMCARY.CMD
C                  Contains The Commands To Accomplish This.
C
C     -------------------------------------------------------------
C
      INTEGER ACCESSORY,ADVANCED,BASELINE,EXIT,INSTRUMENT
      INTEGER LAMP,MENU,PARAMETERS,SPECTRUM,STORE
      INTEGER ASCII,MODE,NARRAY,NCOL,NDATA,PREC,XMODE,YMODE
      INTEGER NPAR(49),OFFSET(49),PARAM(49)
      REAL ORD,ABSC,CELL,CYCLE,SAMPLE,WAVE,TIMER,TEMP,DIST,BAND,CONC
      REAL GAIN,NUMBER,PATH,PMIN,PMAX,RATE,RATIO,SPECBAND,SPECGAIN
      REAL STEP,WAVELENGTH,WMIN,WMAX,XMIN,XMAX,XSTEP,ZERO
      REAL VARIABLE(14),X(10001),Y(10001)
      LOGICAL MATCH,PRINT,SINGLE,TRANSFER
C
C        Dimension Screen Control String Variables
C
      CHARACTER BELL,CLR*2,DOWN*2,ERASE*2,ESC,HOME*2,UP*2
C
C        Dimension Instrument Control String Variables
C
      CHARACTER CSM,Lock*4,Unlock*4,Key*2,Accon*3,Accoff*3
      CHARACTER Par*3,Var*3,Parset*2,Varset*2,Messon*3,Messoff*4
      CHARACTER Setup*4,Command*44,Response*64,String*14
C
C        Dimension Specific Key or Function String Variables
C
      CHARACTER Ready*4,Standby*4,Start*4,Stop*4,Instr*4,Autobal*4
C
C        Dimension Program Parameter Variables
C
      CHARACTER Sstat*10,Bstat*10,Astat*10,Wlength*7
      CHARACTER Directory*40,Fname*20,Name*16,Outfile*63
      CHARACTER Smin*4,Smax*4,Sinc*4,Sdet,Sgain*4,Slamp,Speriod
      CHARACTER Srate,Sref,Sslit,Ssbw*4
      CHARACTER Bmin*4,Bmax*4,Bdet,Bgain*4,Blamp,Bperiod
      CHARACTER Brate,Bref,Bslit,Bsbw*4,Fperiod,Frate
      CHARACTER Omin*4,Omax*4,Oinc*4,Odet,Ogain*4,Olamp,Operiod
      CHARACTER Orate,Oref,Oslit,Osbw*4
C
      CHARACTER DATE*8,INITIALS*2,TITLE*72
      CHARACTER Access(5)*4,Printer(6)*12,Code,Icode,Pcode
      CHARACTER Pname(49)*10,Vname(14)*8,Bscan*14,Btime*14
      CHARACTER Pstr(49,16)*14
```

```
C
C     ----------------------------------------------------------------
C
      COMMON /MODE/NDATA,XMODE,YMODE
      COMMON /CARY/ORD,ABSC,CELL,CYCLE,SAMPLE,WAVE,TIMER,TEMP,DIST
      COMMON /IP/NPAR,OFFSET,/IS/Pname,Vname
      COMMON /DATA/Y,X
C
C         Reference Library IEEE-488 Subroutines
C
      EXTERNAL ABRT
C
C     ----------------------------------------------------------------
C
C         Initialize Cary Command & Status String Variables
C
      DATA CSM,Setup,Lock,Unlock,Key/'0','@@20','@A10','@A00','@D'/
      DATA Accon,Accoff,Par,Var/'@F1','@F0','@C1','@C2'/
      DATA Parset,Varset,Messon,Messoff/'@H','@I','L1','@L00'/
      DATA Ready,Standby,Start/'@DT0','@DS0','@DP0'/
      DATA Stop,Instr,Autobal/'@DQ0','@DC0','@DU0'/
      DATA Sstat,Bstat,Astat/'  OFF','  OFF','  OFF'/
C
C         Initialize Cary Instrument Settings String Arrays
C
      DATA (Pstr(1,I),I=1,6)/'ABSORBANCE','% TRANSMISSION',
     &'TEMPERATURE','% REFLECTANCE','CONCENTRATION','EMISSION'/
      DATA (Pstr(2,I),I=1,4)/'WAVELENGTH','TIME','TEMPERATURE',
     &'DISTANCE'/
      DATA (Pstr(3,I),I=1,11)/'OFF','0.01','0.02','0.05','0.1','0.2',
     &'0.5','1.0','2.0','5.0','10.0'/
      DATA Pstr(4,1)/'OFF'/
      DATA (Pstr(4,I),I=6,15)/'0.2','0.5','1.0','2.0','5.0',
     &'10','20','50','100','200'/
      DATA (Pstr(5,I),I=1,4)/'AUTO SELECT','AUTO GAIN','AUTO SLIT',
     &'SINGLE BEAM'/
      DATA (Pstr(6,I),I=1,5)/'OFF','NORMAL','1ST DERIV','2ND DERIV',
     &'LOG'/
      DATA (Pstr(7,I),I=1,9)/'0.01','0.02','0.05','0.1','0.2','0.5',
     &'1.0','2.0','4.0'/
      DATA (Pstr(8,I),I=10,16)/'2','5','10','20','50','100','200'/
      DATA (Pstr(9,I),I=12,15)/'10','20','50','100'/
      DATA (Pstr(10,I),I=1,5)/'-1.9 TO 0.6','-2.0 TO 0.5',
     &'-2.1 TO 0.4','-2.2 TO 0.3','-2.3 TO 0.2'/
      DATA (Pstr(11,I),I=1,16)/'+/-0.01','+/-0.02','+/-0.05','+/-0.1',
     &'+/-0.2','+/-0.5','+/-1.0','+/-2.0','+/-5.0','+/-10','+/-20',
     &'+/-50','+/-100','+/-200','+/-500','+/-1000'/
      DATA (Pstr(12,I),I=1,16)/'+/-0.01','+/-0.02','+/-0.05','+/-0.1',
     &'+/-0.2','+/-0.5','+/-1.0','+/-2.0','+/-5.0','+/-10','+/-20',
     &'+/-50','+/-100','+/-200','+/-500','+/-1000'/
      DATA (Pstr(13,I),I=1,8)/'+/-0.01','+/-0.02','+/-0.05','+/-0.1',
     &'+/-0.2','+/-0.5','+/-1.0','+/-2.0'/
      DATA (Pstr(14,I),I=1,10)/'0','10','20','30','40','50','60','70',
     &'80','90'/
```

```
      DATA (Pstr(15,I),I=1,4)/'0.5','1.0','3.0','10'/
      DATA (Pstr(16,I),I=1,2)/'NORMAL','REVERSE'/
      DATA (Pstr(17,I),I=1,2)/'OFF','ON'/
      DATA (Pstr(18,I),I=1,2)/'REPEAT SCAN','SGL/MULTI'/
      DATA (Pstr(19,I),I=1,2)/'SERIAL','OVERLAY'/
      DATA (Pstr(20,I),I=1,4)/'BOTH ON','UV ONLY','VIS/NIR ONLY',
     &'BOTH OFF'/
      DATA (Pstr(21,I),I=1,3)/'AUTO','UV','VIS/NIR'/
      DATA (Pstr(22,I),I=1,3)/'AUTO','UV/VIS','NIR'/
      DATA (Pstr(23,I),I=1,2)/'FULL','1/3'/
      DATA (Pstr(24,I),I=1,3)/'AUTO','UV/VIS','NIR'/
      DATA (Pstr(25,I),I=1,3)/'AUTO','UV','VIS/NIR'/
      DATA (Pstr(26,I),I=1,4)/'AUTO SELECT','AUTO GAIN','AUTO SLIT',
     &'SINGLE BEAM'/
      DATA (Pstr(27,I),I=1,2)/'FULL','1/3'/
      DATA (Pstr(28,I),I=1,6)/'0','1','2','3','4','5'/
      DATA (Pstr(29,I),I=1,2)/'STANDARDS','UNKNOWNS'/
      DATA (Pstr(30,I),I=3,6)/'DIRECT','LINEAR','DIRECT-QUAD',
     &'QUADRATIC'/
      DATA (Pstr(31,I),I=7,8)/'NORMAL','AVERAGED'/
      DATA (Pstr(32,I),I=9,13)/'SIGNAL AV','SAMPLE AV','QUICK',
     &'EXTENDED','FIXED'/
      DATA (Pstr(33,I),I=1,5)/'DSPL RESULTS','DSPL SETUP','NEXT CONC',
     &'DELETE SAMPLE','CLEAR RESULTS'/
      DATA (Pstr(34,I),I=1,2)/'OFF','ON'/
      DATA (Pstr(35,I),I=1,2)/'1','2'/
      DATA (Pstr(38,I),I=1,5)/'  OFF','  ON','RECORD',' ','ON/SETUP'/
      DATA (Pstr(40,I),I=1,2)/'INTERVAL','ACCY-DRIVEN'/
C
      DATA (Printer(I),I=1,3)/'WAVELENGTH','TIME','TEMPERATURE'/
      DATA (Printer(I),I=4,6)/'DISTANCE','MAX.mm','MIN.mm'/
C
C         Initialize Screen Control String Variables
C
      BELL=CHAR(7)
      ESC=CHAR(27)
      CLR=ESC//'J'
      HOME=ESC//'h'
      UP=ESC//'A'
      DOWN=ESC//'B'
      ERASE=ESC//'K'
C
C     ---------------------------------------------------------------
C
C         Assign Statement Labels
C
C     ---------------------------------------------------------------
C
      ASSIGN 10  TO MENU
      ASSIGN 90  TO SPECTRUM
      ASSIGN 200 TO BASELINE
      ASSIGN 350 TO ADVANCED
      ASSIGN 390 TO INSTRUMENT
      ASSIGN 400 TO PARAMETERS
```

```
      ASSIGN 570 TO LAMP
      ASSIGN 600 TO ACCESSORY
      ASSIGN 700 TO STORE
      ASSIGN 900 TO EXIT
C
C     -------------------------------------------------------------
C
C         Data Acquisition and Control Menu
C
C     -------------------------------------------------------------
C
      CALL FFRCL(79)                ! Eliminate Line Wrapping Problems
      CALL Send(Setup)              ! Setup Normal Handshaking With Cary
      CALL Send(Ready)              ! Release Cary From Standby Mode
   10 WRITE (1,*) HOME,CLR
      CALL Send(Instr)              ! Display Instrument Settings On Cary
      CALL Send(Messoff)            ! Turn Off Display Messages On Cary
      CALL Send(Unlock)             ! Unlock Keyboard On Cary
      NCOL=70                       ! Set Display To 70 Columns
      TITLE='Cary 2390'
      CALL Center(TITLE)
      TITLE='Spectral Data Acquisition'
      CALL Center(TITLE)
      WRITE (1,'(T61,A2,A8)') UP,'Rev: 1.7'
      CALL Line(NCOL)
      WRITE (1,20) 'CODE','FUNCTION','STATUS','MIN','MAX','INC'
   20 FORMAT (T4,A4,T14,A8,T34,A7,T50,A3,T58,A3,T66,A3)
      CALL Line(NCOL)
      WRITE (1,30) 'A.....Acquire Spectrum.......',Sstat,Smin,Smax,Sinc
      WRITE (1,40) 'B.....Baseline Setup.........',Bstat,Bmin,Bmax
      WRITE (1,50) 'I.....Instrument Settings....'
      WRITE (1,50) 'L.....Lamps/Detectors/Access.'
      WRITE (1,60) 'S.....Store File on Disk.....',Fname
      WRITE (1,50) 'X.....EXIT Data Acquisition..'
   30 FORMAT (/,T4,A30,T35,A8,T50,A4,T58,A4,T66,A4)
   40 FORMAT (/,T4,A30,T35,A8,T50,A4,T58,A4)
   50 FORMAT (/,T4,A30)
   60 FORMAT (/,T4,A30,T35,A20)
      WRITE (1,*)
      CALL Line(NCOL)
      WRITE (1,*)
   70 WRITE (1,*) UP,ERASE,'_'
      WRITE (1,'(T3,A15,A,A2)') 'Enter the CODE:',BELL,'_'
      READ (1,80) Ccde
   80 FORMAT (A1)
      CALL Upper(Code)
      IF (Code.EQ.'A') GO TO SPECTRUM
      IF (Code.EQ.'B') GO TO BASELINE
      IF (Code.EQ.'I') GO TO INSTRUMENT
      IF (Code.EQ.'L') GO TO ADVANCED
      IF (Code.EQ.'S') GO TO STORE
      IF (Code.EQ.'X') GO TO EXIT
      GO TO 70
C
```

```
C     ----------------------------------------------------------------
C
C        Acquire Spectrum: (Instrument Baseline Must Match)
C
C     ----------------------------------------------------------------
C
 90   CALL Partable(PARAM)
      IF ((PARAM(38).NE.1).OR.(Bstat.EQ.'  OFF')) THEN
        WRITE (1,*) UP,ERASE,'_'
        WRITE (1,*) ' Baseline Program Is ABSENT: ',BELL,'_'
        CALL Wait(2.0)
        WRITE (1,*)
        GO TO BASELINE
      END IF
      IF ((PARAM(1).EQ.2).OR.(PARAM(2).NE.0)) THEN
        WRITE (1,*) UP,ERASE,'_'
        WRITE (1,*) ' Ordinate or Abscissa Error: ',BELL,'_'
        CALL Wait(2.0)
        WRITE (1,*)
        GO TO INSTRUMENT
      END IF
      IF (Sstat.EQ.'ACQUIRED') THEN
100     WRITE (1,*) UP,ERASE,'  SPECTRUM NOT STORED:_'
        WRITE (1,*) ' Proceed With Spectrum (Y or N) ? ',BELL,'_'
        READ (1,80) Code
        CALL Upper(Code)
        IF (Code.EQ.'N') GO TO 70
        IF (Code.NE.'Y') GO TO 100
      END IF
C
C     ----------------------------------------------------------------
C
C        Store Previous Spectrum's Parameters For Possible Abort
C
C     ----------------------------------------------------------------
C
      Omin=Smin
      Omax=Smax
      Oinc=Sinc
      Odet=Sdet
      Ogain=Sgain
      Olamp=Slamp
      Operiod=Speriod
      Orate=Srate
      Oref=Sref
      Oslit=Sslit
      Osbw=Ssbw
C     ----------------------------------------------------------------
      WRITE (1,*) HOME,CLR
      TITLE='Scan Parameters'
      CALL Center(TITLE)
      CALL Line(NCOL)
      WRITE (1,*) DOWN,'  BASELINE:'
      WRITE (1,*) DOWN,'  Scan Limits, (nm): ',Bmin,'/ ',Bmax
```

```
      CALL Val(Bmin,WMIN)                     ! Default Spectrum To
      CALL Val(Bmax,WMAX)                     ! Baseline Scan Limits
      WRITE (1,*) DOWN,DOWN,'  SPECTRUM:'
      WRITE (1,*) DOWN,'  Scan Limits, (nm): ',Bmin,'/ ',Bmax,
     &DOWN,DOWN
  110 WRITE (1,*) UP,ERASE,'  A...Accept, C...Change, X...Exit ? ',
     &BELL,'_'
      READ (1,80) Code
      CALL Upper(Code)
      IF (Code.EQ.'X') GO TO MENU
      IF (Code.EQ.'A') GO TO 120
      IF (Code.NE.'C') GO TO 110
      CALL Limits(WMIN,WMAX)
  120 CALL Str(WMIN,String,4)
      Smin=String(2:5)
      CALL Str(WMAX,String,4)
      Smax=String(2:5)
      WRITE (1,*) UP,ERASE,UP,UP,ERASE,'  Scan Limits, (nm): ',
     &Smin,'/ ',Smax,DOWN,DOWN
  130 WRITE (1,*) UP,ERASE,'  Step Size (.01 - 5 nm) : ',BELL,'_'
      READ (1,*,ERR=130) STEP
      IF ((STEP.LT.0.01).OR.(STEP.GT.5.0)) GO TO 130
      CALL Str(STEP,String,4)
      Sinc=String(2:5)
  140 CALL Val(Pstr(3,PARAM(3)+1),RATE)
      RATE=RATE/STEP
      IF (RATE.GT.5.0) THEN
        WRITE (1,*) UP,ERASE,'  Data Rate > 5 Hz - _'
        WRITE (1,*) 'RESET Scan Rate, (Y or N) ? ',
     &  BELL,'_'
        READ (1,80) Code
        CALL Upper(Code)
        IF (Code.NE.'Y') GO TO 130
        N=3
        K=N
        CALL Select(N,PARAM,Pstr)
        PARAM(K)=N-1                          ! Update Parameter Table
        GO TO 140
      END IF
      NDATA=INT((WMAX-WMIN)/STEP+.5)+1
      IF (NDATA.GT.10001) THEN
        WRITE (1,*) UP,ERASE,'  Too Many Data Points - _'
        WRITE (1,*) 'Increase Step Size _',BELL
        CALL Wait(2.0)
        GO TO 130
      END IF
      WRITE (1,*) DOWN,'  Checking Instrument Settings:',BELL
      CALL GOTO(Bmax)        ! Test Matching At Start Of Baseline Scan
C
C     ----------------------------------------------------------------
C
C        Set Spectrum Strings to Match Instrument Parameters
C
C     ----------------------------------------------------------------
```

```
C
      Sdet=CHAR(PARAM(22)+48)
      Slamp=CHAR(PARAM(21)+48)
      Speriod=CHAR(PARAM(15)+48)
      Srate=CHAR(PARAM(3)+48)
      Sref=CHAR(PARAM(5)+48)
      Sslit=CHAR(PARAM(23)+48)
      CALL Vartable(VARIABLE)             ! Update SBW, GAIN at Bmax
      CALL Str(VARIABLE(10),String,4)
      Ssbw=String(2:5)
      CALL Str(VARIABLE(6),String,4)
      Sgain=String(2:5)
C
C     ----------------------------------------------------------------
C
C         Test For Acceptable Instrument Baseline Matching
C
C     ----------------------------------------------------------------
C
      MATCH=.TRUE.
      IF (WMAX.GT.VARIABLE(3)) MATCH=.FALSE.
      IF (WMIN.LT.VARIABLE(4)) MATCH=.FALSE.
      IF (Sref.NE.Bref) MATCH=.FALSE.
      IF (Slamp.NE.Blamp) MATCH=.FALSE.
      IF (Sdet.NE.Bdet) MATCH=.FALSE.
      IF (Sslit.NE.Bslit) MATCH=.FALSE.
C     ----------------------------------------------------------------
      IF ((MODE.EQ.1).AND.(MATCH)) THEN   ! Exit If Already Failed
        IF (Ssbw.NE.Bsbw) THEN
          WRITE (1,*) UP,ERASE,'  Matching To Baseline SBW:',BELL
          Command=Varset//'9'//Bsbw//'!0'
          CALL Send(Command)
          Ssbw=Bsbw
          CALL Wait(1.0)
        END IF
      END IF
C     ----------------------------------------------------------------
      IF ((MODE.EQ.2).AND.(MATCH)) THEN   ! Exit If Already Failed
        IF (Sgain.NE.Bgain) THEN
          WRITE (1,*) UP,ERASE,'  Matching To Baseline GAIN:',BELL
          Command=Varset//'5'//Bgain//'!0'
          CALL Send(Command)              ! Reset AUTOSLIT Gain Level
          Sgain=Bgain
          CALL Wait(2.0)
        END IF
        IF ((Bref.EQ.'0').AND.(Bdet.EQ.'0').AND.(WMAX.LE.800.0)) THEN
          WRITE (1,*) UP,ERASE,'  Matching To Baseline SBW:',BELL
          Wlength='800.5'
          CALL GOTO(Wlength)              ! Reset To NIR Region
          CALL Wait(1.0)
          Wlength='800.0'
          CALL GOTO(Wlength)              ! Set To Start Of UV/VIS
        END IF                            ! With Matching SBW
      END IF
```

```
      IF (MATCH) GO TO 150
C
C     ----------------------------------------------------------------
C
C         Record New Baseline Using Present Instrument Parameters
C         With Period & Scan Rate From The Previous Baseline Scan
C
C     ----------------------------------------------------------------
C
      WRITE (1,*) DOWN,DOWN
      TITLE='### NEW BASELINE REQUIRED ###'
      CALL Center(TITLE)
      WRITE (1,*) BELL
      CALL Wait(2.0)
      MATCH=.TRUE.                          ! Baseline Valid Test On Exit
      CALL Bline(WMIN,WMAX,Sdet,Sgain,Slamp,Fperiod,Frate,Sref,Ssbw,
     &SsLit,Bscan,Btime,MATCH,MODE)
      Command=Parset//'>'//Speriod//CSM     ! Reset To Spectrum's Period
      CALL Send(Command)
      Command=Parset//'2'//Srate//CSM       ! Reset To Spectrum's Rate
      CALL Send(Command)
      IF (.NOT.MATCH) THEN
        Sstat='  OFF'                       ! Aborted Scan Exit
        GO TO MENU
      END IF
C
C     ----------------------------------------------------------------
C
C         Update Baseline Parameter Strings
C
C     ----------------------------------------------------------------
C
      Bmin=Smin
      Bmax=Smax
      Bdet=Sdet
      Bgain=Sgain
      Blamp=Slamp
      Bperiod=Fperiod
      Brate=Frate
      Bref=Sref
      Bsbw=Ssbw
      Bslit=Sslit
      Bstat='ON/MATCH'
C     ----------------------------------------------------------------
  150 WRITE (1,*) HOME,CLR
      TITLE='Acquire Spectrum'
      CALL Center(TITLE)
      CALL Line(NCOL)
      WRITE (1,*) DOWN,'  Wavelength Limits, (nm): ',Smax,'/ ',Smin
      WRITE (1,*) DOWN,'  Step Size, (nm/datum)  : ',Sinc
      WRITE (1,*) DOWN,'  Scan Rate, (nm/sec)    : ',
     &Pstr(3,PARAM(3)+1)
      WRITE (1,*) DOWN,'  Response Time, (sec)   : ',
     &Pstr(15,PARAM(15)+1)
```

```
      IF (MODE.EQ.1) THEN
        WRITE (1,*) DOWN,'  Spectral Bandwidth,(nm): ',Ssbw
        GO TO 160
      END IF
      WRITE (1,*) DOWN,'  AUTOSLIT Gain Level     : ',Sgain
  160 WRITE (1,*) DOWN
      WRITE (1,*) DOWN,'  Place Solution Cell In The SAMPLE Beam:'
      WRITE (1,*) DOWN,'       S.....Start Scan'
      WRITE (1,*) DOWN,'       A.....Abort Scan'
      WRITE (1,*) DOWN,'  Enter the CODE: ',BELL,'_'
  170 READ (1,80) Code
      CALL Upper(Code)
C
C     ------------------------------------------------------------------
C
C        Restore Old Spectrum's Parameter Strings
C
C     ------------------------------------------------------------------
C
      IF (Code.EQ.'A') THEN
        Smin=Omin
        Smax=Omax
        Sinc=Oinc
        Sdet=Odet
        Sgain=Ogain
        Slamp=Olamp
        Speriod=Operiod
        Srate=Orate
        Sref=Oref
        Sslit=Oslit
        Ssbw=Osbw
        GO TO MENU
      END IF
      IF (Code.NE.'S') GO TO 170
C
C     ------------------------------------------------------------------
C
C        Set To Starting Wavelength - Check For Instrument Ready
C
C     ------------------------------------------------------------------
C
      WRITE (1,*) UP,ERASE,UP,UP,ERASE,UP,UP,ERASE,UP,UP,ERASE,'_'
      WRITE (1,*) ' Slewing to Starting Wavelength:',BELL
      CALL GOTO(Smax)
      SINGLE=.FALSE.          ! Scan Mode ON, Single Wavelength OFF
      PRINT=.FALSE.           ! Initialize Print Mode To OFF
  180 WRITE (1,*) UP,ERASE,'  Print to Screen, (Y or N) ? ',BELL,'_'
      READ (1,80) Code
      CALL Upper(Code)
      IF (Code.EQ.'Y') THEN
        PRINT=.TRUE.
        GO TO 190
      END IF
      IF (Code.NE.'N') GO TO 180
```

```
C
C     ------------------------------------------------------------------
C
C         Select Data String Format For Abscissa & Ordinate In
C         SUBROUTINE Acquire Via COMMON Variables XMODE & YMODE
C
C     ------------------------------------------------------------------
C
  190 YMODE=PARAM(1)+1            ! YMODE = 1 - 6 (Only 1 & 2 Allowed)
      XMODE=PARAM(2)+1            ! XMODE = 1 - 4 (Only 1 Allowed)
      SPECGAIN=VARIABLE(6)        ! Save GAIN Value At Smax For Data File
C
      WRITE (1,*) UP,ERASE,'  Scanning Spectrum:',BELL
C
      CALL Send(Instr)            ! Display Instrument Settings On Cary
      CALL Send(Lock)             ! Lock Keyboard On Cary During Scan
      CALL Wait(1.0)              ! Wait For Cary To Finish Housekeeping
C
C     ------------------------------------------------------------------
C                  *** Data Collection Subroutine ***
C
C         Collects NDATA Readings At Sinc (nm) Steps And
C         Returns Spectrum In Arrays (X),(Y) Via EMA COMMON
C         Final Reading Is Returned Via Named COMMON /CARY/
C
      CALL Acquire(Sinc,PRINT,SINGLE,WAVELENGTH)
C
C     ------------------------------------------------------------------
C
      CALL Terminate              ! UNTALK Cary 2390 From IEEE-488 Bus
      CALL Wait(1.0)              ! Wait For Cary To Finish Housekeeping
      CALL Send(Setup)            ! Re-establish Normal Handshaking
      CALL Send(Stop)             ! STOP Key Issued
      CALL Send(Unlock)           ! UNLOCK Keyboard
      CALL Vartable(VARIABLE)     ! Update Instrument Variables To Obtain
      SPECBAND=VARIABLE(10)       ! Value Of Spectral Bandwidth At Smin.
      CALL GOTO(Smax)             ! Return To Starting Wavelength
      NARRAY=NDATA                ! Save # Of Data Points In File Variable
      XMIN=WMIN                   ! Save End Of Scan In File Variable
      XMAX=WMAX                   ! Save Start Of Scan In File Variable
      XSTEP=STEP                  ! Save Step Size In File Variable
      Sstat='ACQUIRED'
      GO TO MENU
C
C     ------------------------------------------------------------------
C
C         Baseline Call and Status Check
C
C     ------------------------------------------------------------------
C
```

```
200 MATCH=.TRUE.
    TRANSFER=.FALSE.
210 WRITE (1,*) UP,ERASE,'  Reading Instrument Baseline: ',BELL,'_'
    CALL Partable(PARAM)
    Bstat=Pstr(38,PARAM(38)+1)
    IF (PARAM(38).GT.1) Bstat='  '//Pstr(38,PARAM(38)+1)
    CALL Vartable(VARIABLE)
    WMAX=NINT(VARIABLE(3))
    WMIN=NINT(VARIABLE(4))
    BAND=VARIABLE(2)/1000.0      ! Only One Of SBW Or GAIN Is Stored
    GAIN=VARIABLE(2)/10.0        ! By The Cary For The Baseline Scan
220 PREC=4                       ! - Decide Below Which Is Valid.
    IF (WMAX.LT.1000.0) PREC=3
    CALL Str(WMAX,String,PREC)
    Bmax=String(2:5)
    PREC=4
    IF (WMIN.LT.1000.0) PREC=3
    CALL Str(WMIN,String,PREC)
    Bmin=String(2:5)
C   ------------------------------------------------------------
    IF (TRANSFER) GO TO MENU    ! EXIT After Return From Bline
C   ------------------------------------------------------------
    IF (WMAX.GT.900.0) THEN
      IF (PARAM(24).EQ.1) PARAM(24)=0    ! Bad UV/VIS Detector Mode
      IF (PARAM(26).EQ.1) PARAM(26)=0    ! Bad AUTO GAIN Ref. Mode
    END IF
    IF (WMIN.LT.700.0) THEN
      IF (PARAM(24).EQ.2) PARAM(24)=0    ! Bad NIR Detector Mode
    END IF
    IF (PARAM(24).EQ.2) THEN
      IF (PARAM(26).EQ.1) PARAM(26)=0    ! Bad NIR Reference Mode
    END IF
    IF ((PARAM(24).EQ.0).AND.(PARAM(26).EQ.1)) THEN
      IF (WMAX.GT.800.0) PARAM(24)=1    ! Bad AUTO Detector Mode
    END IF
    IF (WMAX.GT.400.0) THEN
      IF (PARAM(25).EQ.1) PARAM(25)=0    ! Bad UV Lamp Mode
    END IF
    IF (WMIN.LT.270.0) THEN
      IF (PARAM(25).EQ.2) PARAM(25)=0    ! Bad W Lamp Mode
    END IF
C   ------------------------------------------------------------
    Bperiod=CHAR(PARAM(15)+48)
    Brate=CHAR(PARAM(3)+48)
    Bdet=CHAR(PARAM(24)+48)
    Blamp=CHAR(PARAM(25)+48)
    Bref=CHAR(PARAM(26)+48)
    Bslit=CHAR(PARAM(27)+48)
    IF (Bref.EQ.'2') GO TO 230    ! AUTOSLIT Mode On (Both Detectors)
    IF (Bdet.EQ.'2') GO TO 230    ! NIR Detector  -> AUTOSLIT Mode
    IF (WMAX.GT.900.0) GO TO 230 ! Lambda > 900  -> AUTOSLIT Mode
    IF (WMAX.GT.800.0) THEN
      IF (Bdet.EQ.'0') GO TO 230 ! AUTO Detector -> AUTOSLIT Mode
    END IF
```

```
C     ------------------------------------------------------------------
      CALL Str(BAND,String,4)
      Bsbw=String(2:5)                  ! SBW Fixed At The Start Of Scan
      Bgain=' '                         ! Gain Variable During Scan
      MODE=1
      GO TO 240
  230 CALL Str(GAIN,String,4)
      Bgain=String(2:5)                 ! GAIN Fixed At The Start Of Scan
      Bsbw=' '                          ! SBW Variable During Scan
      MODE=2
  240 Command=Key//'H0'                 ! Display Baseline Menu On Cary
      CALL Send(Command)
      CALL Send(Messoff)                ! Turn Off Any Display Messages
C     ------------------------------------------------------------------
      WRITE (1,*) HOME,CLR
      TITLE='Baseline Setup'
      CALL Center(TITLE)
      CALL Line(NCOL)
      WRITE (1,250) 'INDEX','FUNCTION','SETTING'
      CALL LINE(NCOL)
      WRITE (1,*)
      WRITE (1,260) '0:','.....AUTO BALANCE...........',
     &Astat
      WRITE (1,260) '1:','.....BASELINE STATUS........',
     &Bstat
      WRITE (1,280) '2:','.....WAVELENGTH (Max,Min)...',
     &Bmax,',',Bmin
      WRITE (1,280) '3:','.....SBW (nm), GAIN.........',
     &Bsbw,',',Bgain
      WRITE (1,270) '4:','.....REFERENCE MODE.........',
     &Pstr(26,PARAM(26)+1)
      WRITE (1,270) '5:','.....LAMP SELECT............',
     &Pstr(25,PARAM(25)+1)
      WRITE (1,270) '6:','.....DETECTOR SELECT........',
     &Pstr(24,PARAM(24)+1)
      WRITE (1,270) '7:','.....SLIT HEIGHT............',
     &Pstr(27,PARAM(27)+1)
      WRITE (1,270) '8:','.....SCAN RATE (nm/sec).....',
     &Pstr(3,PARAM(3)+1)
      WRITE (1,270) '9:','.....RESPONSE TIME (sec)....',
     &Pstr(15,PARAM(15)+1)
      WRITE (1,260) 'X:','.....EXIT Baseline Menu.....',
     &' '
  250 FORMAT (T4,A5,T20,A8,T40,A7)
  260 FORMAT (T4,A3,T10,A28,A8)
  270 FORMAT (T4,A3,T10,A28,T40,A14)
  280 FORMAT (T4,A3,T10,A28,T40,A4,A,A4)
      WRITE (1,*)
      CALL Line(NCOL)
      WRITE (1,*)
  290 WRITE (1,*) UP,ERASE,'  INDEX Code: ',BELL,'_'
      READ (1,30) Code
      CALL Upper(Code)
      IF (Code.EQ.'X') GO TO 330
```

```
      N-ICHAR(Code)-48
      IF ((N.LT.0).OR.(N.GT.9)) GO TO 290
C     ------------------------------------------------------------------
      IF (N.EQ.0) THEN
        CALL Send(Autobal)
        Astat-'  SET'
        GO TO 220
      END IF
      IF (N.EQ.1) N-38
      IF (N.EQ.2) GO TO 300          ! Update Wavelength Limits
      IF (N.EQ.3) GO TO 310          ! Update SBW/GAIN
      IF (N.EQ.4) N-26
      IF (N.EQ.5) N-25
      IF (N.EQ.6) N-24
      IF (N.EQ.7) N-27               ! Slit Control Is Manual Only
      IF (N.EQ.8) N-3
      IF (N.EQ.9) N-15
C     ------------------------------------------------------------------
      K-N                            ! Instrument Baseline PARAMETERS Are
      CALL Select(N,PARAM,Pstr)      ! Masked From Direct Changes - The
      PARAM(K)-N-1                   ! NEW Values Are Only Accepted From
      IF (K.EQ.38) THEN              ! SUBROUTINE Bline's '@J' Command.
        WRITE (1,'(T12,A)') '_'
        GO TO 200
      END IF
      GO TO 220
C     ------------------------------------------------------------------
  300 CALL Limits(WMIN,WMAX)
      MATCH-.FALSE.
      GO TO 220
  310 WRITE (1,*) UP,ERASE,'_'
      IF (MODE.EQ.2) GO TO 320
      WRITE (1,*) ' Spectral Bandwidth (0.04 - 3.60 nm) - ',BELL,'_'
      READ (1,*,ERR-310) BAND
      IF ((BAND.LT.0.04).OR.(BAND.GT.3.60)) GO TO 310
      GO TO 220
  320 String-'(1-1275)'
      IF (PARAM(24).NE.2) String-'(1 - 1000)'
      WRITE (1,*) ' Gain Level ',String(1:10),' - ',BELL,'_'
      READ (1,*,ERR-310) NUMBER
      IF ((NUMBER.LT.1.0).OR.(NUMBER.GT.1275.0)) GO TO 310
      IF ((NUMBER.GT.1000.0).AND.(PARAM(24).NE.2)) GO TO 310
      GAIN-VARIABLE(6)
      RATIO-NUMBER/GAIN
      IF (RATIO.GT.10.0) THEN
        WRITE (1,*) UP,ERASE,'_'
        WRITE (1,*) ' Setting Instrument Gain: ',BELL,'_'
        CALL Wait(2.0)
        Command-Parset//'420'             ! Set AUTOSLIT Mode Prior
        CALL Send(Command)                ! To Sending New GAIN Level
        WRITE (1,*)
        TRANSFER-.TRUE.                   ! Transfer To Instrument
        GO TO 490                         ! GAIN Setting Routine
      END IF
```

```
      GAIN=NUMBER
      GO TO 220
C
C     ---------------------------------------------------------------
C
C            Record Baseline Scan In CARY 2390
C
C     ---------------------------------------------------------------
C
  330 WRITE (1,*) UP,ERASE,'_'
      WRITE (1,*) ' Record NEW Baseline, (Y or N) ? ',BELL,'_'
      READ (1,80) Code
      CALL Upper(Code)
      IF (Code.EQ.'N') GO TO 340
      IF (Code.NE.'Y') GO TO 330
      MATCH=.FALSE.
      I=ICHAR(Brate)-48
      Bscan=Pstr(3,I+1)
      I=ICHAR(Bperiod)-48
      Btime=Pstr(15,I+1)
      CALL Bline(WMIN,WMAX,Bdet,Bgain,Blamp,Bperiod,Brate,Bref,Bsbw,
     &Bslit,Bscan,Btime,MATCH,MODE)
      Fperiod=Bperiod
      Frate=Brate
      Astat='  SET'
  340 TRANSFER=.TRUE.  ! Perform An Alternate Return To The Main MENU
      GO TO 210        ! After Reading Instrument Baseline Parameters
C
C     ---------------------------------------------------------------
C
C            Menu of Advanced Setup Operations
C
C     ---------------------------------------------------------------
C
  350 WRITE (1,*) HOME,CLR
      TITLE='Advanced Operations Menus'
      CALL Center(TITLE)
      NCOL=50
      CALL Line(NCOL)
      WRITE (1,'(T15,A5,T30,A14)') 'INDEX','GROUP FUNCTION'
      CALL Line(NCOL)
      WRITE (1,*)
      WRITE (1,360) '1:  .......LAMPS & DETECTORS........'
      WRITE (1,360) '2:  .......ACCESSORY SETTINGS.......'
      WRITE (1,360) '3:  .......AUTOMATIC OPERATION......'
      WRITE (1,360) 'X:  .......EXIT TO SETUP MENU.......'
      WRITE (1,*)
      CALL Line(NCOL)
  360 FORMAT (T17,A35)
      WRITE (1,*)
  370 WRITE (1,'(T15.A2,A2,A9,A,A)') UP,ERASE,'INDEX #: ',BELL,'_'
      READ (1,80) Code
      CALL Upper(Code)
      IF (Code.EQ.'X') GO TO MENU
```

```
      N=ICHAR(Code)-48
      IF (N.EQ.1) GO TO LAMP
      IF (N.EQ.2) GO TO ACCESSORY
      IF (N.EQ.3) GO TO 380
      GO TO 370
  380 WRITE (1,'(T13,A2,A2,A)') UP,ERASE,'_'
      WRITE (1,*) ' Not Supported In Version 1.X ',BELL,'_'
      CALL Wait(2.0)
      GO TO ADVANCED
C
C     ---------------------------------------------------------------
C
C         Display and Update Instrument Settings
C
C     ---------------------------------------------------------------
C
  390 WRITE (1,*) UP,ERASE,'  Reading Wavelength: ',BELL,'_'
      NDATA=1
      OInc='1'
      PRINT=.FALSE.                     ! No Display Required
      SINGLE=.TRUE.                     ! Select Wavelength Update Mode
      CALL Partable(PARAM)
      YMODE=PARAM(1)+1                  ! Set Data String Format
      XMODE=2
      Icode=CHAR(PARAM(2)+48)           ! Save Abscissa Mode
      Command=Parset//'110'             ! Set Abscissa = TIME
      CALL Send(Command)
      CALL Send(Setup)
      CALL Wait(0.5)
      CALL Acquire(OInc,PRINT,SINGLE,WAVELENGTH)
      CALL Terminate
      CALL Wait(0.5)
      CALL Send(Setup)
      CALL Send(Stop)
      Command=Parset//'1'//Icode//CSM
      CALL Send(Command)                ! Restore Abscissa Mode
      WRITE (1,*)
      WRITE (1,*) UP,'_'
  400 WRITE (1,*) ERASE,' Reading Instrument Settings: ',BELL,'_'
      CALL Partable(PARAM)
      CALL Vartable(VARIABLE)
      BAND=VARIABLE(10)                     ! Current SBW (nm)
      GAIN=VARIABLE(6)                      ! Current GAIN Level
      CALL Val(Pstr(8,PARAM(8)+1),PMAX)     ! Pen Limits, %T & %R
      PMIN=VARIABLE(11)
      IF (PARAM(1).EQ.0) THEN               ! Pen Limits, Absorbance
        CALL Val(Pstr(7,PARAM(7)+1),PMAX)
        PMIN=VARIABLE(1)
      END IF
      IF (PARAM(1).EQ.2) THEN               ! Pen Limits, Temperature
        CALL Val(Pstr(9,PARAM(9)+1),PMAX)
        CALL Val(Pstr(14,PARAM(14)+1),PMIN)
      END IF
      PMAX=PMIN+PMAX
```

```
      I=11                                         ! Index For Deriv. Range
      IF (PARAM(6).EQ.4) I=10                      ! Index For Log Zero Range
      String=Pstr(I,PARAM(I)+1)                    ! Pen Range Label For Index
      CALL Send(Instr)                             ! Display Instrument Menu
C     ----------------------------------------------------------------------
      WRITE (1,*) HOME,CLR
      TITLE='Instrument Settings'
      CALL Center(TITLE)
      CALL Line(NCOL)
      WRITE (1,'(T4,A5,T20,A8,T40,A7)') 'INDEX','FUNCTION','SETTING'
      CALL LINE(NCOL)
      WRITE (1,*)
      WRITE (1,410) '0:','.....WAVELENGTH.............',
     &WAVELENGTH
      WRITE (1,420) '1:','.....ORDINATE...............',
     &Pstr(1,PARAM(1)+1)
      WRITE (1,420) '2:','.....ABSCISSA...............',
     &Pstr(2,PARAM(2)+1)
      WRITE (1,420) '3:','.....SCAN RATE (nm/sec).....',
     &Pstr(3,PARAM(3)+1)
      WRITE (1,420) '4:','.....CHART DISPLAY (nm/cm)..',
     &Pstr(4,PARAM(4)+1)
      WRITE (1,420) '5:','.....REFERENCE MODE.........',
     &Pstr(5,PARAM(5)+1)
      WRITE (1,430) '6:','.....SBW (nm), GAIN.........',
     &BAND,',',GAIN
      WRITE (1,420) '7:','.....PEN FUNCTION...........',
     &Pstr(6,PARAM(6)+1)
      WRITE (1,430) '8:','.....PEN LIMITS (Min,Max)...',
     &PMIN,',',PMAX
      IF (PARAM(6).GT.1) WRITE (1,'(T40,A2,A2,A14)') UP,ERASE,String
      WRITE (1,420) '9:','.....RESPONSE TIME (sec)....',
     &Pstr(15,PARAM(15)+1)
      WRITE (1,420) '10:','.....BEAM INTERCHANGE.......',
     &Pstr(16,PARAM(16)+1)
      WRITE (1,420) '11:','.....SLIT HEIGHT............',
     &Pstr(23,PARAM(23)+1)
      WRITE (1,420) 'X:','.....EXIT Instrument Menu...',' '
  410 FORMAT (T4,A3,T10,A28,T40,F6.2)
  420 FORMAT (T4,A3,T10,A28,T40,A14)
  430 FORMAT (T4,A3,T10,A28,T40,F4.2,A,F5.2)
      WRITE (1,*)
      CALL Line(NCOL)
      WRITE (1,*)
  440 WRITE (1,*) UP,ERASE,'  INDEX Code: ',BELL,'_'
      READ (1,'(A2)') Key
      CALL Upper(Key)
      IF (Key.EQ.'X') GO TO MENU
      N=ICHAR(Key(1:1))-48
      IF (Key(2:2).EQ.' ') GO TO 450
      N=N*10+ICHAR(Key(2:2))-48
  450 IF ((N.LT.0).OR.(N.GT.10)) GO TO 440
C     ----------------------------------------------------------------------
```

```
      K-N                                      ! Save Index #:
      IF (N.EQ.0) GO TO 460                    ! Update Wavelength
      IF (N.EQ.6) GO TO 470                    ! Update SBW/GAIN
      IF (N.EQ.7) N-6                          ! Pen Function
      IF (N.EQ.9) N-15
      IF (N.EQ.10) N-16
      IF (N.EQ.8) THEN                         ! Update Pen Limits
        N-1                                    ! Index For Deriv & Log
        IF (PARAM(6).LE.1) THEN                ! PEN - NORMAL Modes
          IF (PARAM(1).NE.2) GO TO 520         ! Absorbance & %T Range
          N-9                                  ! Index For Temp. Range
        END IF
      END IF
      CALL Select(N,PARAM,Pstr)                ! Update Parameters
      IF (K.EQ.5) THEN
        WRITE (1,'(T12,A)') '_'
        GO TO 510
      END IF
      WRITE (1,'(T13,A2,A)') UP,'_'
      GO TO PARAMETERS
C     -------------------------------------------------------------
  460 WRITE (1,*) UP,ERASE,'  Wavelength - ',BELL,'_'
      READ (1,*,ERR-460) NUMBER
      IF ((NUMBER.LT.185.0).OR.(NUMBER.GT.3152)) GO TO 460
      IF ((Bdet.EQ.'1').AND.(NUMBER.GT.900.0)) THEN
        WRITE (1,*) UP,ERASE,'  UV/VIS Detector Limit - 900 nm',BELL
        CALL Wait(2.0)
        GO TO 460
      END IF
      IF ((Bdet.EQ.'2').AND.(NUMBER.LT.700.0)) THEN
        WRITE (1,*) UP,ERASE,'  NIR Detector Limit - 700 nm',BELL
        CALL Wait(2.0)
        GO TO 460
      END IF
      CALL Str(NUMBER,String,6)
      Wlength-String(2:8)
      WRITE (1,*) UP,ERASE,'  Slewing to _'
      WRITE (1,'(F6.2,A4)') NUMBER,' nm:'
      CALL GOTO(Wlength)
      GO TO INSTRUMENT
C     -------------------------------------------------------------
  470 WRITE (1,*) UP,ERASE,'_'
      IF (PARAM(5).EQ.2) GO TO 480     ! AUTOSLIT Mode (Both Detectors)
      IF (PARAM(22).EQ.2) GO TO 480    ! NIR Detector  -> AUTOSLIT Mode
      IF (WAVELENGTH.GT.900.0) THEN
        GO TO 480                      ! Lamda >900 nm -> AUTOSLIT Mode
      END IF
      IF (WAVELENGTH.GT.800.0) THEN
        IF (PARAM(22).EQ.0) GO TO 480 ! AUTO Detector -> AUTOSLIT Mode
      END IF
      WRITE (1,*) ' Spectral Bandwidth: (0.04 - 3.60 nm) - ',BELL,'_'
      READ (1,*,ERR-470) BAND
      IF ((BAND.LT.0.04).OR.(BAND.GT.3.60)) GO TO 470
      CALL Str(BAND,String,4)
```

```
      Command-Varset//'9'//String(2:5)//'!0'
      CALL Send(Command)
      GO TO 510
  480 String-'(1 - 1275)'
      IF (PARAM(22).NE.2) String-'(1 - 1000)'
      WRITE (1,*) ' GAIN: ',String(1:10),' - ',BELL,'_'
      READ (1,*,ERR-470) NUMBER
      IF ((NUMBER.LT.1.0).OR.(NUMBER.GT.1275.0)) GO TO 470
      IF ((NUMBER.GT.1000.0).AND.(PARAM(22).NE.2)) GO TO 470
      TRANSFER-.FALSE.
C     ********************** SPECIAL ENTRY POINT ********************
C         Baseline GAIN Request > 10*GAIN : Reset GAIN and RETURN
C     ***************************************************************
  490 J-0
      RATIO-NUMBER/GAIN
      DO WHILE (RATIO.GT.10.0)
        J-J+1
        NUMBER-NUMBER/10.0
        RATIO-NUMBER/GAIN
      END DO
      CALL Str(NUMBER,String,4)
      Command-Varset//'5'//String(2:5)//'!0'
      CALL Send(Command)
      DO 500 I-1,J
        NUMBER-NUMBER*10.0
        CALL Str(NUMBER,String,4)
        CALL Wait(2.0)
        Command-Varset//'5'//String(2:5)//'!0'
        CALL Send(Command)
  500 CONTINUE
      IF (TRANSFER) THEN          ! Return to Baseline Setup
        GAIN-NUMBER               ! With Instrument GAIN Matched
        TRANSFER-.FALSE.          ! To Requested Baseline Gain
        GO TO 220
      END IF
C     ---------------------------------------------------------------
  510 WRITE (1,*) UP,ERASE,'  Waiting for CARY to settle: ',BELL,'_'
      CALL Wait(5.0)
      WRITE (1,*)
      IF (K.EQ.5) WRITE (1,'(T12,A)') '_'
      GO TO 560
C     ---------------------------------------------------------------
  520 N-8
      IF (PARAM(1).EQ.0) N-7
      I-N
      CALL Select(I,PARAM,Pstr)
      I-I+OFFSET(N)
      CALL Val(Pstr(N,I),NUMBER)
      ZERO-0.0
      IF (N.EQ.8) THEN
        IF (NUMBER.GT.100.0) GO TO 550
        GO TO 530
      END IF
```

```
      IF (NUMBER.GE.1.0) THEN
        NUMBER=4.0-NUMBER
        GO TO 530
      END IF
      NUMBER=3.0
  530 WRITE (1,'(T13,A2,A2,A18)') UP,ERASE,'  Zero Suppress: _'
      IF (N.EQ.8) THEN
        WRITE (1,*) '(0 - 100%) = ',BELL,'_'
        GO TO 540
      END IF
      WRITE (1,'(A9,F4.2,A4,A,A)') '(-0.5 to ',NUMBER,') = ',BELL,'_'
  540 READ (1,*,ERR=530) ZERO
      IF (N.EQ.8) THEN
        IF ((ZERO.LT.0.0).OR.(ZERO.GT.100.0)) GO TO 530
        GO TO 550
      END IF
      IF ((ZERO.LT.-0.5).OR.(ZERO.GT.NUMBER)) GO TO 530
  550 CALL Str(ZERO,String,3)
      Pcode='0'
      IF (N.EQ.8) Pcode=':'
      Command=Varset//Pcode//String(1:5)//'10'
      CALL Send(Command)
      WRITE (1,'(T12,A)') '_'
  560 WRITE (1,*) UP,'_'
      GO TO PARAMETERS
C
C     ------------------------------------------------------------
C
C             Lamp and Detector Mode Selection
C
C     ------------------------------------------------------------
C
  570 CALL Partable(PARAM)
      WRITE (1,*) HOME,CLR
      TITLE='Lamp & Detector Modes'
      CALL Center(TITLE)
      CALL Line(NCOL)
      WRITE (1,'(T15,A5,T27,A8,T47,A4)') 'INDEX','FUNCTION','MODE'
      CALL Line(NCOL)
      WRITE (1,*)
      WRITE (1,580) '1: .....LAMP POWER.......... ',
     &Pstr(20,PARAM(20)+1)
      WRITE (1,580) '2: .....LAMP SELECT......... ',
     &Pstr(21,PARAM(21)+1)
      WRITE (1,580) '3: .....DETECTOR SELECT..... ',
     &Pstr(22,PARAM(22)+1)
      WRITE (1,580) 'X: .....EXIT TO MENU........ ',' '
      WRITE (1,*)
      CALL LINE(NCOL)
  580 FORMAT (T16,A30,A14)
      WRITE (1,*)
  590 WRITE (1,'(T15,A2,A2,A9,A,A)') UP,ERASE,'INDEX #: ',BELL,'_'
      READ (1,80) Code
      CALL Upper(Code)
```

```
      IF (Code.EQ.'X') GO TO ADVANCED
      N-ICHAR(Code)-48
      IF ((N.LT.1).OR.(N.GT.3)) GO TO 590
      N-(N-1)+20
      CALL Select(N,PARAM,Pstr)
      GO TO LAMP
C
C     ------------------------------------------------------------------
C
C        Accessory Mode Selection
C
C     ------------------------------------------------------------------
C
  600 CALL Partable(PARAM)
      DO 610 I-1,2
        Access(I)-'OFF'
        ASCII-(I-1)+48
        Pcode=CHAR(ASCII)
        Command-Accoff//Pcode//CSM
        WRITE (UNIT-38,FMT-*,IOSTAT-N,ERR-999) Command
        READ (UNIT-38,FMT-620,IOSTAT-N,ERR-999) Response
        IF (Response(2:2).EQ.'P') THEN
          Access(I)-'ON'
          Command-Accon//Pcode//CSM
          CALL Send(Command)
        END IF
  610 CONTINUE
  620 FORMAT (A64)
  630 WRITE (1,*) HOME,CLR
      TITLE-'Accessory Control'
      CALL Center(TITLE)
      CALL Line(NCOL)
      WRITE (1,'(T15,A5,T27,A8,T46,A4)') 'INDEX','FUNCTION','MODE'
      CALL Line(NCOL)
      WRITE (1,*)
      WRITE (1,640) '1: ...TEMPERATURE READOUT... ',Access(1)
      WRITE (1,640) '2: ...PRINTER............... ',Access(2)
      IF (Access(2).EQ.'ON') THEN
        WRITE (1,'(T49,A2,A3,A12)') UP,' : ',Printer(IP)
      END IF
      WRITE (1,640) 'X: ...EXIT TO MENU.......... ',' '
      WRITE (1,*)
      CALL Line(NCOL)
  640 FORMAT (T16,A30,A4)
      WRITE (1,*)
  650 WRITE (1,'(T15,A2,A2,A9,A,A)') UP,ERASE,'INDEX #: ',BELL,'_'
      READ (1,80) Code
      CALL Upper(Code)
      IF (Code.EQ.'X') GO TO ADVANCED
      I-ICHAR(Code)-48
      IF ((I.LT.1).OR.(I.GT.2)) GO TO 650
      ASCII-(I-1)+48
      Pcode=CHAR(ASCII)
  660 WRITE (1,'(T14,A2,A2,A)') UP,ERASE,'_'
```

```
      WRITE (1,*) '(OFF=0, ON=1) ? ',BELL,'_'
      READ (1,'(I2)',ERR=660) ASCII
      Code=CHAR(ASCII+48)
      IF ((Code.NE.'0').AND.(Code.NE.'1')) GO TO 660
      Command='@F'//Code//Pcode//CSM
      CALL Send(Command)
      IF (Code.EQ.'0') GO TO 699
      IF (I.EQ.1) THEN
        N=9
        CALL Select(N,PARAM,Pstr)
        GO TO 699
      END IF
C     ----------------------------------------------------------------
      WRITE (1,*) HOME,CLR
      TITLE='Printer Mode'
      CALL Center(TITLE)
      CALL Line(NCOL)
      WRITE (1,'(T15,A5,T27,A8,T46,A4)') 'INDEX','FUNCTION','MODE'
      CALL Line(NCOL)
      WRITE (1,'(T46,A14)') Pstr(40,PARAM(40))
      WRITE (1,670) '1: .....WAVELENGTH.......... '
      WRITE (1,670) '2: .....TIME................ '
      WRITE (1,670) '3: .....TEMPERATURE......... '
      WRITE (1,*)
      CALL Line(NCOL)
  670 FORMAT (T16,A30)
      WRITE (1,*)
  680 WRITE (1,'(T15,A2,A2,A9,A,A)') UP,ERASE,'INDEX #: ',BELL,'_'
      READ (1,'(I2)',ERR=680) IP
      IF ((IP.LT.1).OR.(IP.GT.3)) GO TO 680
      ASCII=(IP-1)+48
      Pcode=CHAR(ASCII)
  690 WRITE (1,'(T15,A2,A2,A11,A,A)') UP,ERASE,'INTERVAL = ',BELL,'_'
      READ (1,*,ERR=690) NUMBER
      CALL Str(NUMBER,String,4)
      Command='@M'//Pcode//String(1:5)//'!0'
      CALL Send(Command)
  699 Command='@DF0'                    ! Update Cary Accessory Display
      CALL Send(Command)
      GO TO 600
C
```

```
C      -----------------------------------------------------------------
C
C          Store Spectrum
C
C      -----------------------------------------------------------------
C
  700 IF ((Sstat.NE.'ACQUIRED').AND.(Sstat.NE.'STORED')) THEN
        WRITE (1,*) UP,ERASE,'  Spectrum is ABSENT: ',BELL,'_'
        CALL Wait(2.0)
        WRITE (1,*)
        GO TO 70
      END IF
      IF (ABS(XMIN-ABSC).GT.0.5) THEN
  710   WRITE (1,*) UP,ERASE,'  SCAN ENDED AT',ABSC,' nm (Expected:',
     &  XMIN,'), Proceed (Y or N) ? ',BELL,'_'
        READ (1,80) Icode
        CALL Upper(Icode)
        IF (Icode.EQ.'N') GO TO 70
        IF (Icode.NE.'Y') GO TO 710
      END IF
      TITLE-'Store Spectrum'
  720 WRITE (1,*) HOME,CLR
      CALL Center(TITLE)
      CALL Line(NCOL)
      WRITE (1,*)
      WRITE (1,*) '  Researcher''s Initials, (AA-ZZ) ? ',BELL,'_'
      READ (1,'(A2)') INITIALS
      CALL Upper(INITIALS)
      String-'.S'//INITIALS
      WRITE (1,*) DOWN
      WRITE (1,*) UP,ERASE,'  Filename: (16 chars.) ? ',BELL,'_'
      READ (1,'(A16)') Name
      CALL Upper(Name)
      K-16
      DO WHILE (Name(K:K).EQ.' ')
        K-K-1
      END DO
      Fname-Name(1:K)//String(1:4)
      WRITE (1,*) DOWN,'  Directory, (Return - /DEFAULT/) ? ',BELL,'_'
      READ (1,'(A40)') Directory
      IF (Directory.EQ.' ') THEN
        Outfile-Fname
        GO TO 730
      END IF
      L-40
      DO WHILE (Directory(L:L).EQ.' ')
        L-L-1
      END DO
      IF (Directory(L:L).EQ.'/') L-L-1
      Outfile-Directory(1:L)//'/'//Fname
  730 L-63
      DO WHILE (Outfile(L:L).EQ.' ')
        L-L-1
      END DO
```

```
  740 WRITE (1,*) DOWN,'  Validating: ',Outfile(1:L),' _'
      OPEN (UNIT=66,FILE=Outfile(1:L),IOSTAT=N,STATUS='NEW')
      WRITE (1,*)
      IF (N.NE.0) THEN
        N=N-500
        WRITE (1,*) UP,ERASE,'_'
        IF (N.EQ.2) WRITE (1,*) ' FILE EXISTS: ',BELL,'_'
        IF (N.EQ.8) WRITE (1,*) ' FILE OPENED: ',BELL,'_'
        IF ((N.NE.2).AND.(N.NE.8)) WRITE (1,*) ' DISK ERROR # ',N,
     &  BELL,' _'
        CLOSE (UNIT=66,STATUS='DELETE')
        CALL Wait(2.0)
        GO TO 720
      END IF
      IF (Code.EQ.'R') GO TO 790
      WRITE (1,*) UP,ERASE,'  Validated Filename: ',Fname
      WRITE (1,*) DOWN,'  Title, (72 chars):'
      WRITE (1,*) '  ',BELL,'_'
      READ (1,750) TITLE
  750 FORMAT (A72)
      WRITE (1,*) DOWN,'  Date, (MM/DD/YY): ',BELL,'_'
      READ (1,760) DATE
  760 FORMAT (A8)
      WRITE (1,*) DOWN
  770 WRITE (1,*) UP,ERASE,'  Concentration, (M): ',BELL,'_'
      READ (1,*,ERR=770) CONC
      IF (CONC.LT.0.0) GO TO 770
      WRITE (1,*) DOWN
  780 WRITE (1,*) UP,ERASE,'  Pathlength, (cm): ',BELL,'_'
      READ (1,*,ERR=780) PATH
      IF (PATH.LT.0.0) GO TO 780
C     ----------------------------------------------------------------
  790 J=49      ! # of Parameters
      K=14      ! # of Variables
      VARIABLE(6)=SPECGAIN        ! Store GAIN At Smax
      VARIABLE(10)=SPECBAND       ! Store SBW At Smin
      WRITE  (1,*) DOWN,'  Storing File: ',Outfile(1:L),BELL
      WRITE (66,FMT=750,IOSTAT=N,ERR=820) TITLE
      WRITE (66,FMT=760,IOSTAT=N,ERR=820) DATE
      WRITE (66,FMT=*,IOSTAT=N,ERR=820) XMIN,XMAX,XSTEP,CONC,PATH
      WRITE (66,FMT=*,IOSTAT=N,ERR=820) ORD,ABSC,CELL,CYCLE,SAMPLE,
     &WAVE,TIMER,TEMP,DIST
      WRITE (66,FMT=800,IOSTAT=N,ERR=820) J,K,NARRAY
  800 FORMAT (I3,I3,I6)
      WRITE (66,FMT=810,IOSTAT=N,ERR=820) (PARAM(I),I=1,J)
  810 FORMAT (I2)
      WRITE (66,FMT=*,IOSTAT=N,ERR=820) (VARIABLE(I),I=1,K)
      WRITE (66,FMT=*,IOSTAT=N,ERR=820) (Y(I),I=1,NARRAY)
      WRITE (66,FMT=*,IOSTAT=N,ERR=820) (X(I),I=1,NARRAY)
      CLOSE (UNIT=66,IOSTAT=N,ERR=820,STATUS='KEEP')
      Sstat='STORED'
      CALL Wait(2.0)
      GO TO MENU
C     ----------------------------------------------------------------
```

```
  820 WRITE (1,*) UP,ERASE,'  Disk Error #',N,BELL,' :_'
      WRITE (1,*) 'R...RESAVE, X...EXIT to Menu ? ',BELL,'_'
      READ (1,80) Code
      IF ((Code.NE.'R').AND.(Code.NE.'X')) GO TO 820
      WRITE (1,*) UP,ERASE,'  Deleting Old File: ',Outfile(1:L),BELL,
     &' _'
      CLOSE (UNIT=66,IOSTAT=N,ERR=820,STATUS='DELETE')
      CALL Wait(2.0)
      IF (Code.EQ.'R') GO TO 720
      Fname=' '
      Sstat='ACQUIRED'
      GO TO MENU
C
C     ---------------------------------------------------------------
C
C         Exit Program
C
C     ---------------------------------------------------------------
C
  900 IF (Sstat.EQ.'ACQUIRED') THEN
        WRITE (1,*) UP,ERASE,'  SPECTRUM NOT STORED:',
     &  '   Exit (Y or N) ? ',BELL,'_'
        READ (1,80) Code
        CALL Upper(Code)
        IF (Code.EQ.'N') GO TO 70
        IF (Code.NE.'Y') GO TO 900
      END IF
  910 WRITE (1,*) UP,ERASE,'  Set To STANDBY, (Y or N) ? ',BELL,'_'
      READ (1,80) Code
      CALL Upper(Code)
      IF (Code.EQ.'N') GO TO 920
      IF (Code.NE.'Y') GO TO 910
      CALL Send(Standby)
  920 WRITE (1,*) UP,ERASF,UP
      STOP
C
C     ---------------------------------------------------------------
C
C         IEEE-488 Error Exit
C
C     ---------------------------------------------------------------
C
  999 WRITE (1,*) ' Error #',N
      STOP
      END
```

```
C
C      ******************** END OF MAIN PROGRAM **********************
C
C          BLOCK DATA FOR NAMED COMMON BLOCK INITIALIZATION
C
C      *************************************************************
C
$ALIAS /MODE/,NOALLOCATE
$ALIAS /CARY/,NOALLOCATE
$ALIAS /IP/,NOALLOCATE
$ALIAS /IS/,NOALLOCATE
       BLOCK DATA Arrays
       INTEGER NDATA,XMODE,YMODE
       INTEGER NPAR(49),OFFSET(49)
       REAL ORD,ABSC,CELL,CYCLE,SAMPLE,WAVE,TIMER,TEMP,DIST
       CHARACTER Pname(49)*10,Vname(14)*8
       COMMON /MODE/NDATA,XMODE,YMODE
       COMMON /CARY/ORD,ABSC,CELL,CYCLE,SAMPLE,WAVE,TIMER,TEMP,DIST
       COMMON /IP/NPAR,OFFSET
       COMMON /IS/Pname,Vname
C
       DATA NDATA,XMODE,YMODE/0,0,0/
       DATA ORD,ABSC,CELL,CYCLE,SAMPLE,WAVE,TIMER,TEMP,DIST/0.0,0.0,0.0,
      &0.0,0.0,0.0,0.0,0.0,0.0/
C
       DATA NPAR/6,4,11,11,4,5,9,7,4,5,11,16,8,10,4,2,2,2,2,4,3,3,2,3,
      &3,3,2,6,2,4,2,5,5,2,2,0,0,5,0,2,0,0,0,0,0,0,0,0,0/
C
       DATA OFFSET/0,0,0,4,0,0,0,9,11,0,0,0,0,0,0,0,0,0,0,0,0,0,0,0,
      &0,0,0,0,2,6,8,0,0,0,0,0,0,0,0,0,0,0,0,0,0,0,0,0,0/
C
       DATA Pname/'Ordinate','Abscissa','Scan Rate','Chart/cm',
      &'Ref.Mode','Pen Functn','A range','%T Range','Temp.Range',
      &'Log Zero','Der.Range','Der.Temp','Kinet.Rnge','Temp.Zero',
      &'Period','Beam Chge','Sequencer','Auto.Op','Chart Op',
      &'Lamp Pwr','Lamp Sel','Det.Sel','Slit Hgt','BLN Det',
      &'BLN Lamp','BLN Ref','BLN Slit','No.cells','Sample',
      &'Curv.Fit','Rec.Prec','Method','Result','Auto Kin',
      &'Samp/Av.',' ',' ','BLN Stat',' ','Printer',' ',' ',
      &'TEST','TEST','TEST','TEST','TEST','TEST','TEST'/
C
       DATA Vname/'A zero','BL SBW/G','BL Wmax','BL Wmin',
      &'Cyc Time','Sel Gain','Ncycles','Nwlngths','Rec Time',
      &'Sel SBW','%T Zero','SEQ Wmax','SEQ Wmin','Distance'/
C
       END
```

```
C
C     ----------------------------------------------------------------
C
C             Select Mode of Operation for Specific Parameter
C
C     ----------------------------------------------------------------
C
$ALIAS /IP/,NOALLOCATE
$ALIAS /IS/,NOALLOCATE
      SUBROUTINE Select(N,PARAM,Pstr)
      INTEGER ASCII,I,J,K,N,NCOL
      INTEGER NPAR(49),OFFSET(49),PARAM(49),INDEX(11)
      CHARACTER Pname(49)*10,Pstr(49,16)*14,Vname(14)*8
      CHARACTER Command*44,CSM,Icode,Key*2,Pcode,Parset*2,TITLE*72
      CHARACTER BELL,CLR*2,ESC,ERASE*2,DOWN*2,HOME*2,UP*2
      COMMON /IP/NPAR,OFFSET,/IS/Pname,Vname
      DATA CSM,Key,Parset/'0','@D','@H'/
      DATA (INDEX(I),I=1,11)/1,3,4,6,7,9,10,12,13,15,16/
      BELL=CHAR(7)
      ESC=CHAR(27)
      CLR=ESC//'J'
      DOWN=ESC//'B'
      ERASE=ESC//'K'
      HOME=ESC//'h'
      UP=ESC//'A'
      NCOL=50
   10 WRITE (1,*) HOME,CLR
      TITLE='Operating Mode Selection'
      CALL Center(TITLE)
      CALL Line(NCOL)
      WRITE (1,'(T15,A5,T30,A10)') 'Index',Pname(N)
      CALL Line(NCOL)
      WRITE (1,*)
      DO 20 I=1,NPAR(N)
        J=I+OFFSET(N)
        IF ((N.EQ.4).AND.(J.EQ.5)) J=1          ! Chart Index Offset
        IF (N.EQ.11) THEN                       ! Derivative Modes
          J=INDEX(I)                            ! Use Valid Index
          IF ((PARAM(1).NE.0).AND.(I.LE.4)) GO TO 20
        END IF
        WRITE (1,30) I,': ........',Pstr(N,J)
   20 CONTINUE
   30 FORMAT (T16,I2,A10,T30,A14)
      WRITE (1,*)
      CALL Line(NCOL)
      WRITE (1,*)
   40 WRITE (1,'(T15,A2,A2,A9,A,A)') UP,ERASE,'Index #: ',BELL,'_'
      READ (1,'(I2)',ERR=40) K
      IF ((K.LT.1).OR.(K.GT.NPAR(N))) GO TO 40   ! Invalid Index Entry
      IF (PARAM(1).NE.0) THEN
        IF ((K.EQ.5).AND.(N.EQ.6)) GO TO 40     ! Only Log(Abs) Valid
        IF ((K.LE.4).AND.(N.EQ.11)) GO TO 40    ! Invalid Deriv Index
      END IF
      IF ((N.EQ.38).AND.(K.GT.2)) GO TO 60      ! Baseline Setup Mode
```

```
      IF (N.EQ.11) K-INDEX(K)                        ! Index To Deriv Mode
   50 ASCII-(K-1)+OFFSET(N)+48
      IF ((N.EQ.4).AND.(K.EQ.1)) ASCII-ASCII-4       ! Chart Index Offset
      Icode-CHAR(ASCII)
      ASCII-(N-1)+48
      Pcode-CHAR(ASCII)
      Command-Parset//Pcode//Icode//CSM
      CALL Send(Command)
      IF ((N.EQ.6).AND.(K.GT.2)) THEN                ! Special Pen Modes
        N-11                                         ! Derivative Modes
        IF (K.EQ.5) N-10                             ! Log(Abs) Mode
        GO TO 10                                     ! Select Setting
      END IF
      N-K
      RETURN
   60 IF (K.EQ.4) GO TO 40
      Pcode-CHAR(48+N-1)
      Command-Parset//Pcode//'0'//CSM            ! Set Status To OFF
      CALL Send(Command)
      Command-Key//'10'                          ! Key - 1
      CALL Send(Command)
      Command-Key//'-0'                          ! Key - ENTER
      CALL Send(Command)
      Command-Key//'h0'                          ! Key - RIGHT CURSOR
      IF (K.EQ.3) GO TO 70
      CALL Send(Command)
   70 CALL Send(Command)
      CALL Send(Command)
      Command-Key//'-0'                          ! Key - ENTER
      CALL Send(Command)
      N-K
      IF (K.EQ.5) N-2
      RETURN
      END
```

```
C
C     -----------------------------------------------------------------
C
C           Baseline Scan Control
C
C     -----------------------------------------------------------------
C
      SUBROUTINE Bline(WMIN,WMAX,Bdet,Bgain,Blamp,Bperiod,Brate,Bref,
     &Bsbw,Bslit,Bscan,Btime,MATCH,MODE)
      INTEGER INDEX,MODE,N,NCOL
      REAL NUMBER,WMIN,WMAX
      LOGICAL MATCH,MONITOR
      CHARACTER*(*) Bdet,Bgain,Blamp,Bperiod,Brate,Bref
      CHARACTER*(*) Bsbw,Bslit,Bscan,Btime
      CHARACTER Bgbw*4,BELL,Code,CLR*2,DOWN*2,ERASE*2,Esc,HOME*2,UP*2
      CHARACTER Bmin*6,Bmax*6,Command*44,Response*64,String*14
      CHARACTER Autobal*4,Blstat*5,Start*4,TITLE*72
      DATA Autobal,Blstat,Start/'@DU0','@C1U0','@DP0'/
      Esc=CHAR(27)
      BELL=CHAR(7)
      CLR=Esc//'J'
      DOWN=Esc//'B'
      ERASE=Esc//'K'
      HOME=Esc//'h'
      UP=Esc//'A'
      MONITOR=.FALSE.                     ! For Testing Routine ONLY
      NCOL=70
      IF (WMAX.GT.800.0) WMAX=WMAX+0.2    ! * Cary Baseline Bug Fix *
      CALL Str(WMAX,String,5)
      Bmax=String(2:7)
      IF (WMIN.GT.800.0) WMIN=WMIN-0.2    ! * Cary Baseline Bug Fix *
      CALL Str(WMIN,String,5)
      Bmin=String(2:7)
      Bgbw=Bsbw                           ! Only One Of SBW Or GAIN Is
      IF (MODE.EQ.2) Bgbw=Bgain           ! Stored By Cary For Baseline
C     -----------------------------------------------------------------
      WRITE (1,*) HOME,CLR
      TITLE='Baseline Scan Control'
      CALL Center(TITLE)
      CALL Line(NCOL)
      WRITE (1,10) DOWN,'  Wavelength Limits, (nm): ',WMAX,' / ',WMIN
   10 FORMAT (T2,A2,A27,F4.1,A3,F4.1)
      WRITE (1,*) DOWN,'  Scan Rate, (nm/sec)     : ',Bscan
      WRITE (1,*) DOWN,'  Response Time, (sec)    : ',Btime
      IF (MODE.EQ.1) THEN
        WRITE (1,*) DOWN,'  Spectral Bandwidth,(nm): ',Bsbw
        GO TO 20
      END IF
      WRITE (1,*) DOWN,'  AUTOSLIT Gain Level     : ',Bgain
   20 WRITE (1,*) DOWN
      WRITE (1,*) DOWN,'  Place Solvent Cells In BOTH Beams:'
      WRITE (1,*) DOWN,'        S.....Start Scan'
      WRITE (1,*) DOWN,'        A.....Abort Scan'
      WRITE (1,*) DOWN,'  Enter the CODE: ',BELL,'_'
```

```
   30 READ (1,'(A1)') Code
      CALL Upper(Code)
      IF (Code.EQ.'A') THEN
        MATCH=.FALSE.
        RETURN
      END IF
      IF (Code.NE.'S') GO TO 30
      WRITE (1,*) UP,ERASE,UP,UP,ERASE,UP,UP,ERASE,UP,UP,ERASE,'_'
      WRITE (1,*) ' Sending Baseline Parameters: ',BELL
      Command='@J'//Bmax//'!'//Bmin//'!'//Bgbw//'!'//Bref//'!'//
     &Blamp//'!'//Bdet//'!'//Bslit//'!'//Brate//'!'//Bperiod//'!0'
      WRITE (UNIT=38,FMT=*,IOSTAT=N,ERR=999) Command
      READ (UNIT=38,FMT=40,IOSTAT=N,ERR=999) Response
   40 FORMAT (A64)
      IF (Response(2:2).EQ.'N') THEN
        INDEX=ICHAR(Response(4:4))-48
        WRITE (1,*) UP,ERASE,'  Parameter Error: ',INDEX,BELL
        CALL Wait(2.0)
        MATCH=.FALSE.
        RETURN
      END IF
      WRITE (1,*) UP,ERASE,'  Recording Baseline:',BELL
      CALL Send(Start)
   50 Command=Blstat
      IF (MONITOR) WRITE (1,*) ' Command - ',Command
      WRITE (UNIT=38,FMT=*,IOSTAT=N,ERR=999) Command
      READ (UNIT=38,FMT=40,IOSTAT=N,ERR=999) Response
      IF (MONITOR) WRITE (1,*) ' Response - ',Response
      INDEX=ICHAR(Response(6:6))-48
      IF (INDEX.NE.1) GO TO 50
      WRITE (1,*) UP,ERASE,'  Performing Auto Balance:',BELL
      CALL Send(Autobal)
      CALL Wait(2.0)
      RETURN
  999 WRITE (1,*) ' Error #',N,' in SUBROUTINE Bline'
      STOP
      END
```

```
C
C     ------------------------------------------------------------------
C
C         Go To Specified Wavelength
C
C     ------------------------------------------------------------------
C
      SUBROUTINE GOTO(Wlength)
      INTEGER LENSTR
      CHARACTER Ascii,CSM,Slew,Model,Ncell,Range,Windex
      CHARACTER Command*4,Key*2
      CHARACTER*(*) Wlength
      CSM-'C'
      Key-'@D'
      Command-Key//'J'//CSM            ! Key - GOTO WAVELENGTH
      CALL Send(Command)
      LENSTR-LEN(Wlength)
      DO 10 I-1,LENSTR
        Ascii-Wlength(I:I)
        IF (Ascii.EQ.' ') GO TO 10
        IF (Ascii.EQ.'.') Ascii-':'
        Command-Key//Ascii//CSM        ! Key - NUMBER (0-9)
        CALL Send(Command)
   10 CONTINUE
      Command-Key//'-'//CSM            ! Key - ENTER
      CALL Send(Command)
   20 CALL Instats(Slew,Model,Ncell,Range,Windex)
      IF (Slew.NE.'0') GO TO 20
      RETURN
      END
C
C     ------------------------------------------------------------------
C
C         Instrument Status Test
C
C     ------------------------------------------------------------------
C
      SUBROUTINE Instats(Slew,Model,Ncell,Range,Windex)
      INTEGER N
      CHARACTER Slew,Model,Ncell,Range,Windex
      CHARACTER Stats*3,Data*12
      Stats-'@B0'
   10 WRITE (UNIT-38,FMT-*,IOSTAT-N,ERR-999) Stats
      READ (UNIT-38,FMT-20,IOSTAT-N,ERR-999) Data
   20 FORMAT (A12)
      Slew-Data(4:4)
      Model-Data(5:5)
      Ncell-Data(6:6)
      Range-Data(7:7)
      Windex-Data(8:8)
      RETURN
  999 WRITE (1,*) ' Error #',N,' in SUBROUTINE Instats'
      STOP
      END
```

```
C
C     ----------------------------------------------------------------
C
C             Read Parameter Table From CARY 2390
C
C     ----------------------------------------------------------------
C
      SUBROUTINE Partable(PARAM)
      INTEGER LENSTR,N,INDEX,PARAM(49)
      LOGICAL TEST
      CHARACTER Command*3,Response*64,Ascii
      TEST=.FALSE.
      Command='@E0'
      WRITE (UNIT=38,FMT=*,IOSTAT=N,ERR=999) Command
      READ (UNIT=38,FMT=10,IOSTAT=N,ERR=999) Response
   10 FORMAT (A64)
      IF (TEST) WRITE (1,*) ' RESPONSE = ',Response
      Ascii=Response(4:4)
      LENSTR=ICHAR(Ascii)-48
      IF (TEST) WRITE (1,*) ' String Length   =',LENSTR
      DO 20 I=1,LENSTR
        J=I+4
        Ascii=Response(J:J)
        IF (TEST) WRITE (1,*) ' ASCII Character = ',Ascii
        INDEX=ICHAR(Ascii)-48
        PARAM(I)=INDEX
        IF (TEST) WRITE (1,*) ' Parameter Index =',PARAM(I)
   20 CONTINUE
      RETURN
  999 WRITE (1,*) ' Error #',N,' in SUBROUTINE Partable'
      STOP
      END
C
C     ----------------------------------------------------------------
C
C             Read Variable Table From CARY 2390
C
C     ----------------------------------------------------------------
C
      SUBROUTINE Vartable(VARIABLE)
      INTEGER LENSTR(14),N
      REAL NUMBER,VARIABLE(14)
      LOGICAL TEST
      CHARACTER Ascii,CSM,Command*5,Response*64,String*14,Varout*3
      DATA (LENSTR(I),I=1,14)/14,11,11,11,10,10,8,8,8,11,11,11,11,11/
      TEST=.FALSE.
      CSM='0'
      Varout='@G2'
      DO 10 I=1,14
        J=I-1
        Ascii=CHAR(J+48)
        Command=Varout//Ascii//CSM
        IF (TEST) WRITE (1,*) ' Command  = ',Command
        WRITE (UNIT=38,FMT=*,IOSTAT=N,ERR=999) Command
```

```
        READ (UNIT-38,FMT-20,IOSTAT-N,ERR-999) Response
          IF (TEST) WRITE (1,*) ' Response - ',Response
          String-Response(6:6+LENSTR(I))
          IF (TEST) WRITE (1,*) ' String - ',String
          CALL Val(String,NUMBER)
          VARIABLE(I)-NUMBER
          IF (TEST) WRITE (1,*) ' VALUE  -',VARIABLE(I)
   10 CONTINUE
   20 FORMAT (A64)
      RETURN
  999 WRITE (1,*) ' Error #',N,' in SUBROUTINE Vartable'
      STOP
      END
C
C     ----------------------------------------------------------------
C
C         Print a TITLE Centered in 72 columns
C
C     ----------------------------------------------------------------
C
      SUBROUTINE Center(TITLE)
      INTEGER I,J,N
      CHARACTER TITLE*72,BLANK*36
      BLANK-'
      I-72
      J-0
      DO WHILE (ICHAR(TITLE(I:I)).EQ.32)
        J-J+1
        I-72-J
      END DO
      N-J/2
      WRITE (1,*) BLANK(1:N),TITLE(1:I)
      RETURN
      END
C
C     ----------------------------------------------------------------
C
C         Print a line of N '-' characters (72 columns max)
C
C     ----------------------------------------------------------------
C
      SUBROUTINE Line(N)
      INTEGER I,N
      CHARACTER BLANK*72,DLINE*72,SPACE*36
      SPACE-'                                    '
      BLANK-SPACE//SPACE
      SPACE-'------------------------------------'
      DLINE-SPACE//SPACE
      IF (N.GT.72) N-72
      I-(72-N)/2
      WRITE (1,*) BLANK(1:I),DLINE(1:N)
      RETURN
      END
```

```
C
C      ------------------------------------------------------------------
C
C          Enter and Validate Wavelength Limits
C
C      ------------------------------------------------------------------
C
      SUBROUTINE Limits(MIN,MAX)
      REAL MIN,MAX,SWAP
      CHARACTER BELL,ERASE*2,ESC,UP*2
      BELL=CHAR(7)
      ESC=CHAR(27)
      ERASE=ESC//'K'
      UP=ESC//'A'
   10 WRITE (1,*) UP,ERASE,'_'
      WRITE (1,*) ' Wavelength Limits: (Min,Max) ',ERASE,BELL,'_'
      READ (1,*,ERR=10) MIN,MAX
      MIN=ABS(MIN)
      MAX=ABS(MAX)
      IF (MIN.LT.MAX) GO TO 20
      SWAP=MIN
      MIN=MAX
      MAX=SWAP
   20 MIN=INT(MIN+.5)
      MAX=INT(MAX+.5)
      IF (MIN.LT.185) GO TO 10
      IF (MAX.GT.3152) GO TO 10
      RETURN
      END
C
C      ------------------------------------------------------------------
C
C          Convert String Entry To Uppercase If Required
C
C      ------------------------------------------------------------------
C
      SUBROUTINE Upper(Code)
      INTEGER LENSTR,N
      CHARACTER*(*) Code
      LENSTR=LEN(Code)
      DO 10 I=1,LENSTR
        N=ICHAR(Code(I:I))
        IF (N.GT.96) Code(I:I)=CHAR(N-32)
   10 CONTINUE
      RETURN
      END
```

```
C
C     -------------------------------------------------------------------
C
C           Read Data In Real Time (INTERVAL) Mode From CARY 2390
C
C     -------------------------------------------------------------------
C
$EMA/DATA/
      SUBROUTINE Acquire(Inc,PRINT,SINGLE,WAVELENGTH)
      INTEGER N,NCOL,NDATA,XMODE,YMODE,XOFF(4),YOFF(6)
      REAL ORD,ABSC,CELL,CYCLE,SAMPLE,WAVE,TIMER,TEMP,DIST
      REAL X(10001),Y(10001),WAVELENGTH
      CHARACTER Command*10,Data*64,Inc*4,Esc,DOWN*2,ERASE*2,UP*2
      CHARACTER S1*8,S2*8,S3,S4,S5*3,S6*8,S7*6,S8*6,S9*7
      LOGICAL CHECK,PRINT,SINGLE,TEST
      COMMON /MODE/NDATA,XMODE,YMODE
      COMMON /CARY/ORD,ABSC,CELL,CYCLE,SAMPLE,WAVE,TIMER,TEMP,DIST
      COMMON /DATA/Y,X
      DATA (XOFF(I),I-1,4)/7,5,5,6/
      DATA (YOFF(I),I-1,6)/7,6,5,6,11,6/
      Esc-CHAR(27)
      UP-Esc//'A'
      DOWN-Esc//'B'
      ERASE-Esc//'K'
      CHECK-.FALSE.                ! Only Used For Testing Routine
      TEST-.FALSE.                 ! Only Used For Testing Routine
      J-2+YOFF(YMODE)              ! The First Two Fields In Data String
      K-J+2                        ! Vary In Length With Choice Of Abscissa
      L-K+XOFF(XMODE)              ! And Ordinate - XMODE & YMODE Select
      M-L+2                        ! The Correct Offsets From XOFF/YOFF
      NCOL-70
      IF (.NOT.PRINT) GO TO 20
      CALL Line(NCOL)
      WRITE (1,10) 'Ordinate','Abscissa','Cell','Cycle','Sample',
     &'Wlength','Time','Temp,C','Dist'
   10 FORMAT (A10,A10,A5,A6,A7,A10,A8,A8,A8)
      CALL Line(NCOL)
      WRITE (1,*) DOWN
   20 Command-'@K11'//Inc//'!0'
      IF (TEST) WRITE (1,*) ' Command  - ',Command
      WRITE (UNIT-38,FMT-*,IOSTAT-N,ERR-999) Command
      IF (SINGLE) THEN
        READ (UNIT-38,FMT-30,IOSTAT-N,ERR-999) Data
        S6-Data(M+9:M+16)
        CALL Val(S6,WAVELENGTH)
        RETURN
      END IF
   30 FORMAT (A64)
      DO 100 I-1,NDATA
        READ (UNIT-38,FMT-30,IOSTAT-N,ERR-999) Data
C       IF (CHECK) WRITE (1,30) Data
        S1-Data(2:J)               ! Ordinate - Variable Length Field
        S2-Data(K:L)               ! Abscissa - Variable Length Field
        S3-Data(M:M)               ! Remaining Fields Are Fixed Length
```

```
         S4=Data(M+2:M+3)
         S5=Data(M+5:M+7)
         S6=Data(M+9:M+16)
         S7=Data(M+18:M+23)
         S8=Data(M+25:M+30)
         S9=Data(M+32:M+38)
C        IF (CHECK) WRITE (1,*) S1,S2,S3,S4,S5,S6,S7,S8,S9
         CALL Val(S1,ORD)
         CALL Val(S2,ABSC)
         CALL Val(S3,CELL)
         CALL Val(S4,CYCLE)
         CALL Val(S5,SAMPLE)
         CALL Val(S6,WAVE)
         CALL Val(S7,TIMER)
         CALL Val(S8,TEMP)
         CALL Val(S9,DIST)
         Y(I)=ORD                  ! Ordinate And Abscissa Stored In Arrays
         X(I)=ABSC                 ! /CARY/ Variables Return Final Reading
       IF (.NOT.PRINT) GO TO 100
       WRITE (1,*) UP,ERASE,UP
       WRITE (1,40) ORD,ABSC,CELL,CYCLE,SAMPLE,WAVE,TIMER,TEMP,DIST
    40 FORMAT (F10.4,F10.2,F5.1,F6.1,F7.1,F10.2,F8.1,F8.2,F8.2)
   100 CONTINUE
       RETURN
   999 WRITE (1,*) 'Error #',N,' in SUBROUTINE Acquire'
       RETURN
       END
```

```
C
C     -----------------------------------------------------------------
C
C            Convert ASCII String To Numeric Value (10 Digits Max'm)
C
C     -----------------------------------------------------------------
C
      SUBROUTINE Val(String,VALUE)
      INTEGER DECPT,EXPON,LENSTR,N,NUM(10)
      REAL VALUE
      DOUBLE PRECISION MULT,SIGN,TEN,DECIMAL
      CHARACTER Ascii
      CHARACTER*(*) String
      LOGICAL INTEGER,TEST
      INTEGER-.TRUE.
      TEST-.FALSE.              ! Only Used For Testing The Routine
      J-1
      K-0
      DECPT-0
      SIGN-1.0
      TEN-10.0
      DECIMAL-0.0
      LENSTR-LEN(String)
      IF (TEST) WRITE (1,*) ' String Number - ',String
      IF (TEST) WRITE (1,*) ' String Length -',LENSTR
      DO 100 I-1,LENSTR
        Ascii-String(I:I)
        N-ICHAR(Ascii)
        IF ((N.GE.48).AND.(N.LE.57)) GO TO 20
        IF (N.EQ.46) INTEGER-.FALSE.
        IF (N.EQ.46) DECPT-K
        IF (N.EQ.45) SIGN--1.0
        GO TO 100
   20 NUM(J)-N-48
      K-J
      J-J+1
  100 CONTINUE
      IF ((DECPT.EQ.0).AND.(INTEGER)) DECPT-K
      DO 200 J-1,K
        EXPON-DECPT-J
        MULT-TEN**EXPON
        DECIMAL-DECIMAL+NUM(J)*MULT
  200 CONTINUE
      VALUE-SIGN*DECIMAL
      IF (TEST) WRITE (1,*) ' Value -',VALUE
      RETURN
      END
```

```
C
C     ------------------------------------------------------------
C
C         Convert Number To ASCII String
C
C     ------------------------------------------------------------
C
      SUBROUTINE Str(VALUE,String,PREC)
      INTEGER ASCII,DECPT,I,J,LENSTR,NDIGIT,NUMBER,PREC
      REAL VALUE
      DOUBLE PRECISION DECIMAL,FRACTION,TEN
      CHARACTER Concat*14,Digit(12),Sign,String*14
      LOGICAL INTEGER,TEST
      INTEGER=.TRUE.
      TEST=.FALSE.              ! Only Used For Testing The Routine
      DECPT=0
      J=0
      TEN=10.0
      Sign=' '
      Concat=' '
      IF (TEST) WRITE (1,*) ' Value Entered = ',VALUE
      IF (VALUE.LT.0.0) Sign='-'
      IF (VALUE.EQ.0.0) GO TO 100
      DECIMAL=ABS(VALUE)
      DO WHILE (DECIMAL.GE.1.0)
        DECIMAL=DECIMAL/TEN
        J=J+1
      END DO
      DECPT=J
      IF (TEST) WRITE (1,*) ' # of Whole Digits: ',DECPT
      IF (DECPT.EQ.0) GO TO 30
      DO 20 J=1,DECPT
        DECIMAL=DECIMAL*TEN
        NUMBER=INT(DECIMAL)
        ASCII=NUMBER+48
        Digit(J)=CHAR(ASCII)
        FRACTION=DECIMAL-NUMBER
        DECIMAL=DINT(FRACTION*TEN**(PREC-J)+.5)/TEN**(PREC-J)
   20 CONTINUE
      IF (.NOT.TEST) GO TO 30
      WRITE (1,*) ' The Whole Digits = ',(Digit(I), I=1,DECPT)
   30 J=DECPT
      IF (TEST) WRITE (1,*) ' Decimal Fraction = ',DECIMAL
      IF (DECIMAL.NE.0.0) INTEGER=.FALSE.
      IF (DECPT.GE.12) GO TO 40
      DO WHILE (DECIMAL.NE.0.0)
        J=J+1
        DECIMAL=DECIMAL*TEN
        NUMBER=INT(DECIMAL)
        ASCII=NUMBER+48
        Digit(J)=CHAR(ASCII)
        FRACTION=DECIMAL-NUMBER
        DECIMAL=DINT(FRACTION*TEN**(PREC-J)+.5)/TEN**(PREC-J)
```

```
          IF (DECIMAL.EQ.1.0) THEN
            DIGIT(J)=CHAR(ASCII+1)
            DECIMAL=0.0
          END IF
          IF (J.GE.12) DECIMAL=0.0
        END DO
   40   NDIGIT=J
        IF (.NOT.TEST) GO TO 50
        WRITE (1,*) ' The Characters  = ',(Digit(I), I=1,NDIGIT)
   50   IF (NDIGIT.GT.12) GO TO 200
        DO 60 I=1,NDIGIT
          Concat(I:I)=Digit(I)
   60   CONTINUE
        IF (INTEGER) GO TO 80
        IF (DECPT.EQ.0) GO TO 70
        String=Sign//Concat(1:DECPT)//'.'//Concat(DECPT+1:14)
        RETURN
   70   String=Sign//'.'//Concat
        RETURN
   80   String=Sign//Concat
        RETURN
  100   String=' 0.0'
        RETURN
  200   WRITE (1,*) ' Error in data: (too many digits)'
        STOP
        END
```

```
C
C     ------------------------------------------------------------
C
C         Send a Command String To CARY 2390
C
C     ------------------------------------------------------------
C
      SUBROUTINE Send(Command)
      INTEGER N
      CHARACTER*(*) Command
      CHARACTER Response*64
      LOGICAL TEST
      TEST=.FALSE.            ! Only Used For Testing The Routine
      IF (TEST) WRITE (1,*) ' Command  = ',Command
      WRITE(UNIT=38,FMT=*,IOSTAT=N,ERR=999) Command
      READ (UNIT=38,FMT=10,IOSTAT=N,ERR=999) Response
   10 FORMAT (A64)
      IF (TEST) WRITE (1,*) ' Response = ',Response
      RETURN
  999 WRITE (1,*) 'Error #',N,' in SUBROUTINE Send'
      RETURN
      END
C
C     ------------------------------------------------------------
C
C         TERMINATE Real Time Transmission from CARY 2390
C
C     ------------------------------------------------------------
C
C     Send UNTALK/UNLISTEN = '_?' to IEEE-488 Bus
C
      SUBROUTINE Terminate
C     CALL CMDW(35,'_?',0)   ! CMDW occasionally fails to UNADDRESS
      CALL ABRT(35,3)        ! The ABRT command sends '_?' reliably
      RETURN
      END
C
C     ------------------------------------------------------------
C
C         Wait Specified Delay (sec)
C
C     ------------------------------------------------------------
C
      SUBROUTINE Wait(DELAY)
      REAL DELAY,PERIOD,Tzero,Time
      PERIOD=0.0
      Tzero=Time(I)
      DO WHILE (PERIOD.LT.DELAY)
        PERIOD=Time(I)-Tzero
      END DO
      RETURN
      END
```

```
C
C      ---------------------------------------------------------------
C
C         Read Time (sec) from the HP 1000's RTE-6 Operating System
C
C         Note: I is a dummy argument, no values are passed
C
C      ---------------------------------------------------------------
C
       REAL FUNCTION Time(I)
       INTEGER ICODE,ITIME(5)
       ICODE=11
       CALL EXEC(ICODE,ITIME)
       Time=FLOAT(ITIME(1))/100.0+FLOAT(ITIME(2))+FLOAT(ITIME(3))*60.0
      &+FLOAT(ITIME(4))*3600.0
       RETURN
       END
```